NASA Conference Publication 10122

Fifth Annual Thermal and Fluids Analysis Workshop

Proceedings of a workshop
held at the Ohio Aerospace Institute
Brook Park, Ohio
August 16–20, 1993

NASA

NASA Conference Publication 10122

Fifth Annual Thermal and Fluids Analysis Workshop

Proceedings of a workshop
held at the Ohio Aerospace Institute, Brook Park, Ohio
cosponsored by NASA Lewis Research Center
and the Ohio Aerospace Institute
August 16–20, 1993

NASA
National Aeronautics and
Space Administration

Office of Management

Scientific and Technical
Information Program

1993

PREFACE

The Fifth Annual Thermal and Fluids Analysis Workshop was held at the Ohio Aerospace Institute, Brook Park, Ohio, cosponsored by NASA Lewis Research Center and the Ohio Aerospace Institute, August 16–20, 1993. The workshop consisted of classes, vendor demonstrations, and paper sessions. The classes and vendor demonstrations provided participants with the information of widely used tools for thermal and fluids analysis. The paper sessions provided a forum for the exchange of information and ideas among thermal and fluids analysts. Paper topics included advances and uses of established thermal and fluids computer codes (such as SINDA and TRASYS) as well as unique modeling techniques and applications.

CONTENTS

Session
One

Thermal Control

ADVANCED X-RAY ASTROPHYSICS FACILITY - IMAGING (AXAF-I) THERMAL ANALYSES USING INTEGRATED THERMAL ANALYSIS SYSTEM (ITAS) PROGRAM

By

Benny Ghaffarian
Sverdrup Technology Inc.
Huntsville, Alabama

and

Ramona Cummings
NASA/MSFC
Huntsville, Alabama

ABSTRACT

The complex geometry and stringent thermal requirements associated with the Advanced X-ray Astrophysics Facility - Imaging (AXAF-I) necessitate a detailed and accurate thermal analysis of the proposed system. A brief description of said geometry and thermal requirements is included in this paper. Among the tools considered for the aforementioned analysis is a PC-compatible version of the Integrated Thermal Analysis System (ITAS). Several bench-mark studies were performed to evaluate the capabilities of ITAS and to compare the corresponding results with those obtained using TRASYS and SINDA. Comparative studies were conducted for a typical Space Station module. Four models were developed using various combinations of the available software packages (i.e. ITAS, SINDA and TRASYS). Orbital heating and heat transfer calculations were performed to determine the temperature distributions along the surfaces of this module. A comparison of the temperature distributions obtained for each of the four cases is presented in this paper. Results of this investigation were used to verify the different ITAS modules including those used for model generation, steady state and transient orbital heating analyses, radiative and convective heat flow analyses, and SINDA/TRASYS model translation. The results suggest that ITAS is well suited to subsequent analyses of the AXAF-I.

INTRODUCTION

The Advanced X-ray Astrophysics Facility (AXAF-I), shown in Figure 1, is a proposed space observatory, designed to address several fundamental questions in astrophysics through celestial observations. The importance of AXAF-I stems from its selective sensitivity to x-rays. Recognizing that x-rays are emitted as a result of fundamental processes affecting the formation, destruction, and behavior of stellar objects, AXAF-I is expected to enhance man's understanding of the history of the universe.

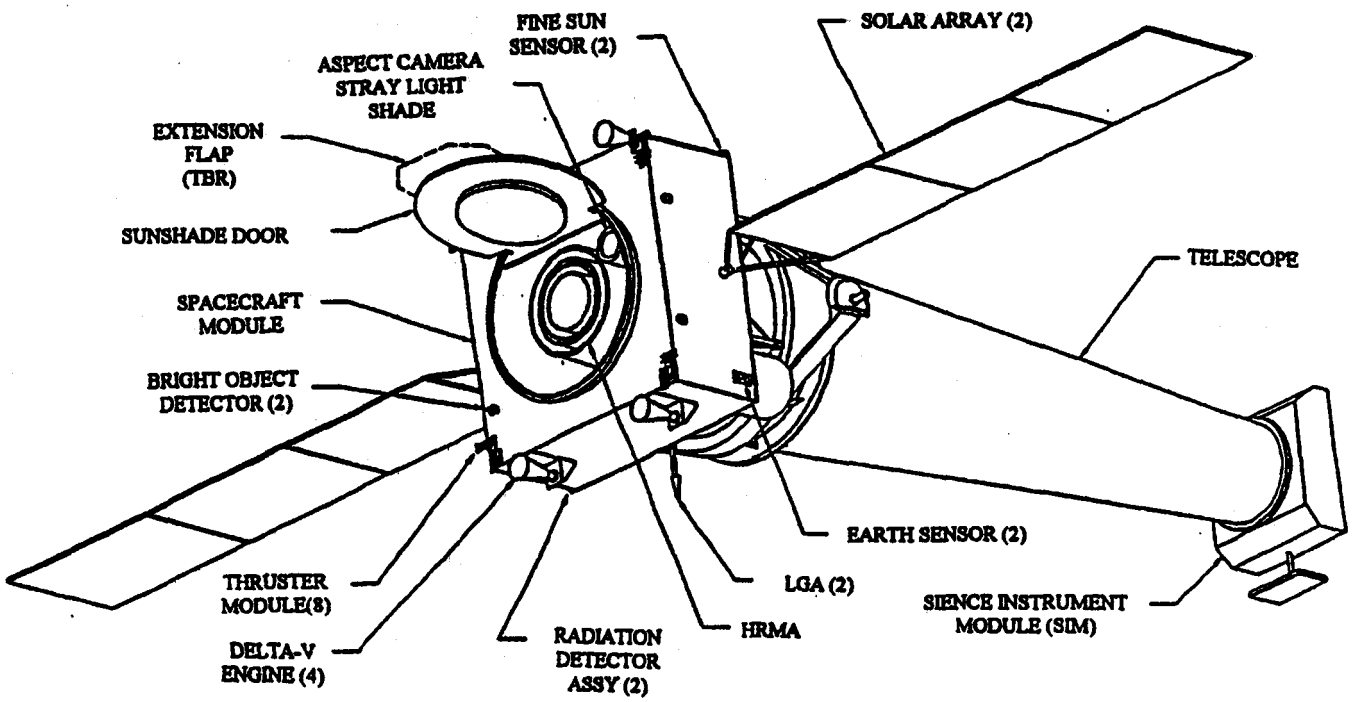

Figure 1: AXAF-I Flight Configuration

AXAF-I is the successor to the Einstein X-ray Observatory, flown between 1978 and 1981. Like the Einstein, AXAF-I will employ special mirrors, capable of projecting high-quality images of stellar objects. This new facility, however, will exceed the capabilities of the short-lived Einstein; AXAF-I will provide 10 times the resolution and 100 times the imaging sensitivity of Einstein. With a life expectancy exceeding 5 years, AXAF-I is scheduled for launch in 1998. The craft will follow an elliptical Earth orbit with minor and major axes of 10000 km and 100000 km, respectively. A 28.5° angle of inclination will be maintained. Under the direction of NASA's Marshall Space Flight Center, the flight system is being developed by a broad-based industry team including TRW Inc. Eastman Kodak, Ball Aerospace, Perkin-Elmer Corporation, The Smithsonian Astrophysical Observatory, MIT, and Martin Marietta Aerospace.

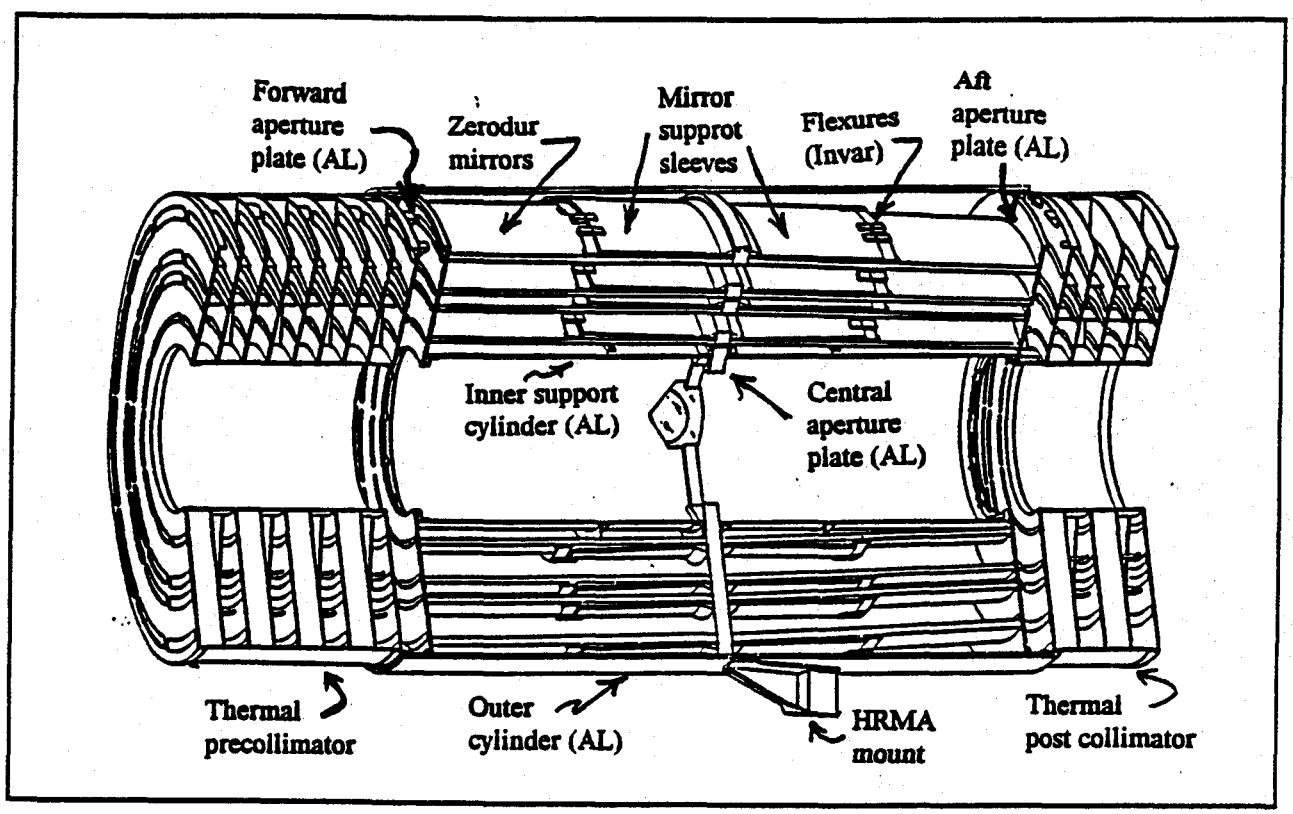

Figure 2: HRMA configuration must meet performance requirement with minimum thermal sensitivity and assembly/alignment risk

AXAF DESIGN AND SYSTEM REQUIREMENTS

The High Resolution Mirror Assembly (HRMA) comprises x-ray imaging mirrors of a special type known as "Wolter, type-1, grazing incidence mirrors." Simply stated, X-rays approaching the mirrors with an angle of incidence between a few degrees and the normal are absorbed (i.e. transmitted) by the mirrors. For angles of less than a few degrees, "soft" x-rays of a few angstroms in wavelength are reflected and imaged using specialized optics. These mirrors are thin-walled cylinders

constructed of Zerodur material. The primary mirrors are parabolic whereas the secondary mirrors are hyperbolic. Because the grazing angle of incidence is low, the collection area of Wolter-type optics is necessarily small. The effective collecting area is increased by nesting concentric sets of mirrors. The AXAF-I HRMA uses four sets of grazing incidence optics, radially and axially parafocalized to a 10 m focal length. The largest parabolic mirror has an inner diameter of 1.2 m; the smallest is 0.68 m. Each mirror is 83.8 cm in length. To satisfy the encircled energy requirement, the polished mirrors must be mounted in a strain-free configuration and assembled to small alignment tolerances. These tolerances must, of course, be maintained during ascent and in the orbital environment. A central aperture plate is the primary structural element in the HRMA; this plate is fabricated using a high-strength aluminum alloy, so chosen because it's high thermal conductivity minimizes temperature gradients which can misalign the mirrors. The forward and aft aperture plates are equipped with ghost image control baffles and multi-zone heater tapes which maintain the assembly at a temperature of 20C. Pre- and post-collimators narrow the view factors (i.e. to cold space and to the 10 C telescope) and minimize heat losses and axial temperature gradients. Heater tapes located on the quarter-point flanges and circumferential MLI blankets minimize diametrical thermal gradients (the HRMA isothermal spatial temperature variation must be maintained to within 2.5 F of the orbital thermistor control set point). The axial, diametrical, and radial temperature gradients must also be maintained to within 1.5 F, 0.5 F, and 1.0 F, respectively.

AXAF-I has provisions for two focal plane Science Instruments (SI's); these include a High Resolution Camera (HRC) and an AXAF CCD (Charge Coupled Device) Imaging Spectrometer (ACIS). The HRMA remains stationary and the SIM will have the capability to move and position the appropriate SI at the focal plane of the HRMA.

In order to make on-orbit observations with the precision required to meet the established scientific objectives, ground calibration of the HRMA in conjunction with the SI's, must be performed. Calibration will take place in the X-ray Calibration Facility (XRCF), at the Marshall Space Flight Center .

OBJECTIVE OF STUDY

A complex geometry, coupled with the need to maintain a strictly defined thermal environment, justify the need for a detailed thermal model of the AXAF-I. Furthermore, the HRMA and other specularly reflective surfaces require an analysis tool that may be used to determine specular (ray tracing/Monte Carlo) view factors/Script-F components of radiation conductors. Among the tools considered for this analysis is an interactive, menu driven, PC-based thermal analysis package known as PC-ITAS. Complex models can be quickly generated using a comprehensive set of integrated surface geometry generation primitives. Figure 3 shows an ITAS-generated representation of the AXAF-I. While the preliminary evaluations of ITAS were particularly encouraging, further studies were needed to determine whether this software is suitable for the task at hand. Therefore, a series of bench-mark studies was performed using a geometry for which the results are accepted and documented. In this case, a Space Station module was considered. Results obtained using TRASYS and SINDA were compared with those obtained from ITAS.

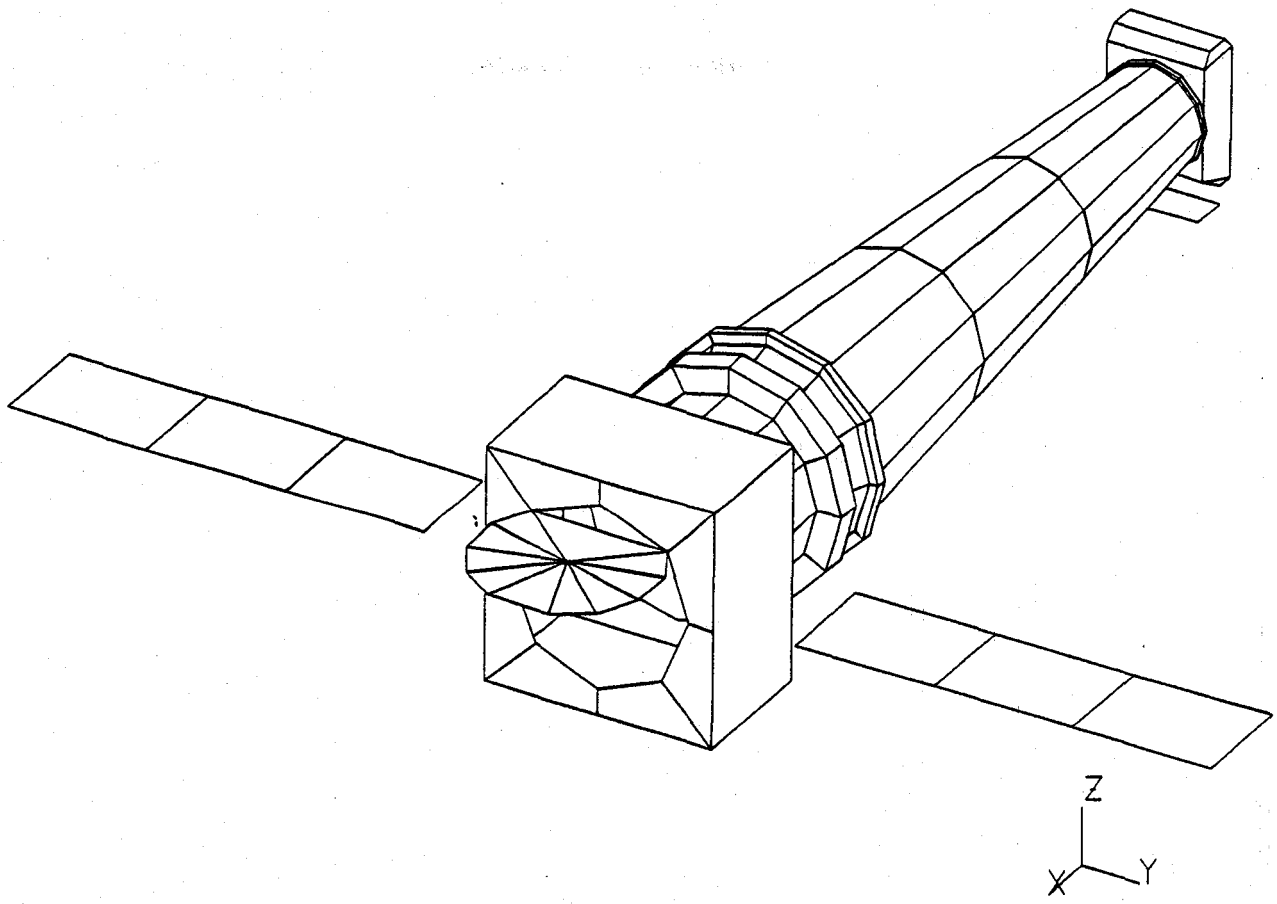

Figure 3: ITAS generated AXAF-I exterior model

METHOD OF EVALUATION

As stated in the previous section, a study was conducted to evaluate PC-ITAS and to compare the performance of this package with that of TRASYS and SINDA. The test case chosen for this evaluation involved a Space Station module in a 250-n.mi., circular earth orbit. A beta-angle of 38°, with respect to the Sun, was assumed for this orbit. Values used for the absorptivity and emissivity of the MLI-covered exterior surfaces of the module were 0.30 and 0.40, respectively. The 0.156-inch-thick Aluminum skin which separates the inner layer of insulation from the interior of the spacecraft was included in the model. An effective emissivity of 0.02 was assumed between interior and exterior surfaces of the spacecraft. Finally, interior surfaces were assumed to exchange heat, via convection, at a rate of 0.20 Btu/sq.ft.hr. to an environment at 70 F. Radiation heat transfer was considered between interior walls of the module, for which the emissivity was assigned a constant value of 0.90. Figure 4 shows a schematic of the model that was generated using ITAS.

Four sets of analyses were conducted. In the first case, ITAS was used (exclusively) to generate a model of the module and to perform orbital heating and subsequent heat flow calculations;

results of these calculations were then used to predict interior and exterior surface temperatures. In the second and third cases, ITAS translators were used to generate SINDA and TRASYS input decks (i.e. using the very same model developed for case one). For the second case, SINDA was run without modifying the respective input deck. In the third case, however, heat fluxes obtained using the ITAS-generated TRASYS input deck were integrated with the ITAS- generated SINDA model. In the fourth and final case, TRASYS and SINDA files were generated and analyzed, independent of ITAS.

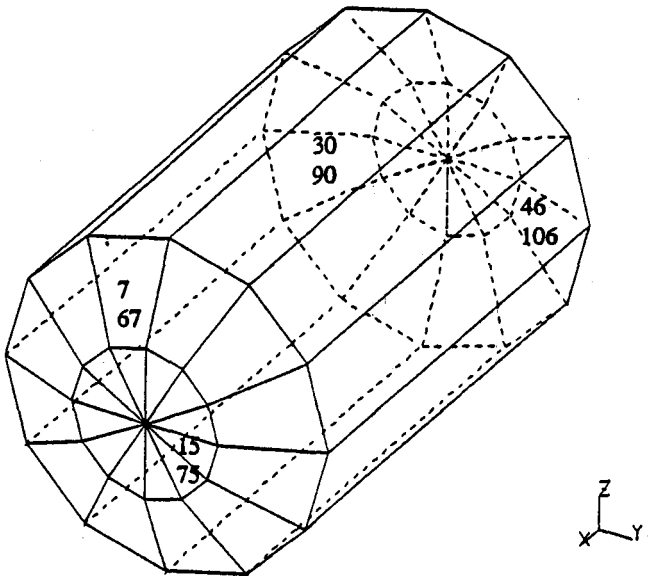

Figure 4: ITAS generated schematic of the space station model.

RESULTS AND DISCUSSION

The temperatures of selected nodes, shown in figure 4, are depicted in Figures 5 through 12. Nodes 7 and 15 are the exterior nodes on the end-cone and have no view of the earth. i.e. the contributing heat source and sink are the solar heat flux and radiation to deep space. Node 30 is on the main cylindrical portion of the module and has partial view of the earth. Node 46 is the exterior node on the other end-cone which is pointing at the earth. Nodes 67, 75, 90 and 106 are the corresponding interior nodes to the above mentioned exterior nodes. As shown in the figures 5 through 12, results corresponding to each of the four cases were in general agreement; hence, the findings of this study suggest that the performance of ITAS is acceptable, at least for cases in which diffuse surface properties may be assumed. These results serve to verify the model definition, steady state and transient orbital heating analysis, radiative and convective heat flow analysis, and translator modules included in the ITAS package.

Additional studies are underway to verify other features of ITAS including the capability for ray tracing and specular surface radiation modeling. These features are of particular interest because they are not accurately handled by COSMIC TRASYS.

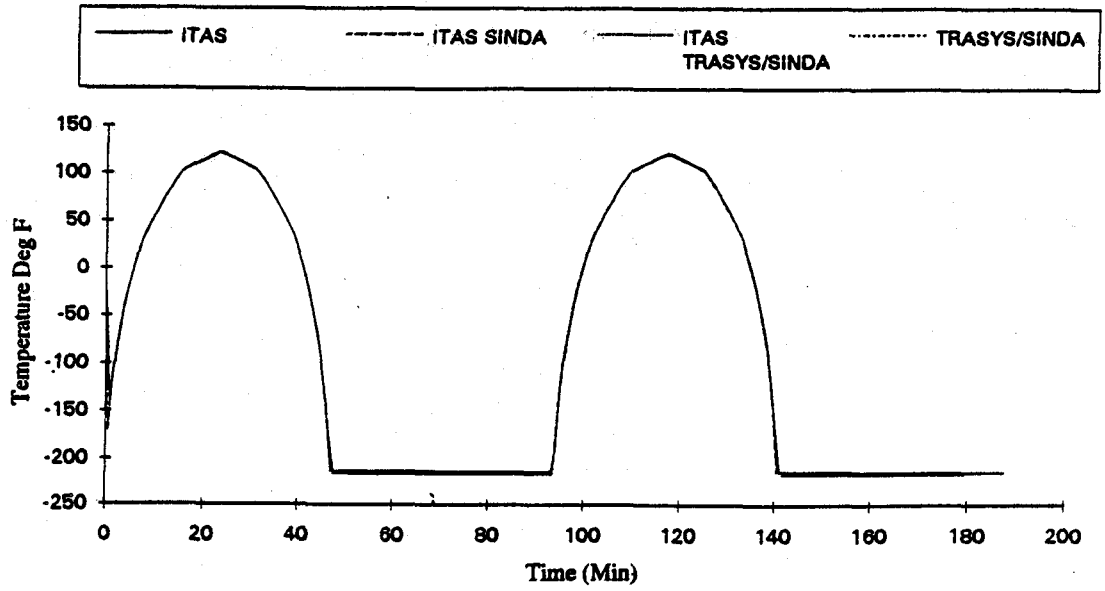

Figure 5: Temperature comparison for interior node 7

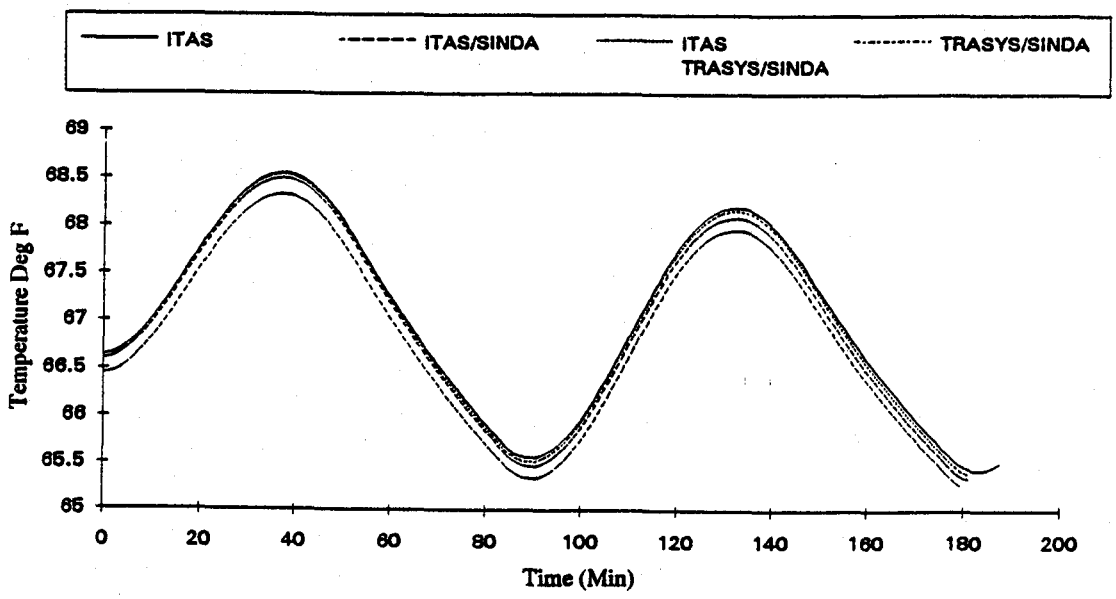

Figure 6: Temperature comparison for interior node 67

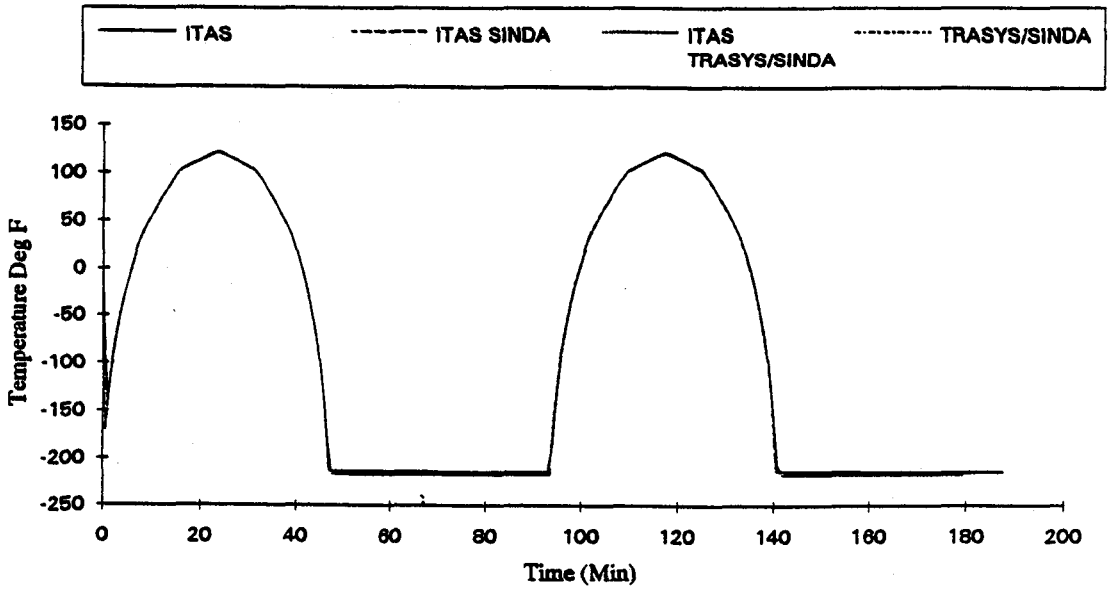

Figure 7: Temperature comparison for interior node 15

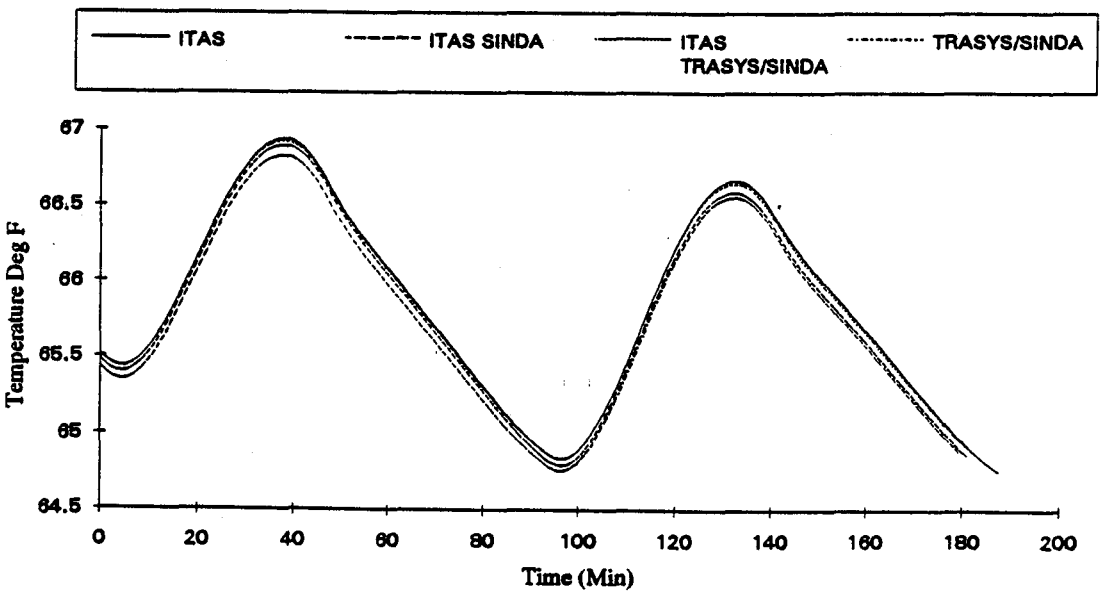

Figure 8: Temperature comparison for interior node 75

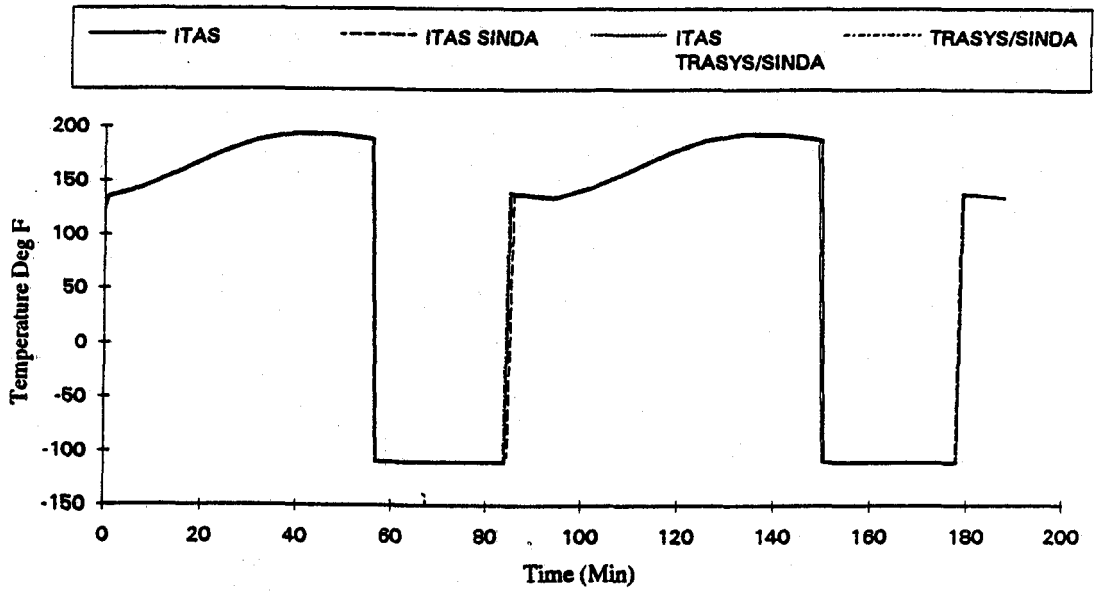

Figure 9: Temperature comparison for interior node 30

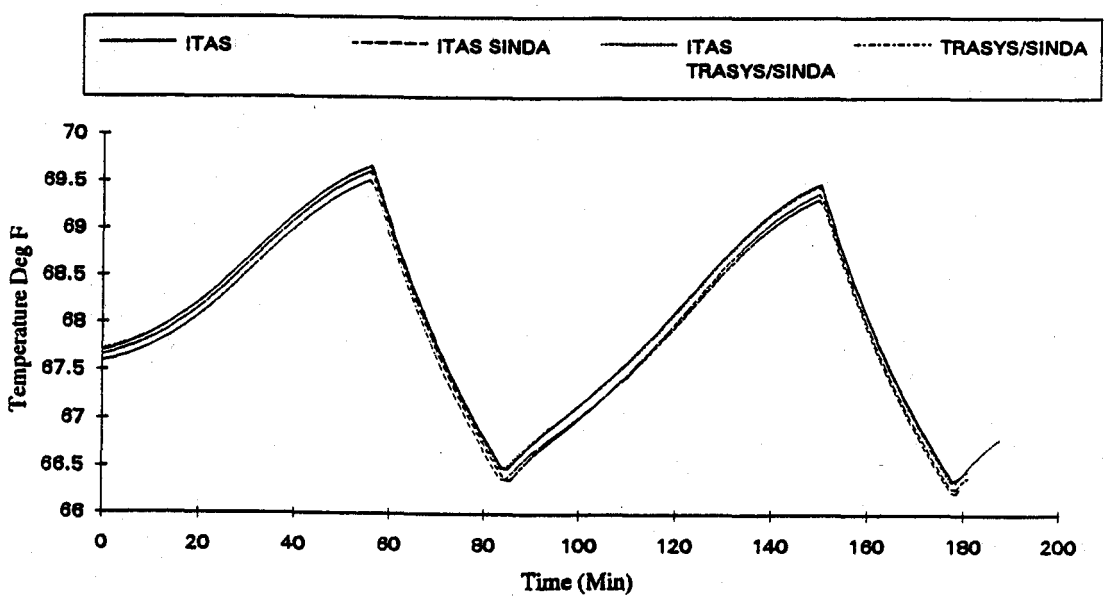

Figure 10: Temperature comparison for interior node 90

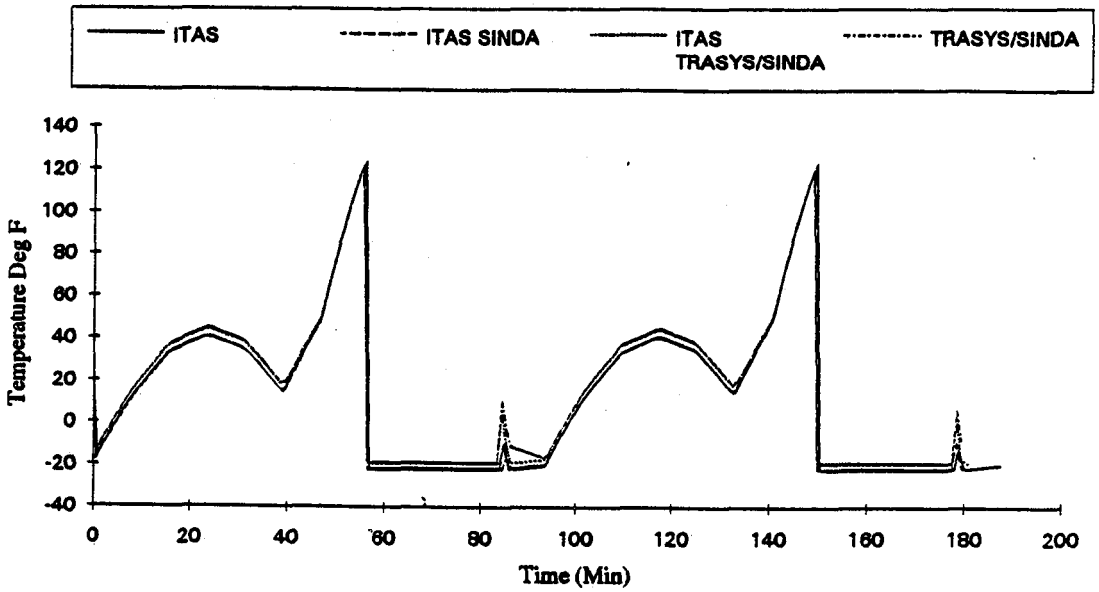

Figure 11: Temperature comparison for interior node 46

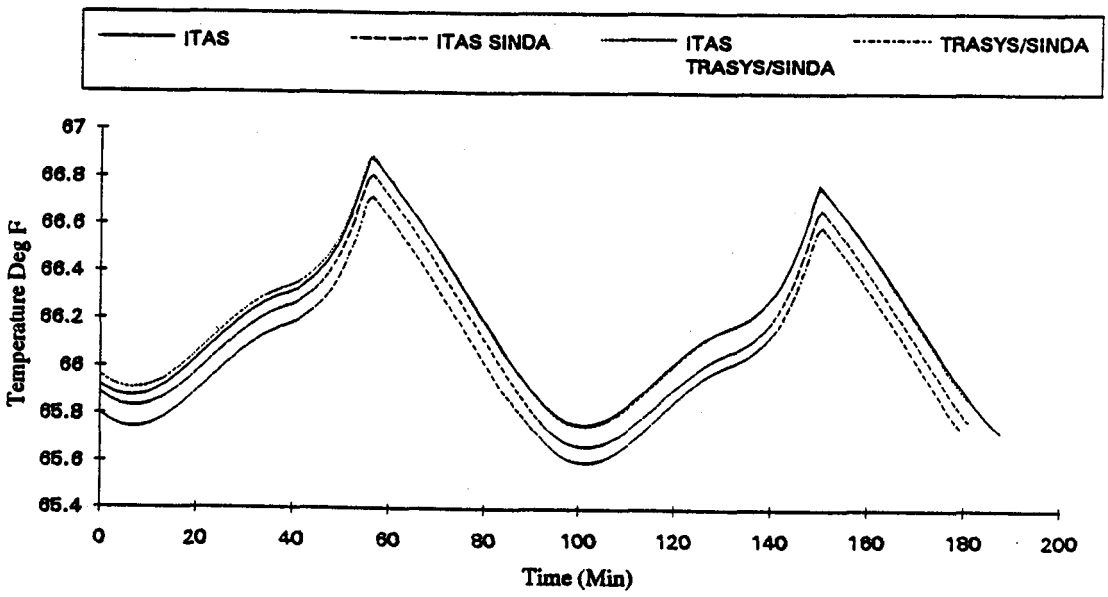

Figure 12: Temperature comparison for interior node 106

AN ENGINEERING CODE TO ANALYZE HYPERSONIC THERMAL MANAGEMENT SYSTEMS

Valerie J. Van Griethuysen
Wright Laboratory
Wright-Patterson AFB, OH

Clark E. Wallace
Science Application International Corporation
Torrance, CA

INTRODUCTION

Thermal loads on current and future aircraft are increasing and as a result are stressing the energy collection, control and dissipation capabilities of current thermal management systems and technology. The thermal loads for hypersonic vehicles will be no exception. In fact, with their projected high heat loads and fluxes, hypersonic vehicles are a prime example of systems that will require thermal management systems (TMS) that have been optimized and integrated with the entire vehicle to the maximum extent possible during the initial design stages. This will not only be to meet operational requirements, but also to fulfill weight and performance constraints in order for the vehicle to takeoff and complete its mission successfully. To meet this challenge, the TMS can no longer be two or more entirely independent systems. Nor can thermal management be an after thought in the design process, the typical pervasive approach in the past. Instead, a TMS that has been integrated throughout the entire vehicle and subsequently optimized will be required. To accomplish this, a method that iteratively optimizes the TMS throughout the vehicle will not only be highly desirable, but advantageous in order to reduce the manhours normally required to conduct the necessary tradeoff studies and comparisons.

This paper will discuss a thermal management engineering computer code that is under development and being managed at Wright Laboratory, Wright-Patterson AFB. The primary goal of the code will be to aid in the development of a hypersonic vehicle TMS that has been optimized and integrated on a total vehicle basis.

BACKGROUND HISTORY

Prior to high speed flight, thermal loads on aircraft were not overtaxing the capabilities of existing cooling approaches, coolants or structural material temperature limits. Consequently, thermal management was not on overriding design consideration. With the advent of high speed flight, this is changing. Previously, aeroheating prediction methods were undergoing development and did not have the fidelity that we are witnessing today. As a result, the extent of thermal protection needed was

not apparent during the initial design stages for vehicles, such as the space shuttle. Consequently, some of the solutions for thermal protection of the shuttle were "fix-it" solutions, ultimately resulting in payload loss potential. With hypersonic vehicle development, we can not afford to take this approach.

Between the lessons learned from previous programs, such as the shuttle, and the current heat loads that are anticipated for hypersonic vehicles, thermal management can no longer be relegated to the tail end of the design cycle. Instead, there must be active involvement during the early design cycle. Furthermore, to enhance the overall vehicle performance and to aid in meeting weight constraints, an integrated engine/airframe thermal management system will have to be developed. This leads to the need for a computer code that will aid in that process.

After a review of available codes and identification of computational requirements, it was decided to base an integrated thermal management code on an engineering code that was under development by Science Applications International Corporation known as HYSTAM (Hypersonic Structural Thermal and Acoustic Management). The primary author submitted a proposal, during autumn 1990, to further develop and enhance the code to meet requirements for a hypersonic vehicle program. The proposed program was approved January 1991 and the effort was under contract before the end of August 1991.

To differentiate HYSTAM from the resulting code to be developed during this effort, a new name was derived and the code became known as the Vehicle Integrated Thermal Management Code or VITMAC. In addition to the code's technical capabilities, it was necessary that it be non-proprietary. This was to ensure that it would be available to the government and government contractor's associated with thermal management for the hypersonic vehicle program in the near term, and eventually to a wider user base. An additional attractive feature of this code was its modularity which easily facilitates the incorporation of non-proprietary codes, subroutines or algorithms from the various sources involved with the program.

CODE ARCHITECTURE

The design approach that went into the development of VITMAC was to simulate a vehicle's thermal management system as a network of open and closed fluid loops with adjacent structures, which may experience external or internal heat loads.[1] Since the networks also included components, such as pumps, tanks, heat exchangers, cooling panels, piping, fittings and turbomachinery, the ability to add them was incorporated into the code. This was possible due to the modular design of VITMAC.

Originally, VITMAC had three primary modules, a general cooling network thermal-fluids response module, a structure thermal response module, and a heat loads module. The heat loads module, for example, contained the capability to compute aerothermal heat

loads and to calculate the heat flux on external surfaces of an earth-orbiting body.[2] After contract initiation, the heat loads module was expanded to include internally generated heat loads. In addition, new modules were added and included a fuel tank module and a component performance module. The role of the fuel tank module is to predict thermal-hydraulic response of the cryogenic tanks and inlet conditions to the cooling networks. The purpose of the component module is to calculate component performance and thermal response and provide coupling with the cooling networks. Figure 1 outlines the code module architecture. A generic VITMAC cooling network is presented in Figures 2 and 3. Figure 2 is a generic cooling network showing various components, with aero-heating and internal heat load inputs and thermal outputs. Figure 3 is the same cooling network that is broken down further to show control volumes, branching and merge points, structure breakout and heat sources and sinks. A more detailed description of the modules follows.

Cooling Network Thermal-Fluid Module.- This module determines the thermal and hydraulic response of a user-defined active cooling network. This module is coupled to the Structure Thermal Response Module. Contained within this module is the capability to have multiple cooling flow loops with multiple coolant sources (i.e. tank) and sinks (i.e. combustor, film cooling). Variable time dependencies can be accepted for the source and sink conditions. Multiple branching and merge points within the loops to simulate parallel flow is also present. Individual coolant loops can thermally interact through designated heat exchangers, as well as allow for coolant (fluid) mass addition and subtraction. The fluid flow can be simulated as being either once-pass through, as in an open system, or recirculating flow, as in a closed system. The code also allows for flow reversal.

VITMAC is currently set up to handle the computation of heat transfer coefficients and friction factors for various flow areas. These include smooth and rough wall for pipe flow and flow between parallel plates for laminar, turbulent and transitional flow. Heat transfer coefficients are based on Nusselt number correlations. Also contained within this module is a loss coefficient library containing several plumbing components, such as valves, tees, elbows and bends. These are listed in Table 1 and can be expanded as needed.

The ability to include pressure drops has been generalized to account for pressure losses due to both skin friction and form drag within the network components. Also contained within this module is the capability to determine hydrogen property data. To accomplish this, NASA Lewis Research Center's code GASPLUS has been coupled with VITMAC as well as built in hydrogen property functions and tables. In addition, a separate submodule for tank operating conditions for hydrogen, oxygen and helium has been developed.

This module is being updated to include correlations for predicting the heat transfer and losses associated with various cooling concepts. Further, industry data pertinent to

configuration and conditions will be incorporated.

Structure Thermal Response Module.- This module predicts structure temperature history and heat loads to the cooling networks. It performs in-depth conduction and radiation heat transfer calculations and convection heat transfer calculations with the coolant, to determine structure thermal response, including through gaps. The module takes a multi-one dimensional approach during its calculations. Further, it takes into account convective, radiative or heat addition boundary conditions. The structures themselves can be actively or passively cooled or heated. In addition, multi-layer composite materials with gaps can be simulated. Thermo-physical properties, such as density and temperature-dependent conductivity and specific heat, for a number of structural materials have been incorporated in with this module. The current list of materials is shown in Table 2. There are plans to expand this list.

Heating Loads Module.- This module addresses aeroheating and internally generated heating loads. The aeroheating portion is based on a cold wall spatial distribution as a function of altitude, while hot wall aeroheating is extracted from surface temperature and edge recovery enthalpy during the flight trajectory. The user has the option to either use the aeroheating module to generate the external heat loads or to input the data directly from other sources. The user has the option to utilize attached boundary layer aeroheating loads generated from a 2-D version of the SAIC 3-D MEIT/3-D inviscid code. The 2-D version was selected to help keep the run times down. A comprehensive survey of the heating effects due to shock boundary layer interaction has been completed, including defining classes of interactions. Development of an algorithm for the code was underway, but due to current funding limits and other priorities, incorporation into VITMAC will be delayed.

Internal heat loads can be either steady-state or transient. VITMAC currently provides the user with three options for specifying internal heat loads on structures. The first option allows the heat loads to be included as part of the input file, i.e. a namelist file, in tabular form. These loads are directly applied to the structure surfaces as specified in the input deck. The second and third options permit the user to define the heat loads on the structures in separate input files, one each for the vehicle's upper and lower surfaces. These heat loads are treated as cold wall aeroheating loads and corrected to hot wall aeroheating loads when read into VITMAC. The second option derives these files from the TRAJIQ code, while the third option requires the user to manually generate these files in the TRAJIQ output file format employing own data.

Algorithms that were previously developed for internal heat generation, such as generic engine heat generation rates and electronic heat generation will be incorporated into VITMAC.

Fuel Tank Module.- This module solves the time-dependent forms of the mass and energy conservation equations for gas, liquid and solid phases for hydrogen and oxygen within a tank. This can be coupled with the injection of a binary gas such as helium for ullage pressure control. Further, the ullage pressure, fuel mass, and fuel level within the tank are predicted as a function of specified heating, venting and recirculation rates. Also, the code has the capability to model equilibrium with phase transition due to heat leakage. Tank pressure can currently be depicted by a pressure-time table. The tank module will be fully integrated with VITMAC and expanded to include heat transfer to local structures and insulation.

Component Performance Module.- This module calculates component responses and provides coupling with the cooling network. The code currently includes simple models for pumps, compressors, and turbines, based on generic component performance and thermodynamic relationships. Pump performance is obtained from head-discharge curves. Compressor performance is based on compression ratio and efficiency. Turbine performance is calculated from expansion ratio and efficiency, coupled with compressor and pump power requirements. The capability to determine power balance between several compressors, pumps and turbines is included. The capability to conduct a complete system power balance will be taking place in the near future.

Engine Module.- VITMAC does not currently support a fully dedicated engine module. However, the code can model at a simplified level, the fuel side of the system. This work was originally scheduled to be developed in FY93. However, funding cutbacks currently preclude the addition of this module. Nonetheless, it is hoped that this can be added in the future.

Input/Output.- While working with the code, it became clear that an alternative approach for inputting the data was needed. The process of inputting a network in a data file was very time consuming. In addition, the learning curve associated with the code was longer than desired. Because of the limited available manpower at contractor and government facilities to conduct cooling network design trade-off and analysis studies, an easier and faster approach to input data into VITMAC was needed. To fulfill this need, the use of a computer graphical user interface (GUI) was recommended.

The possibility of coupling GUI technology with VITMAC was investigated and determined to be highly feasible. The question then became, whether to include GUI capability as soon as possible or to wait until the end of code development. The decision was made to incorporate the GUI during code development. This would make it easier and faster for the user to learn the code, while taking less time to input data. Further this would facilitate feedback to the developer on capabilities, strengths, weaknesses, and areas needing change while the code was still under

development. A contract modification was completed in late August 1992 to add this capability.

Figures 4, 5, and 6 demonstrate generally how the GUI will be used with VITMAC. It is clearly obvious that with the use of the GUI, the network from figures 1 and 2 can literally be generated on the computer screen. This not only aids in visualizing the network, but also aids in input error detection. The GUI will also be used for displaying output, as seen in figure 7 as an example. As a result of these changes, VITMAC is being transitioned to the UNIX operating system, with an XWindows environment.

GENERAL CAPABILITIES

VITMAC has been developed to enable the user to select steady-state, quasi-transient or transient operation. Procedures for ensuring numerical stabilities have been developed and incorporated into the code. These include operations involving division and logarithms, and input error detection. Procedures to minimize storage (i.e. Jacobian matrix within the thermal-fluid module) and run time requirements have been developed. Thermophysical property data for hydrogen and structural materials has been extrapolated to 9000°R, to provide the user with information which may prove helpful during modeling refinement. This is not intended to extend the response of the coolant and materials to this high a temperature. Currently the maximum number of control volumes per loop is 100 and the maximum number of structures is 70 during simulation. This capability can be easily expanded by updating the appropriate parameter statements and recompiling the code.

Several cases, of varying degrees of complexity, were run to assist in the development and checkout of the thermal-fluid network, structure thermal response and tank modules. With the aid of industry in supplying data, several specific simulation cases were performed for both the airframe and engine. The VITMAC User Manual is revised as the code is updated. A manual on the theory of the code will be generated as part of the final report. The code is in the process of being transitioned from a VAX environment to a SUN Workstation environment and should be completed prior to this meeting.

CURRENT STATUS

Mid October 1992, this effort received a drastic budget cut of 76% for FY93. As a result, a stop work order had to be placed on the contract to prevent over expenditure. Damage control was initiated to determine what we could afford to complete and what had to be eliminated, yet still result with a product that would be useful. Downscoped statements of work were written, while budget levels fluctuated. One key area that had to be sacrificed was the engine heat loads module. Since the scope of work had to be reduced to such a large extent, the contract had to be modified and

renegotiated. This was finally completed mid March 1993 and work has been reinitiated at the reduced level. The current contract is scheduled to be completed the end of January 1994. It is hoped that funding will be restored, as a minimum, to the level before the budget cut, in order to complete the originally scoped effort.

CONCLUSION

Despite the uncertainties surrounding the future of hypersonic programs, the need for an engineering computer code that integrates overall thermal management systems remains. This is true, now more than ever, due to the manpower cuts experienced by both airframe and engine companies, particularly in the thermal management community. Not only is the industry personnel base in thermal management small, the same is true for the government in both DOD and NASA. Regardless of whether hypersonic vehicle programs continue, or if there are sub orbital research vehicle programs, or a high speed propulsion system development program, thermal management issues still exist and remains an enabling technology. To conduct complete integrated engine/airframe analyses and trade-off studies to develop an optimum TMS, a code such as VITMAC, is required.

REFERENCES

1. Issacci, F.; Wassel, A.T.; Farr, J.L., Jr.; Wallace, C.E.; and Van Griethuysen, V.J.: "A Thermal Management Assessment Tool for Advanced Hypersonic Aircraft." SAE Aerotech '92, Oct. 1992, p. 2.
2. Wallace, C.E.; Wassel, A.T.; Laganelli, A.; and Carlson, D.: "Systems Integrated Thermal Management Assessment Tool." Science Applications International Corp., Jul. 1990, p. 3.

TABLE 1. Loss Coefficient Library

Component Type	K_{loss}
Elbows:	
Regular 90°, flanged	0.3
Regular 90°, threaded	1.5
Long radius 90°, flanged	0.2
Long radius 90°, threaded	0.7
Long radius 45°, flanged	0.2
Regular 45°, threaded	0.4
180° Return Bends	
Flanged	0.2
Threaded	1.5
Tees:	
Line flow, flanged	0.2
Line flow, threaded	0.9
Branch flow, flanged	1.0
Branch flow, threaded	2.0
Union, threaded	0.08
Valves:	
Globe, fully open	10.0
Angle, fully open	2.0
Gate, fully open	0.15
Gate, 1/4 closed	0.26
Gate, 1/2 closed	2.1
Gate, 3/4 closed	17.0
Swing check, forward flow	2.0
Swing check, backward flow	∞
Ball valve, full open	0.05
Ball valve, 1/3 closed	5.5
Ball valve, 2/3 closed	210.0
Pipe Entrances:	
Inward projecting	0.78
Sharp edged	0.50
Slightly rounded	0.23
Well rounded	0.04
Pipe Exits:	
Projecting	1.0
Sharp edged	1.0
Rounded	1.0

TABLE 2. Structural Material List

Aluminum 2219	Beryllium	Carbon-Carbon
Fibermax	Graphite/Epoxy	Haynes 188
Haynes 230	Incoloy 754	Incoloy 909
Incoloy 956	Lockalloy	Mo-50/Re
Narloy-Z	Niobium	Q-fiber/He purge
Stainless Steel	Titanium 6Al-4V	Titanium 1100

FIGURE 1. VITMAC Architecture

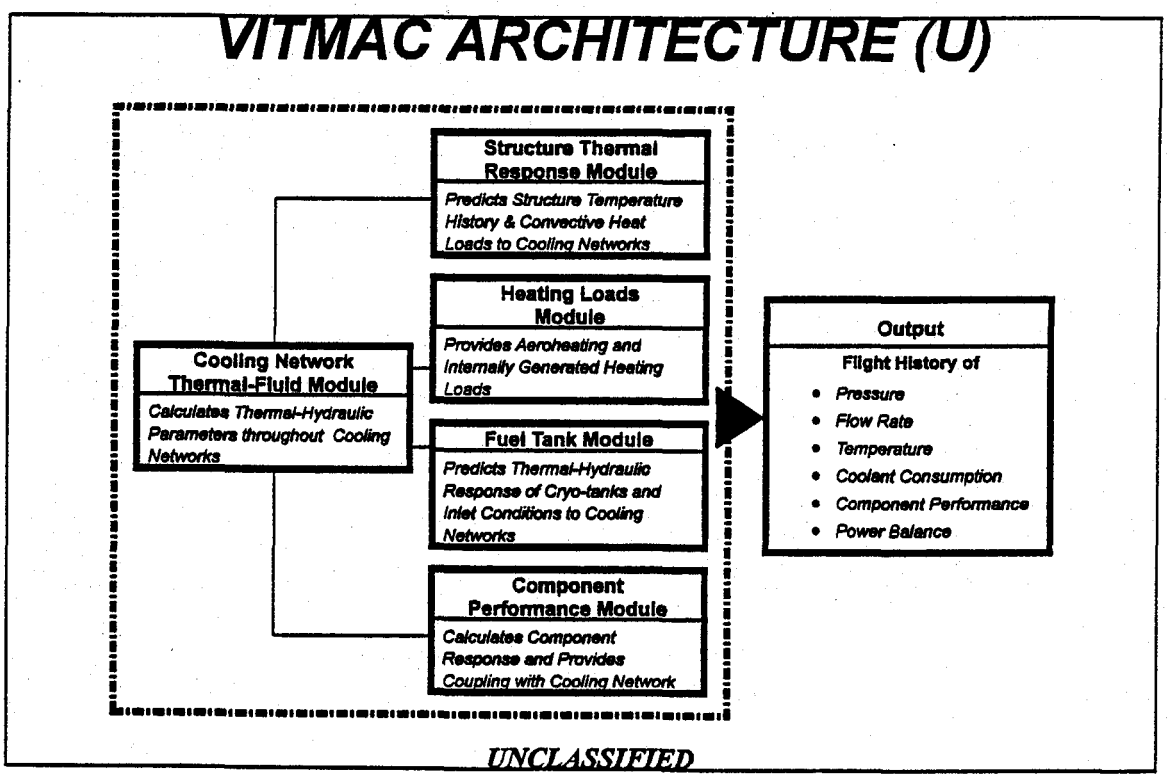

FIGURE 2. VITMAC Cooling Network

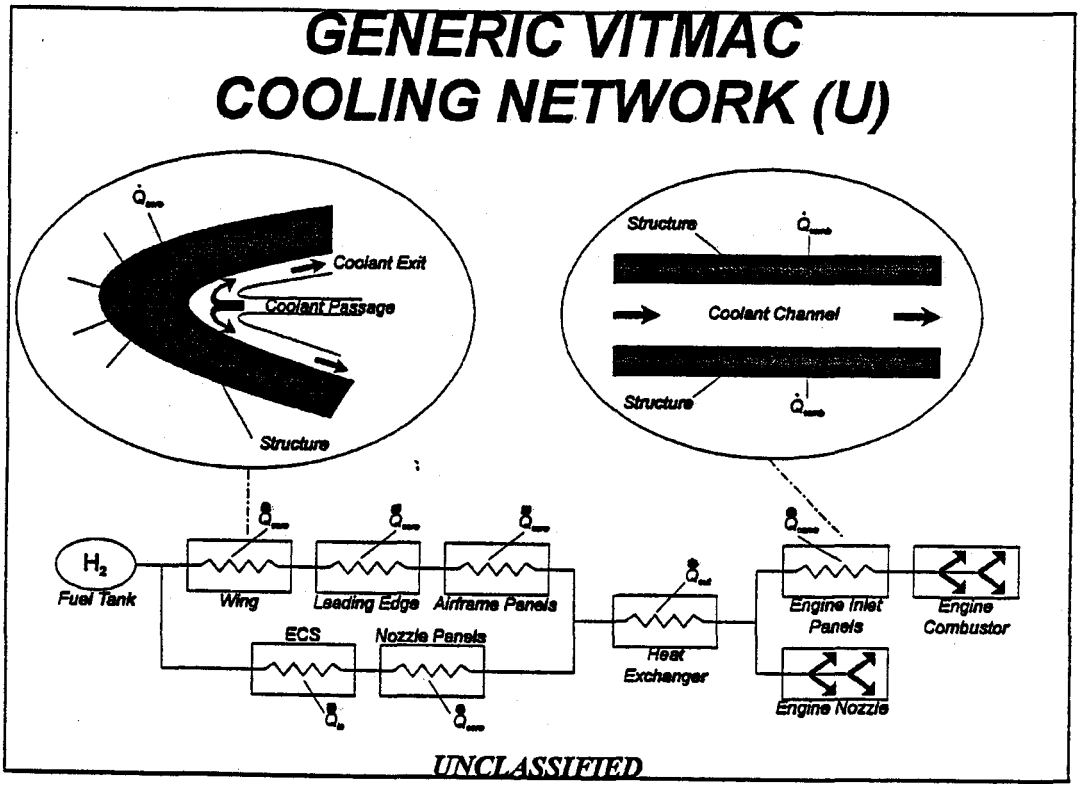

FIGURE 3. Generic Cooling Network

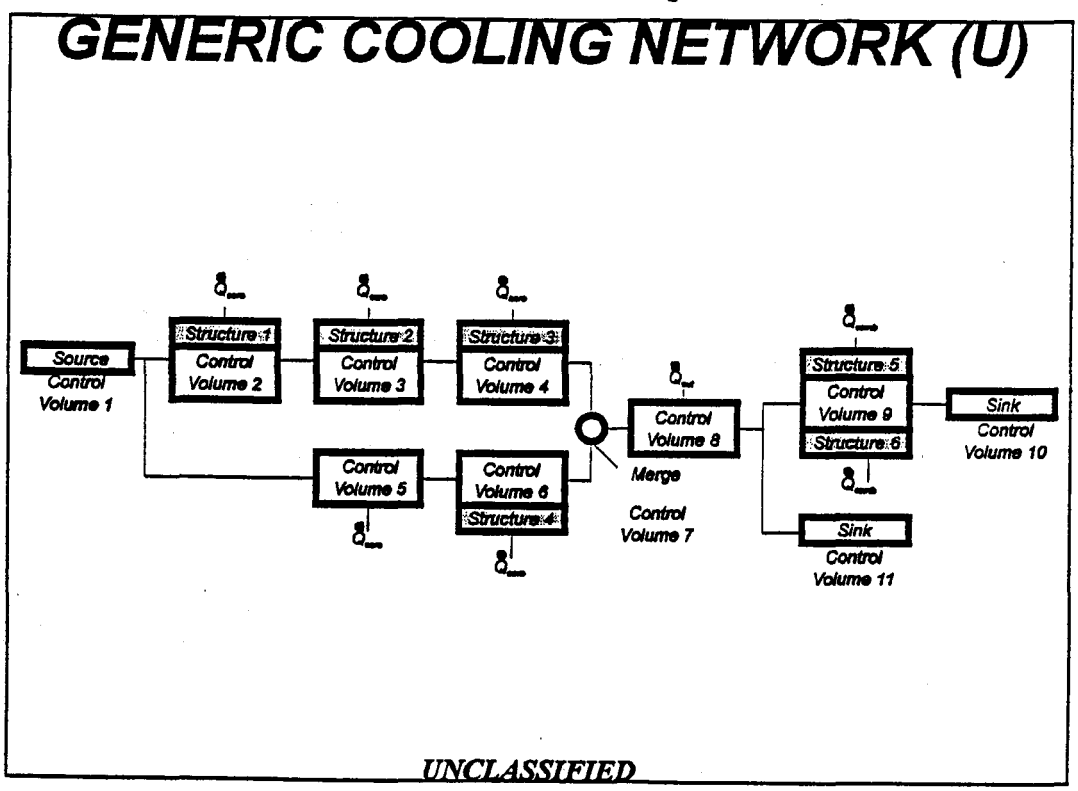

FIGURE 4. VITMAC GUI Generic Cooling Network

VITMAC GUI GENERIC COOLING NETWORK (U)

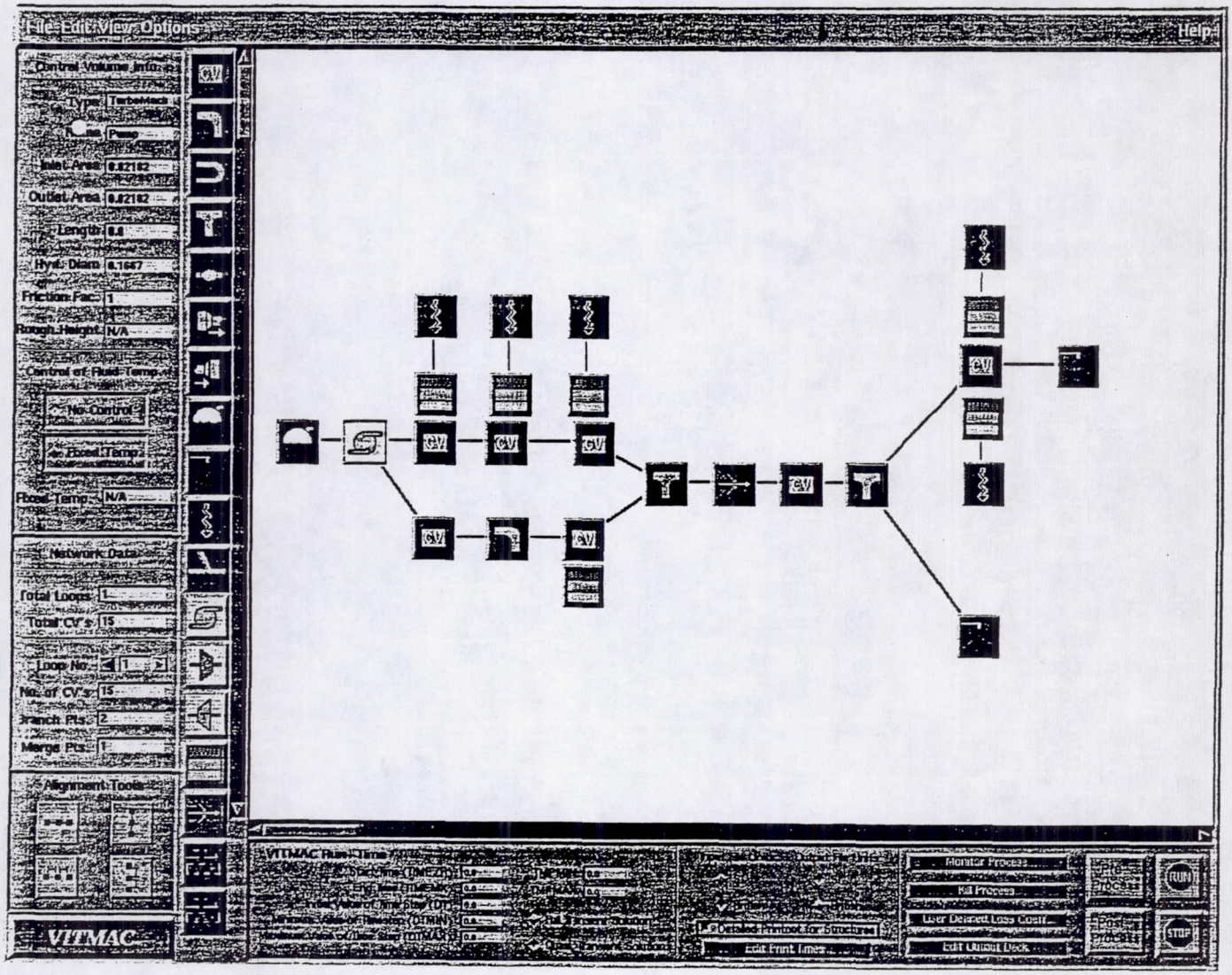

UNCLASSIFIED

FIGURE 5. VITMAC GUI Structure Generation

VITMAC GUI STRUCTURE GENERATION (U)

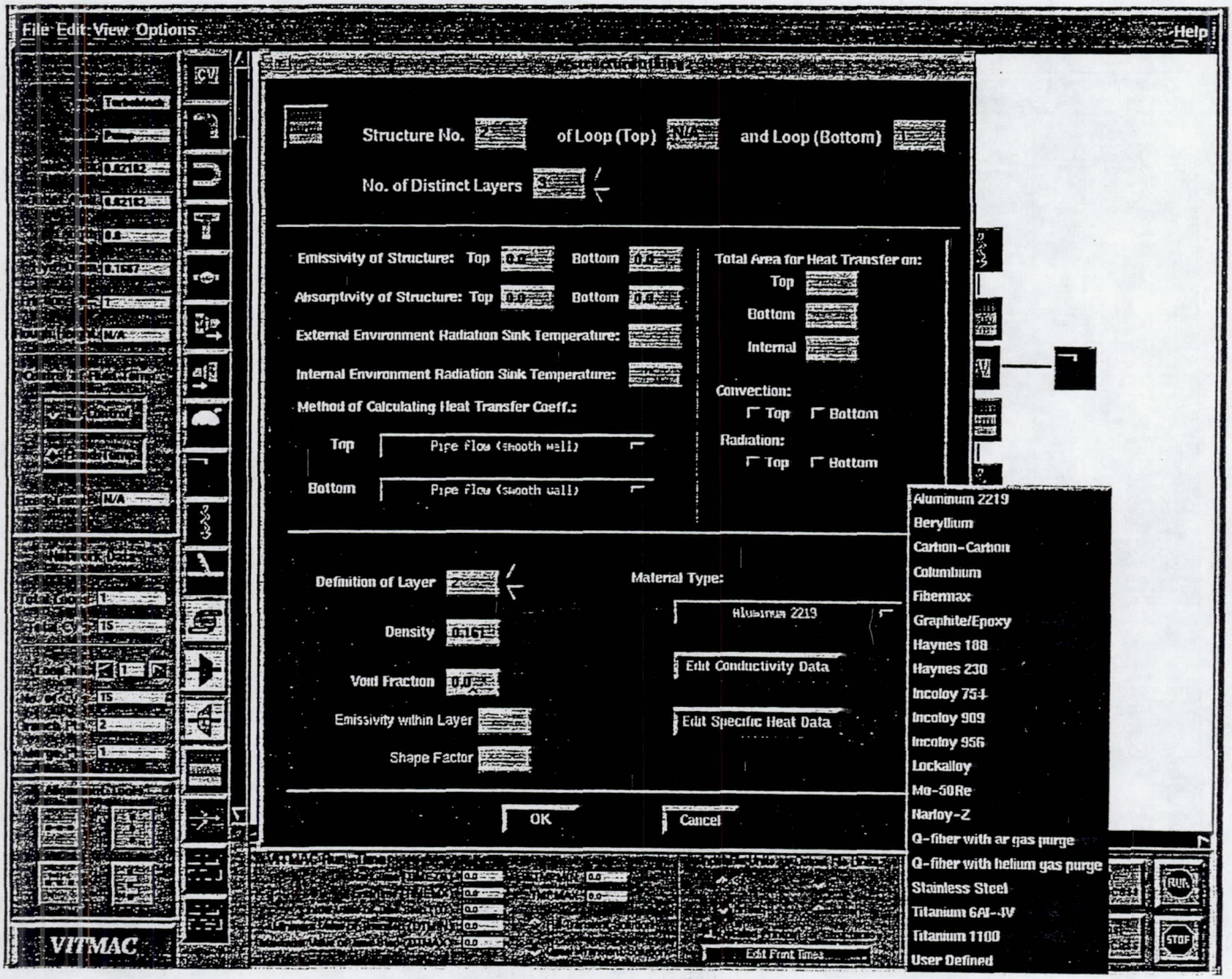

UNCLASSIFIED

FIGURE 6. VITMAC GUI Component Generation

VITMAC GUI COMPONENT GENERATION (U)

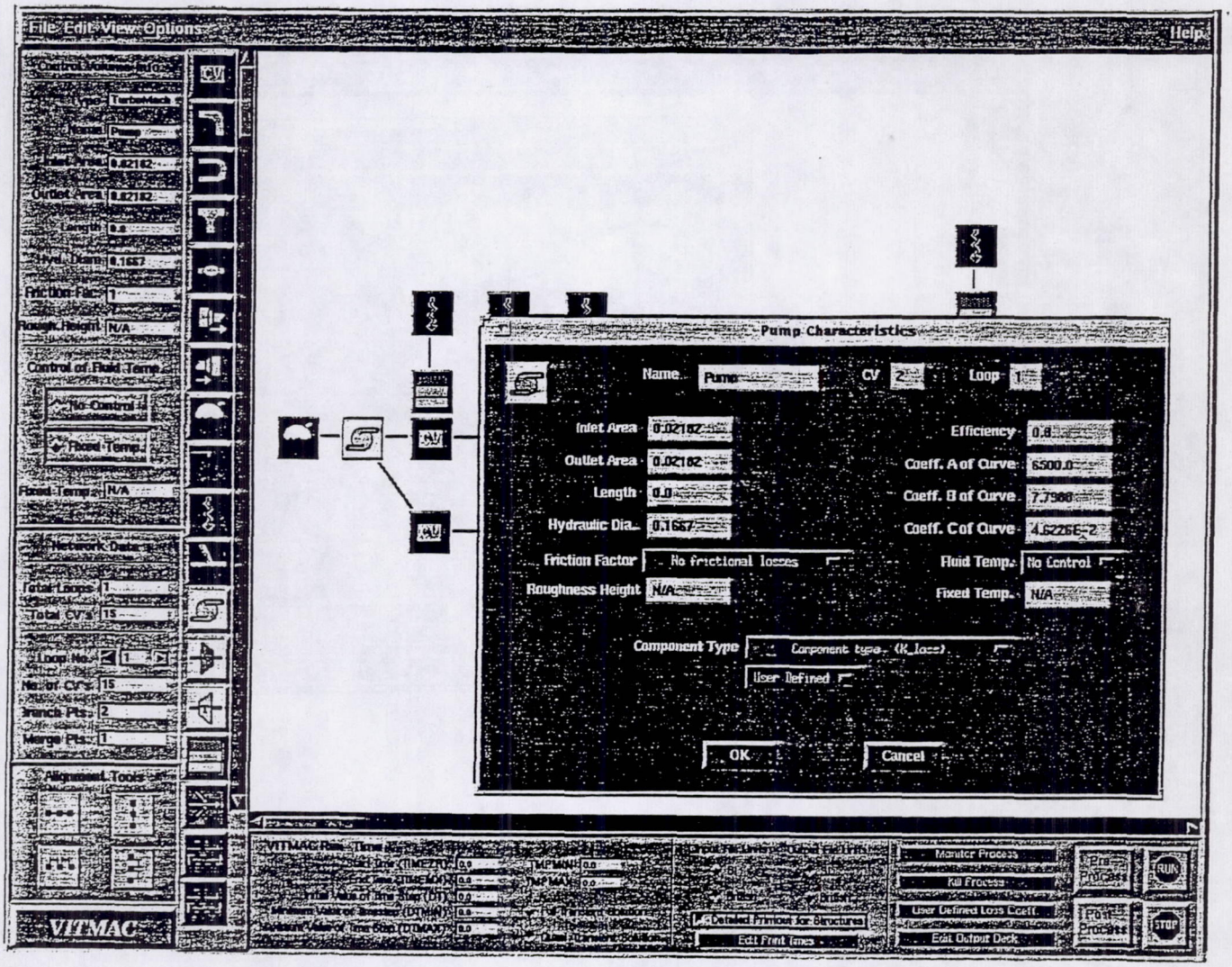

UNCLASSIFIED

FIGURE 7. VITMAC GUI Output

VITMAC GUI OUTPUT EXAMPLE (U)

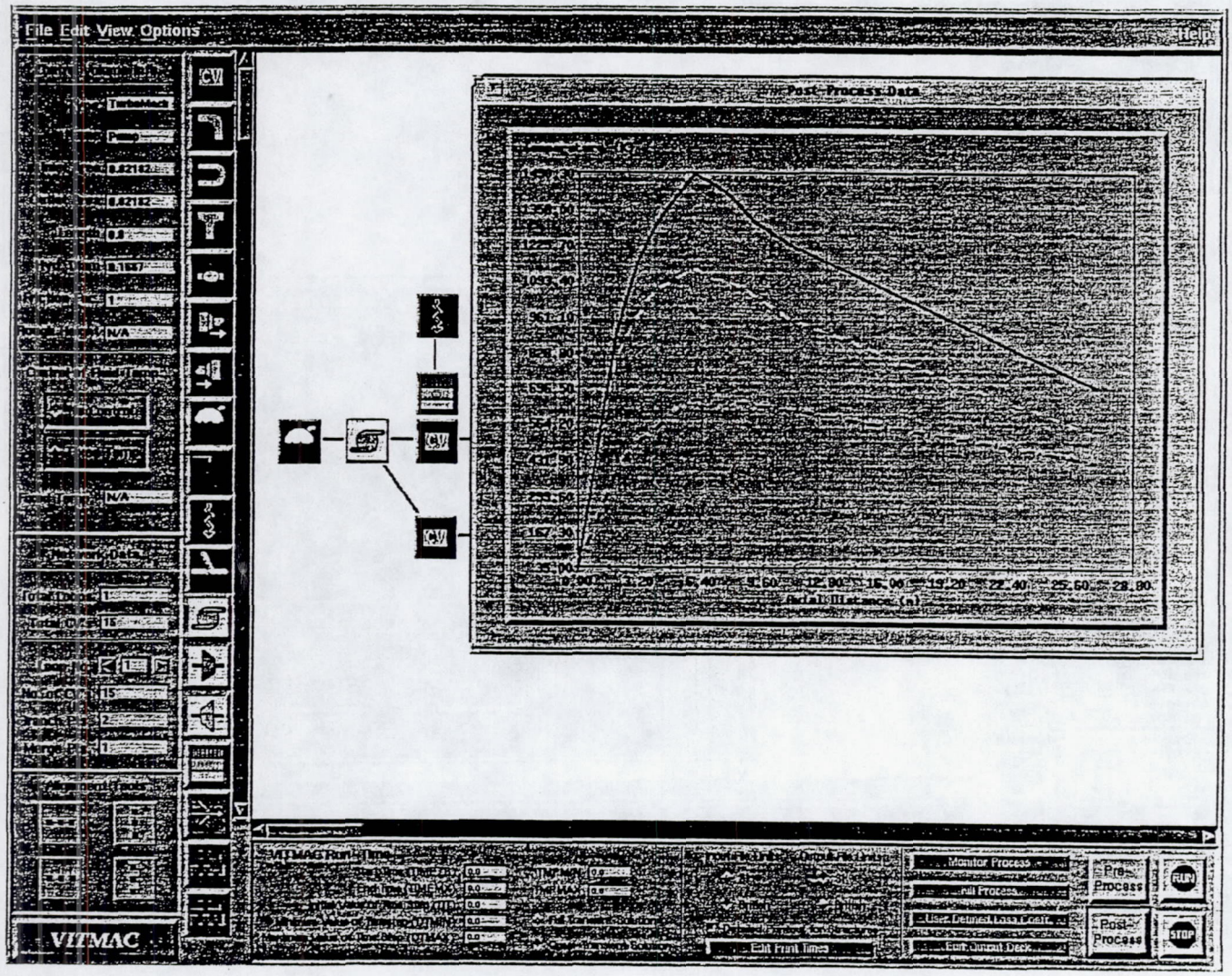

UNCLASSIFIED

UNCERTAINTY ANALYSIS OF DIFFUSE-GRAY RADIATION ENCLOSURE PROBLEMS --A Hypersensivite Case Study

Robert P. Taylor*, Rogelio Luck**, B. K. Hodge*
and W. Glenn Steele***
Thermal & Fluid Dynamics Laboratory
Department of Mechanical Engineering
Mississippi State University
Mississippi State, MS 39762

ABSTRACT

An uncertainty analysis of diffuse-gray enclosure problems is presented. The genesis of this study was a diffuse-gray enclosure problem which proved to be hypersensitive to the specification of view factors. This genesis is discussed in some detail. The uncertainty analysis is presented for the general diffuse-gray enclosure problem and applied to the hypersensitive case study. It was found that the hypersensitivity could be greatly reduced by enforcing both closure and reciprocity for the view factors. The effects of uncertainties in the surface emissivities and temperatures are also investigated.

INTRODUCTION

All thermal analysis computations involve uncertainties. Geometries are imprecisely specified, thermal physical properties are not known exactly, and process data (boundary conditions) such as temperatures, pressures, and velocities are to some degree uncertain. Some of these uncertainties are a natural part of the process being modeled. The thermal-physical properties will naturally vary from point to point in physical space. The thermal conductivity will depend on such local conditions as impurity concentrations, grain structure, and voids in all but the purest and most carefully handled materials. Thermal radiation properties can vary considerably over a surface depending on factors such as roughness and oxidation. Also, the boundary conditions will not be precisely applied in the actual process. Other uncertainties result from a lack of input data. In the early design computation stages, field data may not have been collected and previous project experiences or handbook data must be used to estimate certain process conditions. Finally, all thermal analysis models rely ultimately on experimental measurements for material properties, boundary conditions, or design data bases and correlations. Experimental uncertainty is always present.

The treatment of experimental uncertainties is well developed. National and international standards for the treatment of measurement uncertainty have been published. The ANSI/ASME (1986) standard is one example. The book by Coleman and Steele (1989) gives a good review of current practices for experimental uncertainties. The treatment of thermal analysis uncertainties is not philosophically different from the treatment of measurement uncertainties. A set of basic rules (thermal analysis model/data reduction equation) is applied to a set of data (physical properties and boundary conditions/basic measurements) to produce a result. The goal of the uncertainty analysis is to follow the estimated or measured variances in the data through the rules into uncertainties in the result.

The nuclear engineering community routinely incorporates uncertainty analysis in reactor certification and design calculations and has developed a considerable body of literature on this subject. A recent series of articles in Nuclear Engineering and Design (Boyack et al., 1990, Wilson et al., 1990,

* Professor, ** Assistant Professor, *** Professor and Head

and Wulff et al., 1990) are representative of activity in nuclear engineering. The book edited by Ronen (1988) is also a good source. The fields of sensitivity analysis in control theory (Cruz, 1973) and reliability based mechanical design (Rao, 1992) are closely related to uncertainty analysis.

The use of uncertainty analysis in the mechanical and aerospace engineering thermal analysis community is still rather rare. Emery and Fadale (1990) and Fadale and Emery (1992) present analyses of uncertainties in finite element conduction heat transfer computations. Mehta (1991) discusses aspects of uncertainty in computational fluid dynamics.

This paper presents an uncertainty analysis of diffuse-gray radiation enclosures. Such problems contain uncertainties in the view factor matrix which arise from the geometric specification, in the material properties through the emissivities, and in the process specifications through the surface temperatures. Under the right (or wrong) conditions these uncertainties can have a profound effect on the computed heat flux results. The genesis of this study was a homework problem in the second heat transfer course at Mississippi State University. This genesis is discussed below. This is followed by the development and application of the uncertainty analysis and discussion.

GENESIS

The following problem from the heat transfer text by Incropera and Dewitt (1985) was assigned in the second heat transfer course at Mississippi State University during the Fall 1992 term.

> 13.62 A room is represented by the following enclosure, where the ceiling (1) has an emissivity of 0.8 and is maintained at 40°C by embedded electrical heating elements. Heaters are also used to maintain the floor (2) of emissivity 0.9 at 50°C. The right wall (3) of emissivity 0.7 reaches a temperature of 15°C on a cold, winter day. The left wall (4) and end walls (5A, 5B) are very well insulated. To simplify the analysis, treat the two end walls as a single surface (5). Assuming the surfaces are diffuse-gray, find the net radiation heat transfer from each surface.

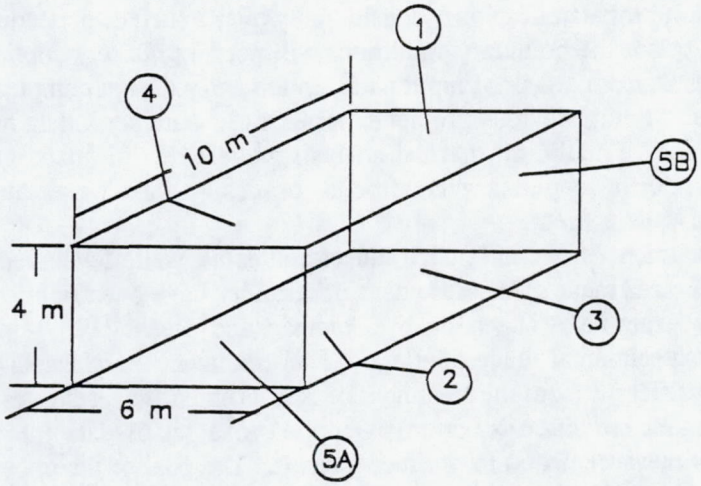

Two students, Miguel and Simon, ignored the simplification and worked the problem as a six-sided enclosure. Miguel computed the view factors from the formulae for opposed parallel plates and perpendicular plates with a common edge and obtained the following view factor matrix:

$$\begin{bmatrix} 0.0 & 0.394 & 0.1921 & 0.1921 & 0.1109 & 0.1109 \\ 0.394 & 0.0 & 0.1921 & 0.1921 & 0.1109 & 0.1109 \\ 0.2881 & 0.2881 & 0.0 & 0.196 & 0.1139 & 0.1139 \\ 0.2881 & 0.2881 & 0.196 & 0.0 & 0.1139 & 0.1139 \\ 0.2774 & 0.2774 & 0.1898 & 0.1898 & 0.0 & 0.066 \\ 0.2774 & 0.2774 & 0.1898 & 0.1898 & 0.066 & 0.0 \end{bmatrix}$$

Simon, on the other hand, obtained values for the view factors from plots provided in the text and obtained the following view factor matrix:

$$\begin{bmatrix} 0.0 & 0.38 & 0.19 & 0.19 & 0.11 & 0.11 \\ 0.38 & 0.0 & 0.19 & 0.19 & 0.11 & 0.11 \\ 0.28 & 0.28 & 0.0 & 0.19 & 0.11 & 0.11 \\ 0.28 & 0.28 & 0.19 & 0.0 & 0.11 & 0.11 \\ 0.28 & 0.28 & 0.19 & 0.19 & 0.0 & 0.07 \\ 0.28 & 0.28 & 0.19 & 0.19 & 0.07 & 0.0 \end{bmatrix}$$

Both students used a diffuse-gray enclosure computer program to find the net radiation heat flux at each surface. This program was based on the net radiation method. This is a two step process. First the following equation is solved for the net radiosity vector, q_o.

$$[I - (I - D_\epsilon)F]q_o = \sigma D_\epsilon D_t^4 i \tag{1}$$

where **I** is the identity matrix, $\mathbf{D}_\epsilon$ is a diagonal matrix with the surface emissivities as members, **F** is the view factor matrix, $\mathbf{D}_t$ is a diagonal matrix with surface temperatures for members, and **i** is a vector of 1's. The heat flux vector is then calculated from the net radiation energy balance.

$$q = (I - F)q_o \tag{2}$$

Both students modeled the adiabatic surfaces as perfect reflections ($\epsilon = 0$). The results are summarized in Table 1.

Simon has slight errors in his view factors, but all in all they look very reasonable. All of the values are within a percent or two. The row sums of view factors are 0.98, 0.98, 0.97, 0.97, 1.01, and 1.01; so, the closure requirement is reasonably met. His radiosites are not seriously in error. The maximum error is 3.5%. However, his heat flux results, which are off by 376%, 18% and 13% for surfaces 1, 2, and 3, respectively, are profoundly in error. Also, his answers are in gross violation of global conservation of energy. For a steady-state analysis such as this one, the net energy stored in the enclosure should be zero. Miguel only has 10 w out of 5000 w left over which is a reasonable error. On the other hand, Simon has 2400 w out of 6000 w left over. Clearly something is terribly wrong. A quick independent check revealed that Simon had executed the program correctly. His radiosity results are indeed solutions of equation (1), and the problem is not numerical. At least not numerical in so far

Table 1. Comparison of Miguel's and Simon's Solutions

	$q_o(w/m^2)$		$q(w/m^2)$		Q(m)	
Surface	Miguel	Simon	Miguel	Simon	Miguel	Simon
1	546.2	542.7	-3.69	10.21	-221.4	612.4
2	609.0	607.3	83.87	99.32	5032.2	5959.2
3	442.6	435.9	-120.53	-105.00	-4821.2	-4200.0
4	543.3	524.4	0.0	0.0	0.0	0.0
5A	543.4	542.4	0.0	0.0	0.0	0.0
5B	543.4	542.4	0.0	0.0	0.0	0.0
				Total	-10.40	2371.6

as the evaluation of the inverse of the matrix in equation (1) goes. Simon's results are the proper solution to the problem as Simon posed it.

Simon's view factor matrix did not strictly enforce closure[1]. It is common practice to force closure by only considering N-1 elements on each row to be independent and computing the remaining element from the closure rule. In fact, Brewster (1992) insists that not only closure but also reciprocity ($a_i f_{ij} = a_j f_{ji}$) must be enforced. He quotes avoidance of singular or poorly conditioned matrixes which cannot be inverted as the reason. As discussed above, inversion is not a problem in Simon's case. In fact, the matrix of coefficients, $[\mathbf{I} - (\mathbf{I} - \mathbf{D}_e)\mathbf{F}]$, which results with Simon's view factors, is well behaved with a condition number of 2.83, compared to a condition number of 2.85 using Miguel's view factors.

Closure is important philosophically and physically; so, we naively adjusted the diagonal elements in Simon's view factor matrix to force closure. The resulting view factor matrix was

$$\begin{bmatrix} 0.02 & 0.38 & 0.19 & 0.19 & 0.11 & 0.11 \\ 0.38 & 0.02 & 0.19 & 0.19 & 0.11 & 0.11 \\ 0.28 & 0.28 & 0.03 & 0.19 & 0.11 & 0.11 \\ 0.28 & 0.28 & 0.19 & 0.03 & 0.11 & 0.11 \\ 0.28 & 0.28 & 0.19 & 0.19 & -0.01 & 0.07 \\ 0.28 & 0.28 & 0.19 & 0.19 & 0.07 & -0.01 \end{bmatrix}$$

The physically unrealistic negative view factors were not corrected. Table 2 shows the revised results which are vastly improved. The heat flux errors are now 21%, 1%, and 2% for surfaces 1, 2, and 3, respectively. This result is an order of magnitude improvement. This result is somewhat surprising since we have enforced a closure where the individual view factors are even more in error. We have forced plane surfaces to see themselves and have forced physically unrealistic negative view factors. However, on the other hand, we have enforced an important physical constraint.

Anecdotically, we can surmise from this experience that this problem is hypersensitive to errors in the view factor specification when all NxN view factors are independent. However, a rather naive enforcement of closure greatly reduces this sensitivity.

---

[1]As is well known, since a ray emitted from a surface must either strike that surface or one of the other surfaces in the enclosure, the rows of the view factor matrix must sum to unity, $\sum_{j=1}^{N} f_{ij} = 1$.

Table 2. Simon's revised results

	$q_o(w/m^2)$		$q(w/m^2)$		Q(m)	
Surface	Miguel	Simon	Miguel	Simon	Miguel	Simon
1	546.2	546.0	-3.69	-2.92	-221.4	-174.6
2	609.0	601.9	83.87	82.92	5032.2	4975.2
3	442.6	441.4	-120.53	-117.89	-4821.2	-4715.6
4	543.3	543.0	0.0	0.0	0.0	0.0
5A	543.4	543.0	0.0	0.0	0.0	0.0
5B	543.4	543.0	0.0	0.0	0.0	0.0
				Total	-10.40	85.6

The computations in equations (1) and (2) are readily amenable to an uncertainty analysis. The sensitivity of the radiosities and heat fluxes to each view factor, emissivity, and temperature can be computed and used with estimates of the uncertainties in the input data to determine estimates of the uncertainties in the computed values for radiosity and heat flux. Such an analysis provides a systematic way to investigate the problems that were apparent in the above discussion, provides a way of determining the source of the hypersensitivity, and provides a means to determine the fidelity of the input data required for a desired model accuracy. This uncertainty analysis is developed below.

UNCERTAINTY ANALYSIS

In the following, we discuss the propagation of uncertainties from the input into the result, the definition of the sensitivity coefficients, and the development of the relations needed to compute the sensitivity coefficients for this problem. In this investigation, uncertainties in view factors, emissivity, and temperatures are considered.

Uncertainty Propagation

The development of the first-order general uncertainty analysis is discussed in detail by Coleman and Steele (1988), and only the result is given here. If all of the uncertainties in the data are taken to be independent (no common or correlated sources of uncertainty), the uncertainties in the results are obtained by taking the root-sum-square of the product of the sensitivity coefficient and the input variable uncertainty.

$$U_{r_k}^2 = \sum_{i=1}^{N} \sum_{j=1}^{N} (\Theta_{k,f_{ij}})^2 U_{f_{ij}}^2 + \sum_{i=1}^{N} (\Theta_{k,\epsilon_i})^2 U_{\epsilon_i}^2 + \sum_{i=1}^{N} (\Theta_{k,t_i})^2 U_{t_i}^2 \qquad (3)$$

Here the result, r_k, is either the heat flux, q_k, or the radiosity, $q_{o,k}$. The sensitivity coefficients are the first partial derivatives of the result with respect to each input variable. For the view factors

$$\Theta_{k,f_{ij}} = \frac{\partial r_k}{\partial f_{ij}} \tag{4}$$

for the emissivities

$$\Theta_{k,\epsilon_i} = \frac{\partial r_k}{\partial \epsilon_i} \tag{5}$$

and for the temperatures

$$\Theta_{k,t_i} = \frac{\partial r_k}{\partial t_i} \tag{6}$$

The terms can be computed efficiently for small problems (considering algebra, programming, and computation time) by direct brute-force finite differences. The forward finite difference formula gives

$$\Theta_{k,x} = \frac{r_k(x + \delta x) - r_k(x)}{\delta x} \tag{7}$$

For the six-surface enclosure considered by Miguel and Simon, this approach would require 49 complete solutions of the enclosure problem to compute the derivatives in equations (4), (5), and (6). For large problems this can become onerous. Also, simple forward differences can be troublesome if the scales are not considered. Fortunately, the direct computation of the sensitivity coefficients is straight forward.

Sensitivity Analysis

The sensitivity computations can be reduced to a series of matrix multiplications by direct expansion of equations (1) and (2). But first a brief consideration of their origin is in order. The radiosity on a surface can be written as the sum of the emitted and reflected radiation

$$q_o = \sigma D_\epsilon D_t^4 i + (I - D_\epsilon) q_i \tag{8}$$

where $\mathbf{q}_i$ is the irradiation. For a diffuse enclosure the irradiation can be written in terms of the radiosities as

$$D_a q_i = F^T D_a q_o \tag{9}$$

where $\mathbf{D}_a$ is the diagonal matrix with the surface areas as members. Solving equation (9) for $\mathbf{q}_i$, substituting into equation (8), and rearranging gives

$$[I - (I - D_\epsilon) D_a^{-1} F^T D_a] q_o = \sigma D_\epsilon D_t^4 i \tag{10}$$

The net heat rate on the surfaces is given by the difference between the radiosity and irradiation as

$$D_e q = D_e q_o - D_e q_i \tag{11}$$

Using equation (9) and rearranging yields

$$q = (I - D_e^{-1} F^T D_e) q_o \tag{12}$$

Usually at this stage of the development the view factor reciprocity relationship

$$F^T D_e = D_e F \tag{13}$$

is substituted into equations (10) and (12) to give equations (1) and (2). However, in this investigation, we are interested in the sensitivity of this analysis to perturbations in the view factors where reciprocity is not strictly enforced. In this case, it is more appropriate to work with equations (10) and (12) directly so that the sensitivities are properly weighted.

A term-by-term differentiation of equation (10) with respect to f_{ij} gives

$$-(I - D_e) D_e^{-1} \frac{\partial F^T}{\partial f_{ij}} D_e q_o + [I - (I - D_e) D_e^{-1} F^T D_e] \frac{\partial q_o}{\partial f_{ij}} = 0 \tag{14}$$

which can be solved for the radiosity sensitivities using the matrix inverse

$$\frac{\partial q_o}{\partial f_{ij}} = [I - (I - D_e) D_e^{-1} F^T D_e]^{-1} [(I - D_e) D_e^{-1} \frac{\partial F^T}{\partial f_{ij}} D_e q_e] \tag{15}$$

A term-by-term differentiation of equation (12) results in

$$\frac{\partial q}{\partial f_{ij}} = -D_e^{-1} \frac{\partial F^T}{\partial f_{ij}} D_e q_o + (I - D_e^{-1} F^T D_e) \frac{\partial q_o}{\partial f_{ij}} \tag{16}$$

Likewise, for the sensitivities with respect to emissivity, a term-by-term differentiation of equation (10) gives

$$\frac{\partial D_e}{\partial \epsilon_i} D_e^{-1} F^T D_e q_o + [I - (I - D_e) D_e^{-1} F^T D_e] \frac{\partial q_o}{\partial \epsilon_i} = \sigma \frac{\partial D_e}{\partial \epsilon_i} D_i^4 i \tag{17}$$

Solving for the radiosity sensitivities yields

$$\frac{\partial q_o}{\partial \epsilon_i} = [I - (I - D_e) D_e^{-1} F^T D_e]^{-1} [\sigma \frac{\partial D_e}{\partial \epsilon_i} D_i^4 i - \frac{\partial D_e}{\partial \epsilon_i} D_e^{-1} F^T D_e q_e] \tag{18}$$

A term-by-term differentiation of equation (12) results in

$$\frac{\partial q}{\partial \epsilon_i} = (I - D_a^{-1} F^T D_a) \frac{\partial q_o}{\partial \epsilon_i} \tag{19}$$

Finally, for the sensitivities with respect to temperature, differentiation of equation (10) gives

$$[I - (I - D_\epsilon) D_a^{-1} F^T D_a] \frac{\partial q_o}{\partial t_i} = \sigma D_\epsilon 4 D_t^3 1_i \tag{20}$$

where 1_i is a vector with 1 at location i and zeros otherwise. Solving for the sensitivities

$$\frac{\partial q_o}{\partial t_i} = [I - (I - D_\epsilon) D_\epsilon F^T D_a]^{-1} [\sigma D_\epsilon 4 D_t^3 1_i] \tag{21}$$

Equation (12) yields as before

$$\frac{\partial q}{\partial t_i} = (I - D_a^{-1} F^T D_a) \frac{\partial q_o}{\partial t_i} \tag{22}$$

The calculation procedure for heat flux and uncertainties is as follows:

1) Invert $[I - (I - D_\epsilon) D_a^{-1} F^T D_a]^{-1}$
2) Compute q_o by multiplication with $\sigma D_\epsilon D_t^4 i$
3) Compute q using equation (12)
4) Compute the radiosity derivatives using equations (15), (18), and (21).
5) Compute the heat flux derivatives using equations (16), (19), and (22).
6) Compute the uncertainties using equation (3).

In this procedure, only one matrix inversion is required. All of the other computations involve only matrix multiplication.

APPLICATION FOR MIGUEL AND SIMON'S PROBLEM

The uncertainty analysis discussed above was added to the diffuse-gray enclosure computer program, and the analysis was carried out using Miguel's input data. For sensitivities with respect to the view factors, four cases are considered: a) all view factors are independently specified, 2) closure is enforced alone, 3) reciprocity is enforced alone, and 4) both closure and reciprocity are enforced simultaneously. That discussion is followed by an examination of the sensitivities with respect to emissivity and temperature and the overall uncertainty problem.

The difference in the four cases for view factor results from the formation of the view factor matrix transpose $\mathbf{F}^T$. If all view factors are independent (closure and reciprocity not enforced) the derivative, $\partial \mathbf{F}^T / \partial f_{ij}$, only has one nonzero element, a 1 at place (j,i). Table 3 shows the normalized sensitivities with respect to the view factors for the heat flux on the three active surfaces. Considering that the view factors are of order 1, the heat flux on surface 1 is seen to be hypersensitive to uncertainties in view factors from the first column of $\mathbf{F}^T$ and strongly sensitive to the other view factor uncertainties. The heat flux on the second surface is much better behaved but still has a strong sensitivity to uncertainty

Table 3: Normalized sensitivities with respect to view factors for the active surfaces in Miguel and Simon's problem with neither closure nor reciprocity enforced.

Surface	$\Theta_{kf_{ij}}/q_k$					
k = 1	124.17	7.47	18.21	53.73	53.72	53.72
	138.46	8.32	20.30	59.91	59.89	59.89
	67.08	4.03	9.84	29.02	29.02	29.02
	82.35	4.95	12.08	35.63	35.62	35.62
	49.41	2.97	7.24	21.38	21.37	21.37
	49.41	2.97	7.24	21.38	21.37	21.37
k = 2	-0.74	-6.02	-0.94	-2.76	-2.76	-2.76
	-0.82	-6.71	-1.04	-3.08	-3.08	-3.08
	-0.40	-3.25	-0.51	-1.49	-1.49	-1.49
	-0.49	-3.99	-0.62	-1.83	-1.83	-1.83
	-0.29	-2.40	-0.37	-1.10	-1.10	-1.10
	-0.29	-2.40	-0.37	-1.10	-1.10	-1.10
k = 3	0.33	0.17	4.99	1.45	1.45	1.45
	0.36	0.19	5.56	1.62	1.62	1.62
	0.18	0.09	2.69	0.78	0.79	0.79
	0.22	0.11	3.31	0.96	0.96	0.96
	0.13	0.07	1.98	0.58	0.58	0.58
	0.13	0.07	1.98	0.58	0.58	0.58

in the second column of $\mathbf{F}^T$. The third surface is relatively less sensitive but is by no means insensitive. The third column has normalized sensitivities of order 3, and the other view factors have normalized sensitivities of order 0.1 to 1.0.

This clearly shows the origin of Simon's difficulty. If all view-factor uncertainties are assumed to be equal (U_{fij} = const) in equation (3) and all uncertainties in emissivity and temperature are ignored, the uncertainty in heat flux is given by

$$\frac{U_{q_k}}{q_k} = U_{f_{ij}} \sqrt{\sum_{i=1}^{N} \sum_{j=1}^{N} \frac{\Theta_{k,f_{ij}}^2}{q_k}} \tag{23}$$

which gives for each active surface

$$\frac{U_{q_1}}{q_1} = 283.74\ U_{f_{ij}} \tag{24}$$

$$\frac{U_{q_2}}{q_2} = 14.12\ U_{f_{ij}} \tag{25}$$

$$\frac{U_{q_3}}{q_3} = 10.20\ U_{f_{ij}} \tag{26}$$

Table 4: Normalized sensitivities with respect to view factors for the active surfaces in Miguel and Simon's problem with closure enforced.

Surface	$\Theta_{kf_{ij}}/q_k$					
k = 1	----	-118.73	-107.81	-71.67	-71.71	-71.71
	132.39	----	12.18	52.48	52.44	52.44
	58.23	-5.90	----	19.52	19.50	19.50
	47.53	-31.21	-23.96	----	-0.02	-0.02
	28.52	-18.70	-14.36	0.01	----	0.00
	28.52	-18.70	-14.36	0.01	0.00	----
k = 2	----	-5.28	-0.20	-2.02	-2.02	-2.02
	5.89	----	5.67	3.63	3.64	3.64
	0.11	-2.75	----	-0.98	-0.98	-0.98
	1.34	-2.16	1.21	----	0.00	0.00
	0.80	-1.30	0.72	0.00	----	0.00
	0.80	-1.30	0.72	0.00	0.00	----
k = 3	----	-0.16	4.66	1.13	1.13	1.13
	0.17	----	5.37	1.43	1.43	1.43
	-2.52	-2.60	----	-1.91	-1.91	-1.91
	-0.75	-0.85	2.34	----	0.00	0.00
	-0.45	-0.51	1.41	0.00	----	0.00
	-0.45	-0.51	1.41	0.00	0.00	----

To obtain 5% accuracy in q_1, $U_{f_{ij}}$ must be less than 0.0001546, or the view factors must be known with approximately 4 digit accuracy. On the other hand, to obtain 5% accuracy in q_3 requires $U_{f_{ij}}$ less than 0.0057 or about 2 digit accuracy. This is in line with Simon's experience. His maximum error was 0.014 on F_{12} and F_{21}. This resulted in 376% error for q_1 but only 13% error for q_3.

If closure is enforced by computing the diagonal elements from

$$f_{ii} = 1 - \sum_{\substack{j=1 \\ j \neq i}}^{N} f_{ij} \tag{27}$$

the derivative $\partial \mathbf{F}^T/\partial f_{ij}$ contains two nonzero terms--a -1 at place (i,i) and a 1 at place (j,i). Table 4 shows the results of the sensitivity analysis for heat flux when closure is enforced. The table shows that closure alone does not reduce the overall sensitivity. Normalized sensitivity coefficients of 100 are still found. In our previous work with Simon's solution it appeared that enforcing closure greatly improved the results. However, equation 1 implicitly assumes that reciprocity exists and Simon's view factors reasonably meet that reciprocity requirement.

When reciprocity is imposed cross-diagonal terms in **F** are related by

$$a_i f_{ij} = a_j f_{ji} \tag{28}$$

In this case, view factors in the lower-left triangle of **F** are computed from those in the upper-right triangle by equation (28). Table 5 shows the results of the sensitivity analysis when only reciprocity is enforced. No improvement is seen. In fact, for this case the overall uncertainty in heat flux would be higher than the case where reciprocity is not enforced.

Table 5: Normalized sensitivities with respect to view factors for the active surfaces in Miguel and Simon's problem with reciprocity enforced.

Surface	$\Theta_{kf_{ij}}/q_k$					
k = 1	124.91	146.78	119.53	178.32	178.26	178.26
	----	8.37	26.51	67.74	67.70	67.70
	----	----	9.89	41.35	41.33	41.33
	----	----	----	35.85	71.67	71.67
	----	----	----	----	21.49	42.98
	----	----	----	----	----	21.49
k = 2	-0.74	-6.84	-1.53	-3.49	-3.49	-3.49
	----	-6.71	-5.92	-9.07	-9.06	-9.06
	----	----	-0.51	-2.11	-2.11	-2.11
	----	----	----	-1.83	-3.66	-3.66
	----	----	----	----	-1.10	-2.19
	----	----	----	----	----	-1.10
k = 3	0.33	0.53	5.25	1.77	1.78	1.78
	----	0.19	5.69	1.79	1.79	1.79
	----	----	2.69	4.09	4.09	4.09
	----	----	----	0.96	1.93	1.93
	----	----	----	----	0.58	1.16
	----	----	----	----	----	0.58

Table 6 shows the results when both reciprocity and closure are simultaneously enforced using equations (27) and (28). An order of magnitude decrease in the sensitivities is observed. If the uncertainties in f_{ij} are again taken to be constant and the uncertainties in emissivity and temperature are ignored, the uncertainties for the active surfaces are given by

$$\frac{U_{q_1}}{q_1} = 27.78\ U_{f_{ij}} \tag{29}$$

$$\frac{U_{q_2}}{q_2} = 1.83\ U_{f_{ij}} \tag{30}$$

$$\frac{U_{q_3}}{q_3} = 1.89\ U_{f_{ij}} \tag{31}$$

Now, to obtain 5% accuracy in q_1, the uncertainty in f_{ij} must be less than 0.0018 which is between 2 and 3 digit accuracy. Recall that, when Simon's view factors were revised to enforce closure, reciprocity was implicitly included in equation (1), and the error for q_1 was 21%, which is in line with equation (29).

The sensitivity analysis has given us a great deal of insight into the hypersensitivity of Simon's problem. It has improved our understanding of why enforcing closure in Simon's case so greatly improved the problem and has shown that this improvement actually requires the simultaneous enforcement of both closure and reciprocity for the view factors. We can draw the conclusion that both closure and reciprocity should be strictly enforced to minimize the sensitivity of the diffuse-gray enclosure analysis to errors in view factors.

For simple geometries such as this one, view factor determination can be made with whatever accuracy is necessary. However, the material properties, emissivities, process specifications, and

Table 6: Normalized sensitivities with respect to view factors for the active surfaces in Miguel and Simon's problem with both closure and reciprocity enforced.

Surface	$\Theta_{k,f_{ij}}/q_k$					
k = 1	----	13.66	-20.46	-0.38	-0.39	-0.39
	----	----	3.33	5.67	5.67	5.67
	----	----	----	-4.45	-4.44	-4.44
	----	----	----	----	0.00	0.00
	----	----	----	----	----	0.00
k = 2	----	0.61	-0.04	-0.01	-0.01	-0.01
	----	----	1.55	0.39	0.39	0.39
	----	----	----	0.22	0.22	0.22
	----	----	----	----	0.00	0.00
	----	----	----	----	----	0.00
k = 3	----	0.02	0.88	0.01	0.01	0.01
	----	----	1.47	0.15	0.15	0.15
	----	----	----	0.43	0.43	0.43
	----	----	----	----	0.00	0.00
	----	----	----	----	----	0.00

temperatures will always contain uncertainties. Table 7 shows the normalized sensitivities for this problem with respect to emissivity and temperature for the three active surfaces. The normalized sensitivities to errors in emissivity are on the order of 10 which is about the same as the view factor sensitivities with both closure and reciprocity enforced. The normalized sensitivity to errors in temperature are on the order of 1. Care must be taken when comparing these normalized sensitivities if the variables have vastly different scales. Emissivity is on the order of 1 while temperature in degrees K is on the order of 100-1000. An absolute error of 5°K will cause much more error in the heat flux result in this problem than a 0.05 error in emissivity.

Using the uncertainty values ($U_{f_{ij}} = 0.0001$; $U_{\epsilon_i} = 0.1$, i = 1,2,3; $U_{\epsilon_i} = 0$, i = 4,5A,5B; U_{t_i} = 1°K, i = 1,2,3; and $U_{t_i} = 0$, i = 4,5A,5B) and Miguel's view factors with both reciprocity and closure enforced, gives the heat flux and uncertainty results shown in Table 8. The table shows that these very reasonable uncertainties result in significant uncertainties in the heat transfer result. The percentage uncertainty on the nearly adiabatic surface 1 is very large. These uncertainties are mainly caused by the uncertainties in emissivity and temperature since Miguel's very precise view factors were used.

CONCLUSIONS

Uncertainty analysis was used to propagate the uncertainties in the view factors, emissivities, and temperatures into uncertainties in the computed heat flux. This analysis allowed us to determine the nature and source of the hypersensitivity to view factor in Simon's case and to find a way to reduce this hypersensitivity. It was found that to avoid hypersensitivity to view factor specification both closure and reciprocity must be simultaneously enforced. Even when the view factors are precisely specified considerable uncertainty remains because of uncertainties in emissivity and temperature specification.

The sensitivity analysis and associated uncertainty analysis are very enlightening. The computational overhead is small since only one matrix is inverted for both the diffuse-gray enclosure solution and the sensitivity analysis. Therefore, it is strongly recommended that all diffuse-gray enclosure solutions be coupled with an uncertainty analysis.

Table 7: Normalized sensitivities with respect to emissivity and temperature for the active surfaces in Miguel and Simon's problem with both closure and reciprocity enforced.

$\Theta_{k,\epsilon_i}/q_k$

Surface	1	2	3	4	5A	5B
			emissivity			
k = 1	1.01	12.97	-12.97	0.01	0.01	0.01
k = 2	0.03	0.84	0.65	0.00	0.00	0.00
k = 3	-0.01	0.29	1.27	0.00	0.00	0.00
			temperature			
k = 1	-1.24	0.96	0.29	0.00	0.00	0.00
k = 2	-0.04	0.06	-0.01	0.00	0.00	0.00
k = 3	0.02	0.02	-0.03	0.00	0.00	0.00

Table 8: Overall uncertainty in Miguel and Simon's Problem: $U_{f_{ij}} = 0.0001$, $U_{\epsilon_i} = 0.1$, $U_{\epsilon_i} = 1°K$.

	Surface		
	1	2	3
q(w)	-3.63	83.9	-120.5
U_q(w)	±8.82	±10.9	±16.4
U_q/q	±270%	±13%	±14%

REFERENCES

1. ANSI/ASME, 1986, Measurement Uncertainty, PTC 19.1-1985, Part 1.
2. Boyack, B. E., Catton, I., Duffey, R. B., Griffith, P., Katsma, K. R., Lillouche, G. S., Levy, S., Rohatgi, U. S., Wilson, G. E., Wulff, W., and Zuber, N., 1990, "Qualifying Reactor Safety Margins Part 1: An Overview of the Code Scaling, Applicability, and Uncertainty Evaluation Methodology," Nuclear Engineering and Design, Vol. 119, No. 1, pp. 1-16.
3. Brewster, M. Q., 1992, Radiative Heat Transfer, John Wiley & Sons, New York.
4. Coleman, H. W. and Steele, W. G., 1989, Experimentation and Uncertainty Analysis for Engineers, John Wiley & Sons, New York.
5. Cruz, J. B., 1973, System Sensitivity Analysis, Dowden, Hutchinson, and Ross, Stroudsburg, PA.
6. Emery, A. F. and Fadale, T. D., 1990, "Stochastic Analysis of Uncertainties in Emissivity and Conductivity by Finite Elements," Paper 90-WA/HT-11, American Society of Mechanical Engineers, New York.
7. Fadale, T. D. and Emery, A. F., 1992, "Transient Effects of Uncertainties on the Sensitivities of Temperatures and Heat Fluxes Using Stochastic Finite Elements," HTD-Vol. 204, General Papers in Heat Transfer, pp. 145-153, American Society of Mechanical Engineers, New York.

8. Incropera, F. P. and Dewitt, D. P., 1985, Fundamentals of Heat and Mass Transfer, John Wiley & Sons, New York.
9. Mehta, U. B., 1991, "Some Aspects of Uncertainty in Computational Fluid Dynamics Results," Journal of Fluids Engineering, Vol. 113, No. 4, pp. 538-543.
10. Rao, S. S., 1992, Reliability-Based Design, McGraw-Hill, New York.
11. Ronen, Y., 1988, Uncertainty Analysis, CRC Press, Boca Raton, FL.
12. Wilson, G. E., Boyack, B. E, Catton, I., Duffey, R. B., Griffith, P., Katsma, K. R., Lillouche, G. S., Levy, S., Rohatgi, U. S., Wulff, W., and Zuber, N., 1990, "Quantifying Reactor Safety Margins Part 2: Characterization of Important Contributions to Uncertainty," Nuclear Engineering and Design, Vol. 119, No. 1, pp.17-32.
13. Wulff, W., Boyack, B. E, Catton, I., Duffey, R. B., Griffith, P., Katsma, K. R., Lillouche, G. S., Levy, S., Rohatgi, U. S., Wilson, G. E., and Zuber, N., 1990, "Quantifying Reactor Safety Margins Part 3: Assessment and Ranging of Parameters," Nuclear Engineering and Design, Vol. 119, No. 1, pp.33-65.

A COMPARISON OF TSS AND TRASYS IN FORM FACTOR CALCULATION

Eric Golliher
Thermal and Fluids Analysis Branch
National Aeronautics and Space Administration
Lewis Research Center
Cleveland, Ohio 44135

INTRODUCTION

As the workstation and personal computer become more popular than a centralized mainframe to perform thermal analysis, the methods for space vehicle thermal analysis will change. Already, many thermal analysis codes are now available for workstations, which were not in existence just five years ago. As these changes occur, some organizations will adopt the new codes and analysis techniques, while others will not. This might lead to misunderstandings between thermal shops in different organizations. If thermal analysts make an effort to understand the major differences between the new and old methods, a smoother transition to a more efficient and more versatile thermal analysis environment will be realized.

DISCUSSION

As dedicated computers becomes more affordable and faster, the method for performing radiation thermal analysis using a "ray-tracing" [1] technique may become the standard. The advantage of some ray-tracing codes lies in their versatility: the ability to account for specular and transmissive surfaces, and to handle boolean geometrical constructions, fence problems, and the box-on-a-plate problem. The disadvantage is that ray-tracing has historically been thought of as less computationally efficient than the traditional method for typical space vehicle thermal design problems, which has been the "unit sphere" or "double summation" method. Since many mainframe computer departments account for costs on a per-CPU hour basis, double summation codes such as TRASYS and VectorSweep currently dominate. However, with the popularity and speed of workstations and personal computers on the rise, many new ray tracing codes and enhancements are taking shape.

Examples of some of the codes with full ray-tracing capability are ESARAD (European Space Agency Research and Technology Center), NEVADA (Turner Associates), OPERA (Boeing Monte Carlo), TMG (Thermal Model Generator from Maya Heat Transfer), and TSS (Thermal Synthesizer System, sponsored by NASA-JSC). Since the workstation costs are typically accounted as a one-time purchase cost, the perceived longer "run-times" with workstations are not a cost issue. Also, since most large satellite/space station thermal problems require many hours of CPU time on a mainframe as well as on a workstation, the "turn-around" time for both is comparable.

This discussion centers on two codes used in form factor radiation thermal analysis for space vehicles: TSS, as an example of a ray-tracing code, and TRASYS, an example of the unit sphere method. A comparison among the different ray-tracing codes is beyond the scope of this paper. Also, a comparison of the orbital heating rate calculations is not the subject of this paper; although

it is acknowledged that the issues described here may cause similar problems with the heating rate algorithms as well.

The motivation for this report came about during a recent project in which NASA-LeRC was involved, called SOHO (Solar and Heliospheric Observatory). The satellite is being integrated by Matra-Marconi of France under contract to ESA/ESTEC in Noordwijk, Holland. The launch vehicle, an Atlas IIAS, is being provided by General Dynamics Commercial Launch Services under contract to NASA-LeRC. The launch date is June 1995. Figure 1 shows the ITPLOT[2] TRASYS plot of the SOHO spacecraft.

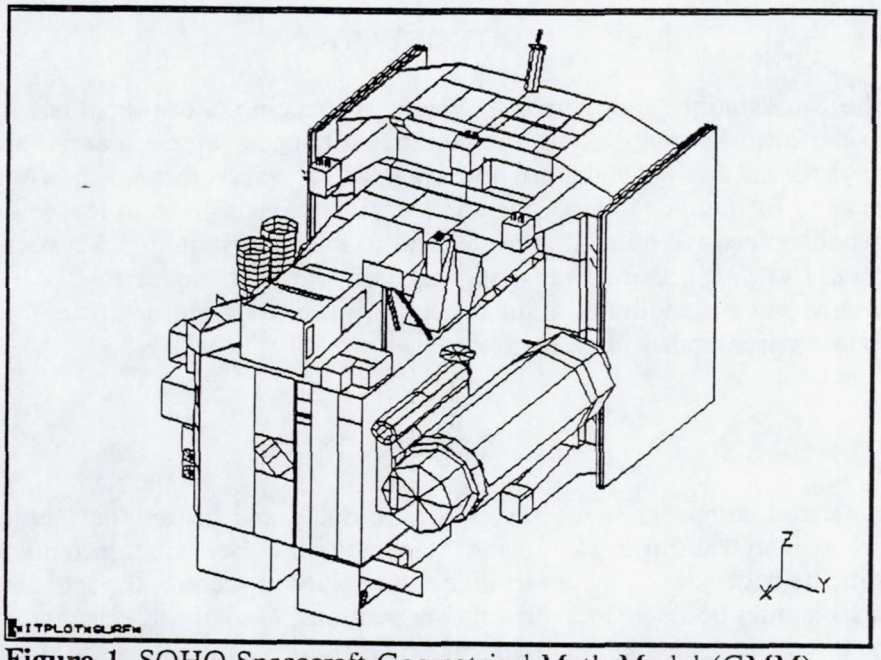

Figure 1 SOHO Spacecraft Geometrical Math Model (GMM)

Recently, ESA/MATRA delivered to NASA/GD simplified thermal models of the satellite which contained approximately 800 surfaces. NASA intended to use TRASYS, a Nusselt sphere-type code, to perform the integrated thermal analysis of the launch phase of the mission. The original GMM was created by Matra in Toulousse, France using ESABASE, a geometry builder for their ray-tracing type radiation thermal analysis code, THERMICA. Therefore, a conversion program had to be written at LeRC to convert ESABASE to TRASYS. The converted GMM was used to generate Hottel-type radiation conductors (RADK's) in TRASYS and then in TSS. After the conversion process, NASA-LeRC plotted the TRASYS surfaces. There appeared to be many surfaces running into each other and many box-on-a-plate problems. It was learned however, that these types of "errors" can, in fact, be handled by ray tracing type codes. Thus, this report can serve as a "lessons learned" from a user's perspective.

It was decided to try using a ray-tracing code at NASA/LeRC to confirm the original TRASYS/SINDA SOHO launch phase temperature predictions[3]. The intent was to compare form factors directly using TSS at NASA/LeRC. However, this became too unwieldy for an 800-node model. A more practical approach was taken. Final temperatures from various SINDA analyses were

compared for the corresponding Thermal Math Model (TMM). In each situation, the original SINDA thermal math model contained only TRASYS-generated heating rates and radiation conductors (RADK's). Then, RADK's generated by TSS were switched for those generated by TRASYS, and the temperatures compared.

When using TRASYS, the analyst has a variety of options in the FFDATA and RKDATA statements which control the accuracy of the resultant form factors. Over the years, typical parameters which seem to work well for most space vehicle analysis have been developed through trial and error. Also, rules and techniques for "good" TRASYS model-building have been established[4]. Since it was known that the model in this case contained box-on-plate problems, it was decided to push TRASYS to its limit with some unreasonably tight FFDATA parameters: NELCT=200, FFRATL=-1.0, and FFACS=0.01. The CPU time for RADK's was approximately 8 hours on a VAX 9410.

When using TSS or any other ray-tracing code, the analyst must deal with a completely different set of control parameters and these are generally not well known to engineers familiar with TRASYS. These parameters include Energy Cut Off Factor, Number of Rays per Surface, Numbers of Levels and Objects in the Oct-Tree Accelerator, Random Number Generator Seed Value, Error Parameter, and the Update parameter[5,6]. The Error Parameter applies to an individual surface and is a function of the confidence level.[6] Also, a working knowledge of engineering statistics is helpful in understanding ray-tracing codes.

ANALYSIS AND RESULTS

Figure 2 shows a plot of CPU time on the Apollo DN10000 versus number of rays and error. The default value was used for the other parameters.

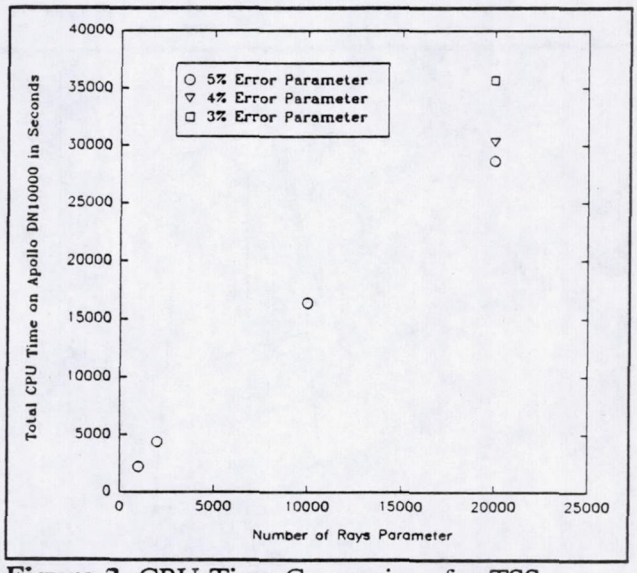

Figure 2 CPU Time Comparison for TSS Parameters

The TSS parameters were successively varied as such: 1000 rays to 20,000 rays with a 5 % Error Parameter, then 20,000 rays with a 4% Error Parameter, and finally 20,000 rays with a 3% Error Parameter. The TSS analyst can effectively use a "restart" file to build upon calculations already performed in previous analyses. For TRASYS, the analyst can increase the accuracy for a particular surface, but the calculations effectively start over for that surface.

As the number of rays per surface increases, the error will decrease. TSS will generate rays from a particular surface until either the Number of Rays or the Maximum Error Parameter is reached. This condition is checked as often as is required by the Update Parameter. For 1000 rays and 5% error, the Number of Rays is the limiting parameter for most surfaces in this problem. For 20,000 rays and 5% error, the Error Parameter is limiting the calculations for some surfaces and fewer than 20,000 rays are generated for many surfaces. As the Number of Rays parameter is increased, it is more likely that the Error Parameter will control the calculations of most surfaces in the problem. The user has the option of forcing practically all surfaces to the same error by setting the Number of Rays equal to a very large number.

If the Error Parameter had the controlled the calculations, the plot would show that the percentage of CPU time increases as the square of the improvement in error. The roughly linear relationship of CPU time to Number of Rays shown in Figure 2 is expected. In this case, the error is different for each surface.

Figure 3 is a close-up view of an instrument which shows a 4-sided boxed protruding through the mounting structure. All surfaces are facing outward. Note that a portion of the active surfaces of the central box view the inactive surfaces of the prism-shaped mounting structure. Also, note that this structure sits directly on a larger rectangle which forms the payload support wall, an example of the box-on-a-plate problem (see Figure 1). This is a typical construction found in the Matra GMM which cannot be handled well by TRASYS, but is acceptable to the Matra ray-tracing package, THERMICA.

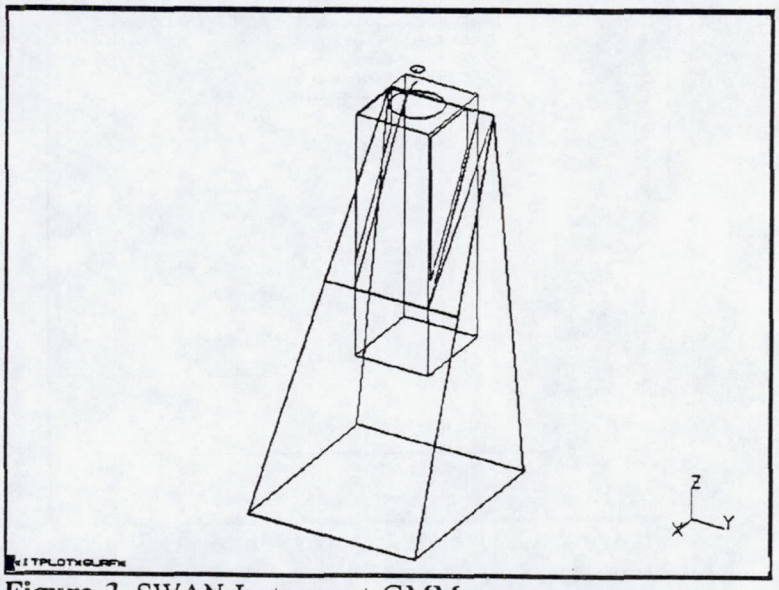

Figure 3 SWAN Instrument GMM

Figures 4 and 5 show the distribution of the difference between temperatures from successive analyses using various TSS and TRASYS RADK's.

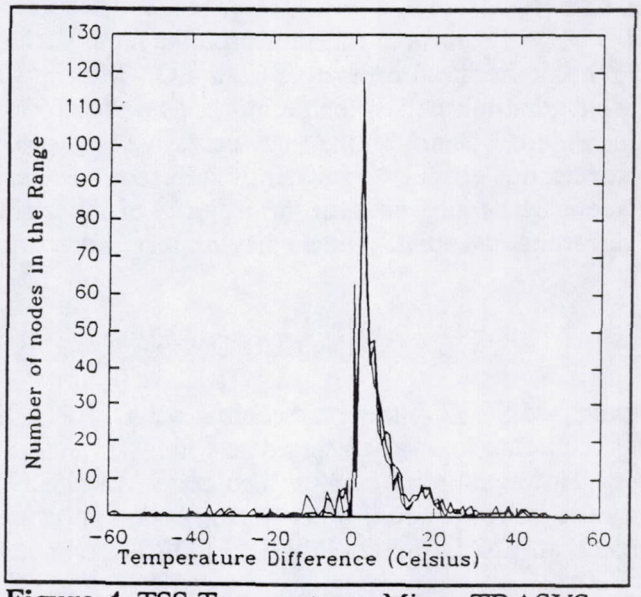

Figure 4 TSS Temperatures Minus TRASYS Temperatures

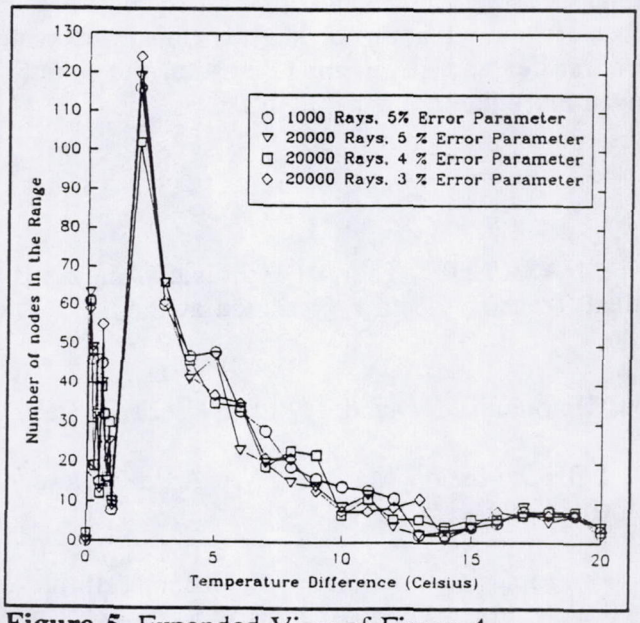

Figure 5 Expanded View of Figure 4

To get this plot, the temperatures produced by TRASYS RADK's were subtracted from those produced by TSS. If the two methods gave exactly the same answers, there would be nothing but a peak at 0 °C. There seems to be a distinct shift in a majority of temperatures by about 2 to 12 °C

warmer for most of the TSS values. This is because TSS has greater view factors to the spacecraft surfaces and therefore smaller views to space. The original TRASYS results showed form factors sums for some surfaces to be far from 1.0. Also, for TSS, weighted error results for several small form factors exceeded 5%. Therefore, for this problem and perhaps for many other similar situations, using TRASYS to generate form factors from a GMM originally constructed for use with a ray tracing code may yield generally colder temperatures as well as in some cases, significant errors, both warmer and colder. Figure 5 clearly shows that successive analyses of TSS using more rays and a smaller error parameter do not produce significantly different results. Therefore, 1000 rays with a 5% Error Parameter seems to be adequate for the majority of the surfaces for a model of this size and type. Of course, different spacecraft models may require more rays.

CONCLUSION

Although the converted SOHO model did contain what TRASYS-trained analysts might call "errors," the model was acceptable to a ray-tracing type code. TRASYS did a surprisingly good job on most of the surfaces. However, results of the two codes do differ for a significant number of surfaces. This model should be reworked if a ray tracing code is not used. Also, as a result of the work on the SOHO project, an ESABASE-to-TRASYS FORTRAN conversion program is available at NASA-LeRC.

If a "cookbook" set of parameters to use with various types and sizes of typical space vehicle thermal models could be provided, this would reduce the confusion and ease the transition to TSS or any ray-tracing program. If, however, TSS and other ray tracing codes must be carefully optimized for each particular spacecraft and situation, or if a ray tracing user must thoroughly understand advanced radiation heat transfer and engineering statistics, the popularity of TSS and other ray tracing codes may be much more limited than TRASYS.

References

1. Baumeister, Joseph F., NASA/LeRC, Thermal and Fluids Analysis Branch, "Application of Ray Tracing in Radiation Heat Transfer," lecture presented at the 1993 Thermal and Fluids Analysis Workshop.

2. Analytix Corporation, Timonium Maryland, ITPLOT User's Guide, December 1990.

3. Sagerman, Gary D., SOHO Mission Manager, NASA/LeRC Launch Vehicle Project Office, personal communication, June 1993.

4. Tsuyuki, Glenn T., Jet Propulsion Laboratory, California Institute of Technology, "Advanced TRASYS" shortcourse at the Thermal Fluids Analysis Workshop.

5. Rickman, Steven L., ES34/Thermal Analysis Section, NASA/JSC,"TSS Tutorial," February 1993.

6. Lockheed Missiles and Space Company, Sunnyvale, California, "User Manual, Thermal Synthesizer System," December 18, 1992.

ACCURACY CONTROL IN MONTECARLO RADIATIVE CALCULATIONS

P. Planas Almazan
Thermal Control and Life Support Division
ESA/ESTEC, P.O. Box 299
2200 AG Noordwijk, The Netherlands

SUMMARY

This paper presents the general accuracy law that rules the MonteCarlo, ray-tracing algorithms used commonly for the calculation of the radiative entities in the thermal analysis of spacecraft. These entities involve transfer of radiative energy either from a single source to a target (e.g., the configuration factors), or from several sources to a target (e.g., the absorbed heat fluxes). In fact, the former is just a particular case of the latter. The accuracy model is later applied to the calculation of some specific radiative entities. Furthermore, some issues related to the implementation of such a model in a software tool are discussed. Although only the relative error is considered through the discussion, similar results can be derived for the absolute error.

INTRODUCTION

Monte Carlo methods are often used in combination with ray-tracing algorithms to perform the radiative analysis of spacecraft (ref. [1]). Using this approach (MCRT from now on), the radiative couplings between the faces of a model, as well as the external heat loads applied on these faces, are calculated. Normally, these radiative values are passed to a thermal solver in order to produce the temperature predictions for the spacecraft model.

While MCRT-based tools present some interesting advantages with respect to other methods, they also show a major drawback, which is the often large computational effort required to produce the radiative values. The results of a MCRT simulation are taken as an estimation of the actual values of the radiative entities. Since these results are of random nature, the accuracy of the estimation depends on the number of rays fired in the simulation. In general, the thermal engineer performs a trade off between the accuracy of the results and the computational effort required to achieve them. This paper presents models which allow the automatic accuracy control of the results in an efficient way.

It is important to point out that the simulation inaccuracies only account for a part of the uncertainty in the results of the thermal analysis. Other sources of error are the validity of the modelling assumptions and the uncertainty of the data used in these models (ref. [2]). The "engineering judgement" shall be used to decide which level of accuracy in the simulation is sensibly required, especially when compared to the uncertainties in the other areas. Once the simulation's accuracy requirements have been established, their efficient achievement can be guaranteed by the techniques presented in this paper.

BASIC ACCURACY MODEL

MCRT methods are based on the repetition of a given random process, which reproduces the physical problem of interest (ref. [3]). For each trial, values of the random parameters that play a role in the process are uniformly sampled from their cumulative distribution functions, and a score T, representative of the physical phenomenon, is tallied. T is a random variable that follows an arbitrary distribution:

$$T - (E(T), V(T)) \qquad \text{(EQ 1)}$$

where E(T) is the expectation of T and V(T) the variance of T. The estimation r* of the radiative parameter R is then calculated by averaging the scores over a large number of trials:

$$r^* = \frac{1}{N} \cdot \sum_{l=1}^{N} t_l \qquad \text{(EQ 2)}$$

where t_l is the score for the l-th trial and N is the total number of trials. In the MCRT simulations, each trial involves firing a ray from the source. Because of the random nature of the process, every simulation produces a different estimated value, and therefore the estimation R* is a random variable itself. By the central limit theorem (ref. [4]), given N reasonably large, R* is normally distributed, regardless of the actual shape of the distribution for the basic random variable T:

$$R^* - N(E(R^*), V(R^*)) \qquad \text{(EQ 3)}$$

where:

$$E(R^*) \equiv \mu_{R^*} = E(T) = R \qquad \text{(EQ 4)}$$

$$V(R^*) \equiv \sigma^2_{R^*} = \frac{V(T)}{N} \qquad \text{(EQ 5)}$$

By definition, the relative error of an estimated value r* is:

$$e \equiv \frac{r^* - R}{R} \qquad \text{(EQ 6)}$$

By applying the algebra of random variables, it is possible to show that the relative error of the estimated values is also normally distributed:

$$E - N(E(E), V(E)) \qquad \text{(EQ 7)}$$

with expectation and variance given by:

$$E(E) \equiv \mu_E = 0 \qquad \text{(EQ 8)}$$

$$V(E) \equiv \sigma^2_E = \frac{V(R^*)}{R^2} = \frac{V(T)}{N \cdot R^2} \qquad \text{(EQ 9)}$$

Given the normal law followed by the simulation error, the probability α of having a relative error smaller than ε is:

$$\alpha \equiv \text{Prob}\,(e < \varepsilon) = \text{erf}\left(\frac{\varepsilon}{\sqrt{2 \cdot \sigma^2_E}}\right) \qquad \text{(EQ 10)}$$

and replacing (eq 9) into (eq 10) the fundamental accuracy model is derived:

$$N_\varepsilon = 2 \cdot \left(\frac{\text{erf}^{-1}(\alpha)}{\varepsilon}\right)^2 \cdot \frac{V(T)}{R^2} \qquad \text{(EQ 11)}$$

This expression is very important for our purposes, because it provides a relationship between the accuracy ε to be achieved and the computational effort (number of rays N_ε) required for it, in terms of the radiative value itself, the variance of the basic random process used in the MCRT simulation and the confidence level α. Furthermore, (eq 11) shows that the accuracy achieved is inversely proportional to the square root of the number of rays fired in the simulation (i. e., to halve the relative error the number of rays has to be multiplied by four).

For a given confidence level α, if N_ε rays are fired to ensure a level of accuracy of ε, the variance of the relative error depends only on ε:

$$V(E_\varepsilon) = \frac{1}{2} \cdot \left(\frac{\varepsilon}{\text{erf}^{-1}(\alpha)}\right)^2 \qquad \text{(EQ 12)}$$

That is, the variance of the relative error is directly proportional to the square of the level of accuracy specified. Once the accuracy requirements are fixed, the variance of the errors associated to the estimation of different values do not depend on the actual values or on the variance of the basic random processes. This is an interesting property which is used later in the paper to introduce an efficient way to calculate reciprocal couplings.

ACCURACY CONTROL FOR RADIATIVE PARAMETERS

Configuration Factors

The configuration (or view) factors represent the fraction of diffuse energy uniformly emitted by a radiative face and reaching directly (i. e., without suffering any intermediate reflection) a target face. The procedure followed in the MCRT approach to determine the configuration factors is based on the repetition of a process consisting of the following steps:

- calculate a random emission point on the emitting radiative face
- calculate a random emission direction
- calculate the intersection between the ray fired from the emission point and directed along the emission direction, and the target radiative face
- tally the ray if the intersection is not void

Finally, the estimated value f* is calculated as the average of all the trials performed:

$$f^* = \frac{1}{N} \cdot \sum_{l=1}^{N} t_l \qquad \text{(EQ 13)}$$

Thus, this algorithm tallies the random variable T, which in this case represents the intersection between a randomly emitted ray and the target radiative face. T is a discrete random variable, which only can take two possible values: 0 if the intersection is void and 1 if the ray strikes the target radiative face. Since this is a rather simple process, the distribution function of the random variable T can be determined by only knowing the value of the configuration factor F, as shown in Figure 1.

The expectation and variance of T can be calculated by applying the expressions used for discrete random variables:

$$E(T) = \sum_{k=1}^{s} t_k \cdot P(t_k) \qquad \text{(EQ 14)}$$

$$V(T) = \sum_{k=1}^{s} (t_k - E(T))^2 \cdot P(t_k) \qquad \text{(EQ 15)}$$

where s is the number of discrete values which the random variable can take. Applying these expressions to T, with s = 2 corresponding to the only two possible values 0 and 1, we obtain:

$$E(T) = F \qquad \text{(EQ 16)}$$

$$V(T) = F \cdot (1 - F) \qquad \text{(EQ 17)}$$

where F is the actual value of the configuration factor.

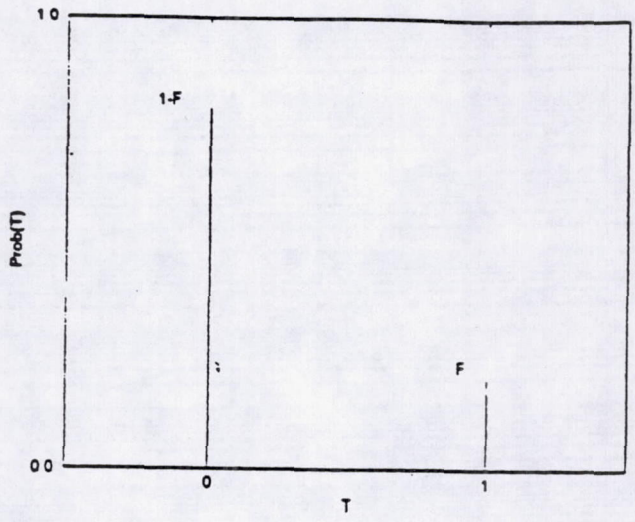

FIGURE 1. Probability distribution function for the random variable T, intersection ray/target face

Introducing these values into the general accuracy model given by (eq 11), the accuracy control law for the configuration factors can be derived:

$$N_\varepsilon = 2 \cdot \left(\frac{\mathrm{erf}^{-1}(\alpha)}{\varepsilon} \right)^2 \cdot \frac{1-F}{F} \qquad \text{(EQ 18)}$$

From this expression it can be appreciated that, in agreement with the experience, bounding the accuracy for small configuration factors is much more computationally demanding than doing so for large values.

Due to the fact that the variance of the basic random process depends exclusively on the value of the configuration factor, once this value F is fixed it is possible to specify the number of rays to be fired in order to achieve the desired accuracy. Figure 2 shows the computational effort (i. e. number of rays fired from the radiative face) required to achieve three different accuracy levels (relative errors of 100%, 10% and 1%) for the whole range of configuration factor values.

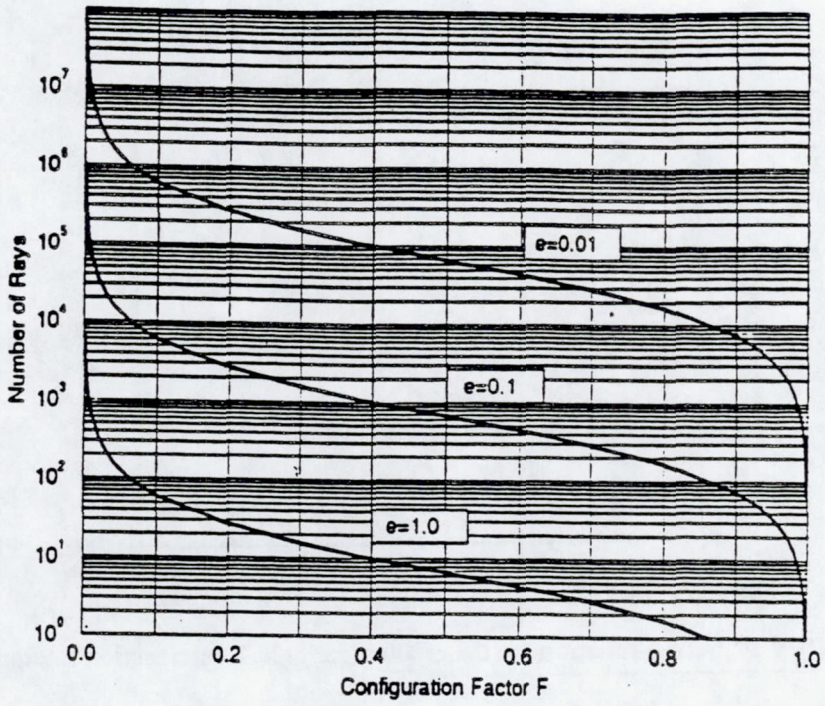

FIGURE 2. Computational effort vs configuration factor value for several levels of accuracy (confidence level of 99%)

Radiative exchange factors

The radiative exchange factors (REF) are defined as the fraction of diffuse energy uniformly emitted by a radiative face and being finally absorbed by a target face. Multi-reflection paths are included in this definition. These values can be derived from the configuration factors, following Gebhart's method (ref. [5]). Alternatively, the MCRT approach offers some advantages, taking into account the non-uniform nature of the radiative transfer exchange between radiative faces, as well as allowing the inclusion of specular behaviour. The procedure followed for each radiative face is in this case:

- calculate a random emission point on the emitting radiative face
- calculate a random emission direction
- propagate the ray fired from the emission point and directed along the emission direction through the model. For the propagation take into account the radiative behaviour of the surfaces
- tally the fraction of the original ray's energy which is finally absorbed by the target face (random variable T)

Following this algorithm, the estimation of the REF value G is calculated by the expression:

$$g^* = \frac{1}{N} \cdot \sum_{l=1}^{N} t_l \qquad \text{(EQ 19)}$$

The main difference with the configuration factors case is that it is not possible to know a priori the nature of the probability distribution function of the random variable T. Indeed, T can take different values depending on the path followed by the rays, and the number of possible paths grows significantly with the number of radiative faces in the model. Nevertheless, regardless of this fact the powerful central limit theorem is valid and (eq 11) still applies. Therefore, the accuracy control model for REF can be expressed as:

$$N_\varepsilon = 2 \cdot \left(\frac{\mathrm{erf}^{-1}(\alpha)}{\varepsilon} \right)^2 \cdot \frac{V(T)}{G^2} \qquad \text{(EQ 20)}$$

Thus, in the REF case, the computational effort depends explicitly not only on the value of the REF but also on the variance of the basic random process.

Direct Solar Flux

The heat flux emitted by the Sun and being intercepted by a given target radiative face can be calculated as:

$$D = SC \cdot A^{\perp} \qquad \text{(EQ 21)}$$

where SC is the solar constant and $A^{\perp}$ is the visible cross section area of the face.

The MCRT method can also be used to calculate an estimation of D. Once the solar constant and the solar aspect ratio are known, the problem is reduced to find the visible cross section area of the radiative face. Although for non-occluded planar faces this is a simple operation, a MCRT procedure can be followed whenever the faces are curved or shading effects exist:

- calculate a random emission point on the radiative face
- fire a ray from the emission point towards the sun
- find whether the emission point "sees" the Sun. A discrete random variable H, taking only two possible values (0 if the Sun is not visible and 1 if it is) shall be tallied for this purpose
- tally the cos θ value (where θ is the angle between the Sun direction and the face's normal vector at the emission point), only if the emission point is not occluded by any other part of the model

An estimation of $A^{\perp}$ is then calculated as:

$$a^{\perp *} = \frac{1}{N} \cdot A \cdot \sum_{l=1}^{N} (\cos\Theta)_l \cdot h_l \qquad \text{(EQ 22)}$$

where A is the radiative node area, h_l is the value of the random variable H and $(\cos\theta)_l$ is the value of the random variable cos θ. The subscript l refers to the l-th trial.

Applying the general accuracy model to this specific case, the following equation is obtained:

$$N_\varepsilon = 2 \cdot \left(\frac{erf^{-1}(\alpha)}{\varepsilon} \right)^2 \cdot (SC \cdot A)^2 \cdot \frac{V(\cos\Theta \cdot H)}{D^2} \qquad \text{(EQ 23)}$$

SOME IMPLEMENTATION ISSUES

Parameter pre-estimation

The application of the accuracy models to the estimation of radiative values presents the paradox of requiring as input the value whose calculation is the goal of the simulation. Furthermore, the variance of the basic random process used to calculate the estimation is not generally known a priori. These apparent drawbacks can be satisfactorily overcome by pre-estimating both the radiative value R and the variance of the basic process V(T), so that the accuracy models can be applied. The pre-estimated values can be obtained after a first batch of M rays is fired in the simulation. Indeed:

$$R = \hat{t} = \sum_{l=1}^{M} \frac{t_l}{M} \qquad \text{(EQ 24)}$$

$$V(T) = S^2_T = \frac{1}{M-1} \cdot \sum_{l=1}^{M} (t_l - \hat{t})^2 \qquad \text{(EQ 25)}$$

The number of rays M to be fired in order to pre-estimate R and V(T) shall be determined as a compromise between having reasonably accurate pre-estimations and not spending too much computational effort in this previous phase of the algorithm. In practice, it has been checked that even with sample sizes which are small when compared to N_ε, the accuracy control based on the accuracy model produces excellent results.

For instance, Figure 3 shows the histogram of the relative error associated to the estimation of a particular configuration factor, with a reference value of 0.01832. To produce the histogram, 1000 different simulations were performed, each of them using a pre-estimation sample size of 1000 rays. The accuracy model was then applied to ensure an accuracy of 3% with a level of confidence of 99%. The application of (eq 11) shows that these requirements are achieved by firing approximately 398000 rays in each simulation. The tails of the histogram, filled in black, show that only 10 out of the 1000 simulations performed had an error beyond the specified limits. This is in agreement with the confidence level used for this particular case.

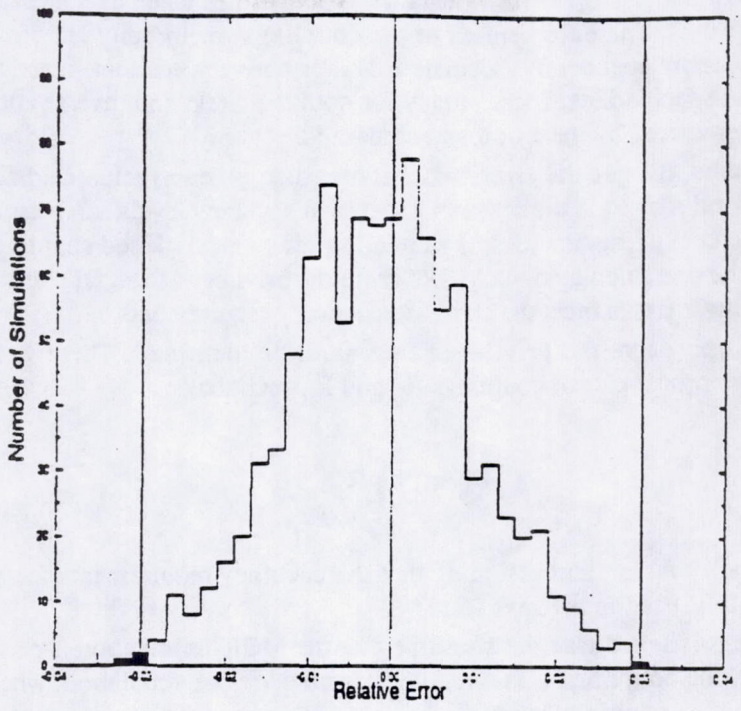

FIGURE 3. Histogram of the relative error associated to the estimation of a configuration factor with reference value 0.01832

A particular problem arising when introducing the pre-estimated values into (eq 11) is that this expression becomes singular for $\bar{\tau} = 0$. A null pre-estimated value can indicate either that:

- the actual radiative value is indeed null, in which case its actual variance will also be null, or that
- the actual radiative value is so small that the size of the sample it is not large enough to provide a non-null pre-estimated value.

In the first case, no additional rays need to be fired. In the second, a very large number of rays are likely to be needed. Practical considerations impose a limit to this number, which for very small couplings might become computationally prohibitive. Generally speaking, once this limit is imposed it will not be possible to guarantee the accuracy of the radiative values below a threshold value.

Enforcement of the reciprocity law

In general, and for efficiency reasons, the software tools that implement MCRT methods do not calculate the couplings individually. Indeed, the couplings from one face to all the other faces in the model are normally calculated in one pass. Due to this fact, the couplings' line sum adds up to 1. However, the reciprocity law between couplings is in principle not satisfied, because of the statistical inaccuracy associated to the estimations.

Often, the manipulation of couplings that satisfy the reciprocity law is preferred, especially because of the reduction in memory requirements. The enforcement of the reciprocity law brings about a

line sum which does not add up to 1. This imbalance is sometimes taken as a measure of the error in the estimation of the couplings. The enforcement of the couplings' reciprocity is normally performed after both couplings have been independently calculated. This is not very efficient, since computational time is wasted to guarantee the specified level of accuracy for both the direct and inverse couplings. Furthermore, a systematic error is introduced by the enforcement method.

On the other hand, the general error model shows that, given a reciprocal pair of faces, one of the associated couplings is privileged in the sense that identical accuracy levels can be achieved with a smaller number of rays. This fact suggests the idea of estimating the non-privileged coupling by simply applying the reciprocity law to the one calculated via MCRT from the privileged face. Of course, this operation shall ensure that both coupling's errors meet the specified accuracy requirements.

To apply this approach, the privileged face shall be identified. Therefore, the question to be answered is: given a reciprocal pair of couplings R_{ij} and R_{ji} such that:

$$R_{ij} = \Psi \cdot R_{ji} \qquad \text{(EQ 26)}$$

where Ψ is the reciprocity factor, and assuming that the accuracy requirements are respectively set to ε_{ij} and ε_{ji}, which face shall be used to fire rays from?

To identify the privileged face, let's assume that the MCRT simulation is performed by firing rays from face i. Therefore, the coupling R_{ij} is directly estimated via the simulation, while the coupling R_{ji} is estimated by enforcing the reciprocity law:

$$r'_{ij} = r^*_{ij} \qquad \text{(EQ 27)}$$

$$r'_{ji} = \frac{r^*_{ij}}{\Psi} \qquad \text{(EQ 28)}$$

The reciprocal values estimated in such a way follow normal distributions:

$$R'_{ij} \sim R^*_{ij} \qquad \text{(EQ 29)}$$

$$R'_{ji} \sim N(E(R'_{ji}), V(R'_{ji})) \qquad \text{(EQ 30)}$$

Furthermore, it can be shown that the variance of the relative error associated to the estimation of R_{ji} via (eq 28) is:

$$V(E'_{ji}) = V(E^*_{ij}) = \frac{V(T_{ij})}{N_{ij} \cdot R_{ij}^2} \qquad \text{(EQ 31)}$$

On the other hand, if the estimation of R_{ji} was calculated by the MCRT procedure, by firing from face j the number of rays needed to meet the accuracy target ε_{ji}, the variance of the relative error would be:

$$V(E_{\varepsilon_{ji}}) = \frac{1}{2} \cdot \left(\frac{\varepsilon_{ji}}{erf^{-1}(\alpha)} \right)^2 \qquad \text{(EQ 32)}$$

Since the accuracy requirements must be also achieved by the enforced estimation R'_{ji}, the variance of its error must be equal to the variance of the error obtained in the MCRT procedure:

$$V(E'_{ji}) = V(E_{\varepsilon_{ji}}) \qquad \text{(EQ 33)}$$

From this equation, it can be proved that i is the privileged face if the following condition holds:

$$V(T_{ij}) \leq \Psi^2 \cdot V(T_{ji}) \qquad \text{(EQ 34)}$$

This expression relates the variance of the basic random processes used to estimate the couplings. If (eq 34) is applied to the configuration factors case, it can be seen that the privileged face is the one with larger associated coupling. In the REF case, the privileged face cannot be determined by simply looking at the relative size of the reciprocal couplings, and (eq 34) shall be used instead.

To clarify the interest of firing rays from the privileged face, let's present an example. For the model in Figure 4, reference values are available in the literature (ref. [6]). In particular, $F_{12} = 0.29176$. Assuming we are interested in the calculation of the view factors with an accuracy of 5%, the most efficient way to proceed is to fire rays from face 1, which is the privileged one. This can be seen by checking the condition given by (eq 34). If the accuracy law for view factors (eq 18) is applied, it can be seen that approximately 6500 rays are needed to guarantee the accuracy requirements for both reciprocal couplings. If the same accuracy level had to be achieved by firing rays from face 2, roughly 25000 rays would be needed.

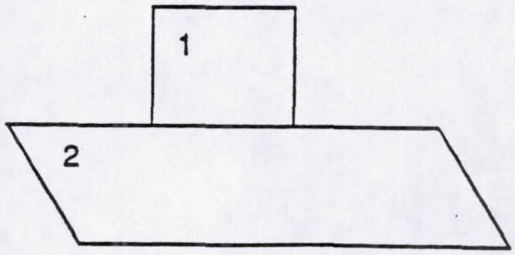

FIGURE 4. Model consisting of two perpendicular rectangular plates, with areas of 1 and 3 units respectively. The reciprocity factor between the configuration factors is in this case $\Psi = 3$.

ACCURACY CONTROL FOR ABSORBED HEAT FLUXES

The estimation of the absorbed heat flux on a radiative face differs of that of the simple radiative values presented above in that the absorbed value can be seen as the contribution of several source terms. Indeed, the heat flux striking the spacecraft follows different multi-reflection paths until it is finally absorbed by the face. Obviously, some multi-reflection paths will contribute more than others to the final absorbed flux. The purpose of this section is to apply the general accuracy model to this problem, taking into account the relevance of the mentioned radiative paths into the final value. The results that follow are applicable to either solar or planetary (infrared and albedo) absorbed heat fluxes.

A proper accuracy control for the absorbed heat flux is especially interesting when trying to quantify the absorbed heat flux on a spacecraft radiator. Because of the radiator's heat rejection requirements, the direct heat loads are generally small, and most of the absorbed flux reaches the radiator after several reflections.

As previously stated, the heat flux Φ absorbed by a given radiative face can be expressed as the addition of a number of contributing terms Φ_j:

$$\Phi = \sum_{j=1}^{n} \Phi_j \qquad \text{(EQ 35)}$$

where each Φ_j is the flux being absorbed by the target face, with origin in the reflection of direct heat flux in the source face j. The summation is therefore extended to the n faces in the model which have non-null direct heat flux.

The concept of source faces is clarified with the help of Figure 5. Assuming an idealised model consisting of 4 surfaces illuminated by the Sun, only faces 1 and 3 are source faces, as far as the calculation of the heat flux absorbed by face 4 is concerned. Face 2 does not see the Sun, and therefore it will not contribute with a source term in (eq 35).

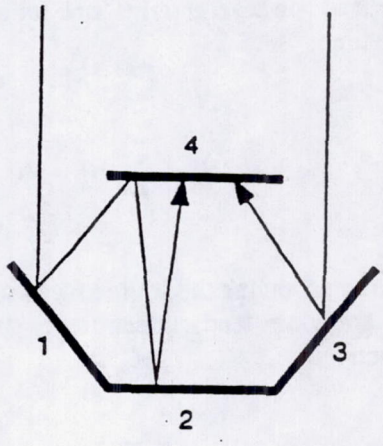

FIGURE 5. Source faces 1 and 3 contribute to the heat flux absorbed by face 4. In this case, face 2 only contributes through multi-reflections.

In the actual MCRT simulation, the Φ_j term is estimated by uniformly firing N_j rays from face j and averaging the random variable T_j, i. e. amount of the energy carried by the ray that is finally absorbed by the target face:

$$\phi_j^* = \frac{1}{N_j} \cdot \sum_{l=1}^{N_j} (t_j)_l \qquad \text{(EQ 36)}$$

The estimated value for the absorbed heat flux is therefore:

$$\phi^* = \sum_{j=1}^{n} \phi_j^* \qquad \text{(EQ 37)}$$

and follows a normal law:

$$\Phi^* - N(E(\Phi^*), V(\Phi^*)) \qquad \text{(EQ 38)}$$

The variance of the relative error associated to the estimation is:

$$V(E) = \frac{1}{\Phi^2} \cdot V(\Phi^*) = \frac{1}{\Phi^2} \cdot \sum_{j=1}^{n} \frac{V(T_j^*)}{N_j} \qquad \text{(EQ 39)}$$

This expression shows that the variance of the relative error, which is directly related to the accuracy achieved by the simulation, depends on several terms, one for each source face. The question here is, given a fixed amount N of rays to be fired:

$$N = \sum_{j=1}^{n} N_j \qquad \text{(EQ 40)}$$

how shall these N rays be distributed among the source faces so that (eq 39) is minimised? The solution to this problem can be found by applying standard techniques of non-linear programming. It can be shown that the optimal solution is given by:

$$N_j^{\circ} = \frac{\sqrt{V(T_j)}}{\sum_{k=1}^{n} \sqrt{V(T_k)}} \cdot N \qquad \text{(EQ 41)}$$

For this optimal distribution of the rays, the variance of the error becomes:

$$V(E) = \frac{1}{\Phi^2 \cdot N} \cdot \left(\sum_{j=1}^{n} \sqrt{V(T_j)} \right)^2 \qquad \text{(EQ 42)}$$

Replacing (eq 42) in the general error model, the accuracy control law for the estimation of the absorbed heat fluxes can be obtained:

$$N_\varepsilon = 2 \cdot \left(\frac{\text{erf}^{-1}(\alpha)}{\varepsilon} \right)^2 \cdot \frac{1}{\Phi^2} \cdot \left(\sum_{j=1}^{n} \sqrt{V(T_j)} \right)^2 \qquad \text{(EQ 43)}$$

This multi-source model is the most general expression of the accuracy law for MCRT calculations. In fact, the accuracy model previously obtained for the simple radiative entities is just a particular case of (eq 43), with n = 1. Indeed, one can regard the calculations of couplings as a mono-source phenomenon, being the unique source the radiative face emitting the radiation. Similarly, the Sun (or the planet) are the unique sources emitting radiation when the direct fluxes are calculated.

The considerations about the pre-estimation of the values are also relevant for the implementation of this accuracy model.

CONCLUSIONS

This paper has presented a model which can be used to control the accuracy of the radiative values estimated by using MCRT methods. The generality of the model allows its application to the radiative values relevant to the thermal analysis of spacecraft.

A prototyping activity has confirmed the validity of the assumptions used in the derivation of the accuracy models, as well as the feasibility of their implementation. The results obtained are in excellent agreement with the values predicted by the statistical models, even if pre-estimation of some parameters is required.

Full scale implementation of the error models is in progress, with the intention to enhance ESARAD, the radiative analysis software developed for the European Space Agency (ref. [7]). Significant improvements in terms of accuracy control, efficiency and performance are expected in relation to other radiative codes currently available in Europe.

NOMENCLATURE

The following conventions have been followed in naming the random variables:

- Star indicates estimation of a radiative entity. For example, F* represents the random variable "estimation of the view factor F".
- Upper case is reserved to denote the distribution of the random variable, while lower case denotes a sample value from this distribution. For example, f* is the estimation of the view factor F, as provided by a single simulation run.

Furthermore, the notation:

$$R - N(E(R), V(R))$$

indicates that the random variable R follows a normal distribution with expectation E(R) and variance V(R).

REFERENCES

[1] Koeck, C.: Improved Ray Tracing Technique for Radiative Heat Transfer Modelling. Proceedings of the 3rd European Symposium on Space Thermal Control & Life Support Systems. ESA SP-288. 1988.

[2] Howell, J. R.: Monte Carlo Treatment of Data Uncertainties in Thermal Analysis. Journal of Spacecraft and Rockets, vol. 10, no. 6, 1973.

[3] Siegel, R. and Howell, J. R.: Thermal Radiation Heat Transfer, 3rd Edition, Hemisphere Publishing Corporation, 1992.

[4] Hoel, P. G., Introduction to Mathematical Statistics, John Wiley & Sons, 1971.

[5] Gebhart, B.: Surface Temperature Calculations in Radiant Surroundings of Arbitrary Complexity for Gray Diffuse Radiation, International Journal Heat Mass Transfer, vol. 3, no. 4, 1961.

[6] Spacecraft Thermal Control Design Data, Volume 1, ESA PSS-03-108, 1989.
[7] ESARAD User Manual, UM-ESARAD-024, jointly published by ESA/ESTEC/YCV & EGT's Engineering Research Centre, 1993.

SAND92-0652C

Thermal Control System for SSF Sensor/Electronics [1]

R. L. Akau

Thermal and Fluid Engineering Department

D. E. Lee

Engineering Design Department

Sandia National Laboratories
Albuquerque, NM 87185

ABSTRACT

A thermal control system has been designed for the SSF sensor/electronics box (SSTACK). Multi-layer insulation and heaters are used to maintain the temperatures of the critical components within their operating and survival temperature limits. Detailed and simplified SSTACK thermal models were developed and temperatures were calculated for worst-case orbital conditions. A comparsion between the two models showed very good agreement. Temperature predictions were also compared to measured temperatures from a thermal-vacuum test.

INTRODUCTION

As part of the Defense Meteorological Support Program (DMSP) with Martin Marieta Astro-Space Division (MMASD), a thermal control system was designed for the SSF (Special Sensor F) sensor/electronics box (SSTACK) located on the precision mounting platform (PMP) of the DMSP satellite. The SSTACK is attached to an aluminum mounting bracket which is thermally isolated from the PMP. The top half of the SSTACK consists of an array of earth facing infrared sensors and a chopper motor, and the bottom half contains a row of electronic circuit boards. Detailed and simplified thermal models of the SSTACK were developed using the thermal analyzer SINDA [1]. The simplified thermal model was integrated into the MMASD PMP thermal model. An SSTACK TRASYS [2] geometric math model of the simplified model was also developed and incorporated into MMASD's TRASYS PMP model.

The boundary temperatures, orbital heat rates, and thermal radiation conductances from MMASD's PMP and TRASYS models for hot (95° sun angle and end-of life (EOL) optical properties) and cold (0° sun angle and beginning-of-life (BOL) optical properties)

[1]This work performed at Sandia National Laboratories, supported by the U.S. Department of Energy under contract DE-AC04-76DP00789

orbits were used in Sandia Labs detailed SSTACK SINDA model. The model guided the development of the SSTACK thermal control system design which maintained the sensors, motor, and electronic board temperatures within their operational and survival temperature limits. Survival/operational heaters were required for SSTACK cold orbit thermal management. Results from the SSTACK thermal models for the different orbits will be presented and results compared to measured temperatures from a thermal-vacuum test.

DESCRIPTION OF SSF SENSOR/ELECTRONICS BOX

The SSTACK is located on the earth-facing side of the precision-mounted platform (PMP) and is attached to an aluminum bracket as illustrated in Figure 1. Figure 1 shows only the PMP and the ESM (equipment support module) sections of the DMSP satellite. The bracket is covered with multi-layer insulation (MLI) and is thermally isolated from the PMP. The PMP temperature range is 5°C ±3°C. A schematic diagram of an earlier SSTACK design is shown in Figure 2. The SSTACK is divided into four quadrants (Q1 to Q4) with Q3 facing outward and Q1 facing inward to the spacecraft. The SSTACK has a mass of 10 kilograms (22 pounds) and produces a power of 11.5±0.2 Watts as summarized in Table 1. Because of redundancy, there are A-side and B-side circuit boards for the SPS-14 and SHM-13 modules with either the A-side or B-side boards powered on. The SSTACK has an overall length and width of 24.8 cm (9.75 inches), and a height of 22.2 cm (8.79 inches). The SSTACK is constructed of thin aluminum sheets (0.10 cm (0.04 inches) average thickness) which are screwed to an inner aluminum frame structure. The SSTACK is attached to the PMP via four feet (1.8 cm by 2.0 cm) located on the bottom of the box. The top section consists of an array of eleven sensors and a chopper motor as illustrated in Figure 3. The bottom half contains an array of electronic circuit boards as shown in Figure 4 with the front covers removed. The circuit boards slide into frame guides and are plugged into a connector board. The front-end of the board frames, except for the two power supply module frames (SPS-14A and SPS-14B), are screwed to the inner frame structure. The front-ends of the power supply frames are attached to the box front cover which enhances heat conduction from the power supplies to the front cover. The operating and survival (power off) component temperature limits are given in Table 2.

Kapton insulated resistive strip heaters (4 Watts each and two per side) are located on the inner wall surfaces (see Figure 4). A thermal control electronics (TCE) device, provided by MMASD, is used to turn the heaters on and off at a temperature set-point of -10±0.2°C. The TCE temperature sensor is located near the chopper motor (see Figure 3). Each of the eleven sensors have apertures located on the earth-facing top cover. The aperture plate is shown in Figure 5.

DESCRIPTION OF SSTACK THERMAL MODELS AND ORBIT RESULTS

The DMSP operates in a 450 NM orbit having a 100 minute orbit period. For the hot orbit, the DMSP satellite encounters an eclipse (earth's shadow) during thiry-percent of the orbit and the SSTACK receives direct solar flux immediately before and after eclipse. However, during the cold orbit, the SSTACK is shaded and does not receive any direct solar flux. MMASD required each sensor contractor to provide simplified SINDA and TRASYS models to be integrated into the MMASD PMP thermal and TRASYS models. The nodes for the reduced model are shown in Figure 6 and in Figure 7 for the detailed model which consisted of 24 and 48 diffusion nodes, resectively. The detailed model was first constructed and the simplified model was developed by maintaining the critical components (motor, sensors, and power supplies). The simplified nodes were formed by combining nodal points and calculating equivalent thermal conductances from the detailed model.

Figure 8 illustrates the MLI design and the thermal radiator surfaces. The SSTACK thermal radiator surfaces include the nadir-facing sensor aperture plate and the bottom half of Q3 which are coated with S-13 GLO white paint. The other surfaces are covered with MLI (8 layers of 0.5 mil thick double-sided aluminized Kapton, 1 mil thick black Kapton outer layer, and 0.5 mil thick Kapton inner layer).

The environmental heat fluxes (direct and reflected solar, and earthshine), boundary temperatures, and thermal radiation conductances for the hot and cold orbits were obtained from MMASD's PMP thermal and TRASYS models. The heat fluxes and boundary temperatures were input into the SSTACK thermal models. The SSTACK temperatures were calculated using the thermal analyzer SINDA until quasi steady-state conditions were obtained (approximately 18 orbits). The thermal parameters used in MMASD's PMP TRASYS model for the cold and hot orbits are shown in Table 3.

Temperature predictions and a comparison between the simplified and detailed thermal models during hot operational conditions (11.7 Watts) are given in Table 4. The temperature uncertainty for model predictions, $\pm 11°C$, according to MIL-1540B [3] was not included in Table 4. Adding the uncertainty, the electronics modules, motor, and sensor temperatures are a few degrees above their desired maximum operating temperatures and are higher than their minimum operating temperatures. A one-Watt operational heater was needed for the morning orbit to keep the motor temperature from going below -10.2°C. A comparison between the simplified and detailed models indicate temperatures that are within $\pm 5°C$. Results for the cold orbit (11.3 Watts) and survival conditions (power off) are shown in Table 5 where temperatures for the simplified and detailed thermal models compare to within $\pm 2°C$. Approximately 12 Watts of survival heater power was needed to maintain the motor temperature from going below -10.2°C. However, Table 5 shows a motor temperature of -11.0°C. This was attributed to thermal lag from the

motor location to the heaters. Adding -11°C to the critical component temperatures in Table 5, indicate temperature limits well above minimum survival temperatures.

THERMAL-VACUUM TEST SET-UP

SSTACK thermal-vacuum tests were recently conducted in a 42 inch diameter by 42 inch high chamber. Thermal balance tests were performed to verify the SSTACK thermal model. The SSTACK was screwed to a block of fiberglass G-10 material to thermally isolate the SSTACK from the chamber baseplate. An MLI test blanket was built and consisted of ten layers of double-sided aluminized Kapton and an outer layer of double-sided aluminized Mylar. The outer surface of the aluminized Mylar was painted with Chemglaze Z-306 black paint. The sensor aperture plate and the bottom of Q3 were painted with S13-GLO white paint. Also included in the chamber was a power distribution box (PSTACK) that accompanies the SSTACK. The PSTACK is located in the ESM section of the DMSP satellite (see Figure 1) and was also bolted to the baseplate. The PSTACK was covered with a separate MLI blanket to minimize thermal radiation interaction with the SSTACK. The baseplate and inner wall of the chamber were controlled to preset temperatures with the chamber pressure maintained at 10^{-6} torr.

The SSTACK has 14 internal AD-590 temperature monitors on each of the sensors, the motor, and the power suppplies. The AD-590's, shown in Figures 3 and 4, have an accuracy of ±2°C, and an output voltage which corresponds to a calibrated temperature. In addition to the internal temperature monitors, copper constantan (Type-T) thermocouples were attached to the external surfaces of the SSTACK using Kapton tape illustrated in Figures 9 to 11. Thermocouples were also located on the inner wall of the chamber (shroud) and baseplate, and on the PSTACK. The thermocouples were calibrated to be ±3°C. The thermal balance tests were conducted at three different shroud and baseplate temperature levels to simulate SSTACK hot-operational (10°C and 20°C) and cold-operational (-100°C and 20°C) conditions. A mid-point operational (-40°C and and 20°C) condition was also performed as a third data point for the SSTACK thermal model. The temperature boundaries were held constant for 15 hours at each condition at which time the SSTACK temperatures changed by no more than 2°C per hour. The A-side was powered on (11.7 Watts) throughout the tests.

The boundary temperatures were determined by a thermal-vacuum thermal model which incorporated the SSTACK, PSTACK, baseplate, and shroud. A TRASYS model was developed for the SSTACK and PSTACK in the vacuum chamber in order to obtain the thermal radiation conductances for the experimental setup. Shroud and baseplate temperatures boundaries were put into the SINDA thermal model and steady-state temperatures were calculated for the three thermal balance tests. Thermal model calculations were done on a Sun Workstation.

COMPARISON OF SSTACK PREDICTED AND MEASURED RESULTS

Preliminary comparisons between the predicted and measured steady-state temperatures are given in Tables 6 to 8 for the hot-operational, cold-operational, and mid-operational tests. The model was first compared to the hot and cold cases with an SSTACK power of 11.7 Watts as shown in Tables 6 and 7. The effective emittance (ϵ^*) of the MLI was 0.02. For the hot case, Table 6, a comparison of the measured and predicted temperatures for the critical components (motor, sensors, and power supply) were within 3°C. For the cold test, Table 7, the component temperatures also compared well, but the measured cover temperatures for Q2 and Q4 (TC5 and TC15) were over 10°C lower than the calculated values even though the measured outer temperatures of the MLI surfaces for Q2 and Q4 (TC9 and TC19) were within 5°C of the calculated values. These discrepencies could be attributed to heat leaks through MLI blanket openings, and thermocouples detaching from the surface. Analysis is continuing to determine these large temperature differences.

SUMMARY AND CONCLUSIONS

A thermal control system was designed for the SSTACK located on the PMP section of the DMSP satellite. The aperture plate and the bottom of Q3 were painted with S13-GLO white paint and the remaining surfaces, except for the bottom plate, covered with MLI. A one-Watt operational heater was needed for the cold orbit and a 12-Watt survival heater for the cold orbit powered off condition. Detailed and simplified SINDA thermal models were developed for the SSTACK with the simplified model integrated into MMASD's PMP thermal model. There was very good agreement between the reduced and detailed thermal models for cold and hot orbital conditions. The model calculations were also compared to measured results from a recent thermal-vacuum test. Preliminary results indicated good agreement between measured and predicted results for the critical components (motor, sensors, and power supply).

REFERENCES

1. User's Manual for the Aerospace Version of J. Gaski's SINDA 1987/ANSI Code.
2. User's Manual Thermal Radiation Analysis System, TRASYS II ANSI Version 1.0, Martin Marietta, February 1987.
3. MIL-1540B (USAF), Military Standard Test Requirements for Space Vehicles, Otober 10, 1982, Department of the Air Force, Washington, D. C. 20301.

Table 1. Nominal Power Distribution for SSTACK.

Component	Power (Watts) A-Side On	B-Side On
Bottom Section		
BMD-10	0.62	0.62
SPS-14A	2.15	0.00
SPS-14B	0.00	2.15
SFR-10	0.01	0.01
PAT-10	0.01	0.01
PAA-10	0.91	0.90
PAA-10	0.91	0.91
PAA-10	0.91	0.91
ARM-10	0.50	0.50
SAA-11	0.53	0.53
SAA-11	1.04	1.04
SAT-10	0.20	0.20
SHM-13A	0.33	0.00
SHM-13B	0.00	0.33
CAS-12	0.48	0.48
CAL-27	0.00	0.00
Top Section		
Motor	0.66	0.66
Pyro Sensors	1.14	1.14
Silicon Sensors	0.74	0.74
Radiometer (2)	0.35	0.35
Total	11.50	11.50

Table 2. SSTACK Component Temperature Limits.

Component	Temperature (°C) Operational	Survival
Sensors	-30 to 35	-40 to 55
Motor	-23 to 35	-40 to 60
Electronics	-40 to 50	-40 to 70

Table 3. Thermal Parameters for Cold (BOL) and Hot (EOL) Orbits.

Parameter	Cold	Hot
Solar Flux (W/cm^2)	0.132	0.142
Earth Infrared (W/cm^2)	0.021	0.026
Earth Albedo	0.275	0.375
	α_s	ϵ_{IR}
S13-GLO White Paint	0.20	0.42
Black Kapton 1 mil	0.87	0.87
MLI effective ϵ^*	0.05	0.02
PMP Temp. (°C)	2	8

Table 4. SSTACK Operational Orbit Temperatures.

Simplified Model					Detailed Model				
Node No.	Temperature (°C) Hot Orbit 11.7 Watts		Cold Orbit 11.3 Watts		Node No.	Temperature (°C) Hot Orbit 11.7 Watts		Cold Orbit 11.3 Watts	
	Min.	Max.	Min.	Max.		Min.	Max.	Min.	Max.
Electronics Modules									
8012	31.9	34.9	-1.6	-0.6	1001	29.6	33.2	-5.2	-2.6
8013	27.9	36.1	-5.8	-4.7	1002	27.4	36.2	-6.5	-4.2
8014	18.4	29.2	-13.6	-12.3	1003	19.7	29.4	-14.1	-11.6
8015	26.2	30.0	-7.2	-5.5	1004,1005	28.1	30.7	-7.5	-5.5
8016	37.8	39.6	3.7	4.6	1006,1007 1008	36.6	38.7	1.2	3.2
8017	34.4	36.2	-0.1	0.8	1009	33.0	35.1	-2.8	-0.7
8018	34.4	36.2	0.3	0.8	1010	33.4	35.5	-2.4	-0.3
8029	36.8	38.1	2.9	3.3	1011-1016	33.2	34.9	-1.7	0.1
Chopper Motor									
8008	24.8	26.3	-10.2	-8.8	1017	26.6	27.8	-10.2	-8.4
Sensors									
8009	23.6	25.9	-11.2	-10.1	1018-1020	24.0	27.4	-11.8	-8.4
8010	23.0	25.8	-11.1	-8.7	1021,1022 1027,1028	25.7	27.3	-11.4	-8.4
8011	22.8	25.9	-11.2	-8.9	1023-1026	24.1	27.2	-11.4	-8.6
External Covers									
8001	16.1	32.2	-14.2	-12.6	8001	17.3	32.4	-14.6	-11.2
8002	23.0	27.8	-10.1	-6.7	8002	22.9	27.9	-11.6	-5.9
8003	23.7	28.1	-9.6	-7.3	8003	23.5	28.2	-10.9	-6.5
8004	22.9	27.8	-10.1	-6.7	8004	22.9	28.0	-11.6	-5.9
8005	17.8	25.1	-13.3	-8.0	8018	19.3	26.2	-13.5	-8.8
8006	25.6	29.3	-7.8	-6.4	8019	25.3	28.9	-9.5	-6.6
8007	27.1	30.4	-6.8	-4.9	8020	24.1	28.8	-10.5	-5.8
8021	18.4	25.4	-13.3	-9.1	8006,8010 8014	20.2	26.7	-13.2	8.3
8022	20.3	25.6	-12.2	-4.9	8007,8011 8015	21.5	26.8	-12.7	-5.9
8023	20.4	25.7	-12.1	-8.2	8008,8012 8016	21.6	26.9	-12.4	-7.6
8024	20.3	25.6	-12.2	-4.9	8009,8013 8017	21.5	26.8	-12.5	-5.8

Note: ±11°C uncertainty not included.

Table 5. SSTACK Cold Orbit Temperatures, Power Off.

Simplified Model			Detailed Model		
Node	Temperature (°C)		Node	Temperature (°C)	
	Min.	Max.		Min.	Max.
Electronics Modules					
8012	-14.1	-13.1	1001	-15.3	-12.2
8013	-18.8	-17.7	1002	-20.1	-17.6
8014	-19.1	-17.7	1003	-20.4	-17.6
8015	-14.2	-12.3	1004,1005	-14.8	-13.0
8016	-13.6	-12.8	1006,1007 1008	-14.3	-12.0
8017	-13.5	-12.8	1009	-14.3	-12.0
8018	-13.5	-12.8	1010	-14.3	-12.1
8029	-13.4	-12.9	1011-1016	-14.1	-12.6
Chopper Motor					
8008	-10.7	-9.7	1017	-11.0	-9.4
Sensors					
8009	-12.0	-10.9	1018-1020	-12.7	-8.7
8010	-11.4	-8.3	1021,1022 1027,1028	-12.2	-8.3
8011	-11.4	-8.7	1023-1026	-12.1	-8.5
External Covers					
8001	-19.9	-17.6	8001	-21.5	-17.7
8002	-14.9	-10.5	8002	-16.5	-9.3
8003	-14.4	-11.1	8003	-15.9	-10.7
8004	-14.9	-10.5	8004	-16.7	-9.5
8005	-15.4	-8.9	8018	-15.6	-8.8
8006	-14.5	-12.7	8019	-15.8	-12.3
8007	-14.2	-11.7	8020	-16.4	-10.1
8021	-15.8	-10.6	8006,8010 8014	-17.0	-11.1
8022	-13.9	-5.8	8007,8011 8015	-15.6	-7.0
8023	-14.3	-9.2	8008,8012 8016	-15.3	-9.3
8024	-13.9	-6.1	8009,8013 8017	-15.6	-7.0
Note: ±11°C uncertainty not included.					

Table 6. Comparsion of Measured and Calculated Temperatures, Hot-Operational.

Thermocouple		AD-590		Model	
TC No.	Temp. (°C)	AD-590	Temp. (°C)	Model Node	Temp. (°C)
			Q1		
1	33.3	Box 1	37.0	8003	35.7
2	30.5	Box 2	37.0	8023	32.9
3	29.4			8023	32.9
4 (MLI)	18.1			8027	15.3
			Q4		
5	28.4			8004	34.5
6	32.0			8024	32.7
7	29.6			8024	32.7
8	28.9			8024	32.7
9 (MLI)	17.7			8028	14.1
			Q3		
10	36.1			8001	33.6
11				8001	33.6
12	29.1			8021	32.3
13	30.0			8021	32.3
14 (MLI)	18.4			8025	14.0
			Q2		
15	26.5			8002	34.6
16	31.2			8022	32.7
17	34.5			8022	32.7
18	29.4			8022	32.7
19 (MLI)	16.7			8026	14.7
			Aperture Plate		
21	33.6			8005	31.6
			Motor		
			36.0	8008	34.5
			Power Supply		
			47.0	8013	50.0
			Sensors		
			37.0	8009-8011	34.0

Table 7. Comparsion of Measured and Calculated Temperatures, Cold-Operational.

Thermocouple		AD-590		Model	
TC No.	Temp. (°C)	AD-590	Temp. (°C)	Model Node	Temp. (°C)
			Q1		
1	-24.5	Box 1	-25.0	8003	-30.6
2	-28.4	Box 2	-25.0	8023	-33.4
3	-33.1			8023	-33.4
4 (MLI)	-63.6			8027	-75.6
			Q4		
5	-42.1			8004	-31.8
6	-34.1			8024	-33.7
7	-39.5			8024	-33.7
8	-37.0			8024	-33.7
9 (MLI)	-83.4			8028	-81.4
			Q3		
10	-25.3			8001	-32.6
11				8001	-34.1
12	-45.0			8021	-34.1
13	-45.3			8021	-34.1
14 (MLI)	-81.6			8025	-82.1
			Q2		
15	-46.3			8002	-31.7
16	-39.5			8022	-33.7
17	-32.7			8022	-33.7
18	-42.9			8022	-33.7
19 (MLI)	-75.4			8026	-79.5
			Aperture Plate		
21	-30.7			8005	-34.8
			Motor		
			-28.0	8008	-31.8
			Power Supply		
			-13.0	8013	-14.6
			Sensors		
			-28.0	8009-8011	-33.0

Table 8. Comparsion of Measured and Calculated Temperatures, Mid-Operational.

Thermocouple		AD-590		Model	
TC No.	Temp. (°C)	AD-590	Temp. (°C)	Model Node	Temp. (°C)
			Q1		
1	3.7	Box 1	5.0	8003	-0.1
2	1.6	Box 2	5.0	8023	-2.9
3	-2.9			8023	-2.9
4 (MLI)	-20.5			8027	-29.4
			Q4		
5	-5.8			8004	-1.3
6	-2.1			8024	-3.6
7	-6.5			8024	-3.6
8	-3.1			8024	-3.6
9 (MLI)	-27.1			8028	-32.3
			Q3		
10	5.1			8001	-2.1
11				8001	-3.6
12	-8.3			8021	-3.6
13	-5.5			8021	-3.6
14 (MLI)	-28.9			8025	-32.3
			Q2		
15	-10.1			8002	-1.3
16	-4.4			8022	-3.1
17	1.1			8022	-3.1
18	-8.0			8022	-3.1
19 (MLI)	-30.4			8026	-31.0
			Aperture Plate		
21	0.1			8005	-4.3
			Motor		
			3.0	8008	-1.3
			Power Supply		
			16.0	8013	15.0
			Sensors		
			4.5	8009-8011	-2.0

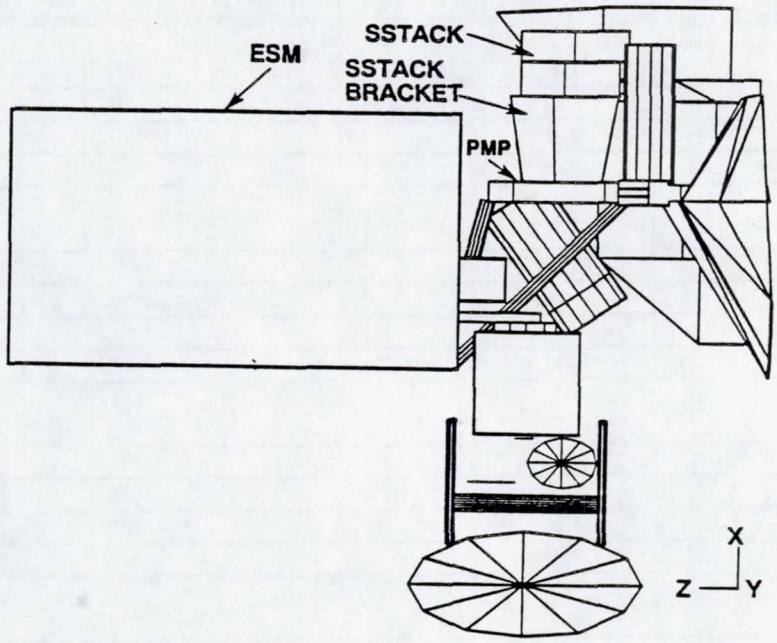

Figure 1. SSTACK location on PMP.

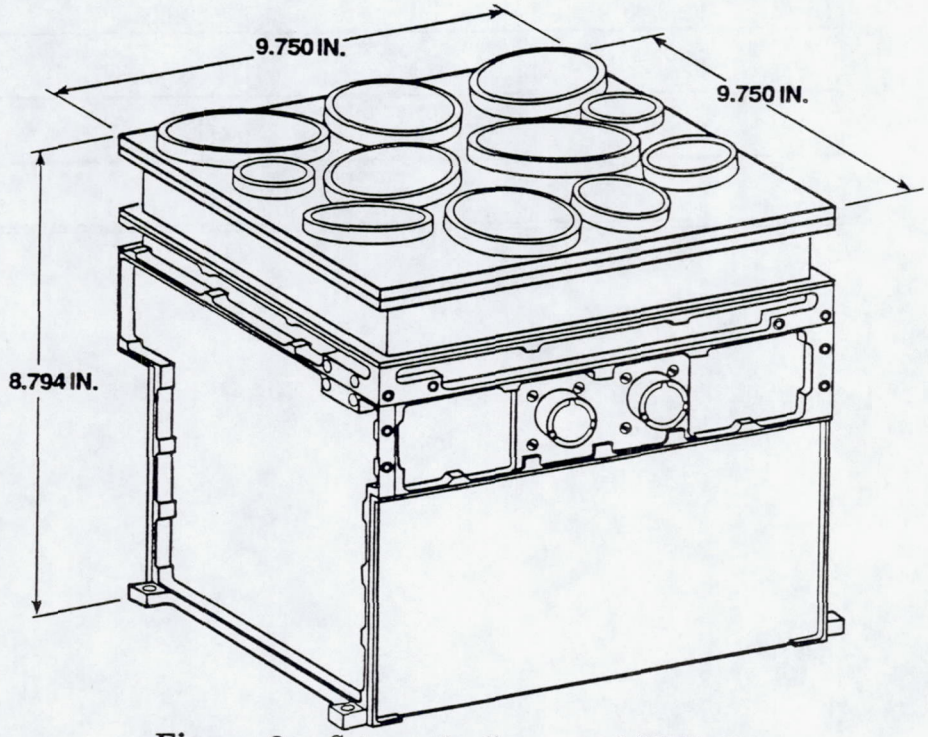

Figure 2. Schematic diagram of SSTACK.

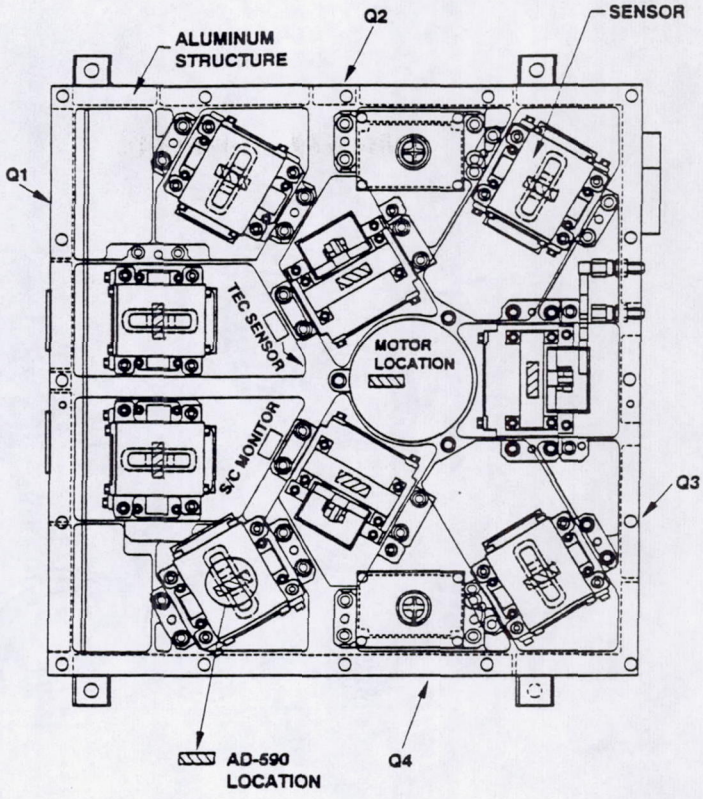

Figure 3. Top view of SSTACK showing motor and sensors.

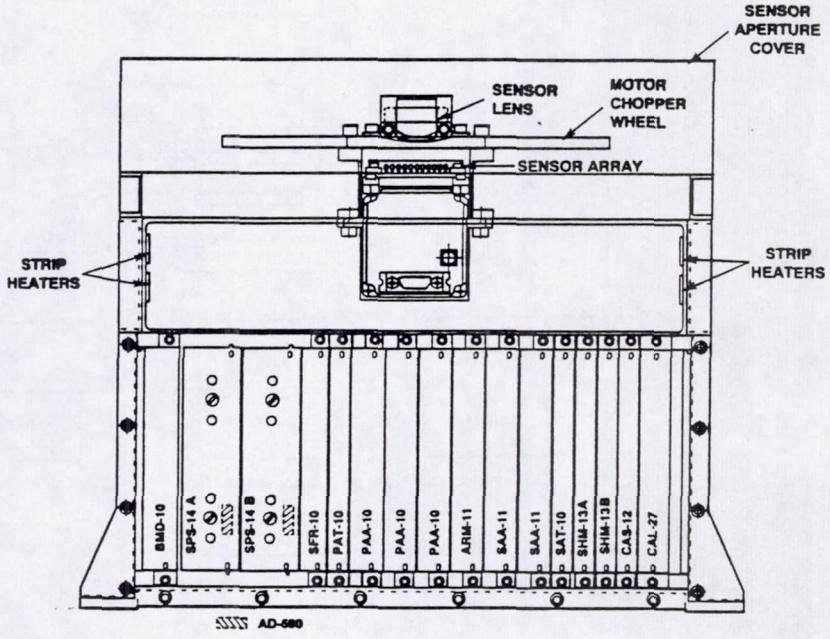

Figure 4. Front-view of SSTACK with front cover removed.

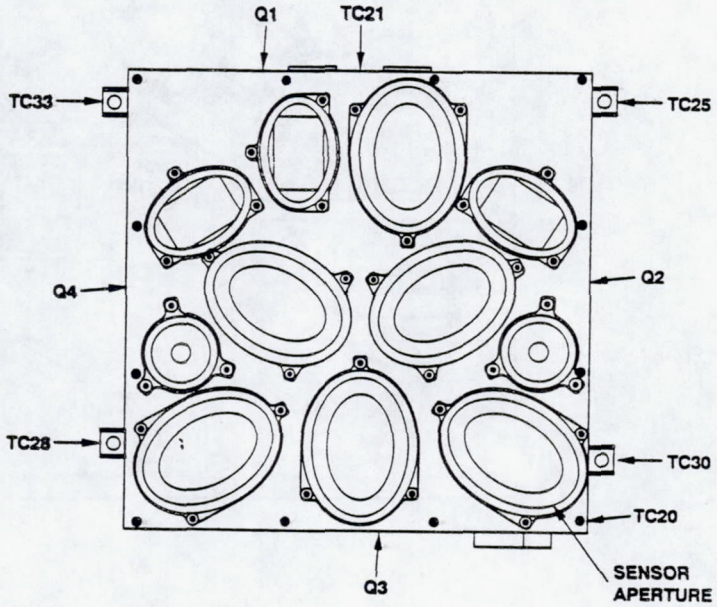

Figure 5. SSTACK aperture plate.

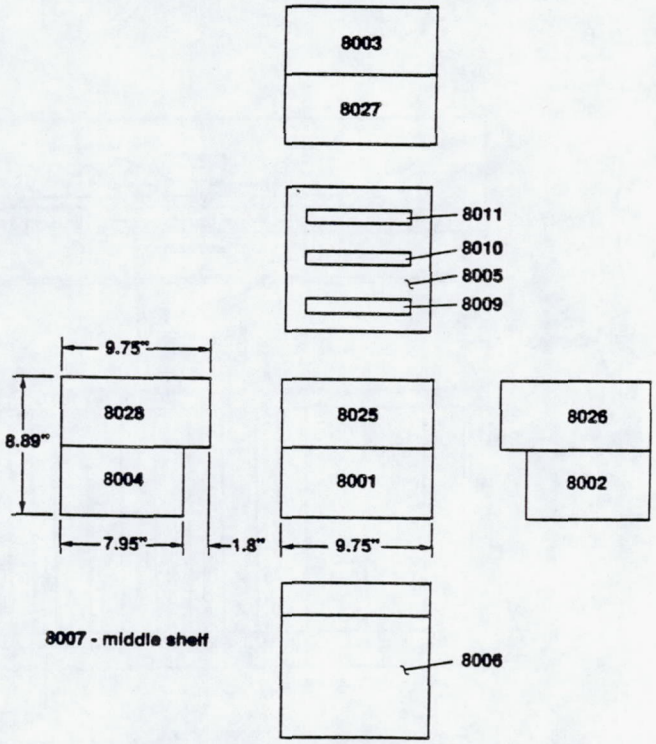

Figure 6. Reduced SINDA thermal model nodes.

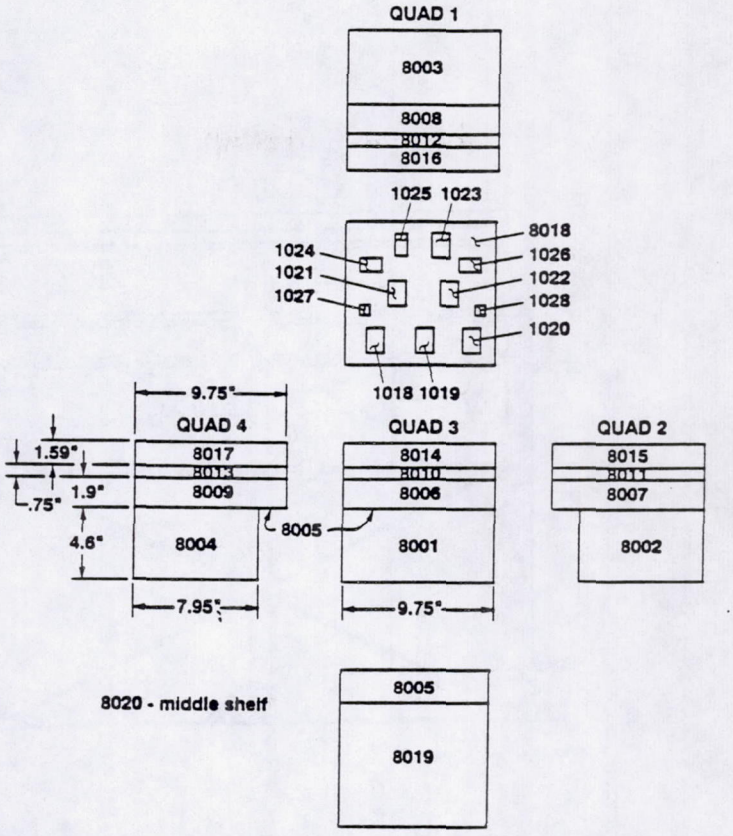

Figure 7. Detailed SINDA thermal model nodes.

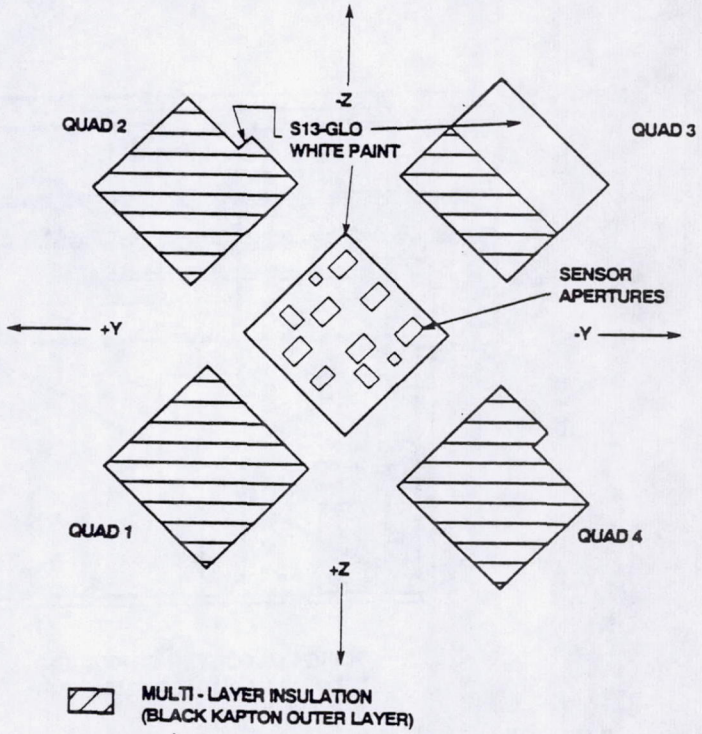

Figure 8. MLI thermal blanket design.

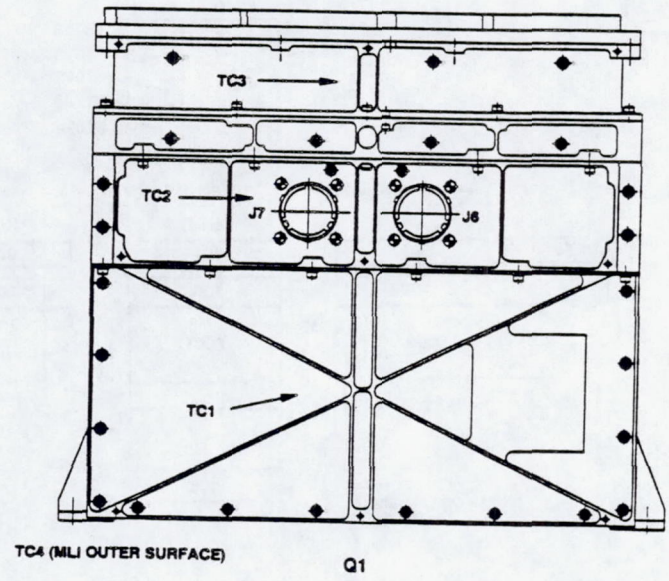

Figure 9. Thermocouples locations on Q1.

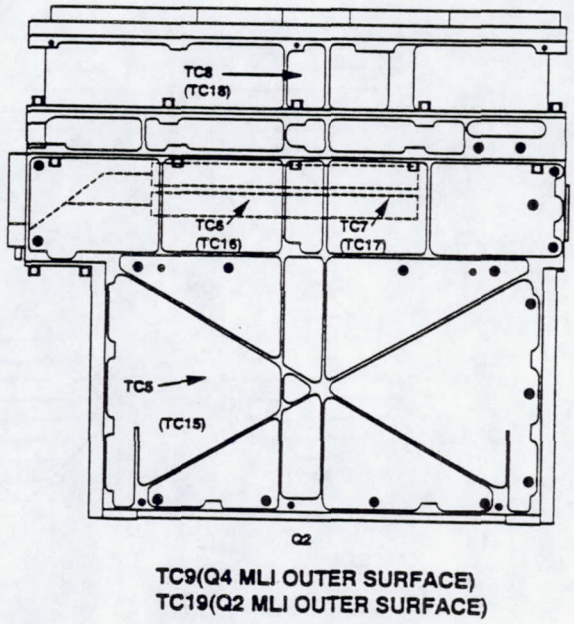

Figure 10. Thermocouples locations on Q2 (paranthesis) and Q4.

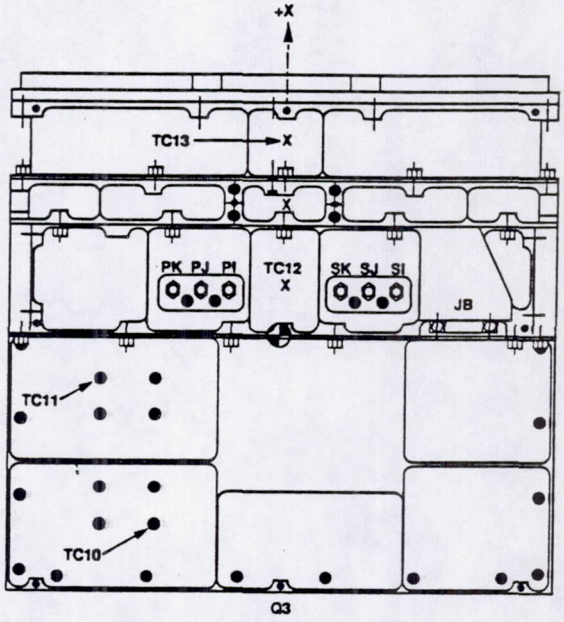

Figure 11. Thermocouples locations on Q3.

Session
Two

Refrigeration/Power Systems

UTILIZATION OF RECENTLY DEVELOPED CODES FOR HIGH POWER BRAYTON AND RANKINE CYCLE POWER SYSTEMS

Michael P. Doherty
National Aeronautics and Space Administration
Lewis Research Center
Nuclear Propulsion Office
Cleveland, OH 44135

SUMMARY

This paper will present two recently developed FORTRAN computer codes for high power Brayton and Rankine thermodynamic cycle analysis for space power applications. The codes were written in support of an effort to develop a series of subsystem models for multimegawatt Nuclear Electric Propulsion, but their use is not limited just to nuclear heat sources or to electric propulsion.

The paper will provide code development background, a description of the codes, some sample input/output from one of the codes, and state future plans/implications for the use of these codes by NASA's Lewis Research Center.

BACKGROUND

Nuclear Electric Propulsion (NEP) is a propellant-efficient type of low thrust-to-weight propulsion for space-based propulsion applications. NEP systems employ a nuclear reactor as a thermal source in a closed heat transport system to generate electricity, which drives an electric thruster. The electric thruster uses the electrical energy to accelerate a propellant, producing mechanical energy or thrust.

Because low thrust is characteristic of electric propulsion, electric propulsion (EP) only realizes its usefulness in microgravity fields. Near planetary bodies, an EP spacecraft's flight is characterized by a spiral trajectory about the planet until escape is achieved. Once free of the planetary gravity well, the spacecraft's trajectory is as direct as need be for target body intercept. Extremely high EP spacecraft velocities are achieved by continual thrusting over a period of time.

Recent studies have shown NEP to be beneficial for robotic planetary

science, as well as Mars piloted and cargo, missions, offering significant advantages over chemical propulsion, including: reduced vehicle initial mass, reduced transit time, wider launch windows, and planetary rendezvous capability (refs. 1 to 4).

Five major subsystems make up an NEP system: a nuclear reactor (with radiation shield), a power conversion subsystem (or heat engine), a waste heat rejection subsystem, a power management and distribution subsystem, and the electric propulsion subsystem (see Figure 1).

Lewis Research Center's (LeRC) Nuclear Propulsion Office (NPO) and Advanced Space Analysis Office (ASAO) have developed subsystem models to improve LeRC's capability to model NEP systems and predict their performance. Greater depth is needed for NEP system models, to verify performance projections and to assess the impact of specific technology developments. The effort to bring greater depth to system models for NEP was initiated with the development of separate software submodules to model each of the five major subsystems inherent to an NEP system.

Subsystem models were developed by the Oak Ridge National Laboratory (ORNL) for the reactor (ref. 5), by the Rocketdyne Division of Rockwell International for power conversion, heat rejection, and power management and distribution (refs. 6 to 9), and by Sverdrup Technology for the thrusters (ref. 10), with at least two inherently different technology options being modeled for each subsystem.

These models are now resident as VAX/FORTRAN source and executable code on one of LeRC's Scientific VAX computers.

DESCRIPTION OF THE CODES

Rankine cycle heat engines produce useful work by heating a fluid to become a gas, employing the heated gas to do useful work, and condensing the gas back into liquid state. Under this modeling effort, the Rankine cycle power conversion option assumes that a primary liquid metal lithium loop supplies heat from the reactor to the boiler and reheater. This is the basis for the schematic shown in Figure 2, which also depicts the other components that make up this power conversion system. Boiler and reheater are modeled as a once-through design with lithium on the shell side and potassium on the tube side. The turboalternator is modeled as a multistage axial reaction turbine with a two-pole toothless

(permanent magnet) alternator. The condenser is modeled as a shear-controlled flow condenser co-serving as a manifold for a heat pipe radiator. The turbopump is modeled as a single stage centrifugal impeller with inducer, driven by a 45% efficient partial admission turbine. Head losses and piping sizes are also computed.

Brayton cycle heat engines are single-phase working fluid engines which produce useful work by heating a gas under a relatively constant pressure process, employing the heated gas to do useful work, and cooling the gas under another relatively constant pressure process to get it back to its original state. This is the basis for the schematic shown in Figure 3, which also depicts the components making up this power conversion system. This Brayton cycle power conversion model has the capability to model the heat input to the gas as either by direct heating (gas circulated through a reactor) or by indirect heating (gas flowing through a liquid-to-gas heat exchanger). The heat exchanger assumes tube and shell configuration with liquid on the tube side. The Brayton turboalternator-compressor can be modeled as either an axial or radial machine, with a two-pole toothless (permanent magnet) alternator. A ducting algorithm computes the ducting diameter, length, and mass, multifoil insulation mass, and total mass for each ducting segment, as well as providing gas Reynolds number and pressure drop. Finally, the code can analyze both recuperated and non-recuperated system designs.

The codes are applicable for electrical ouput power ranges of 100-10,000 kilowatts-electric for system lifetimes of 2-10 years, at turbine inlet temperatures ranging from 1200-1600 K (Rankine) and 1200-1500 K (Brayton). The ranges of inlet-to-outlet temperature ratios considered are 1.25-1.6 (Rankine) and 2.5-4.0 (Brayton).

The products or output of these codes include optimal thermodynamic cycle characteristics, component descriptions, dimensions, efficiencies, and operating parameters, and overall subsystem mass. These outputs are provided as clearly dependent upon the input parameters of turbine inlet temperature, temperature ratio, electrical power level, lifetime, materials of design, turbine design, etc.

SAMPLE INPUT/ OUTPUT

To date, the codes have been reasonably well verified (exercised to see that they work), but only have just begun the process of being

validated (determining the reasonableness of their answers). A parametric analysis of a Brayton power system will be presented to demonstrate the potential of the codes.

Using the Brayton code, a set of cases was run to demonstrate the effect of compressor inlet temperature on the overall mass of a specific space nuclear power system design. The significance of this effect should be clarified. Because of the strong impact that mass has on spacecraft performance, spacecraft power systems may not necessarily be designed for maximum efficiency. Rather, the space power system may be design-optimized for minimum mass. This implies that the system design point ultimately chosen may not be one yielding the highest efficiency, but one yielding the lowest mass.

This implication has interesting consequences for the design of a space electric power generation system. Because a power generation system designed for high efficiency requires moderately low heat rejection, and thus "cold-end", statepoint temperatures, its heat rejection will be encumbered by a low fourth-exponent temperature differential, thus requiring large rejection areas (and encumbent high mass) to achieve the required waste heat rejection capacity. On the other hand, for the same output power requirement, if the power generation system is designed with high heat rejection temperatures, the resulting low power conversion efficiency will demand that a large power source (with encumbent mass) be used. Clearly, for an optimized space electric power generation system, the minimum mass point will be associated with a "cold-end" statepoint (usually the compressor inlet for a Brayton power generation system) temperature somewhere in between these extremes. Detailed analytical modeling of the entire power generation system will help determine minimum system mass versus key parameters such as compressor inlet temperature (or temperature ratio).

To demonstrate this point, a 500 kWe Brayton system was analyzed. The system assumed an 1144 K turbine inlet temperature, a radial compressor having a design pressure ratio of 1.8, a radial turbine design, a Helium-Xenon working fluid mixture having a molecular weight of 20, a recuperator efficiency of .85, and an alternator voltage of 1400 V_{rms}. The compressor inlet temperature was varied from 300 K to 500 K (implying a temperature ratio variance from 3.8 to 2.3). For this analysis, the reactor heat source was modeled with the use of the ORNL lithium liquid metal cooled pin type reactor code (ref. 5), while the heat rejection system was

modeled as being a Sodium-Potassium (NaK) pumped loop having a flat plate, water heat pipe radiator in a 1000 km high Earth orbit, by using the Rocketdyne heat rejection code (ref. 8). Statepoint temperatures, pressures, and required heat flows were manually passed from the Brayton code to the reactor and heat rejection codes to achieve system consistency. System specific mass was calculated versus compressor inlet temperature. In this analysis system specific mass is the sum of the reactor mass; Brayton subsystem mass (including turboalternator-compressor, recuperator, ducting, and intermediate heat exchanger); and heat rejection subsystem mass, divided by the electrical power output.] The results of this parametric variation of compressor inlet temperature (CIT) are shown in Figure 4.

As can be seen from the figure, system specific mass is minimized for a CIT of 400 K, a point somewhere in the midst of the examined range. (It is only coincidental that the minimum happens to occur at the mid point of the chosen range; for the initial conditions of this Brayton design, a CIT design point as low as 250 K is possible, but such a system couldn't operate in Earth orbit. In addition, selection of more data points would have more precisely determined the actual CIT at which the minimum specific mass occurs.) Although the Brayton efficiency at this CIT (24%) is only 73% of the efficiency that could be achieved with a 300 CIT (33%), the mass of its heat rejection system happens to be 33% less. Thus it can be seen that the CIT operating point yielding the minimum system specific mass is not the same point yielding the highest efficiency.

Using the K-Rankine code, a system designer can perform the same kind of trades to determine overall system mass (or specific mass) versus temperature ratio.

UTILIZATION PLANS

A guiding tenet in LeRC's strategic planning for the 1990's is to build upon the strengths of the our Center. At LeRC, our strengths, as evidenced by the roadmap of our history (ref. 11), clearly fall into the disciplines of space power and electric propulsion.

Although these space power and electric propulsion technical areas have had a resurgence in emphasis in recent years - especially so with the potential dawning of major new applications (ref. 12) - there has been a

recent cooling off of intentions to apply these technologies in a major way to new advanced applications. Nevertheless, to indeed build upon the Center's strengths, the Center must maintain a cutting edge in both the technology discipline and systems application of these particular technological areas to the greatest extent possible.

Therefore, these codes, and the system analysis capability they provide, find themselves at the very heart of the future mission of LeRC. Although the Nuclear Propulsion Office will not be formally continued after the end of the fiscal year, the Advanced Space Analysis Office will continue to perform NEP mission and system studies.

Realizing that these studies will be ongoing at LeRC, and recognizing the need for LeRC to maintain a pre-imminence in design, modeling, and analysis of NEP systems for future applications, LeRC is now beginning to implement a new, efficient modeling tool for end-to-end NEP system analysis. This modeling tool will take advantage of an existing generic system modeling, simulation, and analysis environment tool called General Purpose Simulator (or GPS), authored and maintained by the Department of Energy's Argonne National Laboratory (ref. 13). The tool will provide for quick, detailed prototyping of NEP systems that are made up of the subsystem models introduced in this paper (refs. 5 to 10). Such a tool should reduce the analysis time required to create a data curve such as in Figure 4, from as much as 1/2 hour (of analyst's time) per datapoint to mere seconds (the time it takes for a UNIX workstation to respond to the touch of a single kestroke). Before the end of FY93, this system modeling capability is planned to be implemented to some initial degree.

ACKNOWLEDGMENTS

The author gratefully acknowledges Stephen W. Carpenter and John S. Clark for their timely review of the paper.

REFERENCES

1. Hack, K.J.; George, J.A.; and Riehl, J.P.: Evolutionary Use of Nuclear Electric Propulsion. AIAA 90-3821, Sept. 1990.
2. Hack, K.J.; George, J.A.; and Dudzinski, L.A.: Nuclear Electric Propulsion

Mission Performance for Fast Piloted Mars Missions. AIAA 91-3488, Sept. 1991.

3. Yen, C.L.; and Sauer, C.G.: Nuclear Electric Propulsion for Future NASA Space Science Missions. IEPC-91-035, Oct. 1991.
4. Dudzinski, L.A.; Gefert, L.P.; and Hack, K.J.: Nuclear Electric Propulsion Benefits to Piloted Synthesis Missions. Proceedings of the American Nuclear Society Topical Meeting on Nuclear Technologies for Space Exploration, Sept. 1992.
5. Difilippo, F.C.: Scoping Calculations of Power Sources for Nuclear Electric Propulsion. NASA CR 191133.
6. Johnson, G.A.: Potassium-Rankine Power Conversion for Nuclear Electric Propulsion. NASA CR 191134.
7. Ashe, T. and Otting, W.: Brayton Power Conversion System Parametric Design Modeling for Nuclear Electric Propulsion. NASA CR 191135.
8. Moriarty, M.P.: Heat Pipe Cooled Heat Rejection Subsystem Modeling for Nuclear Electric Propulsion Systems. NASA CR 191132.
9. Metcalf, K.J.: Power Conditioning System Modeling for Nuclear Electric Propulsion. NASA CR 191136.
10. Gilland, J.H.: Megawatt Electric Propulsion Thruster Modeling. NASA CR 191137.
11. Dawson, V.P.: Engines and Innovation - Lewis Laboratory and American Propulsion Technology. NASA SP-4306, 1991.
12. Clark, J.S.; Wickenheiser, T.J.; Doherty, M.P.; Marshall, A.; Bhattacharryya, S.K.; and Warren, J.: NASA/DOE/DOD Nuclear Propulsion Technology Planning: Summary of FY 1991 Interagency Panel Results. NASA TM 105703, Aug. 1992.
13. Geyer, H.K.: GPS - A Postscript-like Language for System Simulation. AL-TR-90-085, Jan. 1991.

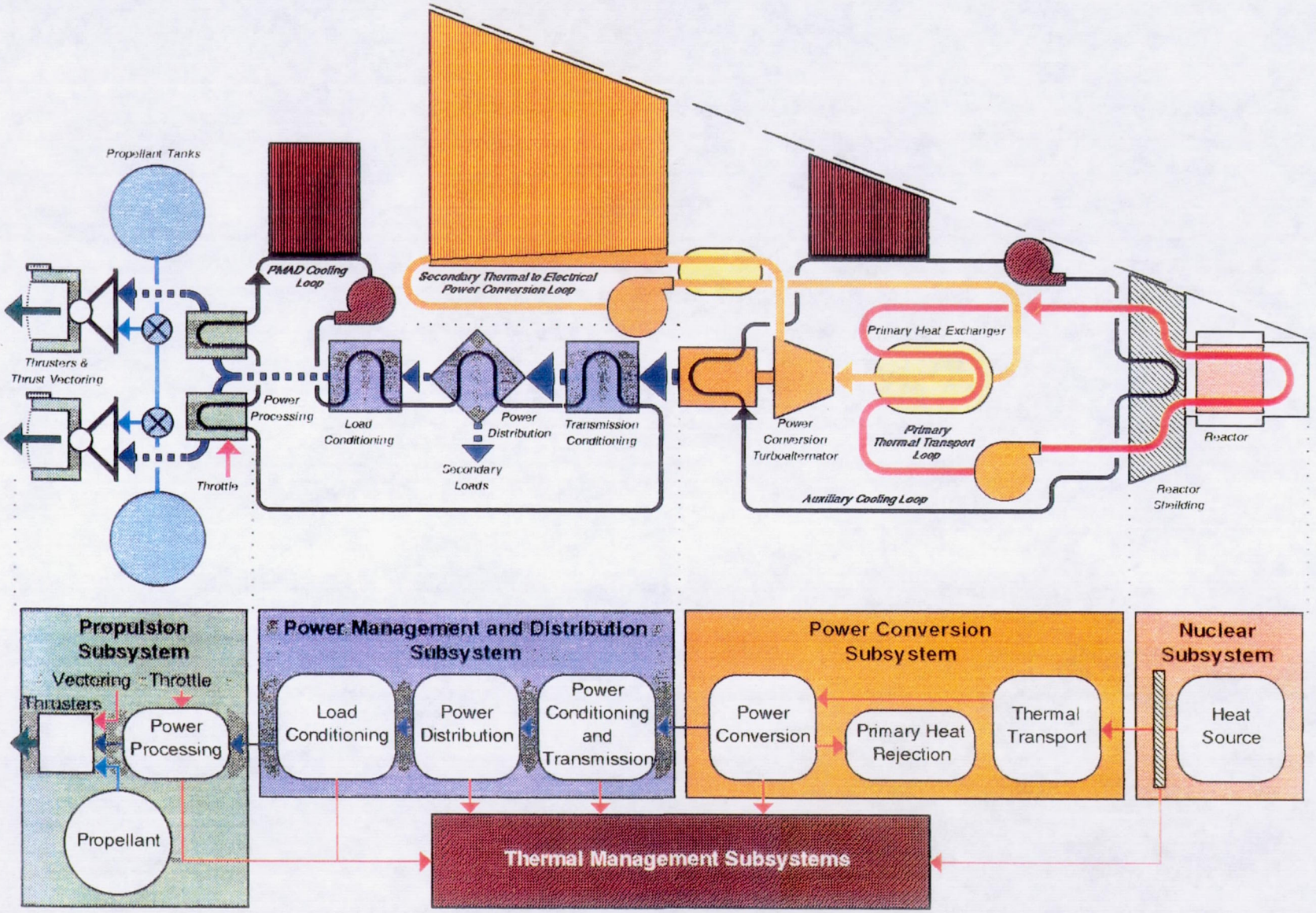

Nuclear Electric Propulsion System Schematic

Example High Power Dynamic System for Piloted Missions

Figure 1.

Figure 2.

POTASSIUM-RANKINE POWER CONVERSION SYSTEM SCHEMATIC

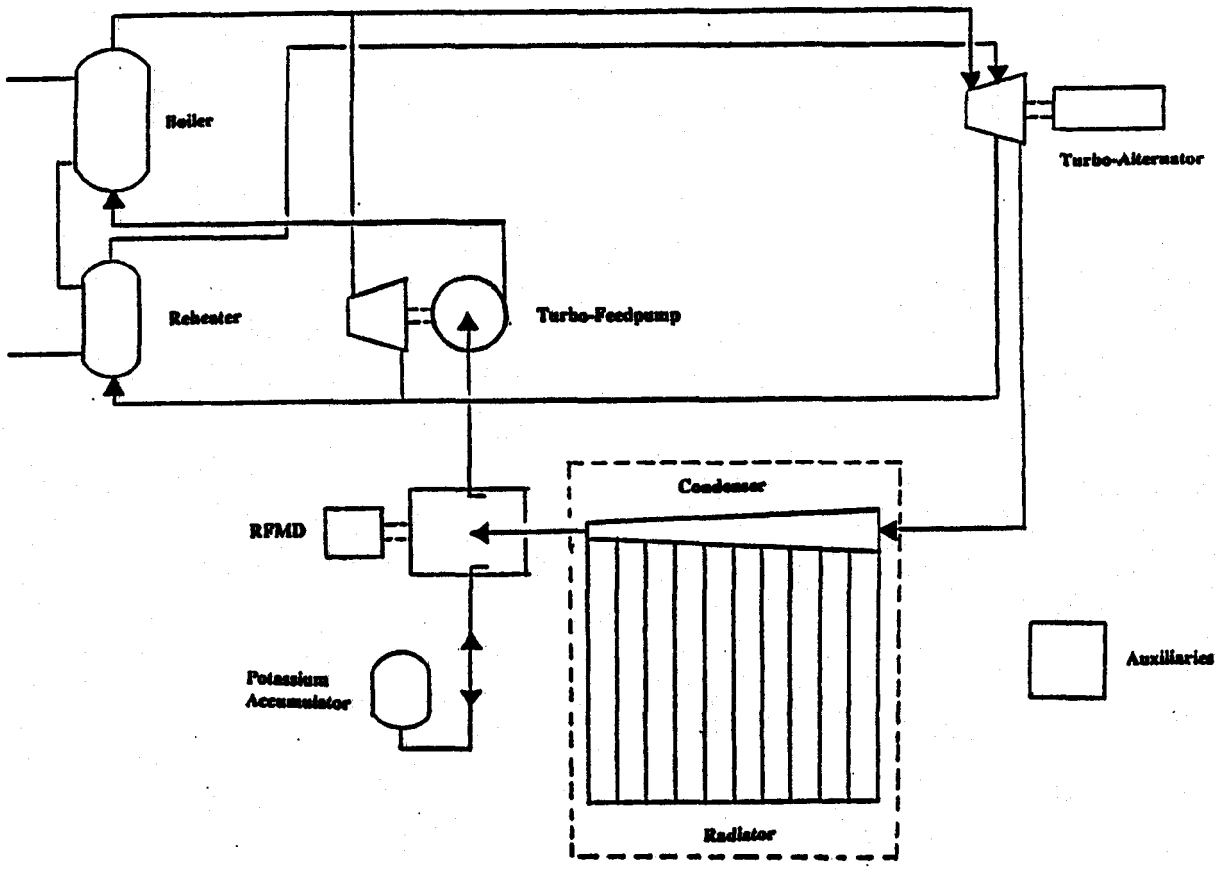

Preceding Page Blank

Figure 3.

Brayton

Power Conversion Module Flow Diagram

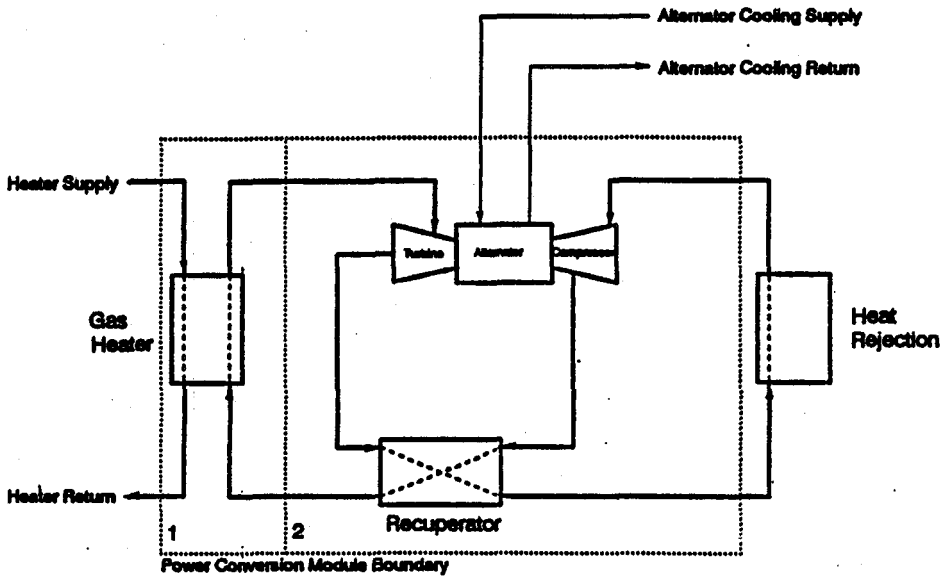

1. Full system module boundary
2. Gas reactor system option module boundary

Figure 4.

Power System Specific Mass vs. Compressor Inlet Temperature

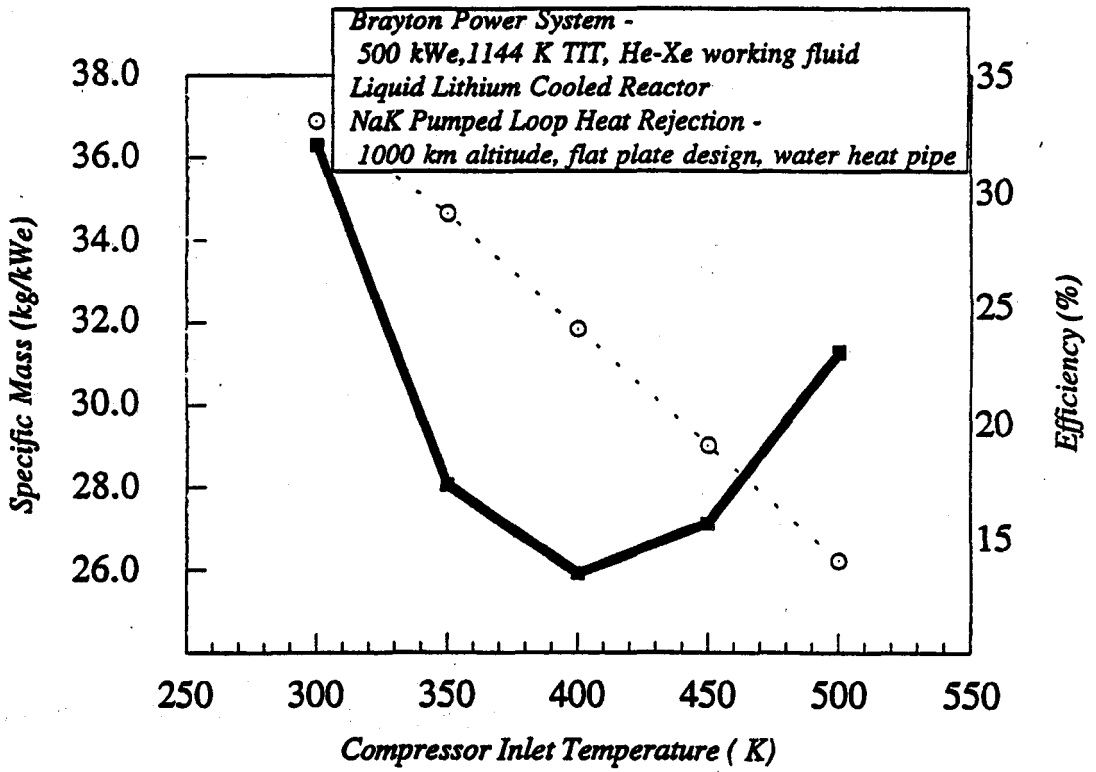

STUDY OF TRANSIENT BEHAVIOR OF FINNED COIL HEAT EXCHANGERS

S.P. Rooke and M.G. Elissa
Department of Mechanical Engineering
The University of Akron
Akron, OH. 44325-3903

SUMMARY

The status of research on the transient behavior of finned coil cross-flow heat exchangers using single phase fluids is reviewed. Applications with available analytical or numerical solutions are discussed. Investigation of water-to-air type cross-flow finned tube heat exchangers is examined through the use of simplified governing equations and an up-wind finite difference scheme. The degenerate case of zero air-side capacitance rate is compared with available exact solution. Generalization of the numerical model is discussed for application to multi-row multi-circuit heat exchangers.

INTRODUCTION

Significant activity has occurred over the last 25 years in the study of the dynamic behavior of heat exchangers. Analytical and numerical solutions of a variety of heat exchanger geometries and applications have appeared. The focus here is specifically with respect to cross-flow heat exchangers for application in the HVAC (and automotive) areas; where geometries are significantly smaller than found in power generation and process industries.

In-depth study of the dynamic behavior of such heat exchangers commenced in the mid-sixties through research aimed at improving dynamic control capabilities of air heating and cooling systems. Numerous simplified first-order transfer function models emerged, such as for bare single tubes in cross flow (refs. 1,2), single pass finned tubes, (ref. 3), serpentine single row (refs. 4,5,6 to 10), and multi-pass cross-counter and cross-parallel flow (refs. 11,12) heat exchangers. Large multi-pass and shell and tube heat exchanger dynamics are discussed in refs. 13 and 14. These references apply to one fluid mixed, liquid to gas cross flow heat exchangers. Most of the results presented are in gain and time constant / frequency response format most useful for control engineering. The aim of all of the above mentioned work was to derive transfer functions relating outlet temperature response of the primary and secondary fluids to changes in flow rate or temperatures of the inlet conditions of primary or secondary fluids. Each of the above references provide up to 4 transfer functions relating the responses of the outlet temperatures to changes in the inlet flow rates and temperatures. Ref. 15 provides for 6 transfer functions, accounting for primary and secondary fluid temperatures and primary fluid flow rate effects on the outlet temperatures. Ref. 16 provides for 8 transfer functions, including the effects of secondary fluid inlet flow rate on the outlet temperatures. Models are also available which include closed-loop feed back analysis of heat exchanger transients (ref. 17) and heating and cooling system simulation (ref. 18).

Most of the above works account for the presence of external fins, but do so by "lumping" the thermal mass of fins with the tubing, thus neglecting thermal diffusion lags due

to conduction in the fins. Work by Waede Hansen and Demandt (ref. 19) and Kabelac (ref. 20) explores distributed effects of heat diffusion in the fins on the overall response of finned tube heat exchangers. Waede Hansen and Demandt concluded that neglecting heat diffusion effects in the fins was reasonable in the frequency range up to 10-15 rads/sec. Kabelac achieved good agreement with experiment using a model which incorporated fin diffusion effects, but did not separate the effects of the fins from the overall model behavior.

Many of the more rigorous analytic and numerical approaches for transient heat exchanger analysis have been developed more recently and have results presented in temperature vs. time format (i.e. the focus is on heat transfer behavior). Some of these studies are more applicable to a wider class of crossflow heat exchangers (i.e. plate heat exchangers, rod bundles, etc.). Rizika (ref. 21) analytically examined a tube in a constant temperature or insulated environment. Evans and Smith (ref. 22) analytically investigated single pass cross flow heat exchangers with neither fluid mixed, but did not include the effects of metal or matrix thermal capacitance. Myers et al. (refs. 23,24) developed an approximate integral method for single row, single pass geometry (solutions developed for both fluids unmixed). Myers et al. (ref. 25) numerically investigated the case of one fluid having an infinite capacitance rate. Jang and Wang (ref. 26) numerically investigated the case of one fluid mixed. Terasaka et al. (ref. 27) used an approximate method of weighted residuals to investigate the case of both fluids unmixed, neglecting metal/matrix capacitance. Spiga and Spiga (ref. 28) utilized the Laplace transform technique (and numerical inversion) to investigate the case of both fluids unmixed, with metal/matrix capacitance incorporated. Gvozdenac (ref. 29), Spiga and Spiga (ref. 28), Romie (ref. 31), and Chen and Chen (ref. 32) used similar Laplace transform approaches to derive analytical solutions for gas-to-gas, neither fluid mixed geometries. Yamashita et al. (ref. 33) used a finite difference technique to numerically investigate heat exchanger transients with both fluids unmixed. Chiang et al. (ref. 34) numerically investigated a cross counter flow automotive application. Numerical investigation of multi-row cooling coils with condensation occurring on the fins has been studied by Reichert et. al (ref. 35).

While significant effort in the above works have been applied to developing analytical solution techniques and presenting the general transient behavior of the broad class of cross flow heat exchangers, less emphasis has been applied to quantifying behavior of particular applications and circuiting arrangements. Numerical analysis remains the strongest and most flexible technique for examining heat exchanger transients. In the same vein as the work of Myers et al. (ref. 23,24, analytical) and Reichert et al. (ref. 35, numerical, cooling coils), the present study further examines the analysis, mathematical/numerical description, and behavior of heat exchangers for air heating in HVAC.

MATHEMATICAL DEVELOPMENT

A length of finned tube exposed to air in crossflow is to be modelled. The tube could be coiled in serpentine manner, laying in a plane which is perpendicular to the external fluid flow, or it could be a single length of tube in cross flow. Situations where multi-row or parallel/counter cross flow circuiting is employed will be discussed later. The following assumptions will be applied:

1. Incompressible flow.
2. "Plug flow" model for water.
3. Convective coefficients constant during transients, equivalent to steady values.
4. Negligible axial conduction in tube and fluids.
5. Negligible radiative effects.
6. Fins/tube are at one unique temperature at a given x location ("lumped thermal mass").
7. The temperature difference between the tube/fin surface and the air is the logarithmic mean temperature difference.
8. Negligible thermal storage in the air.

The primary fluid (water) is treated as mixed (no variation in temperature except in the flow direction) and the secondary fluid (air) is treated as unmixed (variations in temperature both in the flow direction and normal to the flow direction).

Energy balances on an elemental unit of fin/tube (m), water (w), and air (a) gives the governing equations in the primitive variable form:

$$\left(\rho_t c_{p_t} \vartheta_t' + \rho_f c_{p_f} \vartheta_f'\right)\frac{\partial T_m}{\partial t} - \bar{h}_w P(T_w - T_m) + \rho_a V_a A_a' c_{p_a}(T_{ao} - T_{ai}) = 0 \tag{1}$$

$$\rho_w c_{p_w} A_w \frac{\partial T_w}{\partial t} + \rho_w A_w V_w c_{p_w} \frac{\partial T_w}{\partial x} + \bar{h}_w P(T_w - T_m) = 0 \tag{2}$$

$$\rho_a V_a A_a' c_{p_a}(T_{ao} - T_{ai}) = \eta_o \bar{h}_a A' LMTD \tag{3}$$

As will be shown later, this form may be of most usefulness for studying individual effects of physical parameters. The case to be studied here will be for the secondary fluid (air) being heated. Thus, temperatures are non-dimensionalized according to $(T-T_{ai})/(T_{wi}-T_{ai})$. Substitution and rearranging gives:

$$\left(\rho_t c_{p_t} \vartheta_t' + \rho_f c_{p_f} \vartheta_f'\right)\frac{\partial \theta_m}{\partial t} - \bar{h}_w P(\theta_w - \theta_m) + \dot{m}_a' c_{p_a} \theta_{ao} = 0 \tag{4}$$

$$\rho_w c_{p_w} A_w \frac{\partial \theta_w}{\partial t} + \dot{m}_w c_{p_w} \frac{\partial \theta_w}{\partial x} + \bar{h}_w P(\theta_w - \theta_m) = 0 \tag{5}$$

$$\theta_{ao} = \left[1. - \exp\left(-\eta_o \bar{h}_a A' / \dot{m}_a' c_{p_a}\right)\right]\theta_m \tag{6}$$

To reduce the number of variables, dimensionless groupings as follows are helpful:

$$\chi = x/L \ , \quad \tau = tV_w/L$$
$$N_w = \bar{h}_w PL/\dot{m}_w c_{p_w}$$
$$N_a = \eta_o \bar{h}_a A'/\dot{m}_a' c_{p_a}$$
$$C_r = C_m/C_w$$
$$H_r = \eta_o \bar{h}_a A'/\bar{h}_w P$$

Insertion into the governing equations produces

$$\frac{\partial \theta_m}{\partial \tau} + \frac{N_w}{C_r}(\theta_m - \theta_w) + \frac{N_w H_r}{N_a C_r}\theta_{ao} = 0 \tag{7}$$

$$\frac{\partial \theta_w}{\partial \tau} + \frac{\partial \theta_w}{\partial \chi} + N_w(\theta_w - \theta_m) = 0 \tag{8}$$

$$\theta_{ao} = \left[1 - \exp(-N_a)\right]\theta_m \tag{9}$$

Substitution of Eqn.(9) into Eqns. (7) and (8) yields

$$\frac{\partial \theta_{ao}}{\partial \tau} + \left[\frac{N_w}{C_r} + \frac{f(N_a)N_w H_r}{N_a C_r}\right]\theta_{ao} - \left[\frac{f(N_a)N_w}{C_r}\right]\theta_w = 0 \tag{10}$$

$$\frac{\partial \theta_w}{\partial \tau} + \frac{\partial \theta_w}{\partial \chi} + N_w\theta_w - \frac{N_w}{f(N_a)}\theta_{ao} = 0 \tag{11}$$

where $f(N_a)=1-\exp(-N_a)$. Initially, the primary fluid, metal, and secondary fluid temperatures are at zero. The primary fluid (water) temperature is subject to a sudden step change in temperature. The boundary and initial conditions are then

$$\theta_w(\chi,0) = \theta_{ao}(\chi,0) = 0 \tag{12}$$

$$\theta_w(1,\tau) = 1 \tag{13}$$

The dimensionless groupings are the minimum number required to describe the problem. While $N_w=NTU_w$ and $N_a=NTU_a$ have the same form as the conventional "Number of transfer units", they are not actually NTU values. Conversion of these dimensionless variables used into the conventional NTU (ref. 36) can be accomplished as follows:

$$\text{if } \dot{C}_a < \dot{C}_w, \left[\frac{\dot{C}_a}{\dot{C}_w} = \frac{N_w}{N_a}H_r < 1\right] : \quad NTU = \frac{UA}{\dot{C}_a} = \frac{N_a}{1 + H_r} \tag{14}$$

$$\text{if } \dot{C}_w < \dot{C}_a, \left[\frac{\dot{C}_a}{\dot{C}_w} = \frac{N_w}{N_a}H_r > 1\right] : \quad NTU = \frac{UA}{\dot{C}_w} = \frac{H_r N_w}{1 + H_r} \tag{15}$$

N_a and N_w are chosen instead of NTU because they appear naturally in the governing equations, and effectively separate primary and secondary side fluid effects. N_a dictates how close the air temperature comes to the metal temperature (see eqn.6). N_w contains the water flow length L in it, while N_a does not explicitly contain the water flow length. This is a result of the energy equation for the air being lumped and not distributed; thus no characteristic length appears explicitly on the air side. Use of the steady state NTU is not straight forward in parametric studies where the definition can vary. N_a and N_w are also used by Spiga and Spiga (ref. 28) and

Chen and Chen (ref. 32). As will be shown, even the non-dimensional parameters selected do not allow for a perfect separation of all fluid and heat transfer effects. For example, variations in air side resistance affect both the N_a as well as H_r. This duplicity cannot be avoided however, even with a different selection of non-dimensional parameters.

NUMERICAL TECHNIQUE

A forward time backward space finite difference scheme was chosen for the numerical calculations. The explicit formulation was chosen as a "first cut" approach. Eqns. (10) and (11) become

$$\theta_{ao,i}^{n+1} = \left[1 - \frac{N_w \Delta\tau}{C_r} - \frac{f(N_a) N_w H_r \Delta\tau}{N_a C_r}\right] \theta_{ao,i}^{n} + \left[\frac{f(N_a) N_w \Delta\tau}{C_r}\right] \theta_{w,i}^{n} \tag{16}$$

$$\theta_{w,i}^{n+1} = \left[1 - \frac{\Delta\tau}{\Delta\chi} - N_w \Delta\tau\right] \theta_{w,i}^{n} + \frac{\Delta\tau}{\Delta\chi} \theta_{w,i-1}^{n} - \frac{N_w \Delta\tau}{f(N_a)} \theta_{ao,i}^{n} \tag{17}$$

A stability criteria arising from Eqn.(17) is seen to be

$$\Delta\tau \leq \frac{1}{\frac{1}{\Delta\chi} + N_w} \tag{18}$$

N_w in Eqn.(18) arises from the convection term in Eqn.(11). In a purely advective problem, $N_w=0$ and $\Delta\tau=\Delta\chi$ would result (a desirable result, since in dimensional form it is equivalent to $\Delta t \cdot V_w = \Delta x$, which implies that a fluid front properly arrives at a spacial grid point precisely at the time dictated by the fluid velocity.) In the present work the numerical constraint on $\Delta\tau$ is $\Delta\tau < \Delta\chi$, which implies a fluid front will appear at a given grid point prior to what is physically dictated by the fluid velocity. Note that by writing $\Delta\tau = \phi \cdot \Delta\chi$, where $0 \leq \phi \leq 1$, for best representation of the physics, we want $\phi \approx 1$. We can then methodically select grid spacing according to

$$\Delta\chi = \frac{1 - \phi}{\phi N_w} \tag{19}$$

and as ϕ approaches 1, $\Delta\tau$ approaches $\Delta\chi$. Computational effort increases significantly as this is done.

RESULTS AND DISCUSSION

A parametric study is presented using the above parameter definitions over ranges of the parameters found to cover the design and operation of several manufactured air heating coils as determined by a survey of manufacturer's catalogs and designs reported previously in the literature.

An exact solution for the problem at hand is not available. However, Myers et al. (ref. 37) provide an analytic solution for the degenerate case of zero air side capacitance rate. This idealized situation was simulated in the present case by forcing N_a to be very large.

Fig. 1 provides a comparison between the numerical model and the exact solution for the case of negligible air side capacitance. Fig. 1 illustrates a severe test of the numerical model, that of correctly predicting the step response of the primary fluid (water) at the outlet, at a water flush time of one. The comparison is seen to improve as the value of ϕ in Eqn. 19 approaches 1.0 (i.e. decreasing grid and time spacings). A reasonable trade-off between accuracy required for this study and computational effort was to keep ϕ in the neighborhood of 0.995. Figure 2 illustrates that the ϕ criteria has a less dramatic effect on the secondary side fluid (air). For a fixed ϕ less than 1.0, error in temperature is approximately constant versus time, although the magnitude of temperature increases with time and the error appears larger at longer times. The ability to control numerical error is demonstrated; however, since numerically the $\phi \neq 1$ implies some error, the explicit formulation is not particularly attractive on this point and future studies should explore implicit techniques.

Figures 3 and 4 reflect the effects of the metal to water capacitance ratio on outlet water and air temperatures, respectively. The value of C_r does not effect the steady state values of the dimensionless temperatures, but has a strong influence on the transient behavior as expected. Response times can be compared directly between each of the curves on either figure, with greater response times obtained for larger C_r (larger wall capacitance).

Transient heat exchanger efficiency is a useful parameter which compares the energy leaving the heat exchanger via the air stream to the energy that is given up by the water stream, at a given instant during the transient. At steady state, the efficiency will equal one. For heating of the air, we define the transient efficiency as:

$$\textit{Transient Efficiency},\ \epsilon = \frac{(\dot{m}c_p)_a}{(\dot{m}c_p)_w}\frac{(T_{ao} - T_{ai})}{(T_{wi} - T_{wo})}$$

Figure 5 reflects the transient efficiency versus time for the case of varying capacitance ratio. Discontinuities in the curves appear at a dimensionless time of one due to the fact that the water outlet temperature changes abruptly at one flush time. While discontinuities are not an attractive feature for performance diagrams, this is a reflection of what is really occurring. The transient efficiency plot also allows us to compare overall heat exchanger response times for different values of the parameter being studied.

Figures 6 and 7 show the dependence of outlet water and air temperature on N_a, respectively. One can view the N_a variation as a variation in the air flow rate, with smaller N_a values reflecting larger air mass flow rates (with the air side resistance artificially held fixed). As N_a decreases, the water outlet temperature, and hence the air outlet temperature, are seen to decrease. Figure 8 depicts the transient efficiency from which overall response times may be compared. Comparisons of Figs. 6,7, and 8 demonstrate the utility of presenting both outlet temperatures and efficiency; while response time is enhanced by increasing the air mass flow rate (decrease in N_a), one would not want to maximize air mass flow rate in most designs because by doing so the air experiences a negligible rise in temperature.

The effect of the length of the heat exchanger is examined with the N_w parameter. Figs. 9

and 10 show the outlet water and air temperatures, respectively versus the dimensionless time with N_w as a parameter. The x-axis is normalized with respect to the flush time of the water of the $N_w=1$ case so that time durations are equivalent between the different N_w curves. Thus, one flush time is shown at $Tau^*=1$ for the $N_w=1$ case, while for the $N_w=8$ case, the flush time occurs at $Tau^*=8$ since its length is 8 times longer than for $N_w=1$ (assuming the same fluid velocity in each case). As N_w decreases, the outlet water temperature approaches the inlet water temperature, the outlet air temperature approaches the water temperature, and steady state is reached more quickly than for the larger values of N_w. The transient efficiency curves shown in Fig. 11 more directly compare response time for the N_w variations. Note that $N_w=1,4$, and 8 correspond to the conventional units of NTU=0.5, 2.0, and 4.0, respectively, here.

Approximate solutions are available for the cases examined here. The current work is not intended to replace previously available solutions, but rather to complement them. Effort has been aimed at outlining and describing the results and limitations of a simplified numerical solution approach to solve for heat exchanger transients.

Extension of the current work is ongoing to further utilize the flexibility of the numerical approach. Areas being studied include examining the effects of tube rows on transient behavior and examining changes in secondary fluid temperatures and the flow rates of both fluids. Comparisons of solutions between the present modeling approach and a simplified model using ordinary differential equations is also underway. It is anticipated that these efforts will add further insight into modeling requirements as well as insight into design of heat exchangers with consideration of transients.

Acknowledgements

Financial support for this research received from the Ohio Board of Regents Research Challenge Grant (ORSSP#R2444) and from the Faculty Projects Research Committee of the University of Akron (FRG#1244) is gratefully acknowledged.

NOMENCLATURE

A	Area (m^2)
c_p	Specific heat (J/kg·K)
C_r	Dimensionless ratio of metal capacitance to water capacitance.
$\dot{C}$	Capacitance rate (W/K), mass flow specific heat product.
h	Convective heat transfer coefficient ($W/m^2 \cdot K$)
H_r	Dimensionless ratio of water side resistance to air side resistance.
L	Total flow length experienced by water (m)
LMTD	Logarithmic mean temperature difference: $(T_{ao}-T_{ai})/\ln[(T_m-T_{ai})/(T_m-T_{ao})]$
$\dot{m}$	Mass flow rate (kg/s)
NTU	Number of transfer units, $UA/\dot{C}_{min}$.
N_w	(NTU_w) Dimensionless number, inverse of water side resistance-capacitance product.
N_a	(NTU_a) Dimensionless number, inverse of air side resistance-capacitance product.
P	Tube inner perimeter (m)

t Time (s)
UA Overall heat transfer coefficient (W/K)
V Velocity (m/s)
ϑ Volume (m^3)
x Axial position along tube (m)

greek
ρ Density (kg/m^3).
η Surface efficiency
τ Dimensionless time, tV_w/L.
θ Dimensionless temperature $(T-T_{ai})/(T_{wi}-T_{ai})$
χ Dimensionless position, x/L.

subscripts
w water
a air
ai inlet air
ao outlet air
i grid point
m metal (fin plus tubing)
f fin
t tube

superscripts
n time level
$'$ per unit length
$\bar{}$ length or surface averaged

REFERENCES

1. Gartner, J.R.; and Harrison, H.L.: Frequency Response Transfer Function for a Tube in Crossflow. ASHRAE Trans., vol. 69, 1963, pp. 323-330.
2. McNamara, R.T.; and Harrison, H.L.: A Lumped Parameter Approach to Crossflow Heat Exchanger Dynamics. ASHRAE Trans., vol.73, pt.2, 1967, pp. iv.1.1-iv.1.9.
3. Gartner, J.R.; and Harrison, H.L.: Dynamic Characteristics of Water-to-Air Crossflow Heat Exchangers. ASHRAE Trans., vol. 71, pt.1, 1965, pp. 212-224.
4. Tobias, J.R.: Simplified Transfer Function for Temperature Response of Fluids Flowing Through Coils, Pipes or Ducts. ASHRAE Trans., vol. 79, pt.2, 1973, pp. 19-22.
5. Gartner, J.R.: Simplified Dynamic Response Relations for Finned-Coil Heat Exchangers. ASHRAE Trans., vol. 76, pt.2, 1972, pp. 163-169.
6. Gartner, J.R.; and Daane, L.E.: Dynamic Response Relations for a Serpentine Crossflow Heat Exchanger with Water Velocity Disturbance. AHSRAE Trans., vol.75, pt.1, 1969, pp. 53-68.
7. Pearson, J.T.; Leonard, R.G.; McCutchan, R.D.: Gain and Time Constant for Finned Serpentine Crossflow Heat Exchangers. ASHRAE Trans., vol. 80, pt.2, 1974, pp. 255-267.
8. Boot, J.L.; Pearson, J.T.; Leonard, R.G.: An Improved Dynamic Response Model for Finned Serpentine Cross-Flow Heat Exchangers. ASHRAE Trans., vol. 84, pt. 1, 1977, pp. 218-239.

9. Jawadi, Z.: A Simple Transient Heating Coil Model. In Analysis of Time-Dependent Thermal Systems, AES-vol.5, Wepfer, W.J.; Klein, S.A.; Patton, J.S. Eds., ASME, New York, 1988, pp. 63-69.
10. Underwood, D.M.; and Crawford, R.R.: Dynamic Nonlinear Modeling of a Hot-Water-to-Air Heat Exchanger for Control Applications. ASHRAE Trans., vol. pt.1, 1991, pp. 149-155.
11. Tamm, H.: Dynamic Response Relations for Multi-Row Crossflow Heat Exchangers. ASHRAE Trans., vol.75, pt.1, 1969, pp. 69-80.
12. Tamm, H.; and Green, G.H.: Experimental Multi-Row Crossflow Heat Exchanger Dynamics. ASHRAE Trans., vol. 79, pt. 2, 1973, pp. 9-18.
13. Williams, T.J.; and Morris, H.J.: A Survey of the Literature on Heat Exchanger Dynamics and Control. Chem. Eng. Symp. Ser. no. 36, vol. 57, 1961, pp. 20-33.
14. Matsuyama, H.; and O'Shima, E.: Representation of Dynamics of Multipass Heat Exchangers. Heat Transfer Japanese Research, Apr.-Jun., 1975, pp. 1-11.
15. Franck, G.: Dynamisches Verhalten von Kreuzstromwärmeübertragern. Wärme und Stoffübertragung, vol. 20, 1986, pp. 141-149.
16. Bender, E.: Dynamic Response of Crossflow Heat Exchangers for Variations in Temperature and Massflow. Proc. of the 5th IFAC World Congress, 1972, pp. 8.3.1-8.3-10.
17. Maxwell, G.M.; Shapiro, H.N.; Westra, D.G.: Dynamics and Control of a Chilled Water Coil. ASHRAE Trans., vol. 1989, pp. 1243-1255.
18. Clark, D.R.; Hurley, C.W.; Hill, C.R.: Dynamic Models for HVAC System Components. ASHRAE Trans., vol. 91, 1985, pp. 737-751.
19. Waede Hansen, K.; Demandt, K.: Dynamics of a Cross-Flow Heat Exchanger with Fins. Int. J. Heat Mass Transfer, vol. 17, 1974, pp. 1029-1036.
20. Kabelac, S.: The Transient Response of Finned Crossflow Heat Exchangers. Int. J. Heat Mass Transfer, vol. 32, no. 5, 1989, pp. 1189-1192.
21. Rizika, J.W.: Thermal Lags in Flowing Incompressible Fluid Systems Containing Heat Capacitors. ASME, New York, 1954, Paper No. 54-SA-50.
22. Evans, F.; and Smith, W.: Cross-Current Transfer Processes in the Non-Steady State. Proc. Roy. Soc., London, vol. 272 A, 1962, pp. 241-269.
23. Myers, G.E.; Mitchell, J.W.; Nagaoka, R.: A Method of Estimating Cross-Flow Heat Exchanger Transients. ASHRAE Trans., vol. 71, pt.1, 1965, pp. 225-230.
24. Myers, G.E.; Mitchell, J.W.; Lindeman, C.F.: The Transient Response of Heat Exchangers Having an Infinite Capacitance Rate Fluid. J. Heat Transfer, May 1970, pp. 269-275.
25. Myers, G.E.; Mitchell, J.W.; and Norman, R.F.: The Transient Response of Crossflow Heat Exchangers, Evaporators, and Condensers. J. Heat Transfer, Feb. 1967, pp. 75-80.
26. Jang, J.Y.; and Wang, M.T.: Transient Response of Crossflow Heat Exchangers with One Fluid Mixed. Heat and Fluid Flow, vol.8, no.3, Sept. 1987, pp. 182-186.
27. Terasaka, H.; Kanoh, H.; Masubuchi, M.: Approximate Dynamic Analysis of Crossflow Heat Exchanger by the Method of Weighted Residuals. Bull. of the JSME, vol.23, no.177, Mar. 1980, pp. 432-438.
28. Spiga, M.; Spiga, G.: Transient Temperature Fields in Crossflow Heat Exchangers With Finite Wall Capacitance. J. Heat Transfer, vol.110, Feb. 1988, pp. 49-53.
29. Gvozdenac, D.D.: Analytical Solution of the Transient Response of Gas-to-Gas Crossflow

Heat Exchanger with Both Fluids Unmixed. J. Heat Transfer, vol. 108, Nov. 1986, pp. 722-727.
30. Spiga, M.; Spiga, G.: Two-Dimensional Transient Solutions for Crossflow Heat Exchangers With Neither Gas Mixed. J. Heat Transfer, vol. 109, 1987, pp. 281-286.
31. Romie, F.E.: Transient Response of Gas-to-Gas Crossflow Heat Exchangers with Neither Gas Mixed. J. Heat Transfer, vol. 105, May 1987, pp. 518-521.
32. Chen, H.T.; and Chen, K.C.: Transient Response of Crossflow Heat Exchangers with Finite Wall Capacitance. J. Heat Transfer, vol.114, Aug. 1992, pp.752-755.
33. Yamashita, H.; Izumi, R.; Yamaguchi, S.: Analysis of the Dynamic Characteristics of Cross-Flow Heat Exchangers With Both Fluids Unmixed (On the Transient Responses to a Step Change in the Inlet Temperature). Bull. of the JSME, vol.21, no.153, Mar. 1978, pp. 479-485.
34. Chiang, E.C.; Chellaiah, S.; Johnson, J.H.: Modeling of Convective Heat Flow in Radiators for Coolant Temperature Prediction. ASME, New York, 1985, paper 85-WA/HT-22.
35. Reichert, B.A.; Nelson, R.M.; Pate, M.B.: A Computer Simulation of a Cross-Flow Heat Exchanger Operating in a Moist Air Environment. Computer Aided Engineering of Energy Systems, vol.2, ASME, New York, 1986, pp. 89-96.
36. Kays, W.M.; and London, A.L.: Compact Heat Exchangers. Third Edition, McGraw-Hill, New York, 1984, pp. 79-101.
37. Myers, G.E.; Mitchell, J.W.; and Norman, R.F.: The Transient Response of Cross-Flow Heat Exchangers with One Fluid Mixed. Report No. MM-3, Department of Mechanical Engineering, The University of Wisconsin, Madison, Wisconsin, Oct. 1, 1965.

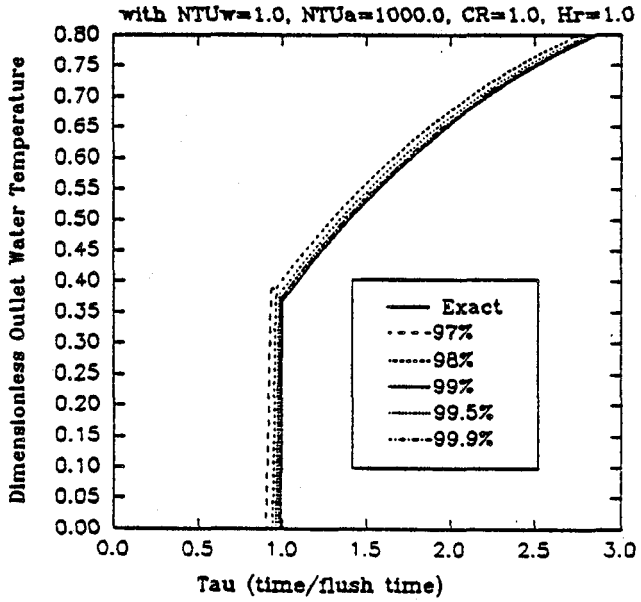

Fig. 1. Comparison of numerical and exact solutions (dimensionless water outlet temperature versus dimensionless time) for the case of negligible air side capacitance, with the grid/time spacing ratio as a parameter.

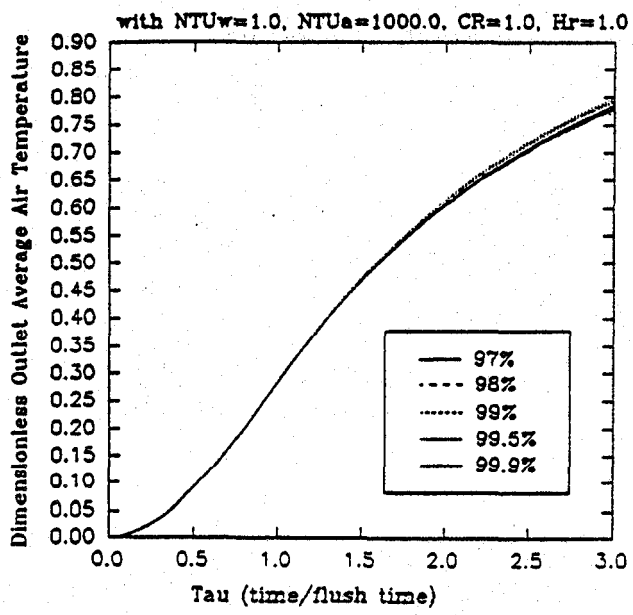

Fig. 2. Comparison of numerical and exact solutions (integrated dimensionless air outlet temperature versus dimensionless time) for the case of negligible air side capacitance, with the grid/time spacing ratio as a parameter.

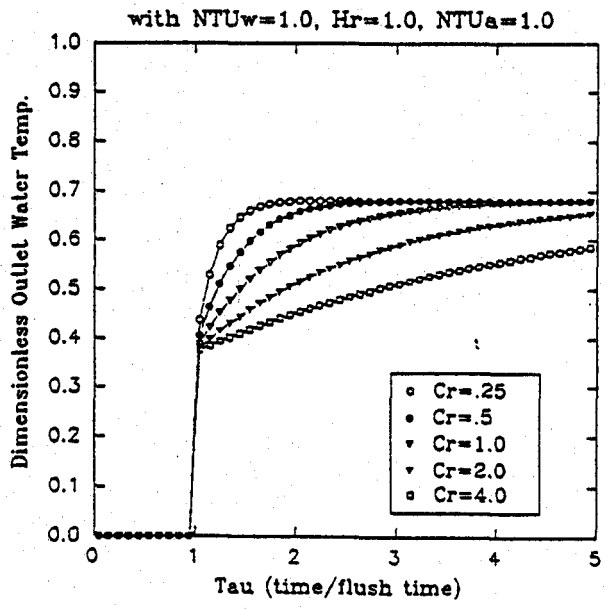

Fig. 3. Dependency of outlet dimensionless water temperature versus dimensionless time on the metal/water capacitance ratio, with all other parameters held fixed.

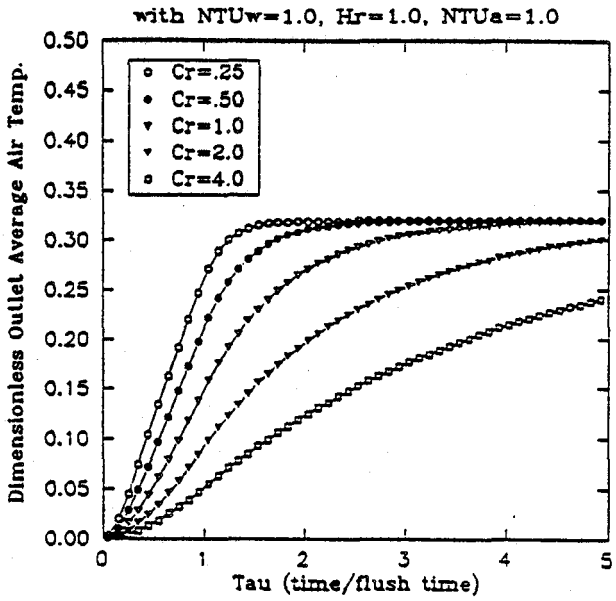

Fig. 4. Dependency of the dimensionless integrated air outlet temperature versus dimensionless time on the metal/water capacitance ratio, with all other parameters held fixed.

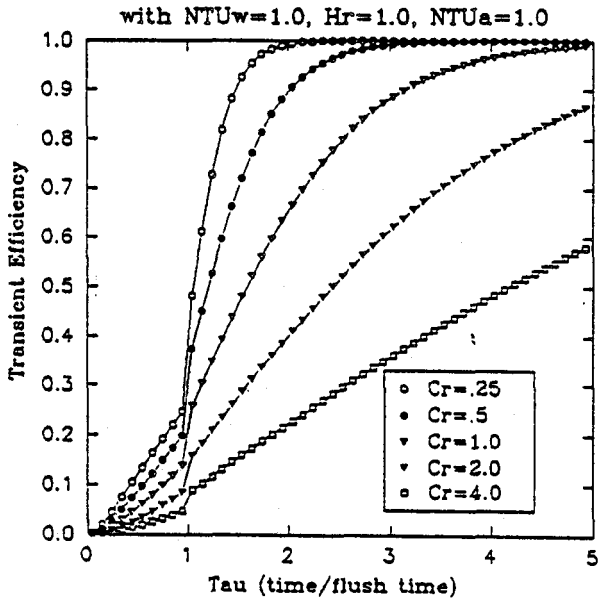

Fig. 5. Dependency of the transient efficiency versus dimensionless time on the metal/water capacitance ratio, with all other parameters held fixed.

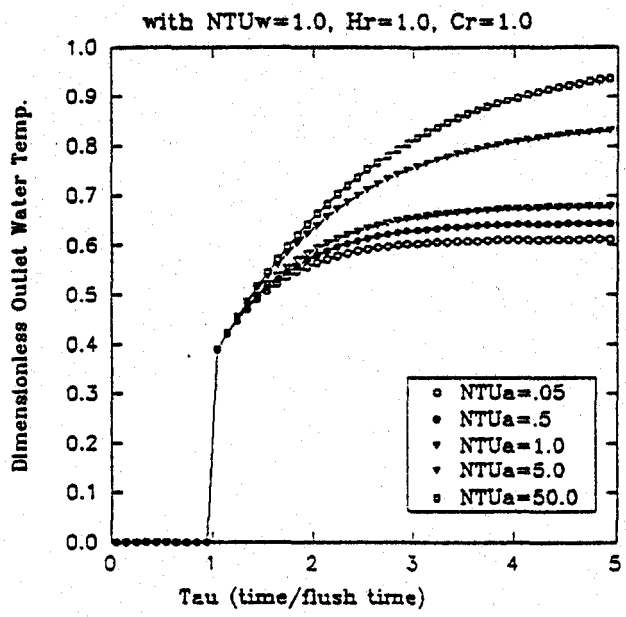

Fig. 6. Dependency of the dimensionless water outlet temperature versus dimensionless time on the N_a parameter, with all other parameters held fixed (simulated air capacitance rate effects).

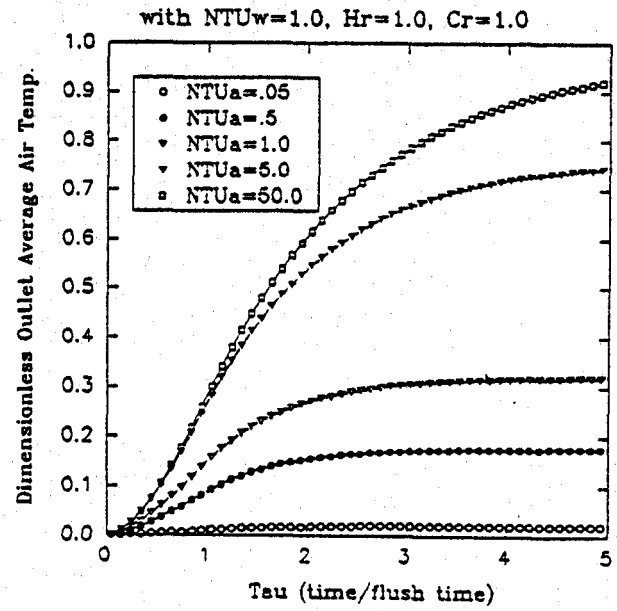

Fig. 7. Dependency of the integrated dimensionless air outlet temperature versus dimensionless time on the N_a parameter, with all other parameters held fixed (simulated air capacitance rate effects).

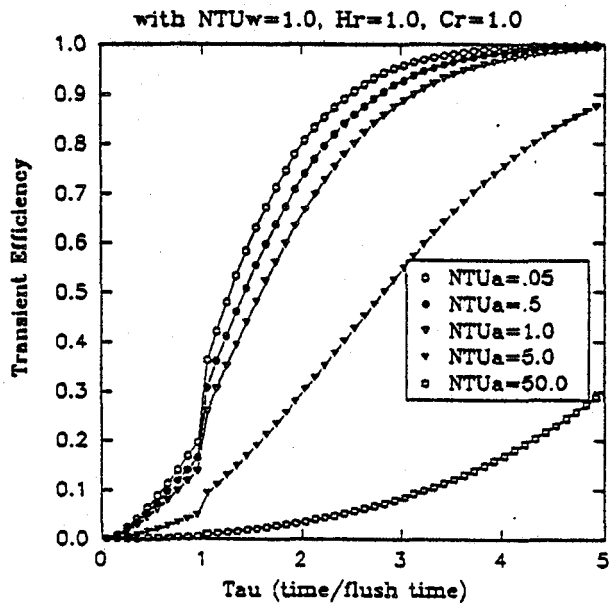

Fig. 8. Dependency of the transient efficiency versus dimensionless time on the N_a parameter, with all other parameters held fixed (simulated air capacitance rate effects).

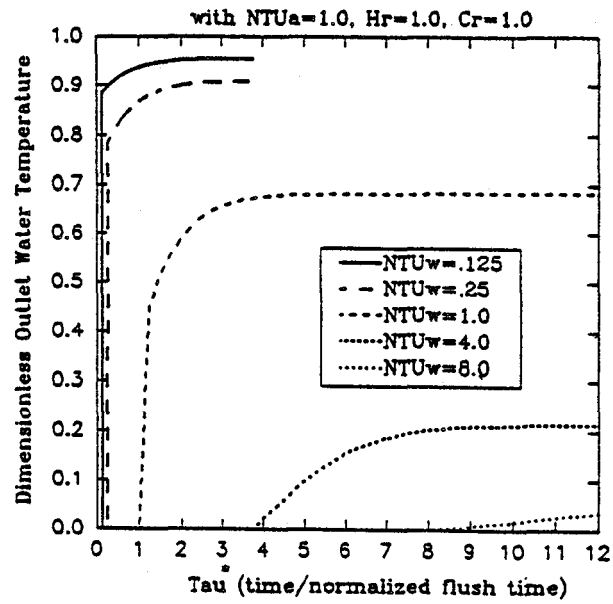

Fig. 9. Dependency of the dimensionless water outlet temperature versus normalized dimensionless time on the N_w parameter, with all other parameters held fixed (simulated heat exchanger length effects).

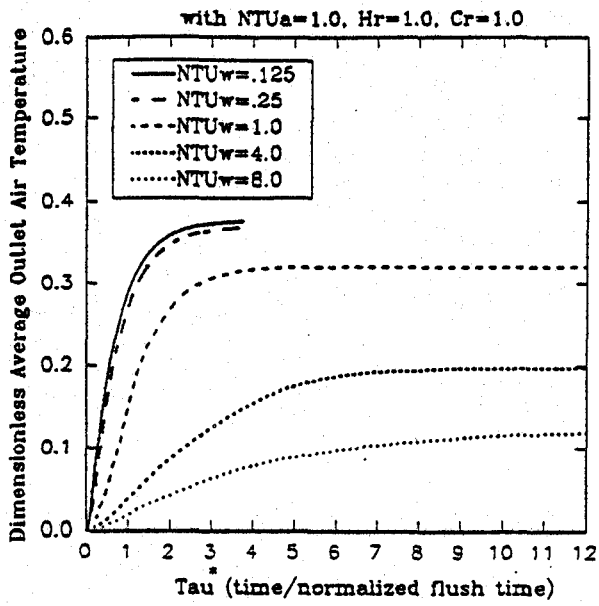

Fig. 10. Dependency of the integrated dimensionless air outlet temperature versus normalized dimensionless time on the N_w parameter, with all other parameters held fixed (simulated heat exchanger length effects).

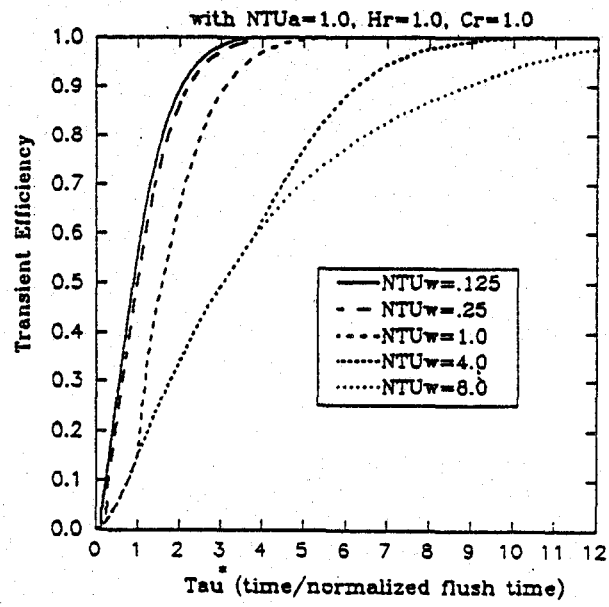

Fig. 11. Dependency of the transient efficiency versus normalized dimensionless time on the N_w parameter, all other parameters held fixed (simulated heat exchanger length effects).

PREDICTION OF PRESSURE DROP IN FLUID TUNED MOUNTS USING ANALYTICAL AND COMPUTATIONAL TECHNIQUES

William C. Lasher*, Amir Khalilollahi*, John Mischler**, Tom Uhric**
The School of Engineering and Engineering Technology
The Pennsylvania State University at Erie, The Behrend College
Station Road, Erie, Pa. 16563

ABSTRACT

A simplified model for predicting pressure drop in fluid tuned isolator mounts has been developed. The model is based on an exact solution to the Navier-Stokes equations and has been made more general through the use of empirical coefficients. The values of these coefficients were determined by numerical simulation of the flow using the commercial CFD package FIDAP.

INTRODUCTION

Fluid-tuned mounts [1] are an effective device for vibration isolation. A simple mount consists of fluid filled chambers connected by a narrow inertia track (Figure 1). When a force is applied to the chamber ends, the fluid is forced through the inertia track causing a pressure drop across the mount. The magnitude and phase of the pressure drop are important parameters in determining the isolation performance of the mount. It is possible to tune the mounts to a specific "notch frequency" by varying the geometric shape of the mount. The shape of the mount and the flow parameters determine the flow resistance, which determines the notch frequency. The design problem then becomes one of determining the shape and flow parameters for a specific notch frequency. This is a complicated fluid dynamics problem; successful design of the mounts requires either sophisticated computational fluid dynamics (CFD) predictions or construction of prototypes for experimental testing. Either of these options requires a considerable amount of time and resources, which makes them difficult to use as design tools. Although this analysis and testing cannot be completely avoided, a simplified empirical model would allow the designer to investigate the effects due to changes in important parameters, and perform preliminary screening on different proposals.

In the present work a model is developed for the simplified geometry shown in Figure 2. The problem can be non-dimensionalized using the mean velocity u_0 and diameter d of the inertia track. The non-dimensional parameters are defined as:

---

* Assistant Professor of Mechanical Engineering

** Undergraduate Student Research Assistant

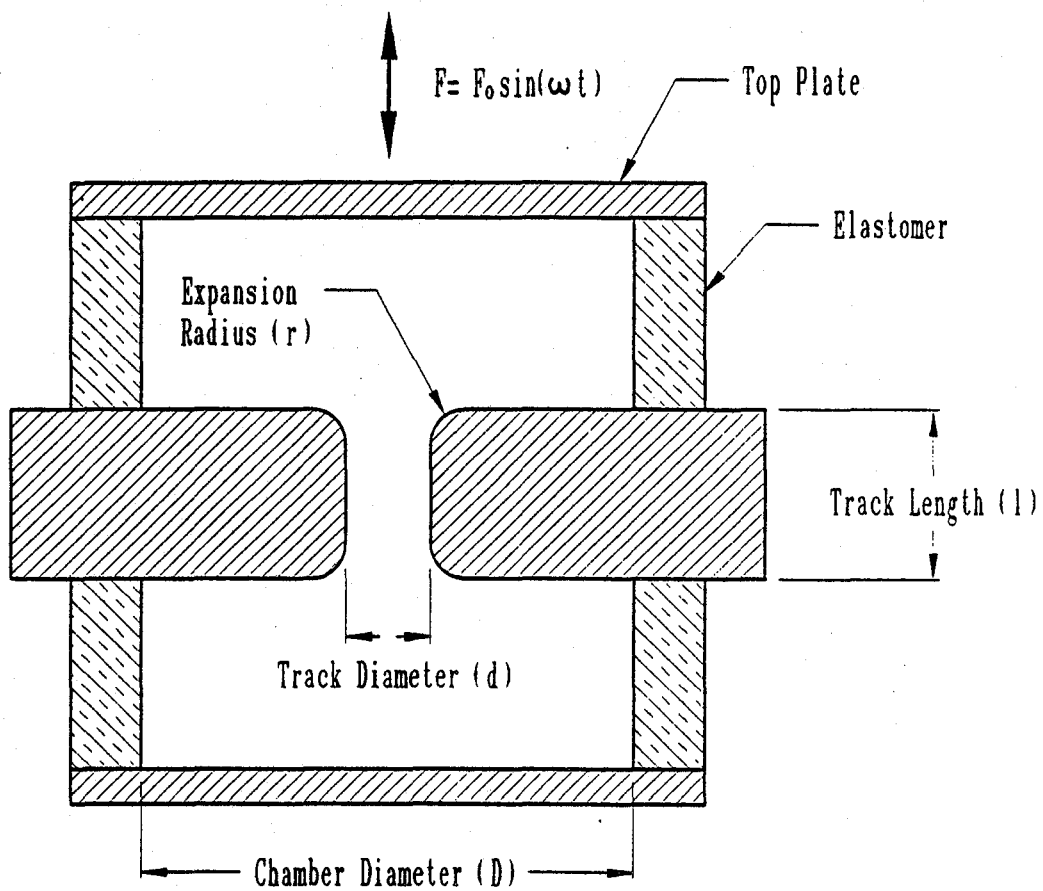

Figure 1
Simple Mount

D/d: expansion ratio
l/d: length/diameter ratio
r/d: radius/diameter ratio
Re: Reynolds Number ($\rho u_o d/\mu$)
St: Strouhal Number ($\omega d/u_o$)
Va: Valenci Number (Re•St)

where

ρ = density
μ = viscosity
ω = angular frequency

A theoretical model for predicting the pressure drop for this geometry was previously developed. The model consists of a series of component models (inertia track, expansion, contraction, and end chamber) which contain coefficients that must be determined by experiment or numerical simulation. In the present work a series of numerical simulations were performed to determine the value of these coefficients, which are a function of mount

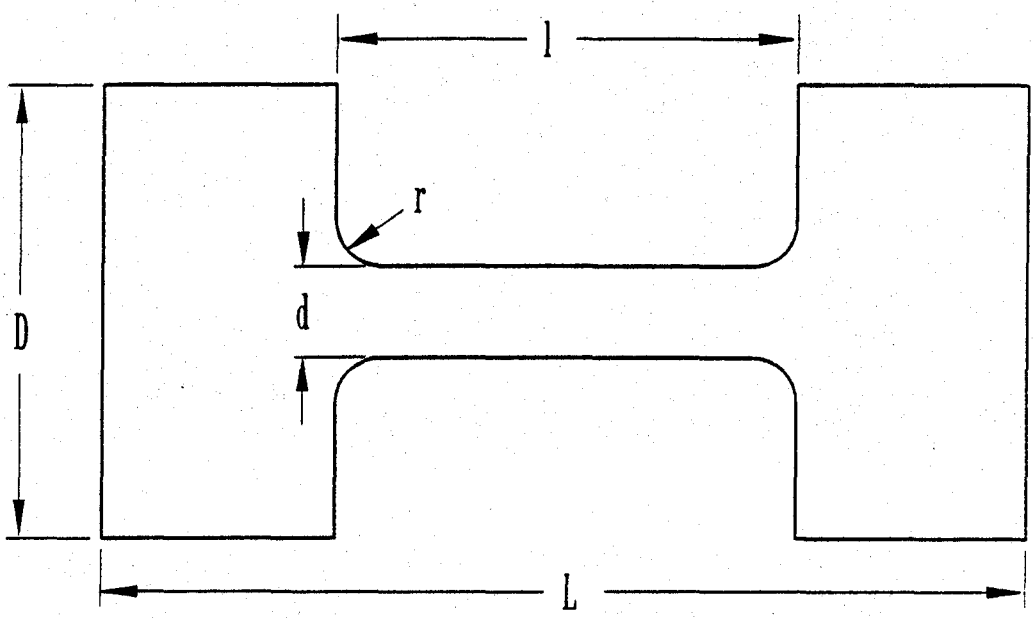

Figure 2
Simplified Mount Geometry

geometry and flow parameters. Completion of the model will require experimental verification, which is in progress.

MATHEMATICAL MODEL

A control volume analysis on the simplified geometry of Figure 2 gives the following equation:

$$A_0 \Delta P = \rho l \frac{dQ}{dt} + F_b \tag{1}$$

where A_0 is the cross-sectional area of the end chambers, P is the pressure, Q is the volume flow rate, and F_b includes the effects of viscous shear, expansion/contraction, and other forces such as body and gravity forces. This equation simply states that the resistance to the pressure difference across the mount is determined by the inertia of the fluid and a general shear/body force.

Presently, the force F_b includes two effects: the viscous resistance, and expansion/contraction terms. The latter are minor contributors and are [2]:

$$\Delta P_{con} / \left(\frac{1}{2}\rho u_0^2\right) = 0.42\left(\frac{1}{A} - \frac{1}{A_0}\right) \tag{2}$$

$$\Delta P_{exp} / \left(\frac{1}{2}\rho u_0^2\right) = \left(1 - \frac{A}{A_0}\right)^2 \tag{3}$$

where A is the cross-sectional area of the inertia track.

The major part of the resistance to the flow occurs within the relatively long inertia track and the end chambers, where the spatial and periodic velocity components exist. The analysis of the oscillatory viscous flow through uniform pipes can be favorably applied to develop the relation between the flow rate and pressure difference across the mount. This phasor relation includes the effects of viscous shear as well as the inertia of the fluid. If a long circular cross-section pipe of radius R undergoes an oscillatory pressure gradient, the volume flow rate through this pipe is [3]:

$$Q = \frac{\pi R^2 \Delta P_0}{\rho l i \omega}\left(1 - \frac{2\alpha i^{3/2} J_1(\alpha i^{3/2})}{i^3 \alpha^2 J_0(\alpha i^{3/2})}\right) e^{i\omega t} \tag{4}$$

where α is equal to $R(\omega/\nu)^{1/2}$ and is referred to as the frequency parameter (α^2 is equivalent to Va/4). J_0 and J_1 are Kelvin functions [4].

It is practical to input the displacement of the mount rather than the force on the mount. In this case the volume flow rate is known

$$Q = Q_0 \sin(\omega t) \tag{5}$$

and the pressure difference ΔP must be calculated from:

$$\Delta P = R_F Q_o \sin(\omega t + \phi) \tag{6}$$

Using the above analytical solution and after some arrangement [5], the unknowns R_F and ϕ are obtained:

$$|Z| = R_F = \frac{\rho \omega l}{\pi R^2 M_{10}} \tag{7}$$

$$\phi = \frac{\pi}{2} - \epsilon_{10} \tag{8}$$

where R_f is the magnitude of the impedance to the flow, and

$$M_{10} = \frac{1}{k}\sqrt{\sin^2\delta_{10} + (k - \cos\delta_{10})^2} \tag{9}$$

$$\delta_{10} = \frac{3\pi}{4} - \theta_1 + \theta_o \tag{10}$$

$$\epsilon_{10} = \tan^{-1}\left(\frac{\sin\delta_{10}}{k - \cos\delta_{10}}\right) \tag{11}$$

$$k = \frac{\alpha M_0}{2M_1} \tag{12}$$

The final assembly of components used in the characterization of the mount impedance is represented by a series circuit diagram (Figure 3) where Q (as current) creates ΔP (as a potential). The theoretical flow impedance of the inertia track, Z, and that of the chambers, Z_0, includes both the inertial and viscous forces that can be found by equations (7) and (8), and are complex values. The contraction/expansion terms are assumed to have negligible inertial resistance but they add to the viscous resistance, so their impedances have only real components. They can be approximated as

$$Z_{con} = \frac{\rho Q_o^2}{2}\left(\frac{1}{A} - \frac{1}{A_o}\right) \tag{13}$$

$$Z_{exp} = \frac{\rho Q_o^2}{2}\left(1 - \frac{A}{A_o}\right)^2 \tag{14}$$

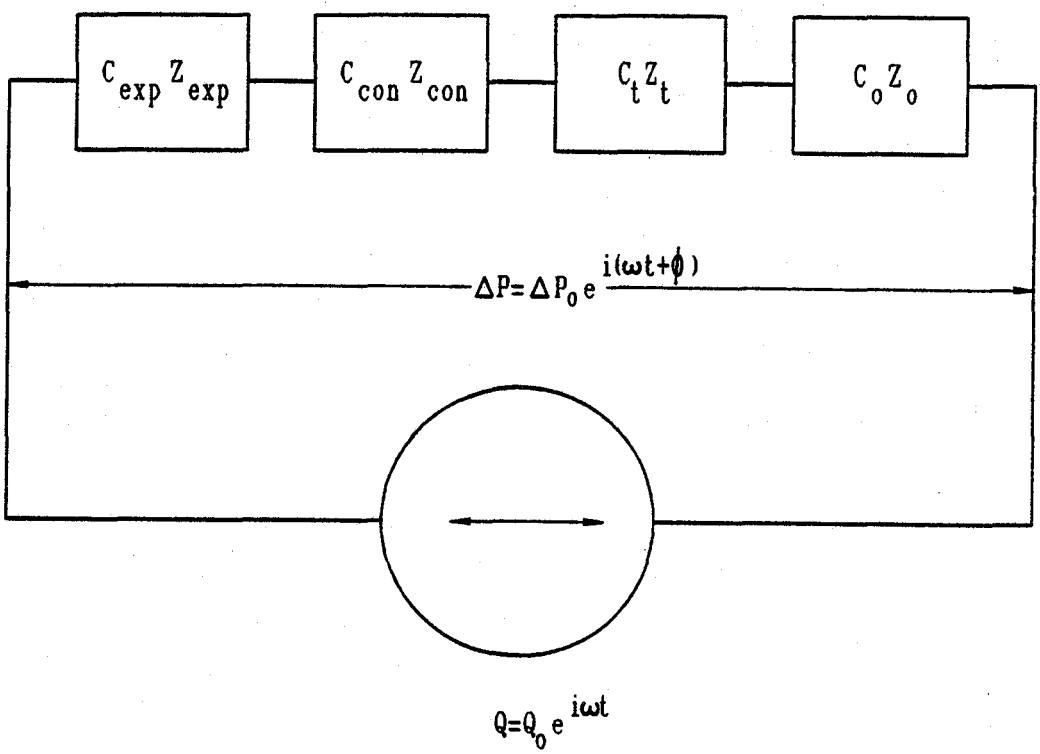

Figure 3
Schematic Representation of Flow Impedances

The total instantaneous pressure difference can be stated as the sum of contributing phasors:

$$\Delta P = (C_{exp}Z_{exp}+C_{con}Z_{con}+C_cZ_c+C_tZ_t)Q \tag{15}$$

The empirical coefficients (C's) are discussed and algebraicly evaluated later in terms of different flow geometries and frequency parameters, upon comparison with the results from numerical simulations.

NUMERICAL COMPUTATIONS

The reason for performing numerical simulations is to extend the range of applicability of the previously described model. For example, the model for the inertia track was developed for infinite length pipes. Simulation of flow in a pipe of finite length provides a correction factor which may be used in predicting the pressure drop for a realistic geometry.

Two computational domains were studied in the present work. In order to determine

coefficients for finite track length and expansion/contraction losses, it is necessary to simulate the full mount, as shown in Figure 4. The problem is axi-symmetric, with the axis of symmetry along the centerline of the inertia track. The boundary conditions are set to zero velocity, except at the ends, where a periodic normal velocity is specified. A systematic series of computations was performed, varying the ratio of track length to diameter and contraction/expansion corner radii.

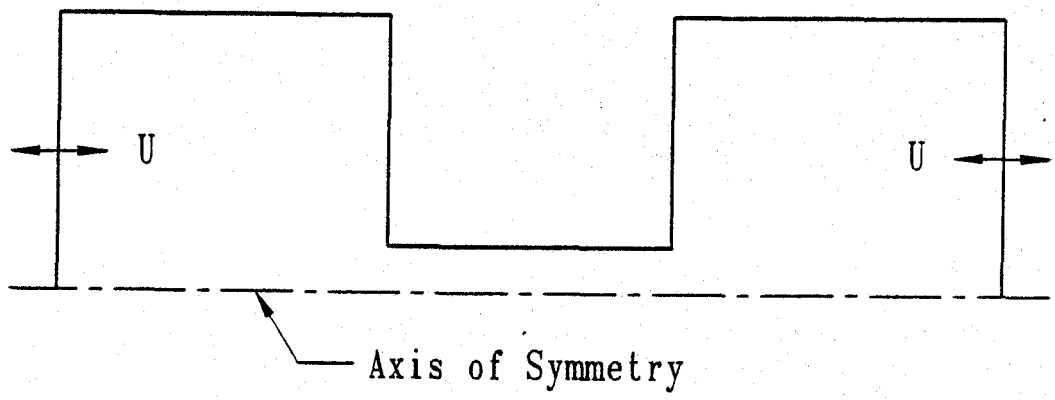

Figure 4
Computational Domain for Full Mount

To determine the effect of different cross-sectional inertia track shapes on pressure drop, the domain shown in Figure 5 was studied. This corresponds to the infinite length pipe by setting the end conditions to zero normal velocity gradient and applying a periodic pressure difference. There are two advantages of this approach over specifying periodic normal velocity - only one element is needed in the x-direction, since all x-derivatives are zero; and the problem is linear, since the convective terms are zero. These advantages greatly reduce the computational time required for solution, which is important when the simulations are for non-circular cross-section, because they must be fully three-dimensional. The disadvantage of this approach is that the flow parameters (i.e., Reynolds number and Strouhal number) are not known until the problem has been solved. In the present work the theoretical model is used to find an approximate pressure drop for non-circular cross sections corresponding to the desired flow parameters. This pressure drop is then used as input, and the exact flow parameters are determined from the simulation.

The incompressible Navier-Stokes equations are solved using the Galerkin formulation of the Finite Element Method provided in the CFD package FIDAP [6]. Each problem was started with an initial velocity of zero. For the full mount case, each problem was run until the pressure history became periodic, which generally occurred in 3 cycles or less. For the infinite length track case, each problem was run until the volumetric flow rate became periodic, which generally occurred in 20 cycles or less.

For each case a preliminary numerical study was performed to optimize FIDAP options. Grid independence was determined for a typical case by doubling the number of elements until there was less than 2% difference in the predicted pressure drop or flow rate.

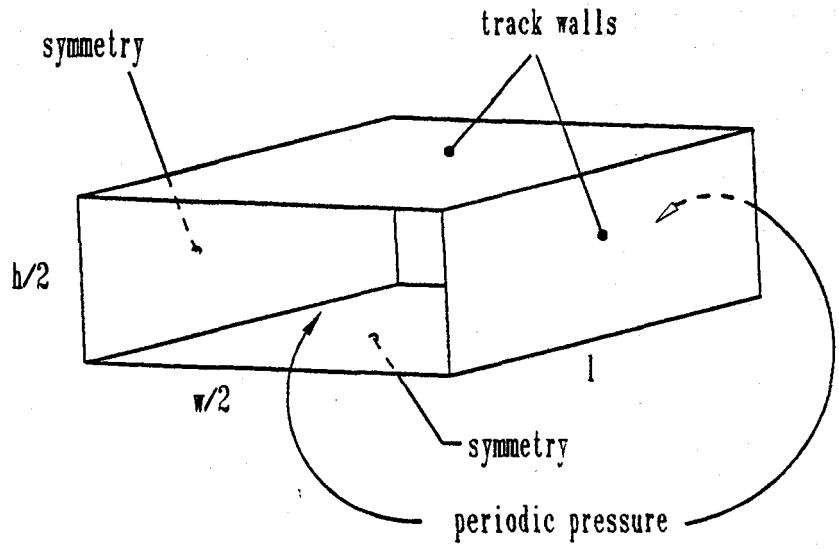

Figure 5
Computational Domain, 3-D Rectangle

The optimal time increment was determined in a similar manner to be 50 time steps per cycle. An acceleration factor of 0.5 was used along with the quasi-Newton solver. The penalty formulation was used for pressure, with the penalty parameter set to 10^{-9}. For the higher Reynolds number cases (above 100) the upwinding option was used to suppress oscillations in the computed velocity field. Backward integration was used for the time derivative.

All of the simulations reported here are for laminar flow. Turbulent simulations for a few cases were performed, but the results were later abandoned for two reasons. First, it is unclear whether the conditions typically found in fluid tuned mounts are in fact turbulent. Ahn and Ibrahim [7] discuss the results of several studies that show transition Reynolds number for periodic flow increases with increasing frequency. The high frequencies typically found in mounts cause the fluid to move as a slug with extremely thin shear layers at the walls. For the frequencies and Reynolds numbers of interest in the present work, the formulas presented by Ahn and Ibrahim indicate laminar flow. Experimental work is in progress to determine if this is in fact the case.

The second problem is that simulation of unsteady turbulent flow is problematic because the k-ϵ turbulence model is based on steady flow, and may not be applicable to oscillating flows. Lasher and Taulbee [8] discuss this problem in more detail. In addition, the form of the model used in FIDAP is a high-Reynolds number model that uses wall functions, and therefore cannot predict transition. As a result of these concerns, turbulent simulations have been deferred until experimental data is available.

FIDAP generally works quite well on this problem, although there were a few difficulties. One of the most significant problems is that the pressure history sometimes developed unrealistic oscillations when the second-order trapezoidal integration was used for the time derivative, which caused the solution to diverge. As a result, the simulations were

performed using the less-accurate backward integration. This is a known problem with the penalty formulation for the pressure, but was unexpectedly found to also occur when the segregated solver (which solves the Poisson equation for the pressure) was used. This problem is currently under investigation.

Simulations were also attempted using FLUENT [9]; however, these did not work as well as FIDAP. It took significantly longer to get a converged solution, and it was found that the interpolation done by the program for time-varying boundary conditions is incorrect. The results obtained by FLUENT did agree well with those obtained by FIDAP.

DETERMINATION OF EMPIRICAL COEFFICIENTS

The empirical coefficients of Equation 15 are developed in terms of nondimensional geometric and flow parameters. Using the pressure drop predicted across a component by computational simulation, the coefficient is found as

$$C = \frac{\Delta P_{computational}}{\Delta P_{model}} \tag{16}$$

Certain geometric components contribute to the flow resistance more than others. Figure 6 shows the centerline pressure drop across a typical mount.

Because most of the pressure drop across the mount occurs in the inertia track, the track component will be the most significant. The pressure drop across the expansion and contraction typically represents 6-10% of the total pressure drop shown. The pressure drop across the chamber is relatively small, so any difference between the model and computational results will not be significant in the overall pressure drop. The chamber coefficient is therefore set to 1. In general the coefficients will be functions of several parameters, such as Reynolds number, Strouhal number, etc. We assume that the coefficients are separable into individual coefficients for each parameter; for example:

$$C = C(R_e) \cdot C(S_t) \cdot C(l/d) \tag{17}$$

RESULTS

Expansion/Contraction Coefficients

Within each cycle, the expansion becomes the contraction and vise versa. Because of this, the expansion and contraction losses are combined as a single loss. The coefficient will be dependent on the following nondimensional geometric and fluid parameters:

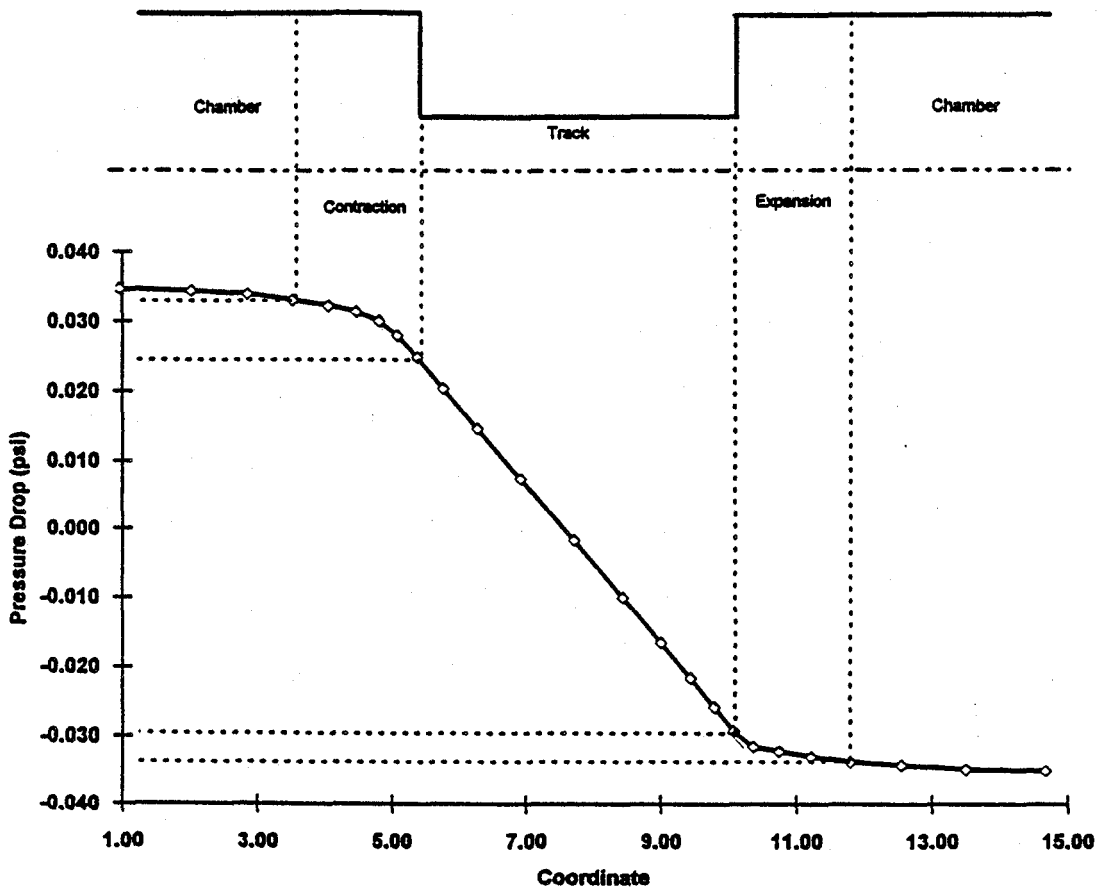

Figure 6
Typical Centerline Pressure Drop

D/d = Expansion Ratio
Re = Reynolds Number
St = Strouhal Number
r/d = Expansion Radius to Diameter Ratio

First, the Reynolds number dependence is considered. In the development of the theoretical model, the pressure drop across the expansion is formulated from the x-momentum equation. The momentum equation contains a viscous term for the wall shear stress, which is neglected in the derivation. If the viscous term is carried through the derivation, it becomes equivalent to adding a term to the nondimensional pressure drop which is proportional to the inverse of the Reynolds Number. Simulations were performed at an expansion ratio of 5 for Reynolds numbers of 1, 10, 100 and 1000. The coefficient was determined by taking the difference between the model and computation and performing a least-squares regression. The resulting corrective term is:

$$A(R_e) = \frac{0.0825}{R_e} \tag{18}$$

The data points and equation (18) are shown in Figure 7. Note that the term asymptotically approaches zero as the Reynolds number increases, as expected.

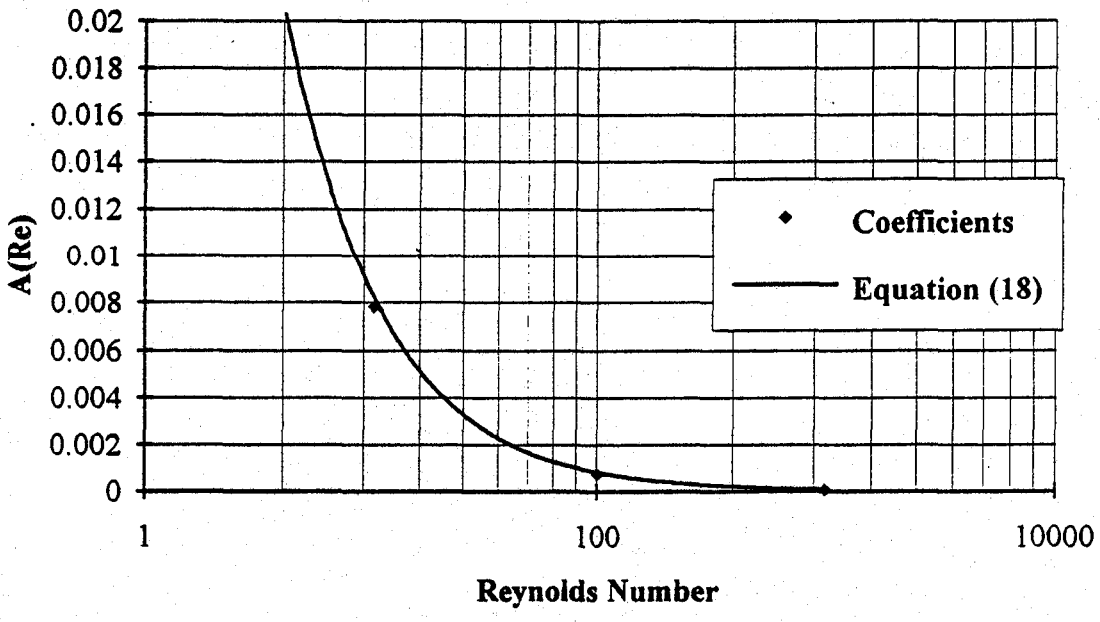

Figure 7
Expansion/Contraction Correction

A similar analysis was performed to determine the coefficient for Strouhal Number dependence. The resulting least squares fit is given by

$$C(S_t) = 1.0 + 0.032 S_t^{0.677} \tag{19}$$

and is shown in Figure 8. Notice that the coefficient approaches 1 for low Strouhal Number (steady flow), as expected, and increases with increasing Strouhal Number.

Other coefficients can be developed for Expansion Ratio and Radius to Diameter Ratio. A comparison of the model predictions to FIDAP simulations is shown in Figures 9 and 10. The good agreement indicates that the assumed separation given in equation (17) produces reasonable results.

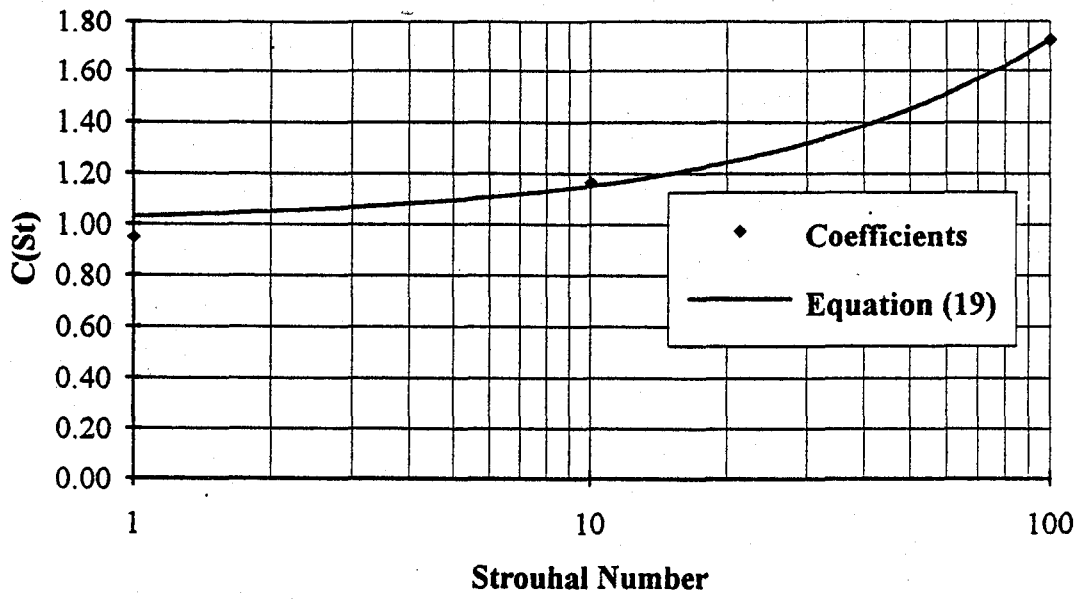

Figure 8
Expansion/Contraction Coefficient vs. Strouhal Number

Track Coefficients

As previously discussed, the theoretical model for the track was derived for periodic fully developed pipe flow. In the developing region the viscous stresses are higher because the velocity profiles are more uniform. The theoretical model will therefore underpredict the pressure drop in this region. For long pipes this error will be negligible; however, the error will increase as the length of pipe decreases. The coefficient for this correction is shown in Figure 11 and given by

$$C(l/d) = 1.0e^{\left[\frac{0.078}{(l/d)^{0.604}}\right]} \qquad (20)$$

For noncircular cross sections the concept of an equivalent diameter is used. Pressure drop in the inertia track correlates well with Valenci number. At high Valenci numbers the pressure drop is mostly inertial, and thus a function of cross sectional area and independent of cross sectional shape. At lower Valenci numbers the cross sectional shape can significantly influence pressure drop. The equivalent diameter ratio (defined as the diameter of a circle that gives the same pressure drop divided by the diameter of a circle of the same area as the rectangle) for various aspect ratios of a rectangular cross section are shown in Figure 12. As expected, the coefficients asymptotically approach 1 at high Valenci number. The Figure also shows that the pressure drop in a square cross section is almost equivalent to that in a circular

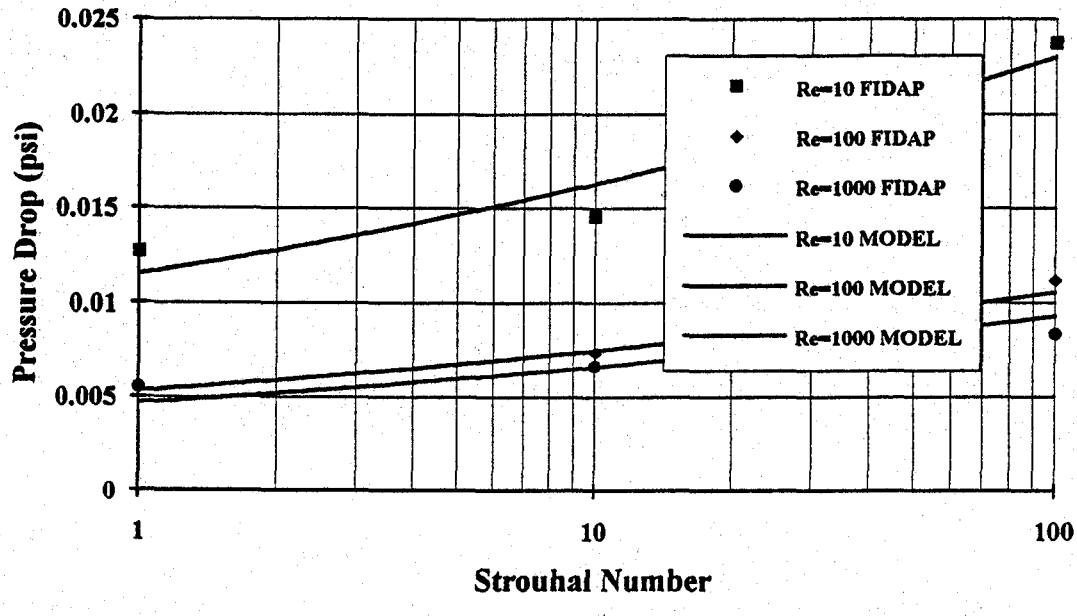

Figure 9
Expansion/Contraction Pressure Drop vs. Strouhal Number Using Corrected Model

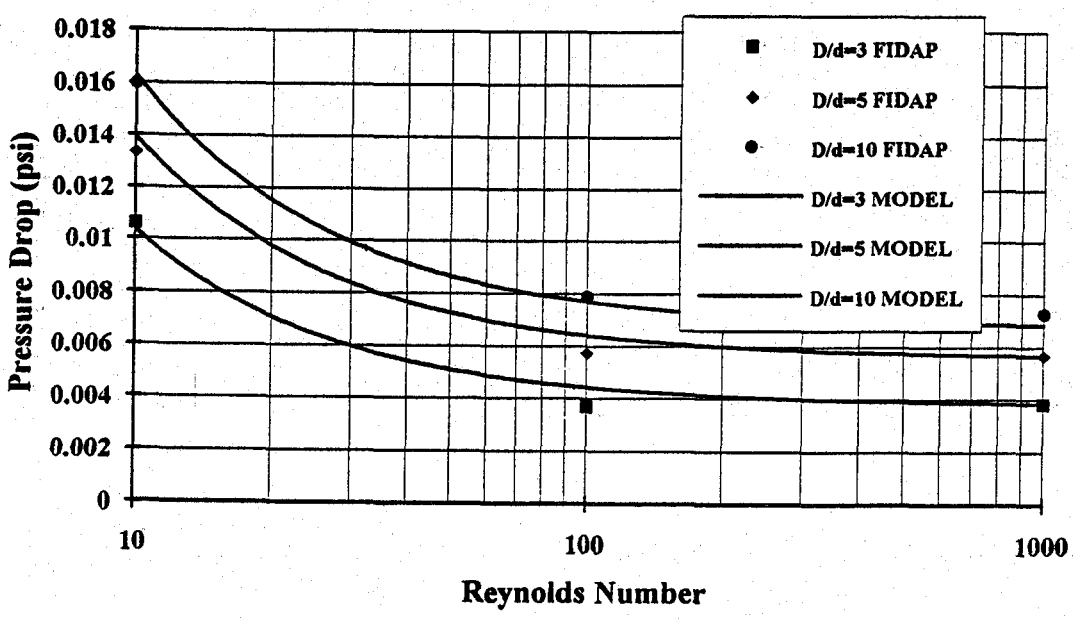

Figure 10
Expansion/Contraction Pressure Drop vs. Reynolds Number Using Corrected Model

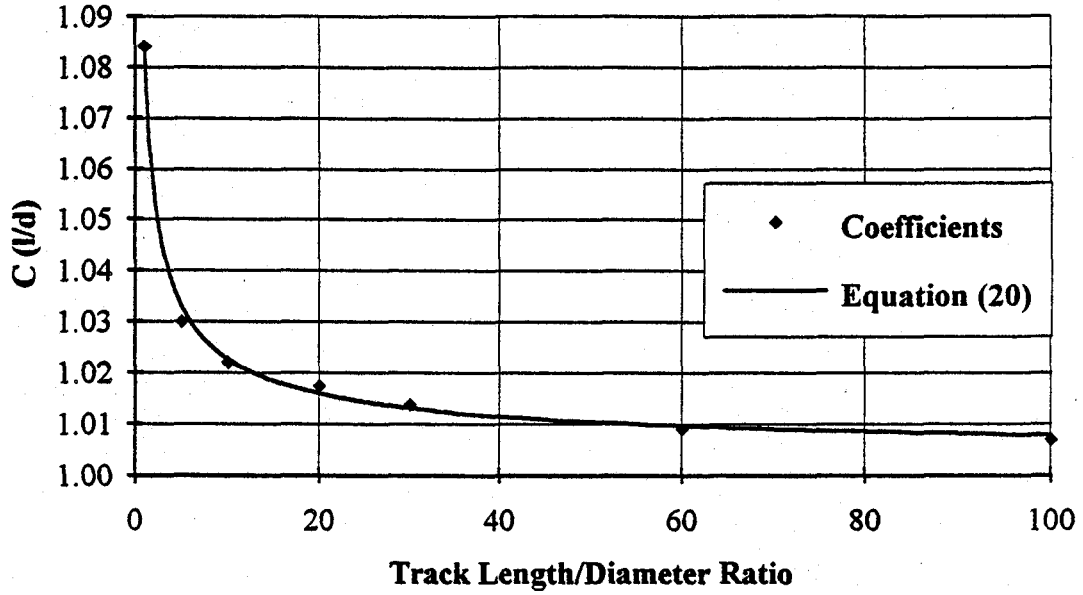

Figure 11
Track Coefficient vs. l/d

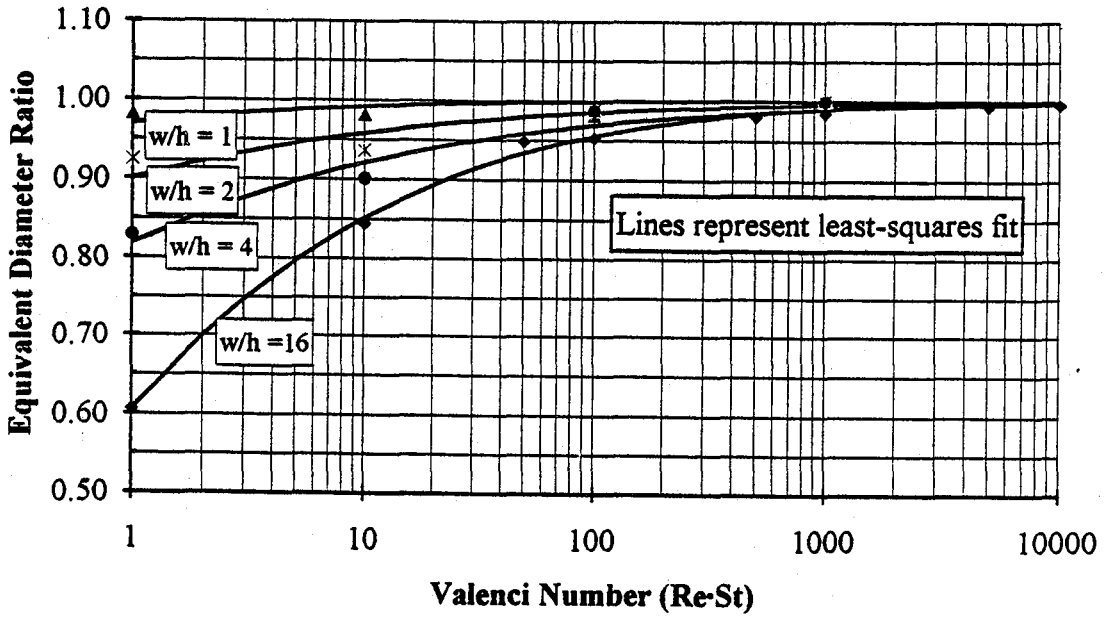

Figure 12
Equivalent Diameter Ratio for Rectangular Cross-Section

cross section of equal area, and increases as the aspect ratio increases.

Coefficients similar to the ones described here can be developed for more complicated geometries. These coefficients will expand the applicability of the model to realistic mount geometries. Work is currently in progress to develop these coefficients.

CONCLUSIONS

A series of component models have been developed for predicting the pressure drop in fluid tuned mounts. Empirical coefficients that will expand the applicability of the models have been developed, and predictions from the adjusted models agree well with computational simulation. As additional coefficients are developed the model will become more useful in the design of realistic mounts.

A major obstacle to completing this model is the problem of determining critical Reynolds number. Further research, including experimental verification, is in progress.

ACKNOWLEDGMENTS

This work was supported by the LORD Corporation and the Ben Franklin Partnership of Pennsylvania.

REFERENCES

1. Flower, W., "Understanding Hydraulic Mounts for Improved Vehicle Noise, Vibration and Ride Qualities", SAE Paper #850975, (1985)
2. Gerhart, P.M. and Gross, R.J., "Fundamentals of Fluid Mechanics", Addison Wesley, Reading, MA. (1985)
3. Wormersley, J.R., "Method for the Calculation of Velocity, Rate of Flow, and Viscous Drag in Arteries When the Pressure Gradient is Known", J. Physiol., **127**, 553-563, (1955)
4. Abramowitz, M. and Stegun, I.A. "Handbook of Mathematical Functions", Dover Publications, N.Y. (1972)
5. Khalilollahi, A., Lasher, W.C. and Weckerly, D.E., "Mathematical Modelling of Fluid Filled Isolator Mounts", submitted for publication in Int. J. of Modelling and Simulation
6. FIDAP Manuals, Fluid Dynamics International, Evanston, IL. (1990)
7. Ahn, K.H. and Ibrahim, M.B., "Laminar/Turbulent Oscillating Flow in Circular Pipes", Int. J. of Heat and Fluid Flow, **13**, #4, 340-346, (1992)
8. Lasher, W.C. and Taulbee, D.B., "On the Computation of Turbulent Backstep Flow", Int. J. of Heat and Fluid Flow, **13**, #1, 30-40 (1992)
9. FLUENT Manuals, FLUENT, Inc., Lebanon, NH. (1992)

SOLUTION OF MIXED CONVECTION HEAT TRANSFER FROM ISOTHERMAL IN-LINE FINS

Amir Khalilollahi*
The School of Engineering and Engineering Technology
The Pennsylvania State University at Erie, The Behrend College
Erie, PA 16563

SUMMARY

Transient and steady state combined natural and forced convective flows over two in-line finite thickness fins (louvers) in a vertical channel are numerically solved using two methods. The first method of solution is based on the "Simple Arbitrary Lagrangian Eulerian" (SALE) technique which incorporates mainly two computational phases: (1) a Lagrangian phase in which the velocity field is updated by the effects of all forces, and (b) an Eulerian phase that executes all advective fluxes of mass, momentum and energy. The second method of solution uses the finite element code entitled FIDAP. In the first part of this study, comparison of the results by FIDAP, SALE and available experimental work were done and discussed for steady state forced convection over louvered fins. Good agreements were deduced between the three sets of results especially for the flow over a single fin. In the second part of the study and in the absence of experimental literature, the numerical predictions were extended to the transient transports and to the opposing flow where pressure drop is reversed. Results are presented and discussed for heat transfer and pressure drop in assisting and opposing mixed convection flows.

INTRODUCTION

Louver arrays are used to enhance the performance of compact heat exchangers. If the orientation of the exchanger is vertical and the flow rates are low, the buoyancy forces would effect the heat transfer and pressure drag characteristics of the fins. Mixed convection near rectangular fins with finite thickness has been studied by Kurosaki et al [1], Sparrow et al. [2], and Suzuki et al. [3]. Reference [1] has provided experimental data for a single fin, two collinear fins, two parallel fins and a staggered array of fins. Suzuki et al. [3] presented finite difference solutions for an array of very thin fins in assisting (upward) flow and discussed heat transfer characteristics of arrays. Transient mixed convection over a single fin was studied by Khalilollahi and Joshi [4] where temperature overshoots and enhanced heat transfer rates were observed for higher Grashof numbers. The transient and steady state assisting flow over two in-line was numerically investigated in Ref. [5] and steady state results were compared with some experimental data reported in Ref. [1].

---

*Assistant Professor of Mechanical Engineering

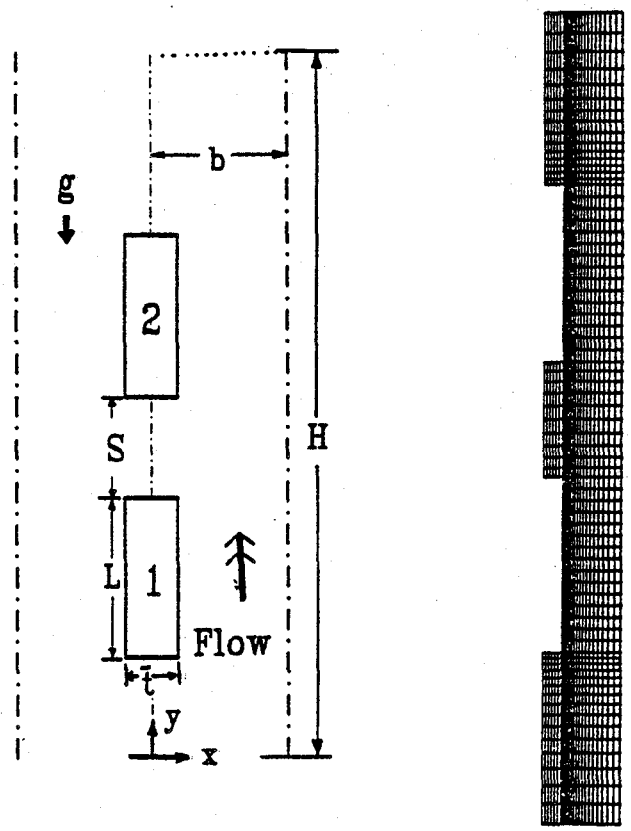

Figure 1. Array geometry and computational domain (L=.022 m, S=.015 m,H=.105 m,b=.01 m,t=.0022 m)

The present study is intended to (1) enhance the confidence in the solution by the finite difference FORTRAN code, SALE (Simple Arbitrary Lagrangian Eulerian) through comparisons with the solution by the finite element package, FIDAP, and (2) to investigate the opposing convective flow where the pressure difference between the top and bottom sections reverses causing pressure field to oppose the buoyancy force.

NUMERICAL PREDICTIONS

Finite Difference Scheme

Figure 1 shows the model geometry, flow domain and computational grid to the left of x-axis. This domain is used in both SALE and FIDAP solutions. The flow field is governed by the conservation equations in dimensionless form,

$$\partial U/\partial X+\partial V/\partial Y=0 \tag{1}$$

$$\partial U/\partial \tau+U\partial U/\partial X+V\partial U/\partial Y=-\partial P/\partial X+\partial \Pi_{xx}/\partial x+\partial \Pi_{xy}/\partial Y \tag{2}$$

$$\partial V/\partial \tau+U\partial V/\partial X+V\partial V/\partial Y=-\partial P/\partial Y+\partial \Pi_{yy}/\partial Y+\partial \Pi_{xy}/\partial X+Gr\theta \tag{3}$$

$$\partial \theta/\partial \tau+U\partial \theta/\partial X+V\partial \theta/\partial Y=[\partial^2\theta/\partial X^2+\partial^2\theta/\partial Y^2]/Pr \tag{4}$$

where

$$\Pi_{xx}=2\partial U/\partial X\ ,\qquad \Pi_{yy}=2\partial V/\partial Y\ ,\qquad \Pi_{xy}=\partial U/\partial Y+\partial V/\partial X\ ,$$

$$Gr=g\beta(T_H-T_C)L^3/\nu^2\ ,\quad Pr=\mu C_p/k\ ,\quad Nu=qL/\Delta T\ k\ ,\quad \theta=(T-T_C)/(T_H-T_C),$$

$$X=x/L,\quad Y=y/L,\quad U=uL/\nu,\quad V=vL/\nu,\quad \tau=t\nu/L^2,\quad P=pL^2/\rho\nu^2$$

The boundary and initial conditions are

$\tau=0,\ U=V=\theta=0,$ *(initial conditions)*

$\tau>0,$

$\partial V/\partial X=U=\partial\theta/\partial X=0$ *(at $X=0,\ b/L$)*

$U=V=0,\quad \theta=1$ *(on fin surfaces)*

$[P]_{Y=0}-[P]_{Y=H}=\Delta P$ *(pressure drop)*

The axes of symmetry are at X=0 and X=b/L, as shown in Fig. 1. The above equations were solved numerically by a Fortran code which incorporates Simple Arbitrary Lagrangian Eulerian

finite difference scheme. This technique is described by Amsden et al. [6]. SALE procedure includes a Lagrangian explicit method where computational cells move with the flow, and an Eulerian phase in which the cells are returned to the original position. This phase estimates the effects of advective fluxes of mass, momentum and energy on the flow parameters.

Finite Element Scheme

The finite element solution of conservation equations governing the laminar flow with boundary/initial conditions in this problem was made possible through the available educational version of the FIDAP package [7]. The grid independence was determined by doubling the number of elements until less than 2% difference in maximum velocity at midsection of the lower fin was observed. The same procedure was incorporated in the finite difference scheme, SALE. An acceleration factor of 0.3 , the quasi-Newton solver, pressure penalty formulation, and a fixed time increment (.05 sec) were used. For both schemes, similar unequally sized grid was assigned with higher cell density near the heated fin surfaces (Fig.1). The convergence in all cases was relatively fast and smooth.

RESULTS AND DISCUSSION

Some transient problems in natural and mixed convection flows have been previously solved by using SALE procedure with favorable results [8,9]. This study intends to apply this technique and finite element analysis to the phenomenon of heat dissipation of in-line finite thickness louvers. In the absence of empirical data, the predictions of transients and thermal characteristics of fins in adverse pressure fields can be valuable. In addition, Comparison of the two set of predictions (by FIDAP and SALE) can evaluate the reliability and accuracy of these methods when applied to thermal design problems.

Figure 2 indicates the heat transfer steady state performance of a single rectangular fin in assisting flow where positive pressure drop assists the buoyancy force. Reynolds number range is between 30 to 600. This is common for air-cooled compact heat exchangers. The aspect ratio t/L has been shown to have minor effect on the overall heat transfer rates [1]. The results are shown for Nusselt number vs. Grashof number and for a fin with t/L=.2 in infinite (air) medium. The correlation for forced convection flow over a flat plate is (shown in Fig. 2)

$$Nu = .644\, Pr^{1/3}\, Re^{1/2} \qquad (5)$$

The agreement between the three sets of predictions is good especially in the range where buoyancy is dominant and Re number is low. The onset of disturbed flow at higher flow rates

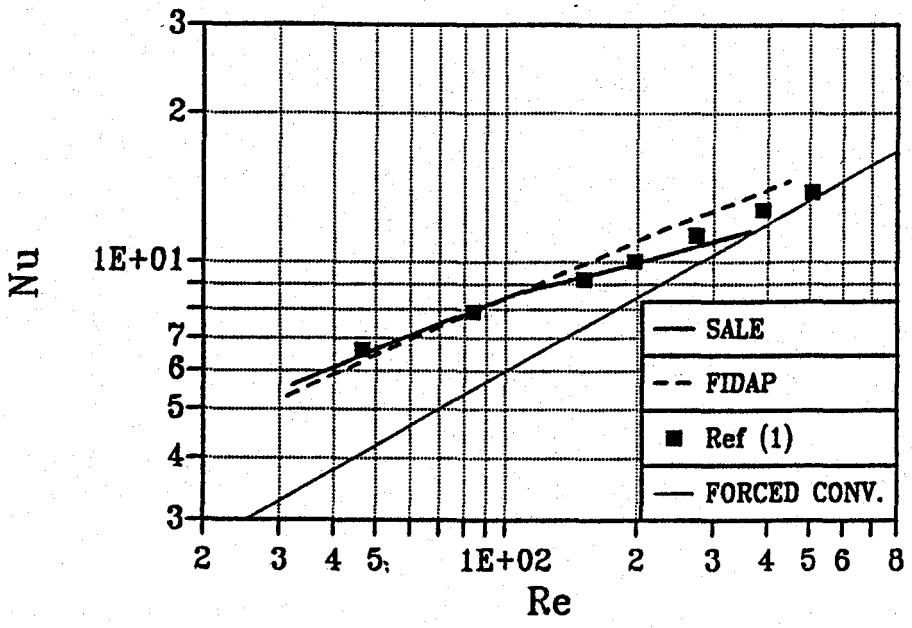

Figure 2. Steady state Nusselt number for single fin in assisting flow

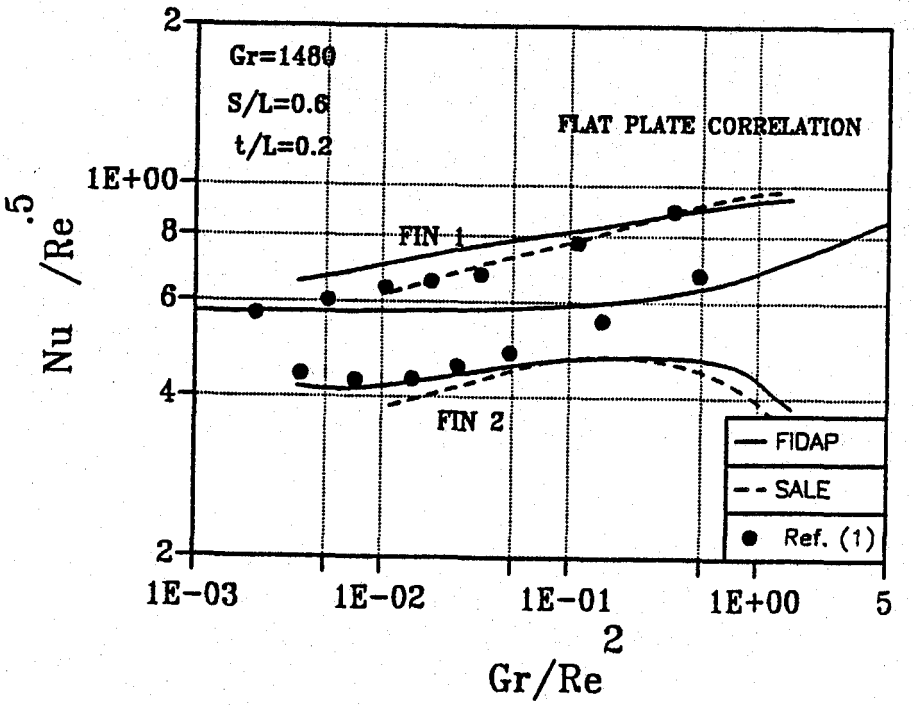

Figure 3. Comparison of steady state Nusselt number for assisting flow

and adjacent to fin corners may be accounted for the small disagreement at Re>200. The experimental values seem to be average of the two numerically predicted sets.

Figure 3 presents the comparison of Nusselt number for assisting steady state flow over two fins (as shown in Fig. 1) which is positioned in an array. The presence of neighboring fins in the array creates the symmetry lines, Y=0 and Y=b/L. The higher values of Gr/Re^2 represents the dominance of natural convection while lower range of Gr/Re^2 indicates the forced convection regime. The experimental data from Ref. [1] is for in-line fins in infinite medium. This explains the difference between the numerical and experimental values for the downstream fin (#2). However, predictions of FIDAP and SALE are in favorable agreement especially in buoyancy dominant regime. For reference, the relation for mixed convection heat transfer for a flat plate is shown in Fig. 3 [10].

The estimation of pressure drop is an important consideration in design of heat exchangers. In the absence of experimental data for fins of present study, numerical predictions by SALE and FIDAP are presented and compared for pressure coefficient and for pure forced (Gr=0) and mixed (Gr=1480) convections as shown in Fig.4. The agreement is very good especially for lower Reynolds number (Re<40) where convection starts by buoyancy action. The difference is steady but higher (about 10%) for higher Re numbers where forced convection is dominant.

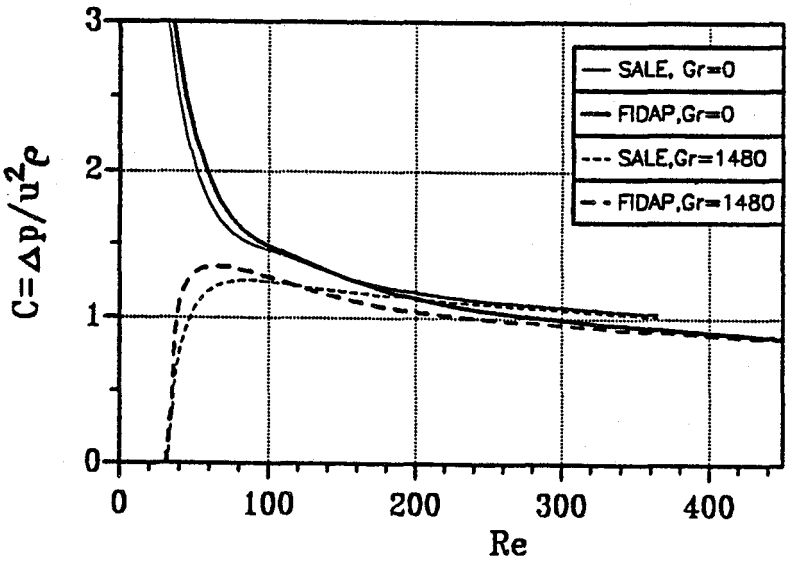

Figure 4. Comparison of pressure coefficient for assisting flow

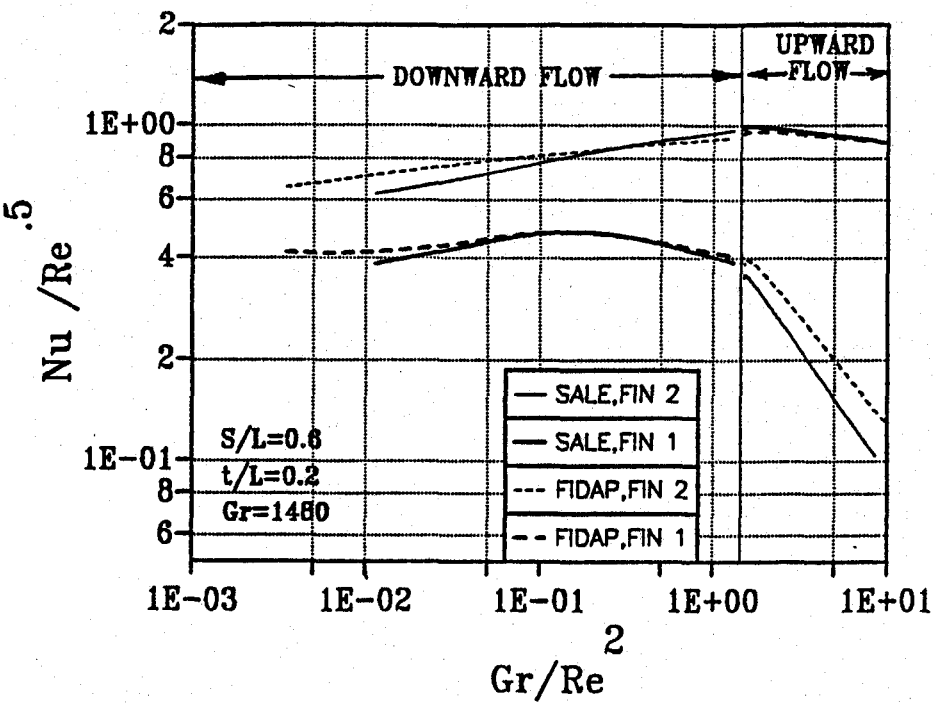

Figure 5. Comparison of steady state Nusselt number for opposing flow

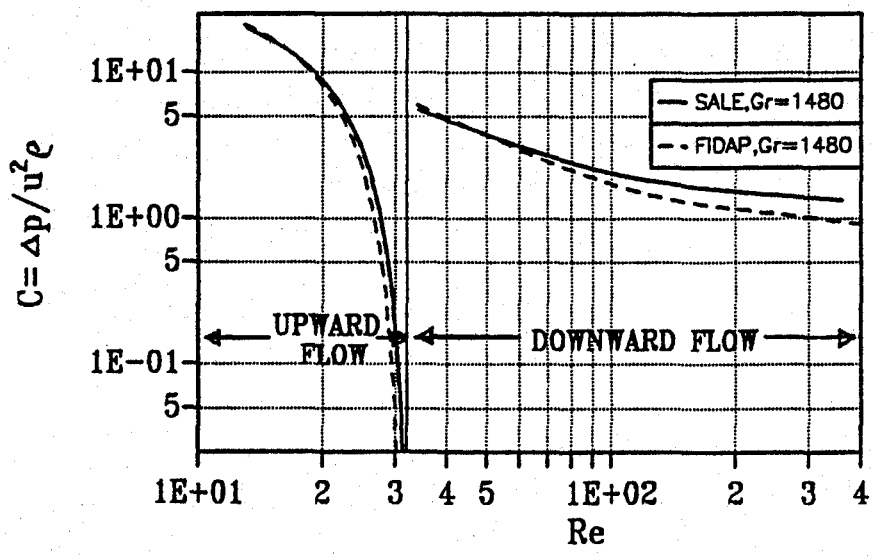

Figure 6. Comparison of pressure coefficient for opposing flow

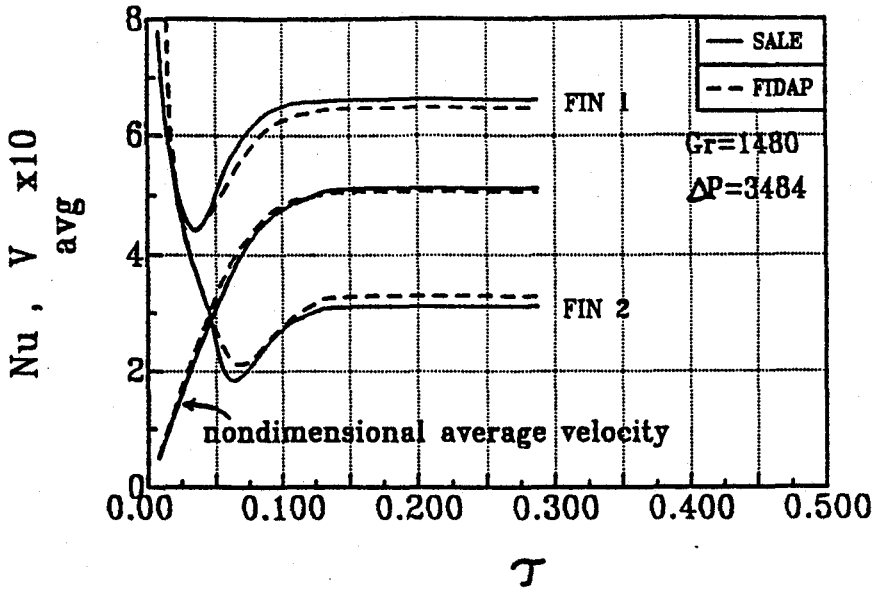

Figure 7. Comparison of transient Nusselt number and average velocity for assisting flow

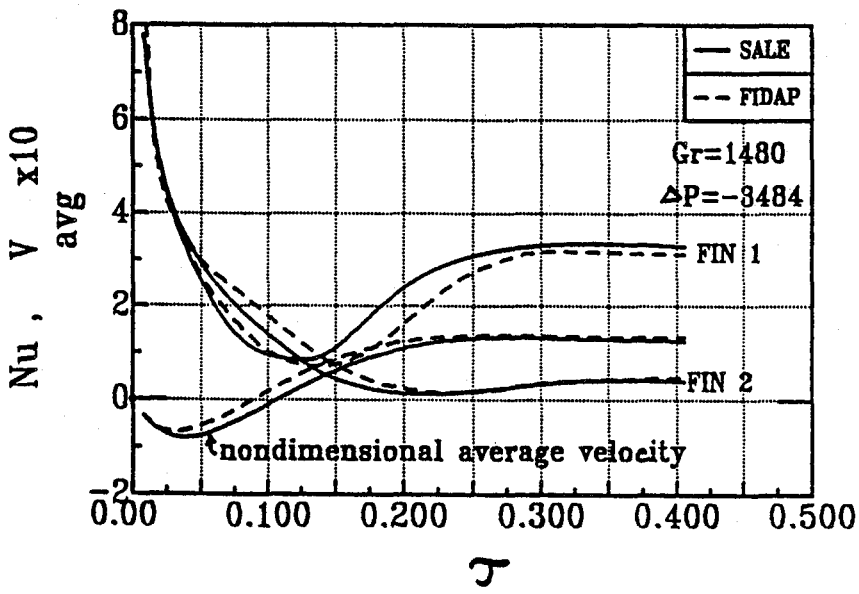

Figure 8. Comparison of transient Nusselt number and average velocity for opposing flow

The term "opposing flow" is given to the case where the pressure drop is reversed. That means the higher pressure at the top section presses the flow downward while opposing the forces of buoyancy. This case presents an interesting discontinuity trend for the flow and heat transfer. Upward free convection begins with $\Delta P=0$ at about $Gr/Re^2=1.3$ ($Re=34$), causing higher heat transfer rates for the downstream fin (#1). Flow stays upward but looses intensity when the magnitude of pressure drop (which is negative) increases. Diminishing flow corresponds to the upper limit of $Gr/Re^2\approx10$ shown in Fig.5. Increasing the magnitude of ΔP will change the direction of the flow downward not gradually but stepwise where a sudden shift is observed for the Nu number of both fins. Thereafter the flow starts from the upper limit ,$Gr/Re^2= 1.3$, in downward mixed convection region and moves to lower Gr/Re^2 region approaching pure forced convection. The differences between SALE and FIDAP predictions are more noticeable for the second fin in the upward flow region and for both fins in the forced convection dominant region.

Similar trend is observed for pressure coefficient in opposing flow (Fig. 6). Lower magnitude of ΔP, ($|\Delta P|<4500$) is not sufficient to push the flow downward in the region where $Re<33$. With increasing $|\Delta P|$, The flow vanishes ($Re=0$) but then suddenly changes direction to a downward flow with Re of about 33. Increasing the magnitude of the pressure difference increases Re where differences between FIDAP and SALE results become more noticeable. Overall the agreement seems to be favorable.

Transient heat transfer and average vertical component of velocity for $Gr=1480$ and $\Delta P=\pm3484$ are shown in Figures 7 and 8, where predictions by SALE and FIDAP are compared. Figure 7 shows the transient Nu vs. dimensionless time, τ , and for assisting flow ($\Delta P=+3484$). The solutions show minima at early times, then reaching steady state values quickly especially for the downstream fin.These minima are caused by the onset of convection and after the early conduction heat transfer lowers. The agreement seems to be fairly good. The underestimation of Nu by FIDAP for fin #1 is opposite to the trend seen for the fin #2. Very good agreement is observed for the average velocity ($V=vL/\nu$).

Figure 8 represents the same trends observed in Fig. 7. The flow is an opposing type since ΔP is negative. Initially the flow is negative or downward, but eventually it reaches steady upward flow since buoyancy effects are more dominant. At early times ($.05<\tau<.15$) under downward pressure force , the flow is downward before the strengthening of buoyancy effects. This region presents higher Nu values for fin #2, since it is the upstream fin. Later the flow direction changes while approaching steady state with fin #1 becoming the upstream fin. The discrepancy between FIDAP and SALE is moderately significant for the first fin and at about $\tau=0.2$. The agreement for the average velocity is fine except at intermediate times ($.05<\tau<.25$) when FIDAP overestimates the predictions by SALE.

CONCLUSION

Transient and steady state heat transfer characteristics of mixed convection were analyzed for assisting and opposing flows over two in-line vertical isothermal fins. Steady state assisting flow was predicted by three means, namely FIDAP and SALE that are numerical schemes, and

by available experimental data in the literature. The trends in pressure coefficient were presented for above cases. A discontinuous trend in Nu number, flow rate, and pressure coefficient was observed for negative ΔP values (opposing flow). Overall predictions by the two schemes, FIDAP and SALE, compared favorably. Future work is planned to study further this discontinuity and to conduct experiments on verification of numerical results especially for opposing flows.

REFERENCES

1. Kurosaki,Y., Kashiwagi, T., Kobayashi, H.,Uzuhashi, H., and Tang, S.,"Experimental Study on Heat Transfer from Parallel Louvered Fins by Laser Holographic Interferometry", Experimental thermal and Fluid Science, 1,59-67 ,1988.
2. Sparrow, E. M., Baliga, B. R.,and Patankar,S.V.,"Heat Transfer and Fluid Flow Analysis of Interrupted Wall Channels, with Application to heat exchangers", J. Heat Transfer, 99, #1, 4-11, 1977.
3. Suzuki,K.,Hirai, E.,Sato, T., and Kieda, S.,"Numerical Study of Heat Transfer System with Staggered Array of Vertical flat Plates used at Low Reynolds Number",Heat Transfer 1982, 3, 483-488, Hemisphere, N.Y.,1982.
4. Khalilollahi A., and Joshi, H.,"Transient and Steady State Solutions for Laminar Flow over a Finite Thickness Fin in a Parallel Plate Channel", Proc. ASME N. H. T. Conf., Houston, July 24-27, 1, 439-444, 1988.
5. Khalilollahi, A.,"Transient Combined Free and Forced Convection over Two In-Line Isothermal Rectangular Fins", Computers and Experiments in Fluid Flow",Springer-Verlag, 429-438,1989.
6. Amsden, A. A., Ruppel, H.M., and Hirt, C.W.,"SALE: A Simplified ALE Computer Program for Fluid Flows at all Speeds", Report No. LA-8095, Los Alamos Scientific Lab., NM., 1980.
7. FIDAP Manuals, Fluid Dynamics International, Evanston, IL., 1990.
8. Khalilollahi A, and Sammakia, B.,"Unsteady Natural Convection Generated by a Heated Surface within an Enclosure," Numerical Heat Transfer, 715-730, 1986.
9. Khalilollahi A., and Sammakia B.,"The Thermal Capacity Effect upon Transient Natural Convection in a Rectangular cavity", ASME J. Electronic Packaging,112, 357-366 ,1990.
10. Churchil, S.W.,"A Comprehensive Correlating Equation for Laminar, Assisting, Forced, and Free Convection", AICHE J., 23, #1,10-16 ,1977.

A DIRECT APPROACH TO FINDING UNKNOWN BOUNDARY CONDITIONS IN STEADY HEAT CONDUCTION

Thomas J. Martin* and George S. Dulikravich**
Department of Aerospace Engineering
The Pennsylvania State University, University Park, PA 16802, USA

SUMMARY

The capability of the boundary element method (BEM) in determining thermal boundary conditions on surfaces of a conducting solid where such quantities are unknown has been demonstrated. The method uses a non-iterative direct approach in solving what is usually called the inverse heat conduction problem (IHCP). Given any over-specified thermal boundary conditions such as a combination of temperature and heat flux on a surface where such data is readily available, the algorithm computes the temperature field within the object and any unknown thermal boundary conditions on surfaces where thermal boundary values are unavailable. A two-dimensional, steady-state BEM program has been developed and was tested on several simple geometries where the analytic solution was known. Results obtained with the BEM were in excellent agreement with the analytic values. The algorithm is highly flexible in treating complex geometries, mixed thermal boundary conditions and temperature-dependent material properties and is presently being extended to three-dimensional and unsteady heat conduction problems. The accuracy and reliability of this technique was very good but tended to deteriorate when the known surface conditions were only slightly over-specified and far from the inaccessible surface.

INTRODUCTION

The objective of the steady-state inverse heat conduction problem is to deduce temperatures and heat fluxes on any surface or surface element where such information is unknown. In many instances it is impossible to place sensors and take measurements on a particular surface of a conducting solid due to the inaccessibility or severity of the environment on that surface. These unknown thermal boundary values may be deduced from additional temperature or heat flux measurements made within the solid or on some other surface of the solid. This problem has been given a considerable amount of attention by a variety of researchers and virtually all work has been directed to the one-dimensional transient problem. The first method proposed to solve the IHCP used inversion of convolution integrals (Stolz 1960) and was subsequently improved by a number of authors (Beck et al. 1988). Many other methods have also been developed using such techniques as Laplace transforms, finite elements, time-marching finite differences and other approaches. A detailed chronological review of the IHCP literature has been provided by Hensel (1992).

A characteristic of most of these inverse techniques is that they tend to produce temporal oscillations in the unknown surface thermal condition estimates that are larger than the temporal oscillations in the over-specified thermal data as it propagates through the solid (Hills and Hensel 1986). In other words, the random noise due to round off errors tends to magnify as the solution proceeds and quickly produces a useless solution, especially as the distance between the surface and the over-specified information increases. A number of authors have presented various smoothing techniques for reducing this error growth, but the effect of these operations on the accuracy of the solution is not easy to evaluate (Murio 1993).

---

* Graduate research assistant.

** Associate professor.

The method presented herein does not utilize any artificial smoothing technique and is not limited to transient or one-dimensional problems. This approach is non-iterative and has been shown to compute meaningful and accurate thermal fields in a single analysis using a straightforward modification to the boundary element method (BEM).

The BEM is a very accurate and efficient technique that can solve boundary value problems such as those governing heat conduction, electromagnetic fields, irrotational incompressible fluid flow, elasticity and many other physical phenomenon. For steady-state heat conduction analysis using the BEM, either temperatures, T, or heat fluxes, Q, are specified everywhere on the surface of the solid where one of these quantities is known while the other is unknown. In the BEM solution to the IHCP, both T and Q must be specified on a part of the solid's surface, while both T and Q are unknown on another part of the surface. Elsewhere on the solid's surface, normal boundary conditions should be applied as either T's or Q's. The surface section where both T and Q are specified simultaneously is called the over-specified boundary and is necessary for the IHCP problem's solution.

Figure 1 illustrates a typical two-dimensional, multiply connected, inverse heat conduction problem. Surfaces labeled Γ_1 are the over-specified boundaries where both T and Q are given. Normal boundary conditions (either T or Q specified) are enforced on the surfaces labeled Γ_2. Thermal data is assumed to be inaccessible on the inner Γ_3 surface and thus has both T and Q unknown on this boundary. The objective of the IHCP is to compute temperatures and heat fluxes on the boundary Γ_3 using only the values of T and Q provided on the surface of the solid and, possibly, additional temperature measurements made within the solid if such data is available.

THEORY

Two-Dimensional Steady-State BEM

Steady-state heat conduction in a homogeneous medium with a constant coefficient of thermal conductivity is governed by the Laplace's equation in the region, Ω, of a conducting solid

$$\nabla^2 T = 0 \tag{1}$$

where T is the temperature. This is a linear boundary value problem having essential boundary conditions, T_0, and natural boundary conditions, Q_0, specified on the surfaces Γu and Γq, respectively. For nonlinear problems with temperature-dependent material properties, the governing equation is given by

$$\nabla \cdot \left(\lambda(T)\, \nabla T \right) = 0 \tag{2}$$

where $\lambda(T)$ is the temperature-dependent thermal conductivity. Equation (2) can be linearized by the application of the classical Kirchoff transformation which defines the heat function, Θ, as

$$\Theta = \int_0^T \frac{\lambda(T)}{\lambda_o}\, dT \tag{3}$$

Here, λ_o is a reference conductivity and $\lambda(T)$ could be an arbitrary function of temperature. Consequently, equation (2) can be transformed into Laplace's equation and solved for the heat function, Θ, instead of temperature, T. Results obtained for the heat function must be transformed back into temperatures using the inverse of the transformation given in equation (3).

Laplace's equation may be solved using the BEM (a weighted residual technique) by introducing an approximation, u, to the exact solution, Θ. Since the approximation is, in general, not equal to the exact solution, an error function or residual is produced in the domain and on the boundary. The residual in the domain is given by $R = \nabla^2 u$ and the residuals at the boundaries are $R_u = u - \Theta_0$ and $R_q = \partial u/\partial n - Q_0$. These error functions are normally non-zero unless u is the exact solution. The weighted average of the residual over the domain and on the boundary may be set to zero by the weighted residual statement

$$\int_{\Omega} u^* \nabla^2 u \, d\Omega - \int_{\Gamma_q} (q - Q_0) u^* \, d\Gamma + \int_{\Gamma_u} (u - \Theta_0) q^* \, d\Gamma = 0 \tag{4}$$

where u^* represents the weight function which is usually called the fundamental solution (Brebbia and Dominguez, 1989), while $q = \partial u/\partial n$, $q^* = \partial u^*/\partial n$ and **n** is the direction of the outward normal to the surface Γ. After integrating by parts twice, the boundary integral equation for Laplace's equation is obtained

$$\int_{\Omega} u \nabla^2 u^* \, d\Omega + \int_{\Gamma} u^* q \, d\Gamma = \int_{\Gamma} q^* u \, d\Gamma \tag{5}$$

The weight function is a Green's function solution for a point-source subject to the homogeneous boundary conditions. For the two-dimensional Laplace's equation it is

$$u^* = \frac{1}{2\pi} \log\left(\frac{1}{r}\right) \tag{6}$$

where $r = | x_i - x_j |$, x_i is the coordinate of the observation point, x_j is the coordinate of the source point and the logarithm function here has base *e*. The bounding surface Γ is discretized into N surface elements bounded by N end-nodes. After discretizing the surface and utilizing the properties of the Dirac delta function, the boundary integral equation (6) can be written as

$$c_i u_i + \sum_{j=1}^{Nsp} \int_{\Gamma_j} u \, q^* \, d\Gamma_j = \sum_{j=1}^{Nsp} \int_{\Gamma_j} q \, u^* \, d\Gamma_j \tag{7}$$

for each ith node. The term c_i indicates the scaled internal angle at the ith surface node. The functions u and q are assumed to vary linearly along each surface element and, therefore, they can be defined in terms of their nodal values and interpolation functions

$$u(\xi) = \phi_1(\xi) u_1 + \phi_2(\xi) u_2 \quad \text{and} \quad q(\xi) = \phi_1(\xi) q_1 + \phi_2(\xi) q_2 \tag{8}$$

where ξ is a localized surface-following dimensionless coordinate, while $\phi_1 = (1 - \xi)/2$ and $\phi_2 = (1 + \xi)/2$. The whole set of equations for the N nodal values of u and q can be expressed in matrix form as

$$[H]\,U = [G]\,Q \tag{9}$$

where $U = (U_1, U_2, U_3, \ldots, U_N)$ and $Q = (Q_1, Q_2, Q_3, \ldots, Q_N)$ are vectors containing the nodal potentials and surface panel fluxes while the terms in the [H] and [G] matrices are assembled by properly adding the contributions from each surface integral

$$H_{ij} = \int_{\Gamma_j} \phi_2\, q^*\, d\Gamma_j + \int_{\Gamma_{j+1}} \phi_1\, q^*\, d\Gamma_{j+1}$$

$$G_{ij} = \int_{\Gamma_j} \phi_2\, u^*\, d\Gamma_j + \int_{\Gamma_{j+1}} \phi_1\, u^*\, d\Gamma_{j+1} \tag{10}$$

The free term, c_i, is produced when the first surface integral of equation (6) is integrated in the sense of the Cauchy principal value. Since $q^* = \partial u^*/\partial n = (\partial u^*/\partial r)\,(\partial r/\partial n) = 0$ when the ith surface integral contains the ith observation point, the diagonal of the [H] matrix is simply the c_i term. This coefficient may be computed explicitly by calculating the internal angle at the surface node or implicitly (Brebbia and Dominguez 1989) by first assuming a constant unit potential throughout the entire domain and then solving for the diagonal component as

$$c_i = H_{ii} = -\sum_{j=1}^{N} H_{ij} \qquad i \neq j \tag{11}$$

When the observation node is on the surface panel of integration, the terms in the [G] matrix are computed analytically from the integral

$$G_{ii} = \frac{1}{2\pi} \int_{\Gamma_i} \phi_2 \log\left(\frac{1}{r}\right) d\Gamma_i + \frac{1}{2\pi} \int_{\Gamma_{i+1}} \phi_1 \log\left(\frac{1}{r}\right) d\Gamma_{i+1} \tag{12}$$

After the [H] and [G] matrices are formed, all boundary conditions are applied and a set of linear algebraic equations, $[A]\,X = F$, is constructed. Known or specified surface potentials, U_j, and fluxes, Q_j, are assembled on the right-hand-side of the equation set and are multiplied by their respective [H] or [G] matrix row thus forming the vector of knowns, F. All unknown potentials or fluxes are assembled on the left-hand-side of the equation set and are represented by a coefficient matrix [A] multiplying a vector of unknown quantities, X.

The set of linear algebraic equations is then solved for the unknown surface potentials, U, and fluxes, Q, using a singular value decomposition (SVD) matrix solver (Press et al. 1992). We used the SVD since the matrix tends to become ill-conditioned or singular (several equations become linearly dependent with other equations in the equation set) whenever the over-specified thermal data are farther away from the surfaces where no boundary conditions are applied. If

additional thermal data within the solid is provided, additional equations may be added to the equation set. Note that the SVD algorithm is capable of providing a satisfactory solution vector even when the [A] matrix is not square. The more rows (i.e. more data points) that are provided to the system, the more accurate the solution vector becomes, although the reverse is true when the matrix has less rows than columns. Once the matrix is solved, the entire thermal field within the solid can be easily deduced.

RESULTS AND DISCUSSION

IHCP for a Square Plate Using the BEM

A BEM computer program was developed using the theory discussed in the previous section. The accuracy of the BEM as a solution to the IHCP was verified for a solid square plate. The plate was 6.0 m on each side and the thermal conductivity of the plate was chosen as 1.0 W/mK. The top and bottom boundaries were specified to be adiabatic ($Q_0 = 0$ W/m^2) while the left side surface of the plate was over-specified with a temperature boundary condition of $T_0 = 300$ K and a heat flux boundary condition of $Q_0 = -50$ W/m^2. The right side boundary was considered to be inaccessible and, as such, both temperature and heat flux were unknown on this boundary. The plate boundary was discretized with 12 panels (3 per each of the four sides) on the boundary of the solid. The BEM was successful in computing a temperature field within the plate that was accurate to almost the floating point precision of the computer. The computed temperature and heat flux on the right side boundary were 0.000161 K and 49.99997 W/m^2, respectively.

Study of the IHCP for an Annular Disk Using the BEM

The behavior of this algorithm for various combinations of boundary conditions was documented for steady-state heat conduction in an annular solid disk. The outer radius of the disk was 1.2 in and the centrally located hole had a radius of 0.5 in. The analytic solution for this problem was developed by applying Dirichlet or essential boundary conditions everywhere on the boundary of the annular region. Temperature boundary conditions of 100°C on the outer boundary and 50°C on the inner boundary were enforced. The thermal conductivity of the solid was considered to be constant, $\lambda = 1.0$ Btu/in sec°R. The analytic solution for the temperature field within the disk is easily found as

$$T(r) = A + B \log r \tag{13}$$

where $A = 89.59$ and $B = 57.11$. The radial heat flux is then

$$Q(r) = -\lambda \nabla T = -\lambda \, dT(r)/dr = B / r \tag{14}$$

which yields $Q_{out} = -47.59$ Btu/in^{2}sec and $Q_{in} = 114.22$ Btu/in^{2}sec as heat fluxes through the outer and inner boundaries, respectively. The BEM algorithm was run on the same problem. The problem was discretized with 36 panels on each outer and inner boundary. The BEM program predicted the temperature field in the solid which averaged only a 0.3% error versus the analytic solution.

In order to study the feasibility and accuracy of the BEM solution to the steady-state IHCP, seven variations to the same problem were performed and the results obtained were compared to those from the previous problem. Each test utilized the same annular geometry and outer boundary thermal data in a variety of combinations.

Test 1. The outer and inner boundaries of the annular domain were each discretized with 36 equally-length flat panels. The entire outer boundary was over-specified with temperature and flux boundary conditions, while both temperature and flux were unknown on the inner boundary. The

BEM formulation detailed in the theory section, can be represented in matrix form by equation (9). For this test case, the solution set of 72 equations included 72 known values given as boundary conditions on the outer surface and 72 unknowns on the inner boundary. The BEM computed the temperature field within the annular solid in addition to the unknown temperatures and heat fluxes on the inner boundary. Figure 2a shows the computed temperature contours for the annular solid disk and also includes the BEM nodes used and the type of boundary conditions specified at each node. The box-shaped nodes have both T and Q known and thus are over-specified, the circles are nodes where both T and Q are unknown, and the triangular nodes have a single boundary condition of temperature applied. The thick solid lines in figures 3 and 4 represent the accuracy of this particular BEM solution. Figure 3 shows the relative percentage error in temperature on the inner boundary for each test as a function of the circumferential angle in radians. Figure 4 is the same as figure 3 except that it gives the relative percentage error in the heat flux on the inner boundary. Notice that this test case had an almost perfectly symmetric result with an average error of only 0.5% in temperature and a somewhat oscillating error in heat flux averaging about -1.5%.

Test 2. This test case was identical to Test 1 except that the outer and inner boundaries were discretized with a coarser grid consisting of 18 panels each. Overall, the BEM solution set had 36 knowns, 36 unknowns and 36 equations. The computed temperature field and boundary discretization are shown in Figure 2b and the relative percentage error in temperature and heat flux on the inner boundary are given as thin solid lines in figures 3 and 4. The temperature field within the solid was nearly perfectly symmetric, but was uniformly biased about 2.5% in temperature and -2.5% in heat flux.

Test 3. This test case was identical to Test 1 except that the boundary of the annular disk was discretized with 36 panels on the outer boundary and 18 panels on the inner boundary. Overall, the BEM solution set was over-specified and had 72 knowns, 36 unknowns and 54 equations. The thick dotted lines in figures 3 and 4 readily show that Test 3 produced the most accurate results for both temperature and heat flux. In addition, the temperature contours in Figure 2c are nearly perfectly symmetric.

Test 4. This test was identical to Test 1 except that the outer boundary was discretized with 18 panels and the inner boundary was discretized with 36 panels. Overall, the BEM solution set was under-specified and had 36 knowns, 72 unknowns and 54 equations. Results of Test 4 are given by the thin dotted line in figures 3 and 4. The temperature was uniformly biased with a 3.0% error, while the heat flux was somewhat oscillatory and similarly biased. The temperature contours in figure 2d were nearly symmetric.

Test 5. Both the outer and inner boundaries of the annular disk were discretized with 36 panels. Temperature boundary conditions were specified everywhere on the outer boundary but the additional heat flux boundary conditions were over-specified in the first and third quadrants of the outer boundary only. The BEM solution set had 54 knowns, 90 unknowns and 72 equations. The temperature field shown in figure 2e was comparable to that of Test 4. The temperature and heat flux on the inner boundary are represented by the finely dotted lines. The temperature distribution on the inner boundary was somewhat oscillatory, but averaged only a 0.75% error. The heat flux on the inner boundary was also oscillatory and averaged an error of about -2.0%.

Test 6. The circular disk was discretized with 36 panels on both the inner and outer boundaries. Temperature boundary conditions were specified on the entire outer boundary, while heat flux boundary conditions were over-specified only on the upper half of the outer boundary. As in Test 5, the BEM solution set contained 54 unknowns, 90 unknowns and 72 equations. The temperature field illustrated in figure 2f was asymmetric about the x-axis, but was very nearly symmetric about the y-axis. The greatest error in the temperature field occurred in the bottom half of the annular solid region. The thick dashed lines in figures 3 and 4 reveal inner boundary errors that are quite oscillatory in nature and noticeably peak at the very bottom of the solid disk (the point farthest from the over-specified data).

Test 7. This test case is identical to Test 5, except that heat flux boundary conditions are over-specified in the first quadrant of the outer boundary only. The BEM solution set contained 45 knowns, 99 unknowns and 72 equations. Figure 2g illustrates the temperature contours within the solid disk. The error in the temperature field obviously worsens as the distance from the over-

specified data increases. The thin dashed lines in Figures 3 and 4 illustrate the error in the temperature and heat flux on the inner boundary. The error is oscillatory and peaks at about 60% at the point farthest from the over-specified data. Notice also that the temperature field is symmetric about the line inclined 45 degrees and passing through the center of the circle.

IHCP for a Rocket Nozzle Wall Section with a Coolant Flow Passage

The BEM solution to the IHCP was attempted on a realistic engineering problem with temperature-dependent material properties. High pressure, reusable rocket thrust chambers encounter a progressive thinning of the coolant flow passage wall after repetitive engine operation. This deformation is caused by high thermal plastic strains that eventually cause cracks to form in the cooling passage wall. An engineer who wishes to reduce or eliminate the plastic strain may obtain experimental data such as hot gas wall temperatures and heat fluxes, shroud temperatures, compressive strains, and thrust chamber total pressure and temperature (Quentmeyer 1978, 1992). Unfortunately, the engineer cannot normally obtain data within the coolant flow passage due to the extremely low temperature of the liquid hydrogen coolant and the small dimensions of the passage..

Figure 5 is a schematic of a cylindrical thrust chamber assembly and figure 6 illustrates a cylinder wall cross section showing typical instrumentation locations and dimensions. These figures were taken from a NASA publication (Quentmeyer 1978) and were subsequently used to generate the geometry of the nozzle wall section. The hot gas wall temperature (1520 ^{o}R), heat flux (-35 Btu/in^{2}sec) and shroud temperature (518.4 ^{o}R) were experimental measurements taken from the same publication. The outer shroud heat flux was assumed to be negligible (0 Btu/in^{2}sec). The coefficient of thermal conductivity of the solid copper region was linearly dependent on the local temperature

$$\lambda = \lambda_o (1 + \alpha T) \qquad (15)$$

where λ_o = 0.004893 Btu/insec^{o}R and α = -0.000055056 ^{o}R^{-1}. In addition, figure 6 shows that the conducting solid region is made up of three different materials; copper, electrodeposited copper, and nichrome ZrO_2. Although the present analysis uses only a single material, the BEM can be modified to handle composite materials with each having distinct thermal properties. The shaded portion in figure 6 is the domain typically used in the two-dimensional heat conduction model. For the BEM analysis of this IHCP, a full section containing the entire cooling passage and half of the surrounding conducting metal was generated in order to examine the symmetry of the results. The meridional or symmetry planes were assumed to be adiabatic. The outer and inner boundaries were discretized in the same manner: 16 panels on the hot gas side , 8 panels on the shroud and 8 panels on each of the two periodic meridional boundaries. The BEM solution set contained 66 knowns, 94 unknowns and 80 equations . The BEM computed both temperatures and heat fluxes on the entire coolant flow passage boundary in addition to the temperatures on the meridional side boundaries. The predicted temperature field within the solid region is illustrated in figure 7. These results show a negligible asymmetry about the meridional centerline and slight oscillations in the temperatures computed near the corners of the coolant passage's cool side.

CONCLUSIONS

The boundary element method computed temperature and heat flux boundary conditions on boundaries of a conducting solid where such quantities were originally inaccessible and unknown. The results presented herein indicate that the direct non-iterative BEM solution method for the IHCP is an accurate, robust and reliable technique that takes only seconds of CPU time on any typical mainframe, workstation or PC. In addition, the results obtained were found to be more accurate when one or both of the following conditions were observed: a) greater amount of over-

specified data was applied, b) the over-specified data locations were in close geometric proximity to the locations of the unknown boundary conditions.

ACKNOWLEDGEMENTS

Sincere thanks are due Mr. Vineet Ahuja for suggesting the use of the SVD algorithm for almost singular matrices, since a standard matrix solver produced meaningless results due to severe accumulation of round-off errors.

REFERENCES

Beck, J.V., Blackwell, B. and St. Clair, C.R., Jr.: Inverse Heat Conduction: Ill-Posed Problems. Wiley-Interscience, New York, 1985.

Brebbia, C.A. and Dominguez, J.: Boundary Elements, An Introductory Course. McGraw-Hill Book Company, New York, 1989.

Hensel, E.C., Jr.: Multi-dimensional Inverse Heat Conduction. Ph.D. dissertation, Mechanical Engineering Dept., New Mexico State University, Las Cruces, NM, 1986.

Hills, R.G. and Hensel, E.C., Jr.: One-dimensional Nonlinear Inverse Heat Conduction Technique. Numerical Heat Transfer, vol. 10, pp. 369-393, 1986.

Martin, T.J.: Inverse Design and Optimization of Two- and Three-Dimensional Coolant Flow Passages. M.S. Thesis, Dept. of Aerospace Engineering, The Pennsylvania State University, May 1993.

Murio, D.A.: The Mollification Method and the Numerical Solution of Ill-Posed Problems. John Wiley & Sons, In., New York, 1993.

Press, W.H., Teukolsky, S.A., Vetterling, W.T. and Flannery, B.P.: Numerical Recipes in FORTRAN. Second Edition, Cambridge University Press, 1992.

Quentmeyer, R.J.: Investigation of the Effect of Ceramic Coatings on Rocket Thrust Chamber Life. NASA TM-78892, 1978.

Quentmeyer, R.J.: An Experimental Investigation of High-Aspect-Ratio Cooling Passages. NASA TM-105679, 1992.

Stolz, G. Jr.: Numerical Solutions to an Inverse Problem of Heat Conduction for Simple Shapes. ASME Journal of Heat Transfer, vol. 82, pp. 20-26, 1960.

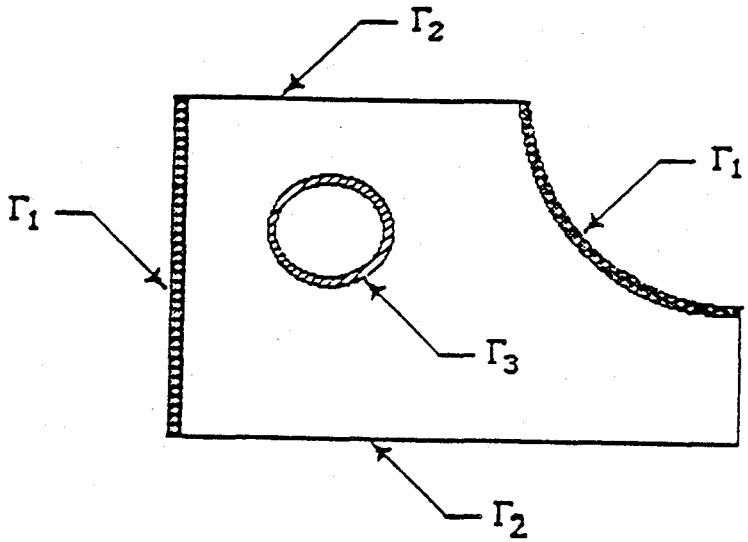

Figure 1. A geometric definition of a two-dimensional inverse heat conduction problem.

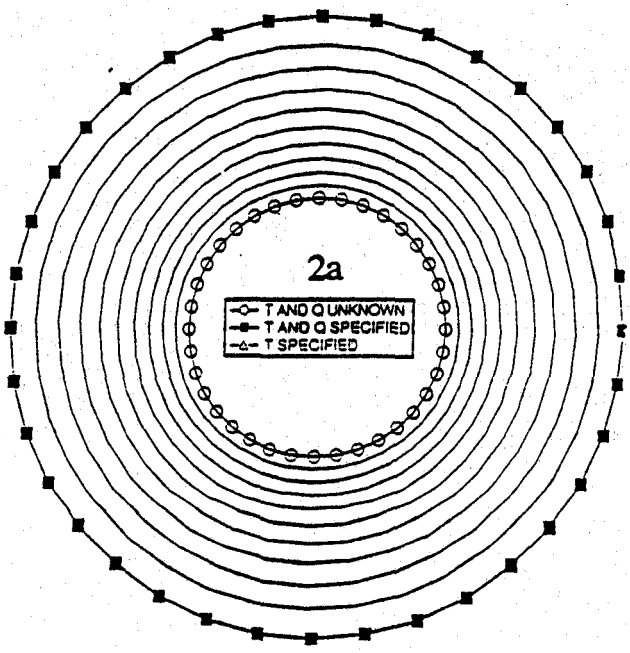
2a
T AND Q UNKNOWN
T AND Q SPECIFIED
T SPECIFIED

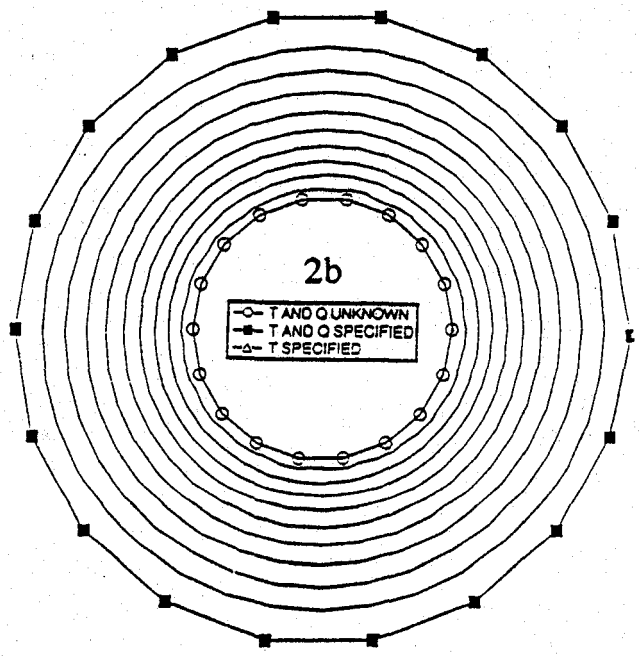
2b
T AND Q UNKNOWN
T AND Q SPECIFIED
T SPECIFIED

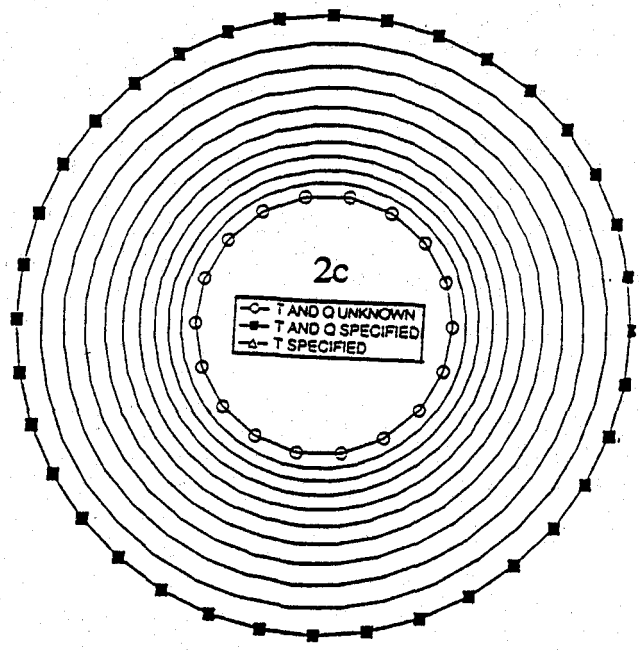
2c
T AND Q UNKNOWN
T AND Q SPECIFIED
T SPECIFIED

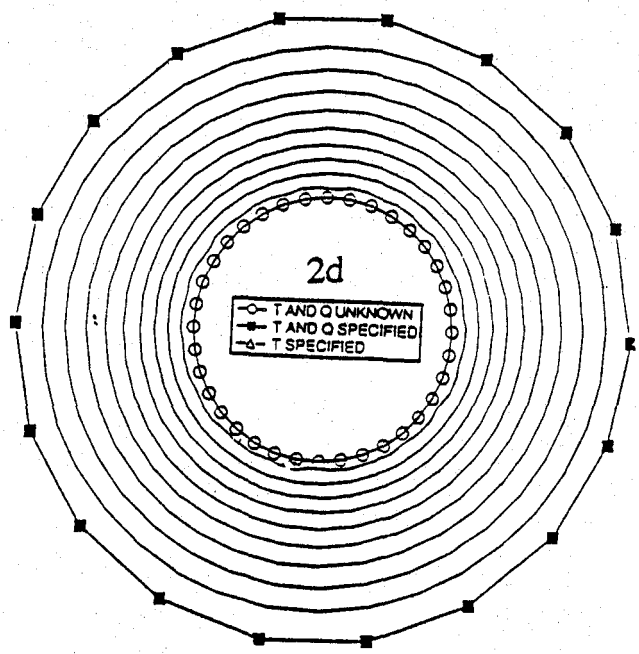
2d
T AND Q UNKNOWN
T AND Q SPECIFIED
T SPECIFIED

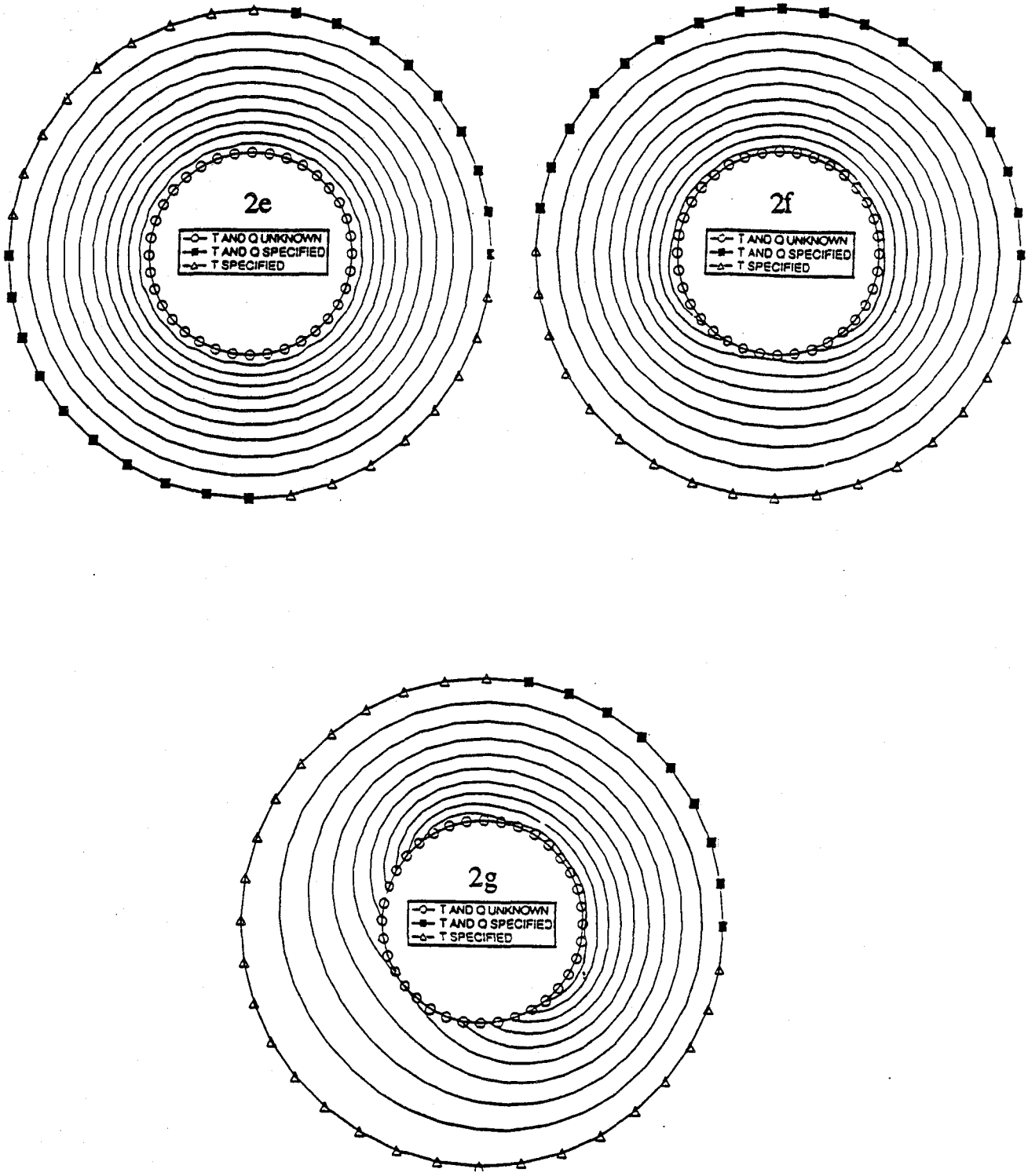

Figure 2. Geometry of the BEM nodes on the outer and inner boundaries, boundary condition types and isotherms computed with the BEM for each of the seven annular disk test cases.

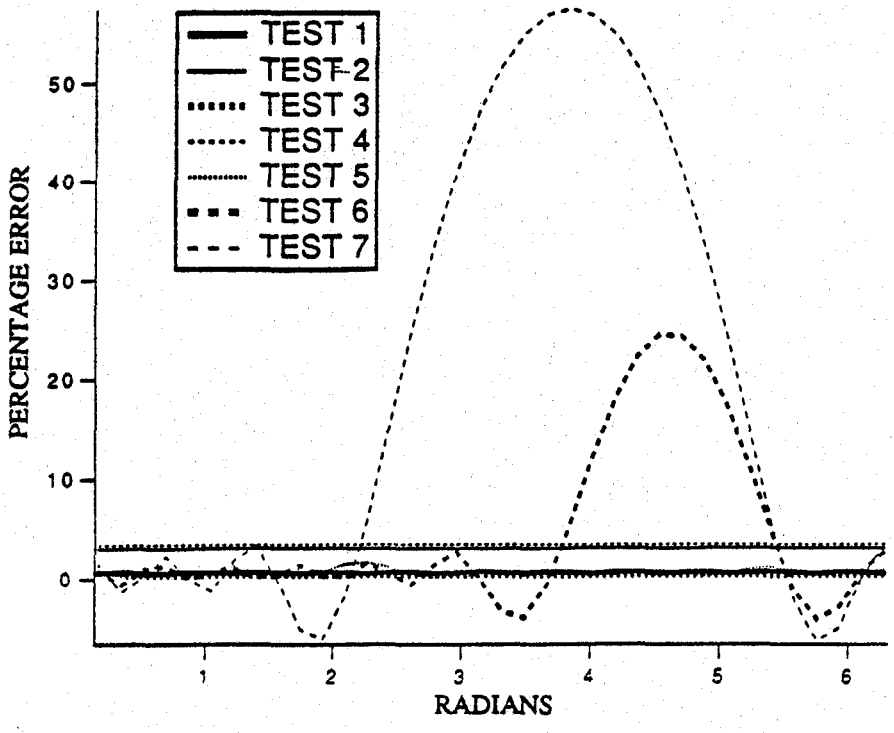

Figure 3. Relative percentage errors (BEM versus analytic solution) of the inner boundary temperatures for each of the seven annular disk test cases.

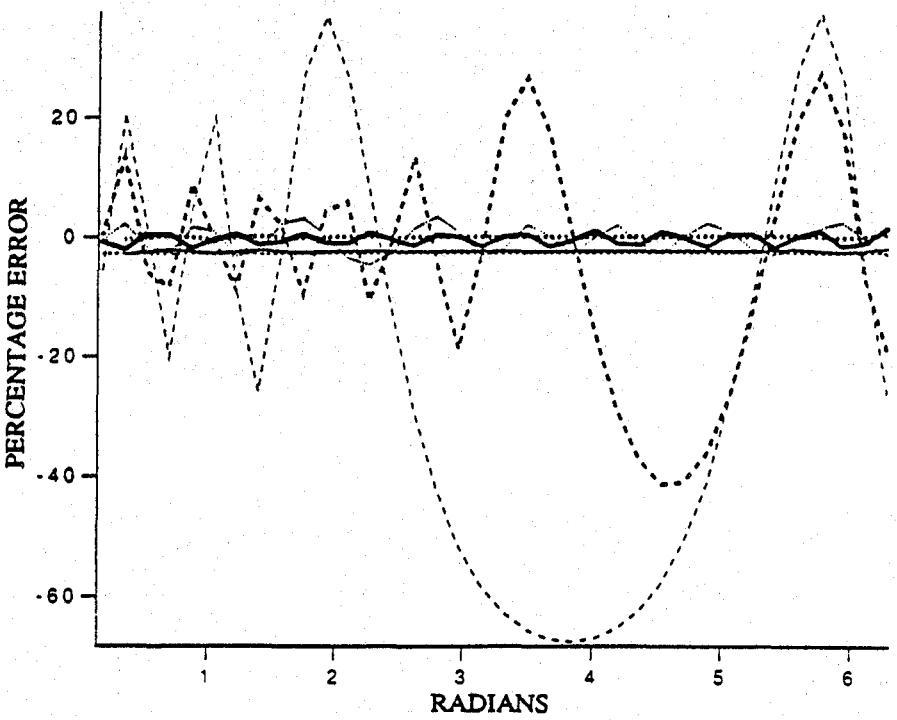

Figure 4. Relative percentage errors (BEM versus analytic solution) of the inner boundary heat fluxes for each of the seven annular disk test cases.

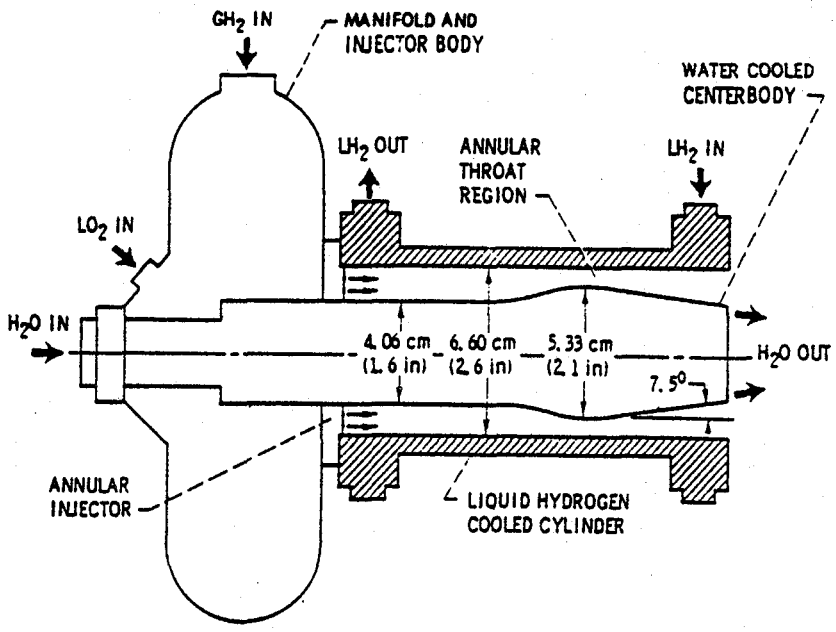

Figure 5. Schematic of cylindrical thrust chamber assembly (Quentmeyer 1978).

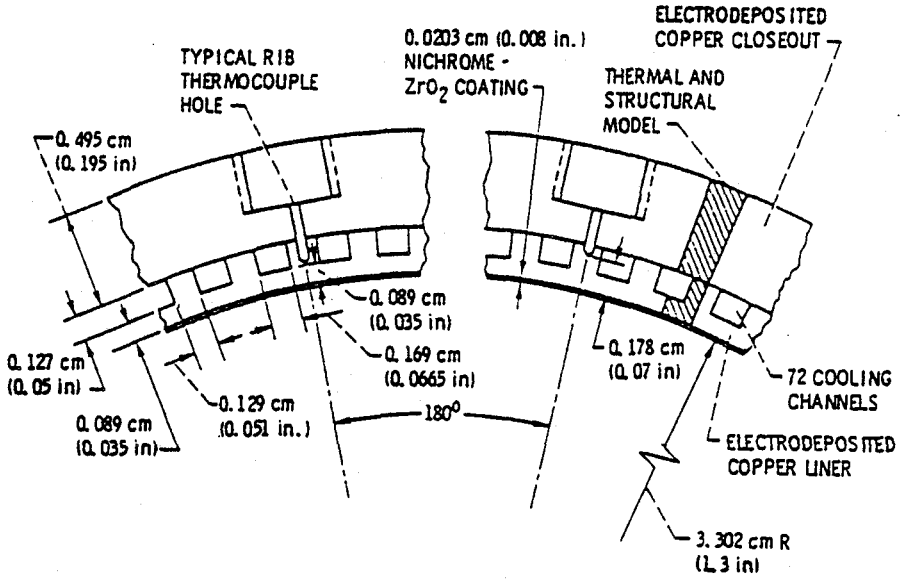

Figure 6. Cylinder wall cross section showing instrumentation locations and dimensions (Quentmeyer 1978).

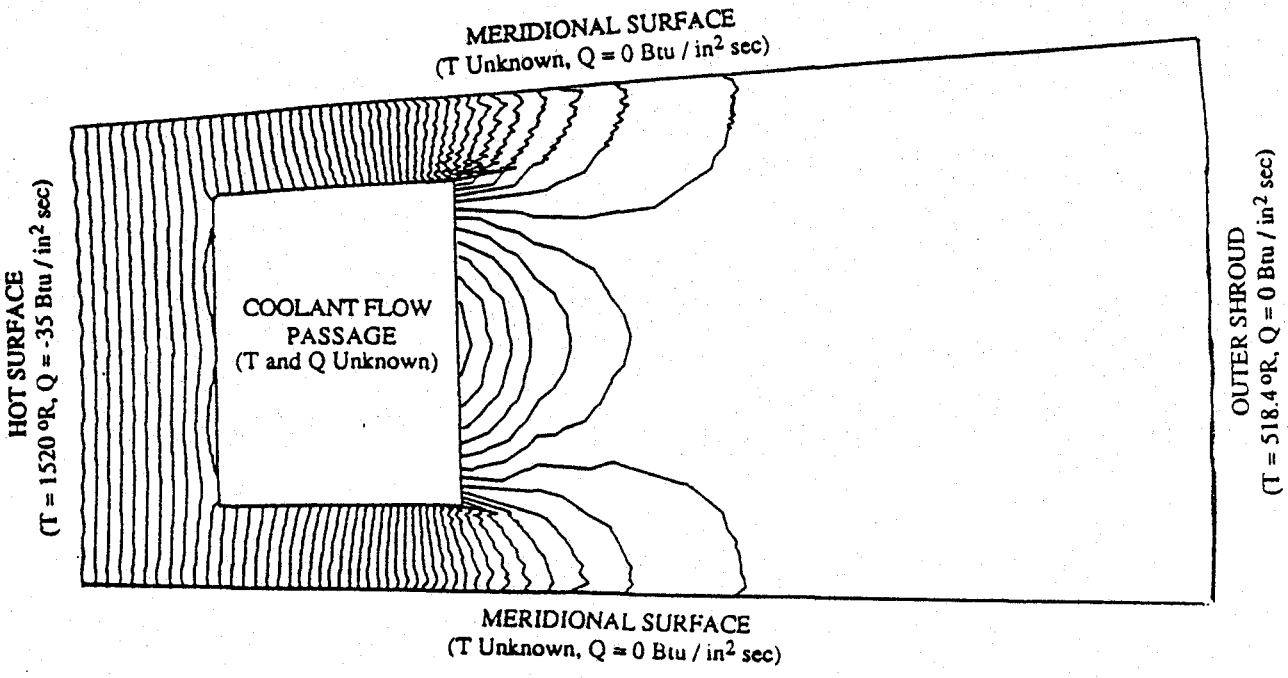

Figure 7. Geometry, boundary conditions and isotherms computed using the BEM for a two-dimensional section of a thrust chamber wall with a coolant flow passage.

SECOND LAW ANALYSIS OF A CONVENTIONAL STEAM POWER PLANT

Geng Liu, Robert H. Turner and Yunus A. Cengel
Department of Mechanical Engineering/312
University of Nevada, Reno
Reno, NV 89557

ABSTRACT

A numerical investigation of exergy destroyed by operation of a conventional steam power plant is computed via an exergy cascade. An order of magnitude analysis shows that exergy destruction is dominated by combustion and heat transfer across temperature differences inside the boiler, and conversion of energy entering the turbine/generator sets from thermal to electrical. Combustion and heat transfer inside the boiler accounts for 53.83 percent of the total exergy destruction. Converting thermal energy into electrical energy is responsible for 41.34 percent of the total exergy destruction. Heat transfer across the condenser accounts for 2.89 percent of the total exergy destruction. Fluid flow with friction is responsible for 0.50 percent of the total exergy destruction. The boiler feed pump turbine accounts for 0.25 percent of the total exergy destruction. Fluid flow mixing is responsible for 0.23 percent of the total exergy destruction. Other equipment including gland steam condenser, drain cooler, deaerator and heat exchangers are, in the aggregate, responsible for less than one percent of the total exergy destruction. An energy analysis is also given for comparison of exergy cascade to energy cascade. Efficiencies based on both the first law and second law of thermodynamics are calculated for a number of components and for the plant. The results show that high first law efficiency does not mean high second law efficiency. Therefore, the second law analysis has been proven to be a more powerful tool in pinpointing real losses. The procedure used to determine total exergy destruction and second law efficiency can be used in a conceptual design and parametric study to evaluate the performance of other steam power plants and other thermal systems.

NOMENCLATURE

A	= area, m^2
C_p	= specific heat, KJ/(kg.c)
E^p	= exergy, MJ
g	= gravitational acceleration, m/s^2
h	= enthalpy, KJ/kg
h^0	= methalpy, KJ/kg, $h^0=h+gz+V^2/2$
HV	= heating value of fuel, KJ/kg
m	= mass flow rate, kg/s
P	= pressure, KPa

Q = heat rate, KW
R = ideal gas constant, for water vapor R=0.461 KJ/(kg.K)
s = entropy, MJ/K.kg
S = entropy, MJ/K
t = time, sec
T = temperature, K or C
v = specific volume, m^3/kg
V = velocity, m/s
W = gross turbine power, KW
x = mass flow rate ratio of mixing
z = elevation, m
Z_h = enthalpy departure factor
Z_s = entropy departure factor

GREEK LETTERS

η_I = first law efficiency
η_{II} = second law efficiency
Δ = (pressure) difference

SUBSCRIPTS

a = ambient (reference)
b = boiler
bfpt = boiler feed pump turbine
cond = condenser
cr = critical point
dc = drain cooler
des = destroyed
fri = due to friction
gen = entropy generation
gsc = gland steam condenser
ht = high pressure turbine
hx = heat exchangers
i = inlet, inflow
it = intermediate pressure turbine
l = liquid
loss = due to loss
lt = low pressure turbine
mak = water makeup
mix = due to mixing
o = outlet, outflow
rh = reheater
ssr = steam seal regulator
v = vapor,steam
w = water

INTRODUCTION

A conventional steam power plant unit located in Valmy, northern Nevada is shown in Fig. 1. In this Plant, steam generated in the coal-fired boiler enters a high-pressure turbine. Most of the steam leaving the high-pressure turbine enters the intermediate-pressure turbine via a reheater. A small fraction of the steam leakage flow from the high-pressure turbine enters the intermediate-pressure turbine directly (without reheating). After passing through the intermediate-pressure turbine, the steam then powers a low-pressure double flow turbine-generator. The main output steam from the turbine-generator is condensed into water through a condenser and is then diverted back to the boiler through a series of heat exchangers and a deaerator. After partial pressurization, the condensed water is heated inside heat exchangers by the steam coming down from three different turbines through bleeds. Two other pieces of auxiliary equipment in the system schematic are the BFPT and SSR. BFPT is the boiler feed pump turbine which supplies direct drive power to the boiler feed pump. The "steam seal regulator" (SSR) can adjust the steam pressure in the turbine gland seals.

Although there have been a considerable number of prior exergy studies on power generation (Salamon et al, 1980; El-Masri, 1985; Ishida et al, 1987; Bejan, 1988; Lozano and Valero, 1988; Stecco and Desideri, 1988; Valero and Torres, 1988; El-Sayed, 1988; Kalina and Tribus, 1989; Dunbar et al, 1991; Kalina, 1991; Horlock, 1991; Bidini and Stecco, 1991; Tsatsaronis et al, 1991), a second law assessment of exergy cascade for this kind of plant is not available.

Properly quantified performance of a steam power plant must not only account for the energy gains and losses as dictated by the First Law of Thermodynamics, it must also account for the quality of the energy. However, energy quality can be only determined from the Second Law. Exergy analysis is a powerful tool for the evaluation of the thermodynamic and economic performance of thermal systems. In this research, the application of exergy analysis in the evaluation of the steam power plant is described in detail. An energy analysis is also performed for purposes of comparison with the exergy analysis.

EXERGY ANALYSIS AND EXERGY EQUATIONS

As described in the above section and Figure 1, the unit is composed of a coal-fired boiler, reheater, high-pressure turbine, intermediate-pressure turbine, low-pressure double flow turbine generator, heat rejector (condenser), gland steam condenser (GSC), drain cooler (DC), deaerator, six heat exchangers, boiler feed pump turbine, steam seal regulator, transportation pipes, pumps, valves and other auxiliary equipment. The working fluid is water/steam. Exergy destruction happens where energy transfer and momentum transportation are involved. In this analysis, only main

components in the system which play important roles in energy transfer and momentum transportation are considered.

Exergy destruction in the boiler manifests from highly irreversible combustion and heat transfer. The fuel oxidation consumes a certain percentage of the usable fuel energy. The huge gap between steam temperature and combustion temperature necessarily causes similarly huge exergy destruction. The value of exergy loss which is obtained by subtracting exergy leaving from exergy arriving at the boiler is the product value of entropy generation and reference temperature. There are several various proposals for the expression of second law efficiency about power plant components (Horlock, 1991). This investigation adopts Fratzscher's definition which is also recommended by Horlock. The second law efficiency is the ratio of exergy leaving over exergy arriving.

$$E_{b,des}=S_{b,gen}T_a=E_{b,i}-E_{b,o} \tag{1}$$

$$\eta_{II,b}=\frac{E_{b,o}}{E_{b,i}} \tag{2}$$

Exergy arriving includes the exergy of fuel input (fuel exergy), the exergy of water returning from heat exchangers and the exergy coming from high-pressure turbine then entering reheater which is built inside the boiler. Exergy gained by the working fluid which is delivered to the high-pressure turbine and the intermediate-pressure turbine respectively is considered as exergy leaving. The fuel exergy is given by

$$E_{fuel}=\int Q_{fuel}\left(1-\frac{T_a}{T_{flame}}\right)dt \tag{3}$$

where

$$Q_{fuel}=m_{fuel}HV \tag{4}$$

Bejan (1988) gives the flow exergy as,

$$E=\dot{m}[h^0-h_a^0-T_a(s-s_a)]\Delta t \quad (5)$$

which is defined as the difference between the flow availability of a stream and that of the same stream at its restricted dead (reference) state. In the above equation, h^0 is methalpy representing the summation of thermal, potential and kinetic energy. After neglecting potential and kinetic energy, the exergy of water from the heat exchangers is expressed by adopting equation (5).

$$E_{b,i,hx}=\int m_{b,i,hx}[h_{b,i,hx}-h_a-T_a(s_{b,i,hx}-s_a)]\,dt \quad (6)$$

The flow exergy entering the reheater from the high-pressure turbine can be described by a same expression.

$$E_{b,i,ht}=\int m_{b,i,ht}[h_{b,i,ht}-h_a-T_a(s_{b,i,ht}-s_a)]\,dt \quad (7)$$

The flow exergy leaving the boiler for the high-pressure turbine is given by

$$E_{b,o,ht}=\int m_{b,o,ht}[h_{b,o,ht}-h_a-T_a(s_{b,o,ht}-s_a)]\,dt \quad (8)$$

The flow exergy leaving the reheater for the intermediate-pressure turbine is given by

$$E_{b,o,it}=\int m_{b,o,it}[h_{b,o,it}-h_a-T_a(s_{b,o,it}-s_a)]\,dt \quad (9)$$

so the exergy destruction and second law efficiency become,

$$E_{b,des}=S_{b,gen}T_a=E_{fuel}+E_{b,i,hx}+E_{b,i,ht}-E_{b,o,ht}-E_{b,o,it} \quad (10)$$

$$\eta_{II,b}=\frac{E_{b,o,ht}+E_{b,o,it}}{E_{fuel}+E_{b,i,hx}+E_{b,i,ht}} \tag{11}$$

Similar analyses of the exergy balance related to exergy destruction and second law efficiency for other components in this steam power plant are based on equation (5) and the following equation for work output or input.

$$E_w=\int W dt \tag{12}$$

Exergy destruction occurs in the flowing fluid throughout the entire system because of energy and momentum loss. Thermodynamic irreversibility in incompressible water flow only depends on temperature drop (Bejan, 1988).

$$S_{f,l,gen}=\int [mC_p \ln\frac{T_o}{T_i}]\, dt \tag{13}$$

or when

$$\Delta P \ll \frac{C_p}{v} T_i \tag{14}$$

then

$$S_{f,l,gen}=\int [\frac{mv}{T_i}\Delta P]\, dt \tag{15}$$

In the case of steam, entropy generated by fluid friction is proportional to the pressure gradient and difference of entropy departure factors.

$$S_{f,v,gen}=\int mR[\ln\frac{P_i}{P_o}+(Z_{s,o}-Z_{s,i})]\, dt \tag{16}$$

The first term in the above expression is based on the ideal gas

assumption (Bejan, 1988). But ideal gas relations should not be used in steam power plant applications where high pressure superheated steam is usually involved. At high pressure, steam deviates considerably from ideal gas behavior. A correction term including enthalpy departure factors and entropy departure factors must be incorporated (Cengel and Boles, 1989). The second term is added to correct for entropy departure.

When two streams of differing temperature and pressure mix with one another, the accompanying energy and momentum exchange necessarily involves exergy destruction. There are many locales where such mixing occurs in the system. Bejan (1988) gives the mixing entropy generation for incompressible fluid as,

$$S_{m,l,gen} = \int mC_{p,w}\left[\frac{x}{2}(1-x)\left(\frac{T_1-T_2}{T_1}\right)^2+\frac{xv}{C_{p,w}T_1}\left(\frac{P_1-P_3}{P_3}\right)+\frac{(1-x)v}{C_{p,w}T_1}\left(\frac{P_2-P_3}{P_3}\right)\right]dt \tag{17}$$

where m is total mass flow rate after mixing, x is ratio of mass flow rate from the inlet with temperature T_1 and pressure P_1 over the total mass flow rate. Variables with subscripts 1 and 2 represent two inlet flow while the outlet flow of mixing is expressed with the subscript 3. The corresponding expression for steam is

$$S_{m,v,gen} = \int m\left[C_{p,v}x(1-x)\left(\frac{T_1-T_2}{T_1}\right)^2+\frac{xR}{C_{p,v}}\left(\frac{P_1-P_3}{P_3}\right)+\frac{(1-x)R}{C_{p,v}}\left(\frac{P_2-P_3}{P_3}\right)\right]+$$

$$xR(Z_{s,3}-Z_{s,1})+(1-x)R(Z_{s,3}-Z_{s,2})\}dt \tag{18}$$

The first three terms in the above equation are based on the ideal gas assumption (Bejan, 1988). Similar to the expression for entropy generated by fluid friction (steam), the last two term is added to correct for entropy departure. Then, exergy destruction can be obtained by multiplying entropy generation and T_a.

Pumps, of course, contribute themselves to the overall destruction of exergy through the system. Like most steam-turbine cycle calculation, their thermodynamic irreversibilities are neglected. Inlet and outlet flows of the steam seal regulator have the same temperature and pressure, so that flow through the steam seal regulator generates no entropy and the net exergy loss is zero.

ENERGY ANALYSIS

Energy balance is based on counting the energy input, energy output and energy losses which is dominated by the first law of thermodynamics. The value of energy loss is obtained by subtracting energy output from energy input.

$$EnergyLoss=EnergyInput-EnergyOutput \tag{19}$$

The first law efficiency is the ratio of energy output over energy input.

$$\eta_I=\frac{EnergyOutput}{EnergyInput} \tag{20}$$

For example, considering energy balance for the boiler.

$$EnergyLoss=\int\{(mHV)_{fuel}+(mh)_{b,i,htr}+(mh)_{b,i,ht}-(mh)_{b,o,ht}-(mh)_{b,o,it}\}dt \tag{21}$$

therefore

$$\eta_{I,b}=\frac{\int\{(mh)_{b,o,ht}+(mh)_{b,o,it}\}dt}{\int\{(mHV)_{fuel}+(mh)_{b,i,hx}+(mh)_{b,i,ht}\}dt} \tag{22}$$

Similar analyses of the energy balance and first law efficiency for other components in the power plant are based on equation (19) and (20).

RESULTS AND DISCUSSION

The preceding integrals are evaluated numerically for a single day using the heating value of coal, temperatures and pressures provided by Sierra Pacific Power Company. Table 1 presents energy and exergy quantities in the energy cascade and exergy cascade from heat source to heat exchanger 7. Comparing the second columns with the third columns for every component in Table 1, it should be noticed that exergy input is always less than energy input. This

means that thermal energy input is not high quality energy and only part of it is available.

Table 2 shows the first law efficiency and the second law efficiency for components and the plant. This table shows that some components, such as the turbine/generator, have high first law efficiencies but low second law efficiencies. The first law efficiency of the turbine/generator set is almost one hundred percent while its second law efficiency is just 54.4 percent. The reason is that a lot of hot steam flows down to the heat exchangers through bleeds. This bleed-off steam can be considered as the hot stream (source) of the heat exchangers and the output of turbine/generator. These thermal energy outputs are much lower quality of energy than the highly refined energy of electrical output. It is also interesting to note that all heat exchangers have a one-hundred percent first law efficiency but not a one-hundred percent second law efficiency, the difference being caused by exergy destruction due to heat transfer. The heat exchanger numbered one has a lower second law efficiency than the other heat exchangers. This datum, crucial to effective energy management, means that heat exchanger one has a larger availability loss; a loss which escapes the methods and techniques of first law analyses.

After the investigation of exergy destruction, it is found that combustion and heat transfer losses in the boiler are responsible for 53.83 percent of the total exergy destruction. Combustion losses can hardly be reduced with present technology because the conventional fuel oxidation via the highly irreversible combustion process consumes about 30 percent of the usable fuel energy (Dunbar et al, 1991). A possible remedy for this waste of exergy would be the application of fuel cells in future, even though fuel-cell technology for large-scale generation of electrical power remains to be determined. The heat transfer loss causing destruction of exergy is due to the difference between high temperature gas and low temperature water/steam. This loss may be reduced by using high temperature and pressure steam.

Conversion of thermal energy into mechanical energy then electrical energy accounts for 41.34 percent of total exergy destruction. Entropy is generated by the expansion of vapor from high temperature and pressure to low temperature and pressure. The magnitude of entropy generated depends on turbine isentropic efficiency.

Heat rejection from steam to the atmosphere is responsible for 2.89 percent of the total exergy destruction. This is due to heat transfer between steam and its ambient surroundings. Lowering the condenser pressure can, of course, reduce temperature differences between working fluid and the atmosphere so that entropy generated in heat rejection can be reduced, but the technical and economical feasibility of doing this should be considered together.

Friction losses account for 0.50 percent of the total exergy destruction. Although it poses a small fraction of the total exergy destruction, it should be noticed that this loss is much bigger than the losses caused by the boiler feed pump turbine, flow

mixing, and any of the heat exchangers in the system. The friction losses may be reduced by installing smooth surface transportation pipes and better insulation on pipes so that pressure and temperature drops are reduced.

The loss caused by the boiler feed pump turbine is responsible for 0.25 percent of the total exergy destruction. Mixing losses account for 0.23 percent of the total exergy destruction. The mixing losses may be reduced by selecting two streams with smaller pressure and temperature difference for mixing purpose. The gland steam condenser, drain cooler, deaerator and other heat exchangers are collectively responsible for 0.96 percent of the total exergy destruction. Theoretically, the irreversibility of heat exchangers depends on two factors, heat transfer across the temperature difference between the hot and cold streams and the pressure drop caused by friction. Large heat exchangers may have a lower exergy destruction rate because they have more heat transfer area and more heat transfer.

CONCLUSION

A methodology is presented to calculate the exergy delivered and the exergy destroyed by operation of a conventional steam power plant. It is shown that combustion and heat transfer inside the boiler and conversion of thermal energy to electricity are responsible for most of the exergy destruction. Heat loss from the condenser makes the next largest contribution. Flow with friction, the boiler feed pump turbine and flow mixing manifest a very small fraction of the total exergy destruction. Heat transfer across temperature differences and frictional pressure drop involved with the gland steam condenser, drain cooler, deaerator and heat exchangers also reduce delivered exergy. The second law analysis is a powerful tool of thermodynamic research for power plants and other thermal systems.

ACKNOWLEDGEMENTS

The authors are very grateful to Mr. David Poole and Mr. Jack McGinley of Sierra Pacific Power Company for providing the system schematic, technical data of the plant and helpful discussion.

REFERENCES

Bejan, A., 1982, Entropy Generation through Heat and Fluid Flow, Wiley Interscience, New York, NY.

Bejan, A., 1988, Advanced Engineering Thermodynamics, Wiley Interscience, New York, NY.

Bejan, A., 1988, "Theory of Heat Transfer-Irreversible Power

Plants," Int. J. Heat and Mass Transfer, Vol.31, No. 6, pp.1211-1219, June, 1988.

Bidini, G. and Stecco, S.S., 1991, "A Computer Code Using Exergy for Optimizing Thermal Plants," ASME J. Engineering for Gas Turbines and Power, Vol. 113, pp.145-150, January, 1991.

Cengel, Y.A. and Boles, M.A., 1989, Thermodynamics: An Engineering Approach, McGraw-Hill Inc., New York, NY.

Dunbar, W.R., Lior, N. and Gaggioli, R.A., 1991, "Combining Fuel Cells with Fuel-Fired Power Plants for Improved Exergy Efficiency," Energy (oxford), Vol.16, No. 10, pp.1259-1274, October, 1991.

El-Masri, M.A., 1985, "On Thermodynamics of Gas-Turbine Cycles: Part 1-Second Law Analysis of Combined Cycles," ASME J. Engineering for Gas Turbines and Power, Vol.107, pp.880-889, October, 1985.

El-Sayed, Y.M., 1988, "A Decomposition Strategy for the Thermoeconomic Optimization of a Given System Configuration," AES-Vol. 7, Approaches to the Design and Optimization of Thermal Systems: The Advanced Energy Systems, ASME WAM, November 27-December 2, 1988, pp. 41-47.

Habib, M.A., 1991, "First and Second Law Analysis of Cogeneration Plant," AES-Vol. 24, Thermodynamics and Energy Systems: Fundamental, Education, and Computer-Aided Analysis, ASME 1991, PP. 31-36.

Horlock, J.H., 1991, "The rational Efficiency of Power Plant and Their Components," 1991 ASME COGEN-TURBO, International Gas Turbine Institute (Publication) IGTI Vol. 6, pp.103-113.

Ishida, M., Zheng, D. and Akehata T., 1987, "Evaluation of a Chemical-Looping Combustion Power-Generation System by Graphic Exergy Analysis," Energy (oxford), Vol.12, No. 2, pp. 147-154, February, 1987.

Kalina A. I. and Tribus M., 1989, "The Kalina Power Cycles A Progress Report," Proceedings of the 51st American Power conference 1989, Chicago, Il, April 24-26, 1989.

Kalina A. I., 1991, "Kalina Cycles and System for Direct-Fired Power Plants," AES-Vol. 25/HTD-vol. 191, Second Law analysis-Industrial and Environmental Applications, Advanced Energy Systems Division, ASME December 1-6 1991, pp.41-47.

Lozano, M.A. and Valero A., 1988, "Methodology for Calculating Exergy in Chemical Process," AES-Vol. 4, Thermodynamic Analysis of Chemically Reactive System, Advanced Energy Systems Division, ASME November 27-December 2 1988, pp.77-86.

Stecco, S.S. and Desideri, U., 1989, " A Thermodynamic Analysis of the Kalina Cycles: Comparisons, Problems and Perspectives," ASME June 4-8 1989, Published by ASME, 89-GT-149.

Tsatsaronis G., Lin, L., Tawfik, T. and Gallaspy, D., 1991, " Exergoeconomic Evaluation of a KRW-based IGCC Power Plant," AES-Vol. 25/HTD-vol. 191, Second Law analysis-Industrial and Environmental Applications, Advanced Energy Systems Division, ASME December 1-6 1991, pp.19-32.

Valero, A. and Torres C., 1988, " Algebraic Thermodynamic Analysis of Energy Systems," AES-Vol. 7, Approaches to the Design and Optimization of Thermal Systems: The Advanced Energy Systems, ASME WAM, November 27-December 2, 1988, pp. 13-23.

Table 1. Energy and Exergy Quantities

COMPONENTS	ENERGY INPUT (MJ)	EXERGY INPUT (MJ)
Boiler	1.51270 E08	8.58632 E07
Turbine/generator	1.29420 E08	5.38873 E07
BFPT	2.71932 E06	776627
Condenser	3.30799 E07	1.75705 E06
GSC	2.77810 E06	58312
DC	2.97503 E06	64511
#1 Heater	5.06362 E06	368189
#2 Heater	6.42929 E06	557701
#3 Heater	9.83891 E06	1.34524 E06
#4 Heater	1.29291 E07	2.16142 E06
#5 Heater	1.53978 E07	2.69885 E06
#6 Heater	1.99722 E07	4.13567 E06
#7 Heater	2.31962 E07	5.59951 E06

Table 2. Efficiencies

COMPONENTS	n_I	n_{II}
Boiler	85.6%	62.8%
Turbine/generator	99.7%	54.4%
BFPT	100%	80.6%
Condenser	8.1%	2.4%
GSC	100%	91.6%
DC	100%	93.0%
#1 Heater	100%	73.4%
#2 Heater	99.9%	91.6%
#3 Heater	100%	92.0%
#4 Heater	100%	95.8%
#5 Heater	100%	98.9%
#6 Heater	100%	98.0%
#7 Heater	100%	98.0%
Total Plant	42.8%	37.8%

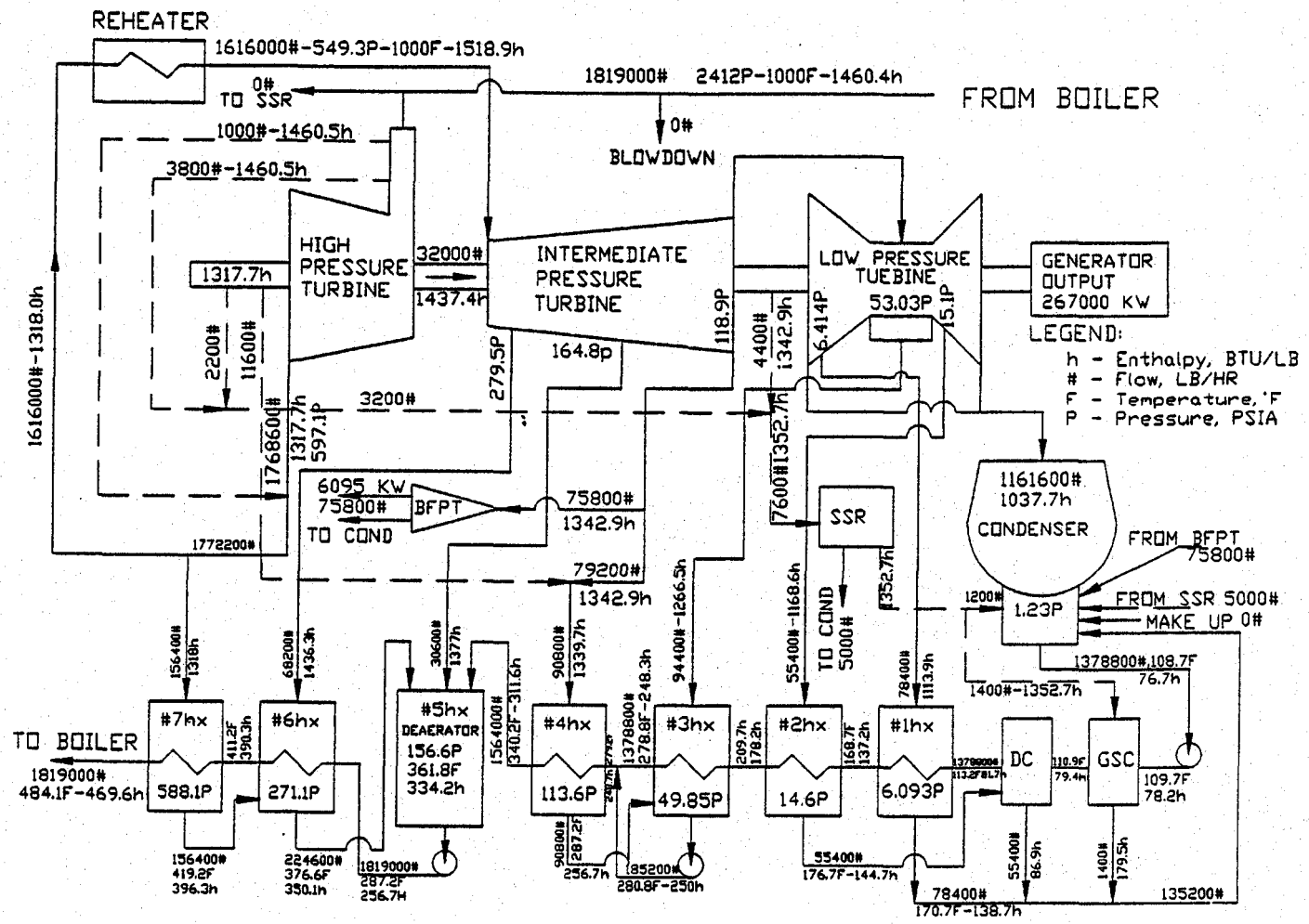

Fig.1 STSTEM SCHEMATIC

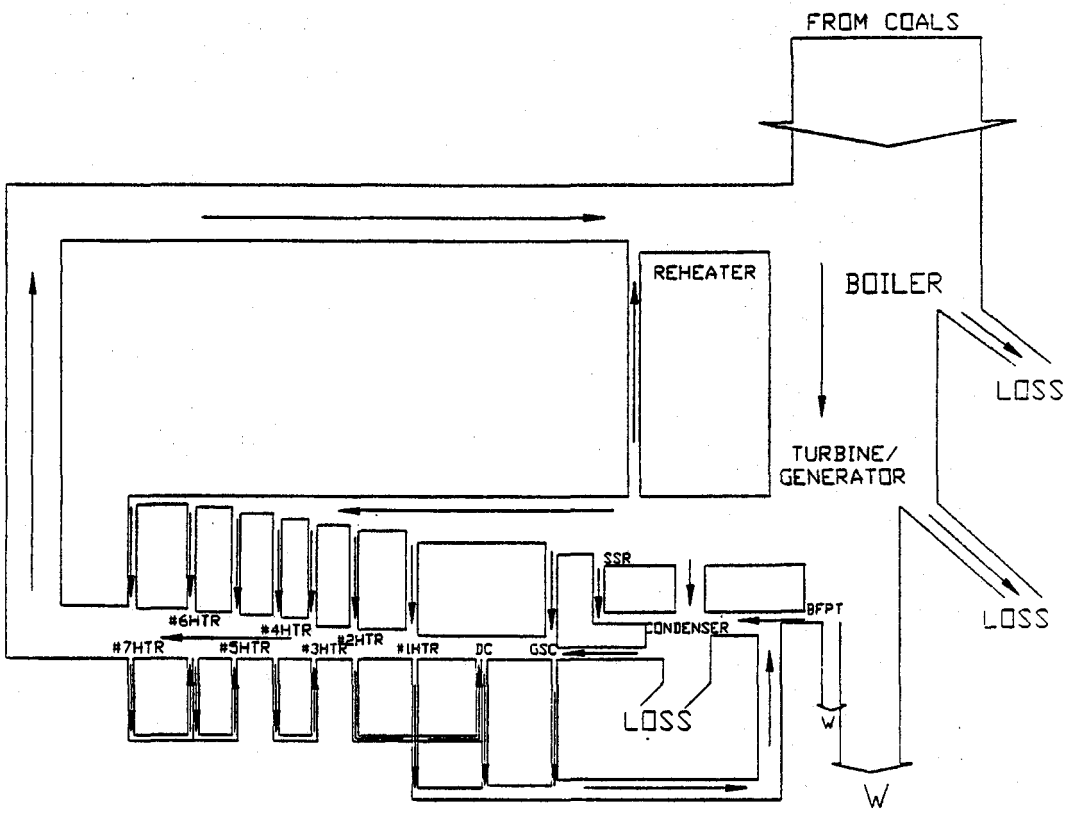

Fig.2 ENERGY CASCADE

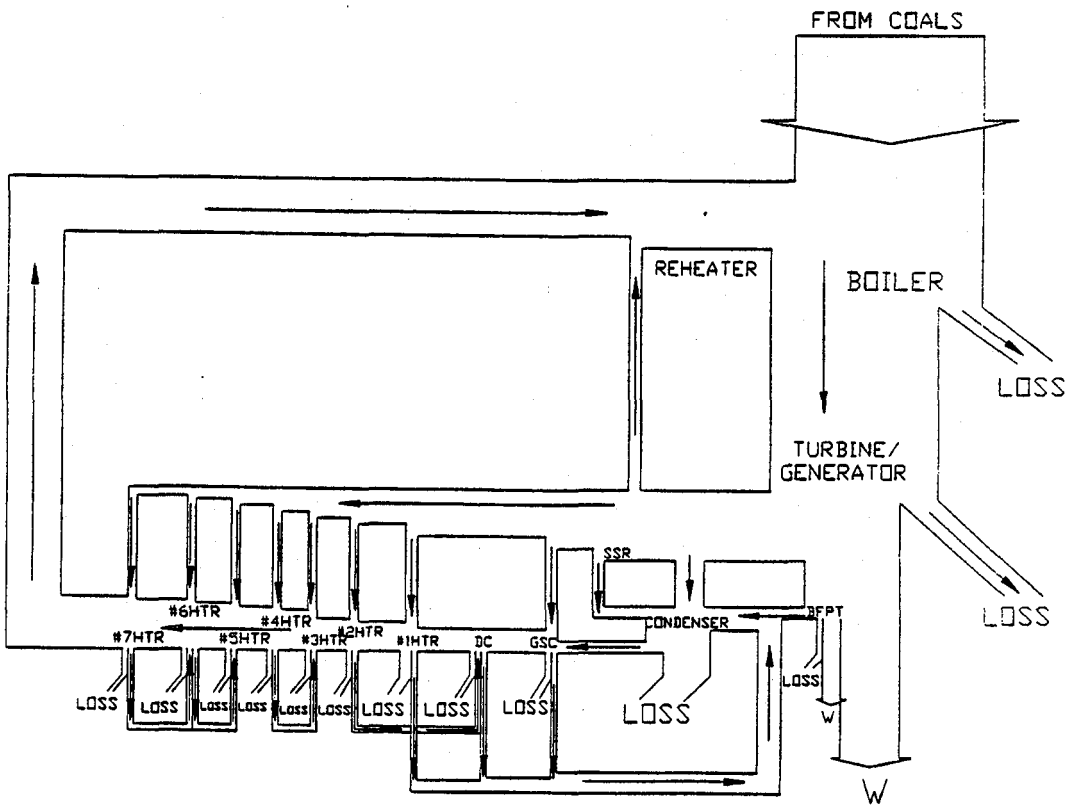

Fig.3 EXERGY CASCADE

Session
Three

Code Innovations

SOME USEFUL INNOVATIONS WITH TRASYS AND SINDA-85

Ruth M. Amundsen
National Aeronautics and Space Administration
Langley Research Center
Hampton, VA 23681

SUMMARY

Several innovative methods have been used to allow more efficient and accurate thermal analysis using SINDA-85 and TRASYS, including model integration and reduction, planetary surface calculations, and model animation. Integration with other modeling and analysis codes allows an analyst to import a geometry from a solid modeling or computer-aided design (CAD) software package, rather than building the geometry "by hand." This is more efficient as well as potentially more accurate. However, the use of solid modeling software often generates large analytical models. The problem of reducing large models has been elegantly solved using the response of the transient derivative to a forcing step function.

The thermal analysis of a lunar rover implemented two unusual features of the TRASYS/SINDA system. A little-known TRASYS routine SURFP calculates the solar heating of a rover on the lunar surface for several different rover positions and orientations. This is used not only to determine the rover temperatures, but also to automatically determine the power generated by the solar arrays. The animation of transient thermal results is an effective tool, especially in a vivid case such as the 14-day progress of the sun over the lunar rover. An animated color map on the solid model displays the progression of temperatures.

INTRODUCTION

In many industries there has recently been a concerted movement toward "quality management" and the issue of how to accomplish work more efficiently. Part of this effort is focused on concurrent engineering: the idea of integrating the design and analysis processes so that they are not separate, sequential processes (often involving design rework due to analytical findings) but instead form an integrated system with smooth transfers of information. Specific examples of concurrent engineering methods being carried out at NASA Langley Research Center (LaRC) are: integration of thermal, structural and optical analyses to predict changes in optical performance based on thermal and structural effects; integration of the CAD design process with thermal and structural analyses; and integration of thermal analysis with animation to show the thermal response of a system as an active color map -- a highly effective visual indication of heat flow.

Electronic integration of design and analysis processes was achieved and refined during the development of an optical bench for a laser-based aerospace experiment. One of the driving requirements for any complex optical system is its alignment stability under all conditions. Accurate predictions of optical bench or test bed deflections are necessary to calculate beam paths and determine optical performance. Another requirement that is increasingly demanded of any analysis process is to do it faster and better; create a more streamlined process and include all known variables to produce the best possible predictions. These goals can be accomplished by using an integrated process to accomplish design and all analyses. This integrated analysis process has been built around software that was already in use by designers and analysts at LaRC. The PATRAN® solid modeling / finite element package is central to this process, since it was already in common use at LaRC. Most of the integration and interface steps described here are also

possible with other packages, although certain of the translators were developed or modified for use with these specific software packages.

Modeling with any solid geometry package, such as PATRAN, tends to encourage the use of larger models than a thermal analyst would tend to produce. Since the geometry is more accurate, it has more complexity and requires finer nodalization. Also, the meshing capability allows quick, automatic generation of models with more nodes than would be generated by hand. These larger models must be reduced to produce the type of model required for a space-flight experiment. One way this has been done at LaRC is to compare the derivative of the transient thermal response to a forcing step function, and correlate this response with the transient response of a smaller model.

In the analysis of a lunar rover, a subroutine in TRASYS called SURFP was used for the first time at LaRC. This routine calculates the solar and IR heating for a spacecraft that is stationary on the planetary surface. By evaluating heating at several different positions on the lunar surface over a lunar day, the entire thermal environment for a traversing rover can be calculated. Also, the solar flux values were used to calculate the power levels generated by the rover's solar arrays, and thus determine what level of charge the battery would achieve.

The process of thermal animation, which is a natural outgrowth of model integration with the solid modeling codes that have this built-in capability, is especially effective for a situation such as the lunar rover, where the angle of the sun to the vehicle is constantly changing.

The efforts of Kelly Smith and Jill Marlowe in structural analysis, Steve Hughes and Al Porter in design, Maria Mitchum in software development, and Greg Herman and Alan Little in optical analysis are gratefully acknowledged.

ANALYSIS INTEGRATION

The heart of the concurrent engineering process described here is the use of a single integrated model for thermal and structural analysis of a system. This allows a savings of time in the thermal and structural analysis work, since only one geometric model must be developed. It facilitates electronic transfer of data between all types of analysis, such as transfer of exact thermal gradients to be used in structural analysis. Finally, it produces greater model accuracy since the model can be directly imported from the design software package.

Interfaces between Analysis and Design Software

The design software most often used in this process at LaRC is Pro-Engineer®. A part is completely designed in Pro-Engineer, which produces a three-dimensional model of the part as well as all the fabrication drawings. A Pro-Engineer solid shaded model of a complex assembly is shown in Figure 1. This example assembly is a laser reference cavity which is mounted on an optical bench. There are three basic methods available to translate from Pro-Engineer CAD software to the PATRAN solid modeling software. All these methods have been used to produce viable models. One is to mesh the solid geometry of the part in Pro-Engineer and translate that mesh to PATRAN. The disadvantages to this method are: only the mesh is transferred, not the underlying solid geometry, so the geometry and mesh cannot be changed in PATRAN; and the mesh is limited to only tetrahedral or triangular elements. The second method is to transfer the part from Pro-Engineer to an IGES file, which is a standard graphics format, and read this file into PATRAN using the CADPAT translator. This translates the phase I (underlying) geometry, but only in the form of surfaces and lines, not PATRAN's solid geometry elements called hyperpatches. Thus the analyst must still define hyperpatches based on the geometry described by the translated surfaces. This can be helpful as the analyst can choose to ignore details such as bolt holes in constructing the analytical model. The disadvantages to this method are the rework in creating the solid form from the transferred

surfaces (which only applies when the part being transferred is a solid rather than plate elements), and that during translation of an assembly of parts, the orientation of the individual parts is lost and the assembly must be reconstructed from the components. The third method is to bring the solid geometry from Pro-Engineer directly into PATRAN. This method is only viable for the newer releases of both Pro-Engineer (Version 10 or later) and PATRAN (3.0). The solid geometry can then be either directly meshed, or used to create hyperpatches. An example component of the laser reference cavity is shown as an IGES file (Figure 2) and as completed with elements (Figure 3). Parts have also been brought into PATRAN from ANVIL, but this brings across only the 2-D shape and position of parts.

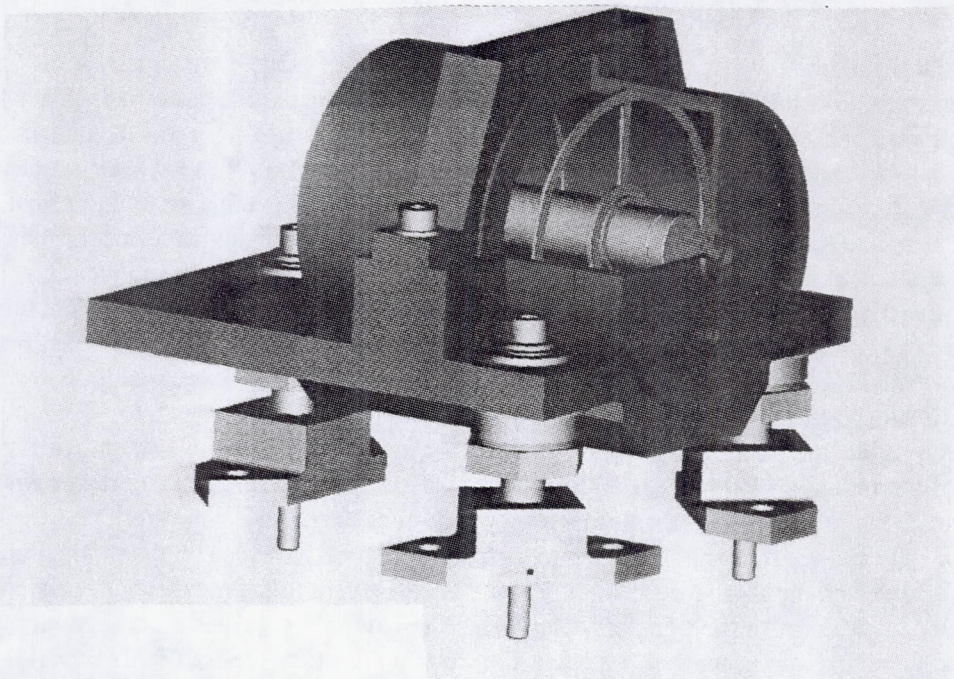

Figure 1. Laser reference cavity as designed and portrayed in Pro-Engineer

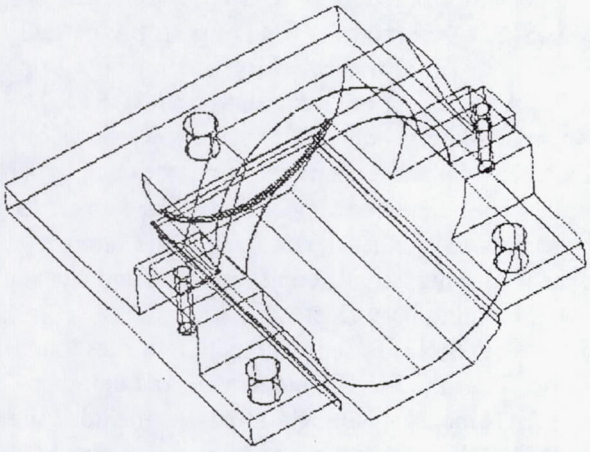

Figure 2. Mount surfaces imported to PATRAN from ProEngineer through IGES file

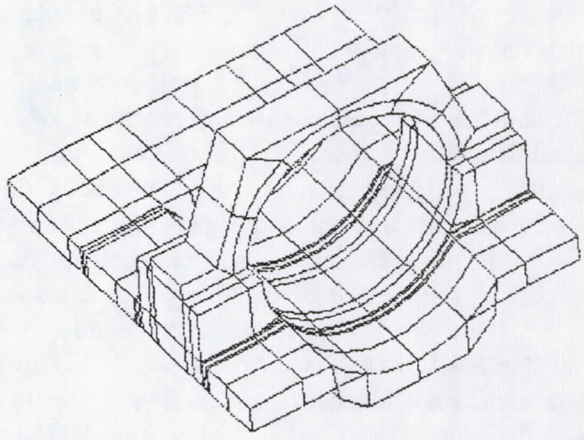

Figure 3. Mount part with solid elements created in PATRAN

The integration of design and analysis has several benefits. In terms of streamlining the process, there is much less work to be done by the analyst since the majority of the geometry is imported automatically. The entire process of taking dimensions from a design drawing and manually building up the geometry is eliminated. Also, the analyst is automatically working with the most current version of the design. Eliminating the repeated step of entering the dimensions lessens the probability of errors in the model. Geometries that are difficult to model and would perhaps be approximated are automatically translated exactly.

Interface between Thermal and Structural Analysis

The translators between structural and thermal analytical models are already built into the PATRAN system. The analysts can easily use the same geometric model, perform analyses through their separate software packages, and share the results electronically. There are a few techniques that make this type of translation easier and more effective. The model can be built in PATRAN by either analyst, but there must be communication between the analysts before the model is built, so that the final model will have a structure and level of detail appropriate for both analyses. One unique aspect of the work described herein is that the structural and thermal analysts determined together what method would be best for both of them in modeling certain parts, before the model was developed. A requirement on the thermal side that must be maintained in the model in order for it to be useful for the thermal analyst, is that between every pair of connected elements all corner nodes must be identical. Also, the best translation to a thermal model is currently achieved by using solid elements rather than plate elements in most cases. Many of the connections between solids and plates and plates-to-plates, that are correct for structural analysis, do not work correctly for thermal analysis. In order for each analyst to be able to easily create their own mesh, or use the same mesh, the phase I geometry must meet the requirements of both analysts.

The only change that must be made to alter the model between use by the thermal and structural analysts is a re-definition of the material properties, usually a five to ten minute task. The material identification is maintained through the transfer; only the actual material properties need be input again. Unfortunately the material properties are exclusive, so that each time the PATRAN model is transferred between analysts, the material properties must be redefined. Normally, the transfer is done only once. Improvements slated for PATRAN 3.0 will do away with this concern.

To perform the thermal analysis, the PATRAN model is translated to SINDA-85, a finite difference thermal analyzer, using the PATSIN translator[1]. This SINDA-85 model is used to perform thermal analysis, with some modifications such as adding power sources. The structural analysis can be performed in P/FEA[2] (a software package that directly interfaces with PATRAN) or after translation to NASTRAN[3]. The analysts sometimes desire different levels of detail; thermal analysis commonly uses a lower level of detail than structural analysis. In that case, an identical PATRAN phase I geometry of patches and hyperpatches is still used; each analyst can create their own mesh. The calculated temperatures can be used to impose accurate thermal loads on the structural model regardless of whether the meshing is the same, as long as the phase I geometry is identical. This has been checked using two different meshings and element numbering schemes on a model; the interpolated values were found to be correct.

One way to use the nodes and conductors created by PATSIN is to separate them into files that are called into the SINDA model using an INCLUDE statement. Thus the SINDA model can contain other data such as heating arrays; if there is a change to the PATRAN model it will only affect the included files, with the main SINDA model left unchanged. The output of PATSIN is often quite bulky, which would make editing of the full SINDA model more difficult. Using included files limits the size of the SINDA model file, and allows several different SINDA files to reference the same PATRAN model.

The thermal results, either from a steady state analysis or from time steps in a transient run, are translated by SINPAT to produce element and nodal temperature files that can be read by PATRAN. These files can be read directly into PATRAN, and the thermal results mapped onto the model geometry.

One advantage to the integrated method is the capability for viewing temperatures that are mapped back onto the geometry of the part. This provides a concrete display which can be used for demonstration of effects, or for de-bugging the model. Some examples of the effectiveness of this display are shown in Figures 4, 5, and 6. In Figure 4, thermal mapping on a laser reference cavity is shown. In this case, it was desirable to have a detailed model and direct transfer of temperatures since the structural analysis was required to predict displacements down to the micron level. In Figure 5, the PATRAN model was created by a designer for display only, and used for thermal mapping to visually verify the position of the rover with respect to the sun. In Figure 6, a cryocooler support bracket and its mounting scheme to a cold bus is portrayed. In this case, the internal heating of the cryocooler is critically dependent on the geometry of the mounting system, so the exact part geometry was imported from Pro-Engineer and used to perform both the thermal and structural analyses.

To use the nodal temperatures as actual thermal loads rather than only for display, the files must be run through a program called READER that translates the files to binary format. The results can be interpolated onto the structural model using a built-in utility of PATRAN (TEMP, ADD/INT)[4]. The thermal results, imported into the PATRAN model, can be used in the structural analysis software to calculate thermally driven stresses and deflections based on the predicted temperature distribution. These thermal stresses can be summed with any load-driven stresses, to produce a total reaction of the system to the environmental constraints.

Exporting Thermal Results to Optical Analysis

Most optical models start with the assumption that the system is aligned and at rest. The optical analyst inputs surfaces, sources and objects at their designed location, and determines the performance of the system. The optical code currently used by many analysts at LaRC is CODE-V®. During actual operation of the optical system, there will often be factors that cause distortions to the aligned system. In the case of an optical bench with optical components mounted on it, there can be thermal gradients across the bench that will cause minute warping of the bench and result in significant distortion of the optical system from its baseline aligned performance. There can also be structural loads imposed which cause deflections, and both the thermal and mechanical loading environments can be changing with time. There is an existing translator that will look at the deformation of a single optical element such as a lens in NASTRAN, and translate the appropriate information to CODE-V to determine the distorted lens performance. However, for the optical bench structure, a method was needed to look at changes in the overall performance based on distortions of the entire bench, not only a single element.

To accomplish this, an output file of nodal deflections is generated by the structural analysis software, with six values for each optical surface (rotations and translations in each of three axes). The deflections can be due to thermal, structural or any combination of loading conditions. A relational file is developed for that model that relates the nodes in the PATRAN model to the optical surfaces in the CODE-V model. Translation software (PATCODV) was developed at LaRC to read the structural analysis deflection file, the relational file, and a copy of the undeflected CODE-V model. It produces a new CODE-V model that has new positions and angles for the optical elements based on summing the predicted deflections and the original positions of the elements. CODE-V can then be run on the new model, and optical performance based on the distorted system is predicted. For any optical system there is usually only one PATRAN model, but there can be a separate CODE-V model for each optical path. The translation must be run for each optical path for which deflection analysis is desired. The translation can be run for a series of time steps, using deflection results files for each time step, to predict the performance of the system as a function of time. Figure 7 demonstrates the steps of this process pictorially by showing: (a) a map of the thermally driven distortions from this distribution; (b) a map of distortions due to structural loading; and (c) and a map of the combined distortions. Development of a user's manual for this translation software is currently underway at LaRC.

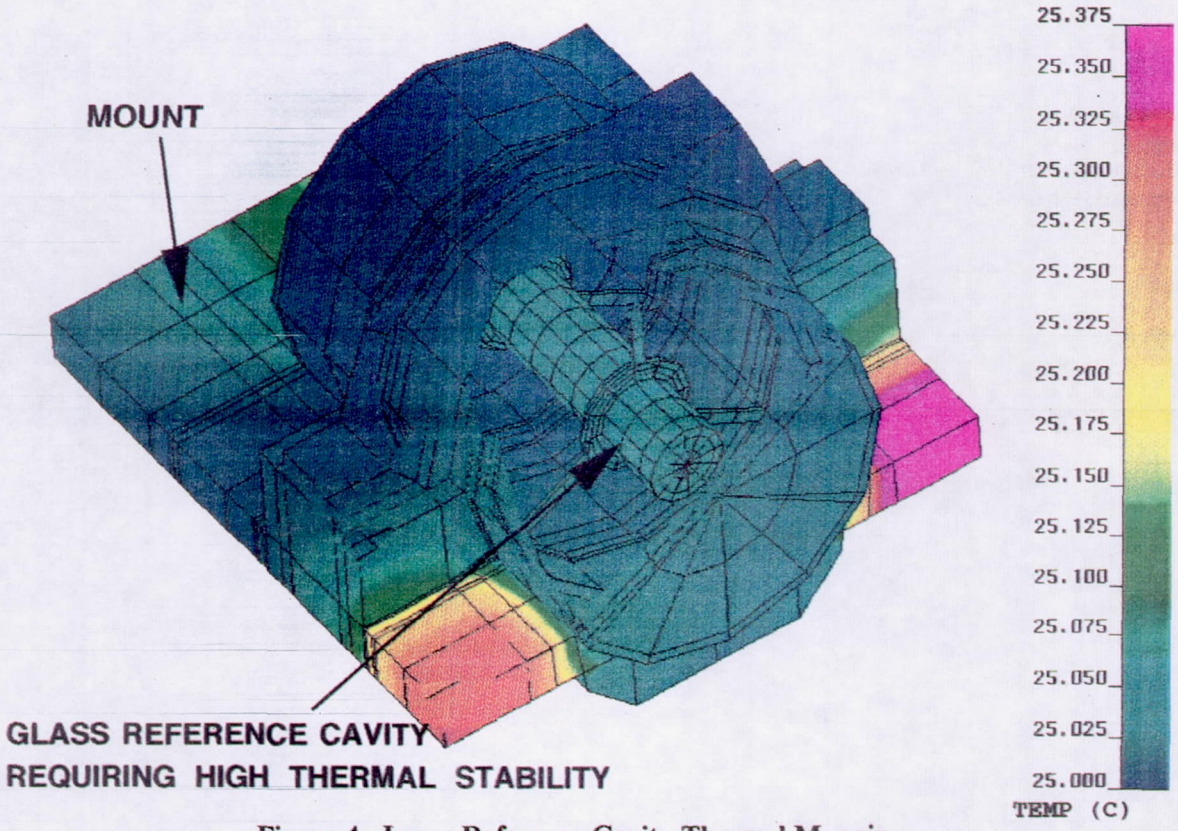

Figure 4. Laser Reference Cavity Thermal Mapping

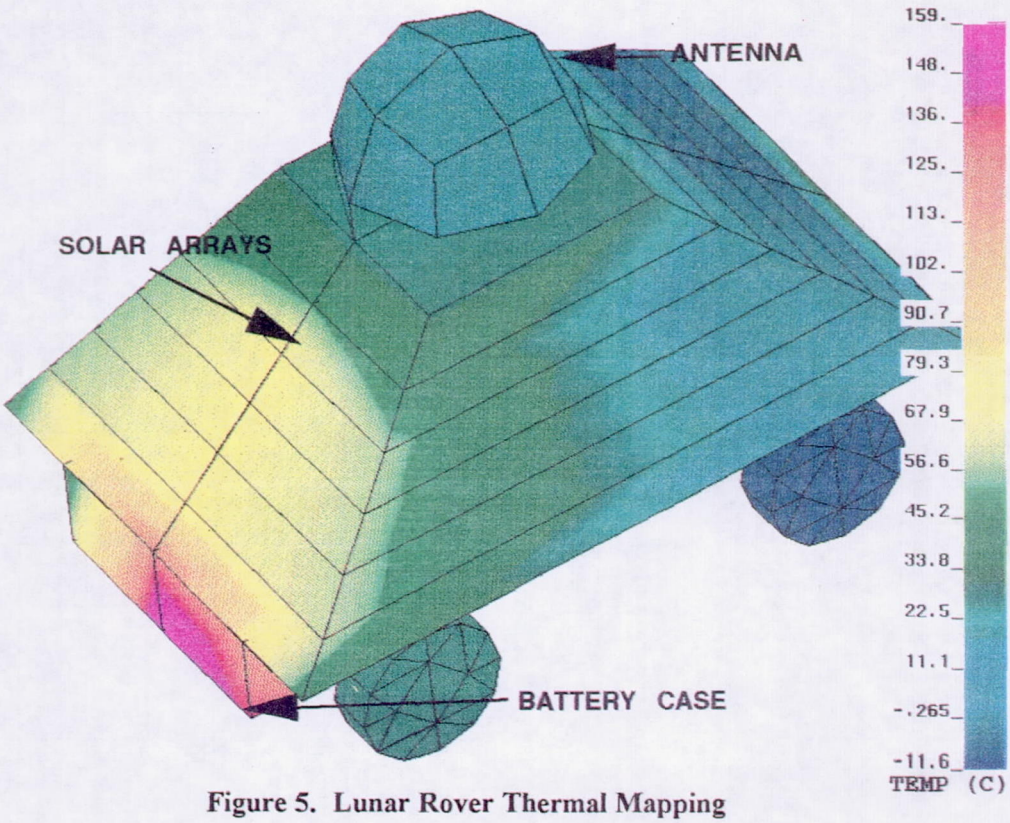

Figure 5. Lunar Rover Thermal Mapping

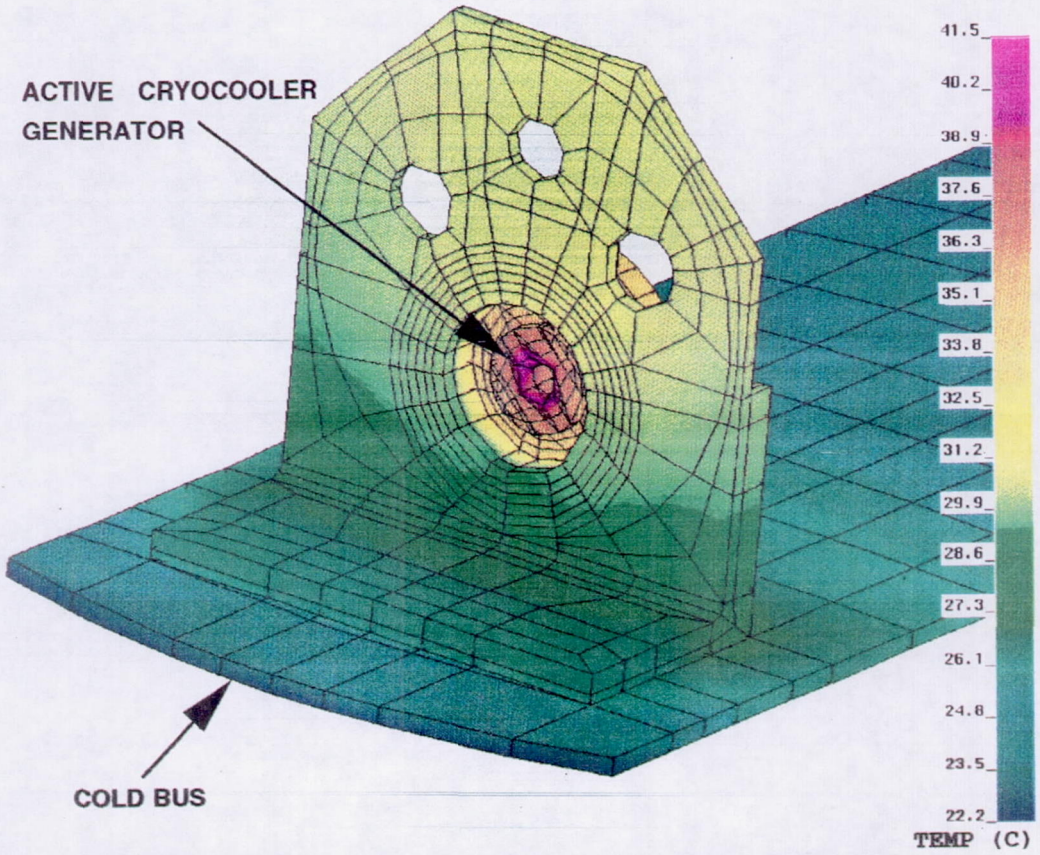

Figure 6. Cryocooler Mounting Bracket Thermal Mapping

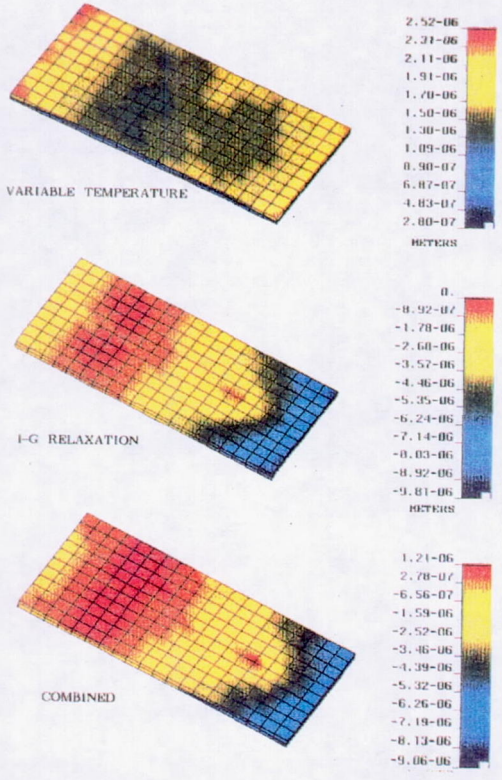

Figure 7. Optical bench deflections: (a) thermally-driven , (b) load-driven, and (c) total

THERMAL CORRELATION USING TRANSIENT

The large thermal models that are developed by using a solid modeling code can be intimidating in size, and can also be unwieldy to correlate with test results. Another disadvantage to the size has to do with the standard procedure for thermal analysis of a space-flight instrument. Normally, a reduced (10 to 12 node) thermal model of an instrument would be delivered to the flight carrier, so that an integrated spacecraft model can be run using all the instrument reduced models. The models developed from PATRAN are too large to be delivered, and they cannot be easily reduced to the required size since they were not developed from hand calculations. The method used here for this model reduction is evaluation of the transient derivative behavior. Key nodes in the model, which are appropriate to be lumped-mass nodes of a reduced model, are selected. The response of those nodes to a forcing step function at an active boundary is evaluated. The best response to evaluate is the derivative of the transient response. In other words, instead of plotting the temperature change of a node, one plots the temperature change per unit time. This leads to a much clearer demonstration of the behavior of the model. The transient derivative response is also useful in correlating models to test data.

Two examples of this method are shown. First, the thermal response of a laser reference cavity that is insulated from the environment is shown in Figure 8. Thermal test data and the predicted data from a large model are plotted; in both cases the same boundary temperature was ramped. It is difficult, from this plot, to evaluate the changes that must be made to the model to correlate it with the test data. In Figure 9, however, the derivative of the transient response is shown. From this plot it is possible to evaluate the exact difference in time and magnitude shown by the transient behavior. The response time of the model lags the test by about 20 minutes (indicating thermal masses that are somewhat too high), and also predicts too low a magnitude for the maximum transient derivative (indicating that the conductances should be increased slightly).

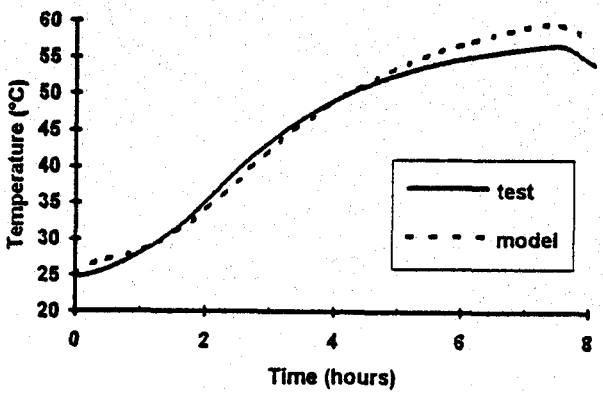

Figure 8. Comparison of Test and Prediction for Thermal Transient

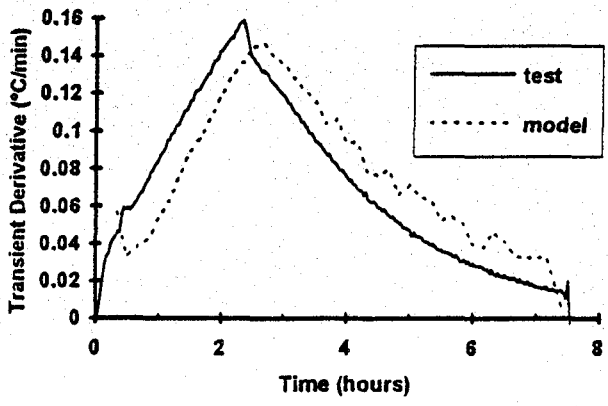

Figure 9. Comparison of Test and Prediction for Thermal Transient Derivative

The second example uses a model of a similar laser cavity placed on an optical bench within a spacecraft. The entire model contained about 3000 nodes. In order to perform an analysis of the noise frequencies of the cavity and their dependence on the orbital period, it was desired to reduce the model to five nodes while still accurately representing the cavity behavior. Nodes were chosen to represent the spacecraft, mounting plate, optical bench, cavity mount, and cavity. The spacecraft temperature was used as the forcing step function. The transient derivative was plotted for the full model, and for an approximate guess of the reduced model. By evaluating the differences, the reduced model predictions were brought into agreement with the full model predictions, as shown in Figure 10. The behavior of the cavity in the five node model could then be described with a single equation.

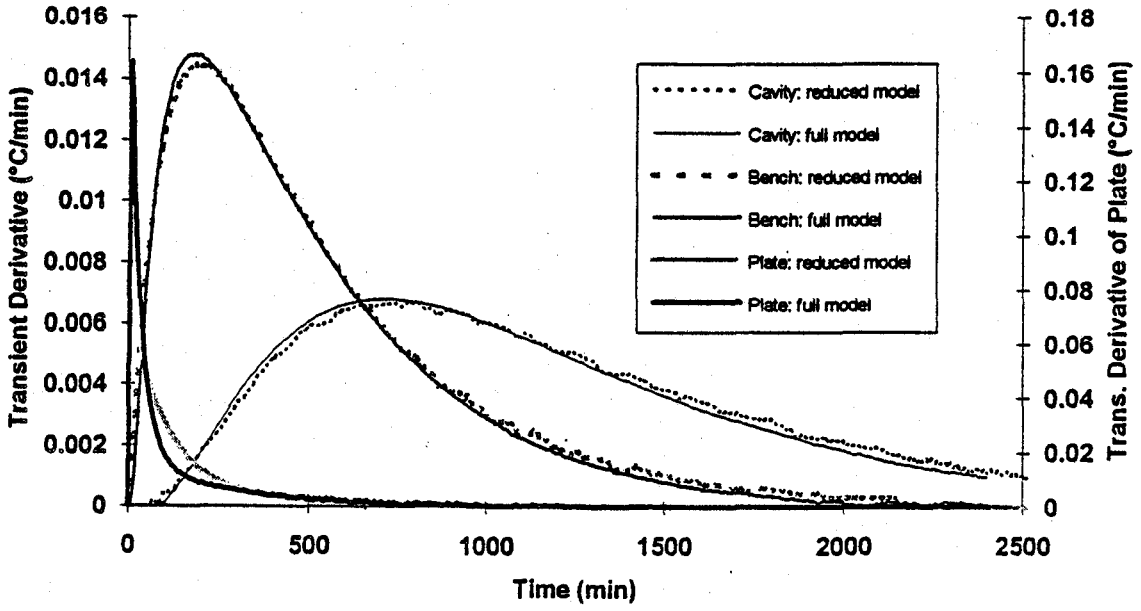

Figure 10. Comparison of Predicted Transient Derivative for Full and Reduced Models

LUNAR SURFACE RADIATION CALCULATIONS

A thermal model was developed for a lunar rover that was designed to be mobile on the surface of the moon. Solar flux radiation calculations in TRASYS had not been previously performed for a spacecraft on the surface of a planet (at least at LaRC). A subroutine in TRASYS called SURFP is available for this type of calculation[5]. In SURFP the user defines the planet, the position on the planet surface, the time of year, and any atmospheric extinction. Table 1 shows the actual code used in the operations data block, after calculation of the radiation conductors.

Table 1. TRASYS Subroutine SURFP Implementation

```
C    ORBITAL DEFINITION USING ROVER ON SURFACE OF PLANET
     CALL SURFP ('MOO',45.,0.,0.)              $ Define position
     CALL DICOMP (0,IZERO,IZERO)
     CALL AQDATA('ZERO','',1.,1.,1.,'')        $ Define format for printout
     AQPRNT='YES'
     CALL QODATA(0,100,'YES','',929.,3.1546E-4, 1., 'BOTH','')
STEP  10000                                    $ Start orbit
    TIMEPR = DAWN                              $ Define each orbit step
desired
L    DICAL
L    AQCAL
...step thru each orbit position...
STEP  10011
     TIMEPR = DUSK+12
L    DICAL
L    AQCAL
L    QOCAL                                     $ Print flux tables
```

A quirk to this subroutine is that only direct solar fluxes to the spacecraft surfaces are automatically computed. To compute infrared (IR) and planetary albedo fluxes, a ground plane with sufficient size and appropriate properties must be constructed to simulate the planet surface. The nodalization of this ground plane surface should be carefully evaluated to ensure it is not distorting the results.

The lunar rover model, plotted in TRAVIEW[6], is shown in Figure 11. The solar fluxes calculated by TRASYS were spot-checked with hand calculations to ensure that the subroutine was being operated correctly. The computed heat fluxes as a function of time over a lunar day cycle were used to calculate the temperatures of the rover over time. The temperature variation over parts of the rover during a lunar day is shown in Figure 12. The radiation calculations were performed for several different rover orientations and positions on the lunar surface.

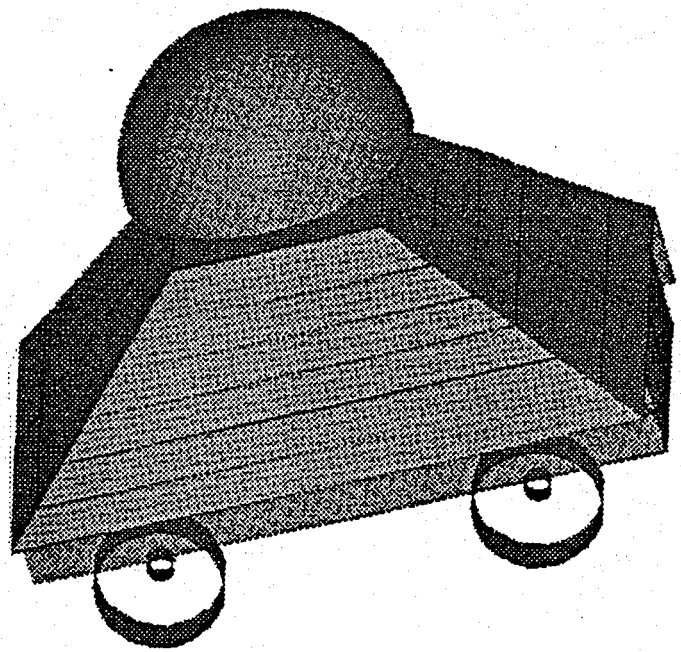

Figure 11. TRASYS Model of Lunar Rover

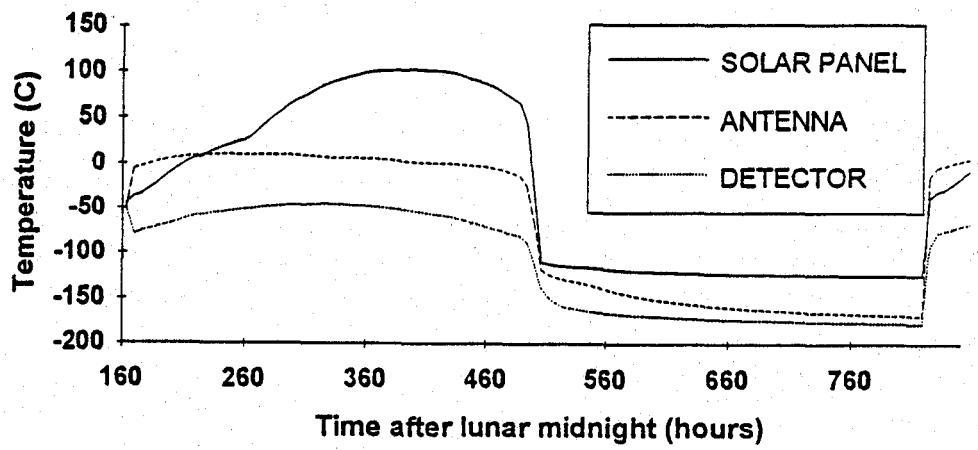

Figure 12. Temperature Variation on Selected Components over Lunar Day

SOLAR ARRAY POWER CALCULATIONS

The solar flux arrays generated by TRASYS were used for more than temperature calculations in SINDA. A key concern in the rover design was correct sizing of the solar arrays and batteries. Before the thermal model was developed, power output of the solar arrays was estimated roughly using a constant temperature for the array material, and approximations for solar flux on the rover geometry. With the combined TRASYS / SINDA model, the solar array power calculation could be done exactly. The solar heating array from TRASYS is included in the SINDA logic block[7]. Instantaneous incident power is calculated at each time step by interpolating the absorbed solar heating for each surface, multiplying by the area fraction that is effective solar array material, and dividing by the absorptivity. The photoelectric efficiency of the material is calculated in SINDA, based on the equation given by the material supplier for efficiency versus temperature, and using the current array temperature calculated by SINDA. The incident power times the efficiency of the array material then gives the total instantaneous power generated by the solar array. Since there were several arrays on the rover, it was necessary to calculate the temperature and power generation of each, and sum them.[7] An example plot of the instantaneous array power generated is shown in Figure 13. The code used to perform the calculations is shown in Table 2.

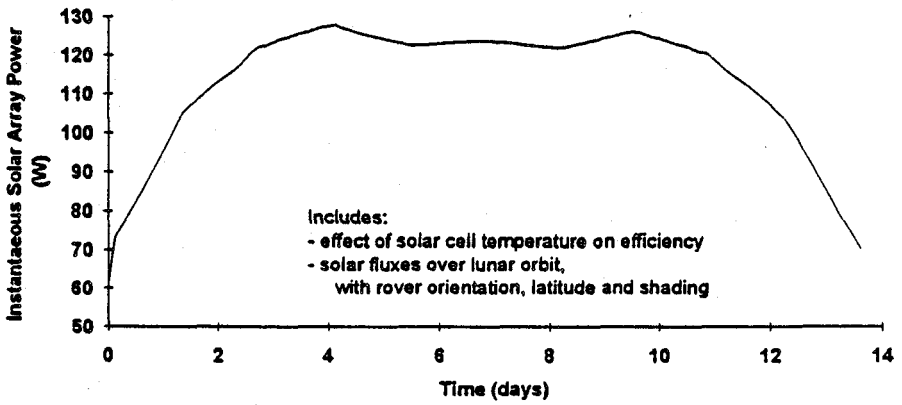

Figure 13. Solar Array Power Generation over Lunar Day for 75 degree Latitude

Table 2. Solar Array Power Calculations in SINDA Logic

```
HEADER ARRAY DATA, ROVER
C       TEMPERATURE DEPENDENCE OF SOLAR ARRAY POWER GENERATION
C       IN DEGREES C AND % (FRACTION) EFFICIENCY
        200 = 28., 0.18, 120., 0.143
...
HEADER OPERATIONS DATA
BUILD LUNAR, ROVER
C
C       OUTPUT FILE FOR SOLAR PANEL POWER GENERATION
F       OPEN (UNIT=27, STATUS='UNKNOWN', FILE='.../rover/solar.pl', RECL=400)
C       PRINT POWER LABELS TO PLOT FILE
        WRITE (27,22) 'TIME', '301 W', '401 W',...,'2501 W', 'TOT W', 'W/ RAD', 'CUM. W/R'
 22     FORMAT(15(A8,1H,),A9)
C
        WTEST = 0.                              $ Zero out total power numbers
...solution execution
        WRITE (27,78) WTEST                     $ Write total generated power at end of file
 78     FORMAT ('TOTAL POWER AVAILABLE IS ',F10.1,' WATT-HRS')
```

Table 2. Solar Array Power Calculations (con't)

```
HEADER OUTPUT CALLS,ROVER
C
C       CALCULATE POWER GENERATION IN SOLAR ARRAYS
C       Qgen  = Qin * 80% area / alpha              Q in already in W
C       Qreal = Qgen * % EFFICIENCY
C
        XK301 = Q301 * 0.80 / 0.88                  $ Power under perfect conditions
        CALL D1D1WM (T301, A200,  1., ETEST)        $ Performance factor (-%/C)
        XK301 = XK301 * ETEST                       $ Actual power generated
C
        XK401 = Q401 * 0.80 / 0.88                  $ Repeat for each array
        CALL D1D1WM (T401, A200,  1., ETEST)
        XK401 = XK401 * ETEST
...
C       CALCULATE TOTAL POWER AVAILABLE
        ATEST = XK301 + XK401 + XK501 + XK2301 + XK2401 + XK2501
        WTEST = OUTPUT * ATEST + WTEST              $ Total watt hours
C
C       PRINT POWERS TO FILE
        WRITE (27,25) TIMEN, XK301, XK401, ..., XK2501, ATEST, BTEST, WTEST
25      FORMAT (15(F8.2,1H,),2(F14.3,1H,),3(F9.3,1H,))
```

The power generation over time can be used to determine total energy available as well as charge of the on-board battery. The total energy available was calculated for different positions and orientations of the rover, to determine the effectiveness of the rover at different lunar positions. This information was used in planning nominal traverses for the rover.

THERMAL ANIMATION

Structural analysts commonly use animation in their presentation of results. Animation of mode shapes or predicted deflection patterns is a vivid method of capturing and conveying all the necessary information. This is done less often with thermal analysis, with the result that many viewers have a less concrete idea of the physical progression of temperatures or heat flows. A visual animation of the thermal map, in color, gives an effective representation of the physical transfer of heat.

Animation of transient thermal results, in combination with an integrated structural-thermal model, is a useful tool that has been utilized through PATRAN and its connection with SINDA. The temperatures of a part are mapped onto the geometry using a color scale. Color maps are generated for several sequential time steps, and the mappings are viewed in a sequence that is run repeatedly on the screen. The progression of temperatures along the part as a function of time is observed as an animated color thermal map. This function is valuable when evaluating the driving force behind a given reaction, and can also give an audience a much clearer understanding of the processes involved in a complex reaction. Cases can be recorded on video tape and used to demonstrate results to a larger audience. This function is also quite valuable to the analyst, as it provides a method for debugging the model and perhaps finding errors that would be time-consuming and tedious to find in any other way.

The specific method for performing this animation is to run SINDA with thermal output at all desired time steps. A virtual temperature (VTE) file must still exist from the PATSIN translation for the SINPAT translator to use in calculating nodal temperatures from element temperatures. Once SINPAT has created the nodal results files, the easiest way to set up an animation is to set up a PATRAN session file

that reads in all the frames. This avoids manual keying of three input lines per frame. The session file sets up the number of frames and the spectrum to be used. For each data frame, RUN, CONTOUR and RUN, HIDE commands are performed. The last line for the last frame must be typed in manually. After the last line is entered, the animation will begin running on the screen. The animation characteristics may be altered in real time using the animation menu. On 3-D workstations the part can be rotated on the screen during animation, so that thermal progressions on all sides of the part may be viewed.

CONCLUSIONS

The innovations that have been used here are useful to reduce modeling time and produce more accurate results. Model integration using a solid modeling package allows direct transfer of information between not only analysts, but designers as well. The technique of using the transient derivative for model reduction and correlation is beneficial in reducing the large solid-model-derived thermal analysis models, and in many other areas such as correlation to test data. The logic used in SINDA and TRASYS, while not unique, is a good example of the wide variety of output that results from the flexibility of incorporating user logic. Finally, the animation of thermal analysis results is a valuable tool for the analyst, and for aiding understanding when results are presented to a wider audience.

REFERENCES

[1]Crouthamel, M.: PAT/SINDA Interface Guide. PATRAN Division, PDA Engineering, March 1990.
[2]PDA Engineering: P/FEA Release 2.5 Notes, October 1990.
[3]PDA Engineering: PAT/MSC-NASTRAN Interface Guide, Release 3.0, January 1991.
[4]PDA Engineering: PATRAN Plus User Manual, Release 2.3, July 1988, p 22-25a.
[5]COSMIC: Thermal Radiation Analyzer System (TRASYS) User's Manual, Job Order 83-388, April 1988.
[6]Purcell, S.: TRAVIEW 3.0, A Model Rendering and Display Program, Hercules Aerospace.
[7]COSMIC: SINDA '85/FLUINT, Systems Improved Numerical Differencing Analyzer and Fluid Integrator, Version 2.3.

ANALYSIS OF HIGH VACUUM SYSTEMS USING SINDA'85

R. A. Spivey , Author
S. E. Clanton and J.D. Moore, Co-authors
Teledyne Brown Engineering, Huntsville, AL 35807

SUMMARY

This paper contains the theory, algorithms, and test data correlation analysis of a math model developed to predict performance of the Space Station Freedom Vacuum Exhaust System. The theory used to predict the flow characteristics of viscous, transition and molecular flow is presented in detail. Development of user subroutines which predict the flow characteristics in conjunction with the SINDA'85/FLUINT analysis software are discussed. The resistance-capacitance network approach with application to vacuum system analysis, is demonstrated and results from the model are correlated with test data.

The model was developed to predict the performance of the Space Station Freedom Vacuum Exhaust System. However, the unique use of the user subroutines developed in this model and written into the SINDA'85/FLUINT thermal analysis model, provides a powerful tool that can be used to predict the transient performance of vacuum systems and gas flow in tubes of virtually any geometry. This can be accomplished using a resistance-capacitance (R-C) method very similar to the methods used to perform thermal analyses.

NOMENCLATURE

A	cross-sectional area of tube in square centimeters
D	diameter of tube (I.D.) in centimeters
G	conductance in liters per second
L	length of tube in centimeters
M	molecular weight in kilograms per mole
P_1	upstream pressure in torr
P2	downstream pressure in torr
P_∞	vacuum pressure in torr
Q	throughput in torr-liters per second
T	temperature in Kelvin
f	friction factor
g	acceleration due to gravity
r	radius of tube in centimeters
γ	specific heat ratio
ρ	density
η	viscosity in poises
r	radius of tube in cm

Subscripts:

mol	molecular regime
trans	transitional regime
visc	viscous regime

INTRODUCTION

The model presented in this text was developed to predict the characteristics of gases as they flow through tubes or other system components. The model is capable of predicting the pressure and throughput of gases in the viscous, transition, and molecular flow regimes. In addition, the model is capable of incorporating a characteristic pump curve as a boundary condition. The model was developed to predict the performance of the Space Station Freedom Vacuum Exhaust System. However, the unique use of the user subroutines developed in this model and written into the SINDA'85/FLUINT thermal analysis model, provide a powerful tool that can be used to predict the transient performance of vacuum systems and gas flow in tubes of virtually any geometry

THEORY

As a gas flows through a tube or system component a pressure drop is experienced. The flow regime that occurs in a tube depends on the size of the tube, temperature of the gas, pressure in the pipe, and the type of gas. From Reference 1, molecular flow prevails at low gas densities where the mean free path or the average distance a molecule travels between successive intermolecular collisions is large compared to the tube cross section. As the mean free path shortens for higher pressure conditions, intermolecular collisions will predominate rather than collisions with the walls of the tube. Such a high density gas flow is called viscous or continuum flow. In this flow regime the velocity profile is nearly parabolic. The mathematical relationships used to describe viscous flow depend on whether it is laminar, turbulent, incompressible, compressible, or critical. A complex transition region exists between the molecular and viscous regimes. Transition flow occurs when the molecular mean free path is about equal to the dimensions of the pipe. At this point, the flow is partially viscous and partially molecular in character.

In space related vacuum systems, a vessel, usually at or above atmospheric pressure, will be allowed to vent through a series of manifolds, pipes and non-propulsive vents to the vacuum of space. The flow will therefore start out in the viscous flow regime and progress through the transition regime to the molecular regime. In the test case discussed later in this paper, a pump was used to evacuate a chamber from 760 Torr down to $1x10^{-4}$ Torr. The following sections will discuss the theory and equations used to characterize the viscous, transition, and molecular flow regimes in this exercise. In addition, the R-C network approach used to model the flow will be discussed.

In the R-C network approach, the fluid flow is divided into discrete sections called nodes. As gas passes through the section of pipe connecting the node centers, a resistance to the flow exists, so that between the points a pressure difference is seen. In fact, no net flow will take place if this pressure difference does not exist. By an analogy with an electrical circuit, we define a *conductance* between the two points such that the flow rate through the system is the product of the conductance and the pressure difference, i.e.,

$$Q=(P_1-P_2)G \qquad (2.1)$$

Where;

- Q = Mass flowrate or throughput from node 1 to node 2 (Torr-liters/sec)
- P1 = Pressure at the center of node 1 (Torr)
- P2 = Pressure at the center of node 2 (Torr)
- G = Conductance from the center of node 1 to the center of node 2 (liters/sec)

Assuming no leaking or accumulation of gas in the system, Q will remain constant for any given time at node 1 and node 2 in the system. The R-C network analogy applied to fluid problems will allow use of the thermal analysis code SINDA'85/FLUINT to solve for transient pressures and throughputs at discrete points which represent the vacuum system. The FWDBK solution routine which applies the "Crank-Nicholson" implicit forward/backward differencing method to the R-C network will be used to perform the required calculations. For further details on the "Crank-Nicholson" method the reader is directed to References 3 & 4.

Since the method developed here applies to a specific type of vacuum system and many characteristics of the flow are known, a number of simplifying assumptions can be made.

1) The flow is isothermal. Past experience in the design and testing of vacuum systems has shown that in piping practice the isothermal assumption is a valid assumption.
2) The gas behaves as an ideal gas. The gas in this case is air which is assumed to be an ideal gas. However, any other ideal gas could be modeled using the methods presented in this paper.
3) Steady Flow. There is no accumulation of gas in the system.
4) The friction factor is constant along the pipe. The piping used in this case was stainless steel. In most vacuum systems, the piping material will be high grade to prevent outgassing. This usually translates into a uniform friction factor.
5) The flow is compressible in the viscous regime (Mach number of greater than 0.3).
6) The flow is fully developed. The velocity profile is the same at any position along the tube length.

The equations illustrated in this paper were developed using these assumptions.

The viscous flow regime is defined as the state in which the main form of energy and momentum transfer of the gas molecules is due to intermolecular collisions. This state occurs for high density gases where the mean free path of the gas molecules is small compared to the physical dimensions of the tube walls. When molecules of the gas collide with each other they do not lose momentum. Only when they collide with the wall of the tube do they reduce their momentum. Therefore, the throughput Q, is expected to be highest in the viscous flow regime. Since the Space Station Freedom Vacuum Exhaust system is designed so that choking will occur at the exit (i.e. the non-propulsive vent valve), the compressibility effects of the gas will dominate the flow equations (see assumption 5).

The maximum velocity of a compressible fluid in a pipe is limited by the velocity at which a pressure wave may be propagated through the fluid medium. This velocity is the speed of sound in the fluid. If the flow is choked, the mass throughput no longer depends own the downstream pressure. Choked areas in the vent system will be identified by a comparison of the downstream and upstream pressure ratio (P_C). From Reference 5, the equation used to determine P_C is given by;

$$P_C = \frac{2}{(\gamma+1)}^{\frac{\gamma}{(\gamma-1)}} \qquad (2.2)$$

Locations in the vent system where the ratio of the downstream node pressure and the upstream node pressure is greater than P_C are considered unchoked. From Reference 5, compressible pipe flow equations used to determine conductance (G) and throughput (Q) for unchoked locations in the system are given by ;

$$G_{unchoked} = \left[\frac{\rho g A^2}{\frac{fL}{D} + 2\ln\left(\frac{P_1}{P_\infty}\right)} \right]^{\frac{1}{2}} \qquad (2.3)$$

$$Q_{unchoked} = G_{unchoked}(P_1 - P_2) \tag{2.4}$$

Locations in the vent system where the upstream and downstream node pressure are less than P_C are considered choked. Again from Reference 5, the conductance and throughput between two nodes in chocked flow is given by

$$G_{choked} = \frac{C_d A \sqrt{\gamma g \rho}}{\sqrt{P_1}} \left(\frac{P_1}{P_1 - P_\infty} \right) \tag{2.5}$$

$$Q_{choked} = G_{choked}(P_1 - P_2) \tag{2.6}$$

The Space Station Freedom Vacuum Exhaust System is designed to choke only at the non-propulsive vent (the exit) however, this method will allow the user to predict where choking may occur.

The transitional flow regime is characterized by both viscous and molecular flow properties. Transition flow occurs over a range of two or three decades of pressure where the molecule-to-wall collision pattern decreases and gives way to the intermolecular collision conditions which characterize viscous or continuum flow. Flow in the transition regime is not well understood but a great deal of experimental work has been done to investigate the region (see References 6, 7 & 8). An empirical expression given by Reference 1 describes the transition flow regime adequately as;

$$Q_{tran} = Q_{visc} + \left(\frac{1 + 0.828\left(\frac{r}{L}\right)^{\frac{1}{2}}}{1 + 1.11\left(\frac{r}{L}\right)^{\frac{1}{2}}} \right) \cdot Q_{mol} \tag{2.7}$$

where Q_{visc} and Q_{mol} are defined as,

$$Q_{visc} = \frac{\pi r^4}{12 \eta L} \left(P_1^2 - P_2^2 \right) \tag{2.8}$$

$$Q_{mol} = \left(\frac{8r}{3L\left[1 + \frac{1}{\left(3 + \frac{3L}{7r}\right)}\right]} \right) \cdot 11.43\, r^2 \left(\frac{T}{M}\right)^{\frac{1}{2}} (P_1 - P_2) \tag{2.9}$$

and the conductance equation is as follows,

$$G_{tran} = \frac{Q_{tran}}{(P_1 - P_2)} \tag{2.10}$$

Transition pressure is the pressure at which the flow departs *significantly* from the parabolic velocity profile that characterizes viscous flow. From Reference 2 the transitional pressure (P_t) is calculated from;

$$P_t = 95.7(T/M)^{1/2}(\eta/D)$$

Where;

P_t = Transition pressure.(Torr)
η = Viscosity of the Gas (Poissions)
T = Temperature of the gas (°K)
D = Diameter of the pipe (cm)
M = Molecular Weight (Kg/Kmole)

From Reference 2 the lower limit of the transition range is given by;

$$P_l = 0.114\ P_t \qquad (2.11)$$

Where;

P_l = Lower pressure limit of the transition regime (Torr)
P_t = Transition pressure (Torr).

This is the pressure where the flow goes from transition to molecular flow. The upper limit of the transition flow regime is given by;

$$P_u = 9.91\ P_t \qquad (2.12)$$

Where;

P_u = Upper pressure limit of the transition regime (Torr)
P_t = Transition pressure (Torr).

This is the pressure where the flow changes from viscous to transition flow.
Using these equations, we can determine when the flow is in the viscous, transition, or molecular flow regimes based on the pressure. With this information, we can calculate conductance and throughput with the correct formulation.

Molecular gas flow is defined by the state at which the mean free path of the gas molecules is very large compared to the dimensional parameters of the tube. Gas molecules move in random straight lines impinging on the tube walls where at impact the molecule is stopped and randomly remitted. Any molecule that strikes the tube wall loses directional momentum because equal probability exists for it to proceed upstream or downstream after impact. The probability of the molecule traveling in any direction depends mainly on a solid angle defined by the length of the tube (l) and the tube radius (r). According to Reference 1, the probability of a molecule passing through the tube without striking the tube wall is a function of the ratio l/r which defines an attenuation factor applicable to the directional energy incident of the tube. Reference 6 has shown that the attenuation factor equals (8/3)x(r/l) for long tubes of circular cross section. From Reference 1, the throughput is given by;

$$Q_{mol} = \left(\frac{8\,r}{3\,L\left[1 + \frac{1}{\left(3 + \frac{3\,L}{7\,r}\right)}\right]} \right) \cdot 11.43\ r^2 \left(\frac{T}{M}\right)^{\frac{1}{2}} (P_1 - P_2) \qquad (2.13)$$

and the conductance equation is as follows;

$$G_{mol} = \frac{G_{mol}}{(P_1 - P_2)} \qquad (2.14)$$

During a point in the transient depressurization process, the outgassing and leakage effects in the system will tend to dominate the throughput results in the molecular flow regime. This will cause the analytical results to trend toward a steady-state solution.

DETAILS OF THE SINDA'85/FLUINT MODEL

The SINDA'85/FLUINT model was developed to provide the analysts a tool to predict the performance of vacuum systems in an accurate and efficient manor. By applying the methods described in the theory section of this paper, the analysts can quickly evaluate proposed vacuum system designs and provide transient data to support any conclusions. The SINDA'85/FLUINT solver is a widely used code that was developed under government contract with the National Aeronautics and Space Administration (NASA) and is available through the Computer Software Management and Information Center (COSMIC) ,located at the University of Georgia, for a nominal fee. The model has the flexibility of predicting characteristics of flow through the viscous, transition, and molecular flow regimes. The model can simulate a blowdown to the space environment or a pumpdown using any pump for which an accurate pump curve exists.The flow block diagrams Shown in Figures one through four illustrate the logic used in the overall model and the major subroutines.

The model requires input from the analysts in several sections. The following paragraphs will identify specific parts of the SINDA'85/FLUINT model that require user input along with specific examples from the test model. The explanations will assume that the reader has some prior knowledge of the SINDA'85/FLUINT solver.

The first step to building any model is to divide the system to be modeled into discreet nodal segments connected by conductors. Figure 5 illustrates how the test setup was nodalized. The size of the nodes is dependent on the geometry and the locations where pressure and throughput data is required. For example, if a test set is to be analyzed, the analysts will want a node center at each location where pressure readings are to be made. In addition, points where diameter changes exists are candidates for node divisions. It should be noted, that runtime on the computer is proportional to the number of nodes present. In our test case, with smooth stainless steal piping, it was found that a course nodalization produced the same results as a fine nodalization.

As with all SINDA'85/FLUINT models, this is the section where the nodalization is defined. The following is the Header Node Data section from the test case model;

```
C ************************************************************************
HEADER NODE DATA,  VAC
C ************************************************************************
C
        1,           760.0,  250000.0      $ Tank
   GEN 2,  5,  1,    750.0,      -1.0      $ Line
   -9999,           760.0,      -1.0      $ Space
```

Of course, the normal SINDA'85/FLUINT designations for boundary nodes and arithmetic nodes is used. However, instead of an initial temperature in the second field, insert the initial pressure guess in Torr (example 760.0 Torr). In field 3, in place of the normal mass entry, insert the volume of the node segment in milliliters (example 250000.0 ml). In the test case all the volume

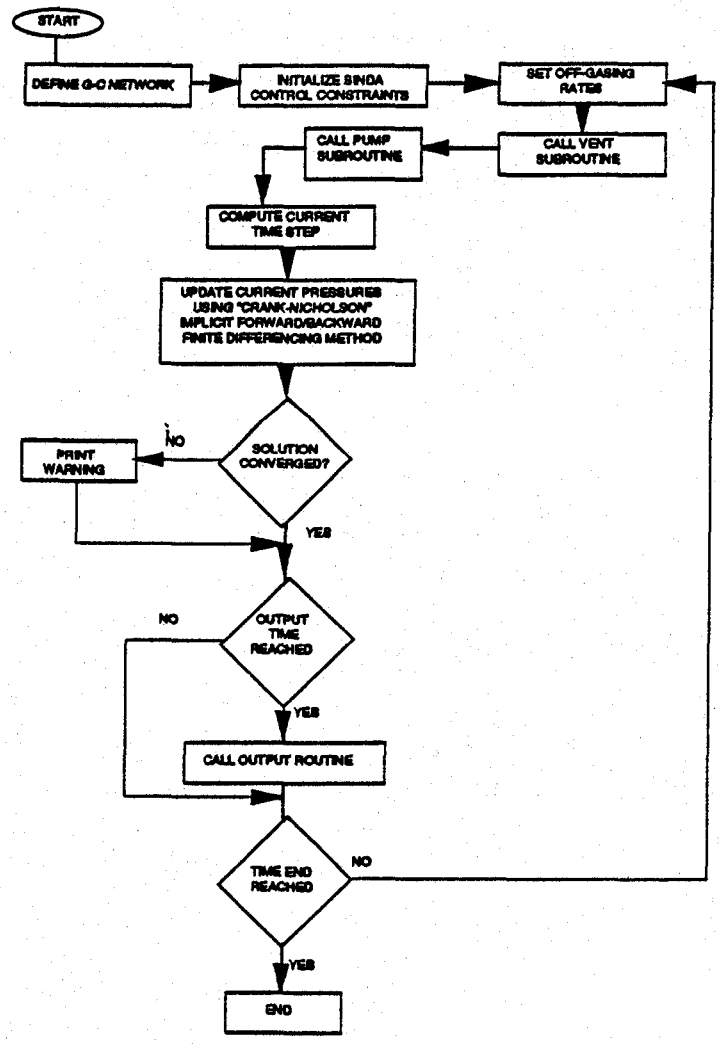

Figure 1. Model Overall Logic Flow Chart

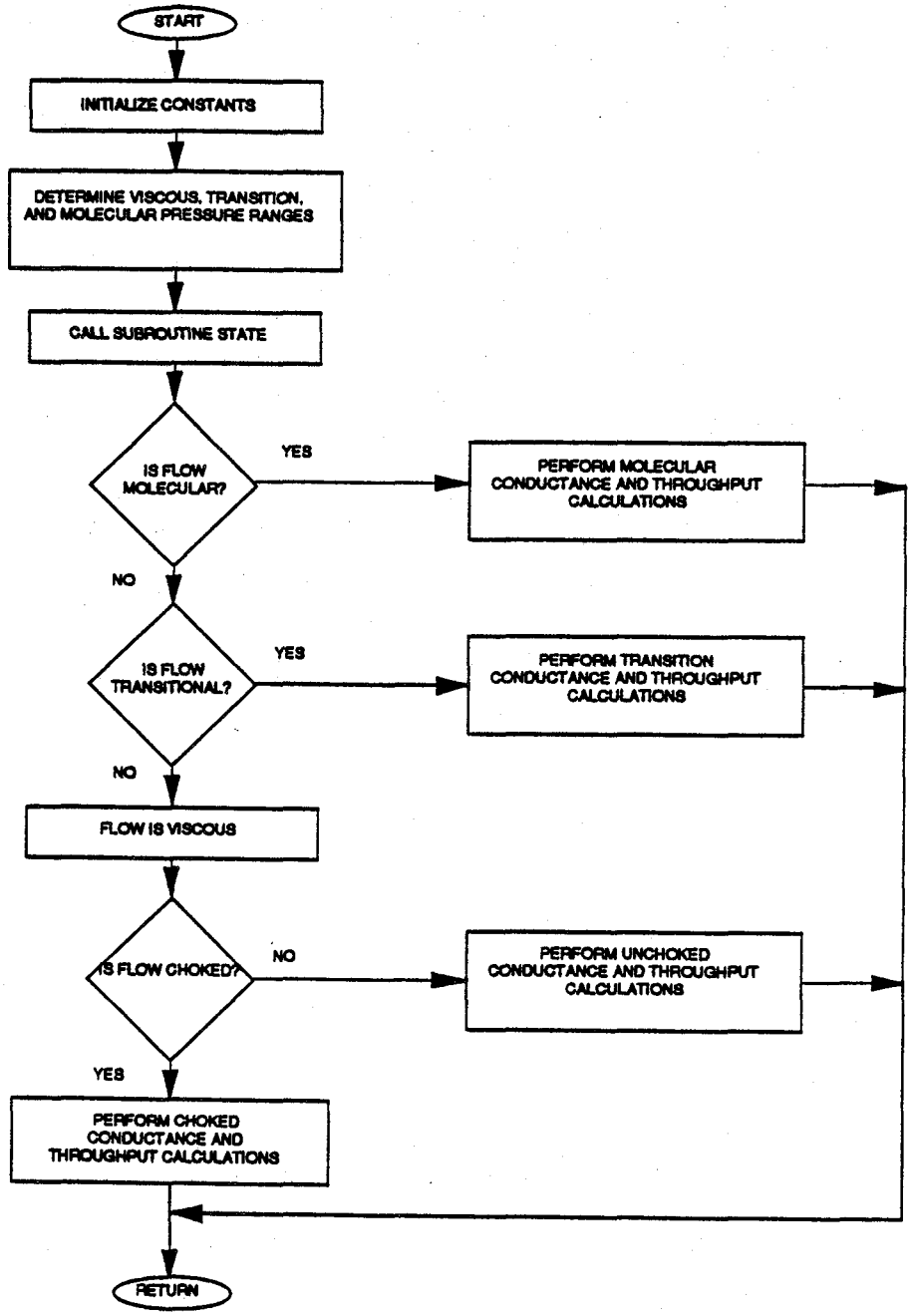

Figure 2. Vent Subroutine Logic Flow

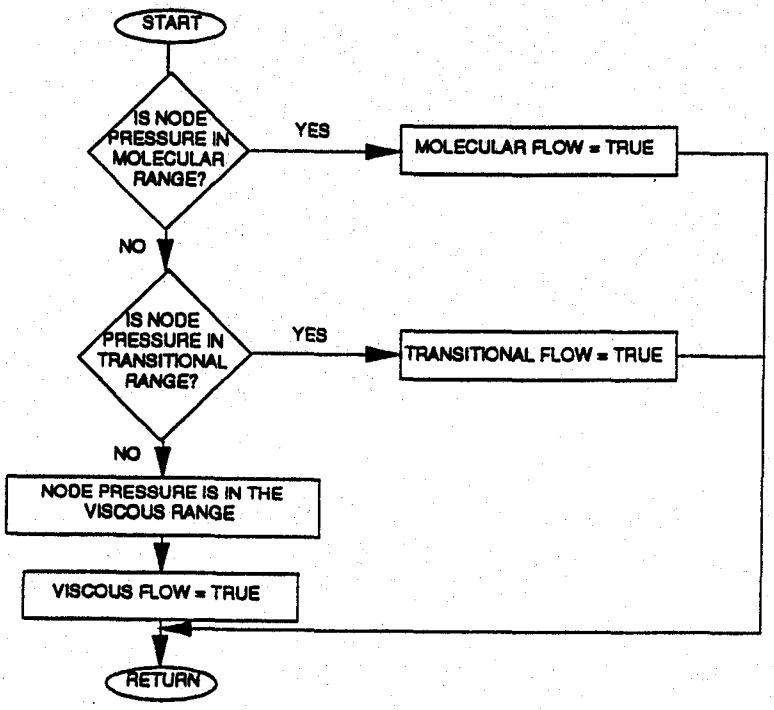

Figure 3. State Subroutine Logic Flow

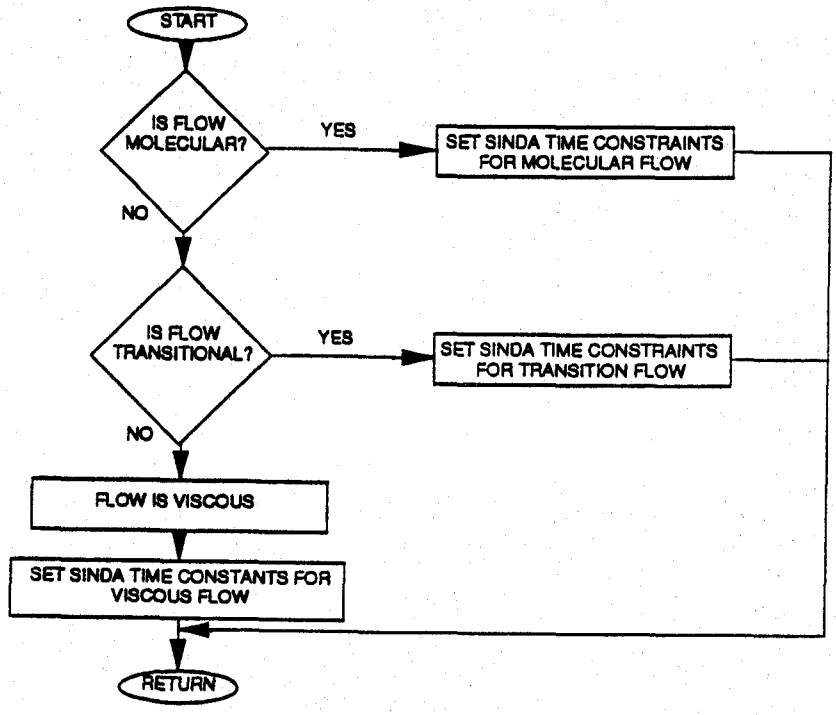

Figure 4. Timestep Subroutine Logic Flow

was lumped into the tank node, and the line nodes were modeled as arithmetic nodes. (See Reference 4 for further definition of an arithmetic node and the Header Node Data section.)

Again, as with all SINDA'85/FLUINT models, this is the section where the conductor designations are made. The following is the Conductor Data section from the test case model;

```
C ******************************************************************
HEADER CONDUCTOR DATA,  VAC
C ******************************************************************
C
C  Main Vent Line
       GEN 1, 5, 1, 1, 1, 2, 1, 1.0   $ Vent Line Conductors
           6,       6, 9999,    1.0   $ G B/t Vent Valve And Space
```

Since the actual conductor values are calculated by the user subroutines developed in this exercise, this section serves mainly to generate and designate the conductors between the nodes defined in the Header Node Data section. Again, the normal rules for developing SINDA'85/FLUINT models is followed in this section. (See Reference 4 for further details concerning SINDA'85/FLUINT models.)

The Header Control Data section of any SINDA'85/FLUINT model is the section where convergence is controlled. Therefore, this is a very important section of the model, especially since the pressure differences in the molecular region can be as small as $1x10^{-6}$ Torr. Therefore, the tolerances must be very tight or the numerical solution will converge to quickly yielding incorrect results. On the other hand, if the tolerances are set to tight, the solution will require several loops and a large amount of computer time to converge. The control data section of the test case model is as follows;

```
C ******************************************************************
Header Control Data,  Global
C ******************************************************************
C
C     Time in Minutes
      ARLXCA  =  1.E-6
      DRLXCA  =  1.E-6
      TIMEO   =  0.0
      TIMEND  =  200.0
      OUTPUT  =  0.01667
      NLOOPT  =  500
      UID     =  SI
      PATMOS  =  0.00
      ABSZRO  =  0.0
```

As with all SINDA'85/FLUINT models, ARLXCA defines the relaxation criteria for the arithmetic nodes defined in the Header Node Data section. In the same way, DRLXCA defines the relaxation criteria for the diffusion nodes defined in the Header Node Data. It should be noted that ARLXCA and DRLXCA are set equal to $1x10^{-6}$ Torr. Since the test case yielded tank pressures of $1x10^{-4}$ Torr, two orders of magnitude lower than the lowest expected pressure is a good first guess. It is not uncommon for it to require 50 to 100 loops for the solution to converge. Therefore, NLOOPT should be set to 200 to 500 loops. In addition, ABSZRO is used in thermal models to tell SINDA that the model requires the absolute temperature scale. Since we are working in an absolute pressure scale and the pressures should never be less than zero, ABSZRO should be set to 0.00 . UID, PATMOS, TIMEO, and TIMEND have the same meaning as in any other SINDA'85/FLUINT model. (See Reference 4 for further details concerning SINDA'85/FLUINT models.)

The HEADER USER DATA, Sbn section of the model is used to initialize the flow through each node so that the model does not fail on the first loop when the flow is just getting started. The flow should be initialized at a very low value but some value greater than zero. From the test case the Header User Data section is as follows;

```
C ************************************************************************
Header User Data,  VAC
C ************************************************************************
C
C  Initialize Nodal Throughput Values
             1 = 0.0001
             2 = 0.0001
             3 = 0.0001
             4 = 0.0001
             5 = 0.0001
             6 = 0.0001
C
```

Note that each node except the boundary node must be initialized.

The Header Variables 1 section of the Vacuum System Analysis Model is the most important. In this section, outgassing rates are defined, the vent subroutines are called, the pump subroutine is called, and the timestep subroutine is called. A detailed explanation of each of these subroutines is included in this paper. The Variables 1 section of the test case is as follows;

```
C ************************************************************************
Header Variables1, VAC
C ************************************************************************
C
C   Outgassing Rates For Tubes, Pumps, Flexlines
          Q1 = 2.358E-1
          Q2 = 7.688E-1
          Q3 = 7.688E-1
          Q4 = 1.24E-1
          Q5 = 2.00E-2
          Q6 = 2.00E-2
C
C   CALL STATEMENT FOR SUBROUTINE - VENT(G, TI, TJ, MDOT, DIA, L)
C   DETERMINES IF THE FLOW IS IN THE TRANSITION PRESSURE RANGE AND       C
CALCULATES A CONDUCTANCE (G), AND MDOT.
C
C   G - CONDUCTANCE (mL/MIN)
C   TI - DOWNSTREAM PRESSURE (TORR)
C   TJ - UPSTREAM PRESSURE (TORR)
C   MDOT - MASS FLOWRATE (KG/MIN)
C   DIA - DIAMETER (CM)
C   L - LENGTH (CM)
C
M       CALL MEPUMP(T9999, TIMEN,DTIMEU)
M       CALL VENT(G1, T1, T2, XK1, 3.81,327.66,ITEST)
M       CALL VENT(G2, T2, T3, XK2, 9.76,523.875 ,ITEST)
M       CALL VENT(G3, T3, T4, XK3, 9.76,1047.75,ITEST)
M       CALL VENT(G4, T4, T5, XK4, 9.76,287.6 ,ITEST)
M       CALL VENT(G5, T5, T6, XK5, 9.76,77.3,ITEST)
M       CALL VENT(G6, T6, T9999, XK6, 3.81, 50.,ITEST)
M       CALL TIMESTEP(T1, 4.76, DTIMEH, OUTPUT)
C
F       ITEST = ITEST + 1
C
```

Outgassing is defined as the release of gases or vapor absorbed by a material. Outgassing rates are a characteristic of the piping material. In the test case the material was stainless steal with an outgassing rate of $1x10^{-9}$ Torr-liters/sec-cm^2. Therefore, to calculate the outgassing rate for a single node the surface area represented by the node is multiplied by the outgassing rate of the pipe material.

The first subroutine called is the MEPUMP subroutine which is used in the test case to determine the pressure of the pump based on the pump curve. The user must make sure that the node representing the pump (in this case 9999) is included with a preceding T as the first entry in the MEPUMP call statement.

Each conductor defined in the Header Conductor Data section must have a corresponding call statement as follows;

```
M       CALL VENT(Gn, Tn1, Tn2, XKn1, D,L ,ITEST)
```

Where;

- Gn1 = Number designation of the conductor to be calculated
- Tn1 = Node number of the first node in the conductor
- Tn2 = Node number of the second node in the conductor
- XKn1 = Designation for the throughput at the first node in the conductor
- D = Diameter of the pipe between the node centers (cm)
- L = Distance between the node centers (cm)
- ITEST= Dummy variable that flags the first timestep.

In order to aid in convergence and reduce the required computation time, the time step is different for each flow regime. The timestep should be smallest in the viscous flow regime, larger in the transition regime and largest in the molecular flow regime. In order to insure that the best time step is chosen for the solution, the user should choose the node most distant from the space node or pump boundary to base the time step calculation. In the call statement;

```
M       CALL TIMESTEP(T1, 4.76, DTIMEH, OUTPUT)
```

The user must enter the number of the node on which the time step is to be based preceded by a "T" (T1 in this case) and the diameter of the tank or pipe that the node represents (4.76cm in this case) in centimeters.

The Header Subroutine Data section of the model is the section that was written to provide SINDA'85/FLUINT with the ability to model vacuum systems. Therefore these subroutines are the heart of the model. The user does not have to provide any input into the TIMESTEP subroutine. However, the MEPUMP & VENT subroutines require the user to input a representation of the pump curve and material constants of the gas.

The vent subroutine is a FORTRAN code that uses the equations discussed in the theory section of this document to calculate the conductance between the two nodes in the call statement The calculations for the conductance are based on the pressure results from the previous time step. The first portion of the routine initializes the material properties of the gas. In the test model the gas was air and the vent subroutine is as follows;

```
C
F       SUBROUTINE VENT(G, TI, TJ, MDOT, D, L, ITEST)
C
FSTART
C
C       THIS SUBROUTINES DETERMINES THE CONDUCTANCE (G) AND MDOT OF THE FLOW
C       UNITS:  G(mL/MIN), TI(TORR), TJ(TORR), MDOT(KG/MIN), D(CM), L(CM)
C
C  DECLARE REAL AND LOGICAL VARIABLES
```

```
      REAL G,TI,TJ,MDOT,D,L,RBAR,MBAR,PI,T,VISC
      REAL AC,LC,F,GRAV,GAM,RA,LP,Z,K,COM,QM,QV,QT
C     REAL K1,K2
C
C
C  INITIALIZE CONSTANTS AND SET AIR PROPERTIES:
C  MBAR(MOL.WT KG/KMOLE),RBAR(UNIV.GAS CONST.(KN-CM/KMOL-K),
C  T(TEMP K),VISC(POSSIONS),AC(THROAT AREA M^2), DENS(KG/M^3)
      MBAR = 28.97
      RBAR = 83.144
      T = 300.0
      VISC = 1.85E-4
      GAM = 1.4
      PI = 3.141592654
      GRAV = 32.2
      DELTAP=TI-TJ
      IF (DELTAP .LE. 0.0) DELTAP = 0.001
C
```

If the vent system is being modeled using a fluid other than air `MBAR, VISC, T & GAM` must be replaced with the appropriate constants. These constants are defined as;

`MBAR`	=	Molecular weight of the gas (Kg/Kmole)
`T`	=	Average temperature of the gas (°K)
`VISC`	=	Viscosity of the gas (Poissions)
`GAM`	=	Ratio of specific heats for the gas

In some cases, the user may want to adjust the time steps used to calculate the transient pressure solution. Since each subroutine stands alone in SINDA'85/FLUINT and variables must be specifically called out in the call statement, the values of `MBAR, VISC,` and `T` must be entered into the `TIMESTEP` subroutine also. The subroutine that controls the timestep is as follows;

```
************************************************************************
F     SUBROUTINE TIMESTEP(TI, D, DTIMEH, OUTPUT)
C
FSTART
C
C  THIS SUBROUTINE DETERMINES THE TIMESTEP IN MINUTES
C  BASED ON THE TANK PRESSURE
C
      MBAR = 28.97
      T = 300.0
      VISC = 1.85E-4
C
C  DETERMINE PRESSURE RANGES
      PT = 95.7 * SQRT(T/MBAR) * (VISC/D)
      PU = 9.91 * PT
      PL = 0.114 * PT
C
C  DETERMINE THE FLOW STATE;  MOLECULAR, TRANSITIONAL, OR VISCOUS
      CALL STATE(PU,PL,TI,IPMOL,IPTRN,IPVISC)
      IF (IPMOL .GT. 1) THEN
        DTIMEH=1.0
        OUTPUT=1.0
      ENDIF
      IF (IPTRN .GT. 1) THEN
        DTIMEH=0.9
```

```
         OUTPUT=0.9
      ENDIF
      IF (IPVISC .GT. 1) THEN
         DTIMEH=0.09
         OUTPUT=0.09
      ENDIF
C
      RETURN
      END
C
FSTOP
C ***************************************************************************
```

The user may also wish to change the timestep for the problem solution. The timestep can be changed by changing the DTIMEH and OUTPUT statements above.

The MEPUMP subroutine was included so the model could analyze a pumpdown rather than a blowdown. The pump curve for the pump used in the pumpdown must be included in the MEPUMP subroutine. The MEPUMP subroutine for the test case is as follows;

```
F       SUBROUTINE MEPUMP(TI,TIMEN,DTIMEU)
C
FSTART
C
      IF(TI .LT. 1.E-4) TI=1.E-4
C
      IF((TI .LT. 11.5).AND.(TI .GT. 1.E-4)) THEN
         TIOLD=11.5
         DT3=DT3+DTIMEU
         G = 7.7362 - 6.4009*ALOG10(TI)
         G = G *1000.*60.
         TI = TIOLD/EXP((G*DT3/350000.))
       ENDIF
C
C
      IF ((TI .GE.11.5) .AND.(TI .LT. 52.5)) THEN
         PMPSP=1.5815
         TIOLD=52.5
         DT1=DT1+DTIMEU
         G=PMPSP*1000.*60.
         TI=TIOLD/EXP(G*DT1/350000.)
         DT3=0.0
       ENDIF
      IF ((TI .GE.52.5).AND.(TI .LT. 272.5)) THEN
         PMPSP=0.7624
         TIOLD=272.5
         DT2=DT2+DTIMEU
         G=PMPSP*1000.*60.
         TI=TIOLD/EXP(G*DT2/350000.)
         DT1=0.0
       ENDIF
      IF (TI .GE.272.5) THEN
         PMPSP=.4274
         TIOLD=755.
         G=PMPSP*1000.*60.
         TI=TIOLD/EXP(G*TIMEN/350000.)
         DT2=0.0
       ENDIF
```

In the test case, the pump was a pump package that was made up of four individual pumps. Note that the quantity that is calculated in this subroutine is the pressure of the boundary node. In most cases, the pump curve supplied by the pump vendor will be in the form of a G vs P curve. Santeler (Reference 1) develops a method of calculating a pressure vs time curve from this data which is as follows;

$$P=P_0\exp(-Gt/V) \qquad (3.1)$$

Where;

P	= New pump pressure (Torr)
P_0	= Pump pressure at previous timestep
G	= Conductance from the pump curve (G vs P) @ P_0
t	= Timestep (min)
V	= System volume

The MEPUMP subroutine used in the test case is discussed further in the next section of this paper.

TEST CASE

The test case was conducted to validate the assumptions, methods, and algorithms described in this paper. The test involved modeling a vacuum test that had two different size pipes, flex lines,valves, and a pump package. The addition of the pump package complicated the modeling because the vendor data was not complete and the pump package contained 4 different pumps that became effective at different pressure ranges.

The layout of the test setup is shown in Figure 5 . The test fixture consisted of a 250 liter chamber connected to the VES1 header (9.78cm I.D.x101.60cm) by a 3.81cm I.D. x 91.44 cm branch line (similar to the line used to attach Space Station payloads to the Vacuum Exhaust System). Also included in the test setup was a pump package connected to the VES1 header by a 3.81cm I.D. X 91.44 cm branch line. The object of the test was to pump the vacuum chamber from atmospheric conditions (760 Torr) down to $1x10^{-4}$ Torr. The tank was filled with air and the VES1 header was made of stainless steal. The pump was a Trybodyne pump package that is made up of four pumps. Data collection consisted of vacuum pressure measurements recorded at the vacuum chamber. Bourdon , cold cathode, and Pirani gauges were use to measure pressure from 760 torr to 10^{-7} torr. Cold cathode gauges were the inverted magnetron design with a pressure range of 10^{-2} to 10^{-11} torr. Pirani gauges measured pressure from 200 torr to 10^{-4} torr. The bourdon gauge measured pressure from 30 psig to 0 mm Hg. The entire system was leak checked with a helium leak detector to 10^{-8} tl/s sensitivity with no measurable leaks indicated. Residual gas analysis was performed to qualify any contamination in the system. Pressure measurements were recorded manually from the gauge controller display and electronically from the gauge controller analog signal. Electronic data recording converted the raw analog signal to pressure units using a curve fit algorithm provided by the manufacturer. Data stored in the computer were then converted to Microsoft Excel and Cricket Graph format for reporting and graphics purposes.

As discussed in above, the pump package presented a modeling challenge due to the design of the Trybodyne pump. This particular model pump consists of 4 pumps in series that are effective at different pressure levels. The pump curve is shown in Figure 6. From Figure 6 we see as the pressure approaches 0 the pump curve goes to infinity and above 11.5 Torr the pump data was found to be inaccurate in previous testing.

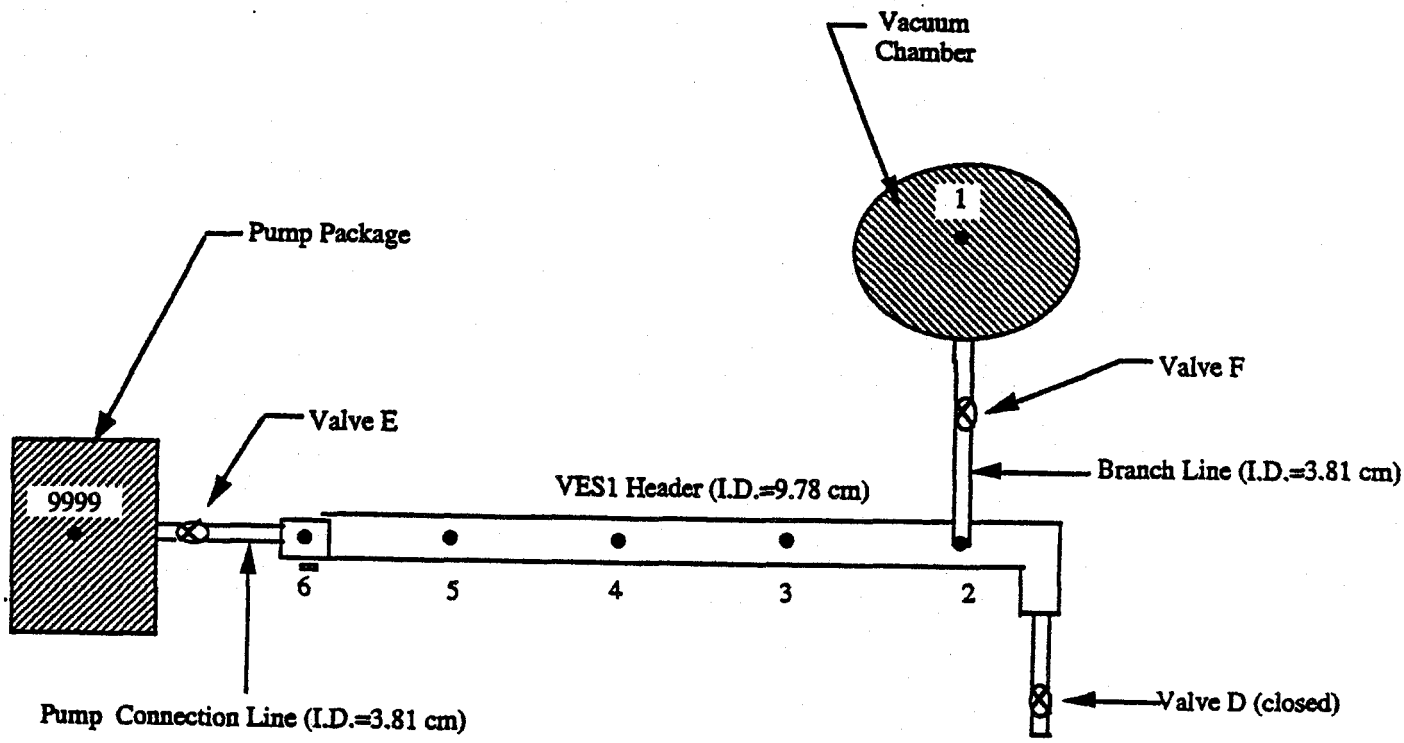

Figure 5. Vacuum Vent Test System Schematic

When the test was performed, it was found that the pump did not provide a pressure of less than $1x10^{-4}$ Torr. In order to model the pump in the pressure range of 760 Torr down to 11.5 Torr, the conductance was assumed to be step wise linear. With this assumption, the pump speed was calculated using equation 3.1 and pump test data. The steps over which the pump conductance was calculated were as follows;

760 Torr to 272.5 Torr
pump speed = 0.4274 l/sec

272.5 Torr to 52.5 Torr
pump speed = 0.7624 l/sec

52.5 Torr to 11.5 Torr
pump speed = 1.5812 l/sec

After the pressure of the system dropped below 11.5 Torr, the pump curve shown in Figure 6 was used to predict the conductance of the pump. It should be noted that, in a blowdown or a pumpdown, the boundary is the driver for the system and any error associated with the pump curve will translate into an error in the analysis. Therefore, it is very important to have accurate data concerning the pump performance when doing this type of analysis. The method used here to model the pump was expected to induce some error into the analysis in the pressure range from 760 Torr to 10 Torr. Greater accuracy might have been achieved if the pressure range had been divided into more steps.

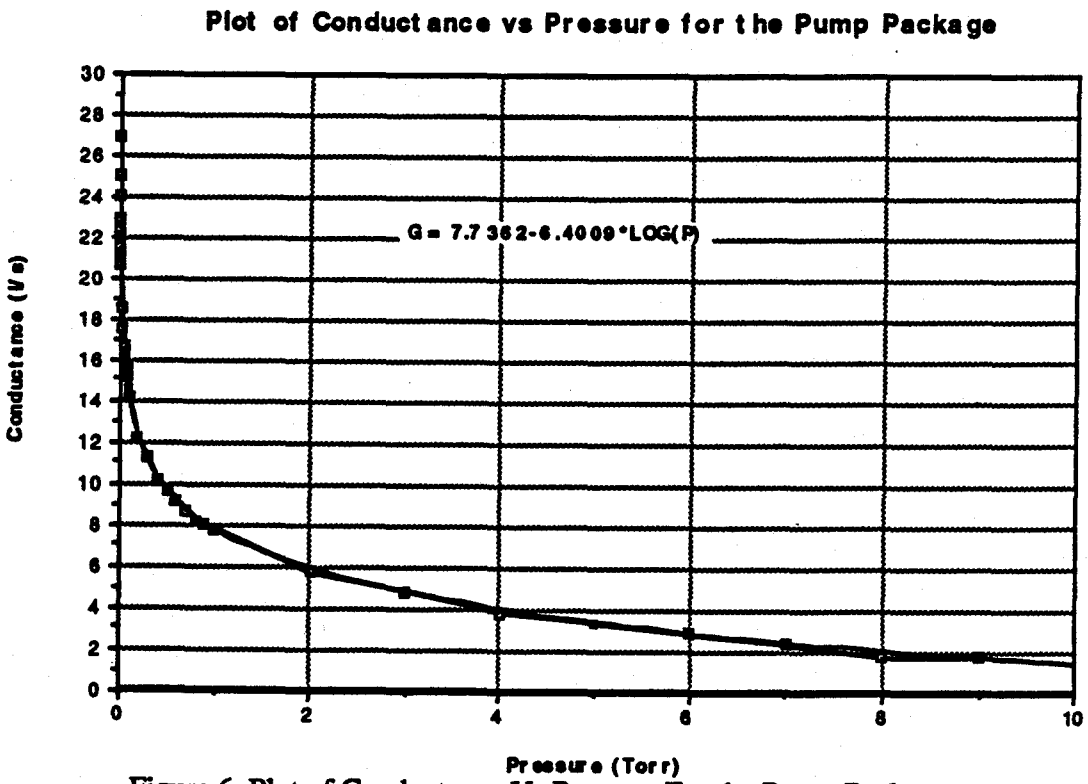

Figure 6. Plot of Conductance Vs Pressure For the Pump Package.

RESULTS AND CONCLUSIONS

Figure 7 shows the correlation between the test data and analytical results. The flow remained in the viscous regime for 33.5 minutes and was in transition for 12 minutes before molecular flow began. Results from the analytical model predicted that the tank pressure would reach steady state at 1.095×10^{-4} Torr. Test results indicate that the tank pressure would reach steady state at 1.06×10^{-4} Torr, yielding an error of 3.3 %. In addition, the trend of the results compares favorably with the test data. The largest deviation was found to be approximately 10 minutes occurring at a pressure of 20 torr. This can be attributed to the assumption of a constant pump speed in this pressure range. A review of the actual test data has shown that speed inflections did occur in this pressure range for the pump.

The results of the correlations support the validity of vacuum flow analysis using numerical solution methods. Any deviations between the test and analysis is largely due to insufficient pump data. The pump in this case was the controlling factor and any discrepancies in pump modeling would have a direct impact on the results. In situations where the evacuation process is due to a blowdown, the analytical results should show greater accuracy. This is because, in a blowdown process the boundary node would remain at a constant pressure and not be based on a pressure vs time dependency such as a pump.

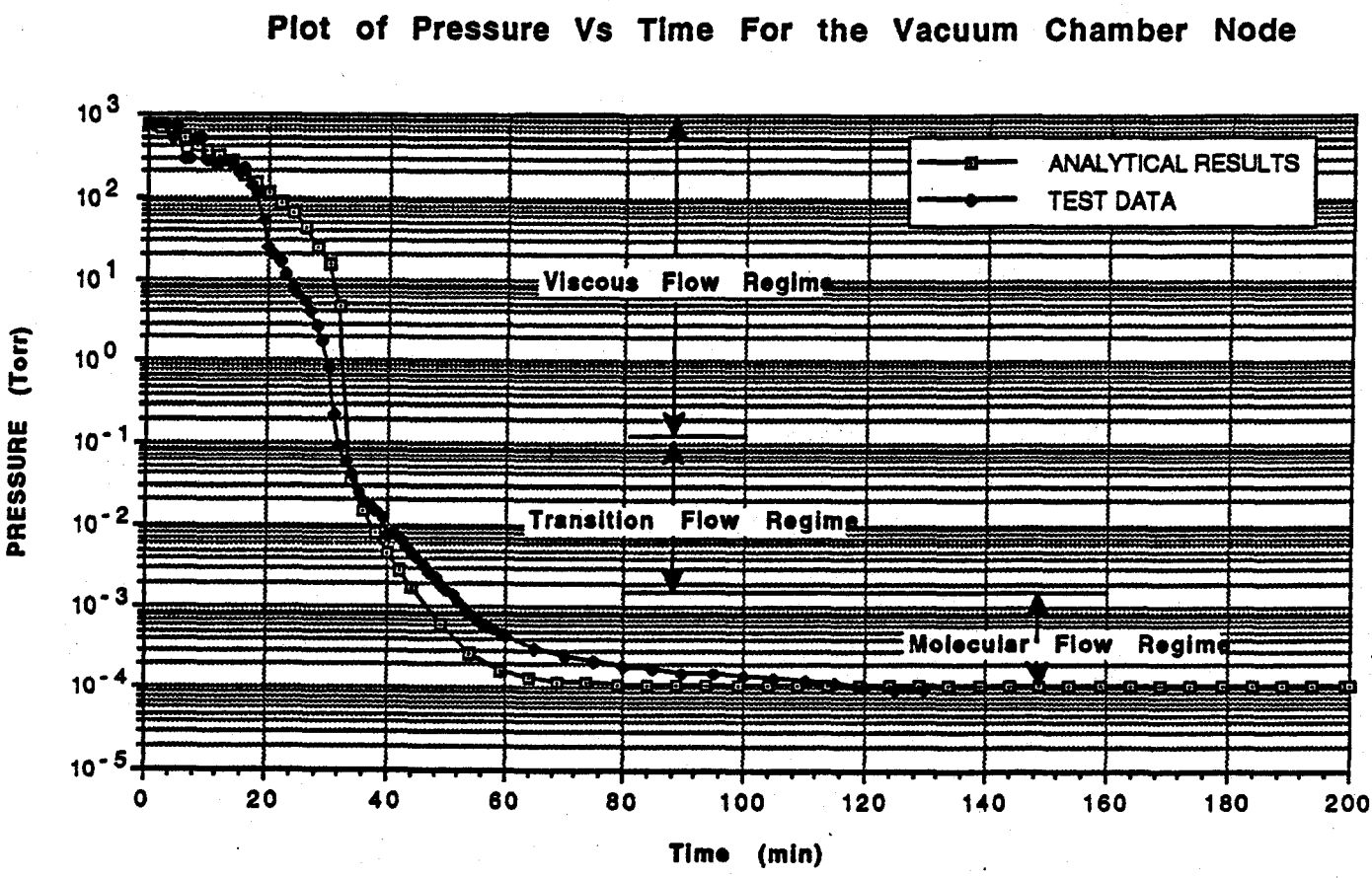

Figure 7. Plot of Analytical Results and Test Results

REFERENCES

1.0 Santeler, Holkeboer, Jones, and Pagano, 1966. Vacuum Technology and Space Simulation. (Prepared for NASA under contract NASw-680), Document No. N66-36129,

2.0 Van Atta, C.M., 1965, Vacuum Science and Engineering, New York; McGraw-Hill Book Company

3.0 Jaluria, Yogesh & Torrance, Kenneth E., 1986, Computational Heat Transfer, New York: Hemisphere Publishing Corporation.

4.0 SINDA User's Manual; Network Analysis Assoc., Inc., 1987.

5.0 Owen, James W.: Thermal Analysis Workbook, NASA (MSFC) and Sverdrup Technologies, Inc. (MSFC Group), Vol I.

6.0 Dushman, S.: Scientific Foundations of Vacuum Techniques. Second ed.. J.M. Lafferty, ed., John Wiley & Sons, Inc. 1962

7.0 Kennard, E. H. 1938, Kinetic Theory of Gases With an Introduction to Statistical Mechanics. First ed., McGraw-Hill Book Co., Inc.

8.0 Dong, Walter; and Bromley, L.A. : "Vacuum Flow of Gases Through Channels With Circular, Annula, and Rectangular Cross Sections". Transactions of the Eighth National Vacuum Symposium and the Second International Congress on Vacuum Science and Technology, vol II. I., E. Preuss, ed., Pergamon Press, 1962, pp. 1116-1132

9.0 Wutz, Adam, and Walcher, 1989, Theory and Practice of Vacuum Technology, Braunschweig/Weisbaden, FRG: Friedr. Vieweg & Sohn,

FEATURES OF A SINDA/FLUINT MODEL OF A LIQUID OXYGEN SUPPLY LINE

Boris G. Simmonds
Sverdrup Technology, Inc.
MSFC Group
Huntsville, Alabama 35806

TOPICS

1. OBJECTIVES

This paper describes the modeling features used in a steady-state heat transfer problem using SINDA/FLUINT. The problem modeled is a 125 feet long, 3 inch diameter pipe, filled with liquid Oxygen flow driven by a given pressure gradient. The pipe is fully insulated in five sections. Three sections of 1 inch thick spray-on foam and two sections of vacuum jacket.

The model evaluates friction, turns losses and convection heat transfer between the fluid and the pipe wall. There is conduction through the foam insulation with temperature dependent thermal conductivity. The vacuum space is model with radiation and gas molecular conduction, if present, in the annular gap. Heat is transferred between the outer surface and surrounding ambient by natural convection and radiation; and, by axial conduction along the pipe and through the vacuum jacket spacers and welded seal flanges.

The model makes extensive use of SINDA/FLUINT basic capabilities such as the GEN option for nodes an conductors (to generates groups of nodes or conductors), the SIV option (to generate single, temperature varying conductors), the SIM option (for multiple, temperature varying conductors) and the M HX macros for fluids (to generate strings of lumps, paths and ties representing a diabatic duct). It calls subroutine CONTRN (returns the relative location in the G-array of a network conductor, given an actual conductor number) enabling an extensive manipulation of conductor (calculation an assignment of their values) with DO loops.

Models like this illustrate to the new an even to the old SINDA/FLUINT user, features of the program that are not so obvious or known, and that are extremely handy when trying to take advantage of both, the automation of the DATA headers and make surgical modifications to specific parameters of the thermal or fluid elements in the OPERATIONS portion of the model.

1. OBJECTIVES (CONT)

1. SHARE SINDA/FLUINT EXPERIENCES WITH OTHER CODE USERS AT TFAWS
2. APPLY TO PRACTICAL PROBLEMS IN THE ENGINEERING FIELD
3. ESTABLISH AN INDUSTRY SOURCE OF TRICKS AND SHORT CUTS FOR USERS OF SINDA/FLUINT
4. ADDRESS SPECIALIZED TECHNIQUES NOT COVERED OR NOT SO OBVIOUS IN THE MANUAL
5. PROVIDE FEEDBACK TO CODE DEVELOPER FOR FUTURE IMPROVEMENTS

2. WHICH SINDA

1. SINDA/FLUINT VERSION 2.5

SYSTEMS IMPROVED NUMERICAL DIFFERENCING ANALYZER AND FLUID INTEGRATOR, VERSION 2.5 DEVELOPED BY MARTIN MARIETTA ASTRONAUTICS GROUP, DENVER, COLORADO UNDER CONTRACT NAS9-18411.

2. PRESENTATION FORMAT:

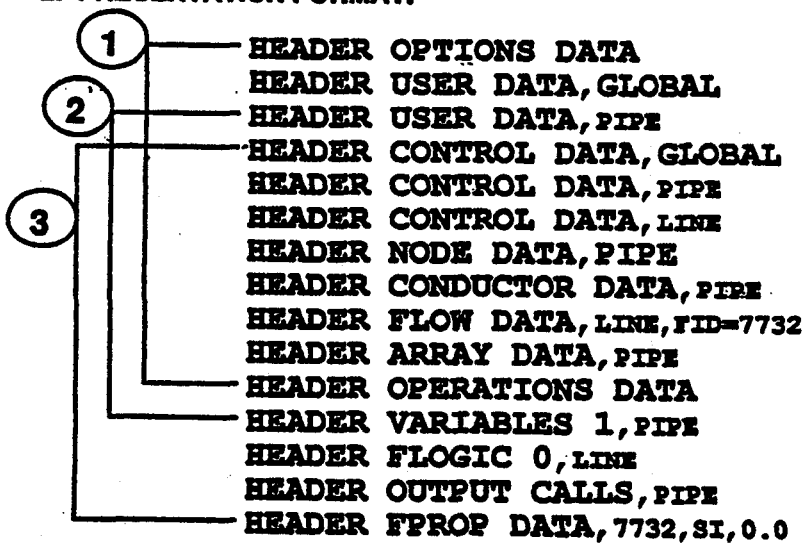

3. LOX SUPPLY LINE

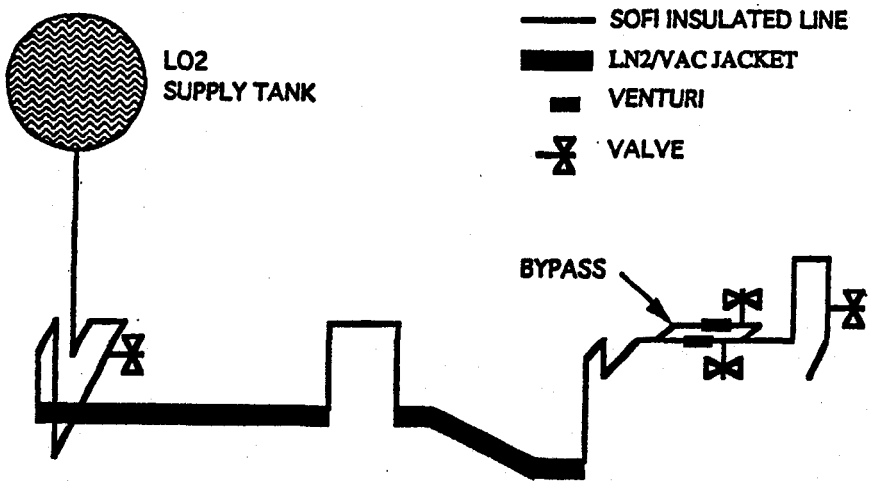

LOX LINE HARDWARE

LINE
- Type 304L CRES 3 SS circular pipe schedule 80
- Length 225 ft
- Bypass length 14 ft
- Diameter (ID) 2.9"
- Wall thickness 0.3"

COMPONENTS
- 90°elbows (qty 22)
- 45° elbows (qty 2)
- Tees (qty 2)
- Venturies (qty 2)

LN2/VACUUM JACKET
- Length (long) 73 ft (from foot 42 to foot 114)
- Length (short) 27 ft (from foot 138 to foot 164)
- Diameter (OD) 6.625"
- Wall thickness 0.143"
- Annular gap 2.857"
- End caps thickness 0.25"
- 11 sliding spacers (contact area=6.0"x0.50" and 6.0"x0.25" , 1.43" tall)
- 4 45° (circular) spacers (contact area 2.1"x0.25", 1.05" tall)

FOAM INSULATION
- Type BX-250 SOFI
- Thickness 1"
- Length 41 ft (from foot 1 to foot 41)
  - 23 ft (form foot 115 to foot 137)
  - 61 ft (from foot 165 to foot 225)
  - 14 ft (bypass from foot 1 to foot 14)
- Thermal Conductivity k=0.00259+0.031696(T°R) Btu/Hr-ft-°F

4. FEATURES

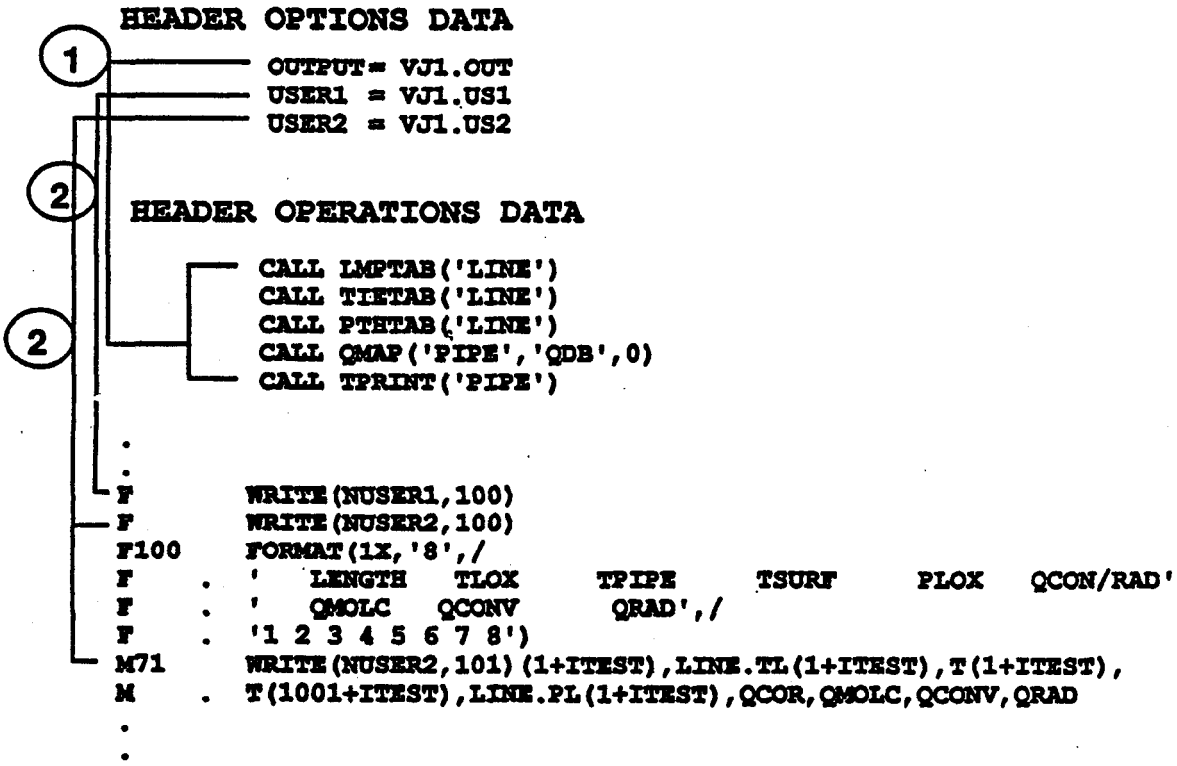

1. OUTPUT

   PROCESSOR PRINT FILE NAME. CAN BE ANY NAME. THIS IS WHERE THE OUTPUT FROM CALLS TO FLOMAP, TPRINT, PRPMAP, ETC. GOES TO AUTOMATICALLY.

2. USER1, USER2

   USER AUXILIARY FILE NAMES. CAN BE ANY NAME.TO PRINT TO THEM USE THE WRITE(NUSER1,100) TO PRINT FOR EXAMPLE TO USER1 FILE USING FORMAT 100.
   WRITE(NUSER2,100) TO PRINT FOR EXAMPLE TO USER2 FILE USING FORMAT 100.

4. FEATURES (CONT)

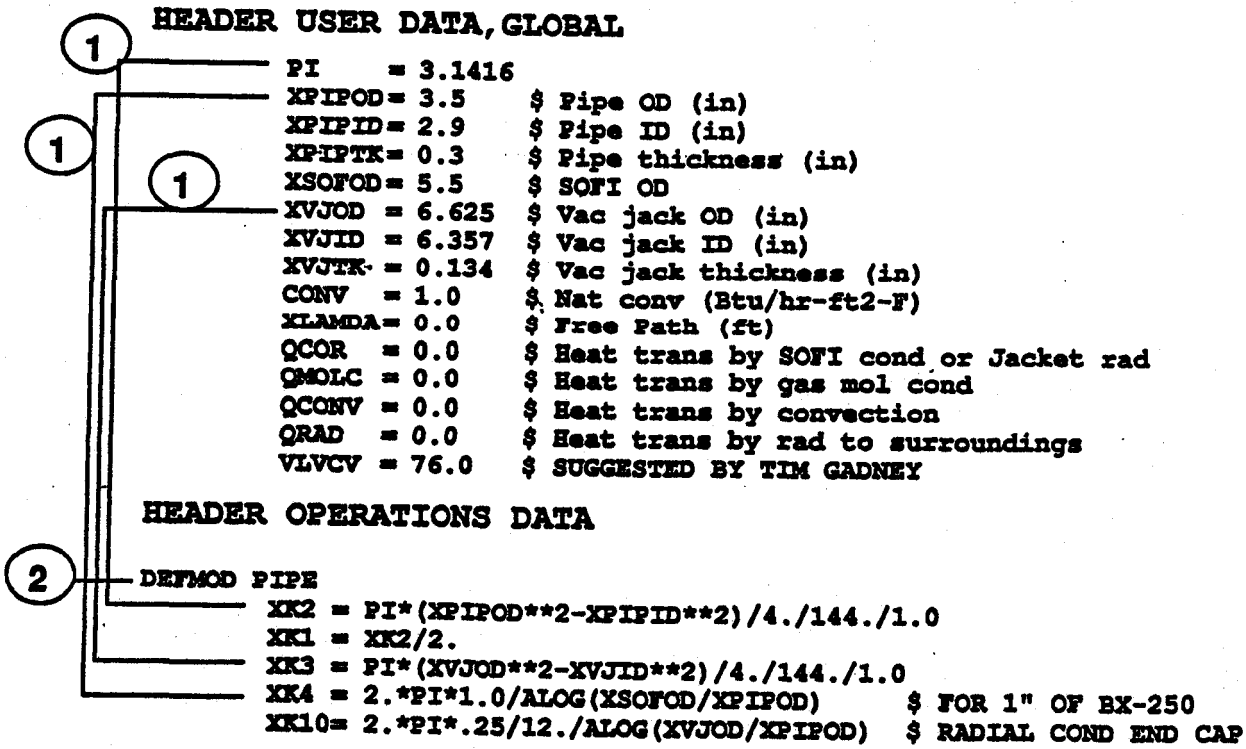

1. THIS IS A HANDY WAY TO DEFINE PI OR ANY OTHER NAME VARIABLE. WATCH FOR PROGRAM RESERVED VARIABLES NAMES SUCH AS G100 (CONDUCTOR 100). VARIABLES ATEST THROUGH ZTEST ARE AVAILABLE BY DEFAULT AND DO NOT HAVE TO BE EXPLICITLY SET.

2. AFTER ENTERING DEFMOD PIPE, YOU CAN ENTER G'S, T'S, ETC. IN THE HEADER OPERATIONS DATA BLOCK WITHOUT THE SUB-MODEL NAME IN FRONT OF IT.

   (EX: ENTER G101=10.0 INSTEAD OF PIPE.G101=10.0).

4. FEATURES (CONT)

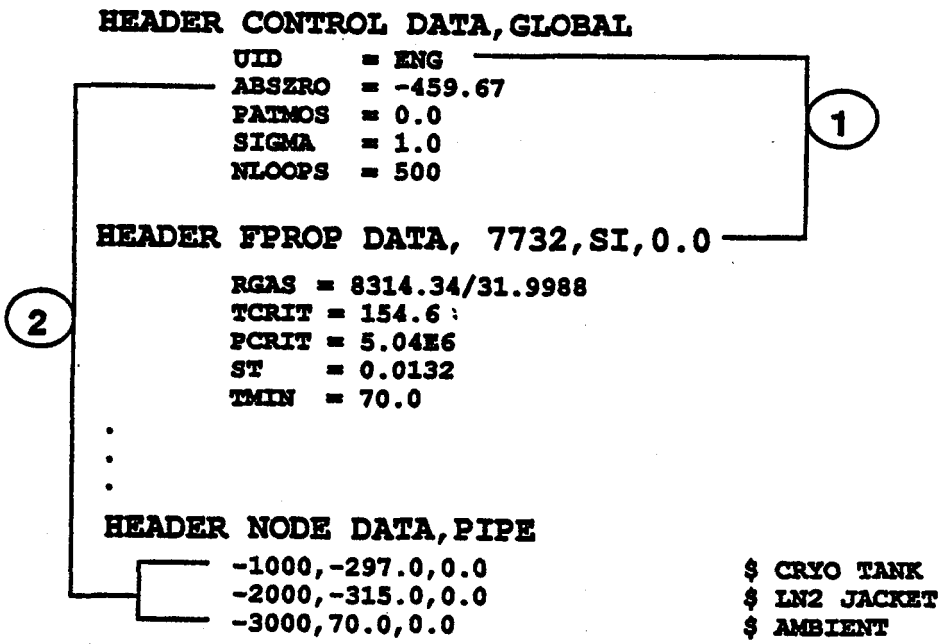

1. UID

   UNIT SYSTEM IDENTIFIER. NOTICE THAT THE LOX LINE PROBLEM IS IN ENG UNITS, WHILE THE FLUID PROPERTIES IN THE HEADER FPROP DATA ARE GIVEN IN SI UNITS.

2. ABSZRO

   VALUE OF ABSOLUTE ZERO IN USER'S TEMPERATURE UNITS

   ABSZRO = -460.0 ALLOWS USE OF TEMPERATURE IN °F INSTEAD OF °R.

4. FEATURES (CONT)

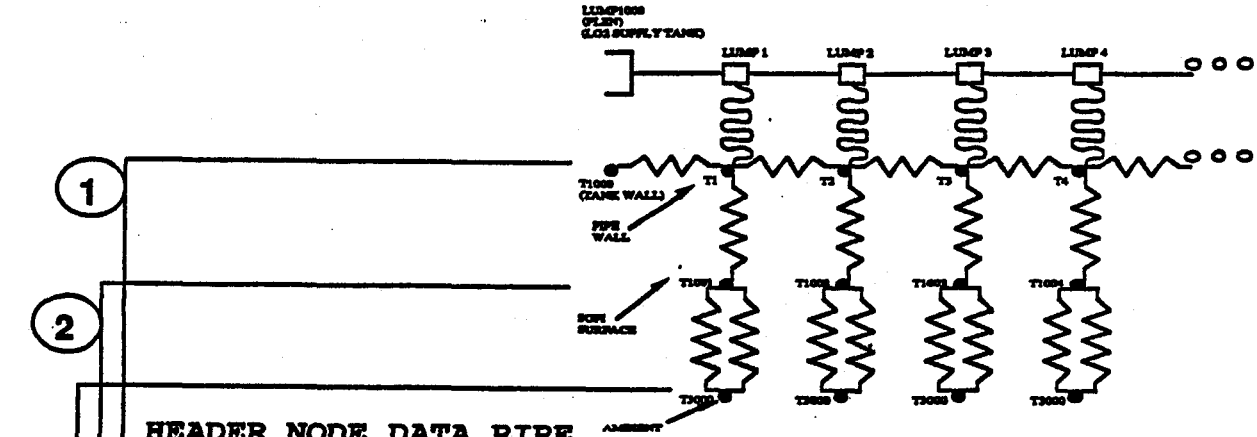

1. GEN

   THIS SINGLE LINE GENERATES 225 DIFFUSION NODES, STARTING WITH NODE 1, IN INCREMENTS OF 1, INITIALLY AT -200°F, WITH A CAPACITANCE VALUE OF 1.0, TO REPRESENT THE LINE. THE CAPACITANCE VALUE IS IMMATERIAL SINCE THIS IS A STEADY STATE MODEL. NODES WILL BE NAMED 1, 2, 3, ETC.

2. THIS SINGLE LINE GENERATES 41 DIFFUSION NODES, STARTING WITH NODE 1001, IN INCREMENTS OF 1, INITIALLY AT 70°F, WITH A CAPACITANCE VALUE OF 1.0, TO REPRESENT THE SOFI SURFACE. NODES WILL BE NAMED 1001, 1002, 1003, ETC.

3. THIS SINGLE LINE GENERATES 1 BOUNDARY NODE 2000 (INDICATED BY THE NEGATIVE SIGN), AT 70°F, TO REPRESENT AMBIENT TEMPERATURE. THE VALUE OF CAPACITANCE IN A BOUNDARY NODE IS MEANINGLESS.

4. FEATURES (CONT)

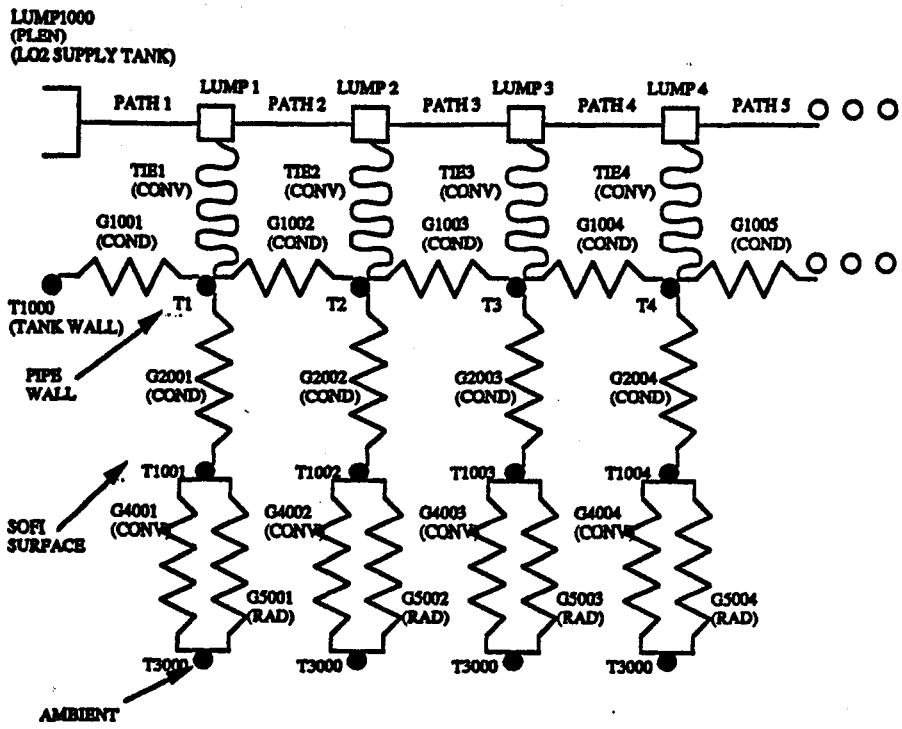

Thermal network schematic of typical section of line with SOFI.

4. FEATURES (CONT)

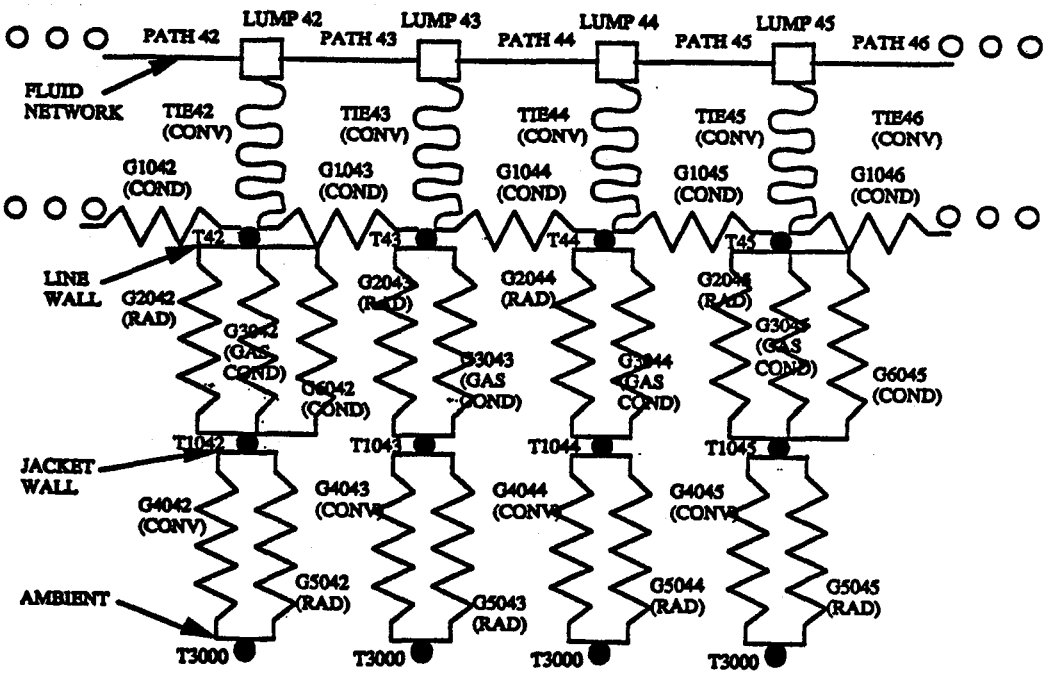

Thermal network schematic of typical section of line with vacuum jacket

4. FEATURES (CONT)

```
1   HEADER CONDUCTOR DATA, PIPE
        GEN 3001,225,1,   1,1,1001,1,0.0        $ GAS MOLEC COND (SOME DUMMIES

    HEADER VARIABLES 1,PIPE
C-CHECK FOR GAS MOL COND
F       DO 10 ITEST=0,72
M       TTEST=(T(42+ITEST)+T(1042+ITEST))/2.+460.
        XK6=(1.4+1.)/(1.4-1.)*((32.2*1545.)/(8.*PI*28.*TTEST))**.5*1.
        XK8=PI*XPIPOD/12.*1.
        CALL CONTRN('PIPE',3042+ITEST,JTEST)
M       GLOBAL.G(JTEST)=XK6*XK7*XK8*3600./778.
        XLAMDA=3.*XK9/XK7*((PI*1545.*TTEST)/(8.*32.2*28.))**.5
M10     IF(XLAMDA.LE.((XVJID-XPIPOD)/2./12.))GLOBAL.G(JTEST)=0.0
C CHECK FOR GAS MOL COND
F       DO 20 ITEST=0,26
M       TTEST=(T(138+ITEST)+T(1138+ITEST))/2.+460.
        XK6=(1.4+1.)/(1.4-1.)*((32.2*1545.)/(8.*PI*28.*TTEST))**.5*1.
        XK8=PI*XPIPOD/12.*1.
M       CALL CONTRN('PIPE',3138+ITEST,JTEST)
M       GLOBAL.G(JTEST)=XK6*XK7*XK8*3600./778.
        XLAMDA=3.*XK9/XK7*((PI*1545.*TTEST)/(8.*32.2*28.))**.5
M20     IF(XLAMDA.LE.((XVJID-XPIPOD)/2./12.))GLOBAL.G(JTEST)=0.0
```

1. GEN

   THIS SINGLE LINE GENERATES 225 CONDUCTION CONDUCTORS,STARTING WITH CONDUCTOR NUMBER 3001, IN INCREMENTS OF 1, CONNECTING NODE 1 IN INCREMENTS OF 1, TO NODE 1001 IN INCREMENTS OF 1, WITH A CONDUCTOR VALUE OF 0.0. CONDUCTORS WILL BE NAMED 3001, 3002, 3003, ETC.

   THESE CONDUCTORS REPRESENT GAS MOLECULAR CONDUCTION IN THE NEAR-VACUUM SPACE, AND THEIR VALUE ARE RE-COMPUTED (FROM 0.0) TO SOMETHING ELSE IN THE HEADER VARIABLES 1 BLOCK BASED ON SOME LOGIC PROGRAMMED THERE.

   NOTICE THAT THERE ARE TWO DO LOOPS OF 73 AND 27 FOR A TOTAL OF ONLY 100 CONDUCTORS TO BE COMPUTED. THE OTHER 125 ONES WILL REMAIN AS 0.0. WHILE THEY ARE NOT NEEDED, THEY WERE LEFT THERE AS DUMMIES FOR FUTURE UTILIZATION.

4. FEATURES (CONT)

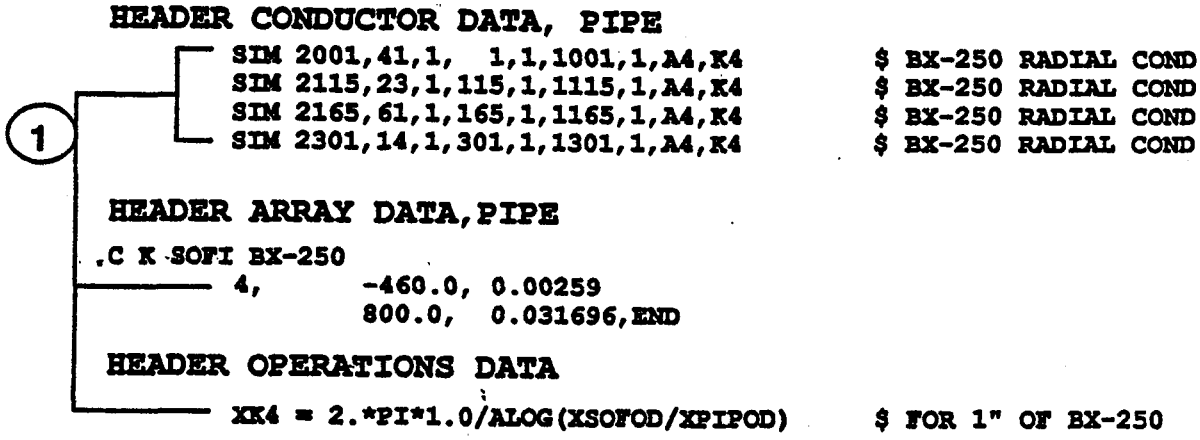

1. SIM

   TO INPUT ONE OR MORE TEMPERATURE-VARYING CONDUCTORS.

   SINDA COMPUTES THE CONDUCTION CONDUCTOR K*A/X BY GETTING K FROM ARRAY 4 (T VERSUS K), AND CONSTANT K4 (A/X) AS XK4, COMPUTED IN THE HEADER OPERATIONS BLOCK, AND MULTIPLYING THE TWO.

1. CONTRN

   THIS ROUTINE RETURNS THE RELATIVE LOCATION IN THE G-ARRAY OF A NETWORK CONDUCTOR, GIVEN THE ACTUAL CONDUCTOR NUMBER.

   THE LOX LINE MODEL MADE EXTENSIVE USE OF THIS ROUTINE IN ORDER TO UTILIZE DO LOOPS TO RECALCULATE THE VALUES OF CONDUCTORS WITHIN SECTIONS OF THE LINE.

2. NOTICE THAT THE RADIATION CONDUCTOR CALCULATION INCLUDES SIGMA (0.1714E-8), WHILE IT IS DEFINED AS 1.0 IN THE HEADER CONTROL DATA, GLOBAL BLOCK. THE DEFAULT VALUE (IF NOT DEFINED) IS 0.1714E-8.

   ONE COMMON ERROR IS TO CALCULATE A CONDUCTOR WITH SIGMA, BUT NOT DEFINING IT AS 1.0 IN THE HEADER CONTROL DATA BLOCK. THIS, OF COURSE, RESULTS IN A CONDUCTOR THAT IS MULTIPLIED TWICE BY SIGMA.

4. FEATURES (CONT)

```
HEADER FLOW DATA,LINE,FID=7732

LU DEF,          XL=0.0,PL=100.0,TL=-297.0
PA DEF,          DH=2.9/12.,UPF=0.5
LU PLEN,1000,    PL=400.0
M HX,1,D, 1,1,1,PIPE.1,1000,NSEG=11,TLENT=11.,DHS=2.9/12.,LU=JUNC,PA=STUBE
M HX,2,D,12,12,12,PIPE.12,11,NSEG=1,TLENT=1.,DHS=2.9/12.,LU=JUNC,PA=LOSS,FK=.35
M HX,3,D,13,13,13,PIPE.13,12,NSEG=2,TLENT=2.,DHS=2.9/12.,LU=JUNC,PA=STUBE
M HX,4,D,15,15,15,PIPE.15,14,NSEG=1,TLENT=1.,DHS=2.9/12.,LU=JUNC,PA=LOSS,FK=.35
M HX,5,D,16,16,16,PIPE.16,15,NSEG=2,TLENT=2.,DHS=2.9/12.,LU=JUNC,PA=STUBE
M HX,6,D,18,18,18,PIPE.18,17,NSEG=1,TLENT=1.,DHS=2.9/12.,LU=JUNC,PA=LOSS,FK=.35
M HX,7,D,19,19,19,PIPE.19,18,NSEG=2,TLENT=2.,DHS=2.9/12.,LU=JUNC,PA=STUBE
.
.
M HX,43,D,201,201,201,PIPE.201,200,NSEG=1,TLENT=1.,DHS=2.9/12.,LU=JUNC,PA=LOSS,FK=
.
.

HEADER FLOGIC 0,LINE

C CONVERT CV TO FK FOR VALVES AND VENTURIES
      FK201=3.0E7*(AF201/VLVCV)**2     $ VENTURI
```

(1) (2)

1. HX MACRO

   TO GENERATE A STRING OF ONE OR MORE LUMPS, PATHS AND TIES REPRESENTING A DIABATIC DUCT (HEAT EXCHANGER SEGMENT).

   SOME ARE PATH PA = STUBE AND PA = LOSS TYPE OF CONNECTOR.

2. IS THERE AN HX DEF LU=JUNC COMMAND TO DEFINE DEFAULTS FOR MACROS ???

3. SOME OF THE LOSSES WERE SPECIFIED BY CV COEFFICIENT. THIS HANDY EQUATION, GIVEN IN THE SINDA MANUAL, CONVERT CV'S TO FK'S.

5. PROGRAM LISTING

```
HEADER OPTIONS DATA
TITLE USTB LOX TRANSFER LINE
      OUTPUT = VJ1.OUT
      USER1  = VJ1.US1
      USER2  = VJ1.US2
      RSO    = VJ1.RSI

HEADER USER DATA,GLOBAL
      PI     =3.1416
      XPIPOD =3.5   $ Pipe OD (in)
      XPIPID =2.9   $ Pipe ID (in)
      XPIPTK =0.3   $ Pipe thickness (in)
      XSOFOD =5.5   $ SOFI OD
      XVJOD  =6.625 $ Vac jack OD (in)
      XVJID  =6.357 $ Vac jack ID (in)
      XVJTK  =0.134 $ Vac jack thickness (in)
      CONV   =1.0   $ Nat conv (Btu/hr-ft2-F)
      XLAMDA =0.0   $ Free Path (ft)
      QCOR   =0.0   $ Heat trans by SOFI cond or Jacket rad
      QMOLC  =0.0   $ Heat trans by gas mol cond
      QCONV  =0.0   $ Heat trans by convection
      QRAD   =0.0   $ Heat trans by rad to surroundings
      VLVCV  =76.0  $ SUGGESTED BY TIM GADNEY

HEADER CONTROL DATA,GLOBAL
      UID    = ENG
      ABSZRO = -459.67
      PATMOS = 0.0
      SIGMA  = 1.0
      NLOOPS = 500

HEADER CONTROL DATA,PIPE
      EBALSA = 0.001

HEADER CONTROL DATA,LINE
      REBALF = 0.001

HEADER NODE DATA,PIPE
C PIPE X SECTION IS pi*od*thick/144 ft2, EACH SEGMENT 1 ft LONG
      GEN  1,225,1,-200.0,1.0          $ PIPE
      GEN 301,14,1,-200.0,1.0          $ BI-PASS
      GEN 1001,41,1,70.0,1.0           $ BX-250 SURFACE
      GEN 1042,73,1,70.0,1.0           $ VAC JACKET
      GEN 1115,23,1,70.0,1.0           $ BX-250 SURFACE
      GEN 1138,27,1,70.0,1.0           $ VAC JACKET
      GEN 1165,61,1,70.0,1.0           $ BX-250 SURFACE
      GEN 1301,14,1,70.0,1.0           $ BI-PASS BX-250 SURFACE
      -1000,-297.0,0.0          $ CRYO TANK
      -2000,-315.0,0.0          $ LN2 JACKET
      -3000,70.0,0.0                   $ AMBIENT

HEADER CONDUCTOR DATA, PIPE
      SIV 1,1000,1,A2,K1               $ AXIAL COND TO TANK
      SIM 2,224,1,1,1,2,1,A2,K2        $ PIPE AXIAL COND
      SIM 300,1,1,194,1,301,1,A2,K2          $ UP PIPE-TO-BI-PASS AXIAL COND
      SIM 301,13,1,301,1,302,1,A2,K2         $ PIPE BI-PASS AXIAL COND
      SIM 314,1,1,314,1,205,1,A2,K2          $ LW PIPE-TO-BI-PASS AXIAL COND
      SIM 1042,72,1,1042,1,1114,1,A2,K3 $ JACKET AXIAL COND
      SIM 1138,26,1,1138,1,1164,1,A2,K3 $ JACKET AXIAL COND
      SIM 2001,41,1,1,1,1001,1,A4,K4         $ BX-250 RADIAL COND
      GEN-2042,73,1,42,1,1042,1,0.0          $ VAC JACKET RAD
      SIM 2115,23,1,115,1,1115,1,A4,K4 $ BX-250 RADIAL COND
```

```
      GEN-2138,27,1,138,1,1138,1,0.0          $ VAC JACKET RAD
      SIM 2165,61,1,165,1,1165,1,A4,K4  $ BX-250 RADIAL COND
      SIM 2301,14,1,301,1,1301,1,A4,K4  $ BX-250 RADIAL COND
      GEN 3001,225,1,   1,1,1001,1,0.0  $ GAS MOLEC COND (SOME DUMMYS)
      GEN 4001,225,1,1001,1,3000,0,0.0  $ BX-250 & JACKET CONV TO AMB
      GEN 4301, 14,1,1301,1,3000,0,0.0  $ BX-250 BI-PASS CONV TO AMB
      GEN-5001,225,1,1001,1,3000,0,0.0  $ BX-250 & JACKET RAD TO AMB
      GEN-5301, 14,1,1301,1,3000,0,0.0  $ BI-PASS BX-250 RAD TO AMB
C SUPPORT CONDUCTORS
      SIM 6042,1,1, 42,1,1042,1,A2,K10  $ END CAP RADIAL COND
      SIM 6045,1,1, 45,1,1045,1,A2,K11  $ COND SLIDING SPACER
      SIM 6048,1,1, 48,1,1048,1,A2,K11  $ COND SLIDING SPACER
      SIM 6049,1,1, 49,1,1049,1,A2,K11  $ COND SLIDING SPACER
      SIM 6051,1,1, 51,1,1051,1,A2,K11  $ COND SLIDING SPACER
      SIM 6052,1,1, 52,1,1052,1,A2,K10  $ END CAP RADIAL COND
      SIM 6053,1,1, 53,1,1053,1,A2,K10  $ END CAP RADIAL COND
      SIM 6054,1,1, 54,1,1054,1,A2,K11  $ COND SLIDING SPACER
      SIM 6058,1,1, 58,1,1058,1,A2,K11  $ COND SLIDING SPACER
      SIM 6066,1,1, 66,1,1066,1,A2,K13  $ COND FIXED ANCHOR WING
      SIM 9066,1,1, 66,1,3000,0,A2,K14  $ COND FIXED ANCHOR TO GROUND
      SIM 6073,1,1, 73,1,1073,1,A2,K11  $ COND SLIDING SPACER
      SIM 6075,1,1, 75,1,1075,1,A2,K11  $ COND SLIDING SPACER
      SIM 6077,1,1, 77,1,1077,1,A2,K11  $ COND SLIDING SPACER
      SIM 6081,1,1, 81,1,1081,1,A2,K11  $ COND SLIDING SPACER
      SIM 6085,1,1, 85,1,1085,1,A2,K11  $ COND SLIDING SPACER
      SIM 6093,1,1, 93,1,1093,1,A2,K11  $ COND SLIDING SPACER
      SIM 6097,1,1, 97,1,1097,1,A2,K11  $ COND SLIDING SPACER
      SIM 6099,1,1, 99,1,1099,1,A2,K11  $ COND SLIDING SPACER
      SIM 6101,1,1,101,1,1101,1,A2,K11  $ COND SLIDING SPACER
      SIM 6109,1,1,109,1,1108,1,A2,K11  $ COND SLIDING SPACER
      SIM 6114,1,1,114,1,1114,1,A2,K10  $ END CAP RADIAL COND
      SIM 6138,1,1,138,1,1138,1,A2,K10  $ END CAP RADIAL COND
      SIM 6145,1,1,145,1,1145,1,A2,K12  $ COND 45 DEG SPACER
      SIM 6147,1,1,147,1,1147,1,A2,K12  $ COND 45 DEG SPACER
      SIM 6151,1,1,151,1,1151,1,A2,K11  $ COND SLIDING SPACER
      SIM 6153,1,1,153,1,1153,1,A2,K11  $ COND SLIDING SPACER
      SIM 6155,1,1,155,1,1155,1,A2,K12  $ COND 45 DEG SPACER
      SIM 6157,1,1,157,1,1157,1,A2,K12  $ COND 45 DEG SPACER
      SIM 6161,1,1,161,1,1161,1,A2,K11  $ COND SLIDING SPACER
      SIM 6163,1,1,163,1,1163,1,A2,K11  $ COND SLIDING SPACER
      SIM 6164,1,1,164,1,1164,1,A2,K10  $ END CAP RADIAL COND
C UNCOMMENT NEXT TWO LINES FOR LN2 CASES
C     GEN 7042,73,1,42,1,2000,0,1000.0  $ LINE TO LN2
C     GEN 7138,27,1,138,1,2000,0,1000.0 $ LINE TO LN2
C     GEN 8042,73,1,2000,0,1042,1,1000.0$ JACKET TO LN2
C     GEN 8138,27,1,2000,0,1138,1,1000.0$ JACKET TO LN2

HEADER FLOW DATA,LINE,FID=7732
LU DEF,      XL=0.0,PL=100.0,TL=-297.0
PA DEF,      DH=2.9/12.,UPF=0.5
LU PLEN,1000,PL=400.0
M HX,1,D, 1,1,1,PIPE.1,1000,NSEG=11,TLENT=11.,DHS=2.9/12.,LU=JUNC,PA=STUBE
M HX,2,D,12,12,12,PIPE.12,11,NSEG=1,TLENT=1.,DHS=2.9/12.,LU=JUNC,PA=LOSS,FK=.35
M HX,3,D,13,13,13,PIPE.13,12,NSEG=2,TLENT=2.,DHS=2.9/12.,LU=JUNC,PA=STUBE
M HX,4,D,15,15,15,PIPE.15,14,NSEG=1,TLENT=1.,DHS=2.9/12.,LU=JUNC,PA=LOSS,FK=.35
M HX,5,D,16,16,16,PIPE.16,15,NSEG=2,TLENT=2.,DHS=2.9/12.,LU=JUNC,PA=STUBE
M HX,6,D,18,18,18,PIPE.18,17,NSEG=1,TLENT=1.,DHS=2.9/12.,LU=JUNC,PA=LOSS,FK=.35
M HX,7,D,19,19,19,PIPE.19,18,NSEG=2,TLENT=2.,DHS=2.9/12.,LU=JUNC,PA=STUBE
M HX,8,D,21,21,21,PIPE.21,20,NSEG=1,TLENT=1.,DHS=2.9/12.,LU=JUNC,PA=STUBE
M HX,9,D,22,22,22,PIPE.22,21,NSEG=1,TLENT=1.,DHS=2.9/12.,LU=JUNC,PA=LOSS,FK=0.0
M HX,10,D,23,23,23,PIPE.23,22,NSEG=4,TLENT=4.,DHS=2.9/12.,LU=JUNC,PA=STUBE
M HX,11,D,27,27,27,PIPE.27,26,NSEG=1,TLENT=1.,DHS=2.9/12.,LU=JUNC,PA=LOSS,FK=.35
M HX,12,D,28,28,28,PIPE.28,27,NSEG=5,TLENT=5.,DHS=2.9/12.,LU=JUNC,PA=STUBE
M HX,13,D,33,33,33,PIPE.33,32,NSEG=1,TLENT=1.,DHS=2.9/12.,LU=JUNC,PA=LOSS,FK=.35
```

```
M HX,14,D,34,34,34,PIPE.34,33,NSEG=2,TLENT=2.,DHS=2.9/12.,LU=JUNC,PA=STUBE
M HX,15,D,36,36,36,PIPE.36,35,NSEG=1,TLENT=1.,DHS=2.9/12.,LU=JUNC,PA=LOSS,FK=.35
M HX,16,D,37,37,37,PIPE.37,36,NSEG=4,TLENT=4.,DHS=2.9/12.,LU=JUNC,PA=STUBE
M HX,17,D,41,41,41,PIPE.41,40,NSEG=1,TLENT=1.,DHS=2.9/12.,LU=JUNC,PA=LOSS,FK=.35
M HX,18,D,42,42,42,PIPE.42,41,NSEG=72,TLENT=72.,DHS=2.9/12.,LU=JUNC,PA=STUBE
M HX,19,D,114,114,114,PIPE.114,113,NSEG=1,TLENT=1.,DHS=2.9/12.,LU=JUNC,PA=LOSS,FK=.35
M HX,20,D,115,115,115,PIPE.115,114,NSEG=7,TLENT=7.,DHS=2.9/12.,LU=JUNC,PA=STUBE
M HX,21,D,122,122,122,PIPE.122,121,NSEG=1,TLENT=1.,DHS=2.9/12.,LU=JUNC,PA=LOSS,FK=.35
M HX,22,D,123,123,123,PIPE.123,122,NSEG=6,TLENT=6.,DHS=2.9/12.,LU=JUNC,PA=STUBE
M HX,23,D,129,129,129,PIPE.129,128,NSEG=1,TLENT=1.,DHS=2.9/12.,LU=JUNC,PA=LOSS,FK=.35
M HX,24,D,130,130,130,PIPE.130,129,NSEG=7,TLENT=7.,DHS=2.9/12.,LU=JUNC,PA=STUBE
M HX,25,D,137,137,137,PIPE.137,136,NSEG=1,TLENT=1.,DHS=2.9/12.,LU=JUNC,PA=LOSS,FK=.35
M HX,26,D,138,138,138,PIPE.138,137,NSEG=8,TLENT=1.,DHS=2.9/12.,LU=JUNC,PA=STUBE
M HX,27,D,146,146,146,PIPE.146,145,NSEG=1,TLENT=1.,DHS=2.9/12.,LU=JUNC,PA=LOSS,FK=.19
M HX,28,D,147,147,147,PIPE.147,146,NSEG=9,TLENT=9.,DHS=2.9/12.,LU=JUNC,PA=STUBE
M HX,29,D,156,156,156,PIPE.156,155,NSEG=1,TLENT=1.,DHS=2.9/12.,LU=JUNC,PA=LOSS,FK=.19
M HX,30,D,157,157,157,PIPE.157,156,NSEG=7,TLENT=7.,DHS=2.9/12.,LU=JUNC,PA=STUBE
M HX,31,D,164,164,164,PIPE.164,163,NSEG=1,TLENT=1.,DHS=2.9/12.,LU=JUNC,PA=LOSS,FK=.35
M HX,32,D,165,165,165,PIPE.165,164,NSEG=7,TLENT=7.,DHS=2.9/12.,LU=JUNC,PA=STUBE
M HX,33,D,172,172,172,PIPE.172,171,NSEG=1,TLENT=1.,DHS=2.9/12.,LU=JUNC,PA=LOSS,FK=.35
M HX,34,D,173,173,173,PIPE.173,172,NSEG=1,TLENT=1.,DHS=2.9/12.,LU=JUNC,PA=STUBEBE
M HX,35,D,174,174,174,PIPE.174,173,NSEG=1,TLENT=1.,DHS=2.9/12.,LU=JUNC,PA=LOSS,FK=.35
M HX,36,D,175,175,175,PIPE.175,174,NSEG=2,TLENT=2.,DHS=2.9/12.,LU=JUNC,PA=STUBE
M HX,37,D,177,177,177,PIPE.177,176,NSEG=1,TLENT=1.,DHS=2.9/12.,LU=JUNC,PA=LOSS,FK=.35

M HX,38,D,178,178,178,PIPE.178,177,NSEG=10,TLENT=10.,DHS=2.9/12.,LU=JUNC,PA=STUBE
M HX,39,D,188,188,188,PIPE.188,187,NSEG=1,TLENT=1.,DHS=2.9/12.,LU=JUNC,PA=LOSS,FK=.35

M HX,40,D,189,189,189,PIPE.189,188,NSEG=6,TLENT=6.,DHS=2.9/12.,LU=JUNC,PA=STUBE
C STRAIGHT SPLIT
M HX,41,D,195,195,195,PIPE.195,194,NSEG=1,TLENT=1.,DHS=2.9/12.,LU=JUNC,PA=LOSS,FK=.15
M HX,42,D,196,196,196,PIPE.196,195,NSEG=5,TLENT=5.,DHS=2.9/12.,LU=JUNC,PA=STUBE
C VENTURI
M HX,43,D,201,201,201,PIPE.201,200,NSEG=1,TLENT=1.,DHS=2.9/12.,LU=JUNC,PA=LOSS,FK=0.0
C VALVE
M HX,44,D,202,202,202,PIPE.202,201,NSEG=2,TLENT=2.,DHS=2.9/12.,LU=JUNC,PA=STUBE
M HX,45,D,204,204,204,PIPE.204,203,NSEG=1,TLENT=1.,DHS=2.9/12.,LU=JUNC,PA=LOSS,FK=.15

M HX,46,D,205,205,205,PIPE.205,204,NSEG=4,TLENT=4.,DHS=2.9/12.,LU=JUNC,PA=STUBE
M HX,47,D,209,209,209,PIPE.209,208,NSEG=1,TLENT=1.,DHS=2.9/12.,LU=JUNC,PA=LOSS,FK=.35
M HX,48,D,210,210,210,PIPE.210,209,NSEG=6,TLENT=6.,DHS=2.9/12.,LU=JUNC,PA=STUBE
M HX,49,D,216,216,216,PIPE.216,215,NSEG=1,TLENT=1.,DHS=2.9/12.,LU=JUNC,PA=LOSS,FK=.35
M HX,50,D,217,217,217,PIPE.217,216,NSEG=1,TLENT=1.,DHS=2.9/12.,LU=JUNC,PA=LOSS,FK=.35
M HX,51,D,218,218,218,PIPE.218,217,NSEG=3,TLENT=3.,DHS=2.9/12.,LU=JUNC,PA=STUBE
M HX,52,D,221,221,221,PIPE.221,220,NSEG=1,TLENT=1.,DHS=2.9/12.,LU=JUNC,PA=STUBE
M HX,53,D,222,222,222,PIPE.222,221,NSEG=1,TLENT=1.,DHS=2.9/12.,LU=JUNC,PA=LOSS,FK=0.0
M HX,54,D,223,223,223,PIPE.223,222,NSEG=1,TLENT=1.,DHS=2.9/12.,LU=JUNC,PA=STUBE
M HX,55,D,224,224,224,PIPE.224,223,NSEG=1,TLENT=1.,DHS=2.9/12.,LU=JUNC,PA=LOSS,FK=.35
C END OF LOX LINE
M HX,56,C,225,225,225,PIPE.225,224,2000,NSEG=1,TLENT=1.,DHS=2.9/12.,LU=JUNC,PA=STUBE
C TURN SPLIT
M HX,57,D,301,301,301,PIPE.301,194,NSEG=1,TLENT=1.,DHS=2.9/12.,LU=JUNC,PA=STUBE
M HX,58,D,302,302,302,PIPE.302,301,NSEG=1,TLENT=1.,DHS=2.9/12.,LU=JUNC,PA=LOSS,FK=.35

M HX,59,D,303,303,303,PIPE.303,302,NSEG=6,TLENT=6.,DHS=2.9/12.,LU=JUNC,PA=STUBE
C VENTURY
M HX,60,D,309,309,309,PIPE.309,308,NSEG=1,TLENT=1.,DHS=2.9/12.,LU=JUNC,PA=LOSS,FK=0.0

M HX,62,D,310,310,310,PIPE.310,309,NSEG=2,TLENT=2.,DHS=2.9/12.,LU=JUNC,PA=STUBE
M HX,63,D,312,312,312,PIPE.312,311,NSEG=1,TLENT=1.,DHS=2.9/12.,LU=JUNC,PA=LOSS,FK=.35

M HX,64,D,313,313,313,PIPE.313,312,NSEG=1,TLENT=1.,DHS=2.9/12.,LU=JUNC,PA=STUBE
M HX,65,C,314,314,314,PIPE.314,313,204,NSEG=1,TLENT=1.,DHS=2.9/12.,LU=JUNC,PA=LOSS,FK=.70
```

```
LU PLEN,2000                $ EXAUST

HEADER ARRAY DATA,PIPE
C K FOR AISI 304L SS (BTU/HR-FT-F)
       2,     -400.0,       2.0
              -350.0,       4.0
              -300.0, 5.1
              -250.0,       6.0
              -150.0,       7.0
              -50.0, 8.0
              100.0, 9.0,   END
C K SOFI BX-250
       4,     -460.0,       0.00259
              800.0, 0.031696,END

HEADER USER DATA, PIPE
       1      =0.0
       2      =0.0
       3      =0.0
       4      =0.0
       5      =0.0
       6      =0.0
       7      =10.E-5*.01934*144. $ IN-HG--->PSIA
       8      =0.0                $ PIPE SURFACE AREA
       9      =.0228/3600.        $ GN2 gas visc (LBM/FT-SEC) @250 R
       10     =0.0          $ A/X FOR RADIAL COND END CAP
       11     =0.0          $ A/X FOR COND SLIDING SPACER
       12     =0.0          $ A/X FOR COND 45 DEG SPACER
       13     =0.0          $ A/X FOR COND FIXED ANCHOR WING
       14     =0.0          $ A/X FOR COND FIXED ANCHOR TO GROUND

HEADER OPERATIONS DATA
BUILD PIPE,PIPE
DEFMOD PIPE
       XK2 = PI*(XPIPOD**2-XPIPID**2)/4./144./1.0
       XK1 = XK2/2.
       XK3 = PI*(XVJOD**2-XVJID**2)/4./144./1.0
       XK4 = 2.*PI*1.0/ALOG(XSOFOD/XPIPOD) $ FOR 1" OF BX-250
       XK10= 2.*PI*.25/12./ALOG(XVJOD/XPIPOD)  $ RADIAL COND END CAP
       XK11= 6.*(.25+.5)/1.43/12.        $ COND SLIDING SPACER
       XK12= 4.*.25*2.1/1.05/12.         $ COND 45 DEG SPACER
       XK13= 6.*.25/1.43/12.             $ COND FIXED ANCHOR WING
       XK14= 8.*.5/9.56/12.       $ COND FIXED ANCHOR TO GROUND

F      DO 10 ITEST=0,40
M      CALL CONTRN('PIPE',4001+ITEST,JTEST)
M      CALL CONTRN('PIPE',5001+ITEST,KTEST)
C SOFI CONVECTION TO AMB
M      GLOBAL.G(JTEST)=CONV*PI*XSOFOD/12.*1.0
C SOFI RADIATION TO AMB
M10    GLOBAL.G(KTEST)=.1714E-8*.9*1.*PI*XSOFOD/12.*1.0

F      DO 20 ITEST=0,72
M      CALL CONTRN('PIPE',2042+ITEST,JTEST)
M      CALL CONTRN('PIPE',4042+ITEST,KTEST)
M      CALL CONTRN('PIPE',5042+ITEST,LTEST)
C VAC JACK INTERNAL RAD
M      GLOBAL.G(JTEST)=.1714E-8*.18*1.*PI*XPIPOD/12./1.0
C VAC JACK CONV TO AMB
M      GLOBAL.G(KTEST)=CONV*PI*XVJOD/12.*1.0
C VAC JACK RAD TO AMB
M20    GLOBAL.G(LTEST)=.1714E-8*.90*1.*PI*XVJOD/12.*1.0

F      DO 30 ITEST=0,22
```

```
M       CALL CONTRN('PIPE',4115+ITEST,JTEST)
M       CALL CONTRN('PIPE',5115+ITEST,KTEST)
C SOFI CONVECTION TO AMB
M       GLOBAL.G(JTEST)=CONV*PI*XSOFOD/12.*1.0
C SOFI RADIATION TO AMB
M30     GLOBAL.G(KTEST)=.1714E-8*.9*1.*PI*XSOFOD/12.*1.0

F       DO 40 ITEST=0,26
M       CALL CONTRN('PIPE',2138+ITEST,JTEST)
M       CALL CONTRN('PIPE',4138+ITEST,KTEST)
M       CALL CONTRN('PIPE',5138+ITEST,LTEST)
C VAC JACK INTERNAL RAD
M       GLOBAL.G(JTEST)=.1714E-8*.18*1.*PI*XPIPOD/12./1.0
C VAC JACK CONV TO AMB
M       GLOBAL.G(KTEST)=CONV*PI*XVJOD/12.*1.0
C VAC JACK RAD TO AMB
M40     GLOBAL.G(LTEST)=.1714E-8*.9*1.*PI*XVJOD/12.*1.0

F       DO 50 ITEST=0,60
M       CALL CONTRN('PIPE',4165+ITEST,JTEST)
M       CALL CONTRN('PIPE',5165+ITEST,KTEST)
C SOFI CONVECTION TO AMB
M       GLOBAL.G(JTEST)=CONV*PI*XSOFOD/12.*1.0
C SOFI RADIATION TO AMB
M50     GLOBAL.G(KTEST)=.1714E-8*.9*1.*PI*XSOFOD/12.*1.0

F       DO 60 ITEST=0,13
M       CALL CONTRN('PIPE',4301+ITEST,JTEST)
M       CALL CONTRN('PIPE',5301+ITEST,KTEST)
C BI-PASS SOFI CONVECTION TO AMB
M       GLOBAL.G(JTEST)=CONV*PI*XSOFOD/12.*1.0
C BI-PASS SOFI RADIATION TO AMB
M60     GLOBAL.G(KTEST)=.1714E-8*.9*1.*PI*XSOFOD/12.*1.0

BUILDF PIPE,LINE
        CALL FASTIC
        CALL LMPTAB('LINE')
        CALL TIETAB('LINE')
        CALL PTHTAB('LINE')
C       CALL QMAP('PIPE','QDB',0)
        CALL TPRINT('PIPE')
F       WRITE(NUSER1,100)
F       WRITE(NUSER2,100)
F100    FORMAT(1X,'8',/
F     .         '   LENGTH    TLOX      TPIPE      TSURF      PLOX    QCON/RAD'
F     . '   QMOLC    QCONV      QRAD',/
F     . '1 2 3 4 5 6 7 8')

F       DO 70 ITEST=0,148
M       CALL CONTRN('PIPE',2001+ITEST,JTEST)
M       CALL CONTRN('PIPE',3001+ITEST,KTEST)
M       CALL CONTRN('PIPE',4001+ITEST,LTEST)
M       CALL CONTRN('PIPE',5001+ITEST,MTEST)
M       CALL QMETER(T(1+ITEST),T(1001+ITEST),GLOBAL.G(JTEST),QCOR)
M       IF(1+ITEST.GT.41.AND.1+ITEST.LT.114)THEN
M       CALL RDTNQS(T(1001+ITEST),T(1+ITEST),GLOBAL.G(JTEST),QCOR)
M       CALL QMETER(T(1+ITEST),T(1001+ITEST),GLOBAL.G(KTEST),QMOLC)
M       ELSE IF(1+ITEST.GT.136.AND.1+ITEST.LT.165)THEN
M       CALL RDTNQS(T(1001+ITEST),T(1+ITEST),GLOBAL.G(JTEST),QCOR)
M       CALL QMETER(T(1+ITEST),T(1001+ITEST),GLOBAL.G(KTEST),QMOLC)
F       ELSE
        QMOLC=0.0
F       END IF
M       CALL QMETER(T(1001+ITEST),T3000,GLOBAL.G(LTEST),QCONV)
```

```
M       CALL RDTNQS(T3000,T(1001+ITEST),GLOBAL.G(MTEST),QRAD)
M70     WRITE(NUSER1,101)(1+ITEST),LINE.TL(1+ITEST),T(1+ITEST),
M     . T(1001+ITEST),LINE.PL(1+ITEST),QCOR,QMOLC,QCONV,QRAD

F       DO 71 ITEST=149,224
M       CALL CONTRN('PIPE',2001+ITEST,JTEST)
M       CALL CONTRN('PIPE',3001+ITEST,KTEST)
M       CALL CONTRN('PIPE',4001+ITEST,LTEST)
M       CALL CONTRN('PIPE',5001+ITEST,MTEST)
M       CALL QMETER(T(1+ITEST),T(1001+ITEST),GLOBAL.G(JTEST),QCOR)
M       IF(1+ITEST.GT.41.AND.1+ITEST.LT.114)THEN
M       CALL RDTNQS(T(1001+ITEST),T(1+ITEST),GLOBAL.G(JTEST),QCOR)
M       CALL QMETER(T(1+ITEST),T(1001+ITEST),GLOBAL.G(KTEST),QMOLC)
M       ELSE IF(1+ITEST.GT.136.AND.1+ITEST.LT.165)THEN
M       CALL RDTNQS(T(1001+ITEST),T(1+ITEST),GLOBAL.G(JTEST),QCOR)
M       CALL QMETER(T(1+ITEST),T(1001+ITEST),GLOBAL.G(KTEST),QMOLC)
F       ELSE
        QMOLC=0.0
F       END IF
M       CALL QMETER(T(1001+ITEST),T3000,GLOBAL.G(LTEST),QCONV)
M       CALL RDTNQS(T3000,T(1001+ITEST),GLOBAL.G(MTEST),QRAD)
M71     WRITE(NUSER2,101)(1+ITEST),LINE.TL(1+ITEST),T(1+ITEST),
M     . T(1001+ITEST),LINE.PL(1+ITEST),QCOR,QMOLC,QCONV,QRAD

F101    FORMAT(1X,I5,1X,1PE9.2,1X,1PE9.2,1X,1PE9.2,1X,1PE9.2,1X,1PE9.2,
F     . 1X,1PE9.2,1X,1PE9.2,1X,1PE9.2)

HEADER VARIABLES 1,PIPE
C CHECK FOR GAS MOL COND
F       DO 10 ITEST=0,72
M       TTEST=(T(42+ITEST)+T(1042+ITEST))/2.+460.
        XK6=(1.4+1.)/(1.4-1.)*((32.2*1545.)/(8.*PI*28.*TTEST))**.5*1.
        XK8=PI*XPIPOD/12.*1.
        CALL CONTRN('PIPE',3042+ITEST,JTEST)
M       GLOBAL.G(JTEST)=XK6*XK7*XK8*3600./778.
        XLAMDA=3.*XK9/XK7*((PI*1545.*TTEST)/(8.*32.2*28.))**.5
M10     IF(XLAMDA.LE.((XVJID-XPIPOD)/2./12.))GLOBAL.G(JTEST)=0.0
C CHECK FOR GAS MOL COND
F       DO 20 ITEST=0,26
M       TTEST=(T(138+ITEST)+T(1138+ITEST))/2.+460.
      . XK6=(1.4+1.)/(1.4-1.)*((32.2*1545.)/(8.*PI*28.*TTEST))**.5*1.
        XK8=PI*XPIPOD/12.*1.
M       CALL CONTRN('PIPE',3138+ITEST,JTEST)
M       GLOBAL.G(JTEST)=XK6*XK7*XK8*3600./778.
        XLAMDA=3.*XK9/XK7*((PI*1545.*TTEST)/(8.*32.2*28.))**.5
M20     IF(XLAMDA.LE.((XVJID-XPIPOD)/2./12.))GLOBAL.G(JTEST)=0.0

HEADER FLOGIC 0,LINE
C CONVERT CV TO FK FOR VALVES AND VENTURIES
        FK22=3.0E7*(AF22/VLVCV)**2 $ VALVE
        FK201=3.0E7*(AF201/VLVCV)**2      $ VENTURI
        FK202=3.0E7*(AF202/VLVCV)**2      $ VALVE
        FK222=3.0E7*(AF222/VLVCV)**2      $ VALVE
        FK309=3.0E7*(AF309/VLVCV)**2      $ VENTURI
        FK310=3.0E7*(AF310/VLVCV)**2      $ VALVE

HEADER OUTPUT CALLS, PIPE
C-----------------------------
HEADER FPROP DATA,7732,SI,0.0
C
C MORE COMPLETE OXYGEN TWO-PHASE (FROM 70 TO 120K, NEAR 90 K)
C VAPOR PROPERTIES ARE FOR SATURATED VAPOR
C
        RGAS   = 8314.34/31.9988
```

```
      TCRIT  = 154.6
      PCRIT  = 5.04E6
      ST     = 0.0132
      TMIN   = 70.0
      PGMAX  = 1.0E6
C     TGMAX  = 120.0
C
C *** ALTERNATE INPUTS FOR SUPERHEATED VAPOR PROPERTIES AT 1 ATM
C     THEN USE THE FOLLOWING LINES INSTEAD:
      TGMAX         = 700.0
AT,VG, 80.0,6.27E-6, 100.0,7.68E-6,      120.0,9.12E-6,      130.0,9.85E-6
      140.0,10.6E-6,      155.0,11.6E-6,      170.0,12.7E-6,      200.0,14.7E-6
      300.0,20.7E-6,      400.0,25.9E-6,      500.0,30.5E-6,      600.0,34.7E-6
      700.0,38.5E-6
AT,KG, 100.0,9.1E-3, 120.0,0.0109, 130.0,0.0119, 140.0,0.0128
      155.0,0.0142, 170.0,0.0156, 200.0,0.0182, 300.0,0.0267
      400.0,0.0342, 500.0,0.0412, 600.0,0.0480, 700.0,0.0544
C *** END ALTERNATE INPUTS
C
C THE NEXT TWO LINES ARE FOR SATURATED VAPOR
CAT,VG,      80.0,6.27E-6, 100.0,7.72E-6,      120.0,9.49E-6,      130.0,1.057E-5
CAT,KG,      100.0,9.3E-3, 120.0,0.0124, 130.0,0.015
C
AT,DOME,     54.34, 145.3,       242.37E3
C ELSE:            60.0,  724.9,       238.26E3
C ELSE:            70.0,  6253.0,            230.50E3
             90.19, 101325.0,    213.03E3
C ELSE:            100.0, 0.254E6,     202.57E3
C ELSE:            110.0, 0.534E6,     189.69E3
C ELSE:            120.0, 1.022E6,     173.75E3
AT,KL, 80.0,0.1623,  100.0,0.1372, 120.0,0.1096, 130.0,0.0949
C     140.0,0.0796, 150.0,0.0610
AT,VL, 80.0,2.57E-4, 100.0,1.56E-4,      120.0,1.117E-4,     130.0,9.6E-5
C     140.0,7.8E-5, 150.0,5.1E-5
C
AT,CPG,      80.0,909.8,  170.0,909.8,  200.0,910.2,  300.0,918.4
      400.0,941.5,  500.0,970.9,  600.0,1002.,  700.0,1031.
AT,DL, 53.34,1309.,  60.0,1282.,  65.0,1259.,  70.0,1238.,
      75.0,1214.,  80.0,1190.,  85.0,1167.,  90.0,1142.
      95.0,1116.,  100.0,1091.,  105.0,1064.,  110.0,1035.
      115.0,1006.,  120.0,973.7,  125.0,939.8
C     130.0,902.5,  135.0,861.3,  140.0,813.0,  145.0,755.3
END OF DATA
```

THERMAL ANALYSIS OF COMBINATORIAL SOLID GEOMETRY MODELS USING SINDA

Capt Diane Gerencser
Mr George Radke
Capt Rob Introne
Phillips Laboratory, Kirtland AFB, NM

Mr John Klosterman
Mr Dave Miklosovic
Battelle, Columbus, OH

SUMMARY

Algorithms have been developed using Monte Carlo techniques to determine the thermal network parameters necessary to perform a finite difference analysis on Combinatorial Solid Geometry (CSG) models. Orbital and laser fluxes as well as internal heat generation are modeled to facilitate satellite modeling. The results of the thermal calculations are used to model the infra-red (IR) images of targets and assess target vulnerability. Sample analyses and validation are presented which demonstrate code products.

INTRODUCTION

CSG models of targets have been used for many years in performing various phenomenologic analyses such as nuclear particle transport, kinetic energy weapon effects, survivability, susceptibility, and lethality studies. Many CSG vehicle target description databases are under construction and include highly detailed, three dimensional solid geometry models of red and blue, high value strategic and tactical targets. Ideally, these data sets include all of the information necessary to perform detailed thermal analysis for thermal performance simulation. Applications of thermal analysis on these data sets include thermal design analysis, laser weapon effects survivability analysis, and IR image synthesis for sensor and seeker performance of target susceptibility, acquisition and tracking, simulation of system IR imaging, and automatic target recognition algorithm training.

SINDA and other network methods for thermal analysis algorithms have been successfully employed to model many complex thermophysical systems. Their success may be partially credited to the simplicity of modeling very complicated thermal control, radiative transfer and nonlinear thermal problems. However, these codes are not usually linked directly to geometric solid geometry models, and therefore the burden of constructing the input data has been placed on the code user. Often, the only cross correlation for temperature predictions is a sketch or drawing and a node number penciled in by hand.

At the Phillips Laboratory and Battelle Memorial Institute, algorithms have recently been developed to marry the two technologies, allowing high resolution thermal analysis of these CSG target sets for such studies. The algorithms include three dimensional geometry discretization, thermal network parameter computation including interelemental radiative transfer computation,

orbital and external thermal environment simulation, transient source computation including internal heat generations and thermal control. The computed data is then reformatted to a SINDA input file format for transient or steady state thermal predictions. The resultant thermal profiles are explicitly linked to the geometric models. This correlation increases the usefulness of the data by allowing IR image and signature predictions from the total set of geometry, thermophysical, thermoradiative and temperature data. Although originally created for imagery analysis, the algorithms were modified to include time and space resolved laser fluxes. The thermal results of the laser loads on a target can be used in vulnerability analysis. All of the algorithms are combined in a suite of codes collectively named AutoSINDA.

THERMAL SOLVER CHOSEN

SINDA was chosen as the thermal solver for AutoSINDA for a variety of reasons. Its application is flexible, able to model time and temperature dependent parameters, convection, conduction, internal and external radiation, heat pipes, thermal control systems, and phase changes. SINDA also allows programmable access through user defined variables and has many solution schemes which allow both transient and steady state solutions. In addition, SINDA has been used and tested for many years and has a heritage as a thermal analysis code in the satellite community. The SINDA code has a broad base of users within the community from which to draw expertise.

ALGORITHM DEVELOPMENT

Overview

An overview of the AutoSINDA codes is presented in Figure 1. The model is first discretized. The discretized model has the same format as the original model and has lost no geometric fidelity. Next the thermal network parameters are calculated using a Monte Carlo technique. Orbital loadings are applied using only first incident absorption of solar and earth fluxes. Diffuse fluxes such as earth shine is modeled as a distributed impressed flux. The result is an element/load table as a function of time. All thermal network parameters and loads are reformatted for SINDA input. SINDA is then used for transient thermal analysis. There is a one to one correspondence between the discretized elements in the solid model and the SINDA nodes. The temperatures correlated to the discretized geometry are used to determine laser effects or the resulting IR image of the target.

Assumptions

The AutoSINDA model is limited by the following assumptions: 1) all materials are opaque, 2) all materials are perfect diffuse or perfect specular, and 3) only first incident external radiative flux absorption is modeled.

CSG Geometric Description

A combinatorial solid geometry model is described by Boolean combinations of solid primitives. The lowest hierarchial unit of these models is called the "element" (not related to element as in Finite Element). Each element should be composed of a contiguous solid material and have a

single surface property or coating. An example of a single element would be a base plate for an antenna or a panel for a structural housing.

Each element is a built by a combination of solid primitives. This entails complex intersections and unions of void and solid ellipsoids, elliptical cones and polyhedra. Note that in general these combinatorial intersections of volumes allows very complex solid descriptions in a compact format.

The target model is comprised of many elements assembled in a series of hierarchial sets to describe the complete system model. Many of these models are quite detailed, modeled down to the electronic card level.

Algorithm Basic Processes

In order to perform thermal analyses on the CSG descriptions, five basic processes are executed on the geometry model. These are:

Process 1: Model Discretization
Process 2: Thermal Network Parameter Computation
Process 3: Environmental Simulation
Process 4: Application of Environmental Flux & Internal Heat Generations
Process 5: Data Reformatting to SINDA Input Deck

Model Discretization

For each element in the CSG model, a bounding box is found using the minimum and maximum x, y, and z coordinates for the element. The number of divisions in each direction which will produce a length less than or equal to the maximum mesh size, l_{max} for that element is determined by,

$$n_r = int[(r_{max} - r_{min})/l_{max}] + 1 \qquad (1)$$

where r is the axis being divided and "int" takes the truncated integer of the expression. Each axis is divided into n_r equal segments. A plane going through each division is cut perpendicular to the axis. Planes which cut through the x, y, and z axis intersect to form new boxes whose sides are at most l_{max} long. Each box created that overlaps with any part of the original element is "ANDed" with the original element using boolean algebra. This creates a new element in the discretized model. This algorithm discretizes all elements in this "rectangular" manner and may create "strange" or very small new elements. If an element from the original model has a convex surface, this discretization scheme is undesirably susceptible to creating elements that are in two discontiguous pieces. In this case, increasing the discrete resolution will reduce this anomaly.

Thermal Network Parameter Computation

A Monte Carlo technique is employed to determine volumes, surface areas, conductive resistances, and radiative resistances. For each element, **I**, a sphere is found which completely surrounds the element. The sphere is found by determining the minimum and maximum coordinates for each primitive in the element (an element can be composed of several primitives which are "ANDed" and "ORed" together). The maximum coordinate for the element is determined by the maximum coordinate of all element primitives that are "Ored" and the minimum maximum coordinate for all the primitives that are "ANDed". The minimum coordinate for the element is found similarly.

Note that this technique is very simply and efficiently evaluated but does not necessarily find the smallest sphere containing the element, which may be extremely complex.

The radius of this sphere is determined by,

$$R_{sphere} = \frac{\sqrt{(x_{max} - x_{min})^2 + (y_{max} - y_{min})^2 + (z_{max} - z_{min})^2}}{2} \tag{2}$$

The center of the sphere is located at the average coordinate,

$$x_c = \frac{x_{max} + x_{min}}{2}$$

$$y_c = \frac{y_{max} + y_{min}}{2} \tag{3}$$

$$z_c = \frac{z_{max} + z_{min}}{2}$$

The cross-sectional area through the center of the sphere is given by,

$$A_{cross} = \pi R_{sphere}^2 \tag{4}$$

Rays are shot in an inward random direction from a random location on the surface of the surrounding sphere. A total of n_{rays} are shot. The number of times a ray hits the surface of the element, n_{hits} is recorded. Every time a ray hits the surface of the element, there is one entrance and one exit point. For every hit, the distance traveled through the element from the entrance to the exit point, dL, is recorded. The total length traveled through the element is determined by summing the distances traveled through the element from each hit,

$$L = \sum_{i=1}^{n_{rays}} \sum_{j=1}^{n_{hits}(i)} dL_j \tag{5}$$

The volume of the element is determined by,

$$V_I = \frac{LA_{cross}}{n_{rays}} \tag{6}$$

The surface area of the element is determined by,

$$A_{s,I} = \frac{4\, n_{hits}\, A_{cross}}{n_{rays}} \tag{7}$$

For every entrance and exit point that a ray found, a ray is shot from that location on the surface of the element in the outward normal direction. The ray is tracked until it either hits another element or escapes to space. If the ray hits another element, k, the distance traveled to the element k is determined. If the distance traveled is less than a tolerance distance for conduction, the point

where the ray originated is located on a conductive surface. The number of times a point on a conductive area is found from the element I to element k, is collected in $n_{cond,k}$. If the origination point is located on a conductive surface, a ray is shot from that location in the inward normal direction until it exits the element. The distance traveled to the exit of element I is recorded in the array d_k. When the ray exits element I, a check is made to see if it conducts to the same element, k, at that location. If it does, d_k is divided by two. The distance to the conductive center from element I to k will be determined by half the average value of d_k. The reason d_k is divided by two if the ray conducts to element k on both sides of element I, is that instead of heat flowing through element I, heat will flow in the inward/outward direction from the element.

For every entrance and exit point found that is not located on a conductive area, the energy that is emitted from the element to all the other elements and space is found. A ray is shot in a random outward direction. The ray is given an initial energy weight, ω, of:

$$\omega = \sigma e_I \frac{2A_{cross}}{n_{rays}} \tag{8}$$

The ray is tracked until it either hits another element or escapes to space. If the ray escapes to space, the remaining weight, ω, is added to $E_{space,I}$ and the ray is terminated. If the ray hits an element, k, the energy deposited in $E_{I\to k}$ is determined by,

$$E_{I,k} = E_{I,k} + e_k \omega \tag{9}$$

The weight of the ray is reduced by the energy deposited in the element it hit,

$$\omega = \omega - e_k \omega \tag{10}$$

The ray continues in a random direction from the point it hit on element k until an exit criteria is met. Exit criteria are in the form of a maximum number of reflections made by the ray and fraction of original weight left in the ray.

The thermal network from element I to all other elements and space is determined. For every element k that element I conducts to, the conductive area between I and k is found by,

$$A_{cond,I\to k} = \frac{2\, n_{cond,k}\, A_{cross}}{n_{rays}} \tag{11}$$

The average length, $l_{ave,I\to k}$, from the "center" of element I that is normal to the conductive area, $A_{cond,I\to k}$ is found by,

$$l_{avg,I\to k} = \frac{1}{2n_{cond,k}} \sum_{i=1}^{n_{cond}(k)} d_i \tag{12}$$

The non-linear radiative conductance (inverse of resistance) from element I to element k is contained in $E_{I\to k}$.

Upon completion of this algorithm for every element, the arrays from i to j and j to i are combined. Since the conductive area between element i and j is computed separately for element i and element j, they must be combined. A weighted average between the two areas is taken. They are weighted by the cross-sectional area of the other's surrounding cylinder,

$$w_1 = \frac{A_{cross,j}}{A_{cross,i} + A_{cross,j}}$$

$$w_2 = \frac{A_{cross,i}}{A_{cross,i} + A_{cross,j}} \tag{13}$$

$$A_{ij} = w_1 A_{cond,i-j} + w_2 A_{cond,j-i}$$

The conductive resistance from element i to element j can then be determined by,

$$R_{cond,i-j} = \frac{l_{avg,i-j}}{k_{therm,i} A_{ij}} \tag{14}$$

where k_{therm} is the thermal conductivity. The "resistive" conductor between element i and element j is found by adding the two resistors in series from the elements to the conductive area,

$$R_{i-j} = R_{i-j} + R_{j-i} \tag{15}$$

The conductive heat flow between element i and j is then found by taking the inverse of the resistance.

To find the radiative heat flow between element i and j, a weighted average between E_{i-j} and E_{j-i} is taken. They are weighted the same way as the areas,

$$E_{ij} = w_1 E_{i-j} + w_2 E_{j-i} \tag{16}$$

Environmental Simulation

Environmental simulation is accomplished using a standard orbital code which reads the orbital elements and epoch of the satellite and writes the satellite ephemeris to a data file. This information includes the direct solar flux and direction, the earth shine flux, the solar albedo flux and the orientation of the satellite with respect to the earth.

Application of External Fluxes & Internal Heat Generations

The direct sun, laser flux, and earth albedo are modeled as collimated loads. Although the earth albedo is by no means collimated, this model is implemented for computational simplicity. This model does conserve the energy of the earth albedo, primarily making the gross approximation in the directional distribution.

Earthshine is modeled in a distributed fashion. The distributed earthshine is modeled as originating from a flat earth disk, broken into 13 sections of equal area. Each area radiates one thirteenth of the total earth flux on the space object. The disk radius is defined as,

$$r_d = r_e \sin\theta \tag{17}$$

where

$$\theta = a\tan\sqrt{\alpha^2 + 2\alpha} \tag{18}$$

and

$$\alpha = \frac{altitude\ of\ satellite}{r_e} \tag{19}$$

and r_e is the IR apparent radius of the earth,

$$r_e = 6378.2\ km + 30\ km(IR\ apparent\ atmosphere) \tag{20}$$

The disk is broken into an inner disk, a four-piece middle annulus, and an eight-piece outer annulus.

The area of each of the thirteen sections is,

$$A_{section} = \frac{\pi R_d^2}{13} \tag{21}$$

The radius of the inner circle is,

$$r_{inner} = \frac{r_d}{\sqrt{13}} \tag{22}$$

The outer radius of the middle annulus is,

$$r_{middle\ annulus} = r_d\sqrt{\frac{5}{13}} \tag{23}$$

The middle annulus is sectioned at 0, 90, 180, and 270 degrees. The outer annulus is sectioned at 0, 45, 90, 135, 180, 225, 270, and 315 degrees.

The effective directions for each section to impinge the satellite is modeled deterministically as coming from a point at the center of each sector. The center is defined by the area average radius for the annulus sectors and the center of the circle for the inner circle sector. Each direction is assigned one thirteenth of the total earthshine flux.

The flux and direction of all external loads are applied to the solid model by ray tracing. Currently only first-incidence actions of externally applied loads are modeled. The absorbed flux going into each element is numerically evaluated by ray tracing the entire model in a semi-systematic uniform grid. The grid is defined by the square which surrounds the circle defined by the model-enveloping sphere. The enveloping sphere is defined as the sphere centered on the models bounding rectangular box with a radius extending to the bounding box's corner. Ray tracing is accomplished through a user-specified mesh size.

The radiant heat transfer into each element from loads other than laser loads is calculated by multiplying the number of hits on the element, the area each ray represents, the spectral (or banded) absorptivity of each element, and the uniform incident flux of the load. Since laser loads do not have

uniform flux, the laser model employs rays with an energy equal to its representative area times the radial variation of flux according to the gaussian laser profile,

$$q = q_p \, e^{-\left[\frac{r^2}{2\sigma^2}\right]} \tag{24}$$

where q_p is the peak flux (central intensity) of the laser, r is the radial distance from the ray being traced to the aim point of the target, and σ is the Gaussian deviation parameter for characterizing the spot size.

Internal Heat Generations

Internal loadings can be specified as a constant heat generation or an on/off thermal control heat generation. The internal heats are assigned to the geometry model's original elements before discretization and are then distributed to the discrete elements based on mass fraction.

Data Reformat to SINDA Input Deck

Upon completion of the four previous processes, all necessary data to perform thermal analysis now exists. The data is formatted to a SINDA compatible input deck and subsequently submitted to the SINDA process. This reformatting operation allows the use of both temperature dependent or independent material properties. The option to cyclically repeat a single orbit is also allowed. Any of the SINDA transient solution schemes may be used as well as the steady state solvers.

SAMPLE CASES

Conductive Model Validation

Case 1: Solid Cube with a Zero Temperature Boundary Condition

Two samples cases were created to test the validity of the conduction method, the first sample case is a box with sides length 5 cm. The temperature of the box is initially 100 K when a zero temperature is imposed at the boundary for times greater than 0. In order to apply the above algorithms, a thin shell .1 cm thick is modeled around the box. The analytical solution for a box with sides of 5 and 5.1 cm is compared to the solution predicted by the algorithms for different mesh sizes in Table 1. In the table, n is the number of divisions in the x, y, and z directions.

As the mesh size gets finer (n gets larger), the algorithms approach the analytical solution with the exception of the finest discretization. The final column in Table 1 shows a divergent behavior as the number of divisions was increased to 17 in each direction. This is probably caused by numerical round-off errors.

Case 2: Sphere with a Zero Temperature Boundary Condition

The second sample case is a sphere with radius 5 cm initially set to 100 K when a zero temperature is imposed at the boundary for times greater than 0. Again, in order to apply the above algorithms, a thin shell 0.1 cm thick is modeled around the sphere. The analytical solution for the sphere with radii of 5 and 5.1 cm is compared to the solution predicted by the algorithms for different mesh sizes in Table 2.

Table I Comparison of the temperature at the center of the box between the analytical solution and the numerical approximation

time (s)	anal (5cm)	anal (5.1cm)	n=3	n=6	n=9	n=11	n=17
1	69.8	72.0	88.2	79.7	74.2	71.6	73.8
2	26.9	29.0	33.2	21.7	29.8	28.8	30.4
3	9.8	11.0	0.0	7.4	11.2	10.9	11.7
4	3.5	4.1	0.0	2.3	4.2	4.1	4.5
5	1.3	1.6	0.0	0.7	1.6	1.5	1.7
6	0.5	0.6	0.0	0.2	0.6	0.6	0.7
7	0.2	0.2	0.0	0.1	0.2	0.2	0.3
8	0.1	0.1	0.0	0.0	0.1	0.1	0.1

Radiative Transfer Validation

In order to validate the radiative transfer model, a simple test geometry was constructed using the solid geometry modeling software. A 6 sided hollow box was created 3 x 4 x 5 cm in internal dimensions x, y and z respectively. Note that the radiative transfer mechanism accounts for both internal and external radiative heat transfer, so it was necessary to ensure that this box was constructed with no external view factors. Two methods were used to compute the radiative heat transfer coefficients.

The first method involved using a 6 facet analytical model for 6 simple view factors. This method assumes uniform distribution of all irradiance and radiosity. The method of Gebhart was used to find the radiative interchange factors and the K_{rad} matrix.

The second method involved discretizing each face of the box and numerically computing view factors for each small element within the faces. Upon determining the hundreds of view factors, the method of Gebhart was used to compute the radiative transfer factors. The large matrix of radiative interchange factors then had to be summed over each face using the appropriate summation principles. Note that the AutoSINDA algorithms inherently model the second case more accurately as it does not assume the uniform irradiance and radiosity distribution.

The two distinct methods were chosen to allow complete comparison, knowing that the second method models the radiative transfer more accurately. Table 3 summarizes the model of the 6 sided box and its 300K broad band radiative properties.

Case 1: 6 Node Analytical Radiative Transfer

The internal radiative interchange factors for this geometry, K_{rad}, were computed using a simple 6 node view factor analysis of the 6 sides of the box. This was done analytically using the view factor formula for two right plates with a common edge. The method of Gebhart was used to

Table II Comparison of the temperature at the center of a sphere between the analytical solution and the numerical solution

time (s)	anal (5.0)	anal (5.1)	n=4	n=6	n=11	n=13
1	99.6	99.7	93.3	97.1	99.4	99.5
2	88.7	90.0	78.5	84.7	91.1	91.2
3	68.9	71.2	62.8	68.5	75.1	74.9
4	50.6	53.2	49.2	53.2	58.3	57.9
5	36.5	38.9	38.0	40.5	44.2	43.7
6	26.1	28.2	29.2	30.6	33.1	32.6
7	18.6	20.4	22.4	22.9	24.6	24.2
8	13.3	14.7	17.1	17.2	18.3	17.9
9	9.5	10.6	13.1	12.9	13.6	13.3
10	6.7	7.7	10.0	9.6	10.1	9.8
11	4.8	5.5	7.6	7.2	7.5	7.3
12	3.4	4.0	5.8	5.4	5.6	5.4
13	2.4	2.9	4.4	4.0	4.1	4.0
14	1.7	2.0	3.4	3.1	3.1	3.0

mathematically compute the radiative interchange factors and the resultant K_{rad} matrix.

Case 2: 6 Node, Discretized Radiative Transfer

The internal radiative transfer was modeled by discretizing each face of the box. Ideally this will increase the accuracy of the radiative interchange. However, since the AutoSINDA radiative transfer algorithms only tabulate this data in the 6x6 matrix, this very large set of data had to be summed over the subelements within each face to back out the net radiative interchange for each of the six faces.

Radiative Transfer Validation Results

AutoSINDA was executed on the 6 sided solid geometry model using 10 thousand rays per element, allowing a maximum of 30 reflections per ray. A mixed mode reflective model was chosen allowing both photon analog radiative transfer propagation as well as the continuous ray progression. The execution time for this case is on the order of 30 seconds wall clock time for a SunSPARC 10.

Table III Physical Model of the 3x4x5 cm Box for Validation

Box Face	Outward Normal	Face Area, cm^2	Material	Broadband Emissivity
1	-X	20.0	Cast Aluminum Alloy, Type 360	0.200
2	+X	20.0	Aluminized Kapton 1, Kapton side out	0.740
3	-Y	15.0	Carbon Black Tedlar Film	0.800
4	+Y	15.0	Highly Reflective Aluminum Alloy, 2024-Al	0.030
5	-Z	12.0	White Paint, Chemglaze A276	0.881
6	+Z	12.0	Black Paint, Chemglaze A382	0.975

Table IV shows the results of AutoSINDA in comparison to both of the methods described above. Overall, the mean deviation for the six node view factor method is about 4% with a maximum deviation of 24%, so the comparison against the simple 6 node model is quite unacceptable.

However, using the more accurate many node model, the mean deviation falls to only 2% with a maximum deviation on the order of 5%, an increase of almost 5 times the accuracy. Hence it is concluded that the AutoSINDA algorithms compare very well with the more accurate method of computing the radiative transfer.

SAMPLE OF COMPLICATED GEOMETRY

As a sample of a complicated geometry, Figure 2 shows a spiral antenna attached to a flat plate which has been subjected to orbital and laser loadings. This example is not presented to compare to analytical or measured data, but merely to show the range of applications and the usefulness of data visualization.

Table IV Results of the Radiative Transfer Validation

Box Faces	AutoSINDA Results K_{rad} [W/K⁴]	Analytic Results			
		6 Surface Elements		600 Surface Elements	
		K_{RAD}	%ϵ	K_{RAD}	%ϵ
1-2	7.06995×10^{-12}	7.22104×10^{-12}	2.14	7.16098×10^{-12}	1.29
1-3	5.04044×10^{-12}	5.10710×10^{-12}	1.32	5.10193×10^{-12}	1.22
1-4	1.65488×10^{-13}	1.68235×10^{-13}	1.66	1.73681×10^{-13}	4.96
1-5	4.52019×10^{-12}	4.55183×10^{-12}	0.70	4.56767×10^{-12}	1.05
1-6	4.87479×10^{-12}	5.09267×10^{-12}	4.47	5.06076×10^{-12}	3.82
2-3	2.11906×10^{-11}	2.18800×10^{-11}	3.26	2.17028×10^{-11}	2.42
2-4	7.23058×10^{-13}	7.20755×10^{-13}	-0.32	7.32650×10^{-13}	1.33
2-5	1.90117×10^{-11}	1.95011×10^{-11}	2.58	1.93365×10^{-11}	1.71
2-6	2.09295×10^{-11}	2.18181×10^{-11}	4.25	2.14510×10^{-11}	2.49
3-4	5.39125×10^{-13}	5.66541×10^{-13}	5.09	5.40254×10^{-13}	0.21
3-5	1.47630×10^{-11}	1.56077×10^{-11}	5.72	1.53137×10^{-11}	3.73
3-6	1.68516×10^{-11}	1.74621×10^{-11}	3.63	1.69953×10^{-11}	0.85
4-5	5.11129×10^{-13}	5.14137×10^{-13}	0.59	5.19854×10^{-13}	1.71
4-6	5.64379×10^{-13}	5.75225×10^{-13}	1.92	5.75496×10^{-13}	1.97
5-6	1.10285×10^{-11}	1.36538×10^{-11}	23.8	1.12036×10^{-11}	1.5

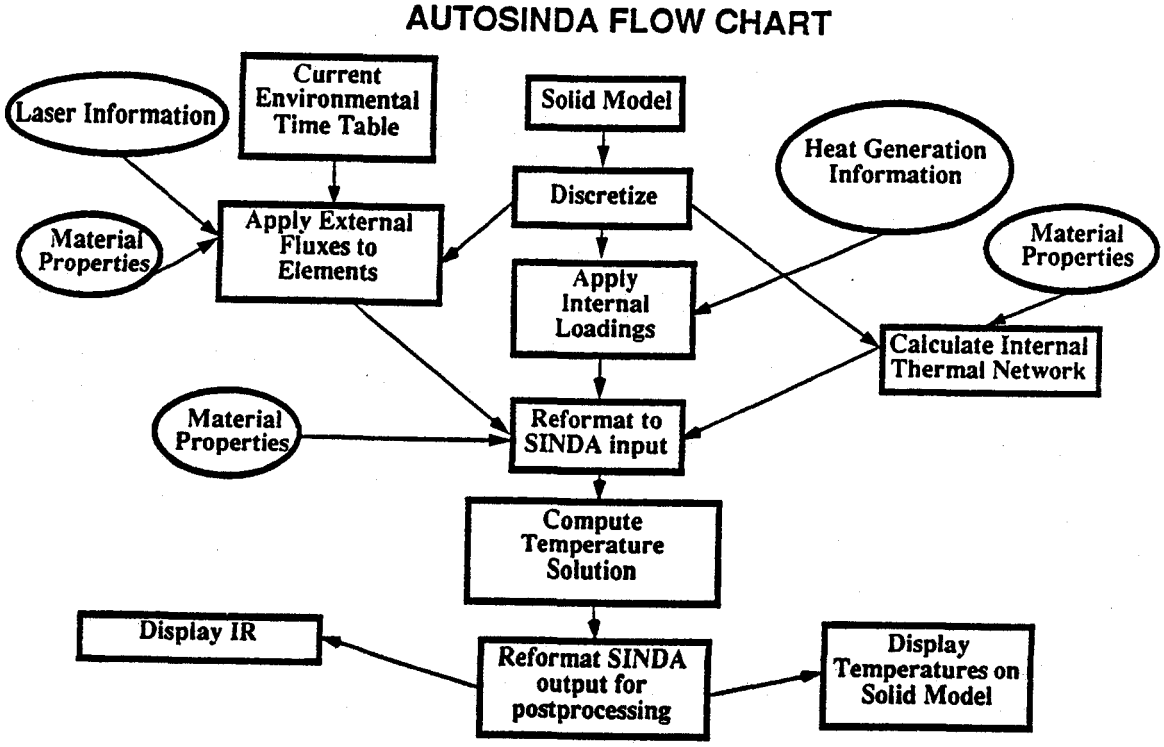

Figure 1. Flow Chart of the AutoSINDA Process.

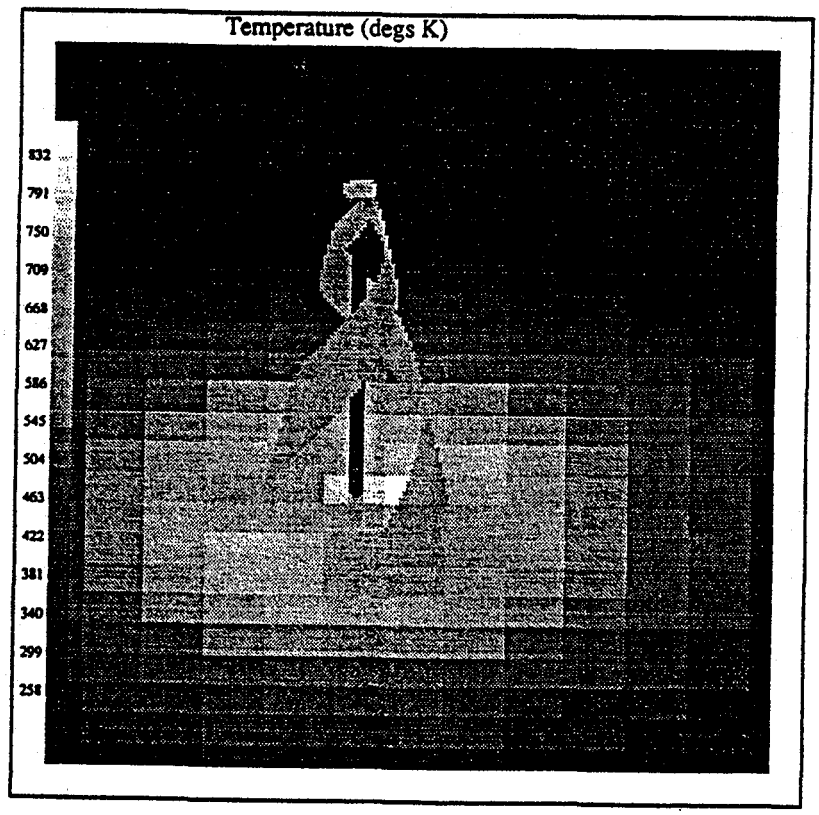

Figure 2. Temperature profile of a spiral antenna mounted on a flat plate with an applied laser flux.

CONVECTION EQUATION MODELING: A NON-ITERATIVE DIRECT MATRIX SOLUTION ALGORITHM FOR USE WITH SINDA

Dean S. Schrage
Sverdrup Technology Inc.
Lewis Research Center Group
Brook Park, Ohio 44142

ABSTRACT

The determination of the boundary conditions for a component-level analysis, applying discrete finite element and finite difference modeling techniques often requires an analysis of complex coupled phenomenon that cannot be described algebraically. For example, an analysis of the temperature field of a coldplate surface with an integral fluid loop requires a solution to the parabolic heat equation and also requires the boundary conditions that describe the local fluid temperature. However, the local fluid temperature is described by a convection equation that can only be solved with the knowledge of the locally-coupled coldplate temperatures. Generally speaking, it is not computationally efficient, and sometimes, not even possible to perform a direct, coupled phenomenon analysis of the component-level and boundary condition models within a single analysis code. An alternative is to perform a disjoint analysis, but transmit the necessary information between models during the simulation to provide an indirect coupling. For this approach to be effective, the component-level model retains full detail while the boundary condition model is simplified to provide a fast, first-order prediction of the phenomenon in question. Specifically for the present study, the coldplate structure is analyzed with a discrete, numerical model (SINDA) while the fluid loop convection equation is analyzed with a discrete, analytical model (direct matrix solution). This indirect coupling allows a satisfactory prediction of the boundary condition, while not subjugating the overall computational efficiency of the component-level analysis. In the present study a discussion of the complete analysis of the derivation and direct matrix solution algorithm of the convection equation is presented. Discretization is analyzed and discussed to extend of solution accuracy, stability and computation speed. Case studies considering a pulsed and harmonic inlet disturbance to the fluid loop are analyzed to assist in the discussion of numerical dissipation and accuracy. In addition, the issues of code melding or integration with standard class solvers such as SINDA are discussed to advise the user of the potential problems to be encountered.

NOMENCLATURE

C	=	Courant Number ($U \Delta t / \Delta x$)	
C_p	=	specific heat	(W s / kg °C)
e	=	total specific energy	(W s / kg)

E_∞	=	global error	
G	=	thermal conductance	(W / °C)
h	=	enthalpy	(W s / kg)
h^*	=	effective heat transfer coefficient	(W / m^2)
H	=	enthalpy flux	(W)
k	=	thermal conductivity	(W / m °C)
L	=	total tube length	(m)
$\dot{m}$	=	mass flowrate	(kg / s)
P	=	pressure	(N / m^2)
$\dot{Q}$	=	heat load	(W)
t	=	time	(s)
T	=	temperature	(°C)
$\tilde{T}$	=	temperature, actual equation solved	(°C)
u	=	specific internal energy	(W s / kg)
U	=	flow velocity	(m / s)
x	=	space	(m)

Greek

α	=	thermal diffusivity ($k / \rho C_p$)	(m^2 / s)
α^*	=	effective thermal diffusivity flux	(s^{-1})
Δ	=	denotes difference	
ρ	=	density	(kg / m^3)
τ	=	fluid transit time	(s)

Superscripts and Subscripts

i	=	space increment
j	=	time increment

INTRODUCTION

The process of convection (or advection) involves the transport of a scalar property within the confines of a motive flow, traveling a finite velocity. If the convected quantity represents the fluid enthalpy (or temperature as will be shown), then energy is transported by the convection of the fluid at a particular enthalpy and flow velocity. In this case, a disturbance in the inlet temperature (enthalpy) would be convected along the length of a conduit in space and time. By constructing a differential control volume and performing a transient energy balance, the first-order wave or convection equation can be derived by balancing heat addition with transient heating and convection enthalpy. Figure 1 shows the control volume with an inlet and outlet enthalpy flux (H) and differential heating (dQ) from a target sink surface (coldplate). The transient energy balance can be written according to:

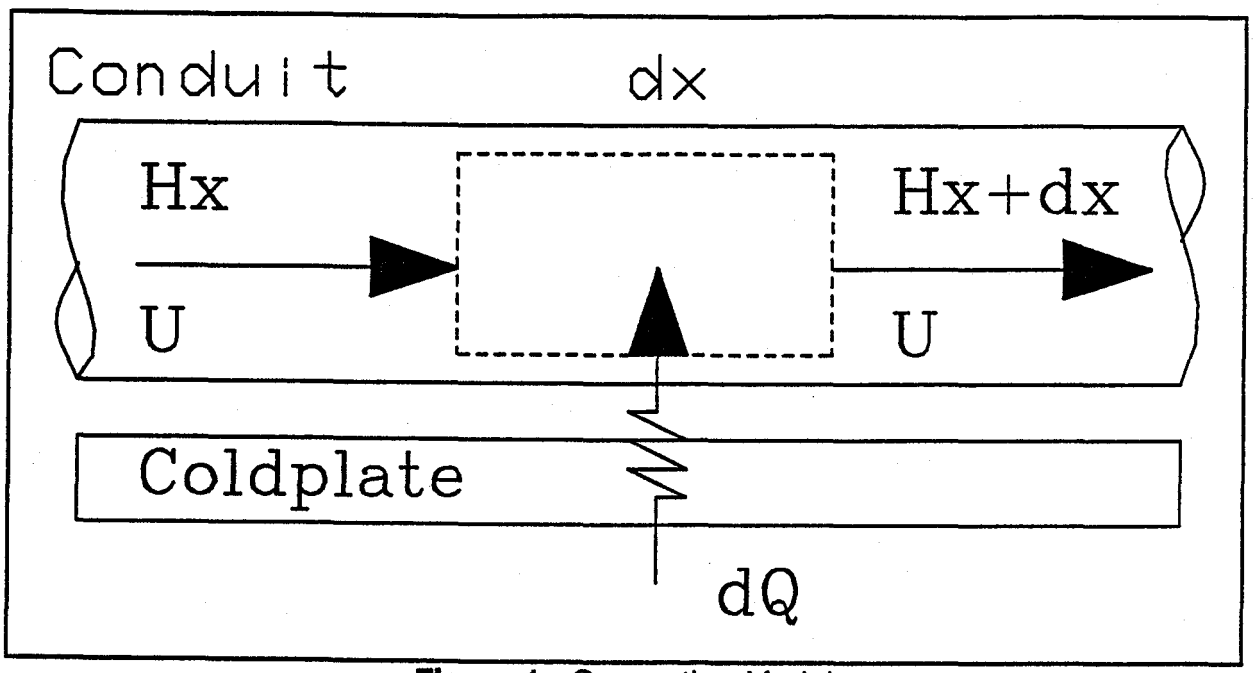

Figure 1. Convection Model

$$d\dot{Q} = \frac{\partial}{\partial t}\int_{dM} e\, dM + H_{x+dx} - H_x \qquad (1)$$

$$d\dot{Q} = d\dot{Q}_T + d\dot{Q}_A$$

Terms e, H, dQ are the total specific energy, enthalpy flux and total heat conduction respectively. The total specific energy is the sum of the internal, kinetic and potential energies while the enthalpy flux is a product of the local mass flowrate and local flow enthalpy. Terms dQ_T and dQ_A are transverse and axial heat conduction terms, respectively. The transverse heat conduction term represents the conduction into the control volume from the local coldplate, while the axial heat conduction term represents the net heat conduction into the control volume from the upstream and downstream fluid layers. Generally, the axial heat conduction term is assumed to be small in comparison to the convection process and for the present study, axial conduction is neglected[1]. The above terms can be expanded according to:

---

[1] *By normalizing the equations, assuming the convection term is of the same magnitude as the capacitance term, it can be shown that the axial conduction term will be negligible provided that:*

$$\frac{\tau K}{L^2 \rho C} = \frac{\tau \alpha}{L^2} \ll 1$$

For the present study this ratio is approximately 0.1.

$$H_{x+dx} - H_x = \dot{m}h_x - \left(\dot{m}h_x + \frac{\partial \dot{m}h}{\partial x}dx\right)$$

$$e = u + KE + PE$$

$$u = h - \frac{P}{\rho} \qquad (2)$$

$$d\dot{Q} = dG\,(T_\infty - T)$$

At this point it is appropriate to make several simplifying assumptions. First, we can generally neglect changes in kinetic and potential energy. Next, if we assume an incompressible fluid, then the pressure dependence can be eliminated and we can formulate a simple state equation to relate enthalpy to temperature. With this, Eqns. 1 and 2 can be combined to yield:

$$\frac{\partial T}{\partial t} + U\frac{\partial T}{\partial x} = \alpha^*(T_\infty - T)$$

$$U = \frac{L}{\tau} \qquad (3)$$

Equation 3 is the first-order convection equation that describes the local fluid temperature (T) as a function of both time and one-dimensional space along the length of the conduit. Parameters U and α^* are the fluid flow velocity and effective thermal diffusivity flux, respectively, and is a compact notation to describing the relevant features of the convection process (geometry, flow velocity and coldplate coupling, thermal-physical properties). The effective thermal diffusivity flux is written:

$$\alpha^* = \frac{h^* D_H L}{\tau \dot{m} C} \qquad (4)$$

This parameter describes the relative strength of the thermal coupling between the tube and the local sink surface. For Example, when $\tau \rightarrow 0$, the energy transport is dominated by local conduction to the sink; when $h^* \rightarrow 0$, the energy transport is dominated by fluid convection.

In its appearance, Eqn. 3 is linear, in-homogeneous[2] with constant coefficients and should yield to an analytical solution.[3] However, as addressed in the abstract, the present

---

[2] *The equation is in-homogeneous because of the presence of the source term, T_∞ which varies in time and space.*

[3] *An inhomogeneous ordinary differential equation can be described along a characteristic line ($\Psi = x - Ut$) and solved specifically for those regions where either the initial conditions or the boundary conditions effect the solution.*

study deals with the feature of a coupled boundary condition. The source term in Eqn. 3 is determined from the coupled boundary condition of the local coldplate temperature.[4] Thus the source term cannot be decoupled from the dependent variable - at least not analytically. This interdependence between boundary conditions is the impetus for the present study - to develop a suitable means to coordinating a solution of Eqn. 3 with the boundary conditions (coldplate temperatures) put forth from a discrete finite difference model.

ANALYSIS

If, because of the coldplate coupling, that analytical solutions to Eqn. 3 are intractable, we must resort to a numerical solution, preferably a finite difference technique. Consider then a discrete numerical approach. Equation 3 appears innocuous. The partial derivatives are first order, not mixed and the equation is linear. It would be desirable to develop an explicit discrete equation, or discretization, that would not require iteration at each time step - this in order to generate a rapid disjoint solution discussed in the abstract. To satisfy this, we could use forward differencing in time and central differencing in space:

$$\frac{\partial T}{\partial t} \approx \frac{T_i^{j+1} - T_i^j}{\Delta t}$$
$$\frac{\partial T}{\partial x} \approx \frac{T_{i+1}^j - T_{i-1}^j}{2\Delta x} \qquad (5)$$

Superscripts (j) indicate time and subscripts (i) indicate space. Substituting Eqns. 5 into Eqn. 3, and assuming for the sake of convenience that the fluid loop is thermally decoupled from the coldplate ($\alpha^* = 0$), we can write the discrete difference equation (kernel):

$$T_i^{j+1} = T_i^j + \frac{C}{2}(T_{i+1}^j - T_{i-1}^j)$$
$$C = \frac{U\Delta t}{\Delta x} \qquad (6)$$

This kernel is referred to as the Euler forward, centered difference (EFCD). Equation 6 is explicit such that we solve for the future time (j+1) temperatures based on old (j) values, so the numerical solution would consist of a simple marching scheme. Without the need for iteration, the EFCD kernel is computationally efficient. However, this is not a sufficient criteria to select this kernel - above all, the scheme must also be numerically stable. We can evaluate stability in a macroscopic manner by computing the

---

[4] *The coldplate temperature is given from the solution of the parabolic heat equation with the boundary conditions determined from the local fluid temperature.*

actual equation solved by the discrete representation of Eqn. 6. We do this by letting the discrete values interpolate the continuous values of an effective temperature ($\tilde{T}$), where $T_i^j \rightarrow \tilde{T}(t_j, x_i)$. If we expand, in a Taylor series, those discrete values away from i,j, then the actual equation solved is simply the original convection equation with a remainder term:

$$\frac{\partial \tilde{T}}{\partial t} + U\frac{\partial \tilde{T}}{\partial x} = -\frac{U^2 \Delta t}{2}\frac{\partial^2 \tilde{T}}{\partial x^2} + Order(\Delta t^2, \Delta x^2) \qquad (7)$$

The remainder term is composed of a second partial of T with respect to x (and other higher order mixed partials). This term is exactly representative of axial diffusion or conduction, but it is numerically generated and not physical. It is true that the magnitude of the axial conduction is small for a small value of Δt, but the fact that the leading coefficient is negative results in a solution that will always grow without bound after a finite number of recursive solutions of Eqn. 6. Thus, the Euler forward, centered difference kernel (Eqn. 6) is unstable and should not be used.

While the use of Taylor series to determine the actual equation solved is a suitable approach to eliminate those kernels that create deleterious artificial phenomenon, there are more sophisticated approaches to determining the subtleties of numerical stability of a differencing kernels (Strauss, 1992). These techniques are used to analyze some 12 difference kernels applied to the one-dimensional convection equation in Anderson et al. (1984); some general conclusions from the Anderson et al. study are:

- all differencing kernel possess inaccuracy as a result of truncation error
- truncation error creates numerical dissipation and dispersion phenomenon[5]

Crank-Nicolson Kernel

Selection of a kernel requires a careful trade of the computational requirements (explicit versus implicit solutions) and the effects of the spurious numerical phenomenon weighed against the assumptions applied to the system at hand[6]. In the present study, we desire a kernel that will produce a negligible dissipation and will require a minimum of computation. The former criteria tends to associate with implicit, centered point kernels, while the latter criteria, with non-iterative explicit kernels.

The Crank-Nicolson centered-difference (CNCD) kernel is implicit, can be

---

[5] *Dissipation results from even order partial derivative terms and has the effect of introducing a spurious axial conduction. Dispersion results from odd order partial derivative terms and has the effect of changing the phase relationships between waves. The combination of dissipation and dispersion is terms diffusion (Anderson et al., 1984).*

[6] *To elaborate, one should weigh the assumptions made in the analysis with the noted effects created by the kernel. For example, if the convection equation is derived by neglecting an axial conduction term, then a comparable amount of spurious dissipation would be considered acceptable. However, it is difficult to determining the magnitude of the injected numerical dissipation.*

described in a matrix form suitable for a direct matrix inversion and possess second order accuracy in time and space. The kernel is formed analogous to the EFCD kernel above, but includes a present-time space difference for stability:

$$\frac{\partial T}{\partial t} \approx \frac{T_l^{j+1} - T_l^j}{\Delta t}$$

$$\frac{\partial T}{\partial x} \approx \frac{\dfrac{T_{l+1}^{j+1} - T_{l-1}^{j+1}}{2\Delta x} + \dfrac{T_{l+1}^{j} - T_{l-1}^{j}}{2\Delta x}}{2} \qquad (8)$$

The actual equation solved by the CNCD kernel creates numerical dispersion, (a remaining odd-ordered partial derivative term), but is unconditionally stable for any time step.

At this point, we have discussed the development of the kernel with a constant space incremental (Δx). We can generalize the CNCD kernel to apply a variable spatial step size[7]. We begin by creating a differencing scheme to approximate the space derivative with varying step size according to:

$$\frac{df}{dx} \approx a\, f_{l-1} + b\, f_l + c\, f_{l+1} \qquad (9)$$

[7] *This is necessary in order to simulation fluid networks that have variable sized nodes - a feature in the present study.*

The leading coefficients, a, b, c are determined by applying a Taylor series expansion to approximate the function away for the discrete local i values[8]:

$$a = \frac{-1}{\Delta x_1(1+R)}$$

$$b = \frac{1 - R^2}{\Delta x_1(1+R)}$$

$$c = \frac{R^2}{\Delta x_1(1+R)} \qquad (10)$$

$$R = \frac{\Delta x_1}{\Delta x_2}$$

$$\Delta x_1 = x_i - x_{i-1}$$

$$\Delta x_2 = x_{i+1} - x_i$$

By combining Eqns. 9, 10 with Eqn. 3, the extended CNCD kernel can be written:

$$A\,T_{i-1}^{j+1} + B\,T_i^{j+1} + C\,T_{i+1}^{j+1} = D\,T_{i-1}^{j} + E\,T_i^{j} + F\,T_{i+1}^{j} + \alpha^* T_{\infty,i}$$

$$A = \frac{a\,U}{2}$$

$$B = \frac{1}{\Delta t} + \frac{b\,U}{2} + \frac{\alpha^*}{2}$$

$$C = \frac{c\,U}{2} \qquad (11)$$

$$D = -A$$

$$E = \frac{1}{\Delta t} - \frac{b\,U}{2} - \frac{\alpha^*}{2}$$

$$F = -C$$

Equation 11 describes a system of discrete equations for each node (i = 1 to N). In order to apply the kernel over the discrete domain from i = 1 to N we need to perform a conditioning of the first and last equations. At the first node (i = 1), a boundary value of $T_{i-1=0}$ is required. This value is the specified inlet fluid temperature to the fluid loop (as a function of time). At the last node, the kernel requires a value of T_{N+1}, but this value does not exist. This is circumvented by simply adjusting the local values of the derivative

[8] *The details of this are excluded, but can be found in most treatise on numerical analysis techniques. Briefly, the method involves substituting the Taylor series expansions for each discrete value and observing the coefficients of each derivative terms. Three independent equations are created to solve for a, b, c.*

coefficients, a, b, c to apply a backwards-differencing in space at this last node[9]:

$$\begin{aligned} &\text{for } i=N \\ &\tilde{a} = \frac{-1}{\Delta x_1} \\ &\tilde{b} = \frac{1}{\Delta x_1} \\ &\tilde{c} = 0 \end{aligned} \tag{12}$$

We can now generate a tri-diagonal matrix equation according to:

$$\begin{bmatrix} B & C & & & & & \\ A & B & C & & & & \\ & A & B & C & & & \\ & & \bullet & \bullet & \bullet & & \\ & & & \bullet & \bullet & \bullet & \\ & & & & A & B & C \\ & & & & & \tilde{A} & \tilde{B} \end{bmatrix} \begin{bmatrix} T_1 \\ T_2 \\ T_3 \\ \bullet \\ \bullet \\ T_{N-2} \\ T_{N-1} \\ T_N \end{bmatrix}^{j+1} = \begin{bmatrix} E & F & & & & & \\ D & E & F & & & & \\ & D & E & F & & & \\ & & \bullet & \bullet & \bullet & & \\ & & & \bullet & \bullet & \bullet & \\ & & & & D & E & F \\ & & & & & \tilde{E} & \tilde{F} \end{bmatrix} \begin{bmatrix} T_1 \\ T_2 \\ T_3 \\ \bullet \\ \bullet \\ T_{N-2} \\ T_{N-1} \\ T_N \end{bmatrix}^{j} + \begin{bmatrix} \alpha^* T_{\infty,1} + D\,T_0^j - A\,T_0^{j+1} \\ \alpha^* T_{\infty,2} \\ \alpha^* T_{\infty,3} \\ \bullet \\ \bullet \\ \alpha^* T_{\infty,N-2} \\ \alpha^* T_{\infty,N-1} \\ \alpha^* T_{\infty,N} \end{bmatrix} \tag{13}$$

In compressed form, Eqn. 13 can be simplified and we can solve for the future time (j+1) values of temperature by multiplying both sides by the inverse of the leading matrix:

$$\begin{aligned} [M][T]^{j+1} &= [N][T]^j + [\tilde{T}_\infty] \\ [T]^{j+1} &= [M]^{-1}[N][T]^j + [M]^{-1}[\tilde{T}_\infty] \end{aligned} \tag{14}$$

At this stage, Eqn. 14 is usually solved numerically, typically with a Gauss-Siedel or an over-relaxation method. Under the best of conditions, either of these methods converge to a solution with a finite number of iterations with sucessive substitutions of pervious solutions. This process can be computationally expensive especially if the boundary conditions need to be updated frequently. Alternatively, because matrix M is sparse, square, tri-diagonal, we can apply a direct solution technique to determine M^{-1}. A well-established approach to finding the solution of Eqn. 14 is to use LU decomposition. Briefly, this technique involves creating lower and upper diagonal matrices that are manipulated to yield a direct solution with minimal storage requirements. Development

---

[9] *Because the backwards difference is only first order accurate in space at the last node, the overall order of the entire solution is somewhat less than second order - unfortunate indeed but unavoidable.*

of this method is quite standard and is excluded for the sake of brevity. The interested reader is referred to Gerald and Wheatly (1984).

The necessary conditions for the LU decomposition is that M must be diagonally dominant. This in effect, does pose a limit on the selection of time step Δt for a given Δx because these parameters describe the respective diagonals of M. Diagonal dominance will be observed if:

$$\left|\frac{1}{\Delta t} + \frac{b\,U}{2} + \frac{\alpha^*}{2}\right| \geq \left|\frac{a\,U}{2}\right| + \left|\frac{c\,U}{2}\right| \qquad (15)$$

In the special case of b = 0 (uniform node size) and $\alpha^* = 0$ (coldplate decoupled), Eqn. 15 can be more appropriately expressed as a function of the Courant number (C):

$$C = \frac{\Delta t\,U}{\Delta x} \leq 2 \qquad (16)$$

This restriction is mitigated by the fact that diagonally dominance will be enhance by coldplate plate coupling. Therefore, Eqn. 16 should be considered a rough criteria in selecting the time step. Regardless, the user should be aware that accuracy decreases with increasing time step, and so in general, C should be made as small as possible.

CASE STUDIES

In this section, the direct solution to Eqn. 14 is presented in both time and space for the cases of the inlet fluid temperature described by: a pulse function; a harmonic function. The pulse function will be used to demonstrate the features of spurious dispersion. The harmonic function, for which an exact solution exists, is used to determine the global error and method order. In both cases, the fluid is decoupled from the baseplate in which case we are solving the homogeneous convection equation. The space domain is divided into 100 equal sized nodes with C = 1.

Pulse Inlet Temperature

A pulse boundary condition is analogous to a sudden burst change in inlet fluid temperature for a finite length of time, then reverting back to the original pre-disturbance value. The pulse or square wave, in the absence of any dissipation, should retain its original shape and form along the characteristics. That is, the temperature disturbance should be convected at the velocity U and should retain the stepped nature of the original disturbance along lines where x - Ut is a constant. In this test, the magnitude and time duration of the pulse are both unity. Figure 2 presents a three dimensional plot of temperature versus time and space. The general trends indicate that the pulse does not dissipate forward into the flow as indicated by the sharp ridge that defines the leading characteristic. However, in regions behind or downstream of the pulse, the surface is

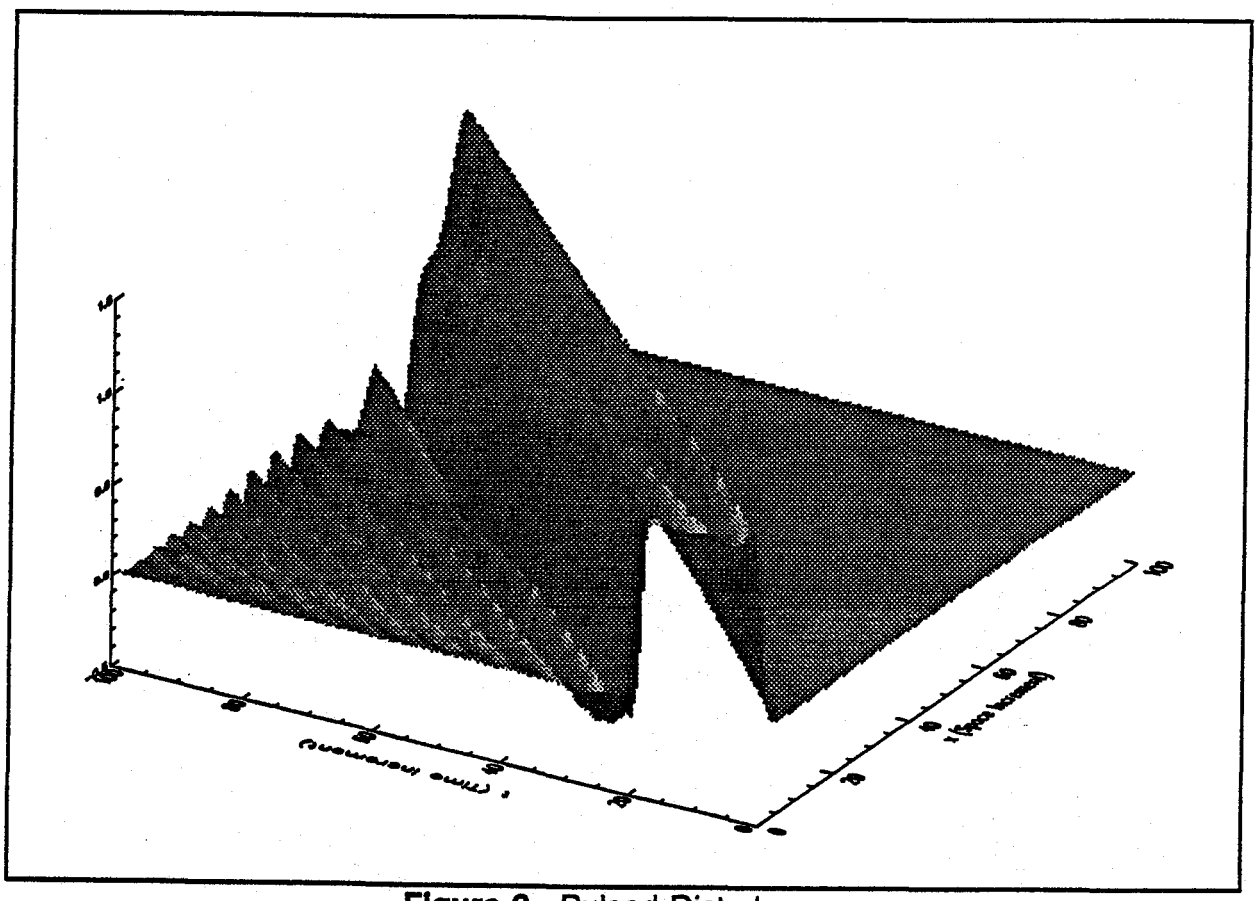

Figure 2. Pulsed Disturbance

wavy which means that there are residual effects of the disturbance that has since left the region. This is the result of dispersion, and is exacerbated by the fact that we have used a discontinuous step function for the disturbance.

Harmonic Inlet Temperature

A harmonic disturbance is useful to study from the standpoint of determining the global error and the overall method order. In this case we define the inlet temperature as $T_0 = \sin(2\,\pi\,t)$; the exact solution is given:

$$T(t, x) = \sin(2\,\pi(t - \frac{x}{U})) \qquad (17)$$

Figure 3 presents the time-space plot of temperature. We immediately see that dispersion of the waves is diminished in comparison to the pulse disturbance.

The global error (E_∞) of a method is the maximum absolute difference between the numerical and exact solutions. We can compute E_∞ for several values of Courant number to establish the dependence between discretization on accuracy. In general, the global error increases with Courant number as depicted in Figure 4. We can determine an approximate method order if we assume that the global error is a function of the time and

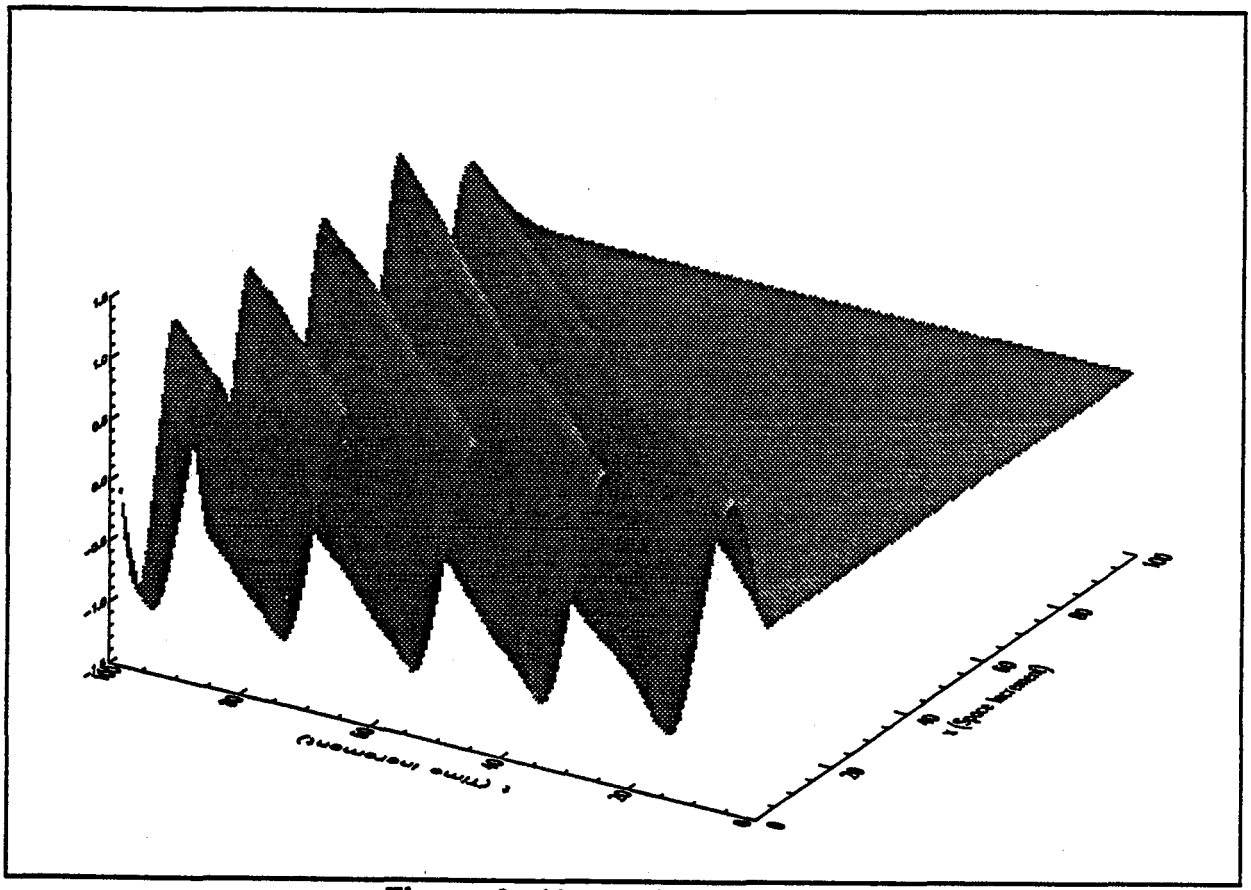

Figure 3. Harmonic Disturbance

space increments according to:

$$E_\infty \sim a\,\Delta t^P + b\,\Delta x^Q \tag{18}$$

For a constant space increment, we can rewrite Eqn. 19 as a function of the Courant number:

$$E_\infty = \bar{a}\,C^P + \bar{b} \tag{19}$$

Now if we have two successive values of E_∞ for corresponding values of C, and if we assume the coefficients $\bar{a}$, $\bar{b}$ do not change for the small change in C, then we can compute the method order P according to:

$$P = \frac{\log(E_{\infty,1}) - \log(E_{\infty,2})}{\log(C_1) - \log(C_2)} \tag{20}$$

Equation 20 predicts a nominal value P = 1.8. This means that the overall order of the method is slightly less than second order. This is expected because a backwards

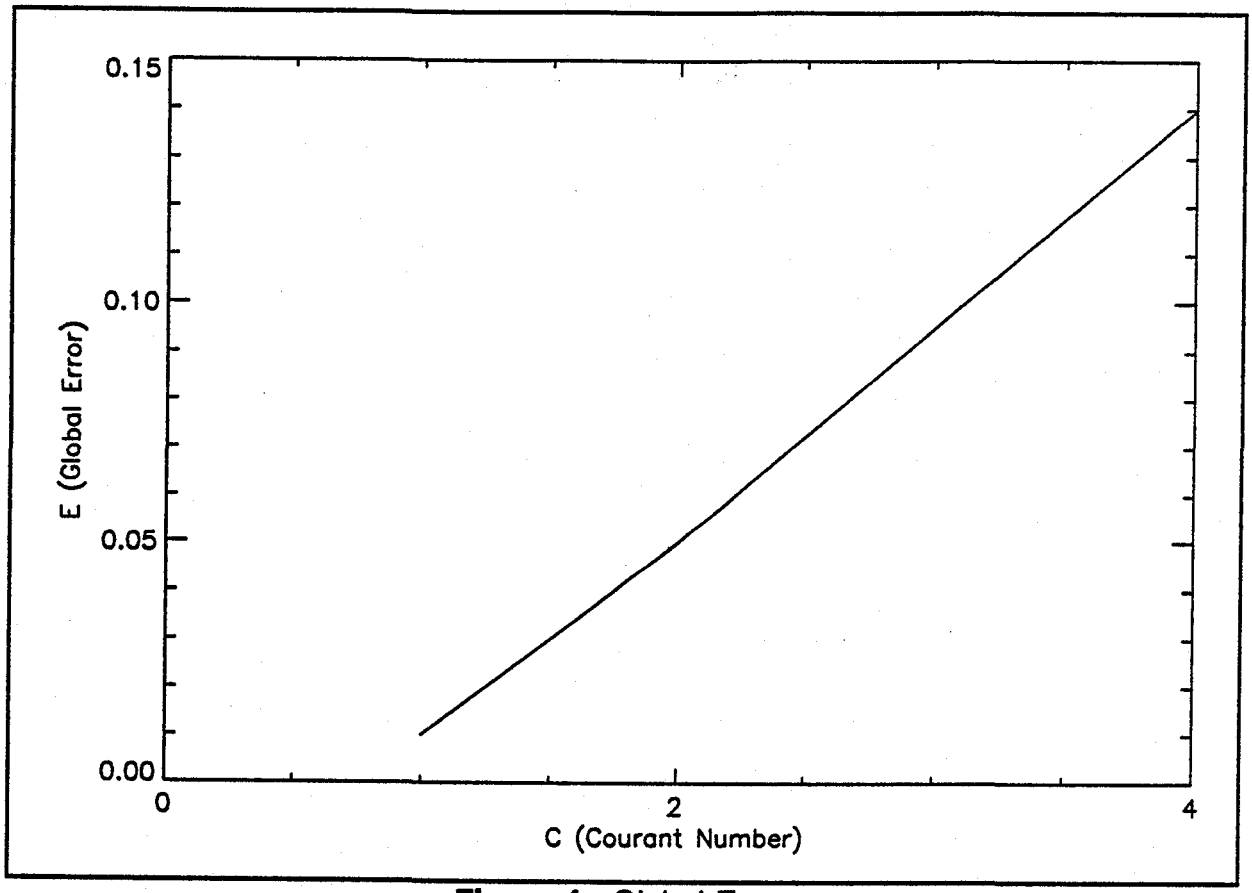

Figure 4. Global Error

difference kernel, of first order accuracy, is applied at the node N. First order inaccuracies generated at the last node tend to propagate into the solution domain, reducing the overall solution order. Overall, a specified method order should be considered approximate and will yield to the practical considerations of discretization and the application of boundary conditions.

MELDING WITH STANDARD CLASS SOLVERS

The CNCD solution algorithm with LU matrix decomposition routine was programmed in FORTRAN in a structured subroutine form. The inputs to the code are the time, time step (Courant number), appropriate geometry and thermal physical properties and boundary and initial conditions (coldplate and inlet fluid temperatures respectively). The code can be executed independently to return a temperature array describing the local time and space values of the fluid temperature. This would be an acceptable output as a utility routine if the code could be melded and referenced (called) within a standard class solver such as SINDA. Of this melding or integration, there are several important considerations that the user must be aware of:

- clashing of variable names between the convection code and the general purpose code (SINDA)

- creating common blocks required by the convection routine and defining global parameters

- conversion of absolute and relative node locations to the temperature values in array format to be referenced[10]

Without elaboration, these above problems with code melding are considered rudimentary and can be managed with careful programming. However, the most important consideration is that of time-step synchronization.

Standard solvers that analyze transient phenomenon, have internal discretization structures, similar to those of the present study, but are typically removed from the user. Removed in the sense that the local variables are not known, these discretization structures select the appropriate time step during the simulation to ensure a specified accuracy. Because the present algorithm is not an integral accessory to the standard solver, the time and time-step of the standard solver must be sampled during a melded simulation between solver and convection equation algorithm. Ideally, we desire to make a single subroutine call to the convection code to update the boundary conditions. However, as observed from the present study, the time-step used in the standard solver is typically larger than that limited by the Courant criteria (Eqn. 16). Thus we cannot make a single call to the convection routine to update the boundary conditions, rather, a sub-integration must be performed.

This sub-integration is simply a moving time window. If the standard solver is sampled to indicate a local time of 1 and time step if 0.1, and if the Courant criteria requires a time step of 0.01 (say for C = 1), then we must perform 10 sub-integrations of the convection equation to integrate from time t = 1 to t = 1.1. Upon completion of the sub-integration, the user must whether decide to update the outer integration.[11] If the outer integration step is large (the step internal to SINDA), then it may be necessary to reenter the outer-integration upon completion of the sub-integration and iterate the solution. If a relative small outer-loop time step is applied (this can be done by limiting the time step selection mechanism in SINDA) then this iteration step can be eliminated.

CONCLUSIONS

A numerical study of the solution of the one-dimensional convection equation is

---

[10] This is a SINDA convention specific to the SINDA code. The user names nodes with absolute numbers, i.e. nodes 1 to 100. While, SINDA applies a relative numbering convention internally. To reference the temperatures of those nodes that are boundary conditions, the user must convert the numbering convention with a utility routine.

[11] An update or iteration is required because the convection solution forms a coupled boundary conditions with the standard solver.

presented. A solution kernel has been presented that will yield satisfactory accuracy with minimal computation complexities. The features of stability, accuracy and spurious numerical phenomenon have been addressed in a general fashion to provide the user with a cursory insight into problematic features of numerical convection equation solutions. The key feature of time-step synchronization, as it applies to standard solver code melding, has been discussed in considerable detail.

REFERENCES

Anderson, D. A., Tannehill, J. C., and Pletcher, R. H., Computational Fluid Mechanics and Heat Transfer, McGraw Hill, New York, 1984, pp. 88-107.

Gerald, C. F., and Wheatley, P. O., Applied Numerical Analysis, Addison Wesley, Reading, Massachusetts, 1984, pp. 139-143.

Strauss, W. A., Partial Differential Equations - an Introduction, John Wiley & Sons, Inc., New York, 1992, pp. 194-197.

Session
Four

Aeronautics

Simulation of Unsteady Flows Through Stator and Rotor Blades of a Gas Turbine Using the Chimera Method

S. Nakamura† and J. N. Scott††

†Mechanical Engineering Department
††Aeronautical and Astronautical Engineering Department
The Ohio State University
Columbus, Ohio 43210, USA

Abstract

A two-dimensional model to solve compressible Navier-Stokes equations for the flow through stator and rotor blades of a turbine is developed. The flow domains for the stator and rotor blades are coupled by the Chimera method that makes grid generation easy and enhances accuracy because the area of the grid that have high turning of grid lines or high skewness can be eliminated from the computational domain after the grids are generated. The results of flow computations show various important features of unsteady flows including the acoustic waves interacting with boundary layers, Karman vortex shedding from the trailing edge of the stator blades, pulsating incoming flow to a rotor blade from passing stator blades, and flow separation from both suction and pressure sides of the rotor blades.

1. Introduction

Most of computer codes currently used to simulate aerodynamics in compressors and turbines are based on the steady basis with a turbulence model. However these time-averaged steady-state approaches are limited in their capabilities to compute some of the most critical features encountered in turbomachinery. Among their most serious shortcomings are their inability to predict phenomena associated with unsteady nature of the flows, and their inability to accurately simulate heat transfer. This is particularly evident when computing flow through a stator and rotor combination. Because of the non-uniform flow velocities from the stator exit plane, the moving rotor blades always encounter a time-varying, or pulsating, inlet flow. This constantly changing flow distribution of the inlet flow causes deviations from the steady inflow and changes the flow characteristics in the rotor blade passage. The importance of simulation of unsteady flows in the rotor blade passages has been recognized as a critical capability for performance analysis and design.

The development of a code to analyze the three-dimensional transient flow through a stator and rotor is a difficult task for various reasons. To analyze the flow through a stator and rotor blades, it is necessary to include at least 5 to 6 blades in the computations because of differences in the blade pitches between the rotor and stator blades. The rotor blades are constantly moving relative to the stator blades. The computation takes significantly more cpu time not only because of the large number of blades to be considered but also because of the unsteady flow simulation. The development of more advanced codes requires both new mathematical methods for numerical computations and significantly more powerful computer resources.

The present study [1] was initiated with the background thus stated. Two major objectives of the study are, first, (a) to examine some numerical methods suitable for the flow through stator and rotor rows, and second, (b) to analyze the effect of unsteady flow from the stator to the rotor. The present work is performed using a two-dimensional model. However, the experience and results of the investigation will be useful in developing three-dimensional models.

The remainder of this paper describes a computational model for the transient flow through stator and rotor blades based on the two-dimensional compressible Navier-Stokes equations and shows results of flow computations. We assume the pitch of stator blades is identical to that of the rotor blade. Therefore, only one stator blade that is stationary and one rotor that moves linearly to the negative direction of the y-coordinate are considered in the computations. For the direction tangential to the rotor movement, periodic boundary conditions are used for both rotor and stator flow channels. The body-fitted grids are used in both stator and rotor regions, but the grid for the rotor region moves with the rotor blade. The compressible Navier-Stokes equations are solved in each domain, and coupled to each other by the Chimera method[2].

2. Basic Equations and the Solution Methods

The compressible Navier-Stokes equation for the stator domain is written as

$$Q_t + E_x + F_y = R_x + S_y \tag{1}$$

where

$$Q = \begin{bmatrix} \rho \\ \rho u \\ \rho v \\ e \end{bmatrix}, \quad E = \begin{bmatrix} \rho u \\ \rho u^2 + p \\ \rho uv \\ u(e+p) \end{bmatrix}, \quad F = \begin{bmatrix} \rho v \\ \rho uv \\ \rho v^2 + p \\ v(e+p) \end{bmatrix}, \quad R = \begin{bmatrix} 0 \\ \tau_{xx} \\ \tau_{xy} \\ r \end{bmatrix}, \quad S = \begin{bmatrix} 0 \\ \tau_{xy} \\ \tau_{yy} \\ s \end{bmatrix} \tag{2}$$

with

$$\tau_{xx} = [(\lambda + 2\mu)u_x + \lambda v_y]/Re$$

$$\tau_{xy} = \mu(u_y + v_x)/Re$$

$$\tau_{yy} = [(\lambda + 2\mu)v_y + \lambda u_x]/Re \tag{3}$$

$$r = u\tau_{xx} + v\tau_{xy} + \beta(a^2)_x$$

$$s = u\tau_{xy} + v\tau_{yy} + \beta(a^2)_y$$

Here, ρ is the density, u and v are the velocity components, p is the pressure, e is the total energy, and all the variables are non-dimensionalized by

$$x = \bar{x}/\bar{L}, \quad y = \bar{y}/\bar{L}$$

$$\rho = \bar{\rho}/\bar{\rho}_o, \quad u = \bar{u}/\bar{a}_o, \quad v = \bar{v}/\bar{a}_o$$

$$p = \bar{p}/(\bar{\rho}_o\bar{a}_o), \quad e = \bar{e}/(\bar{\rho}_o\bar{a}_o) \tag{4}$$

$$\mu = \bar{\mu}/\bar{\mu}_o, \quad \lambda = \bar{\lambda}/\bar{\lambda}_o$$

$$t = \bar{a}_o \bar{t}/\bar{L}, \quad Re = \bar{\rho}_o \bar{a}_o L/\bar{\mu}_o$$

Here the quantities with an overbar is the dimensional quantity, and those with subscript o is the value at the inlet. The variables x and y are coordinates, L is a reference length, μ and λ are viscosities, a is the sound speed. The pressure is related to the conservative flow variables by

$$p = (\gamma-1)\left(e - \frac{1}{2}\rho(u^2 + v^2)\right) \tag{5}$$

For the rotor domain that moves with the rotor blade, Eq.(1) holds but the variables are redefined by

$$Q = \begin{bmatrix} \tilde{\rho} \\ \tilde{\rho}\tilde{u} \\ \tilde{\rho}\tilde{v} \\ \tilde{e} \end{bmatrix}, \quad E = \begin{bmatrix} \tilde{\rho}\tilde{u} \\ \tilde{\rho}\tilde{u}^2 + \tilde{p} \\ \tilde{\rho}\tilde{u}\tilde{v} \\ \tilde{u}(\tilde{e}+\tilde{p}) \end{bmatrix}, \quad F = \begin{bmatrix} \tilde{\rho}\tilde{v} \\ \tilde{\rho}\tilde{u}\tilde{v} \\ \tilde{\rho}\tilde{v}^2 + \tilde{p} \\ \tilde{v}(\tilde{e}+\tilde{p}) \end{bmatrix}, \quad R = \begin{bmatrix} 0 \\ \tilde{\tau}_{xx} \\ \tilde{\tau}_{xy} \\ \tilde{r} \end{bmatrix}, \quad S = \begin{bmatrix} 0 \\ \tilde{\tau}_{xy} \\ \tilde{\tau}_{yy} \\ \tilde{s} \end{bmatrix} \tag{6}$$

$$\tilde{\tau}_{xx} = [(\lambda + 2\mu)\tilde{u}_x + \lambda\tilde{v}_y]/Re$$

$$\tilde{\tau}_{xy} = \mu(\tilde{u}_y + \tilde{v}_x)/Re \tag{7}$$

$$\tilde{\tau}_{yy} = [(\lambda + 2\mu)\tilde{v}_y + \lambda\tilde{u}_x]/Re$$

$$\tilde{s} = \tilde{u}\tilde{\tau}_{xy} + \tilde{v}\tilde{\tau}_{yy} + \beta(\tilde{a}^2)_y$$

The pressure is related to the conservative flow variables by

$$\tilde{p} = (\gamma-1)\left(\tilde{e} - \frac{1}{2}\tilde{\rho}(\tilde{u}^2 + \tilde{v}^2)\right) \tag{8}$$

Other nondimensional variables are

$$\tilde{x} = \bar{x}/\bar{L}, \quad \tilde{y} = \bar{y}/\bar{L}$$

$$\tilde{\rho} = \bar{\tilde{\rho}}/\bar{\rho}_o, \quad \tilde{u} = \bar{\tilde{u}}/\bar{a}_o, \quad \tilde{v} = \bar{\tilde{v}}/\bar{a}_o$$

$$\tilde{p} = \bar{\tilde{p}}/(\bar{\tilde{\rho}}_o \bar{a}_o), \quad \tilde{e} = \bar{\tilde{e}}/(\bar{\tilde{\rho}}_o \bar{a}_o)$$

$$\mu = \bar{\tilde{\mu}}/\bar{\mu}_o, \quad \lambda = \bar{\tilde{\lambda}}/\bar{\lambda}_o$$

and t and Re are common for the two domains.

$$t = \bar{a}_o \bar{t}/\bar{L}, \quad Re = \bar{\rho}_o \bar{a}_o L/\bar{\mu}_o \tag{9}$$

At the interface between the stator region and the rotor region, the relations between the

variables are

$$\tilde{u} = u, \quad \tilde{v} = v - \tilde{V}, \quad \tilde{\rho} = \rho, \quad \tilde{p} = p \tag{10}$$

where $\tilde{V}$ is the nondimensional velocity of the rotor given by

$$\tilde{V} = \bar{\bar{V}}/a_o$$

Introducing Eq.(4) and Eq.(8) into

$$\tilde{p} = p$$

yields

$$e - \frac{1}{2}\rho(u^2 + v^2) = \tilde{e} - \frac{1}{2}\tilde{\rho}(\tilde{u}^2 + \tilde{v}^2)$$

or equivalently

$$\tilde{e} = e - \frac{1}{2}\rho[v^2 - (v - \tilde{V}^2)]$$

or

$$e = \tilde{e} + \frac{1}{2}\rho[(\tilde{v} + \tilde{V})^2 - \tilde{v}^2] \tag{11}$$

3. Computational Procedure

The Navier-Stokes equations are transformed onto a rectangular computational domain, and solved by the implicit method based on the LU decomposition [4]. The Navier-Stokes code is based on the second-order accurate implicit method. However, the boundary condition along the trailing cut and the Chimera coupling both use the computed results from the previous times step. Therefore, the accuracy of the whole solution reduces to the first order in time at least locally. The grid for each region is generated independently by the elliptic-hyperbolic method[3]. Two grid systems are used, one 38x220 points per blade, and another 55x658 points per blade. The grid points along the trailing cut in the gird are not made continuous across the cut because otherwise very high skewness of grid occurs under the periodicity constraints of the grid.

The inflow boundary conditions for the rotor domain are taken from the most updated computational results for the stator domain by the Chimera method. At the same time, the exit boundary conditions for the stator domain are taken from the most updated computational results from the rotor flow domain. The points along the inlet for the rotor regions are not same as the left boundary of the rotor grid so the front area of the rotor grid with significant turning can be avoided. Likewise, the exist boundary for the stator domain does not coincide with the right boundary of the stator grid.

The conventional method of coupling the two domains is as follows. The grid line which is vertical at the exit of the rotor domain would match the vertical grid line at the flow entrance of the rotor grid. However, the rotor grid is moving with the rotor blades, so flow boundary conditions are exchanged between the two domains by means of one-dimensional interpolations. Since the rotor grid is constantly moving relative to the stator grid, the interpolation relations also constantly changes. With the conventional approach, the grid for the flow exit of the stator and the grid at the

entrance to the rotor should be carefully aligned. Whenever the distance between the stator and the rotor is altered, a new set of grids should be generated. Generally the grid lines in a c-grid for a turbomachinery blade have high turns at the top left and bottom left corner of the grid for a blade where the accuracy of the coordinate transformation is poor.

With the Chimera method, a code developed for a single rectangular computational domain is applied for each of the flow domain belonging to one blade. Therefore, it is not necessary to match the grid line of the exit boundary of the stator domain with the grid line of the inlet boundary of the rotor domain. With the Chimera coupling, the front area of the rotor grid with high turning of grid lines may be removed from the actively used computational domain. Likewise the rear domain of the stator where high skewness of the grid tend to occur can be removed. The Chimera coupling requires two-dimensional interpolation to exchange boundary conditions between the stator and rotor. The interpolative exchanges of the boundary conditions disturb continuity of the field values across the boundaries of the two domains, but the conventional methods have the same problem. The Chimera method may be applied not only for the blade rows, but can be easily applied when additional flow domains are involved. This feature will become attractive in three-dimensional simulation particularly when the additional flow geometries such as inlet eye, volute, and exit diffuser are included (for a radial turbine).

4. Illustration of Results

The coarser grids for the stator and rotor are shown in Figures 1, where only every other grid lines that are parallel to the blade surface are omitted for clarity. The finer grids of 55x658/blade were generated by interpolation of the coarser grids (not shown here).

Figures 2 illustrates density distribution at two different stator-rotor positions, which were developed as follows. The coarser grids of 38x220/blade were used for this flow computation. There are some overlapping between the computed flow domains for the stator and the rotor blades. The mid point in the overlapping area will be denoted by x=A. The density distribution is plotted for x<A, and the density distribution from the rotor calculation is plotted for x>A. Discontinuity of the density contours is due to the interpolating scheme to couple the two domains in the Chimera scheme. Note, however, that even if no smearing effect due to interpolation exists, the wake from the trailing edge of the stator blade does not go into the rotor domain, because the plotting on the rotor domain is based on the relative coordinate. The grid size in the wake region of the stator is significantly smaller than that in front of the rotor blade. The difference of the grid sizes is also responsible to the discontinuity of the contours than Chimera coupling effects.

An examination of Fig.2 reveals that shapes of density contours at these different time points, namely at different stator-rotor positions, are different. It is caused by the unsteady inlet flow to the rotor primarily because of changing relative position of the rotor to the stator blades. To show the effect of the moving relative positions, distribution of several flow quantities along a vertical line indicated in Figure 1 are plotted in Figure 3 in order of increasing time in cycle 8. The initial numerical transient of the solution such as propagation of acoustic waves disappears after two cycles. At the eighth cycle, the same time-dependent flow distribution repeats during each cycle.

The computation with the finer grid of 55x658 was performed for the same geometry and physical constants as for the computation illustrated in Figure 2 and 3. Because of a massive amount of data from the finer grid computations, we have not yet been able to analyze the results to a full extent. However, snapshots of density distribution for a few selected time steps are illustrated in Figure 4. Figure 4a is a density distribution that occurs during the initial numerical transient and shows interaction between acoustic waves and boundary layers. Although the initial numerical transient is not a true physical phenomena, the flow behavior during that period still provides important information because similar transient should occur in case a sudden change of

inlet or exit flow conditions change or the load to the turbine impulsively changes. Figure 4b is for a later time than Fig. 4a but still in a late stage of the initial numerical transient. This figure shows Karman vortex shedding from the trailing edge of the stator blade, and flow separation from the suction side of the rotor blade. Figure 4c is for a time step after the rotor blades has passed stator blades seven times. The figure shows a flow separation at the lower surface of the rotor blade and a vortex being shed. A periodic shedding of vortices from the same location has been observed. At this time of writing it is not certain, however, if this vortex shedding phenomena is simply due to periodic change of the inlet flow to the rotor blade or induced by the Karman vortices from the trailing edge of the stator. But the latter is be highly likely. Karman vortices from the trailing edge are also observed in Figure 4c (Karman vortices are more clearly shown in the next figure). Figure 4d (the number of contour lines are significantly increased to show details more clearly) shows Karman vortex street from the trailing edge of the stator blade at a different time step. Unlike the vortex shedding from a simple circular cylinder, the geometrical pattern of Karman Vortices from a turbine blade seem to be much irregular.

5. Concluding Remarks

Two dimensional modeling of the flow through stator and rotor rows based on the Chimera method has been described. The computational results show several important aspects of the unsteady flow through stator and rotor passages. The unsteady flow phenomena captured in the present computational simulation are not only interesting from academic curiosity but also worth further investigation of practical interest, particularly to understand the mechanism of heat transfer in turbomachinery.

Acknowledgements

The authors are thankful to R. V. Chima and K. C. Civinscus of NASA Lewis Research Center for providing data and comments that were very useful for the present study. The Chimera-coupled compressible Navier-Stokes code described here was developed by modification of the compressible Navier-Stokes code originally developed by S. Obayashi for a single airfoil. A part of the grid generation was performed by a computer at NASA Lewis. The flow solution was obtained on Cray YMP at Ohio Supercomputer Center. The first author also thank Ohio Aerospace Institute for their support for an initial stage of this study

References

[1] S. Nakamura, J. N. Scott, " Computational Simulation of Unsteady Flows through Stator and Rotor Passage of a Gas Turbine," Proc. International Symposium of Experimental and Computational Aerothermodynamic of Internal Flows, Prague, Czech Republics, July 12-15, 1993

[2] J. L. Steger, F. C. Dougherty, and J. A. Benek, "A Chimera Grid Scheme," in *Advances in Grid Generation*, ed. K. Ghia and U. Ghia, ASME FED Vol-5, 1983

[3] S. Nakamura, M. Spradling, D. Fradl, and K. Kuwahara, "A Grid Generating System for Automobile Aerodynamic Analysis," in *Vehicle Aerodynamics: Recent Progress*, SAE SP-855, 1991

[4] S. Obayashi, K. Kuwahara, and H. Kubota, "Computation of Unsteady Schock-Induced Vortex Separation," AIAA 85-0183, 1985

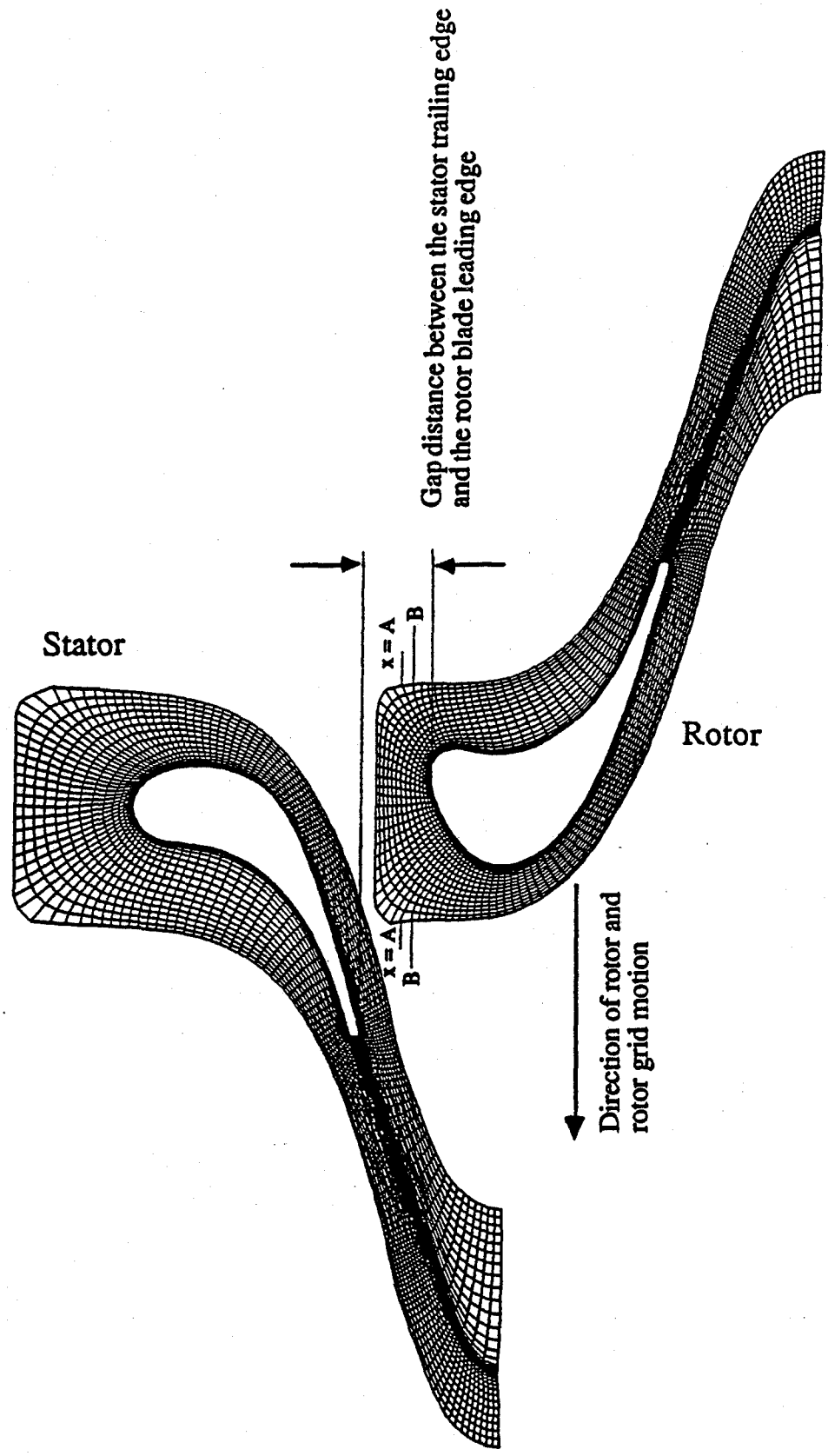

Figure 1 Grids for the stator and rotor domains (only half of the points in the directions intersecting the blades and trailing cut are plotted)

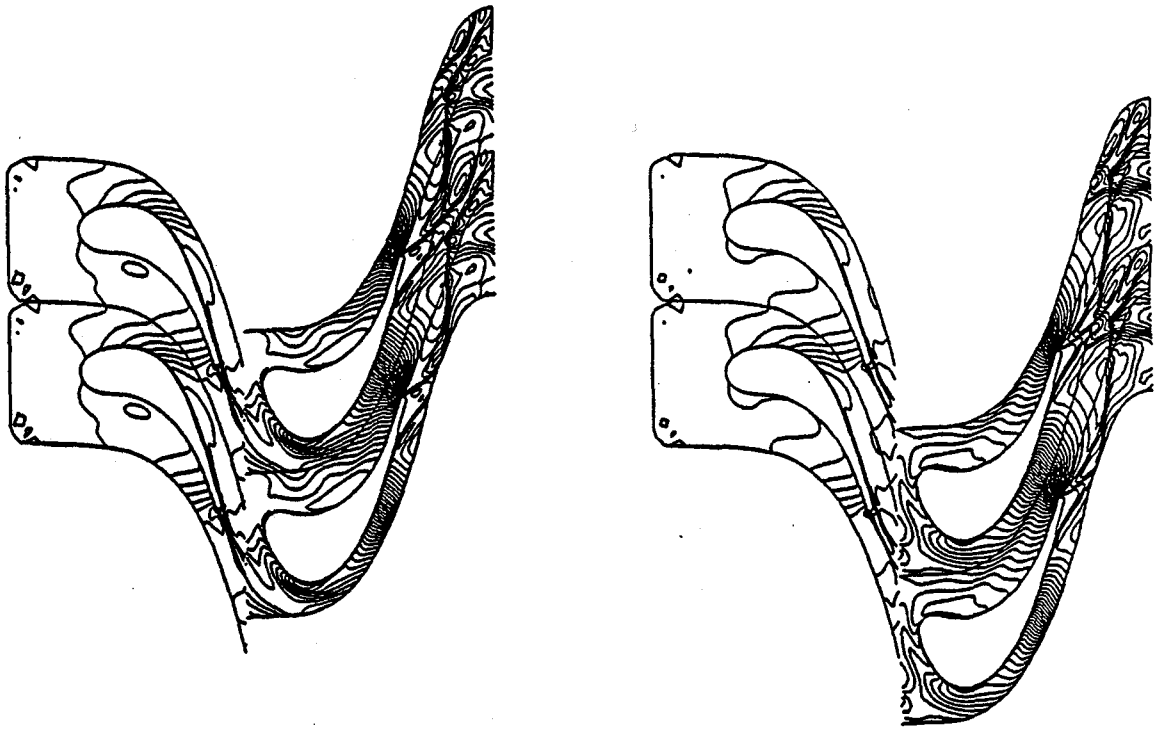

Figure 2 Density contour plot for two different positions of rotor blades relative to stator blades

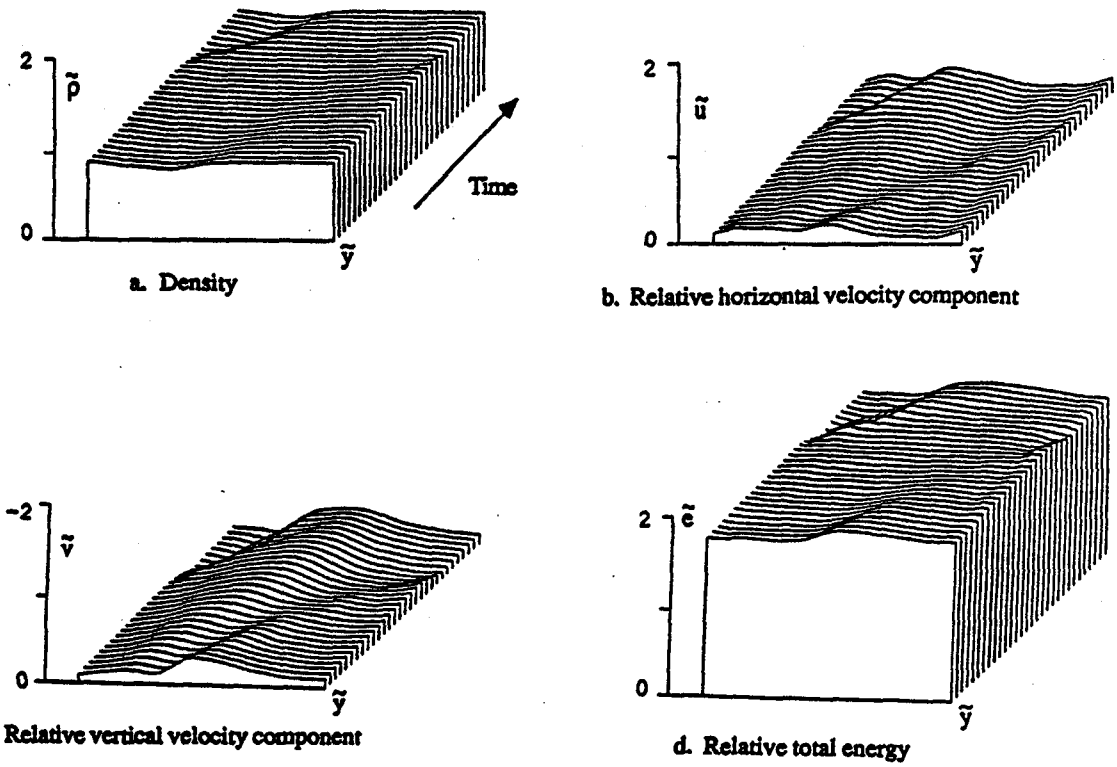

Figure 3 Time-dependent variations of spatial distributions of field variables in front of the rotor blade leading edge (see A-A line in Figure 1)

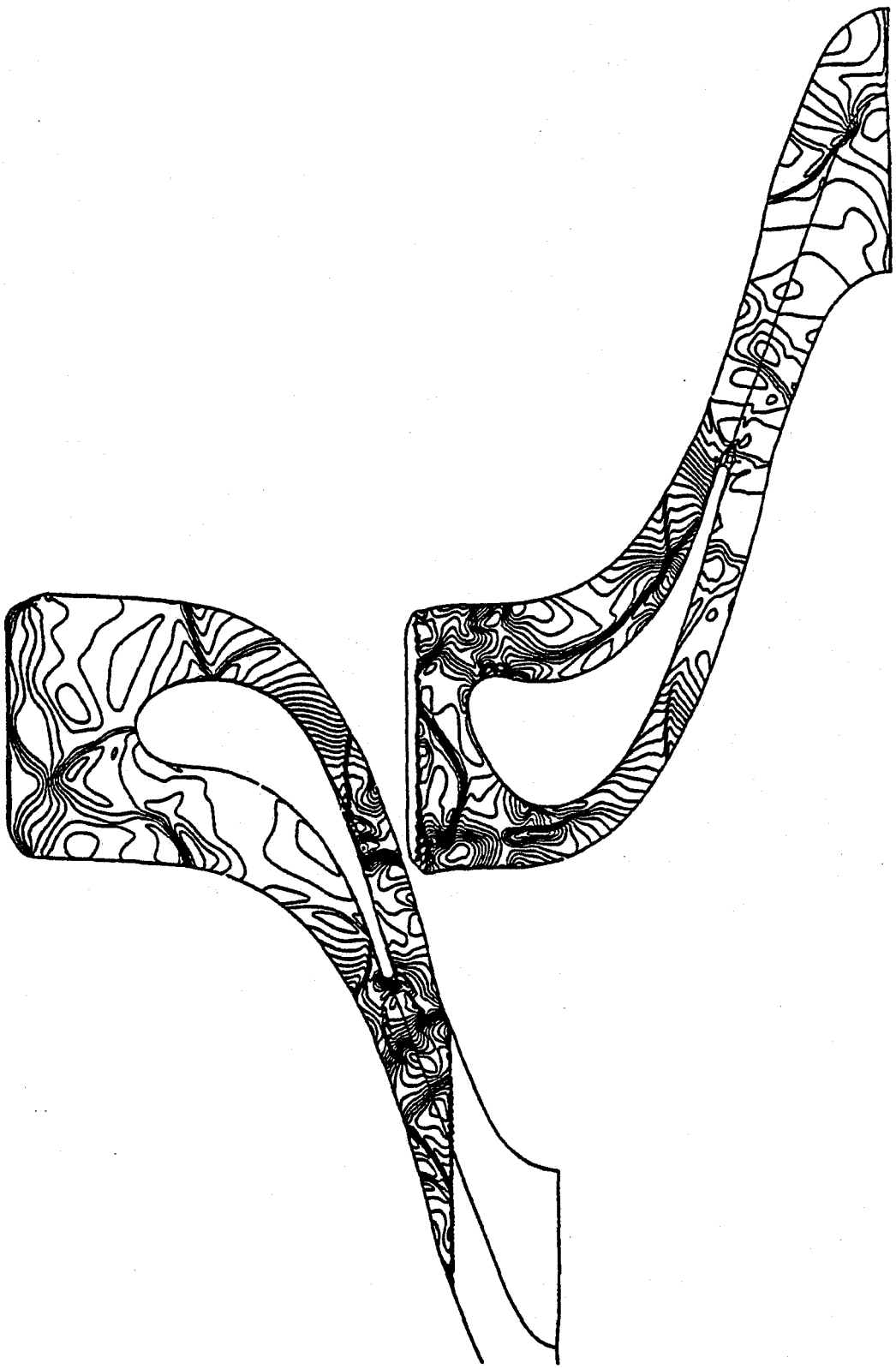

4a: during the initial numerical transient

Figure 4 Snapshots of density contours at different time steps (55x658 points/blade)

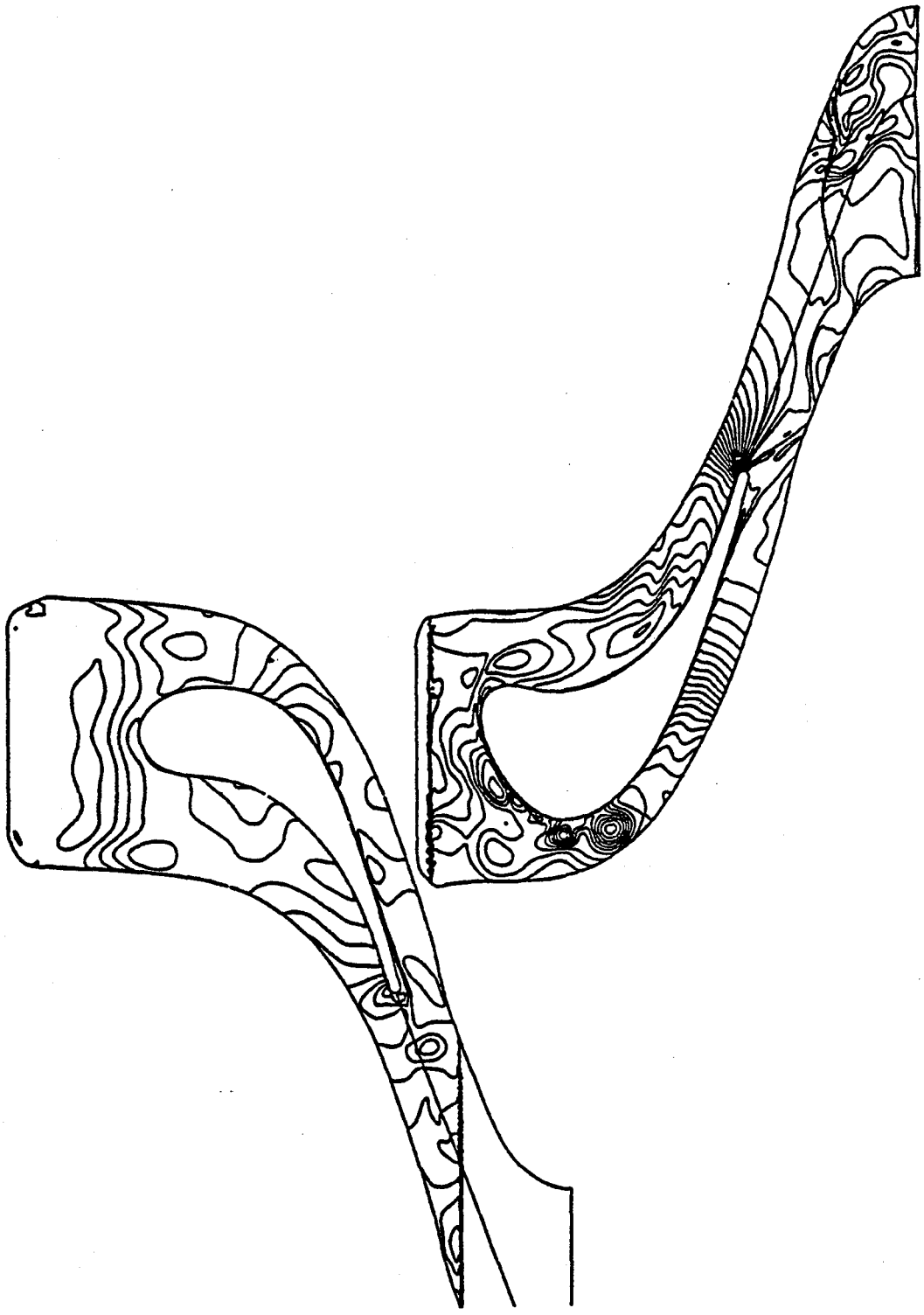

4b: a later stage of the initial numerical transient

Figure 4 continued

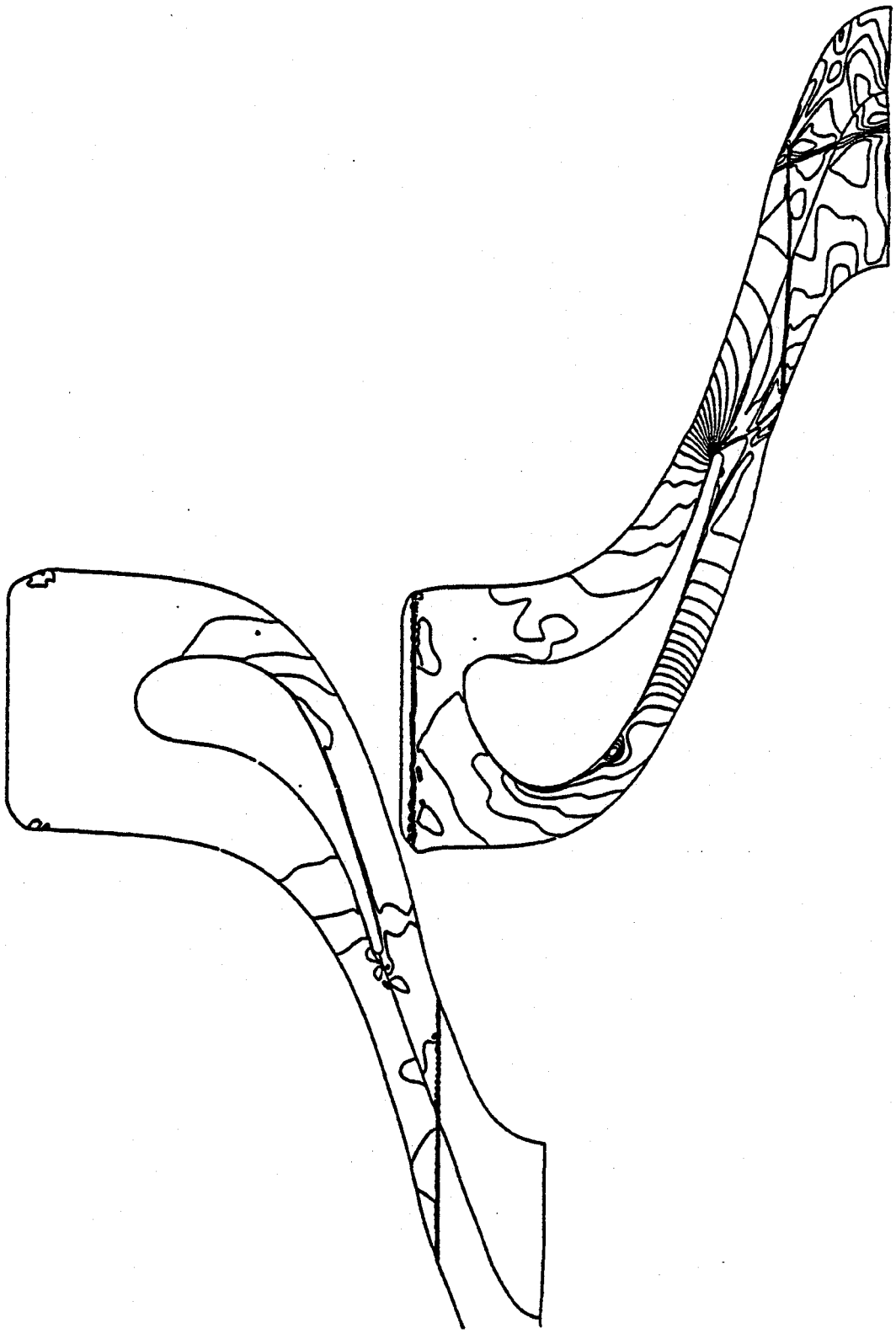

4c: a time step long after the initial numerical transient

Figure 4 continued

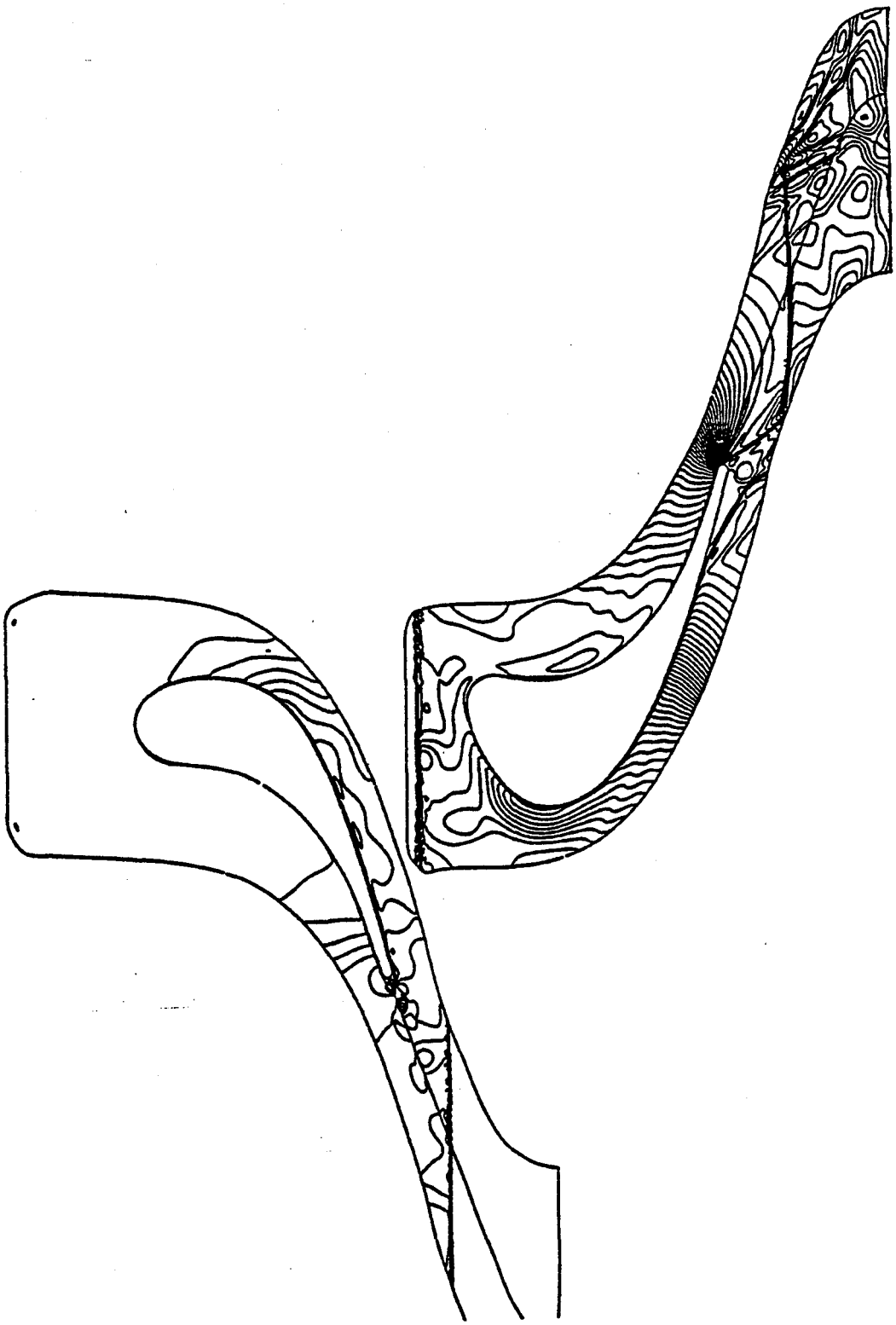

4d: another time step long after the initial numerical transient
(with a higher contour density than 4c)

Figure 4 continued

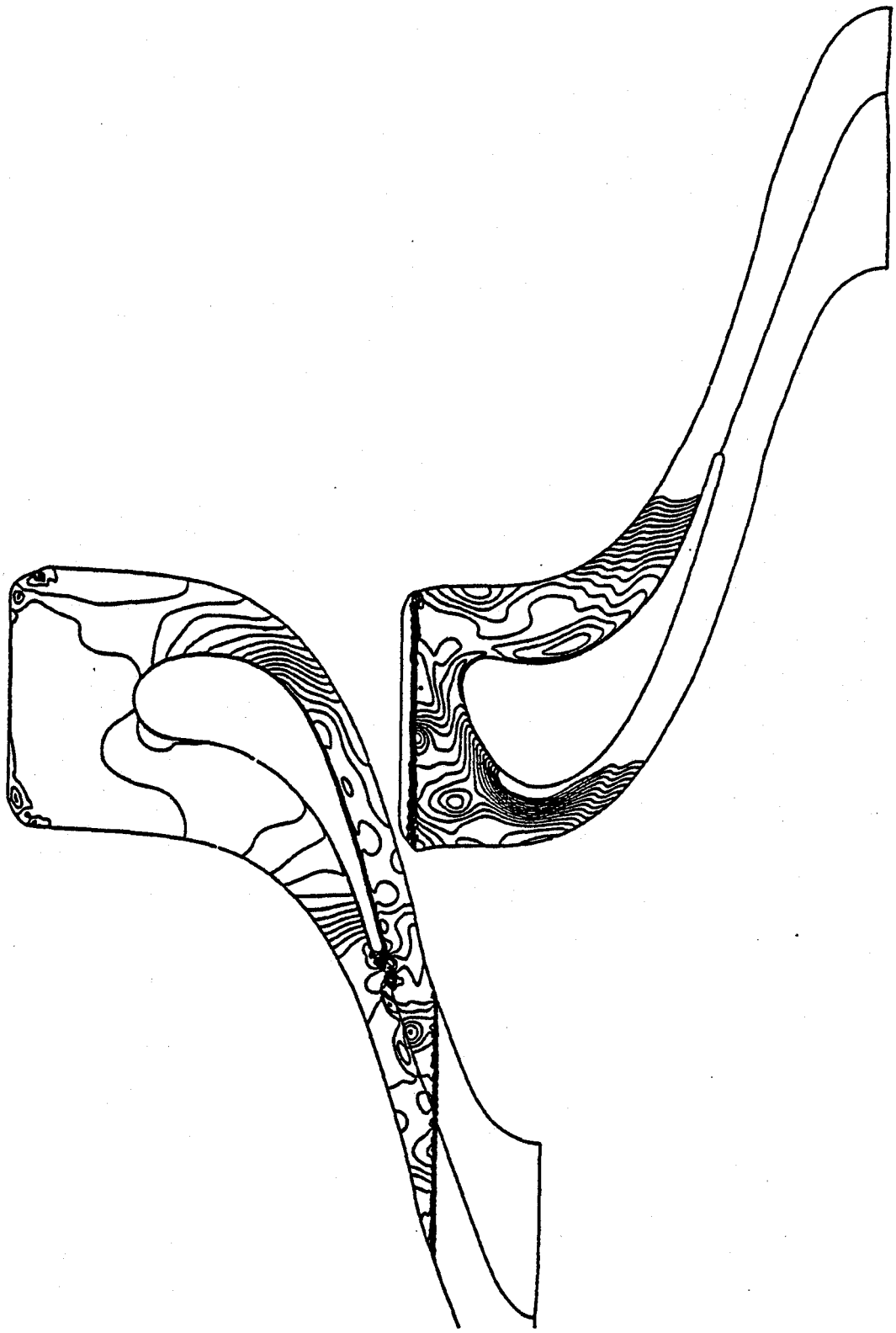

4d': repeat of 4d (with a much higher contour density)

Figure 4 continued

DEVELOPMENT AND APPLICATION OF AN EMPIRICAL PROBABILITY DISTRIBUTION FOR THE PREDICTION ERROR OF RE-ENTRY BODY MAXIMUM DYNAMIC PRESSURE

R. James Lanzi
National Aeronautics and Space Administration
Goddard Space Flight Center
Wallops Flight Facility
Wallops Island, VA 23337

Brett T. Vincent
Computer Sciences Corporation
Wallops Flight Facility
Wallops Island, VA 23337

ABSTRACT

The relationship between actual and predicted re-entry maximum dynamic pressure is characterized using a probability density function and a cumulative distribution function derived from sounding rocket flight data. This paper explores the properties of this distribution and demonstrates applications of this data with observed sounding rocket re-entry body damage characteristics to assess probabilities of sustaining various levels of heating damage. The results from this paper effectively bridge the gap existing in sounding rocket re-entry analysis between the known damage level/flight environment relationships and the predicted flight environment.

1.0 INTRODUCTION

Figure 1 shows a schematic of a typical re-entry configuration for a Terrier-Black Brant sounding rocket payload. Historically at NASA/GSFC/Wallops Flight Facility, 5 degree-of-freedom trajectory simulations (Reference 1) have been used to predict sounding rocket re-entry body flight environment parameters such as maximum dynamic pressure, Mach 1 altitude and parachute deployment conditions. The aerodynamic characteristics used in these simulations have been computed using the CDCG computer program which incorporates a hybrid theoretical / empirical nonlinear crossflow aerodynamics model.

As the NASA Sounding Rocket Program has shifted toward larger payload size and increased vehicle performance capability, concern over aerodynamic heating during re-entry has become more than just an academic issue. Re-entry heating damage to sounding rocket recovery systems has been a source of refurbishment cost, and a cause for apprehension over possible recovery system failure. The level of heating damaged sustained by any given

sounding rocket payload during the re-entry leg of the flight has been found to be directly related to the peak level of dynamic pressure encountered and the static margin of the re-entry body. A crude characterization of the relationship between the aerodynamic heating damage and maximum dynamic pressure was determined in Reference 2. In this report, a "damage line" is defined which separates values of flight dynamic pressure and re-entry body static margin that constitute a "cool region", within which no heating damage has been experienced, from values of flight dynamic pressure and static margin which constitute a "hot" region where varying degrees of heating damage have been experienced.

Flight levels of maximum dynamic pressure can vary significantly from the predicted values. In Reference 2, the limitations of the analysis tools used to make predictions of the re-entry environment parameters were investigated, and several sources of prediction error were isolated. In particular, a statistical characterization of the prediction error in the aerodynamic properties was determined.

Before the study of Reference 2, NASA/GSFC/Wallops Flight Facility imposed a fixed limit on predicted maximum dynamic pressure to prevent recovery system failure due to re-entry heating. Payloads were ballasted to meet this constraint. Once the study of Reference 2 was published, NASA began using the observed properties of the prediction error of re-entry body aerodynamic characteristics to analytically determine the dispersion of re-entry environment parameters such as maximum dynamic pressure (q_{max}) and Mach 1 altitude (References 2 and 3). Re-entry bodies are then ballasted to bring the envelope of predicted levels of maximum dynamic pressure beneath the "damage line" given in Reference 2. Although this technique does address the variability in predicted re-entry dynamic pressure levels, the inherent noise involved in the determination of the prediction error of the body aerodynamics combined with the extreme sensitivity of the re-entry environment to variations in body aerodynamic characteristics makes it difficult to interpret the results from this approach.

During the post flight mission analyses of Terrier-Black Brant V Flights 36.079 and 36.089 it was observed that the predicted re-entry maximum dynamic pressures (q_p) were 20.2% and 15.3% lower, respectively, than the actual re-entry maximum dynamic pressures (q_a). Flight 36.089 was a refly of the 36.079 payload. Further analysis revealed that there was an apparent center of pressure shift away from the S-19 canards for both flights. Reference 2 noted that for the 28 analyzed cases, the apparent center of pressure shift was towards the S-19 canards. Approximately 9 Lbs. of re-entry ballast were incorporated on these flights to bring q_p below the "damage line" of Reference 2. These flights illustrate the difficulty in applying the results of Reference 2 to payload ballast design.

In this report, the direct statistical relationships between predicted and actual maximum dynamic pressure are developed, and the relationship between re-entry heating damage and maximum dynamic pressure is refined. These results are combined into a coherent method for relating results from simulation to probability of sustaining various levels of aerodynamic heating damage during re-entry.

2.0 CHARACTERISTICS OF RE-ENTRY ENVIRONMENT PREDICTION ERROR

2.1 Prediction Error Determination

The re-entry environment prediction error is characterized by the percent error in predicting q_a ($\%q_{err}$), which is given by:

$$\%q_{err} = \left(\frac{q_p - q_a}{q_a}\right) * 100\%. \quad (1)$$

The percent error was determined for the 49 flights listed in Table 1. As was done in References 2 and 4, q_p was determined by initializing a GEM 5-DOF re-entry simulation (containing nonlinear aerodynamics from the CDCG program) with radar data at some time prior to re-entry. This was done to eliminate trajectory dispersion effects.

2.2 Generation of an Empirical Probability Density Function

It can be seen in Table 1 that $\%q_{err}$ varies widely, from -54.5% to +232.5%. However, closer inspection of the data reveals that the majority of cases fall within ±30% error range. A distribution for $\%q_{err}$ was determined by generating a normalized relative frequency histogram h(x); that is, dividing the $\%q_{err}$ values into 10 $\%q_{err}$ class intervals and determining the frequency of $\%q_{err}$ values within each interval. The intervals are represented mathematically by

$$[c_0, c_1),\ [c_1, c_2),\ \ldots,\ [c_{k-1}, c_k),$$

where k is the number of class intervals (10 in this case). The above notation denotes that the class intervals are closed on the left; that is, a value on a boundary point is assigned to the class interval that has this value as its lower boundary. The interval widths were chosen

to give a more or less continuous distribution. The normalized relative frequency histogram is defined by

$$h(x) = \frac{f_i/n}{c_i - c_{i-1}} \quad for\ c_{i-1} \leq x\ c_i, \quad i=1,2,...,10, \tag{2}$$

where n is the number of observations and f_i is the frequency of the class $[c_{i-1}, c_i)$. The normalized relative frequency histogram is an approximation of the probability density function for $\%q_{err}$. Probability values for the event that a random variable, x, falls within a certain interval are given by the area beneath the probability density function, f(x), over the interval. Figure 2 presents the normalized relative frequency histogram for the $\%q_{err}$ of the 49 subject cases. As was observed in Table 1, the distribution of $\%q_{err}$ is skewed to the right with the majority of cases being between ±30%.

The relative frequency of an interval [a, b), where $c_0 \leq a < b \leq c_k$, can be computed by the integral

$$\int_a^b h(x)dx.$$

Since the relative frequency is an approximation to probability, this integral can be thought of as an approximation to the probability that X, the random variable under consideration ($\%q_{err}$), is in the interval [a, b). It follows that a cumulative distribution function F(x) can be derived from

$$F(x) = P(X \leq x) = P(X < x) = \int_{-\infty}^{x} f(w)dw, \tag{3}$$

where f(x) is the limit of h(x) as n increases and the lengths of the class intervals go to zero.

2.3 Discussion of the Cumulative Distribution Function

The cumulative distribution function (c.d.f.) in Equation 3 gives the probability of having a value of the variable X (in this case, $\%q_{err}$) less than some given value x. Figure 3 presents the c.d.f. for $\%q_{err}$. The c.d.f. shows that while there is a 47.7% probability of

having a negative $\%q_{err}$ (that is, q_a greater than q_p), there have been no recorded cases of $\%q_{err}$ exceeding -60%. Qualitatively, the c.d.f. shows that most of the time the re-entry q_{max} prediction is fairly accurate, and is about as likely to be under the flight value as it is over, but the over predictions are of a much larger magnitude than the under predictions. Of course, it is the under predictions of re-entry q_{max} that are of greater concern, in terms of re-entry heating damage.

3.0 COMPUTING DAMAGE RISK USING THE EMPIRICAL ERROR DISTRIBUTION

Figure 4 shows the re-entry flight envelope of maximum dynamic pressure and re-entry static margin for the Terrier-Black Brant V family. The different symbols on the plot represent the different levels of heating damage sustained during the flight according to the following classifications:

Re-entry Heating Damage Classifications

0 - No damage. (36.096)

1 - Exterior discoloration. (36.053)

2 - Minor exterior erosion, especially near surface discontinuities. (36.049)

3 - Melting at surface discontinuities and erosion making its way into interior. (36.034)

4 - Major exterior damage. Skin eroding and peeling away from joint. (36.057)

5 - All above exterior damage plus significant interior damage. (36.086)

6 - Failure due to re-entry heating (no known cases)

The lower line in Figure 4 separates the region in the flight envelope of Level 0 and 1 heating damage from the region of Level 2 and 3 heating damage. This line was previously published in Reference 2 and is given by the equation

$$q_{\max}^{(1)} \leq 4200 - 17.5 * SM^2, \tag{4}$$

where

q_{max} = Flight maximum dynamic pressure (psf)

SM = |xcg - xcla| (% Total Body Length).

The upper line in Figure 4 separates the Level 2/3 region from the higher level heating damage regions in the flight envelope. This line is defined by several borderline flights and is given by the equation

$$q_{\max}^{(2)} \leq 4600 - 10.5 * SM^2. \tag{5}$$

For a re-entry body with a fixed static margin, values of $q_{max}^{(1)}$ and $q_{max}^{(2)}$ can be computed using Equations 4 and 5. A value of q_p is determined using the nonlinear aerodynamics of the CDCG program and the GEM 5-DOF simulation. At this point the probability of falling into the three regions of the flight envelope can be computed using the cumulative distribution function derived in Section 2.2. This is done as follows:

1. Calculate the prediction errors associated with flight values of maximum dynamic pressure equal to $q_{max}^{(1)}$ and $q_{max}^{(2)}$:

$$\%q_{err}^{(1)} = \frac{q_p - q_{\max}^{(1)}}{q_{\max}^{(1)}} * 100\%$$

$$\%q_{err}^{(2)} = \frac{q_p - q_{\max}^{(2)}}{q_{\max}^{(2)}} * 100\%$$

2. Compute the following probability values from the cumulative distribution curve (CDF) of Section 2.2:

$$p_1 = 1 - CDF(\%q_{err}^{(1)})$$

$$p_2 = CDF(\%q_{err}^{(2)})$$

$$p_3 = 1 - p_1 - p_2$$

where

p_1 = Probability of flight q_{max} (q_a) falling into the level 0/1 region.

p_2 = Probability of q_a falling into the higher level damage region (3/4/5/6).

p_3 = Probability of q_a falling into the level 2/3 damage region.

The procedure outlined above has been automated in a FORTRAN program called REPROB. The damage demarcation curves and the empirical cumulative distribution function will be updated as new cases are added to the re-entry database.

CONCLUSIONS

An empirical probability density function describing the re-entry environment prediction error has been derived by comparing predicted re-entry maximum dynamic pressure (q_p) to flight maximum dynamic pressure (q_a) for 49 flights. From this, a cumulative distribution function has been generated relating q_p to q_a; allowing the mission analyst to predict, to a given probability, if q_a will be in a possible heating damage region. The re-entry error distribution and the damage region definitions can easily be updated as new cases are flown and as previous flight data is found.

The methods given in this report utilize the properties of the re-entry environment prediction error to give a more direct means of assessing possible re-entry heating difficulties. Future work in refining the aerodynamic models should address the effect of changes on the prediction error distribution.

REFERENCES

1. 841.1 Wallops Flight Facility Computer Programs:
   WFF CDCG - Crossflow Drag Computer Program
   WFF GEM - 6-DOF Simulation Program
2. Lanzi, R. J.: A Quantitative Evaluation of the Mission Analysis Tools Used for the Prediction of Reentry Body Aerodynamic Characteristics and Reentry Trajectory Parameters. NASA Internal Memo, 9/91.
3. Lanzi, R. J.: A Procedure for the Determination of Sensitivities of Reentry Trajectory Predictions with Known Error Bands in Predicted Aerodynamic Coefficients. NASA Internal Memo, 12/91.

4. Vincent, B. T.: Preliminary Findings of the Comparison Between the Current CDC Code and a Modified CDC Code (CDCG) With Flight Data. CSC Memorandum, November 30, 1990.

5. Hogg, R. V.; Ledolter, J.: Engineering Statistics. Macmillan Publishing Co., 1987.

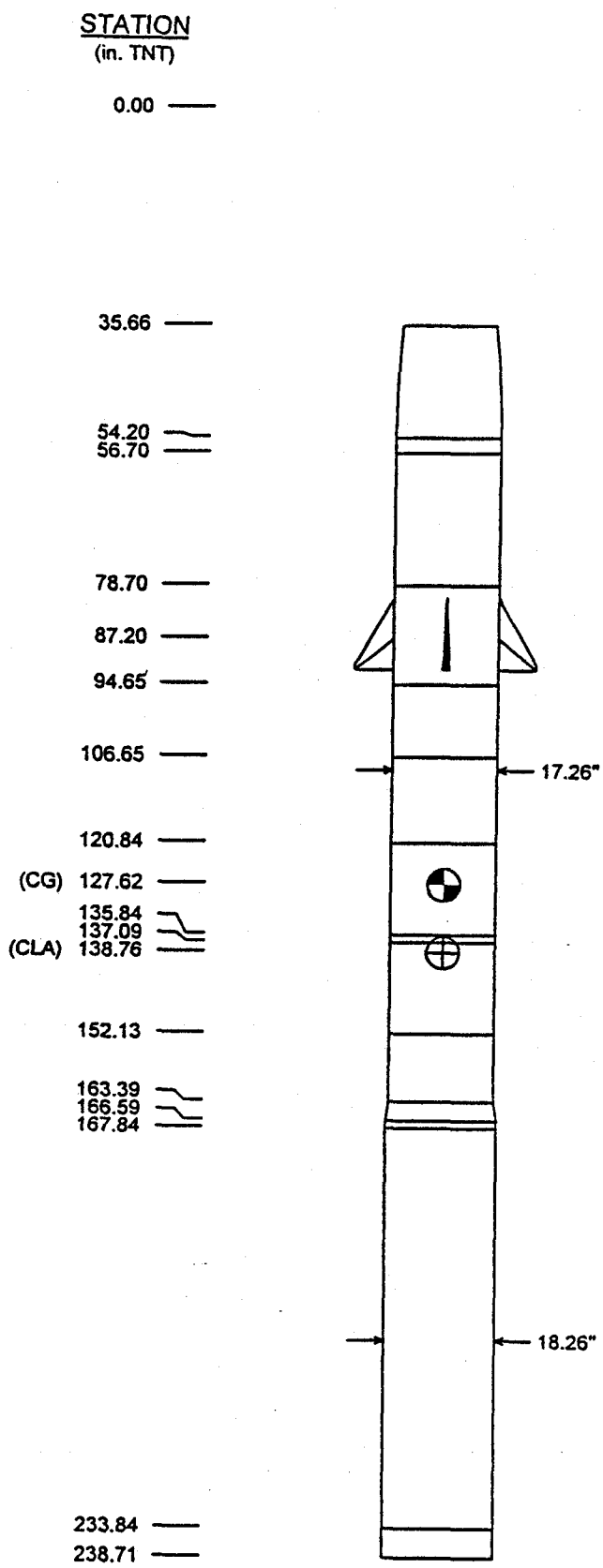

RE-ENTRY GRAVIMETRICS

Weight	=	875.00	lbs.
Length	=	203.05	in.
CG	=	127.62	in. TNT
CLA	=	138.76	in. TNT
[CG-CLA]	=	11.14	in.
Ix	=	8.61	slug-ft^2
Iy	=	665.47	slug-ft^2

Figure 1. Terrier - Black Brant VC 36.068 GG

Re-entry Configuration

Table 1. CDCG Comparison with Flight Data

Flight	Pred. Qmax	Flight Qmax	%Qerr
27.075	3565.6	2481.5	43.69%
27.106	2502.1	3071.5	-18.54%
27.121	2599.4	781.7	232.53%
27.122	945.6	821.0	15.17%
27.123	1888.3	1317.0	43.38%
27.124	2335.9	2388.0	-2.18%
27.129	1057.0	1116.0	-5.29%
27.130	1160.0	894.0	29.75%
27.133	1056.5	305.5	245.83%
36.016	2305.0	5061.6	-54.46%
36.025	3740.1	4271.6	-12.44%
36.027	2703.4	1505.4	79.58%
36.030	2616.5	4103.5	-36.24%
36.032	2609.4	3090.7	-15.57%
36.034	2067.7	4110.0	-49.69%
36.035	3317.0	2673.2	24.08%
36.041	2874.5	3778.3	-23.92%
36.043	2730.0	1408.5	93.82%
36.047	1808.0	1230.9	46.88%
36.048	2800.0	2700.0	3.70%
36.049	3607.7	4334.9	-16.78%
36.052	1536.0	919.4	67.07%
36.053	1965.0	2938.5	-33.13%
36.054	1635.0	2344.1	-30.25%
36.057	4949.0	4739.7	4.42%
36.058	4643.0	4285.0	8.35%
36.059	2749.9	1277.2	115.31%
36.060	1633.0	622.2	162.46%
36.062	3958.0	4744.6	-16.58%
36.063	2342.0	3888.7	-39.77%
36.066	3383.1	3760.3	-10.03%
36.067	2715.3	1946.0	39.53%
36.068	4907.0	5238.2	-6.32%
36.069	3443.3	3352.5	2.71%
36.070	3365.0	3701.2	-9.08%
36.072	1916.3	1888.9	1.45%
36.073	4964.0	4267.6	16.32%
36.074	3146.4	2608.9	20.60%
36.077	5020.6	3268.3	53.62%
36.078	4584.0	4341.1	5.60%
36.079	3794.8	4757.0	-20.23%
36.085	4190.0	4230.0	-0.95%
36.086	4919.0	4413.5	11.45%
36.087	3153.2	3500.0	-9.91%
36.088	2124.7	2600.0	-18.28%
36.089	3921.0	4631.0	-15.33%
36.090	3800.0	3940.0	-3.55%
36.096	1907.7	812.7	134.74%
36.098	2740.0	2740.0	0.00%

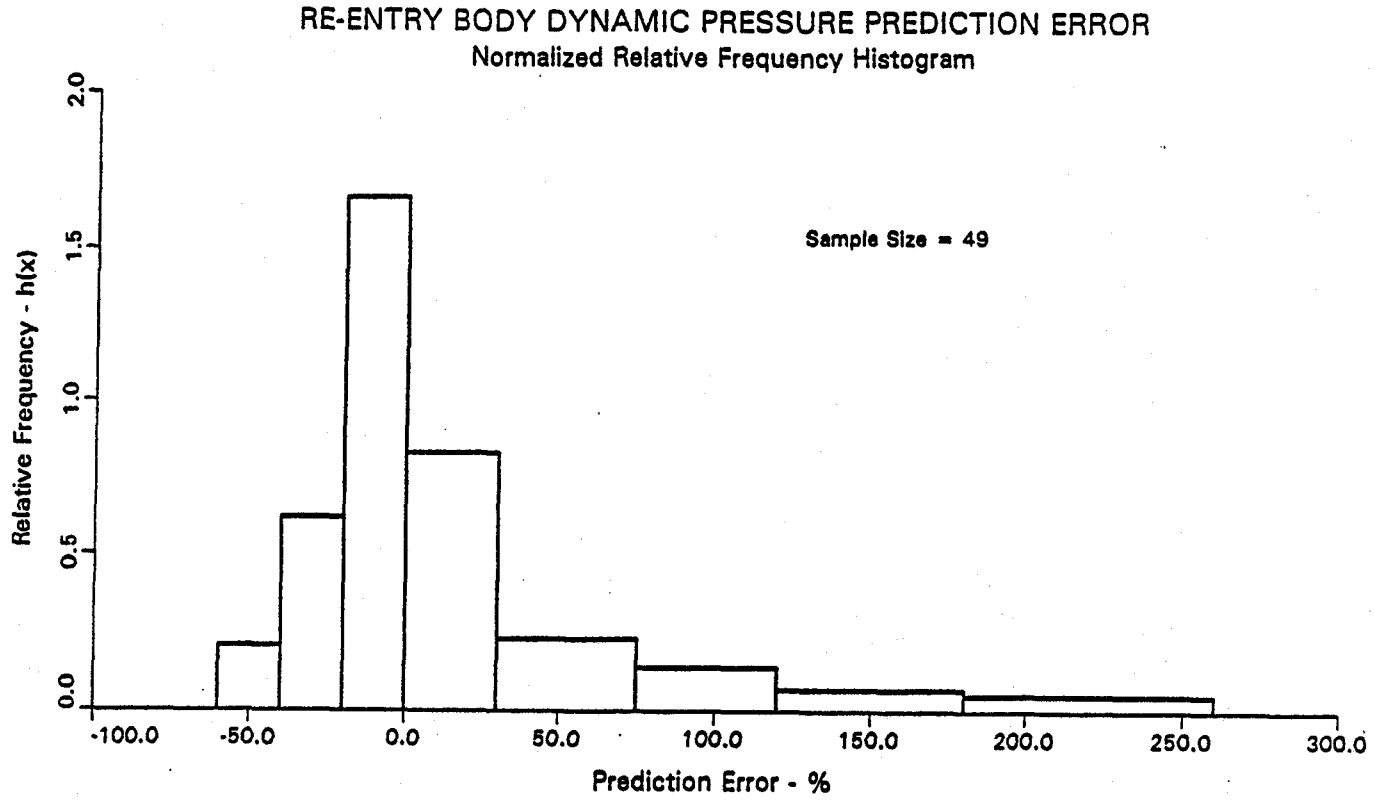

Figure 2

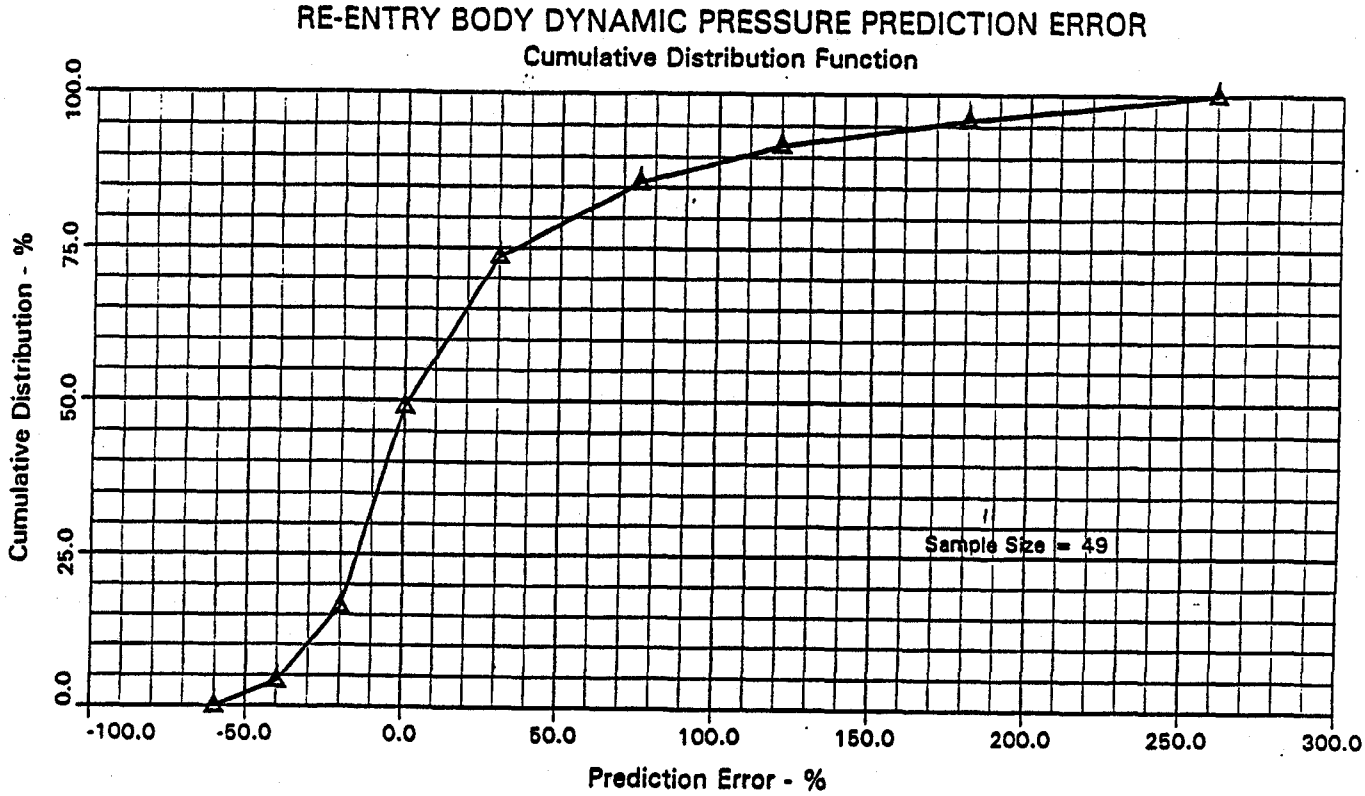

Figure 3

Terrier-Brant Reentry Study

Qmax vs SM

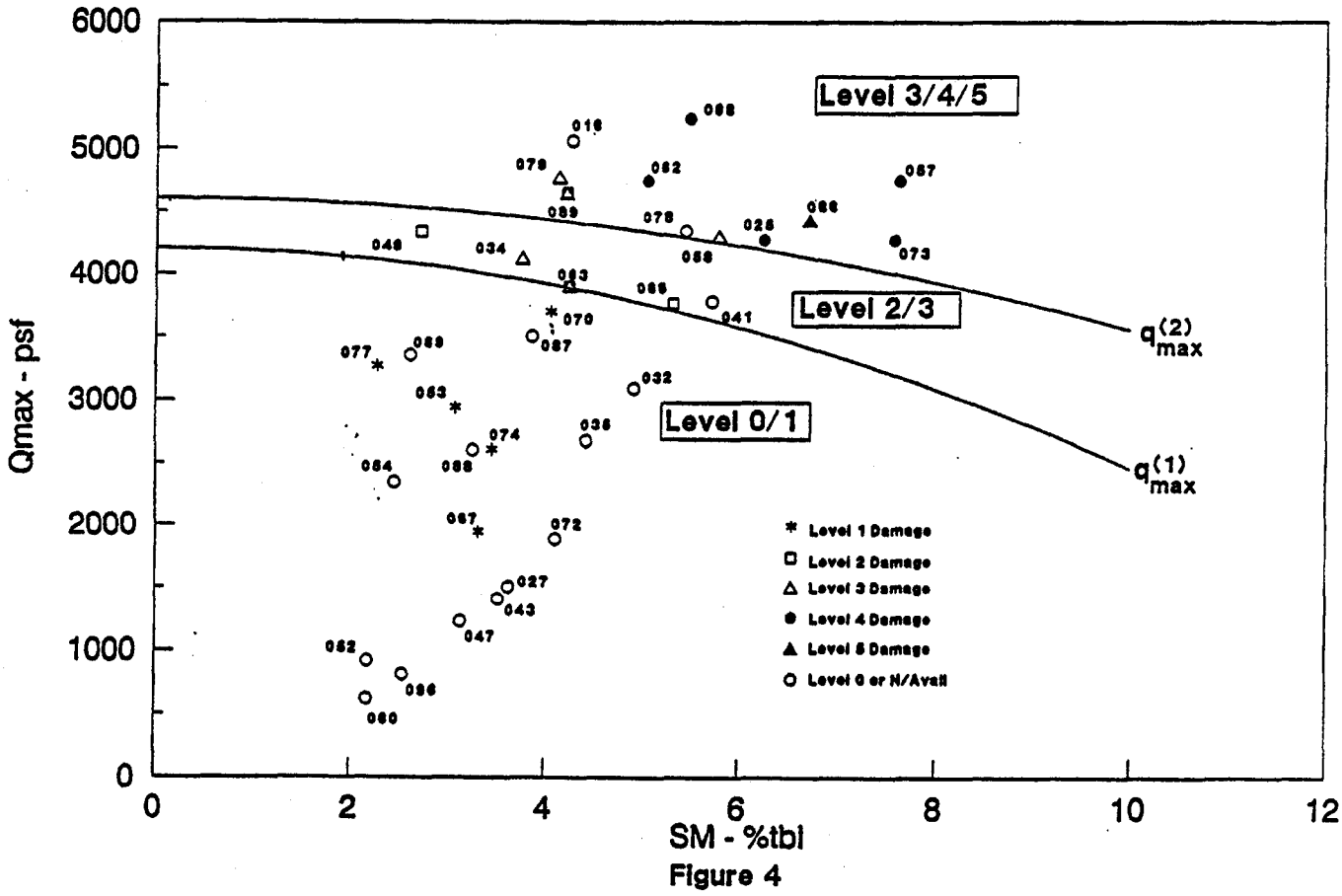

Figure 4

PREDICTION OF THREE SIGMA MAXIMUM DISPERSED DENSITY FOR AEROSPACE APPLICATIONS

Terri L. Charles
Michael D. Nitschke
General Dynamics Space Systems Division
San Diego, California 92186-5990

SUMMARY

Free molecular heating (FMH) is caused by the transfer of energy during collisions between the upper atmosphere molecules and a space vehicle. The dispersed free molecular heating on a surface is an important constraint for space vehicle thermal analyses since it can be a significant source of heating. To reduce FMH to a spacecraft, the parking orbit is often designed to a higher altitude at a the expense of payload capability. Dispersed FMH is a function of both space vehicle velocity and atmospheric density; however, the space vehicle velocity variations are insignificant when compared to the atmospheric density variations. The density of the upper atmosphere molecules is a function of altitude, but also varies with other environmental factors, such as solar activity, geomagnetic activity, location, and time.

A method has been developed to predict three sigma maximum dispersed density for up to 15 years into the future. This method uses a state-of-the-art atmospheric density code, MSIS 86, along with 50 years of solar data, NASA and NOAA solar activity predictions for the next 15 years, and an Aerospace Corporation correlation to account for density code inaccuracies to generate dispersed maximum density ratios denoted as 'K-factors'. The calculated K-factors can be used on a mission unique basis to calculate dispersed density, and hence dispersed free molecular heating rates. These more accurate K-factors can allow lower parking orbit altitudes, resulting in increased payload capability.

FREE MOLECULAR HEATING

Free molecular heating (FMH) is caused by the kinetic transfer of energy during the collisions between the rarefied upper atmosphere molecules and a space vehicle traveling at high velocities. The dispersed free molecular heating on a surface normal to the velocity vector can be a significant portion of the space heating environment (Figure 1). Therefore, the FMH during the period between payload fairing (PLF) jettison and spacecraft separation is an important constraint for space vehicle thermal analysis.

Nominal FMH is predicted by the following equation which relates the free molecular heat flux, q_{fmh}, to the atmospheric density, ρ, and to the vehicle velocity relative to the atmosphere velocity, v_{rel}:

$$q_{fmh} = {}^1/_2 \, \rho_{nom} \, v_{rel}^3 \qquad (1).$$

Units conversion factors for Equation 1 are listed in Table 1 for various standard English units of density and velocity. Dispersed free molecular heating is predicted by using the dispersed density, ρ_{disp}, in Equation 1:

$$q_{fmh,disp} = {}^1/_2 \, \rho_{disp} \, v_{rel}^3 \qquad (2).$$

Table 1. Units Conversion Factors for Free Molecular Heating Equation (1)

Common Density Units	Common Velocity Units	Common FMH Units	Conversion Factor Value 1.	Conversion Factor Units
$slug/ft^3$	ft/sec	$BTU/hr\text{-}ft^2$	4.62268	$\frac{BTU/hr\text{-}ft^2}{(slug/ft^3)(ft^3/sec^3)}$
lb_m/ft^3	ft/sec	$BTU/hr\text{-}ft^2$	0.143677	$\frac{BTU/hr\text{-}ft^2}{(lb_m/ft^3)(ft^3/sec^3)}$
$lb_f\text{-}sec^2/ft^4$	ft/sec	$BTU/hr\text{-}ft^2$	4.62268	$\frac{BTU/hr\text{-}ft^2}{(lb_f\text{-}sec^2/ft^4)(ft^3/sec^3)}$

Note 1. The following values were used to determine the conversion factors:
J = mechanical equivalent of heat, 778.770 ft-lb_f/BTU
g_c = proportionality constant between mass and force, 32.174 lb_m-ft/lb_f-sec^2

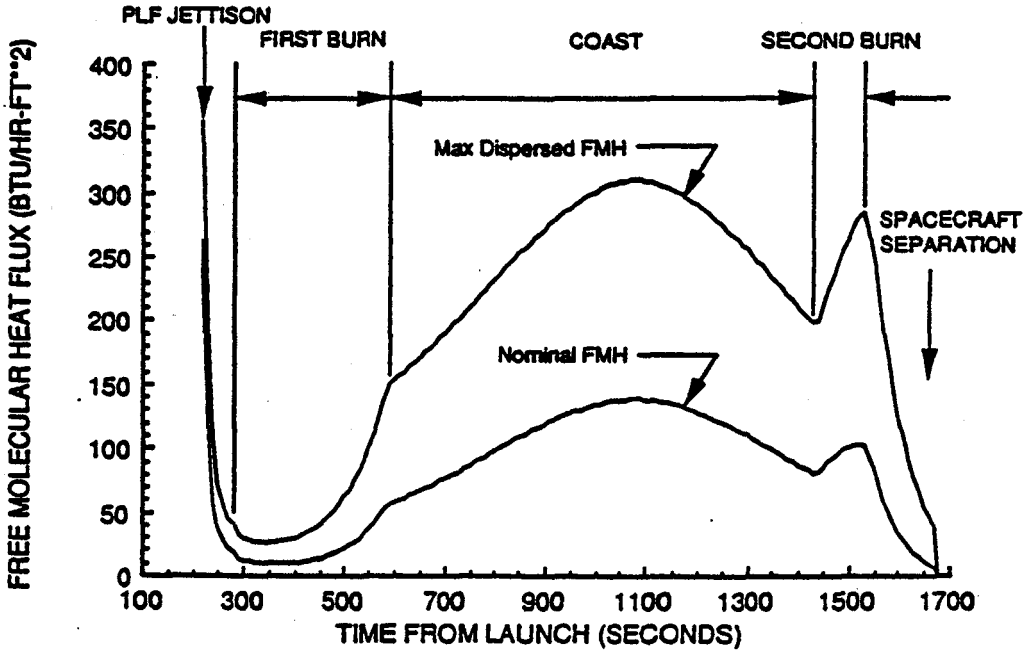

Figure 1 Example of Nominal and Dispersed Free Molecular Heating Fluxes for a Standard Atlas/Centaur Launch Vehicle Parking Orbit

The dispersed density, ρ_{disp}, can be calculated from the Equation 3 which relates the dispersed density to the U.S. Standard 1976 nominal density (Reference 1), ρ_{76}, by a density dispersion factor, K, also called a 'K-factor':

$$\rho_{disp} = K\,\rho_{76} \qquad (3).$$

Both the density and the density dispersion factor are functions of altitude. The U.S. Standard 1976 density is a nominal, mid-solar cycle density which is tabulated as a function of

altitude. The density dispersion factor 'K' is a function of several parameters, but is affected primarily by altitude and level of solar activity.

Free Molecular Flow Regime

In the upper atmosphere, the density of the gas molecules is so low that the intermolecular collisions are negligible. This is the free molecule flow regime where the kinetic theory of gasses takes over from the continuum fluid mechanics of the lower atmosphere. The basic free molecular flow assumption is that the flow of atmospheric gas molecules incident on a body is undisturbed by the presence of that body. Thus, there is no boundary layer and no flow around a body, and collisions between the body and the gas molecules only take place on surfaces which are normal to the velocity vector (Reference 2).

The transition between the free molecule and continuum flow regimes depends on whether or not the molecules' collisions with each other affect their collisions with the body. In other words, the free molecule regime is characterized by single collisions between the gas molecules and the body, which means that the mean-free path of the molecules has to be much greater than the characteristic length of the body. The ratio of the mean-free path in the gas, λ, to the characteristic dimension, d, is called the Knudsen number, Kn:

$$Kn = \lambda / d \qquad (4).$$

Free molecule flow is assumed for $Kn \geq 10$. The mean-free path varies with density and is a function of altitude. Assuming a space vehicle characteristic dimension of 3.0 m, the vehicle will be fully in free molecule flow when the molecules have a mean-free path greater than 10 x 3.0 m or 30 m. This mean-free path length has been measured at about 130 km (70 nmi or 425 kft, Reference 1), which is below the 80 to 100 nmi typical low Earth parking orbits.

Free Molecular Heat Flux

Free molecular heating occurs when the incident rarefied molecules are reflected from a surface. These reflections are characterized as diffuse, specular, or some combination of these two extremes. A diffuse reflection is one in which the molecules are momentarily absorbed by the surface and then emitted according to a Maxwell velocity distribution corresponding to the surface temperature. A specular reflection is one in which the nominal velocity of the molecules is reversed and the tangential velocity remains the same. Diffuse reflections are very common for most surfaces, whereas, specular reflections are only common for very highly polished, non-oxidized metals or for very small grazing angles (Reference 3).

The thermal accommodation coefficient, α, is the measure of how close the actual energy transfer to the wall is to the purely diffuse energy transfer. For purely diffuse reflections, α=1.0 and for purely specular reflections, α=0.0. The accommodation coefficient increases with increasing oxidation, with increasing surface roughness, and with increasing wall temperature (Reference 4). For most cases involving space vehicles, diffuse reflections are predominant and accommodation coefficients of at least 0.9 are appropriate (Reference 3). An accommodation coefficient of 1.0 is often used for a maximum heating analysis and an accommodation coefficient of 0.0 is often used for a minimum heating analysis (Reference 5). The heat flux absorbed by a surface normal to the flow is calculated by

$$q_{fmh,absorbed} = \alpha \left({}^{1}/_{2} \rho_{disp} v_{rel}^{3} \right) \qquad (5).$$

The velocity and altitude are determined from the trajectory. The dispersed density is determined from the altitude and the appropriate density dispersion K-factors (Equation 3). The derivation of this equation from the kinetic theory of gasses is described in Reference 4 and requires many simplifying assumptions. The main assumptions are:

1) free molecular flows, $Kn \geq 10$
2) surfaces are normal to the flow
3) vehicle velocities much greater than molecular velocities
4) surface temperatures much lower than gas stagnation temperatures.

Nominal Atmospheric Density

The nominal free molecular heating from Equation 1 is calculated using a nominal atmospheric density from a standard atmosphere model. The most widely used nominal atmosphere model is the U.S. Standard Atmosphere, 1976 (Reference 1). This atmosphere model is a hypothetical, constant, vertical distribution of atmospheric temperature, pressure and density which, by international agreement, is roughly representative of year-round, mid-latitude conditions for the range of solar activity that occurs between sunspot minimum and sunspot maximum. In the model, the gasses of the atmosphere are assumed to obey the perfect gas law, $P = \rho R T$, and hydrostatic equation, $dP/dh = -\rho g_c$, which, when taken together, relate temperature, pressure and density with altitude. The U.S. Standard 1976 Atmosphere is the base atmosphere on which the density dispersion factors (K-factors) are calculated.

These nominal atmosphere models are designed to fit the available atmospheric data. From 50 to 90 km, the atmospheric measurements of temperature, density, and pressure were made almost exclusively with rocket-borne instruments, mass spectrometers and density gauges. From 140 to 1000 km, these values were determined from satellite-related observations (satellite drag calculations and satellite-borne instruments) and radar incoherent scatter techniques (Reference 1).

Atmospheric densities calculated from both composition measurements made with rocket-borne mass spectrometers and from values inferred from satellite drag calculations have been compared over the range from 100 to 200 km (54 to 108 nmi). The mass spectrometer-calculated densities were usually lower than satellite drag-calculated densities (Reference 1). The U.S. Standard 1976 atmosphere (Reference 1) relies principally on the satellite drag data.

Dispersed Atmospheric Density

The atmospheric density, though principally a function of altitude, is dynamic and variations in it occur frequently. The range of density variation which occurs is illustrated in Figure 2. Several types of variations occur which are attributed to: different levels of solar activity, fluctuations in geomagnetic activity, geographical location, seasonal variations, and variations between day and night levels. Low Earth orbiting satellites passing through the upper atmosphere are significantly affected by these density variations due to increased satellite drag and increased free molecular heating. Changes in satellite drag due to density variations can cause satellite lifetimes to vary by a factor of ten between minimum to maximum conditions (Reference 6). The sudden density variations from solar storms can significantly change satellite orbits, which requires relocation and reacquisition of the satellites and uses on-board propellant to correct deviations (Reference 7). For launch vehicles, the main effect of this dispersed density is from increased free molecular heating on vehicle and payload surfaces.

Solar Cycle Effects

The largest atmospheric density dispersion is from the variation in the solar flux received by Earth's atmosphere. The waning and waxing of the solar flux, known as the solar cycle, lasts approximately 11 years (Figure 3). At the peak of the solar cycle, large energetic events occur on the Sun which greatly increase the extreme ultraviolet (EUV) radiation arriving at the Earth. All of the EUV is absorbed in the Earth's lower thermosphere, a layer which is located approximately between 83 to 120 km (45 to 65 nmi) in altitude. The lower thermosphere layer absorbs the EUV energy and expands outward, decreasing the density at the very lowest altitudes but greatly increasing the density in the higher altitudes where the low earth parking orbits are (from 148 to 185 km) and above. Above 296 km (160 nmi) the density can vary by an order of magnitude due to solar cycle effects (Figure 2).

Because none of the EUV radiation reaches the ground, the EUV cannot be monitored using ground-based techniques. Measurements have been made by a few specially equipped satellites over relatively short periods. The solar 10.7 cm (radio wavelength) flux is measurable from Earth and varies closely with the EUV flux as can be seen in Figure 4, which compares satellite EUV measurements with coincident ground measurements of 10.7 cm flux. Therefore, the F10.7 index, which is a measure of the 10.7 cm radio flux levels with units of 10^{-22} Watts m^{-2} Hz^{-1}, is used as a proxy index in atmospheric density models in place of the EUV flux levels (Reference 7).

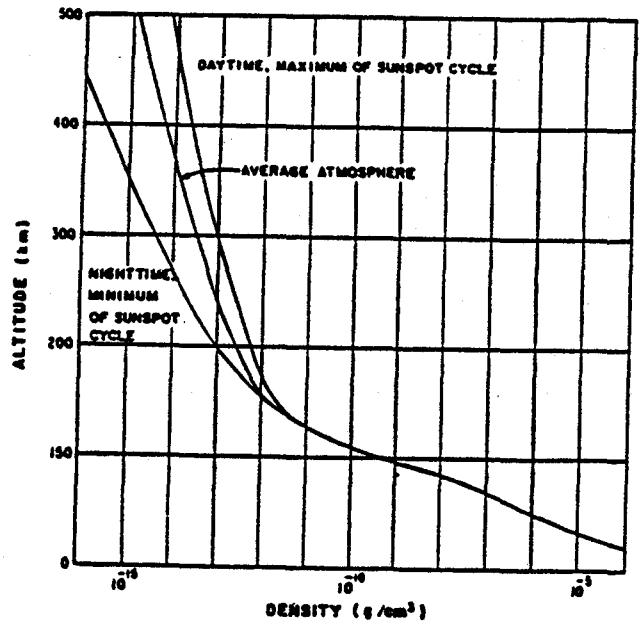

Figure 2. Atmospheric Density Variation: Nominal, Minimum and Maximum (Reference 8)

The solar cycle, as recorded from the 10.7 cm flux, shows significant daily variation (Figure 5). The trend is difficult to see in this data; therefore, a 13-month running mean, using data from both sides of the given day, is used to eliminate the daily fluctuations. Use of this mean allows easier tracking of the solar cycle progress and easier comparison from one solar cycle to another. The 10.7 cm flux also correlates well with the historical method of recording solar cycles by the number of appearances of sunspots (used in Figure 3). This correlation is clearly seen over the last few solar cycles in Figure 6. There are significant differences between the activity levels during different solar cycles, with Cycle 19 having the highest activity level recorded to date.

The National Oceanic and Atmospheric Administration (NOAA) provides regular updates on solar 10.7 cm radio flux activity and also provides a nominal prediction of the F10.7

index with 90% bounds for a full solar cycle (approximately 11 years) which is used in dispersed density predictions. The F10.7 index over the last few solar cycles is shown in Figure 7 along with the NOAA prediction for the current solar cycle.

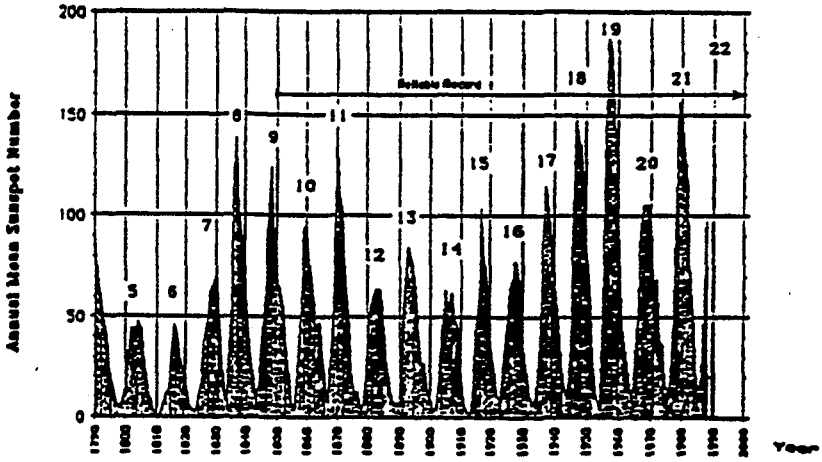

Figure 3. Solar Cycles from 1790 to 1988 (Reference 9)

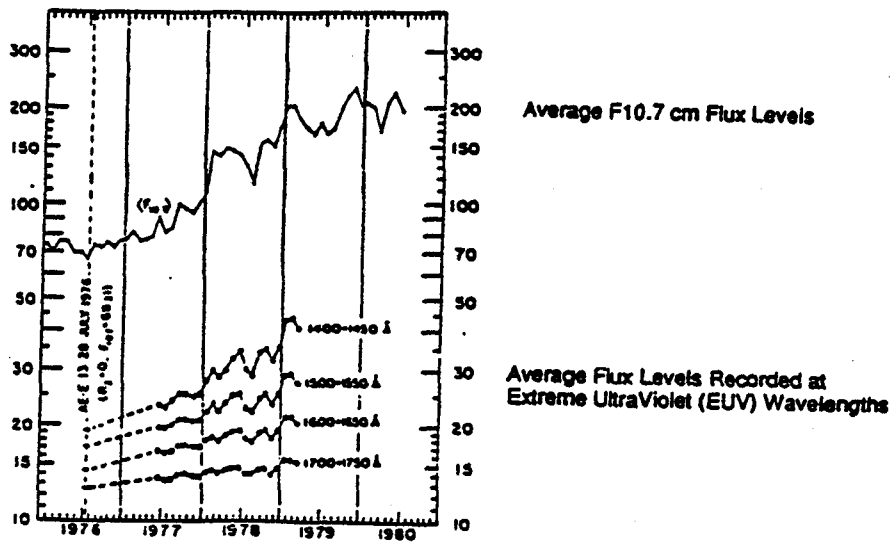

Figure 4. Comparison for Solar 10.7 cm Flux Levels Recorded on Earth to EUV Flux Levels Recorded by the AE-E Satellite During Solar Cycle 21 (Reference 7).

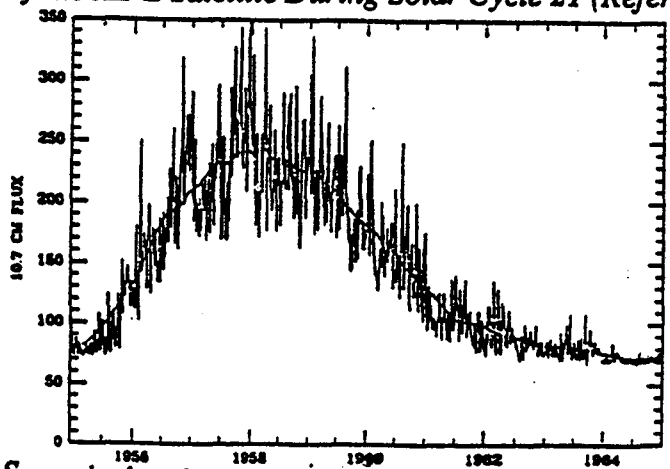

Figure 5. Smoothed and Daily 10.7 cm Flux for Solar Cycle 19 (Reference 9)

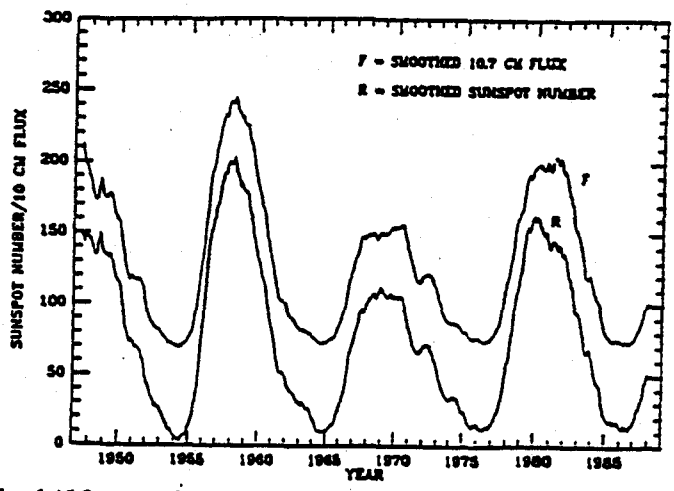

Figure 6. Smoothed (13-month Running Mean) Sunspot Number R and Solar Flux (Ref. 9)

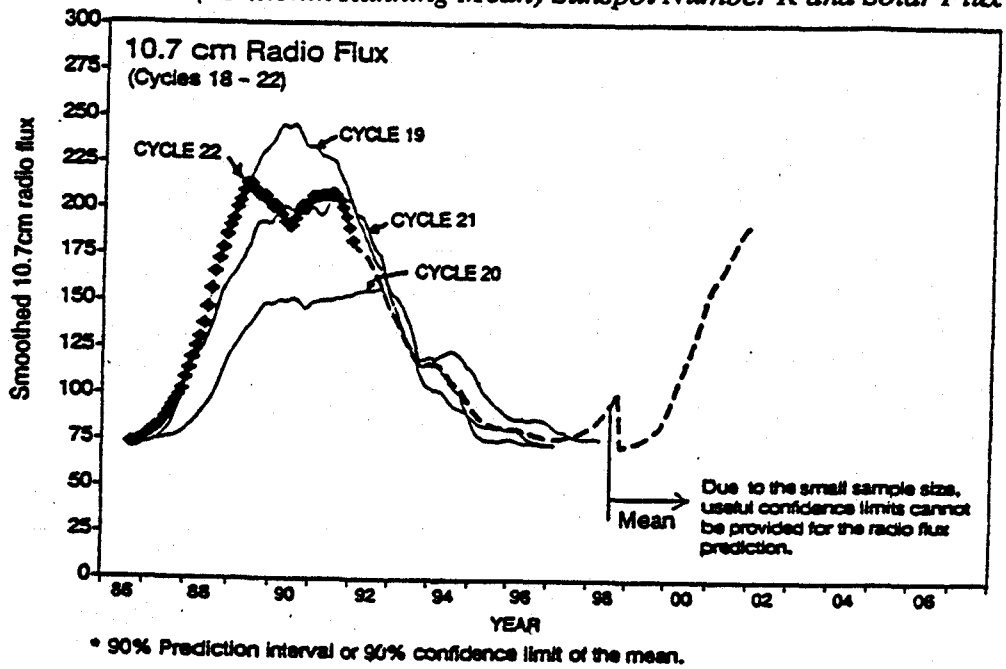

Figure 7. Smoothed Solar 10.7 cm Flux for Past and Predicted Cycles (Reference 10)

Geomagnetic Activity Effects

Geomagnetic storms are caused by bursts of charged particles from the sun colliding with the Earth's magnetosphere. Large amounts of energy are deposited at high latitudes during these storms and can significantly increase the atmospheric density at low Earth parking orbit altitudes in a matter of hours. Unlike the 10.7 cm radio flux, the geomagnetic activity has a relatively short term effect of only a few days. The geomagnetic activity effects are a strong function of latitude and are much stronger near the poles than at the equator (Reference 7).

The Ap index is a measure of the intensity of atmospheric activity due to geomagnetic storms. It is a derived index which is unitless and varies from 0 (quiet) to 400 (maximum storm activity). There is a pronounced maximum magnetic storm frequency during the declining phase of the solar cycle, which is illustrated in Figure 11. Increased geomagnetic activity begins about halfway between the solar maximum and the solar minimum and continues until the solar cycle minimum is reached (Reference 7).

The Ap level is determined by mapping the Kp level, which varies from 0 to 9, onto the Ap range of 0 to 400. The Kp index is a quasi-logarithmic measure of the amplitude of geomagnetic disturbances, where the change from 1 to 2 represents a small increase in amplitude while the change from 8 to 9 represents a major increase in amplitude. The Kp index is a 24-hour combination of the eight 3-hour K indices reported from twelve observatories around the world. The K index varies from 0 to 9 like the Kp index and is a measure of the local magnetic character for each 3-hour period recorded at each location (Reference 8). Marshall Space Flight Center (MSFC) produces a monthly update on the geomagnetic activity and provides a nominal Ap prediction with 97% bounds for a full solar cycle.

Diurnal, Seasonal, and Geographical Variations

There is a diurnal or daily variation in atmospheric density which also occurs. The time at which the maximum occurs is around 1400 local solar time and varies with altitude (see Appendix). The amount of variation in density levels is latitude- and altitude-dependent. At the higher altitudes, above 200 km (108 nmi), the density during the day can be up to eight times higher than the density at night (References 11 and 12). However, the effects are not as pronounced at the lower parking orbit altitudes.

There is a semiannual variation in the atmospheric density levels. This variation is clearly shown in the figures in the Appendix. There is a primary minimum in July, followed by a primary maximum in October, a secondary minimum in January, followed by a secondary maximum in April (References 11 and 12). This variation depends principally on solar activity levels.

The atmospheric density also varies depending on the latitude and longitude. This variation extends down to about 150 km (81 nmi) and is shown in the Appendix. Some of the latitude variation is due to the geomagnetic activity having a more pronounced effect nearer the poles (Reference 12).

Atmospheric Density Codes

There are two principal atmospheric density calculation codes available for altitudes above 90 km (50 nmi). These are the Jacchia model, developed by L. G. Jacchia from satellite drag data, and the MSIS model, developed by A. E. Hedin from mass spectrometer and incoherent scattering measurements made from satellites and ground stations respectively. Both have been shown to have an estimated error of around 15%. These codes require the user to input values for all of the principle density variations mechanisms: altitude, F10.7, Ap, time of day, day of year, latitude, and longitude. Based on these inputs, these atmospheric models calculate nominal atmospheric densities. The Free Molecular Heating K-Factor Calculation Section discusses the use of the MSIS code to calculate K-factors.

K-Factors

To calculate a three-sigma dispersed density, the nominal atmospheric densities have to be increased to account for the solar activity and other dispersion mechanisms. The atmospheric density calculation codes, with suitably dispersed input parameters and suitably applied error estimates, could be used in each calculation of dispersed density; however, an easier approach is generally used. Atmospheric density dispersion factors called "K-factors" have been developed to disperse the nominal densities, for different altitudes and for different times in the solar cycle. These K-factors can be conservatively calculated to bound a given time period by dividing the three sigma dispersed density calculated from the density codes by the nominal density.

The dispersed density is then regenerated by multiplying the nominal density at a given altitude by the corresponding K-factor for that altitude and for the range of years desired as in Equation 3. The method for deriving K-factors is discussed in the following section.

FREE MOLECULAR HEATING K-FACTOR CALCULATION

Free molecular heating (FMH) is calculated by cubing the relative velocity and multiplying it by one half the atmospheric density (Equation 1). Given nominal atmospheric density and velocity, nominal FMH fluxes can be calculated. However, standard engineering practices require additional conservatism to account for possible dispersions. These dispersions are accounted for by multiplying the nominal density by a dispersion factor or K-factor .

To calculate dispersed atmospheric density, four primary sources are used: 1) Atmospheric density model, which predicts nominal atmospheric density given the atmospheric location with respect to the Earth, and the solar, and geomagnetic index parameters; 2) Forecasts of solar activity; 3) Measured daily solar and geomagnetic index data collected over the past 59 years; and 4) Atmospheric model uncertainty equation used to disperse nominal predicted densities. Using a Monte Carlo statistical technique and the U.S. Standard 1976 atmospheric density (Reference 1), K-factors can be determined. To automate this process a computer program has been developed by the authors.

Atmospheric Density Model (MSIS-86)

Due to the significant effect that the upper atmospheric density has on space vehicles and satellites, a great deal of work has been done in developing a method for determining atmospheric densities and temperatures. Through the years, several mathematical models have been developed (Figure 8) based on atmospheric calculations from satellite drag data, incoherent scatter data from ground sites, and measured atmospheric conditions from mass spectrometer measurements on numerous satellites. Not only can these models provide estimates of density, but atmospheric composition, temperature, molecular mass, pressure scale height, and density scale height for altitudes between 85 and 2500 km (46 and 1350 nmi).

The MSIS-86 (Mass Spectrometer and Incoherent Scatter) model (Reference 13) is one of the latest in the series of empirical models developed. This model uses user-provided values of day of year, time of day, altitude, latitude, longitude, local solar time, geomagnetic index, predicted three month average F10.7 cm radio solar flux (F10.7), and daily F10.7 solar flux. The model predicts atmospheric temperature, total density, and densities of N2, O2, O, N, He, Ar, and H. This model is based on atmospheric composition and temperature data from eight scientific satellites (OGO-6, San Marc-3, Aeros-A, AE-C, -D, -E, ESRO-4, and DE-2) and numerous rocket probes, as well as five ground-based incoherent scatter stations (Millstone Hill, St. Santin, Arecibo, Jicamarca, and Malvern) (Reference 14).

GDSS has adopted the MSIS-86 atmospheric code to predict nominal atmospheric densities as a function of altitude and year. This decision was based on the Reference 14 comparison study, identifying the MSIS-86 model as the most up-to-date atmospheric model. However, an additional study (Reference 15) was performed that showed discrepancies in the MSIS-86 predicted density results for latitudes near the north pole. To overcome this discrepancy, atmospheric densities calculated with latitudes greater than 60 degrees were changed to reflect the southern hemisphere values.

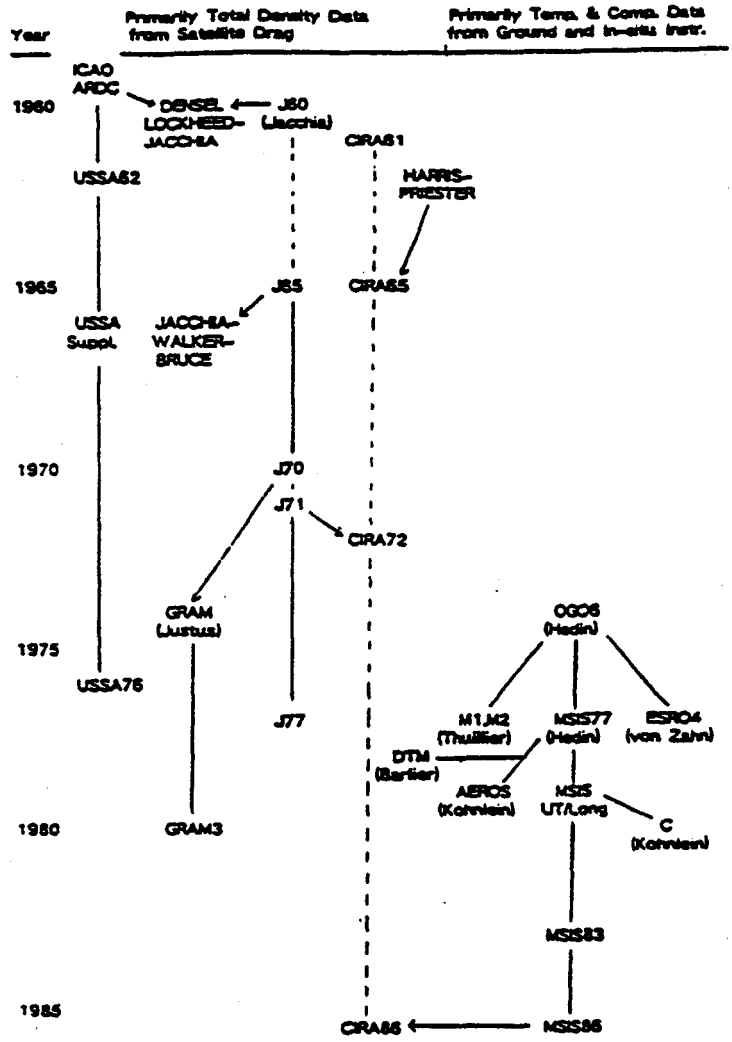

Figure 8. Historical Development of Empirical Thermoshpere Models (Reference 14).

Solar and Geomagnetic Activity Forecast

Upper atmospheric density fluctuations are strongly influenced by changing levels of solar activity. The F10.7 cm solar flux and geomagnetic index inputs are ground measurements used to indicate the level of solar activity. This solar activity data is collected and summarized in monthly publications provided by NASA-Marshall Space Fight Center (MSFC) (Reference 16) and National Oceanic and Atmospheric Administration (NOAA) (Reference 10). This data is used as input data to upper atmospheric models to predict upper atmospheric conditions.

The MSFC solar flux (F10.7) and geomagnetic index (Ap) long range statistical estimates are based upon historical F10.7 cm solar flux and geomagnetic index measurements. These estimates (1992 to 2008) are based on the statistical data of solar cycles 9 through 22 (1850 to 1992). Figure 9 illustrates the MSFC 13-month average F10.7 cm solar flux predictions. As shown in Figure 9, nominal predictions as well as 2-sigma dispersed high and low predictions are provided. The nominal curve represents the most likely curve that is expected in the future based on the most recent observed data. To provide additional conservatism to the calculation of FMH, the 2-sigma (97.7%) high 13-month F10.7 solar flux average predictions were used.

Due to the variations in daily F10.7 cm solar flux and geomagnetic index, these parameters cannot be projected into the future with any acceptable degree of statistical confidence. Because these parameters are required input to the MSIS-86 program, alternate techniques of determining these values have been developed (see Measured Solar and Geomagnetic Index Data and Computer Program Sections).

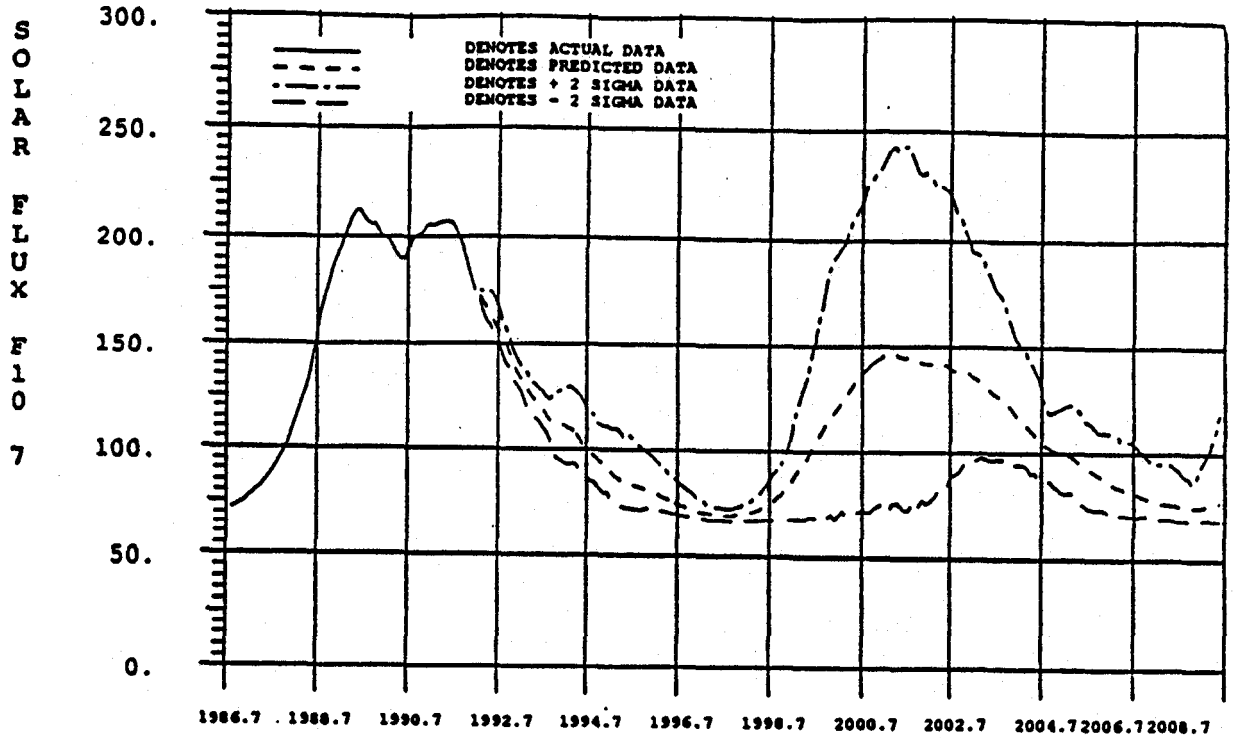

Figure 9. MSFC (Ref. 18) Long Range Estimates of Solar Activity for Solar Cycles 22 and 23.

Measured Solar and Geomagnetic Index Data

Measured daily geomagnetic and solar activity summaries were obtained through the National Geophysical Data Center (Reference 17). The available data contains daily summary records from January 1, 1932 through June 30, 1990. The planetary geomagnetic index (ap) is provided every three hours throughout the day and represents the planetary average based on 13 observations between 46 degrees north and 63 degrees south latitudes. The daily Ap average is determined from the arithmetic mean of the day's eight ap values. The daily Ap index is used in the calculation of atmospheric density. The daily F10.7 cm solar flux represents the value measured in Ottawa, Canada at 1700 GMT. The F10.7 cm solar flux measurements began on February 14, 1947 and are expressed in units of 10^{-22} Watts m^{-2} Hz^{-1}. Figures 10 and 11 illustrate the measured daily F10.7 cm solar flux and Ap values for solar cycles 18 through 22.

Based on this measured data, a new data file was generated which consists of the date, daily average Ap and daily F10.7 cm solar flux. Additionally, for each day, the 3-month and 13-month F10.7 cm solar flux averages were calculated and added to the data file. Because the F10.7 predictions are only available in 13-month averages and the MSIS-86 program requires 3-month F10.7 averages as input, it was necessary to generate these 3-month averages. The 3-month F10.7 cm average solar flux for a given day was calculated by averaging the preceding and following 45 daily F10.7 cm solar flux measurements (90 total values). Similarly the 13-month F10.7 cm solar flux averages were calculated by averaging the previous and following 195 daily F10.7 cm solar flux measurements (390 total values). Figure 12 illustrates the resulting 3 and 13-month averages for solar cycle 19.

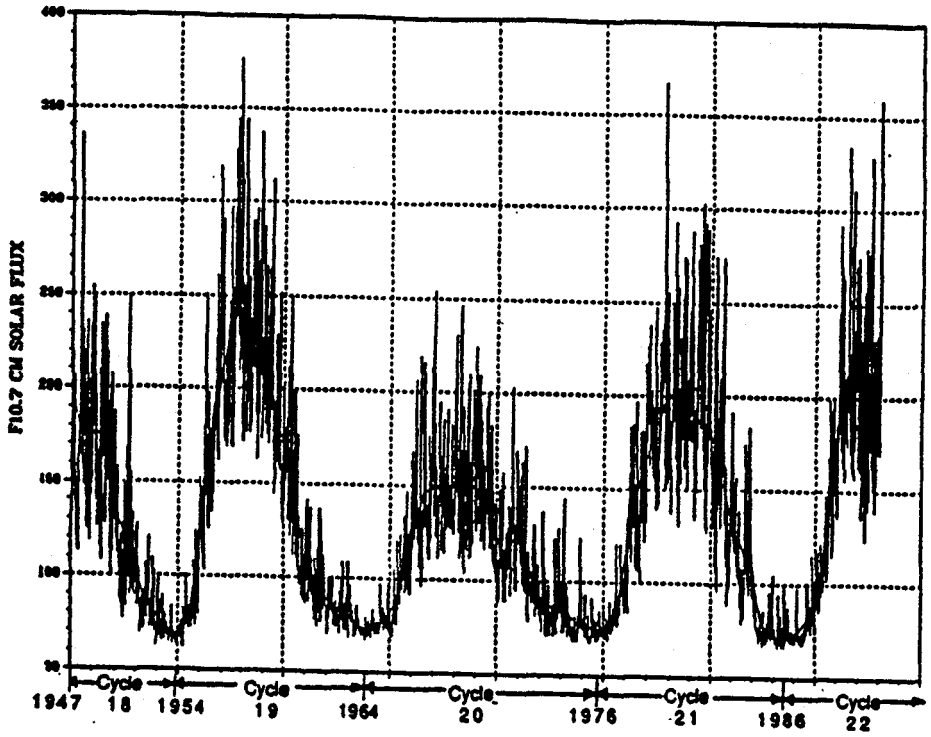

Figure 10. Measured Daily F10.7 cm Solar Flux for Solar Cycles 18 through 22 (Ref. 17).

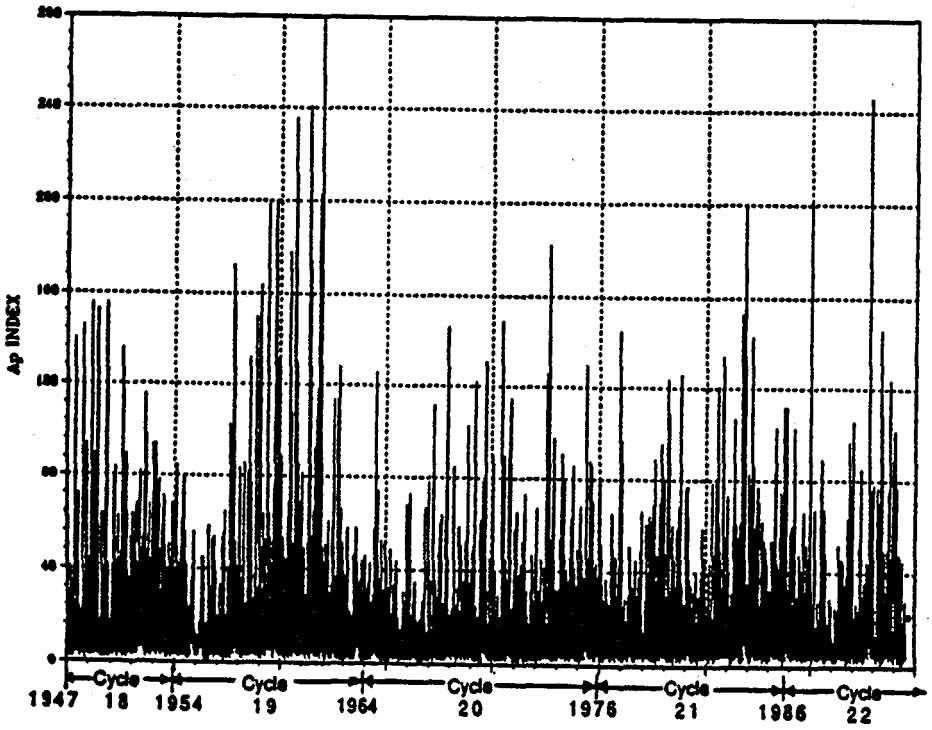

Figure 11. Measured Daily Geomagnetic Index (Ap) for Solar Cycles 18 through 22 (Ref. 17).

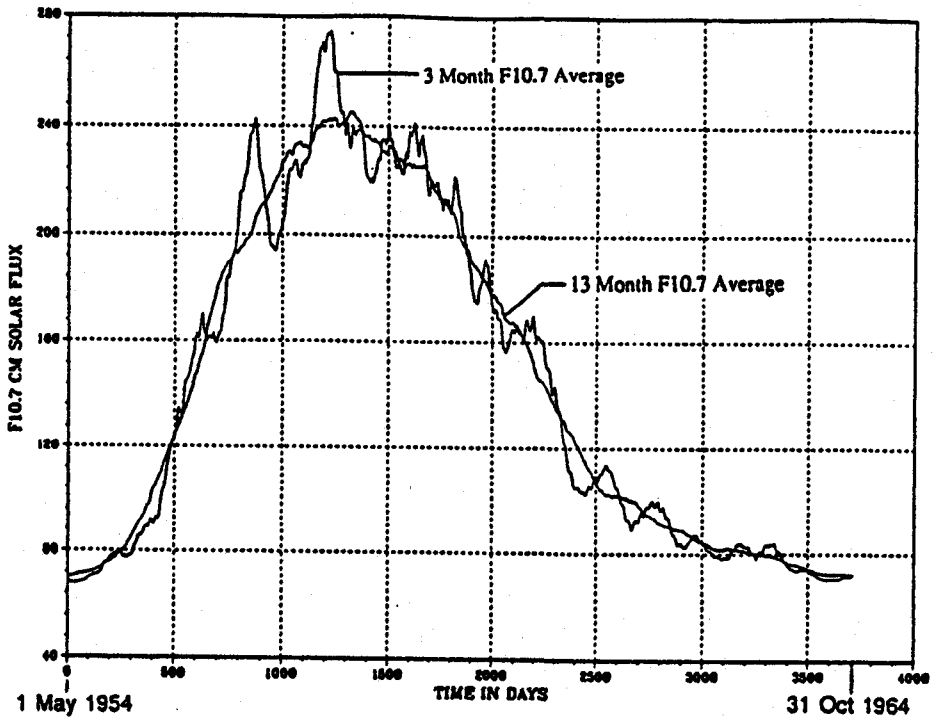

Figure 12. Calculated 3 and 13-month F10.7 Solar Flux Averages for Solar Cycle 19.

Atmospheric Model Uncertainty

Even though the inputs to MSIS-86 are selected so as to maximize density, the atmospheric densities calculated by MSIS-86 represent the best approximation of density and are considered nominal values. To account for MSIS model prediction uncertainties another dispersion factor was incorporated. D. Kayser, Aerospace Corp., developed analytical functions to predict dispersed atmospheric density within 99.865% (approximately 3-sigma) confidence level relative to MSIS-83 atmospheric model (Reference 15). Predictions from the MSIS-83 model were compared to the available Aerospace density data base to derive these equations. Knowing that the differences in predicted atmospheric density between the MSIS-83 and MSIS-86 models are small between latitudes -90 and 60 degrees, the authors applied the model uncertainty equations developed for the MSIS-83 model to the MSIS-86 model.

The Reference 15 derived expression for the calculation of dispersed density as a function of altitude is provided below:

$$r_c(h) = (0.769\text{-}0.307 \exp\{-[(h\text{-}102.5)/126.21]^4\}) \quad (6)$$

where:

$r_c(h)$ is the 3-sigma confidence level as a function of altitude (h) in kilometers.

$$\rho_{disp} = \rho_{nominal} \exp(r_c(h)) \quad (7)$$

where:

ρ_{disp} = 3-sigma dispersed atmospheric density

$\rho_{nominal}$ = MSIS-86 predicted density

Monte Carlo Statistical Technique

There have been a large number of calculations of the drag exerted by the atmosphere on satellites and measurements made by density gauges and mass spectrometers aboard rockets and satellites. These calculations and measurements have revealed several different effects other than altitude that result in variations of density, temperature, and composition of the upper atmosphere. The parameters and assumed ranges used as input to the MSIS-86 program are listed below:

IYD - Day of the year (1 through 365 days)
UT - Universal time or GMT (0 to 86400 seconds)
ALT - Altitude (440 to 1000 kft)
LAT - Latitude (user provided)
LONG - Longitude (0 to 360°)
LST - Local solar time (0 to 24 hours)
F107A - Predicted 3-month average F10.7 cm solar flux
F107 - Daily F10.7cm solar flux
Ap - Geomagnetic index

The MSIS-86 input parameters associated with defining solar activity are F107A, F107, and Ap. The remaining input parameters define the Earth's position relative to the sun (IYD, UT), point of interest within the Earth's atmosphere (ALT, LAT, and LONG), and location on Earth with respect to the sun (LST). A parametric analysis was performed to identify the sensitivity of atmospheric density as a function of each parameter. Results from this study are shown in the Appendix.

Since these parameters are dependent on each other, it is not a simple task to identify which combination of parameters will result in maximizing atmospheric density for a given set of solar conditions. To simplify this procedure, a Monte Carlo statistical approach was incorporated to predict maximum dispersed atmospheric density values.

For a given altitude, random values of IYD, UT, LAT, LONG, and LST were selected within their valid ranges. Additionally, daily and 3-month average F10.7 solar fluxes and Ap values for a given day were randomly selected from a generated data file (see Measured Solar and Geomagnetic Index Data Section). Based on these inputs atmospheric density was calculated using the MSIS-86 program. Using this process, 1000 density values were calculated and a 3-sigma dispersed density was determined using the following equation:

$$RHO3SIG = RHOAV + 3\left[\frac{\sum_{i=1,n}(RHO_i - RHOAV)^2}{N-1}\right]^{.5} \quad (8)$$

where:

RHO3SIG = 3-sigma dispersed density
RHOAV = calculated average density
RHO_i = a given density value
N = number of density values calculated

K-Factor Computer Program

To automate the calculation of K-factors, a computer program was developed. Figure 13 illustrates the program flow chart. The only program inputs required are the predicted 13-month F10.7 cm solar flux, and latitude range for which the K-factors are to apply. Variations in latitude were incorporated to allow flexibility for missions which may have unique parking orbit

latitudes. Results presented herein were based on latitudes between ±60 degrees which will encompass all typical geosynchronous transfer orbit trajectories and latitudes between ±90 degrees to include polar orbit trajectories. Based on the parametric study results (see the Appendix), K-factors tend to increase as a function of increasing latitude.

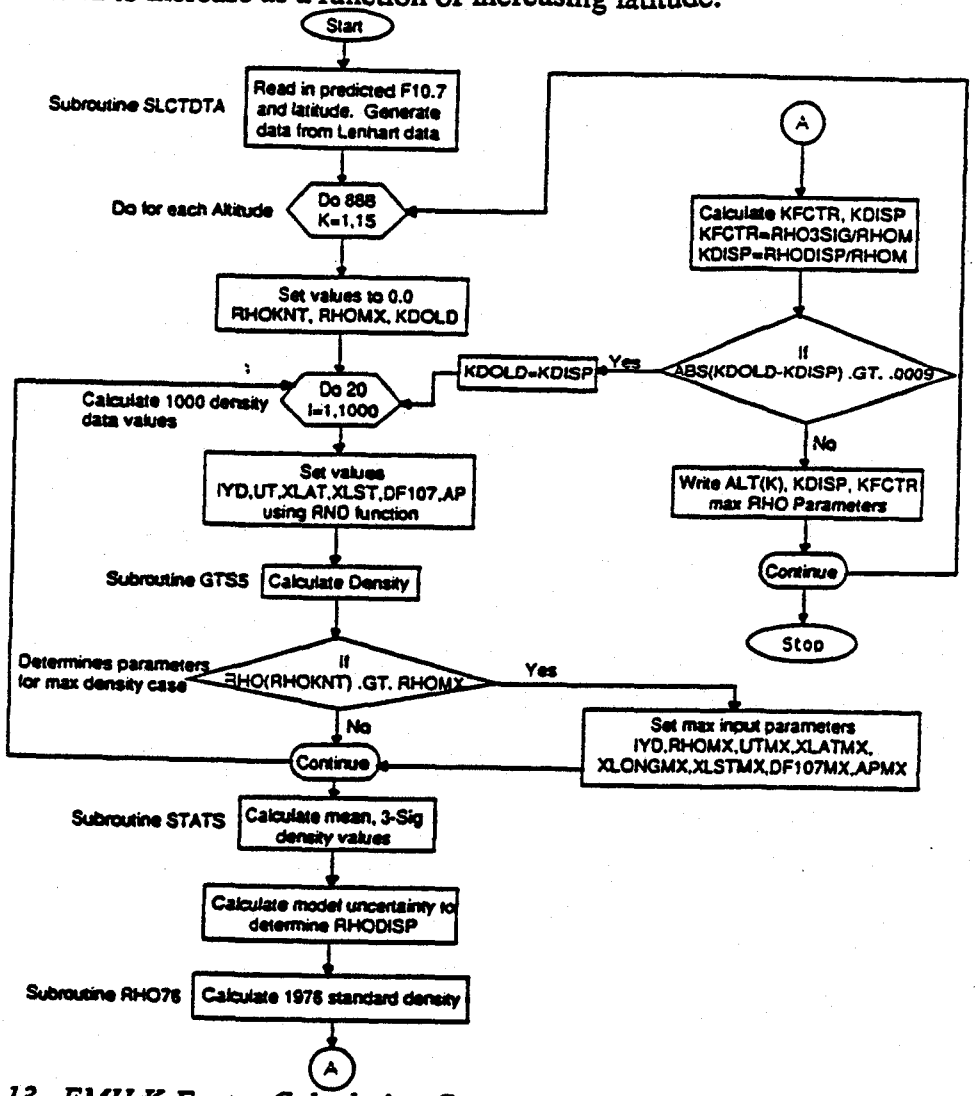

Figure 13. FMH K-Factor Calculation Computer Program Flow Chart

FMH K-factors were calculated at various altitude heights ranging from 134 to 305 km (72 to 165 nmi). For altitudes up to 133 km (72 nmi), 3-sigma dispersed densities calculated specifically for the Atlas/Centaur launch vehicle (Reference 18) are used. For altitudes greater than 305 km (165 nmi) the density is assumed to be negligible.

The entered F10.7 cm solar flux 13-month predicted average is used to determine the data set of daily values of F10.7, Ap, and calculated 3-month F10.7 averages extracted from measured historical data (see Measured Solar and Geomagnetic Index Data Section). The 13-month F10.7 average solar flux value, for a given day, represents the average of the 195 preceding and following F10.7 measured daily values. Using the Reference 17 measured historical data, a data set of daily F10.7 and corresponding Ap values can be determined which are representative of the predicted 13-month F10.7 solar flux value (user provided). When the predicted 13-month F10.7 value intersects the measured 13-month F10.7 value for past solar cycles, the previous and following daily measured F10.7 and Ap values are written to a data file for each intersection of measured 13-month F10.7 values. Additionally, because the MSIS-86 atmospheric model

requires 3-month F10.7 averages as input, these values are calculated and included in this data set. Figure 14 illustrates the methodology of this data selection process.

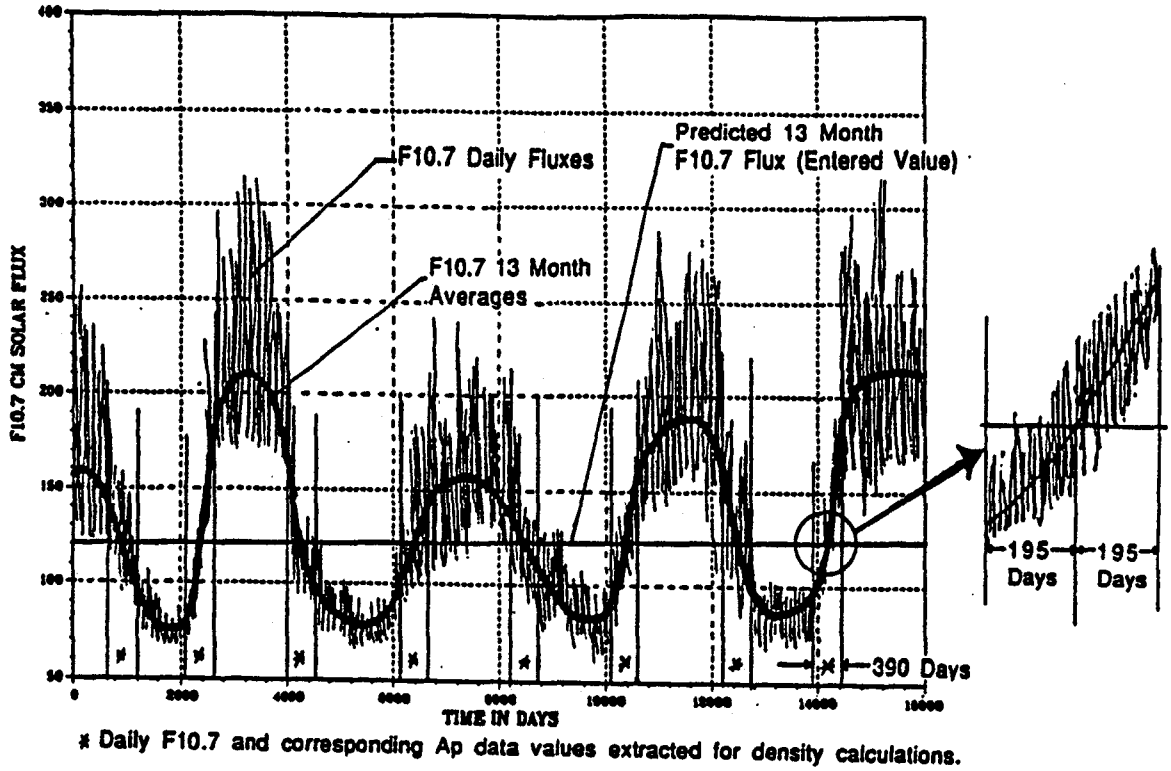

Figure 14. Illustration of the Data Selection Methodology in Determining Daily F10.7 and Ap Measured Values for the Calculation of FMH K-Factors.

Values of Ap and F10.7 daily and 3-month averages are randomly selected from this data file in performing the Monte Carlo statistical method (see Monte Carlo Statistical Technique Section). After performing this operation 1000 times, the 3-sigma dispersed atmospheric density is calculated using Equations 7 and 8.

After another 1000 density values are calculated and added to the data set, a new 3-sigma dispersed density is determined and compared to the original calculated 3-sigma density value. If the difference between these two values is less than the convergence criterion (set to 0.0009) it is assumed that a solution has been determined. If the convergence criterion has not been satisfied, the process is repeated. Once the convergence criterion has been satisfied, the FMH K-factor for a given altitude is calculated by dividing the 3-sigma dispersed density by the U.S. Standard 1976 atmospheric density (Reference 1).

K-Factor Results

Tables 2 and 3 list the calculated 3-sigma K-factors for the maximum recorded solar flux value (worst case) and worst case yearly values from 1992 to 2008. Table 2 lists the K-factors which are valid for missions with low Earth parking orbits circling the Earth between latitudes of ±60 degrees and Table 3 lists K-factors valid for all latitudes (±90 degrees). The predicted K-factor for a given year is based on the Reference 16 largest monthly predicted 2-sigma high 13-month F10.7 cm solar flux average for that year. If the month of a scheduled launch is known, less conservative K-factors could be calculated based on actual monthly values; however, it is recommended that yearly values be used to avoid invalidating analysis results due to a possible launch delay.

Because the K-factors are calculated using atmospheric densities based on random inputs, slight variations in the results can occur. The magnitude of these variations has been observed to be a function of altitude and entered 13-month average F10.7 solar flux with the variations increasing with increasing altitude and F10.7 value. Table 4 illustrates the calculated worst case predicted K-factors from six separate runs using the same input values. For low altitudes (less than 191km (625 kft)) differences in results are approximately ±0.02. For altitudes greater than 191 km (625 kft) the variation in the results were found to be approximately ±0.03.

It is noted here that the results of this analysis are only as good as the F10.7 cm solar flux predictions. The farther into the future the FMH K-factors are calculated, the greater the uncertainty of the prediction. Even though great effort has been made to predict conservative K-factors there have been recorded instances where abnormally high levels of geomagnetic disturbances and solar fluxes have occurred (Reference 19). In the unlikely event this were to happen, the predicted K-factor values would not be bounding. Even though there is a chance (beyond 3-sigma) this could occur, it would be unrealistic to design a space vehicle to withstand these levels.

Table 2. Worst Case Free Molecular Heating K-Factors vs. Altitude as a Function of Year for Latitudes Between ±60°

Altitude		Worst Case (244.0)	1992 (188.9)	1993 (151.0)	1994 (134.0)	1995 (112.3)	1996 (96.6)	1997 (78.5)	1998 (97.4)	1999 (186.6)
Kft	nmi									
440.0	72.42	1.86	1.79	1.73	1.72	1.69	1.68	1.66	1.68	1.78
450.0	74.06	1.91	1.82	1.77	1.75	1.72	1.70	1.68	1.69	1.82
475.0	78.18	2.08	1.95	1.86	1.83	1.78	1.74	1.70	1.75	1.95
500.0	82.29	2.26	2.09	1.97	1.93	1.86	1.81	1.73	1.82	2.09
525.0	86.40	2.49	2.25	2.09	2.03	1.94	1.87	1.77	1.87	2.23
550.0	90.52	2.69	2.41	2.21	2.15	2.03	1.93	1.80	1.95	2.41
575.0	94.63	2.96	2.59	2.36	2.26	2.13	2.00	1.84	2.01	2.59
600.0	98.75	3.24	2.81	2.52	2.44	2.24	2.10	1.87	2.08	2.81
625.0	102.86	3.55	3.06	2.70	2.59	2.38	2.19	1.91	2.20	3.06
650.0	106.98	3.92	3.31	2.89	2.78	2.50	2.29	1.98	2.30	3.31
675.0	111.09	4.31	3.60	3.10	2.95	2.66	2.39	2.03	2.40	3.59
700.0	115.21	4.72	3.96	3.34	3.16	2.80	2.51	2.07	2.53	3.89
800.0	131.66	6.71	5.33	4.34	4.02	3.45	2.95	2.26	2.99	5.32
900.0	148.12	8.93	6.73	5.29	4.77	3.94	3.28	2.32	3.36	6.72
1000.0	164.58	11.15	8.04	5.95	5.31	4.23	3.37	2.26	3.45	7.97

Altitude		2000 (231.4)	2001 (243.0)	2002 (231.0)	2003 (200.5)	2004 (154.3)	2005 (122.6)	2006 (109.9)	2007 (96.7)
Kft	nmi								
440.0	72.42	1.84	1.86	1.84	1.79	1.74	1.70	1.69	1.68
450.0	74.06	1.89	1.91	1.88	1.84	1.78	1.73	1.71	1.69
475.0	78.18	2.04	2.07	2.05	1.95	1.87	1.81	1.78	1.75
500.0	82.29	2.22	2.28	2.21	2.09	1.98	1.89	1.85	1.80
525.0	86.40	2.41	2.48	2.42	2.27	2.12	1.99	1.94	1.87
550.0	90.52	2.61	2.69	2.63	2.43	2.26	2.08	2.02	1.93
575.0	94.63	2.87	2.94	2.85	2.62	2.40	2.21	2.12	1.99
600.0	98.75	3.15	3.23	3.13	2.85	2.56	2.34	2.23	2.09
625.0	102.86	3.43	3.56	3.43	3.10	2.76	2.46	2.35	2.19
650.0	106.98	3.78	3.90	3.76	3.34	2.95	2.62	2.49	2.29
675.0	111.09	4.13	4.29	4.12	3.67	3.17	2.80	2.63	2.38
700.0	115.21	4.53	4.75	4.55	3.97	3.44	2.96	2.78	2.50
800.0	131.66	6.46	6.76	6.42	5.44	4.49	3.71	3.40	2.95
900.0	148.12	8.44	8.94	8.43	6.96	5.41	4.35	3.85	3.26
1000.0	164.58	10.42	11.12	10.38	8.31	6.27	4.70	4.15	3.39

Note: Values in parentheses are entered 13-month averaged F10.7 values

Table 3. Worst Case Free Molecular Heating K-Factors vs. Altitude as a Function of Year for Latitudes Between ±90°

Altitude		Worst Case (244.0)	1992 (188.9)	1993 (151.0)	1994 (134.0)	1995 (112.3)	1996 (96.6)	1997 (78.5)	1998 (97.4)	1999 (186.6)
Kft	nmi									
440.0	72.42	1.90	1.82	1.79	1.77	1.74	1.72	1.70	1.73	1.82
450.0	74.06	1.97	1.87	1.83	1.79	1.78	1.75	1.73	1.75	1.87
475.0	78.18	2.14	2.00	1.93	1.90	1.86	1.82	1.77	1.83	2.00
500.0	82.29	2.36	2.16	2.06	1.99	1.94	1.90	1.82	1.89	2.16
525.0	86.40	2.56	2.34	2.19	2.13	2.04	1.98	1.88	1.99	2.33
550.0	90.52	2.78	2.51	2.33	2.26	2.14	2.05	1.93	2.03	2.49
575.0	94.63	3.06	2.71	2.46	2.38	2.26	2.12	1.96	2.14	2.69
600.0	98.75	3.34	2.91	2.66	2.56	2.36	2.22	2.02	2.25	2.93
625.0	102.86	3.70	3.16	2.83	2.72	2.50	2.33	2.08	2.33	3.17
650.0	106.98	4.05	3.46	3.01	2.90	2.64	2.43	2.11	2.44	3.41
675.0	111.09	4.44	3.74	3.24	3.10	2.78	2.53	2.18	2.56	3.72
700.0	115.21	4.88	4.05	3.50	3.29	2.93	2.63	2.20	2.65	4.04
800.0	131.66	6.90	5.43	4.48	4.18	3.55	3.05	2.39	3.09	5.42
900.0	148.12	9.03	6.83	5.35	4.92	4.01	3.31	2.40	3.38	6.74
1000.0	164.58	11.05	7.99	5.96	5.35	4.20	3.38	2.25	3.42	7.94

Altitude		2000 (231.4)	2001 (243.0)	2002 (231.0)	2003 (200.5)	2004 (154.3)	2005 (122.6)	2006 (109.9)	2007 (96.7)
Kft	nmi								
440.0	72.42	1.88	1.90	1.87	1.81	1.79	1.76	1.75	1.73
450.0	74.06	1.92	1.97	1.93	1.87	1.82	1.79	1.78	1.75
475.0	78.18	2.09	2.13	2.10	2.00	1.93	1.88	1.85	1.83
500.0	82.29	2.29	2.33	2.27	2.15	2.06	1.98	1.95	1.90
525.0	86.40	2.49	2.57	2.49	2.33	2.22	2.07	2.05	1.98
550.0	90.52	2.69	2.79	2.71	2.51	2.35	2.18	2.14	2.05
575.0	94.63	2.98	3.03	2.96	2.71	2.51	2.32	2.24	2.13
600.0	98.75	3.24	3.36	3.19	2.96	2.69	2.44	2.39	2.21
625 0	102.86	3.54	3.70	3.55	3.20	2.88	2.59	2.49	2.32
650 0	106.98	3.89	4.07	3.90	3.48	3.08	2.75	2.62	2.45
675.0	111.09	4.27	4.41	4.26	3.78	3.30	2.90	2.75	2.50
700.0	115.21	4.68	4.85	4.68	4.14	3.56	3.09	2.91	2.66
800.0	131.66	6.56	6.90	6.57	5.49	4.59	3.82	3.50	3.08
900.0	148.12	8.50	9.03	8.49	7.03	5.54	4.38	3.93	3.32
1000.0	164.58	10.26	10.97	10.30	8.17	6.17	4.71	4.12	3.40

Note: Values in parentheses are entered 13-month averaged F10.7 values

Table 4. Worst Case Variations in the Calculation of FMH K-Factors

Altitude		Calculated K-Factors Assuming Latitude 90 deg and F10.7 = 244.0						Average	Max Delta
Kft	nmi								
440.0	72.42	1.90	1.90	1.90	1.90	1.90	1.89	1.90	0.01
450.0	74.06	1.97	1.96	1.95	1.97	1.96	1.96	1.96	0.01
475.0	78.18	2.14	2.12	2.14	2.13	2.13	2.14	2.13	0.01
500.0	82.29	2.36	2.33	2.34	2.33	2.33	2.36	2.34	0.02
525.0	86.40	2.56	2.57	2.56	2.56	2.55	2.56	2.56	0.01
550.0	90.52	2.78	2.80	2.79	2.80	2.78	2.78	2.79	0.01
575.0	94.63	3.06	3.06	3.04	3.04	3.07	3.05	3.05	0.02
600.0	98.75	3.34	3.36	3.36	3.35	3.35	3.35	3.35	0.01
625.0	102.86	3.70	3.69	3.68	3.68	3.68	3.70	3.69	0.01
650.0	106.98	4.05	4.04	4.05	4.04	4.01	4.04	4.04	0.03
675.0	111.09	4.44	4.42	4.47	4.43	4.45	4.45	4.44	0.03
700.0	115.21	4.88	4.90	4.87	4.88	4.87	4.90	4.88	0.01
800.0	131.66	6.90	6.89	6.88	6.90	6.86	6.89	6.89	0.03
900.0	148.12	9.03	9.01	9.00	9.02	9.02	9.01	9.01	0.02
1000.0	164.58	11.05	11.07	11.03	11.01	11.01	11.04	11.04	0.03

Note: Max Delta = Maximum difference between average and predicted value for a given altitude

REFERENCES

1. *US Standard Atmosphere*, 1976, National Oceanic and Atmospheric Administration, National Aeronautics and Space Administration, United States Air Force, October 1976, US Government Printing Office, Washington DC 20402, NOAA-S/T 76-1562
2. Schaaf, Samuel A. and Lawrence Talbot, "Handbook of Supersonic Aerodynamics," Section 16, Mechanics of Rarefied Gasses, Navord Report 1488, 1957.
3. Koelle, Heinz H., *Handbook of Astronautical Engineering*, McGraw-Hill, New York, 1961.
4. Caruso, Paul. S. Jr. and Charles. R. Naegeli, "Low-Perigee Aerodynamic Heating During Orbital Flight of an Atmosphere Explorer," NASA TN D-8308, NASA Goddard Space Flight Center, Maryland, September 1976.
5. Stitt, M. C.,"Payload Integration Departmental Instruction, Thermal Control (Dept. 890-0)," Report No. 10.41, Chapter 2, Issue 1, 20 December 1989.
6. Wertz, James R. and Wiley J. Larson, *Space Mission Analysis and Design*, Kluwer Academic Publishers, Norwell, MA, 1991.
7. Walterscheid, R. L.,"Solar Cycle Effects on the Upper Atmosphere: Implications for Satellite Drag," Journal of Spacecraft, Vol. 26, No. 6, Nov-Dec 1989, pages 439-444.
8. Johnson, Francis, S., *Satellite Environment Handbook, 2nd Edition*, Stanford University Press, California, 1965.
9. Withbroe, George L.,"Expectations for Solar Activity in the 1990's," AAS, 89-147, pages 727-743.
10. NOAA/SESC Monthly Newsletter, Aug. 1992, National Oceanic and Atmospheric Administration, Space Environment Services Center, Colorado, August 1992.
11. *Models of Earth's Atmosphere (90 to 2500 KM)*, NASA SP-8021, March 1973.
12. Burgess, Eric and Douglass Torr,"Into the Thermosphere, the Atmosphere Explorers," NASA SP-490, 1987.
13. Hedin, Alan E., "MSIS-86 Thermospheric Model," Journal of Geophysical Research, Vol. 92, No. A5, p. 4649-4662, 1 May 87.

14. Hedin, Alan E., "High Altitude Atmospheric Modeling," NASA Technical Memo 100707, October 1988.
15. Kayser, D. C., "A Study of Recent Thermospheric Density Models," Internal Aerospace Technical Memo ATM-88 (3531-02)-10, 17 June 1988.
16. NASA - George C. Marshall Space Flight Center, "Solar Activity Inputs for Upper Atmospheric Models Used in Programs to Estimate Spacecraft Orbital Lifetime," 5 October 1992.
17. National Oceanic and Atmospheric Administration (NOAA) National Geophysical Data Center, Lenhart Data Disk 1932-1990.
18. Erickson, J. W.,"Empirical Curve Fit for an Approximate Plus Three-Sigma Atmospheric Density Function for Altitudes Above 160,000 Feet," 697-0-81-114, 7 August 1981.
19. Hecht, J., "Solar Activity Wreaks Havoc in Heaven and Earth," New Scientist, p. 47, 30 June 1990.

APPENDIX

MSIS-86 Input Parameters Parametric Analysis

To determine the trends and sensitivity each MSIS-86 input parameter has on the calculation of K-factor, a parametric analysis was performed. For this analysis "standard" values were assumed for each input (Table A1). By varying one parameter at a time between its minimum and maximum value, while constraining the remaining inputs, nominal K-factors were calculated as a function of altitude and MSIS-86 inputs. Table A1 lists the assumed standard values and the dispersed ranges for each parameter.

Table A1. MSIS-86 Input Parameters Standard Values and Dispersions Assumed in the Parametric Analysis

PARAMETER	STANDARD VALUE	DISPERSION
Latitude (deg)	-30	-60 to 60
Longitude (deg)	150	0 to 360
Local Solar Time (hr)	13	0 to 24
Universal Time (sec)	25200	0 to 90000
Day of Year (day)	300	0 to 360
Average F10.7 Solar Flux	125	75 to 250
Daily F10.7 Solar Flux	150	75 to 300
Geomagnetic Index	20	5 to 80

The results for each input parameter are illustrated in Figures A1 through A8. Since these parameters are dependent on each other, a different set of standard values can significantly change the results. These results are only presented to show the sensitivity and trends for each input in the calculation of K-factor, and are not to be used as a method to determine K-factors.

MSIS-86 INPUTS
LONG = 150 (deg)
LST = 13 (Hr)
UT = 25200 (sec)
IYD = 300 (day)
AF10.7 = 125
DF10.7 = 150
Ap = 20

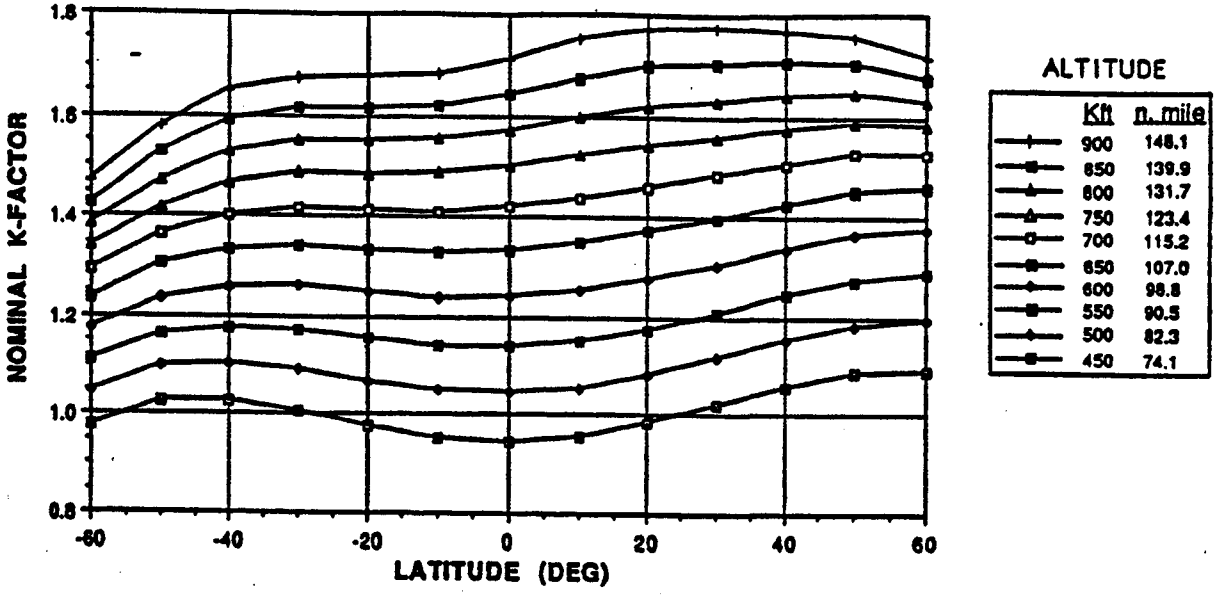

Figure A1. Nominal K-factor Calculation as a funciton of Altitude and Latitude For a Given Set of MSIS-86 Inupt Parameters.

MSIS-86 INPUTS
LAT = -30 (deg)
LST = 13 (Hr)
UT = 25200 (sec)
IYD = 300 (day)
AF10.7 = 125
DF10.7 = 150
Ap = 20

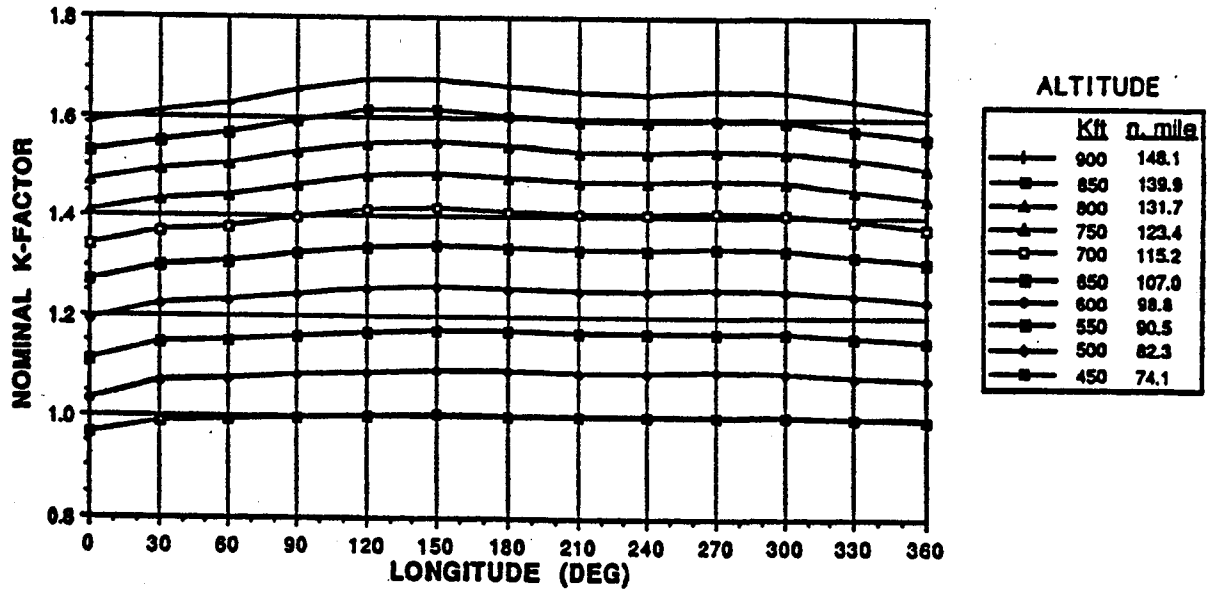

Figure A2 Nominal K-factor Calculation as a funciton of Altitude and Longitude For a Given Set of MSIS-86 Inupt Parameters.

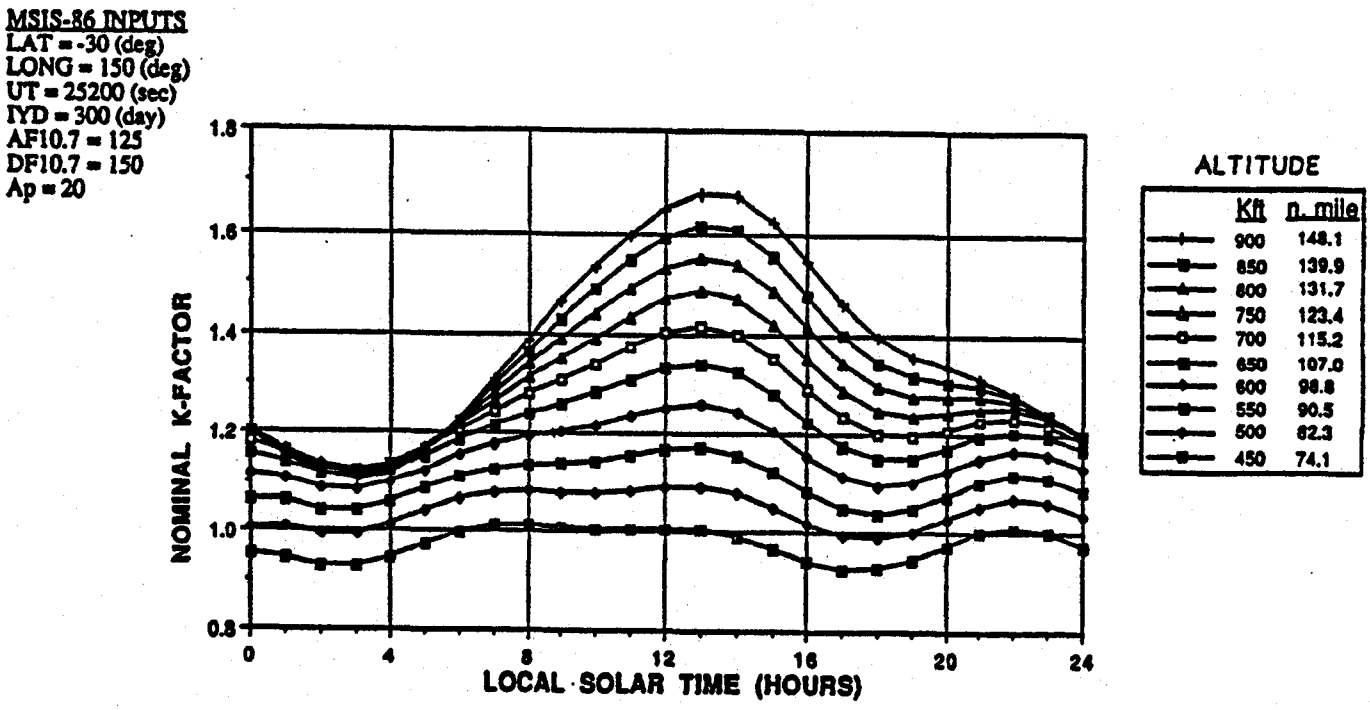

Figure A3. Nominal K-factor Calculation as a funciton of Altitude and Local Solar Time For a Given Set of MSIS-86 Inupt Parameters.

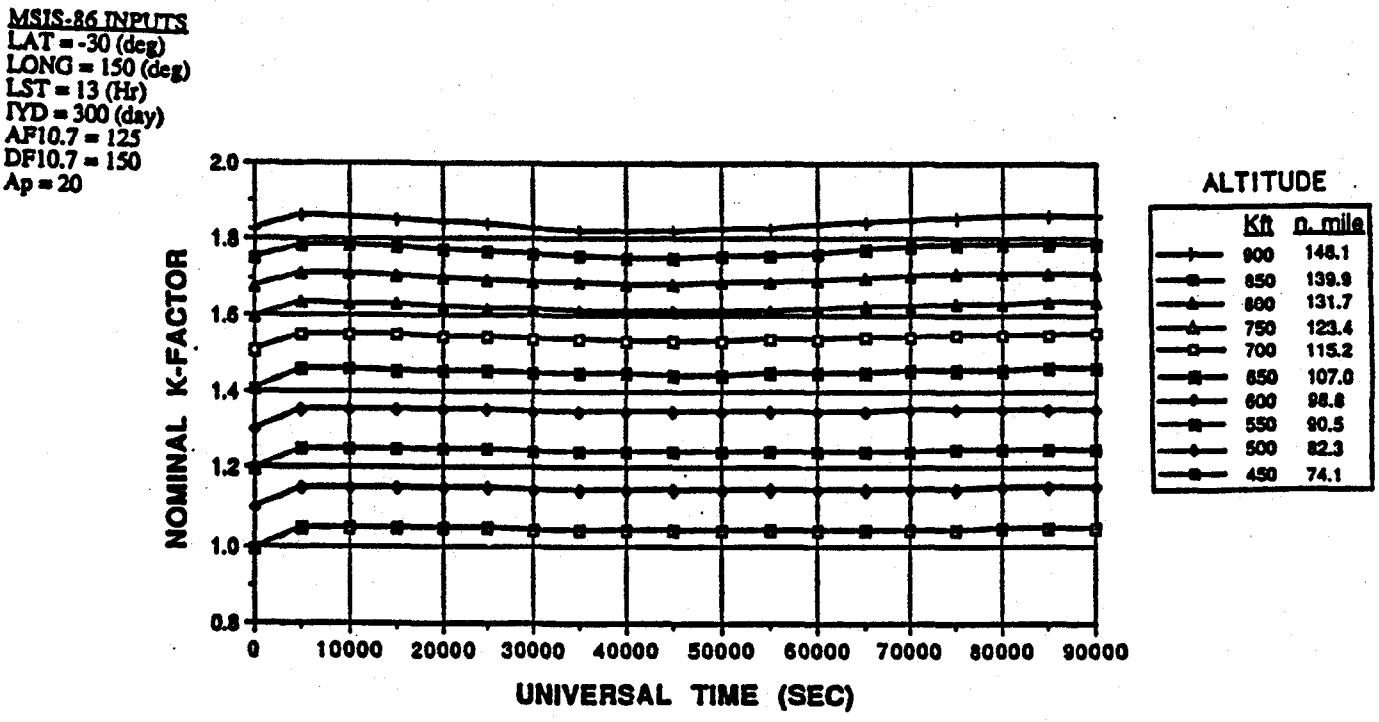

Figure A4. Nominal K-factor Calculation as a funciton of Altitude and Universal Time For a Given Set of MSIS-86 Inupt Parameters.

MSIS-86 INPUTS
LAT = -30 (deg)
LONG = 150 (deg)
LST = 13 (Hr)
UT = 25200 (sec)
AF10.7 = 125
DF10.7 = 150
Ap = 20

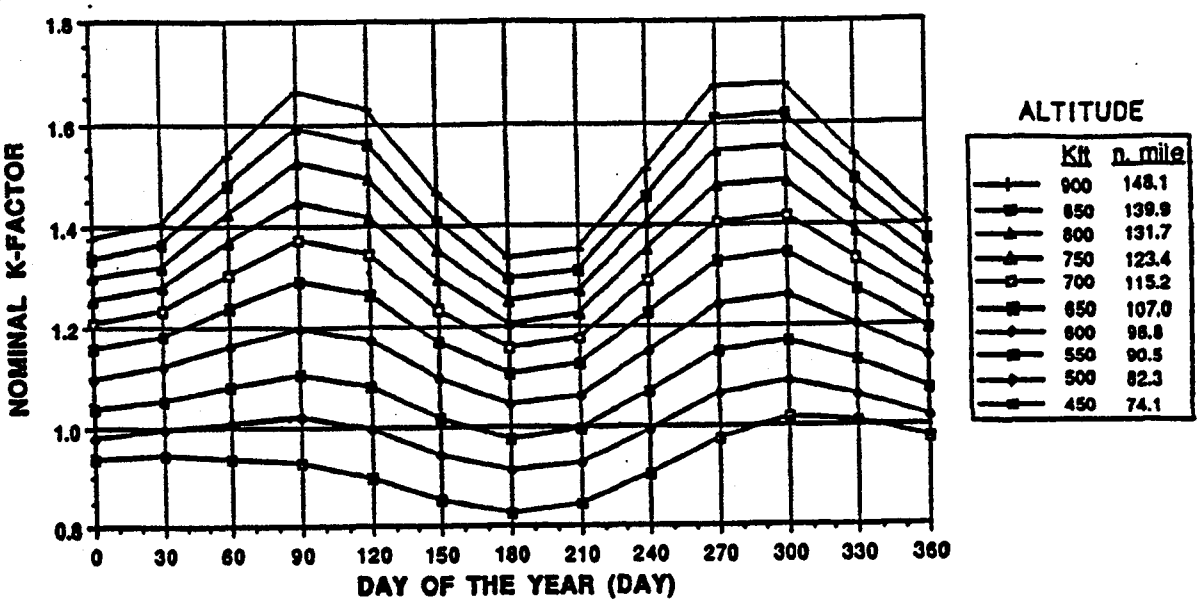

Figure A5. Nominal K-factor Calculation as a funciton of Altitude and Day of Year For a Given Set of MSIS-86 Inupt Parameters.

MSIS-86 INPUTS
LAT = -30 (deg)
LONG = 150 (deg)
LST = 13 (Hr)
UT = 25200 (sec)
IYD = 300 (day)
DF10.7 = 150
Ap = 20

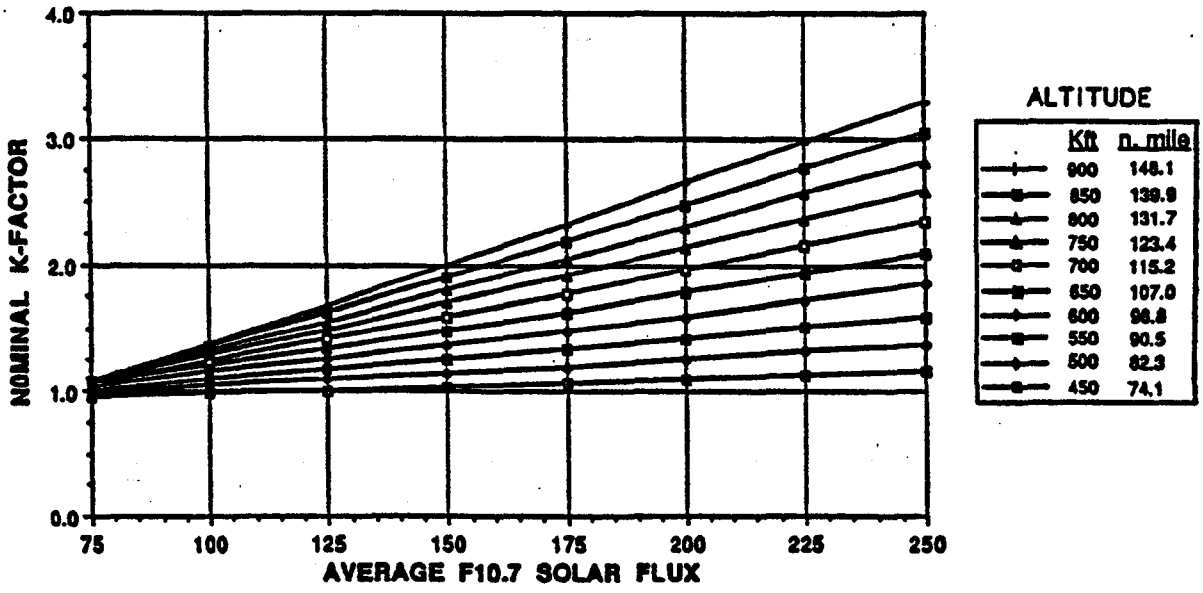

Figure A6. Nominal K-factor Calculation as a funciton of Altitude and Average F10.7 Solar Flux For a Given Set of MSIS-86 Inupt Parameters.

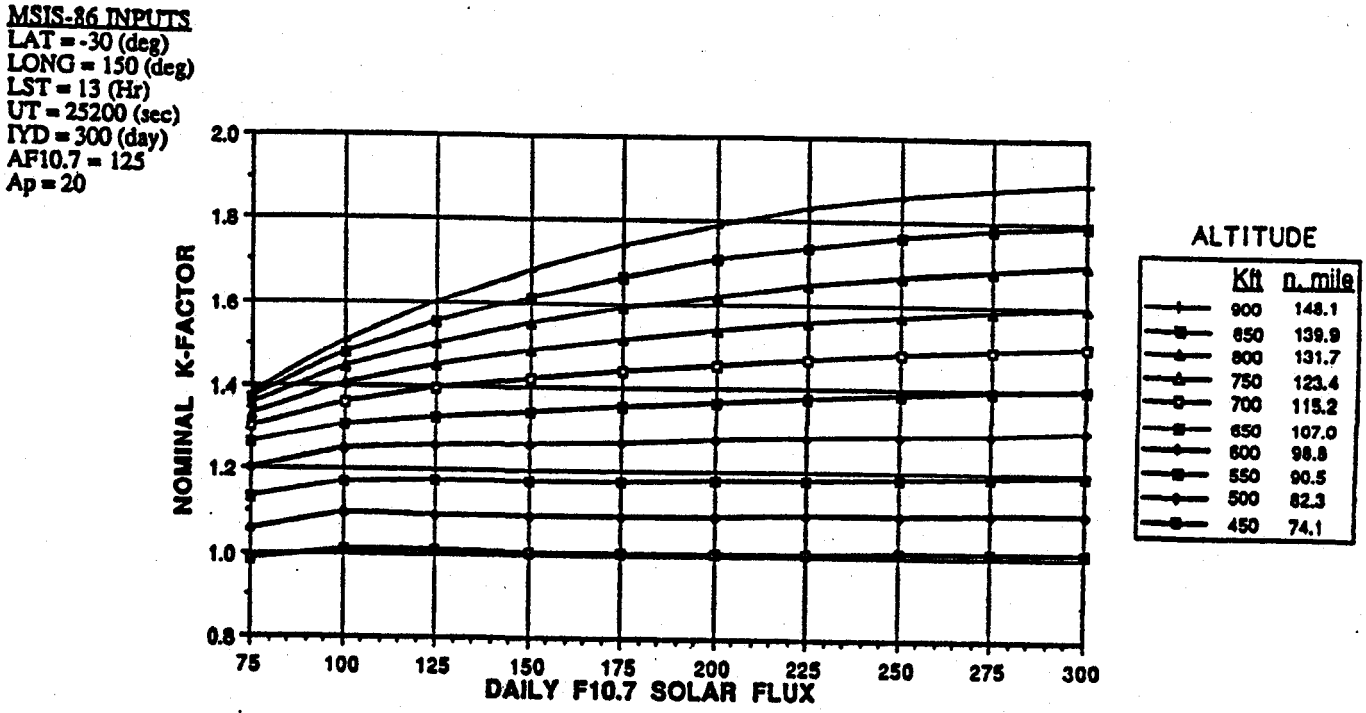

Figure A7. Nominal K-factor Calculation as a funciton of Altitude and Daily F10.7 Solar Flux For a Given Set of MSIS-86 Inupt Parameters.

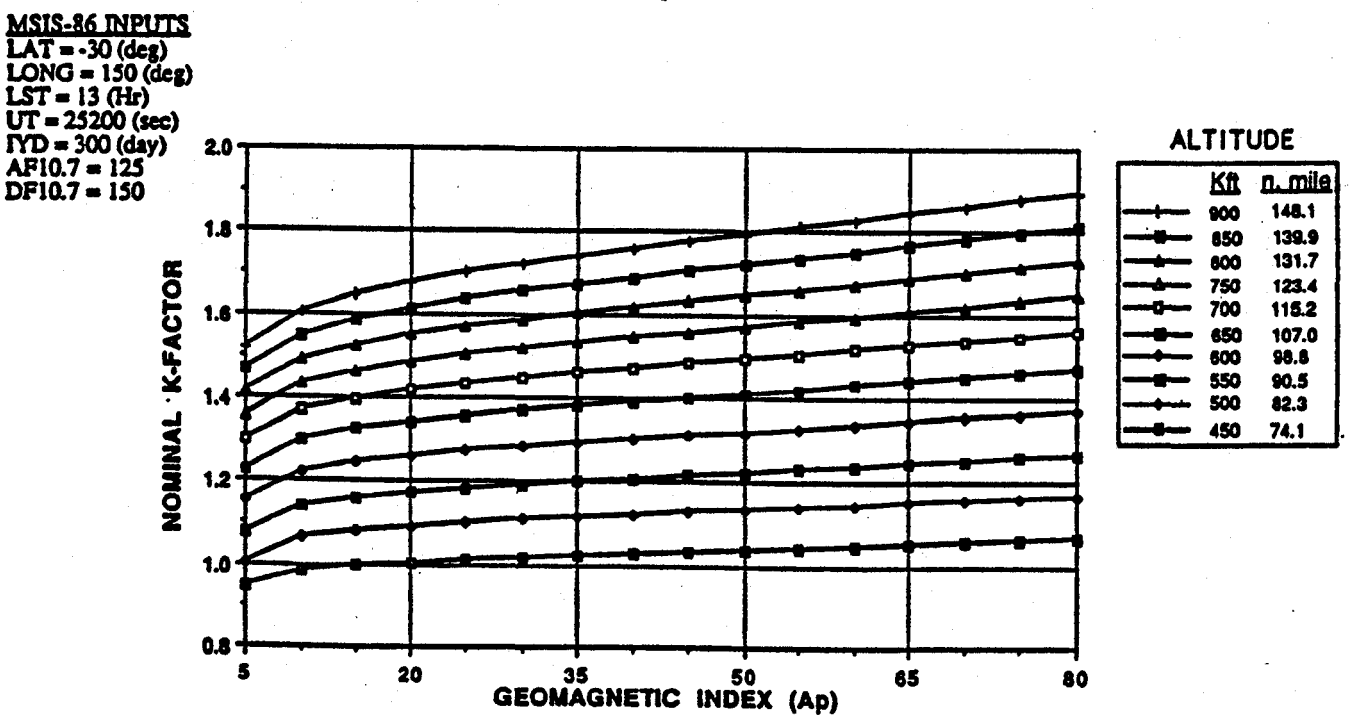

Figure A8. Nominal K-factor Calculation as a funciton of Altitude and Geomagnetic Index For a Given Set of MSIS-86 Inupt Parameters.

MIXING AND UNMIXEDNESS IN PLASMA JETS 1: NEAR-FIELD ANALYSIS

Olusegun J. Ilegbusi
Department of Mechanical Engineering
Northeastern University
Boston, MA 02115

SUMMARY

The flow characteristics in the near-field of a plasma jet are simulated with a two-fluid model. This model accounts for both gradient-diffusion mixing and uni-directional sifting motion resulting from pressure-gradient-body-force imbalance. This latter mechanism is believed to be responsible for the umixedness observed in plasma jets. The unmixedness is considered to be essentially a Rayleigh-Taylor kind instability. Transport equations are solved for the individual plasma and ambient gas velocities, temperatures and volume fractions. Empirical relations are employed for the interface transfers of mass, momentum and heat. The empirical coefficients are first established by comparison of predictions with available experimental data for shear flows. The model is then applied to an Argon plasma jet ejecting into stagnant air. The predicted results show the significant build-up of unmixed air within the plasma gas, even relatively far downstream of the torch. By adjusting the inlet condition, the model adequately reproduces the experimental data.

INTRODUCTION

Plasma jets have important applications in materials processing, some of which include spray deposition, melting and refining, heat treatment and materials synthesis. In a typical reactor, the hot plasma stream entrains a surrounding gas and the resulting heat and mass transfer and the condition of operation of the torch, determines to a large extent, the performance of the unit. The entrainment may prevent uniform mixing and produce regions of unmixed hot/cold gases and non-uniform deposits as a result of insufficient melting of deposit in cold regions. This phenomenon may also affect chemical reaction rate in plasma systems for NOx reduction in exhaust gases.

The study of plasma phenomena is often conveniently divided into three parts namely, the plasma torch, the plasma jet and analysis of the particles carried in the jet. The present work concerns processes occuring in the near-field of the plasma jet i.e. just downstream of the torch.

The early modeling approaches on plasma jets were based on the solution of momentum integral equations (refs. 1 and 2), and on highly simplified boundary layer equations (refs. 3 and 4). These techniques, while providing useful insights into the gross behavior of plasma jets, were inadequate due to their inherent approximations. A fully elliptic approach was employed later by several workers (refs. 5-10), with varying degrees of success. Such works ranged in complexity, depending on the assumptions made for the inlet conditions, property variation and treatment of the surrounding gas. They have shown that:

(i) the velocity and temperature profiles within the reactor are strongly dependent on the torch exit conditions,
(ii) plasma jets operating in a fully laminar regime could be adequately modeled by existing methodologies, and,
(iii) plasma jets operating in a fully turbulent regime could not be adequately simulated with existing conventional turbulence models. Specifically, such models could not account for the inherent non-isotropic, intermittent nature of the turbulence field.

Recent studies (refs. 11 to 14) have shown that contrary to earlier beliefs, the flow emanating from most standard torches is highly transitional over most of the domain of the reactor, and mixing of the plasma jet with the cold surrounding gas is dominated by large scale coherent structures. Clearly, prediction methods which assume uniform properties resulting from small-scale mixing processes (such as the popular k-ε model) will be highly unreliable. Specifically, the phenomenon of unmixedness cannot be predicted by conventional turbulence models.

The objective of this study is to employ a two-fluid model (refs. 15 to 17) to predict the degree of mixing and unmixeness in the near-field region of a typical plasma reactor. The two-fluid idea has been employed in various forms by many authors (refs. 18 to 23). The present model has however refined those ideas by employing the mathematical techniques that have been developed for two-phase flows. The model requires solution of conservation equations of two sets of velocities and temperatures, and also of the volume fractions. It also requires mathematical representation of each of the processes of interaction between the the two fluids such as momentum and heat exchange and entrainment of one fluid by the other. Additional relations are required to express the transport of fluid fragments due to relative motion of the two fluids. The model has been applied successfully to boundary layers and internal flows in earlier publications (refs. 16,17, and 24 to 26). In the present paper, the main features of the model are presented and applied to flow in a plasma reactor.

A parabolic solution technique has been employed to ensure adequate grid resolution and numerical accuracy of the results. It should be mentioned that while a fully elliptic model does not suffer from the approximations to the governing equations imposed by the parabolic scheme, it requires calculation of the whole domain of the reactor, including the stagnant region outside the jet, where little or no property variations occur. Indeed, ellipticity (or flow recirculation) is confined essentially to this outer ambient region and its neglect is not expected to have significant effect on the results within the plasma jet. The present parabolic approach allows us to concentrate the computational grid within the jet region of interest.

The paper is divided into five main sections of which this introduction is the first. In the following section, we describe a brief mathematical formulation of the two fluids model. Section 3 provided details of the computational method employed to solve the governing transport equations. The results are presented and discussed in section 4. Finally, section 5 contains the concluding remarks.

MATHEMATICAL FORMULATION

The Two-Fluid Idea

We propose that the observed mixing and unmixedness in plasma jets could be explained to a significant extent, by a "sifting" phenomenon, in which fragments of fluid subjected to larger body forces move through those subjected to smaller body forces in a pressure gradient field. This phenomenon is similar to the Rayleigh-Taylor kind instabilities.

The body forces are here due to the large thermal field gradient between the plasma gas and the ambient air. This sifting motion is essentially one-dimensional. Conventional turbulence models such as the k-ε model have terms to express gradient diffusion fluxes or shear stresses which in the present situation represents only an additional mechanism responsible for mixing. These models have no terms to account for the often counter-gradient unmixing phenomenon.

The sifting phenomenon can be represented mathematically by considering space as containing a mixture of fragments of two distinct fluids, separated by sharp (but flexible and permeable) boundaries on which surface tension are inactive. In effect, while conventional models are concerned with time-averaged properties of fluid, the present two-fluid model focuses on averages of conditioned quantities. At any location, we thus have two average densities, two velocities in each coordinate direction and two temperatures.

The most general means of distinguishing between the two fluids is to suppose that fluid 1 has a greater time-averaged velocity v_1, and fluid 2 a lesser one, v_2, in the body-force direction. This definition allows a direct qualitative physical relationship to Prandtl's mixing-length theory (ref. 19). Fortunately, in the present situation, this implies that fluid 1 is the hot plasma gas while fluid 2 is the cold ambient air surrounding the jet. The two fluids are assumed to share space in proportion to their existence probabilities or volume fractions, r_1 and r_2, such that:

$$r_1 + r_2 = 1.0 \tag{1}$$

In this and subsequent equations, subscript 1 refers to the plasma gas (Argon) while subscript 2 refers to the ambient air (or Nitrogen).

Transport equations are required for each fluid, with empirical relations to express the entrainment and transfer of momentum and heat at the interface.

General Conservation Equation (Fluid i)

In light of the above, the set of partial differential conservation equations governing the transport of a generic flow variable ϕ for fluid i (i=1 for plasma gas, i=2 for ambient air) in plasma jet can be represented as:

$$\frac{\partial}{\partial t}(r_i\rho_i\phi_i) + \nabla \cdot (r_i\rho_i U_i\phi_i - \Gamma_i\nabla\phi_i) = S_i + S_i^* \tag{2}$$

in which,

- ϕ ≡ dependent variable (= 1 for continuity)
- r ≡ volume fraction
- Γ ≡ relevant transport property (exchange coefficient, representing effect of diffusion within one fluid)
- U ≡ velocity vector
- S ≡ intra-fluid source terms (e.g. pressure gradient and buoyancy forces)
- S^* ≡ inter-fluid source terms (friction, entrainment, heat conduction at interface)

The dependent variables and the associated definitions of Γ, S and S* are presented in Table 1. Details of the derivation of these expressions are contained in refs. 16 and 17. The

set of values of the model constants employed in the analysis is presented in Table 2. These values have been established in earlier work on boundary layers and free shear flows (refs. 16, 17 and 24). In Table 1, subscripts i and j refer to the two fluids, E represents the entrainment rate, F is the interface friction and Q is the heat conduction at the interface. Auxiliary relations are employed to express these terms as follows:

Entrainment Rate: We assume that the rate of entrainment is proportional to the relative velocity of the two fluids and to the surface area of the fragment. Assuming j represents the fragment phase, the entrainment rate per unit volume can thus be expressed as:

$$E_{ij} = c_m \rho_i r_i r_j (r_j - 0.5) |\Delta U| / l \tag{3}$$

where c_m is an empirical constant and l is a measure of the linear scale of the fragment and characterizes the interaction processes between the two fluids, $|\Delta U|$ represents the relative velocity between the fluid and its surrounding. The term $(r_j - 0.5)$ is used to enforce symmetry and ensure generality of application of the model to free and confined flows.

Inter-Fluid Friction Forces: The friction forces per unit volume that fluid j exterts on fluid i is expressed as:

$$F_{ij} = c_f \rho_i r_i r_j (U_j - U_i) |\Delta U| / l \tag{4}$$

in which c_f is an empirical constant and U represents either the cross-stream or streamwise velocity components, depending on the momentum equation of interest. Equation (4) implies that the slower-moving fluid gains momentum from the fast-moving fluid. This momentum transfer is of course in addition to that due to the mass transfer as a result of entrainment between the fluids.

Inter-Fluid Heat Transfer: The heat conduction at the interface from fluid j to fluid i is expressed in analogy to the above inter-fluid momentum flux as:

$$Q_{ij} = c_h c_p \rho_i r_i r_j (T_j - T_i) |\Delta U| / l \tag{5}$$

where c_h is an empirical constant (established in ref. 24) and c_p is the specific heat of the hot fluid at constant pressure. In effect, the hot fluid looses heat to the cold fluid at any spatial location.

Shear Source S_{vi}: By analogy to Prandtl's hypothesis, we postulate that there should be a shear-related source in the cross-stream momentum equations (for v_1 and v_2) that is proportional to the gradient of the mean streamwise velocity. This source term can be expressed as:

$$S_{vi} = c_v \rho_i |\Delta U| \left| \frac{\partial w}{\partial y} \right| \tag{6}$$

in which c_v is an empirical constant and w is the mean velocity in the main flow direction. This equation implies that v_1 will increase and v_2 will decrease, whenever the two fluids are in relative motion and the main flow exhibits shear (i.e. $|\partial w/\partial y| > 0$). This term thus expresses

the well-known instability of shear layers and their tendency to break up into a succession of eddies or train of vortices which are convected downstream at the mean-flow velocity.

Length Scale *l*: While the actual entrainment process in shear flows and perhaps plasma jets may depend in detail on viscous action, evidence abounds indicating that the entrainment rate is controlled by the large-scale motion (refs. 11 and 26). We here employ the following transport equation to obtain the length scale thus:

$$\frac{\partial l}{\partial t} + \mathbf{U} \cdot \nabla l = A|U| - B\, l \left(\frac{\partial v}{\partial z} + \frac{\partial w}{\partial y} \right) \tag{7}$$

in which A and B are constants. The first term on the right hand side expresses the growth of fragment size by entrainment and agglomeration. The second term represents the decrease of fragment size by shear distortion. The preliminary values employed for the constants are $A = 0.05$ and $B = 0.01$.

Boundary and Initial Conditions

Symmetry Plane: The physical situation considered is symmetrical about the jet axis, and so calculations are performed only over one half of the flow. A no-flux boundary condition is thus imposed at the symmetry plane.

Free stream: At the outer edge of the computational domain which is located in the ambient air stream just beyond the jet boundary, a fixed pressure condition is imposed. Thus, mass transfer or entrainment of air across this boundary is calculated from continuity. The main-stream velocities and temperatures are prescribed to equal the values in the surrounding air.

The parabolic numerical approach employed implies there is a predominant direction of flow. The nature of the governing equations is such that the downstream boundary condition is of no consequence and needs not (and indeed, should not) be prescibed.

Initial Conditions: Since the calculations must start from an inlet plane, the initial distribution of the dependent variables (velocities, temperatures, volume fractions) must be specified. At the torch exit which represents the inlet plane to the computational domain, parabolic velocity and temperature profiles are prescibed within the jet using the following relations:

$$v_1 = v_{max} [\, 1 - (r/r_o)^2] \tag{8}$$

$$T_1 = T_{max} [\, 1 - (r/r_o)^2] \tag{9}$$

wherein v_{max}(=400m/s), T_{max} (=11500K) are the maximum velocity and temperature at the axis, v_1 and T_1 are the velocity and temperature of the Argon (plasma gas) respectively, r is the radial coordinate and r_o is the radius of the torch. The values employed for these parameters are contained in Table 3. The volume fraction of the plasma gas (r_1) is also specified to be unity at this location.

COMPUTATIONAL DETAILS

Grid: A total of 40 non-uniform grids are employed in the radial direction, with about 90% located within the jet. The computational domain is allowed to expand linearly with the downstream direction in the form:

$$r_g/r_o = a + bz \tag{10}$$

where r_g is the radial extent of the grid, r_o is the torch exit radius (jet radius at inlet plane), z is the streamwise distance from the inlet and a and b are empirical constants. The established spreading rate of axisymmetric jets is used to estimate the initial magnitudes of a and b. The estimated values are then systematically modified until the computational grid spreads slightly faster than the jet. The values employed in the present study are a = 1.0 and b =18.50.

Solution Procedure: The above governing differential equations are solved using the Inter-Phase Slip (IPSA) algorithm embodied in the PHOENICS computational code (ref. 27). The IPSA algorithm has been described in detail in several publications (refs. 28 to 30). This algorithm allows for shared pressure between the two fluids and employs a Partial Elimination Algorithm (PEA) to accelerate convergence of the solutions of the finite domain equations for the temperatures and velocities.

The thermodynamic and transport properties of the plasma gas (Argon) and air are obtained from the literature (refs. 31 to 33). The principal input parameters employed in the computation are presented in Table 3.

RESULTS

Prelimianry Application to Shear Flows

Figs. 1 shows a comparison of the mean and conditioned temperature similarity profiles with the experimental data (refs. 34 to 39), for a plane jet ejecting into stagnant environments. The corresponding results for an axisymmetric jet are presented in Fig.2. The predicted and measured shear stresses and heat fluxes are presented in Figs.3 and 4 for a plane jet and an axisymmetric jet, respectively. The predicted gross characteristics of jets are compared with the values deduced from the experimental data in Table 4.

The mean characteristics and fluxes in the above and subsequent figures are calculated from the individual fluid variables and the volume fractions using the following relations:

$$\phi = r_1\phi_1 + r_2\phi_2 \tag{11}$$

$$\overline{v\phi} = r_1 r_2 (v_1 - v_2)(\phi_1 - \phi_2) \tag{12}$$

where ϕ represents velocity or temperature.

These results have shown that the two-fluid model, employing the model constants presented in Table 2, can adequately predict the flow characteristics of turbulent shear flows.

Application to Plasma Jets

Fig. 5 shows a schematic sketch of the calculation domain considered. The initial width of the grid is located at the torch exit, and the forward step size is progressively increased until a distance of about 8 torch diameters is reached. This ensures that predictions are restricted to the near-field region of the jet. Figs. 6 and 7 show respectively the velocity vectors and mean temperature profiles in the plasma jet. These figures clearly show the spread of the jet along the reactor, and the decay of the jet velocity and temperature downstream of the torch. The hot and fast-moving core of the plasma is clearly visible from these figures, as well as the slow, cold region near the edge of the jet.

The decay of centerline mean velocity and temperature are shown in Figs. 8 and 9. Fig. 10 shows the increase in fraction of Nitrogen (or ambient air) along the centerline while Fig. 11 presents the profiles of the volumetric entrainment rate in the jet. Clearly, there occur sharp decreases in the velocity and temperature profiles at locations corressponding to the increase in entrainment rate. Fig. 11 shows that at any axial location, the entrainment rate reaches a maximum near the edge of the jet . It should be remarked that the outer edge of Fig. 11 (as in other figures showing the complete domain) corresponds to the outer edge of the computational grid, while the edge of the jet is somewhat narrower.

Equally significant is that Fig. 10 indicates that a significant portion of the core region of the jet consists of ambient Nitrogen downstream of the torch. While subsequent mixing might allow this to decay farther downstream, this result clearly confirms the occurence of unmixed fragments of ambient fluid within the plasma.

Figs 12 and 13 show the radial profiles of predicted conditioned velocities and temperatures respectively, at a location z/D=5, downstream of the torch, D being the diameter of the torch exit. Figs. 14 and 15 show the field profiles of Argon temperature and Nitrogen (Air) temperature respectively. In Figs. 16 and 17 are presented the Argon and Nitrogen temperature profiles, respectively, at three axial locations (z/D=3, 5 and 8). These figures show that Argon temperature is generally higher than Nitrogen temperature; the difference progressively decreasing downstream as entrainment increases. At a location just downstream of the torch (z/D=3), the plasma temperature decreases rapidly due to large entrainment of Nitrogen, and then decreases towards the free stream. Fig. 16 shows that at large radial locations, the plasma temperature near the torch is smaller than that far downstream due to the spread of the jet. For instance, while location r = 6mm might be located in the low temperature, ambient region at z/D=3, the same radial position would be located well within the expanding jet at z/D=8, father downstream of the torch.

In Figs. 18 and 19 are presented a comparison of the predicted temperature centerline and radial temperature profiles respectively with the experimental data (ref. 40). To obtain this fit, the inlet velocity and temperature profiles have been expressed using the following relations:

$$v = v_{max} [\, 1 - (r/r_o)^3]$$ (13)

$$T = T_{max} [\, 1 - (r/r_o)^3]$$ (14)

where v_{max}=600m/s and T_{max} = 11500 K. This approach was taken due to lack of available data for the conditions at the torch exit. While the results appear satisfactory, the work is still very preliminary at this stage. A more detailed study of this problem will be considered in a subsequent publication. These figures however show that, with the appropriate inlet and

boundary conditions, the experimental data on jets can be well simulated by the two-fluids model.

CONCLUSION

A two-fluid model of turbulence has been presented that accounts for unidirectional "sifting" resulting from body-force-pressure gradient imbalnace, as well as the stress induced (gradient diffusion) mechanism. The sifting mechanism is believed to be responsible for the observed unmixing in many systems including plasma reactors.

Empirical correlations are employed to represent interfluid phenomena including entrainment rate, friction and heat conduction at the interface. The model constants were established from prior work by comparison of predictions with available mean and conditional sampling data for shear layers.

The model was then applied to predict the flow characteristics in a plasma jet issuing into a stagnant ambient air in a reactor. It allows for the prediction of not only the mean velocity and temperature profiles, but also, the spatial distribution of the Argon (Plasma gas) and Nitrogen velocity and temperature, volume fractions and entrainment rate.

The results appear to be qualitatively realistic and the model appears to be a useful tool for predicting mixing and unmixedness in plasma jets. We have been able to predict the decay in flow velocity and temperature as a result of entrainment of ambient Nitrogen. There appears to be a significant concentration of Nitrogen in the core of the plasma even at relatively long distance downstream of the torch, indicating the occurence of unmixed zones. A preliminary calculation also shows that by adjusting the inlet profiles, we can successfully reproduce the experimental data for a plasma jet. Details of this work will appear in a subsequent paper.

Further work is being planned to compare predictions with more experimental data. The ultimate objective is to combine this model with a large eddy simulation scheme to predict the large structures observed experimentally, and to study the transitional flow behavior in the plasma reactor.

REFERENCES

1. Grey, J; Sherman,M.P.; Williams, P.M.; and Frodkin, D.B.: AIAA J., vol. 4, 1966, p.986.
2. Donaldson,C.P.; and Gray, K.E.: AIAA J., vol.4, 1966, p.2017.
3. Incropera, I.P.; and Leppert, G.: Int. J. Heat Mass Transfer, vol. 10, 1967, p.1861.
4. Lee, Y.C.; and Pfender, E.: Plasma Chem. Plasma Proc., vol. 7, (1), 1987, p.1.
5. Mckelliget, J.; Szekely, J.; Vardelle, M.; and Fauchais, P.: Plasma Chem. Plasma Proc., vol. 2, 1982, p.317.
6. Dilawari, A.H.; and Szekely, J.: Int. J. Heat Mass Trans. vol. 30, (11), 1987, p.2357.
7. Dilawari, A.H.; Szekely, J.; Coudert, J.F.; and Fauchais, P.: Int. J. Heat Mass Trans., vol. 32, (1), 1989, p.35.
8. Chyou, Y.P.; and Pfender, E.: Plasma Chem. Plasma Proc., vol. 9, (2), 1989, p.291.
9. Chang, C.H.; and Pfender, E.: Plasma Chem. Plasma Proc., vol. 10, (3), 1990, p. 473.
10. Chang, C.H.; and Pfender, E.: Plasma Chem. Plasma Proc., vol. 10, (3), 1990, p. 493.
11. Pfender, E.; Finke, J.; and Spores, R.: Entrainment of Cold Gas into Thermal Plasma Jets, Plasma Chem. Plasma Proc., vol. 11, (4), 1991, pp. 529-543.

12. Fincke, J.R.; and Pentecost, C.G.: Laminar-to-Turbulent Transition and Entrainment in Thermal Plasma Jets, ASME Heat Transfer in Thermal and Plasma Processing, HTD vol. 161, 1991, pp. 101-106.
13. Fincke, J.R.; Swank, W.D.; and Haggard,D.C.: Entrainment and Demixing in Subsonic Argon/Helium Thermal Plasma Jets, Proc. 1993 National Thermal Spray Conf., Anaheim, CA, 7-11 June, 1993, pp. 49-54.
14. Fincke, J.R.; Swank, W.D.; and Haggard,D.C.: Plasma/Particle Interaction in Subsonic Argon/Helium Thermal Plasma Jets, Proc. 1993 National Thermal Spray Conf., Anaheim, CA, 7-11 June, 1993, pp. 25-30.
15. Spalding, D.B.: Two-Fluid models of turbulence, NASA Langley Workshop on Theoretical Approaches to Turbulence, Hampton, VA (1984).
16. Ilegbusi, O.J.; and Spalding, D.B.: A Two-Fluids Model of Turbulence and its Application to Near-Wall Flows, PCH Physico Chemical Hydrodynamics, vol. 9, (1/2), 1987, p.127.
17. Ilegbusi, O.J.; and Spalding, D.B.: Application of a Two-Fluids Model of Turbulence to Turbulent Flows in Conduits and Free Shear Layers, PCH Physico Chemical Hydrodynamics, vol. 9, (1/2), 1987, p.161.
18. Reynolds, O.: On the Extent and Action of the Heating Surface for Steam Boilers, Proc. Manchester Lib Phil Soc., vol 8, 1874.
19. Prandtl L.: Bericht uber Untersuchungen zur ausgebildeten Turbulenz, Z. angew Math. Mech. (ZAMM), vol 5, (2), 1925, pp.136-139.
20. Libby, P.A.: On the Prediction of Intermittent Turbulent Flows, J. Fluid Mech, vol. 68 (2), 1975, pp. 273-295.
21. Moss, J.B.: Simultaneous Measurements of Concentration and Velocity in an Open Pre-Mixed Flame, Comb. Sci. Tech., vol 22, 1980, pp. 115-129.
22. Bray, K.N.C.; and Libby, P.A.: Countergradient Diffusion in Pre-Mixed Turbulent Flames, AIAA J. vol 19, 1981, p.205.
23. Kollman, W.: Prediction of Intermittency Factor for Turbulent Shear Flows, AIAA J., vol. 22, 1983, pp. 486-492.
24. Ilegbusi, O.J.; and Spalding, D.B.: Prediction of Fluid Flow and Heat Transfer Characteristics of Turbulent Shear Flows with a Two-Fluid Model of Turbulence, Int. J. Heat Mass Trans., vol. 32, (4), 1989, pp. 767-773.
25. Malin, M.R.; and Spalding, D.B.: A Two-Fluid Model of Turbulence and its Application to Heated Plane Jets and Wakes, PCH Journal, vol. 5, 1984, pp.339-361.
26. Townsend, A.A.: The Structure of Turbulent Shear Flow, 2nd Edition, Cambridge University Press, 1980.
27. Rosten H.; and Spalding, D.B.: PHOENICS Beginner's Guide and User's Manual, CHAM Limited (UK) Technical Report TR/100, 1986.
28. Spalding, D.B.: Numerical Computation of MultiPhase Fluid Flow and Heat Transfer, In Recent Advances in Numerical Methods, Ed. C. Taylor and K. Morgan, 1980.
29. Spalding, D.B.: IPSA 1980 - Developments in the Procedure for Numerical Computation of Multi-Phase Flow Phenomena with Interphase Slip, Unequal Temperatures, etc., In Numerical Properties and Methodologies in Heat Transfer, Proc. 2nd Nat. Symp., Ed. T.M. Shih, Maryland, USA, 1981.
30. Spalding, D.B.: Four Lectures on the PHOENICS Computer Code, Imperial College, London, Technical Report CFD/82/5, 1982.
31. Evans, D.C.; and Tankin, R.S.: Phys. Fluids, vol. 10, 1967, p.1137.
32. Morris, J.C.; Bach,G.R.; and Yos, J.M.: Report No. ARL-64-180, Aerospace Research Laboratories, 1964.

33. Yos, J.M.: Technical Memorandum RAD-TM-63-7, Research and Advanced Development Division, AVCO Corporation, Wilmington, MA, 1983.
34. Wygnanski, I; and Fiedler, H: Some measurements in the self-preserving jet, J. Fluid Mech., vol.38, 1969 p.599.
35. Chevray, R.; and Tutu, N.K.: Intermittency and Preferential Transport of Heat in a Round Jet, J. Fluid Mech., vol. 88 (1), 1978, p.133.
36. Van der Hegge Zijnen, B.G.: Measurement of the distribution of heat and matter in a plane turbulent jet of air, Appl. Scient. Res., vol. 4, 1968, p.405.
37. Rodi,W.: A Review of Experimental Data on Free Turbulent Boundary Layers, In Studies in Convection, Theory, Measurements and Applications, Ed. B.E. Launder, Academic Press, London, 1975.
38. Davies, A.E.; Keffer, J.F.; and Baines,W.D.: Spread of a Heated Turbulent Jet, Phys. Fluids, vol. 18, (7), 1975, p.770.
39. Rodi, W.: The Prediction of Free Turbulent Boundary Layers by the use of Two-Equation Model of Turbulence, PhD. Thesis, University of London, 1972.
40. Brossa, M.; and Pfender, E.: Plasma Chem. Plasma Proc., vol. 8, 1988, p.75.

List of Symbols

D	Diameter of torch at exit
E_{ij}	Volumetric entrainment rate of fluid j by fluid i
F_{ij}	Volumetric inter-fluid friction
k	Turbulence kinetic energy
l	Length scale
P	Static pressure
Q_{ij}	Heat transfer by conduction at the interface
r	Volume fraction
r	Radial coordinate
r_o	Radius of torch at exit (D/2)
r_g	Radial extent of computational grid
S	Intra-fluid source term
S^*	Inter-fluid source term
S_v	Shear source in radial velocity equations
T	Temperature
U	Velocity vector
v	Velocity component in radial direction
w	Velocity component in streamwise direction
$\overline{vT}$	Turbulent heat flux
$\overline{vw}$	Turbulent shear stress
y	Radial coordinate direction
z	Streamwise coordinate direction
δ	Momentum boundary layer thickness
δ_T	Thermal boundary layer thickness
ε	Rate of dissipation of turbulence energy
ϕ	Generic flow variable
Γ	Diffusion flux coefficient
ρ	Fluid density
σ	Prandtl number

Table 1: Exchange Coefficients and Source Terms

Equation	Γ_i	S_i	S^*_i
Mass balance	0	0	E_{ij}
Momentum (Radial)	$c_t\acute{r}_i\acute{r}_j\|V\|$	$-r_i\nabla P + S_{vi}$	$F_{ij} + U_jE_{ij}$
Momentum (Axial)	$c_t\acute{r}_i\acute{r}_j\|V\|$	$-r_i\nabla P$	$F_{ij} + U_jE_{ij}$
Energy	$c_t\acute{r}_i\acute{r}_j\|V\|/\sigma_T$	0	$Q_{ij} + c_pT_jE_{ij}$

Table 2: Values of the Two-Fluid Model Constants

Constant	Value
c_m	10.00
c_v	0.30
c_d	1.00
c_f	0.05
c_t	10.00
c_h	0.05
σ_t	1.00

Table 3: Principal Input Parameters

Plasma Torch Diameter	8mm
Maximum Plasma Temperature	11500K
Maximum Plasma Velocity	400m/s
Nitrogen Temperature	300K

Table 4: Predicted and Measured Integral Characteristics of Jets

Parameter	Round Jet		Plane Jet	
	Data	Prediction	Data	Prediction
$d\delta/dz$	0.086	0.087	0.110	0.120
$d\delta_T/dz$	0.110	0.105	0.140	0.145
$\overline{vw}_{max}$	0.019	0.014	0.024	0.020
$\overline{vT}_{max}$	0.021	0.020	0.028	0.029
E_{max}	0.051	0.050	-	0.060

FIGURE CAPTIONS

Fig.1 Predicted mean and fluid temperatures compared with measured similarity profiles of mean and conditioned data for plane jet

Fig.2 Predicted mean and fluid temperatures compared with measured similarity profiles of mean and conditioned data for round jet

Fig.3 Predicted and measured similarity profiles of shear stress and heat flux for a plane jet

Fig.4 Predicted and measured similarity profiles of shear stress and heat flux for a round jet

Fig.5 Schematic sketch of the calculation domain employed for plasma jet

Fig.6 Velocity vectors in the plasma jet

Fig.7 Mean temperature profile in the plasma jet

Fig.8 Mean velocity decay along the jet axis

Fig.9 Mean temperature decay along the jet axis

Fig.10 Volume fractions of Argon and Nitrogen along jet axis

Fig.11 Profile of volumetric entrainment rate in the plasma jet

Fig.12 Predicted radial variation of velocities of Argon and Nitrogen at z/D=5

Fig.13 Predicted radial variation of temperatures of Argon and Nitrogen at z/D=5

Fig.14 Profile of Argon temperature in the jet

Fig.15 Profile of Nitrogen temperature in the jet

Fig.16 Radial variation of Argon temperature at z/D=3,5 and 8.

Fig.17 Radial variation of Nitrogen temperature at z/D=3,5 and 8

Fig.18. Predicted centerline profile of mean temperature compared with the experimental data of ref. 40.

Fig.19. Predicted radial profile of mean temperature at z=20mm compared with the experimental data of ref. 40.

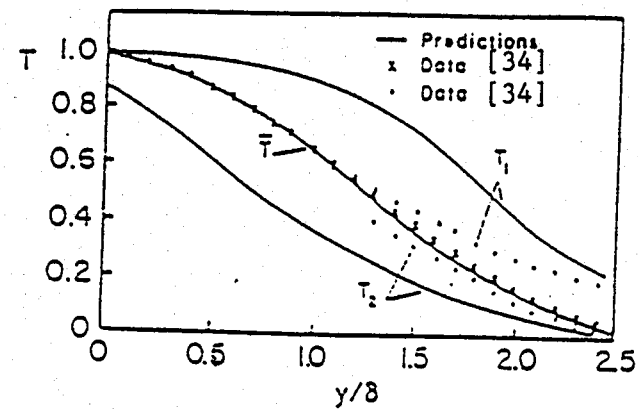

Fig.1 Predicted mean and fluid temperatures compared with measured similarity profiles of mean and conditioned data for plane jet

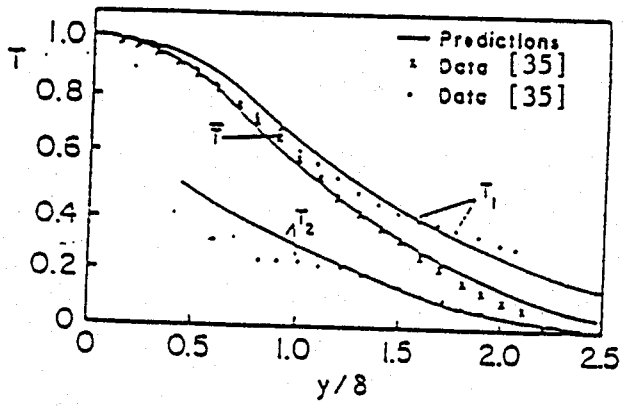

Fig.2 Predicted mean and fluid temperatures compared with measured similarity profiles of mean and conditioned data for round jet

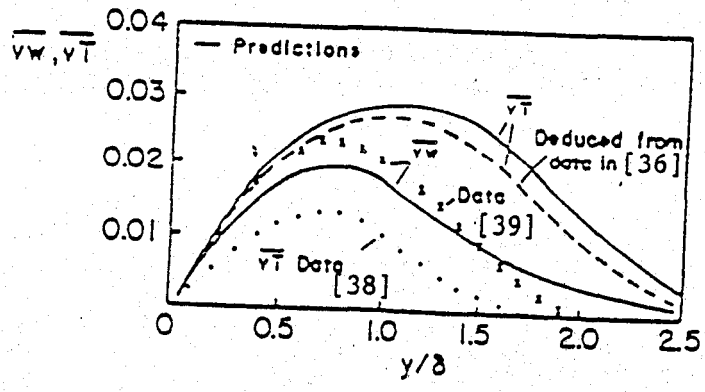

Fig.3 Predicted and measured similarity profiles of shear stress and heat flux for a plane jet.

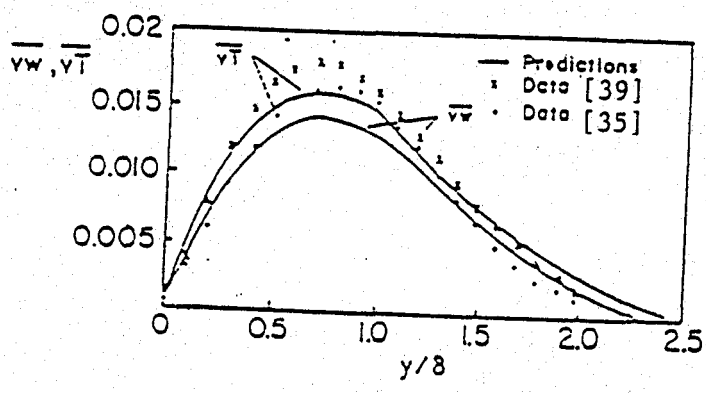

Fig.4 Predicted and measured similarity profiles of shear stress and heat flux for a round jet

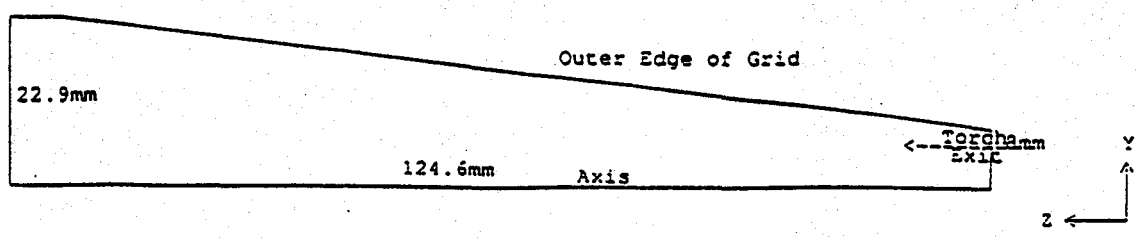

Fig.5 Schematic sketch of the calculation domain employed for plasma jet

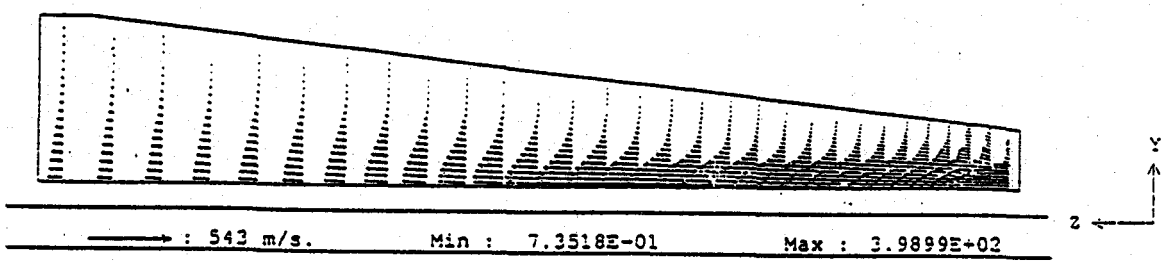

Fig.6 Velocity vectors in the plasma jet

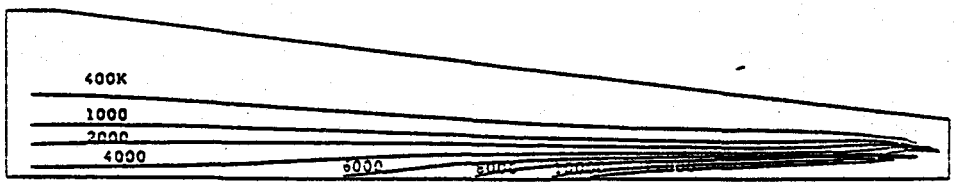

Fig.7 Mean temperature profile in the plasma jet

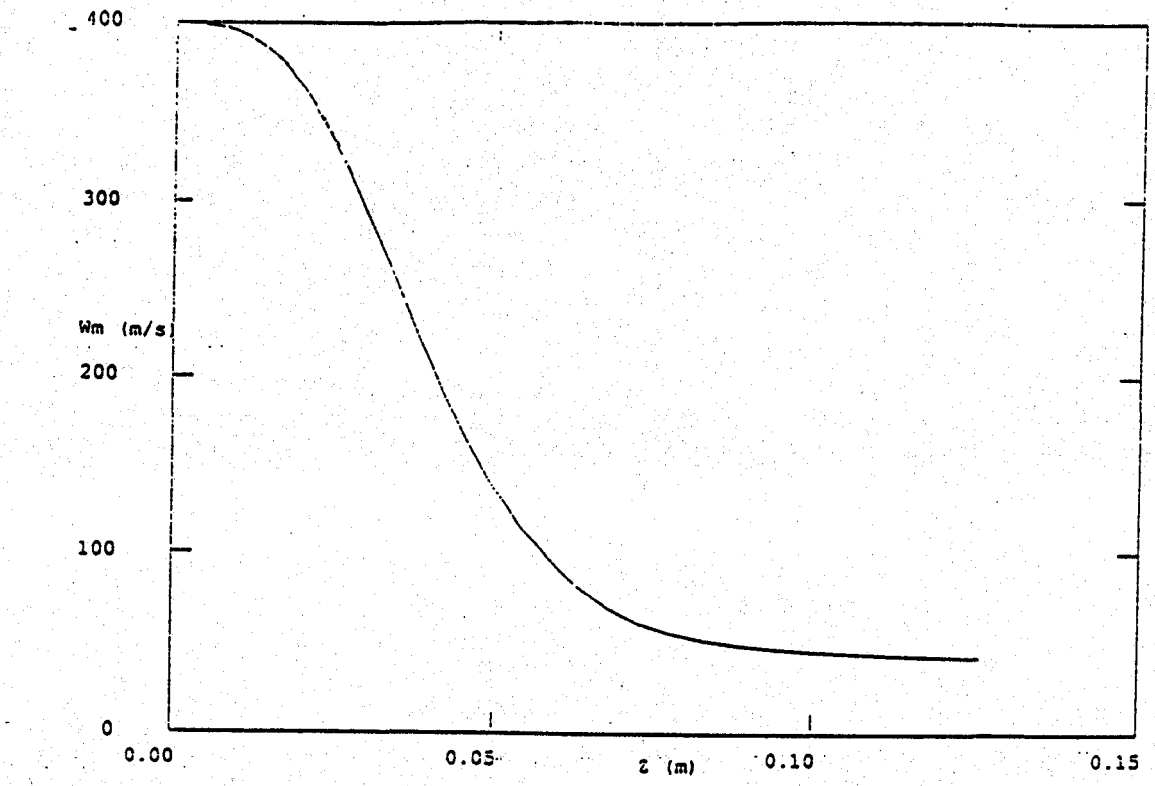

Fig.8 Mean velocity decay along the jet axis

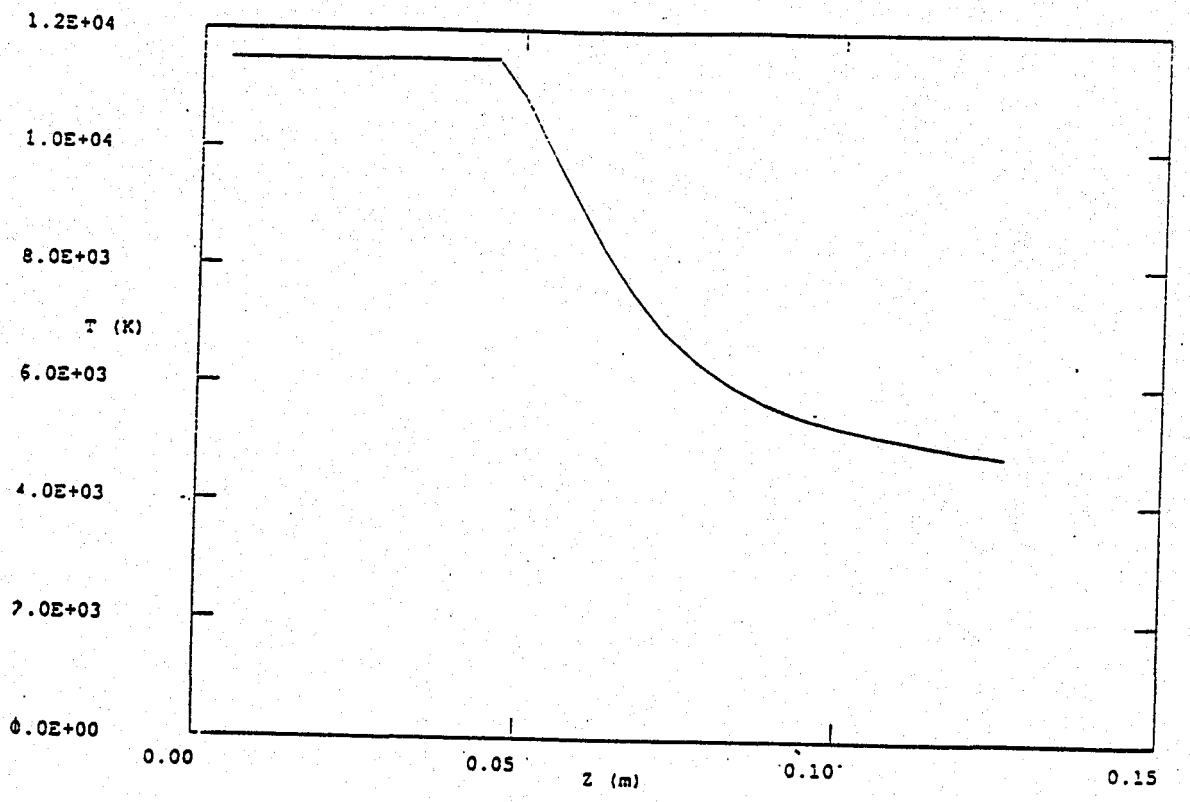

Fig.9 Mean temperature decay along the jet axis

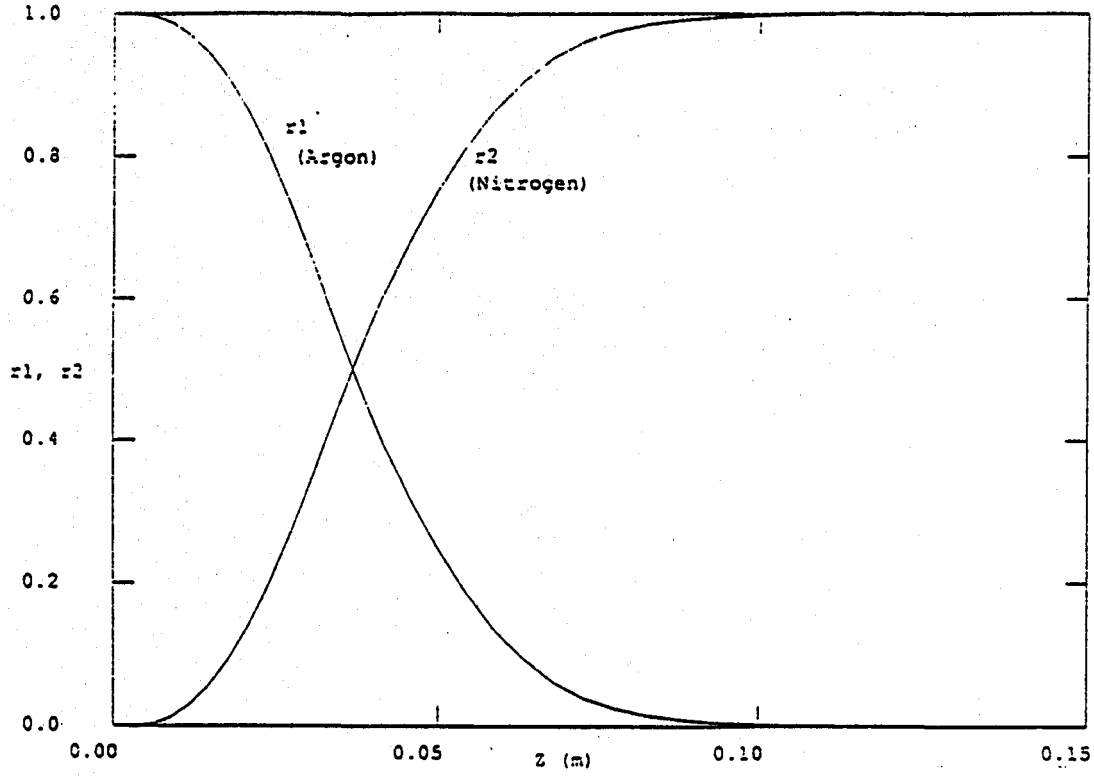

Fig.10 Volume fractions of Argon and Nitrogen along jet axis

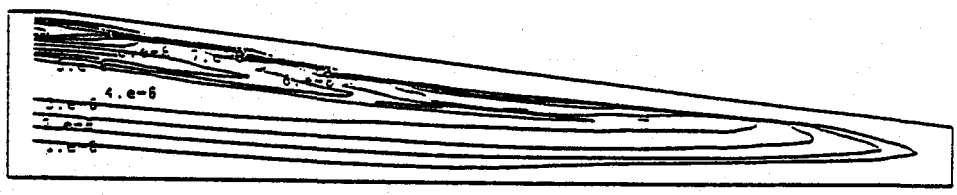

Fig.11 Profile of volumetric entrainment rate in the plasma jet

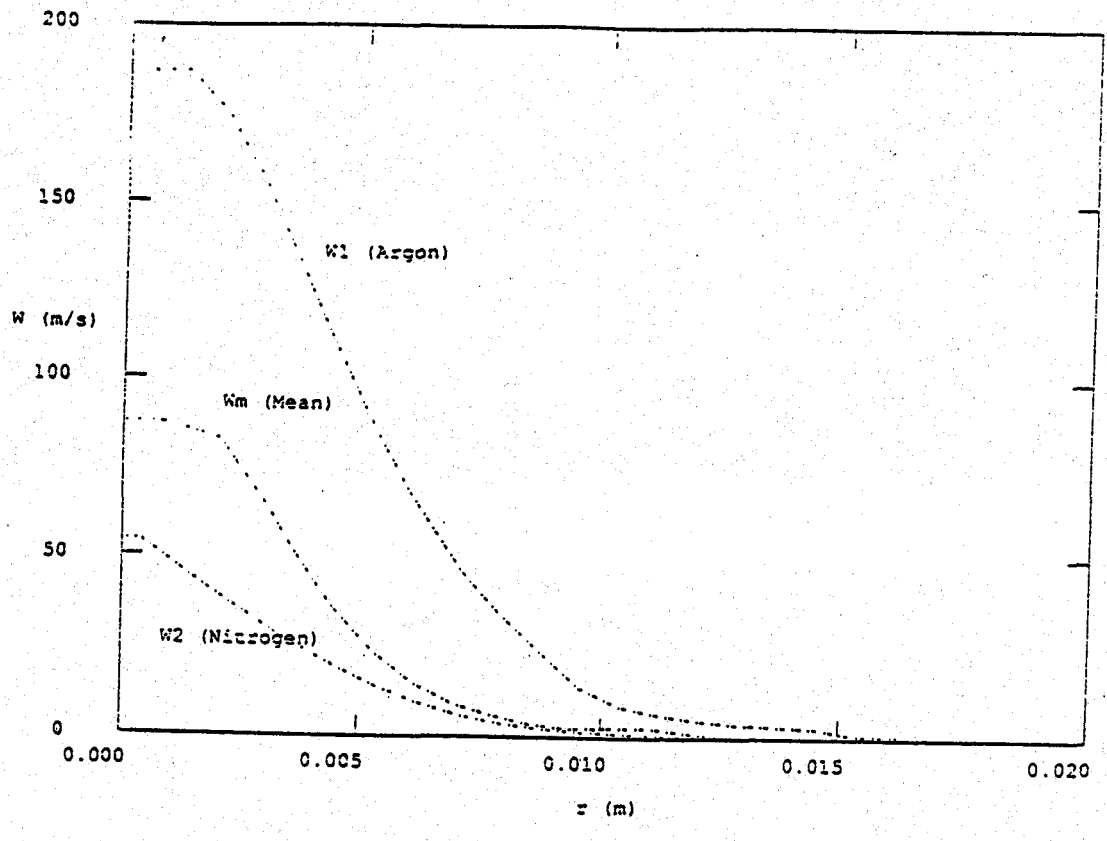

Fig.12 Predicted radial variation of velocities of Argon and Nitrogen at z/D=5

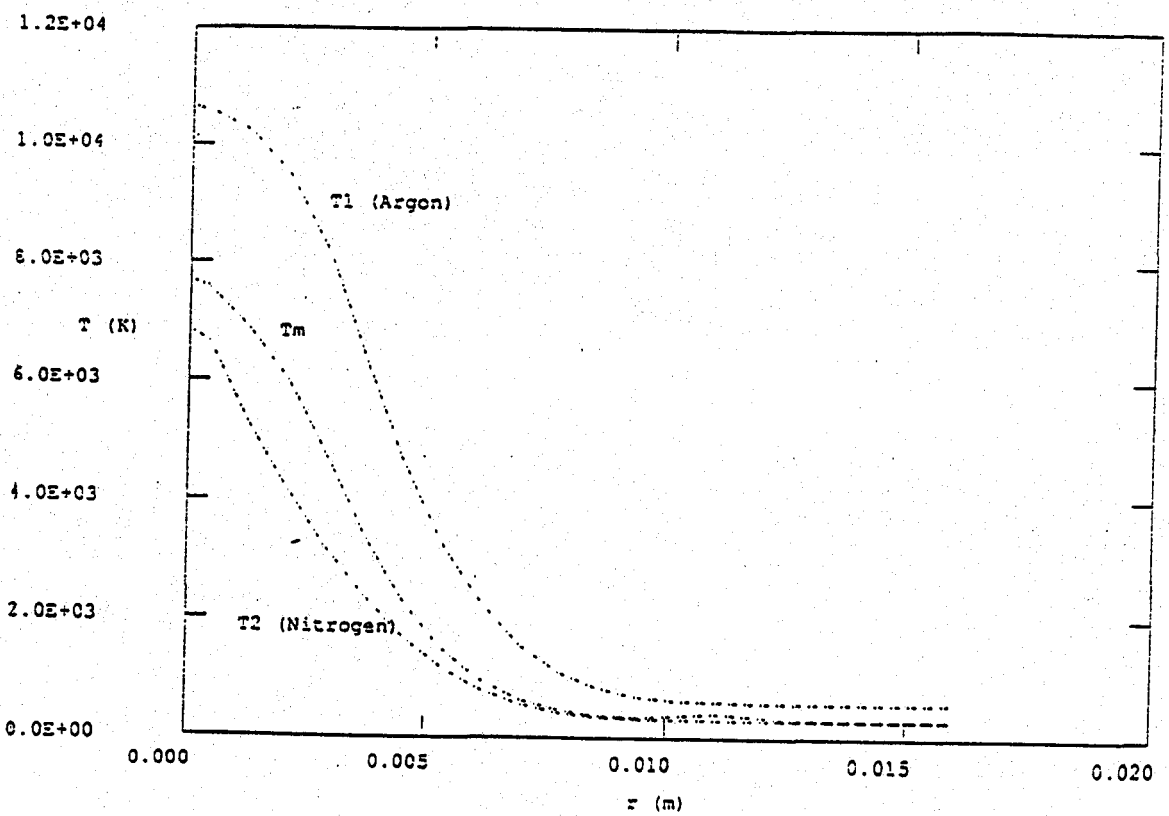

Fig.13 Predicted radial variation of temperatures of Argon and Nitrogen at z/D=5

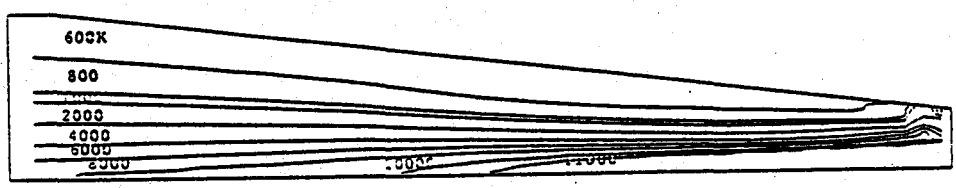

Fig.14 Profile of Argon temperature in the jet

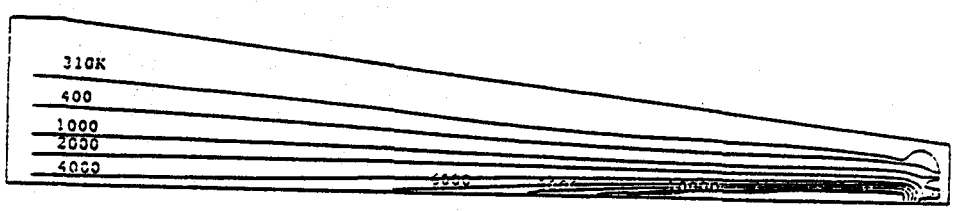

Fig.15 Profile of Nitrogen temperature in the jet

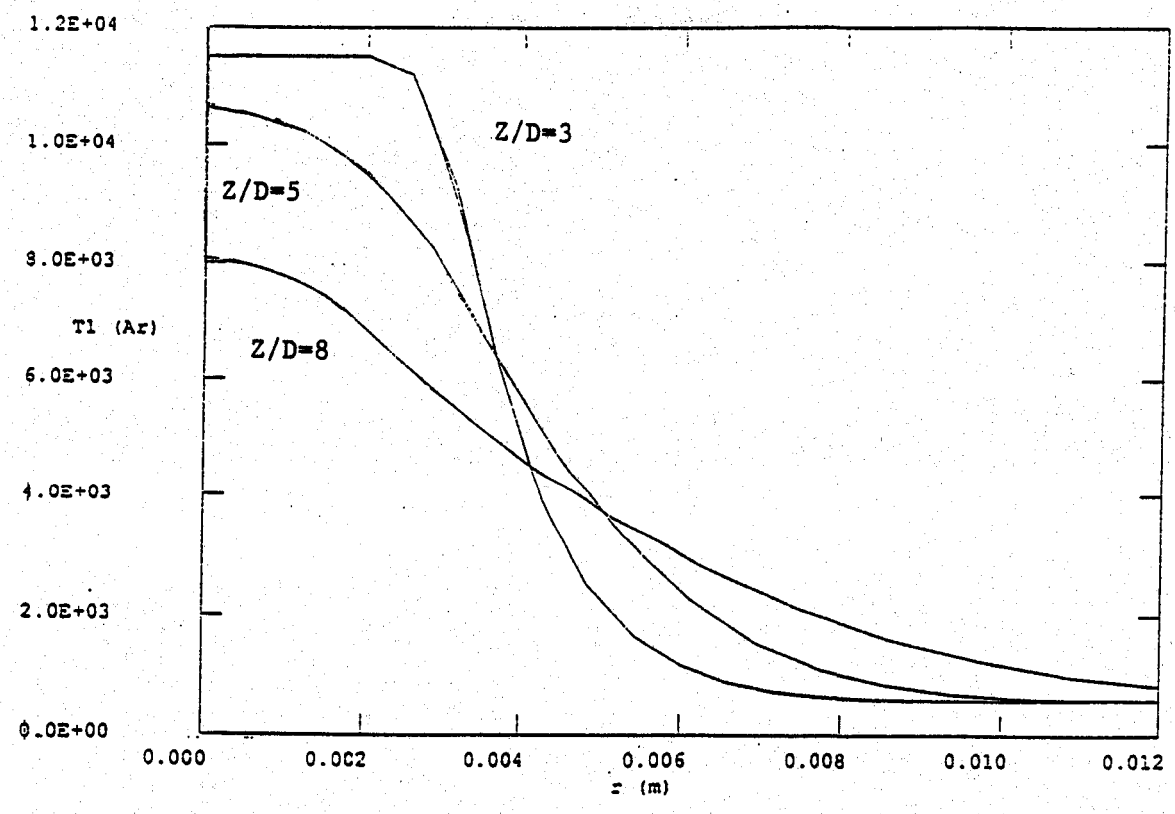

Fig.16 Radial variation of Argon temperature at z/D=3,5 and 8.

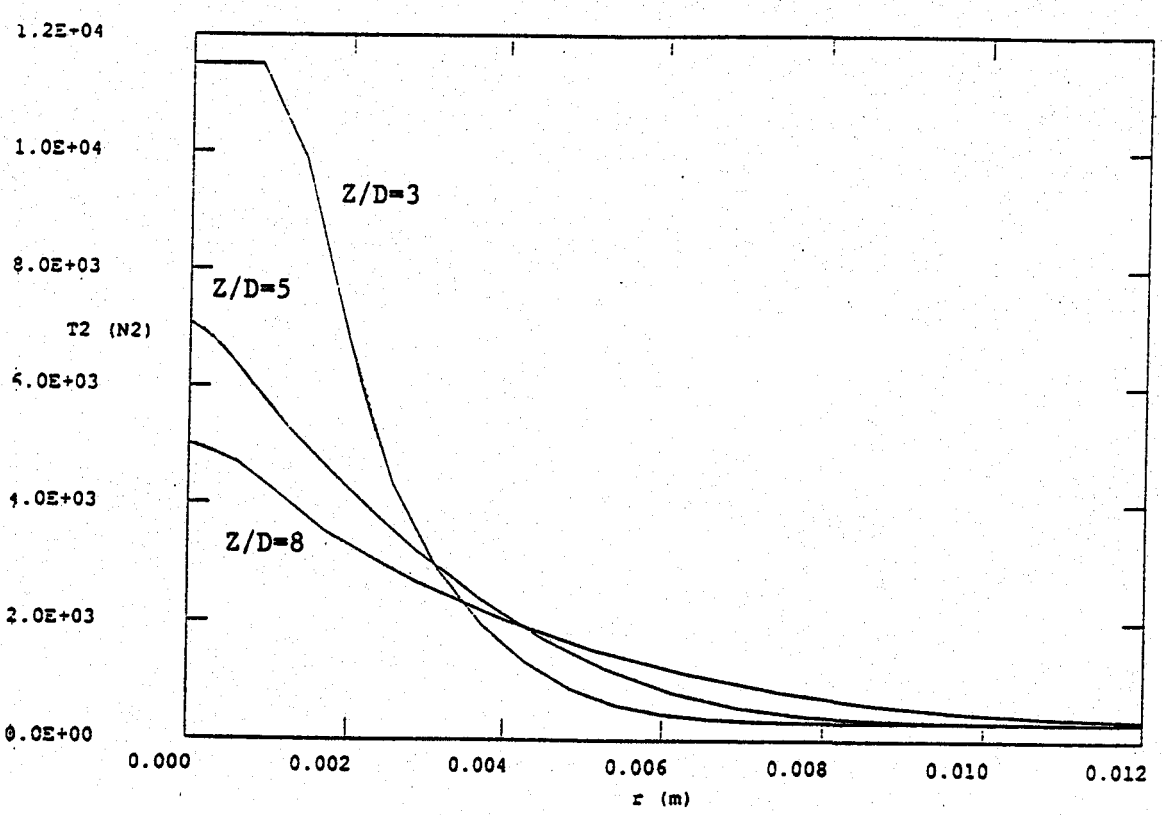

Fig.17 Radial variation of Nitrogen temperature at z/D=3,5 and 8

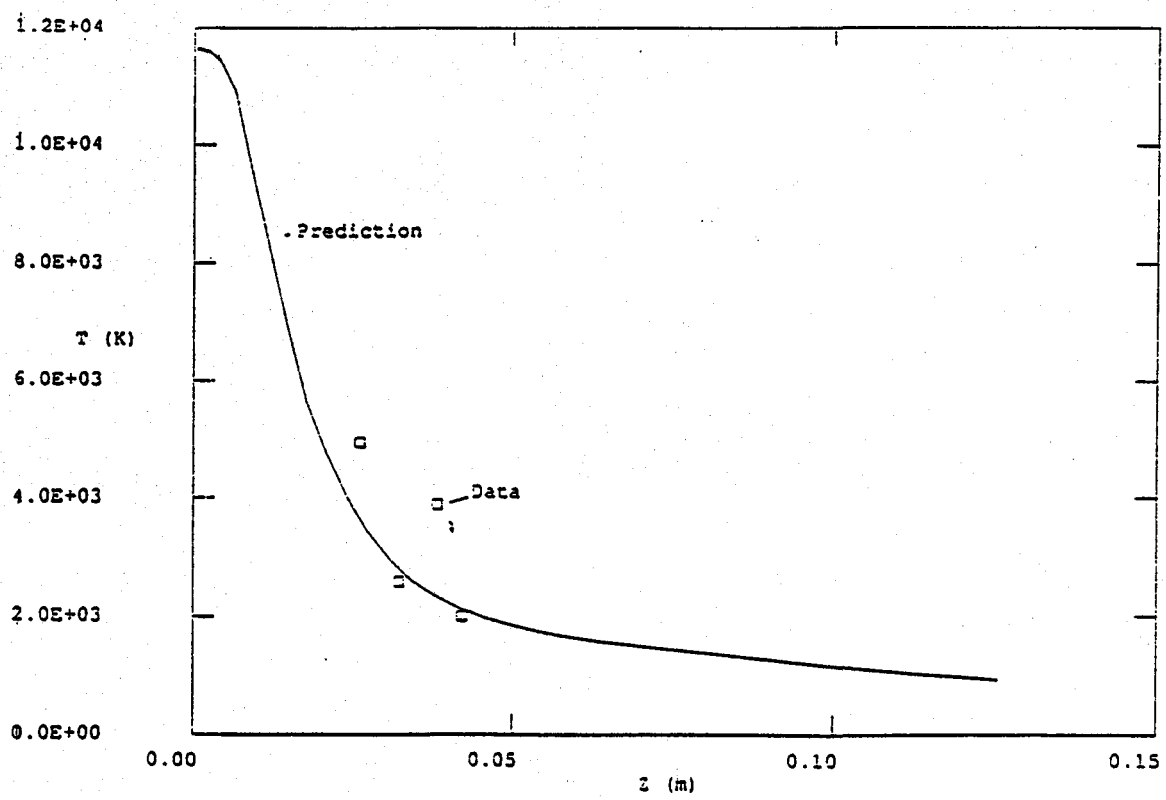

Fig.18. Predicted centerline profile of mean temperature compared with the experimental data of ref. 40.

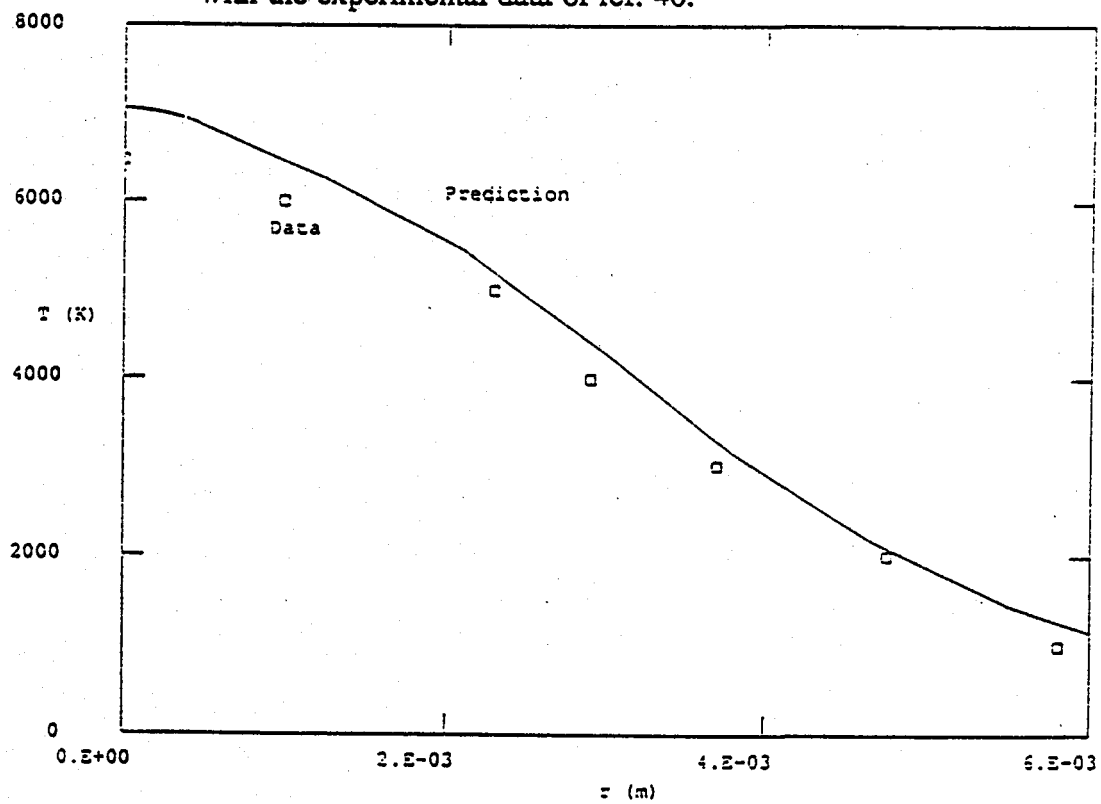

Fig.19. Predicted radial profile of mean temperature at z=20mm compared with the experimental data of ref. 40.

SUPERSONIC MINIMUM LENGTH NOZZLE DESIGN FOR DENSE GASES

Andrew C. Aldo* and Brian M. Argrow**
Department of Aerospace Engineering Sciences
University of Colorado
Boulder, Colorado 80309

ABSTRACT

Recently, dense gases have been investigated for many engineering applications such as for turbomachinery and wind tunnels. Supersonic nozzle design for these gases is complicated by their nonclassical behavior in the transonic flow regime. In this paper a method of characteristics (MOC) is developed for two-dimensional (planar) and, primarily, axisymmetric flow of a van der Waals gas. Using a straight sonic line assumption, a centered expansion is used to generate an inviscid wall contour of minimum length. The van der Waals results are compared to previous perfect gas results to show the real gas effects on the flow properties and inviscid wall contours.

INTRODUCTION

A minimum length nozzle (MLN) produces a uniform supersonic flow with a minimum ratio of throat height or radius to total nozzle length. Argrow and Emanuel (refs. 1, 2) present detailed discussion of MLN designs, comparisons of different types, computational flow field analysis, and engineering applications. Until this paper, all MLN analyses, that we are aware of, have focused only on perfect gas results. Several authors (refs. 3–10) have recently investigated nozzle flows for nonideal gases. References 3–5 and 8–11 discuss steady flows of dense gases. Cramer (ref. 11) refers to these gases as BZT (Bethe-Zel'dovich-Thompson) to recognize the individuals that first theorized their nonclassical behavior. Such behavior includes local a minimum of the Mach number during steady isentropic expansion, expansion shocks, increase in the critical Mach number, and other nonclassical behaviors. BZT fluids typically have large polyatomic molecules with comparatively large specific heats.

All the previously mentioned references that investigate BZT fluids discuss the thermodynamic condition that governs the classical or nonclassical behavior. The governing thermodynamic parameter is

$$\Gamma = 1 + \frac{\bar{\varrho}}{\bar{a}}\left(\frac{\partial \bar{a}}{\partial \bar{\varrho}}\right)_{\bar{s}}$$

where

$$\bar{a} = \left(\frac{\partial \bar{p}}{\partial \bar{\varrho}}\right)_{\bar{s}}^{1/2}$$

is the speed of sound, $\bar{\varrho}$, $\bar{p}$, and $\bar{s}$ are the density, pressure, and entropy, respectively. The overbar indicates dimensional quantities. The parameter Γ is referred to by Thompson (ref. 13) as the fundamental derivative of gas dynamics.

For most fluids $\Gamma > 0$ under normal conditions, but for BZT fluids may have $\Gamma < 0$. The $\Gamma < 0$ region of a BZT gas (dense gas) occurs in the dense gas region near the saturated vapor curve in the pv plane. Practical uses for the nonclassical behavior of BZT fluids include turbomachinery and heavy-gas

*Graduate Student
**Assistant Professor

wind tunnels. Discussion of the various applications that may capitalize on the nonclassical behavior of BZT fluids can be found in refs. 3, 5, and 8–12.

The most apparent application of a MLN designed for dense-gas flow is for heavy-gas wind tunnels. Anderson (ref. 9) shows Navier-Stokes calculations for the flow of sulfur hexaflouride (HF_6) over a NACA 0012 airfoil. This study investigated the feasibility of using this large-molecule gas for wind tunnel applications. While most of the previous references speculate that nozzles can be designed to produce supersonic flow of a BZT fluid, the calculations have been limited to one-dimensional cases (refs. 3–5, 8, 10, 11).

THERMODYNAMIC MODEL

The van der Waals equation of state is

$$\bar{p} = \frac{\bar{R}\bar{T}}{\bar{v} - \bar{b}} - \frac{\bar{a}}{\bar{v}^2},$$

where $\bar{R}$ is the specific gas constant, $\bar{v}$ is the specific volume, and

$$\bar{b} = \frac{\bar{R}\bar{T}_c}{8\bar{p}_c} \quad \text{and} \quad \bar{a} = \frac{27}{64}\frac{\bar{R}^2\bar{T}_c^2}{\bar{p}_c}.$$

The c subscript refers to conditions at the critical point. The following thermodynamic development and nondimensionalization scheme follows that of ref. 12. The enthalpy $\bar{h}$ and speed of sound $\bar{a}$ are given by

$$\bar{h} = \bar{e}_r + \frac{\bar{R}\bar{T}}{\delta}\left(1 + \delta\frac{\bar{v}}{\bar{v} - \bar{b}}\right) - \frac{2\bar{a}}{\bar{v}},$$

$$\bar{a} = \left[\left(\frac{\bar{v}}{\bar{v} - \bar{b}}\right)^2 \bar{R}\bar{T}(1 + \delta) - \frac{2\bar{a}}{\bar{v}}\right]^{1/2},$$

Here $\bar{e}_r$ is an arbitrary reference energy and

$$\delta \equiv \bar{R}/\bar{c}_v$$

Because there is minimal temperature variation for the flows investigated, we assume a constant $\bar{c}_v = \bar{c}_{v\infty}$, where $\bar{c}_{v\infty}$ is the ideal gas specific heat. The temperature variation for isentropic flow of a van der Waals gas is given by

$$\frac{\bar{T}}{\bar{T}_0} = \left(\frac{\bar{v}_0 - \bar{b}}{\bar{v} - \bar{b}}\right)^{\delta},$$

where the 0 subscript refers to stagnation conditions.

The nondimensional (reduced variable) form of the van der Waals equation is written as

$$p = \frac{8T}{3v - 1} - \frac{3}{v^2},$$

and the critical compressibility is

$$Z_c = \left(\frac{pv}{RT}\right)_c = \frac{3}{8}$$

with the reduced variables

$$p = \frac{\bar{p}}{\bar{p}_c}, \quad T = \frac{\bar{T}}{\bar{T}_c}, \quad v = \frac{\bar{v}}{\bar{v}_c}.$$

The nondimensional form of the other thermodynamics relations are

$$T = T_0\left(\frac{v_0 - b}{v - b}\right)^{\delta},$$

$$h = \frac{T}{\delta}\left(1 + \delta\frac{v_0}{v_0 - b}\right) - \frac{2a}{v_0},$$

$$a = \left[T(1 + \delta)\left(\frac{v}{v - b}\right)^2 - \frac{2a}{v}\right]^{1/2},$$

$$M = \frac{\sqrt{2(h_0 - h)}}{a},$$

where

$$h \equiv \frac{\bar{h} - \bar{e}_r}{\bar{R}\bar{T}_c}, \quad a \equiv \frac{\bar{a}}{\sqrt{\bar{R}\bar{T}_c}}, \quad b \equiv \frac{\bar{b}}{\bar{v}_c} = \frac{1}{8Z_c}, \quad \alpha \equiv \frac{\bar{a}}{\bar{R}\bar{T}_c\bar{v}_c} = \frac{27}{64}\frac{1}{Z_c}.$$

METHOD OF CHARACTERISTICS FOR REAL GASES

The method of characteristics (MOC) used by Argrow and Emanuel (ref. 1) assumes an isentropic, irrotational flow of a perfect gas. For this case, the governing two-dimensional partial differential equation reduces to a set of four algebraic equations, two characteristic and two compatibility equations. For the axisymmetric case, the characteristic and compatibility equations form a set of four ordinary differential equations that are solved simultaneously. Details of the solution procedures can be found in ref. 1.

A MOC for the isentropic two-dimensional or axisymmetric flow of a real gas (ref. 14) is used for the present study. The method is completely general and we use the van der Waals thermodynamic model more for simplicity than for accuracy. The governing partial differential equations (PDEs) are given by the gas dynamic equation, the irrotationality condition, and the speed of sound relation,

$$(V_x^2 - a^2)V_x + (V_y^2 - a^2)V_y + 2V_xV_y\frac{\partial V_x}{\partial y} - \sigma\frac{a^2V_y}{y} = 0,$$

$$\frac{\partial V_x}{\partial y} - \frac{\partial V_y}{\partial x} = 0,$$

$$a = a(V) = a(V_x, V_y),$$

where $\sigma = 0$ for two-dimensional flow or $\sigma = 0$ for axisymmetric flow, x and y are the axial and radial (transverse) coordinates nondimensionalized with respect to throat radius or half-height, V_x and V_y are the corresponding velocity components, and V is the velocity magnitude, all velocities are nondimensionalized in the same manner as the speed of sound $\bar{a}$. Along the characteristic lines, that correspond to Mach lines in the flow, this system of PDEs reduces to two ordinary differential equations called compatibility equations. Fig. 1 is a schematic of the supersonic flow field showing the MLN geometry and the flow geometry associated with an arbitrary point on a streamline. The angle θ^* is the initial inclination of the supersonic contour. The left and right running characteristics designated as C_+ and C_- are Mach lines inclined at the Mach angle μ with respect to the velocity vector V. The corresponding characteristic and compatibility equations are

$$C_\pm \text{ characteristic equation}: \left(\frac{dy}{dx}\right)_\pm = \lambda_\pm = \tan(\theta \pm \mu), \tag{1a}$$

$$C_\pm \text{ compatibility equation}: (V_x^2 - a^2)dV_{x_\pm} + [2V_xV_y - (V_x^2 - a^2)\lambda_\pm]dV_{y_\pm} - \sigma\frac{a^2V_y}{y}dx_\pm = 0. \tag{1b}$$

The gas is assumed to enter the supersonic portion of the nozzle along the straight sonic line OA uniform and parallel to the axis. It is then expanded and accelerated (or possibly decelerated in the $\Gamma < 0$ region) through the nozzle and exits the nozzle with a uniform flow crossing the terminating characteristic BC at the exit Mach number M_f. For the two-dimensional nozzle, the centered expansion generated by the sharp throat is a Prandtl-Meyer expansion. In the axisymmetric case, the flow at the wall is locally two-dimensional, thus at the throat the expansion is locally Prandtl-Meyer. Construction of the flow field begins by discretizing the centered expansion into equally-spaced velocity increments. Each velocity increment ΔV has an associated isentropic flow turn angle increment $\Delta\theta$. The angle increment $\Delta\theta$ is computed from the relation

$$\theta_2 - \theta_1 = \int_{V_1}^{V_2} \frac{\sqrt{M^2 - 1}}{V} dV. \tag{2}$$

For a perfect gas, the ΔM associated with an angular deflection $\Delta\theta$ can be easily determined from the Prandtl-Meyer function. For a real gas, the Prandtl-Meyer computation requires the solution of a system of ordinary differential equations as shown by Cramer (ref. 10). We avoid the Prandtl-Meyer computation by using the angle-velocity relation, equation (2).

With the position of the throat specified and the velocity components (V_x, V_y) computed from V and θ, the necessary independent variables are determined at the throat. Equations (1) are solved simultaneously using the second-order average-property Euler predictor-corrector scheme described in ref. 14. The characteristic net of the kernel region OAB and the transition region ABC is constructed using the unit processes described in ref. 1. The wall contour corresponds to the streamline that passes through points A and C. This streamline is determined by also using the average-property Euler predictor-corrector scheme to integrate the equation

$$\frac{dy_w}{dx} = \tan\theta_w$$

from the initial condition, $\theta_w = \theta^*$ at $x = 0$ to the exit condition $\theta_w = 0$ at $x_f = 0$.

The accuracy of the characteristic computations and the wall contour are affected by the spacing of the characteristic nodes. The C_- characteristics that emanate from the corner at point A reflect from the axis as C_+ characteristics and bend away from the center of the expansion. This causes relatively large spacing between characteristic node points and the subsequent computed wall points just downstream of the throat where the gradients are largest. To alleviate this situation, the characteristic net is compressed toward the sonic line by decreasing the step size of the speed increments in the centered expansion discretization. The Prandtl–Meyer and turn angles in ref. 1 are discretized and compressed in a similar manner.

RESULTS

For the nominal case of T_0 =1.01, δ = 0.02, and ν_0 = 0.70, $dV \cong \delta V = 10^{-6}$ for equation (2). The first characteristic is chosen at δV, then the step size is increased until a characteristic is generated at every $20\delta V$. This allows characteristics to be compressed towards the sonic line for improved accuracy. For the nominal case, the limits of integration for equation (2) are set at the sonic speed $V_1 = 0.26$ to $V_2 = 0.9V_{max}$ with $V_{max} = 9.93$. Characteristic spacing in the transition region is controlled by an aspect ratio that keeps the shape of the characteristic cells as uniform as needed. For the relatively short nozzles produced in this study, the aspect ratio was set at 0.5. Reference 1 gives a complete description of how the characteristic compression and transition region aspect ratio affect the overall computational accuracy.

Figures 2 show the wall contour and the variation of M, ϱ, and Γ along the axis and along the wall for a two-dimensional nozzle with T_0 =1.01, δ =0.02, and ν_0 =0.70, 0.85. Figure 2(a) indicates the increase in nozzle length required for the more dense gas. Note that θ^* is fixed at 2.5° for the comparisons in Figs. 2. This is near the maximum value of θ^* where the C_- characteristic, near AB of Fig. 1, begin to overlap other C_- characteristics in the kernel, or there is overlapping from C_+ characteristics near BC with both instances producing an oblique expansion shock. Once a shock occurs (compression or expansion), the flow is no longer isentropic and the MOC cannot be applied without some special procedure to account for the placement of the shock (We do not to incorporate such a procedure in the MOC used for this study.)

For Figs. 2(b–d), the axis curves are terminated at the end of the kernel because the uniform flow region begins at point B as shown in Fig. 1. The wall curves extend to the end of the contour at point C as also shown in Fig. 1. The density ϱ decreases smoothly along the axis and wall for both cases as shown in Fig. 2(b). Figure 2c shows that the gas is expanded into a $\Gamma < 0$ region that extends through the nozzle exit for the nominal ν_0 =0.70 case. This produces a uniform supersonic flow with $\Gamma < 0$. For this case, the Mach number reaches a maximum of about 1.88 along the axis and along the wall, as shown in fig. 2d. This agrees with the quasi one-dimensional results obtained by Cramer and Best (ref. 12).

A comparison of the wall contours at the maximum M_f for the two-dimensional and axisymmetric nominal cases is shown in Fig. 3. Note that in the contour plots, the y-axis is not to scale. Although difficult to see, the axisymmetric contour contains an inflection point just downstream of the throat that is not present in the two-dimensional contour. Also, θ^* is larger for the two-dimensional case as will be shown in more detail in the following figures. The results of this plot agree with the perfect gas results of Argrow and Emanuel (ref. 1).

Figures 4(a) and 4(b) show the θ^* vs. M_f variation for the axisymmetric and two-dimensional cases, respectively. These figures show the nominal case, a perfect gas with nominal conditions, and nominal conditions with $\nu_0 = 0.85$. Varying stagnation conditions for the perfect gas does not effect the nondimensional results. The dense gas case, $\nu_0 = 0.7$, shows BZT gas behavior, reaching a maximum M_f of about 1.88 for θ^* near 1° for the axisymmetric case shown in Fig 4(a). Then M_f decreases until reaching a maximum θ^* value of about 2.5°. The maximum M_f for the two-dimensional case is at $\theta^* \cong 2.5°$. The decrease of M_f for $\theta^* > 2.5°$ is not shown in Fig. 4(b), although the maximum θ^* for this case is about 3.5°.

Figures 5 and 6 also show θ^* vs. M_f for the for the nominal axisymmetric case. Figure 5 shows the effect of varying T_0, keeping other nominal conditions fixed, compared to a perfect gas. This shows that slightly increasing T_0 moves the flow away from the dense gas region. Figure 6 shows the effect of varying

c_v/R, keeping the other nominal conditions fixed, compared to a perfect gas. This shows a tendency to approach perfect gas behavior as c_v/R is decreased.

Figures 7 and 8 show the variation of the kernel length x_B and nozzle length x_f vs. M_f, respectively. Note that for the two-dimensional case, the figures show the increase to the maximum lengths but the decrease as θ^* increases (and M_f decreases from the maximum) is not shown in these plots. The BZT gas behavior is indicated in the nominal cases. Because the gas is more dense, the lengths are longer and reach a maximum before decreasing.

CONCLUSIONS

The MOC is applied to the steady isentropic flow of a dense gas. A method is presented for generating inviscid MLN contours to produce a uniform supersonic flow. The MLN procedure presented is limited to cases where there is only one sonic point. Inclusion of more than one sonic point will require the coupling of the present method with a subsonic contour design procedure. In order to continuously isentropically expand the gas from a stagnation state to $M \to \infty$, reference 12 shows that for the nominal case investigated in the present study, M first reaches a local maximum value of about 1.88 before decreasing to a supersonic minimum of about 1.05. We have shown that it is not possible for a nozzle to use a single centered expansion to accomplish this. At best, the single centered-expansion MLN can generate an isentropic expansion slightly beyond the local maximum before an expansion shock is generated. The maximum allowable θ^* appears to occur as the $\Gamma < 0$ region approaches the throat, resulting in a shock. We speculate that a design that employs two centered expansions separated by a finite converging wall may be able to accomplish the expansion in a minimum length. This will be investigated in the future.

It was shown that the nozzle designs presented may be used to produce a steady supersonic flow of a BZT gas in a $\Gamma < 0$ state. This raises the possibility of producing interesting wind tunnel experiments to study the supersonic external flow of a dense gas over airfoils and other aerodynamic shapes.

ACKNOWLEDGEMENT

The authors gratefully acknowledge Mark. S. Cramer and George Emanuel for their insightful correspondence and suggestions.

REFERENCES

1. Argrow, B. M. and Emanuel, G,, "Comparison of Minimum Length Nozzles," J. of Fluids Engineering
2. Argrow, B. M.; and Emanuel, G.: Computational Analysis of the Transonic Flow Field of Two-Dimensional Minimum Length Nozzles. J. Fluids Eng., vol. 113, Sept. 1991, pp. 479-488.
3. Cramer, M. S.; and Fry, R. N.: Nozzle Flows of Dense Gases. Phys. Fluids A, vol. 5, May 1993, pp. 1246-1259.
4. Chandrasekar, D.; and Prasad, P. P.: Transonic Flow of a Fluid with Positive and Negative Nonlinearity through a Nozzle. Phys. Fluids A., vol. 3, Mar. 1991, pp. 427-438.
5. Schnerr, G. H.; and Leidner, P.: Diabatic Supersonic Flows of Dense Gases. Phys. Fluids A, vol. 3, Oct. 1991, pp. 2445- 2458.
6. Bober, W.; and Chow, W. L.: Nonideal Isentropic Gas Flow Through Converging-Diverging Nozzles. J. Fluids Eng., vol. 112, Dec. 1990, pp 455-460.
7. Vinokur, M.: Discussion of Nonideal Isentropic Gas Flow Through Converging-Diverging Nozzles. J. Fluids Eng., vol. 112, Dec. 1990, pp. 460-461.
8. Kluwick, A.: Transonic Nozzle Flow of Dense Gases. J. Fluid Mech., vol. 247, 1993, pp. 661-688.
9. Anderson, W. K.: Numerical Study on Using Sulfur Hexaflouride as a Wind Tunnel Test Gas. AIAA J., vol. 29, Dec. 1991, pp. 2179-2180.
10. Cramer, M. S.; and Crickenberger, A. B.: Prandtl-Meyer Function for Dense Gases. AIAA J., vol. 30, Feb. 1992, pp. 561-564.

11. Cramer, M. S.: Nonclassical Dynamics of Classical Gases. Nonlinear Waves in Real Fluids, Springer-Verlag, 1991, pp. 91–145.
12. Cramer, M. S.; and Best, L. M.: Steady, Isentropic Flows of Dense Gases. Phys. Fluids A, vol. 3, Jan. 1991, pp. 219–226.
13. Thompson, P. A.: A Fundamental Derivative in Gasdynamics. Phys. Fluids, vol. 14, 1971, pp. 1843–1849.
14. Zucrow, M. J.; and Hoffman Gas Dynamics. Vol. 1. Wiley, 1976, vol. 2 Krieger, 1977.

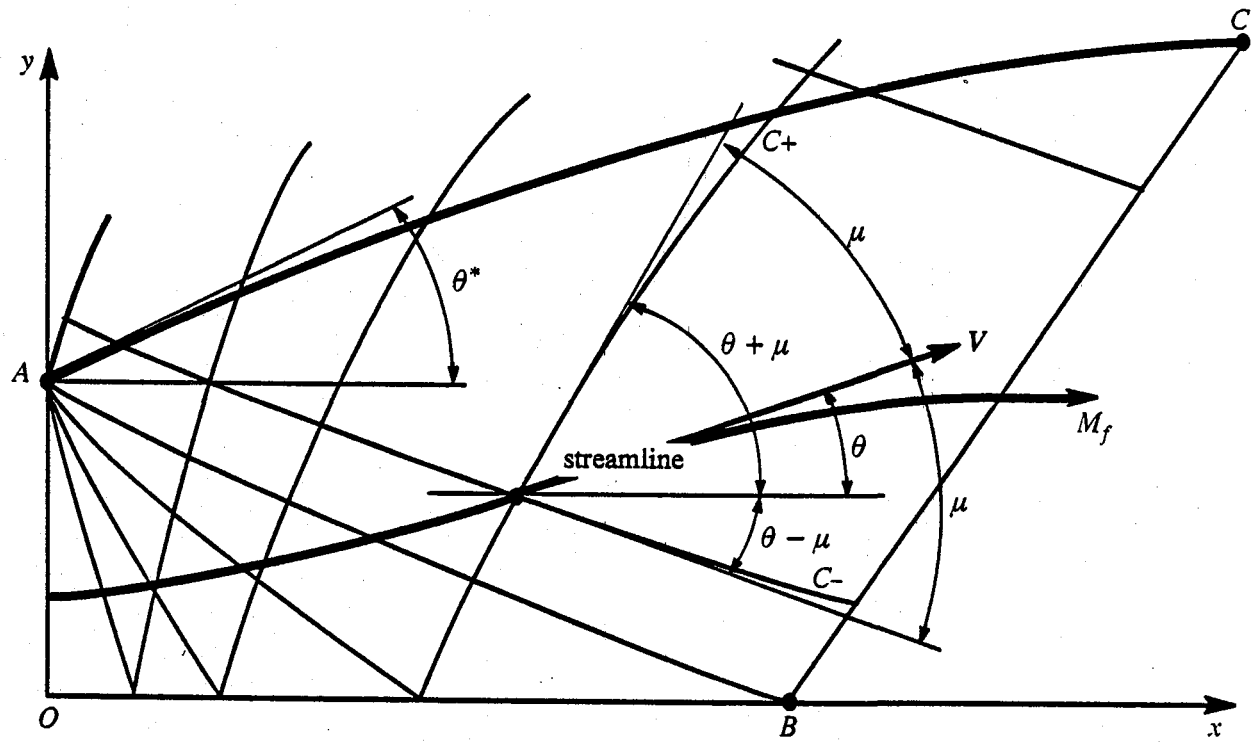

Fig. 1 MLN supersonic flow field geometry, upper half-plane.

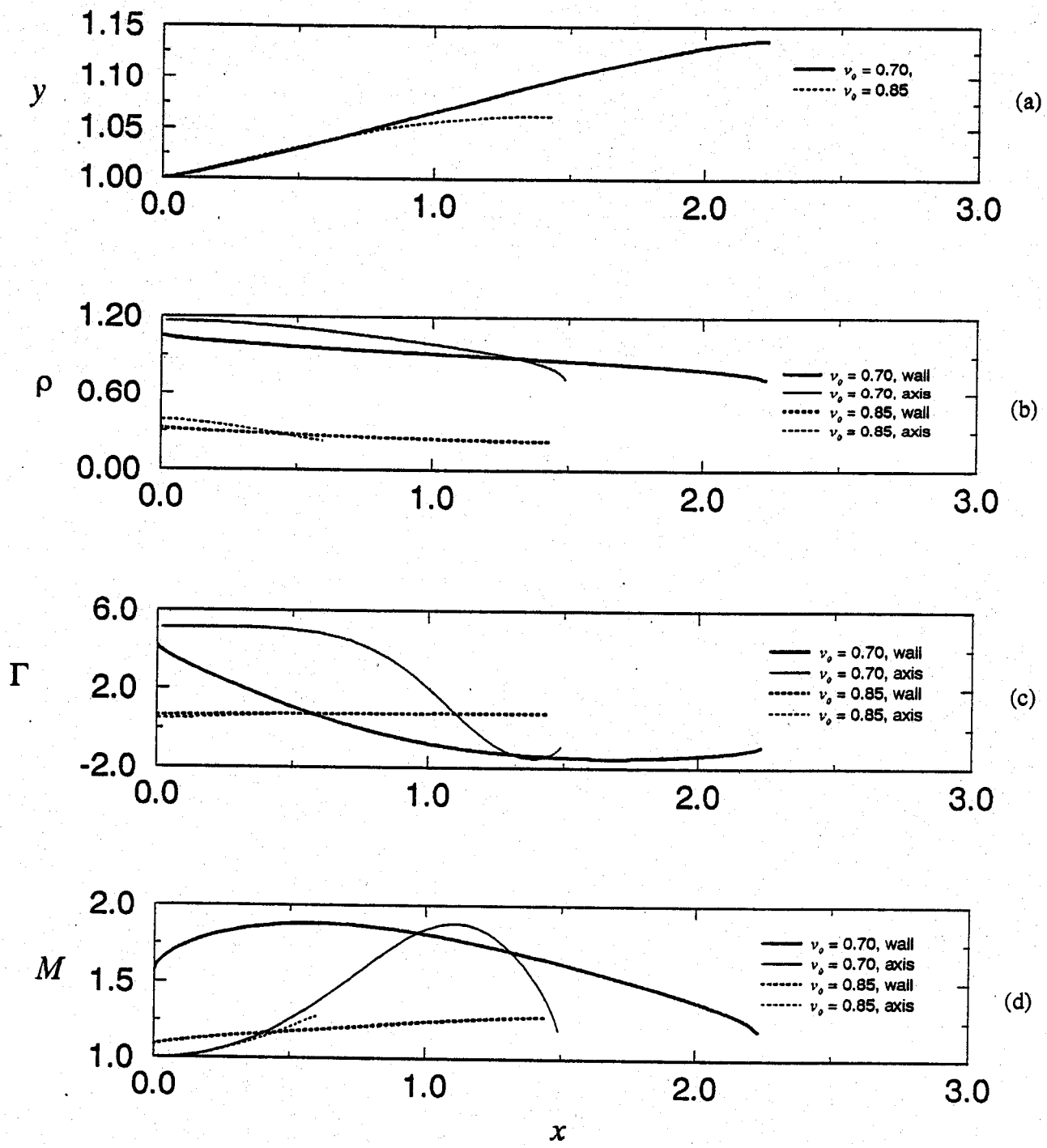

Fig. 2 (a) Wall contour, (b) density, ϱ, distributions (c) fundamental derivative, Γ, distributions; (d) Mach number, M, distributions, along the wall and the axis, all for the axisymmetric case, nominal and for $\nu_0 = 0.85$.

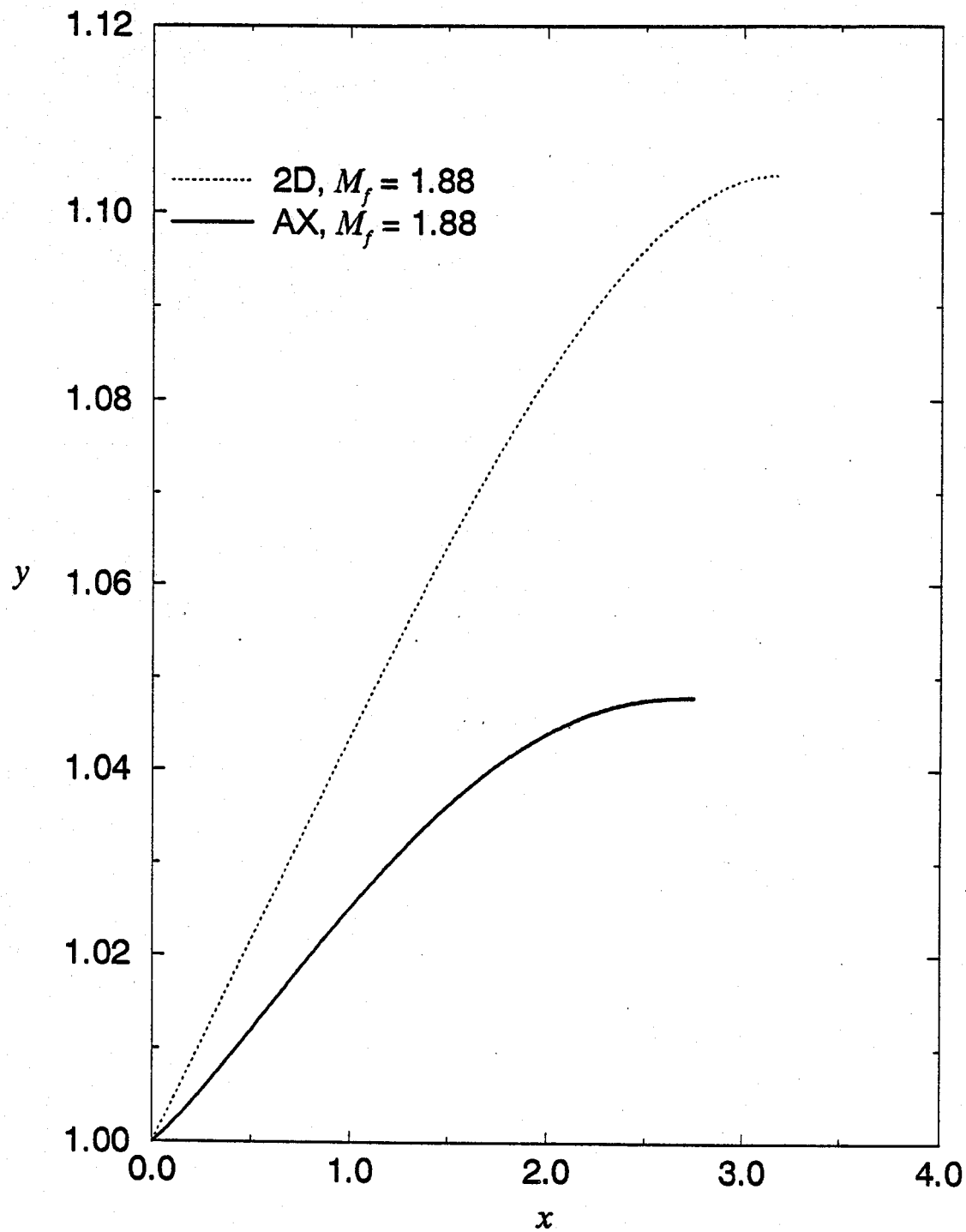

Fig. 3 Comparison of two-dimensional and axisymmetric contours for maximum M_f, nominal case.

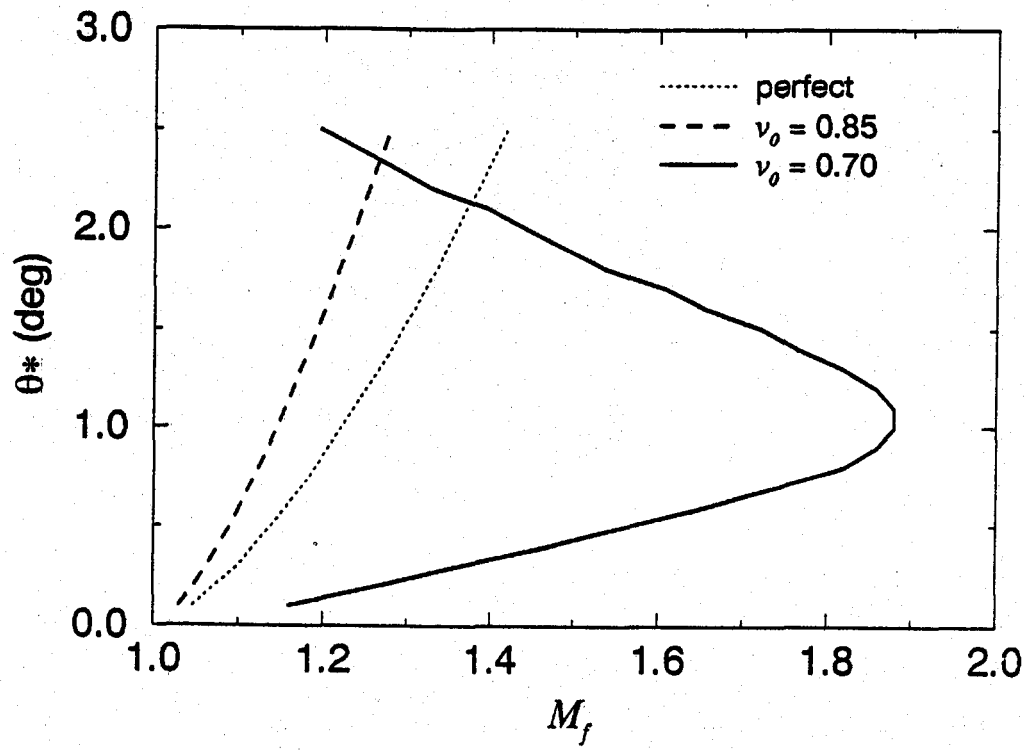

Fig. 4 (a) Initial wall turn angle θ^* vs. M_f, nominal conditions, variable ν_0, axisymmetric case.

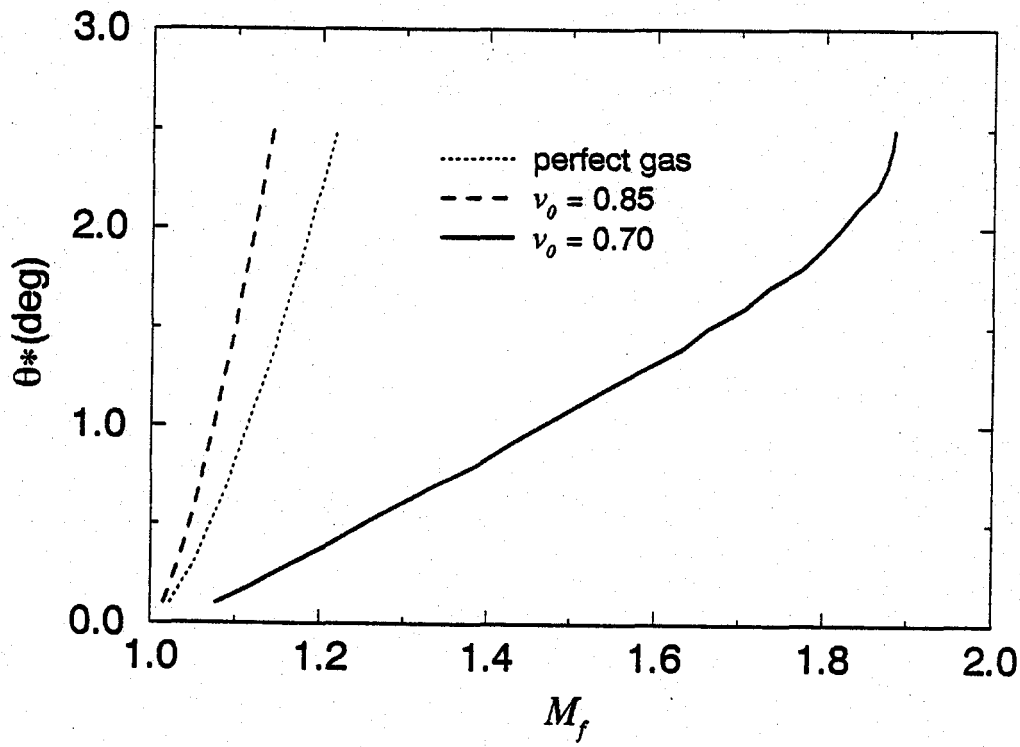

Fig. 4 (b) Initial wall turn angle θ^* vs. M_f, nominal conditions, variable ν_0, two-dimensional case.

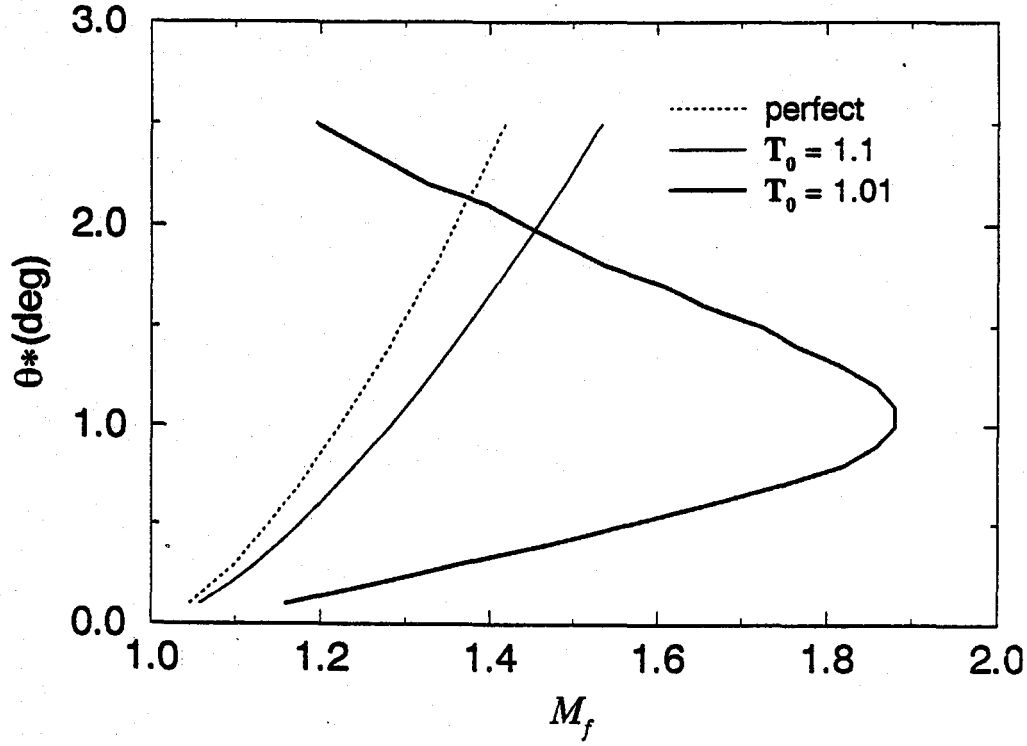

Fig. 5 Initial wall turn angle θ^* vs. M_f, nominal conditions, variable T_0, axisymmetric case.

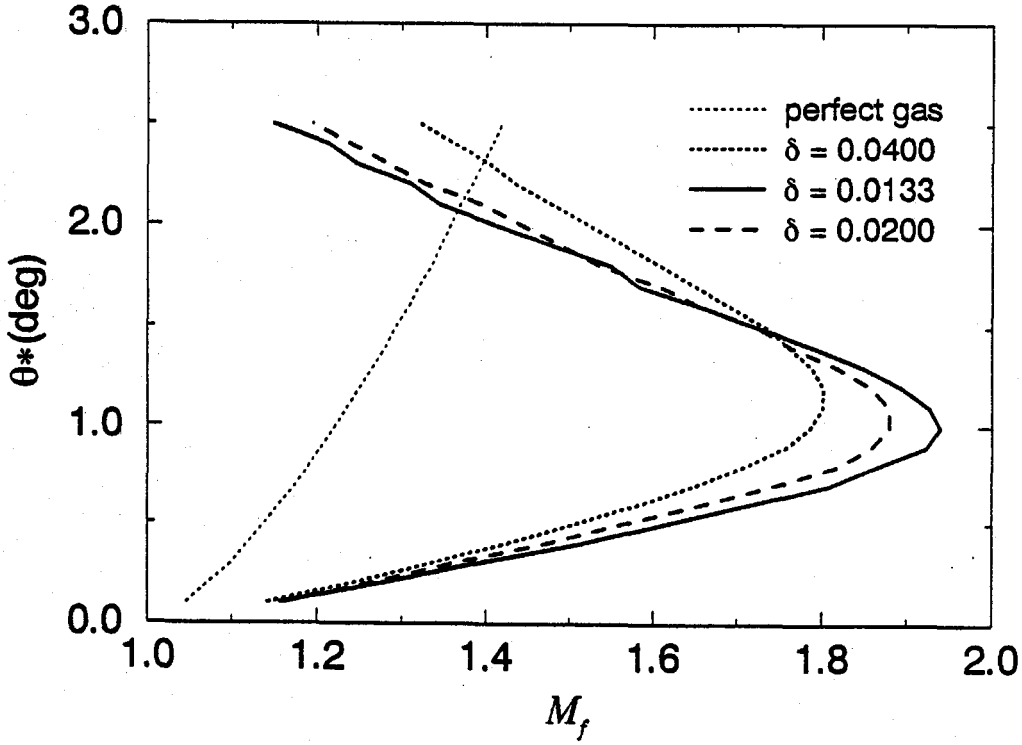

Fig. 6 Initial wall turn angle θ^* vs. M_f, nominal conditions, variable c_v/R, axisymmetric case.

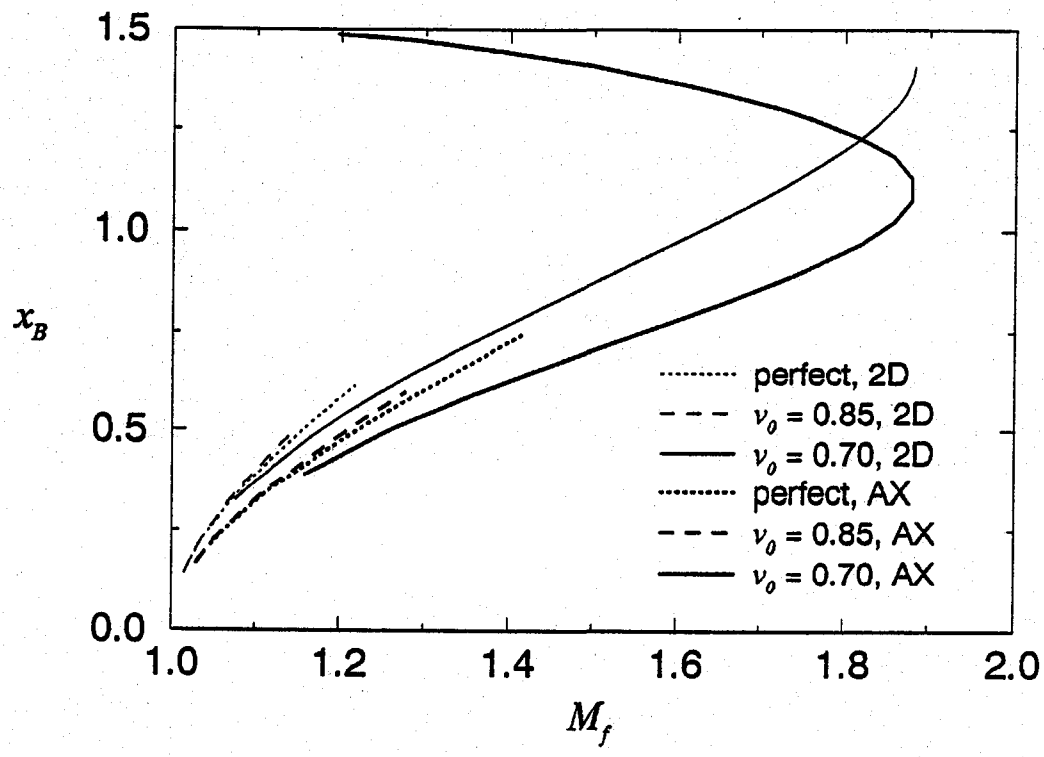

Fig. 7 Kernel length x_B vs. M_f, nominal two-dimensional and axisymmetric cases with variable ν_0.

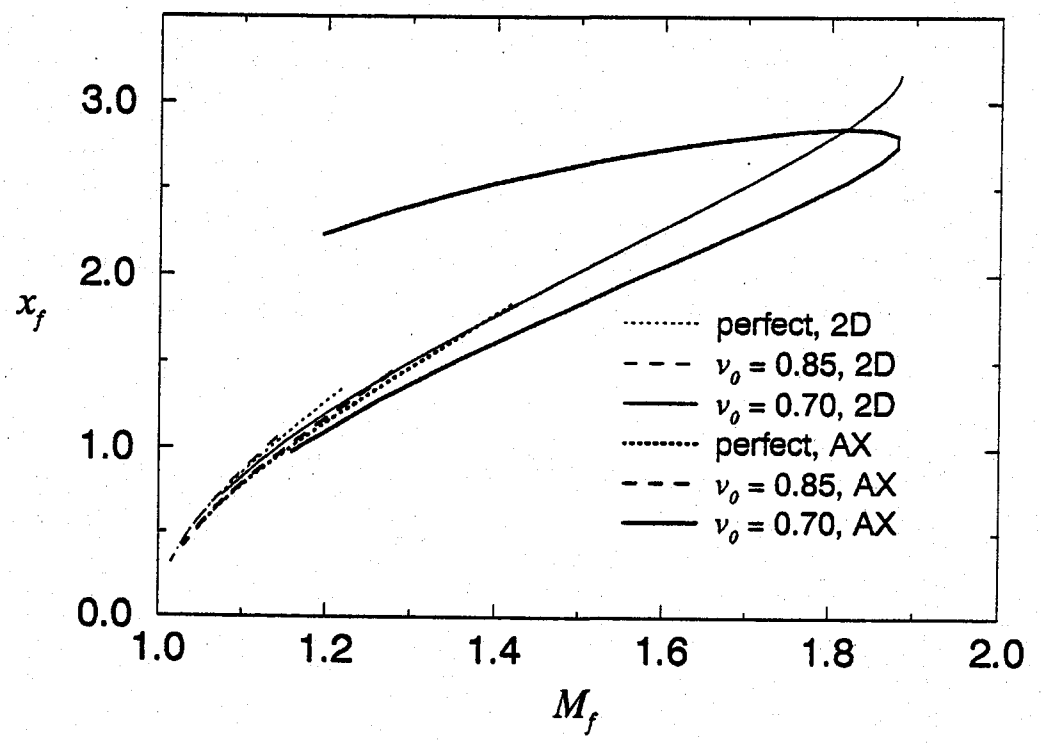

Fig. 8 Nozzle length x_f vs. M_f, nominal two-dimensional and axisymmetric cases with variable ν_0.

EXPERIMENTAL AND ANALYTICAL STUDY OF CRYOGENIC PROPELLANT BOILOFF TO DEVELOP AND VERIFY ALTERNATE PRESSURIZATION CONCEPTS FOR SPACE SHUTTLE EXTERNAL TANK USING A SCALED DOWN TANK

K. M. Akyuzlu
Department of Mechanical Engineering
University of New Orleans
New Orleans, Louisiana 70148

S. Jones and T. Meredith
Advanced Programs
Martin Marietta Manned Space Systems
New Orleans, Louisiana 70189

SUMMARY

Self pressurization by propellant boiloff is experimentally studied as an alternate pressurization concept for the Space Shuttle external tank (ET). The experimental setup used in the study is an open flow system which is composed of a variable area test tank and a recovery tank. The vacuum jacketed test tank is geometrically similar to the external LOx tank for the Space Shuttle. It is equipped with instrumentation to measure the temperature and pressure histories within the liquid and vapor, and viewports to accommodate visual observations and Laser-Doppler Anemometry measurements of fluid velocities. A set of experiments were conducted using liquid Nitrogen to determine the temperature stratification in the liquid and vapor, and pressure histories of the vapor during sudden and continuous depressurization for various different boundary and initial conditions.

The study also includes the development and calibration of a computer model to simulate the experiments. This model is a one-dimensional, multi-node type which assumes the liquid and the vapor to be under non-equilibrium conditions during the depressurization. It has been tested for limited number of cases. The preliminary results indicate that the accuracy of the simulations is determined by the accuracy of the heat transfer coefficients for the vapor and the liquid at the interface which are taken to be the calibration parameters in the present model.

INTRODUCTION

The analytical study conducted previously [1] has demonstrated that self-pressurization due to boiloff during discharge of liquid from a cryogenic tank is possible under certain boundary and initial conditions. The boiloff phenomena depends on various parameters such as: initial pressure and temperature of the vapor, initial temperature of the liquid, initial ullage volume, discharge rate (exit valve setting), initial concentration of bubbles in the liquid, impurities in the liquid, external heat transfer, nucleation sites on the walls of the container, and variation in liquid-vapor interfacial area that are due to changes in cross-sectional area [2,3, and 4]. It also depends on parameters that are directly related to the thermophysical properties of the cryogenic fluid. It is important to know which of these parameters play an important role in determining the rate of pressure recovery in the ullage and to what extent. Such information helps one to explore the possibility of passive type of self-pressurization in cryogenic tanks.

The scope of this study includes the investigation of the important parameters that effect the self-pressurization phenomena. They are chosen to be the parameters that are set at the beginning of the discharge such as : initial ullage volume, discharge rate (exit valve setting), and initial ullage pressure. The study was planned to be conducted under a controlled environment; therefore, a scaled down model of the liquid Oxygen (Lox) tank [5] with the necessary piping and recovery system was constructed and equipped with various instrumentation in the Cryogenics Laboratory at the University of New Orleans.

A numerical analysis is also carried out to predict the time dependent pressure, temperature, density, and velocity distributions within the liquid and vapor phases of the Nitrogen in the tank as it goes through a sudden depressurization. The mathematical model adopted for this purpose is a one-dimensional, non-equilibrium thermal-hydrodynamic model. A more simplistic but practical model approach that is cited in the literature [6,7, and 8] assumes a single temperature and pressure for both of the phases. These thermal equilibrium models cannot predict the evaporation rates correctly during the initial stages of depresurization; therefore are not reliable in predicting the pressure transients. This fact may lead to underestimation (or overestimation) of the time for pressure recovery within the tank. More elaborate models use three-dimensional, incompressible Navier-Stokes equations [9] which fail to predict the transient behavior of the vapor in the ullage which exhibit non-equilibrium characteristics during the depressurization process.

DESCRIPTION OF THE EXPERIMENTAL SETUP

The schematic of the Space Shuttle Liquid Oxygen (LOx) External Tank (ET) is given in Figure 1. The tank is filled from an eccentrically placed pipe at the bottom which serves also as the outlet. The LOx tank has slosh baffles on the lower interior and anti-vortex baffles at the bottom as shown in Figure 1. The gaseous Helium is injected from the bottom of the LOx tank for geysering protection and is injected from the top for pressurization. There is also a vent/relief valve at the top of the tank. The model tank and the rest of the experimental setup is described below [10 and 11]. Nitrogen - which has thermodynamical properties similar to that of Oxygen - was chosen as the working fluid because it is safe and cheaper to obtain.

Model Tank and Flow System

The flow diagram for the experimental setup is shown in Figure 2. The setup consists of a test tank which is filled with liquid Nitrogen (LN2) that is supplied through a 1/2 inch line from a supply tank. The 1 1/2 inch discharge line from the test tank leads to a recovery tank within five feet or to a dewar which is open to the atmosphere. The liquid line is equipped with four monitoring stations and also accommodates a cryogenic liquid pump. The recovery tank exhausts to the atmosphere through a 2 inch pipe which is also equipped with a monitoring station. The exhaust piping is designed to accommodate a cryogenic vapor blower. Both the liquid and vapor lines are equipped with ball valves to shut-off or control the flow of Nitrogen. There is a 1/2 inch Helium line which is used to pressurize the liquid in the test tank. A 1/4 inch line diverts the flow of Helium through a needle valve to the bottom of the test tank for Helium injection simulation. The gas is supplied from a high pressure Helium tank. The test and recovery tanks and all the monitoring stations have individual relief lines which open to the 2 inch exhaust line.

Test Tank: The test tank is vacuum jacketed and has a capacity of 55 gallons. The inner tank was designed in order to simulate both changing and constant liquid surface area as the liquid is drained from the tank. This is accomplished with a conical section at the top tapering out to a cylindrical mid section and a dome section on the bottom. The test tank currently has six penetrations: one 1 1/2" outlet (liquid) on the bottom, four 1/2" outlets (instrumentation ports and a vent port) and one 2" instrument port at the top. A 1/4" Helium inject port is located on the elbow of the 1 1/2" bottom outlet. In addition, two 2" viewing ports, 180 degrees apart, are located on the cylindrical section of the tank to be used in

conjunction with a Laser Doppler Anemometry and a video camera to capture the velocity and geometry of the bubbles formed in liquid during sudden depressurization. The viewing ports consist of quartz lenses attached to the inner tank and a Pyrex glass attached to the outer shell of the test tank. The test tank is made of stainless steel 304L and has a maximum operating pressure of 150 psig. Figure 3 is a drawing of the test tank.

Recovery Tank and Dewar: The recovery tank has a volume of 100 gallons in a cylindrical shape with a diameter of 28 inches. It is also vacuum jacketed. It has one 1 1/2 inch vacuum jacketed inlet at the bottom and one 1 1/2 inch outlet at the top. The recovery tank is also made from stainless steel 304L and has a maximum operating pressure of 150 psig. It is designed to stand pressures up to 150 psig. The dewar is a vacuum jacketed stainless steel tank which is open at the top. It can hold liquid Nitrogen in excess of 20 gallons.

Liquid Nitrogen Supply Tank: During the experiments, the liquid Nitrogen is supplied from a DURA-MAX 550 dewar. The dewar is vacuum jacketed and has a capacity of 55 gallons. It has a maximum operating pressure of 350 psig.

Instrumentation

The tanks and the piping are equipped with various types of instrumentation to monitor the pressure, temperature and flow rate at appropriate locations. There are five monitoring stations that are located along the liquid and vapor line. Each monitoring station has a pressure gage and a transducer, a flow-thru thermocouple, a purge valve and a pressure relief valve.

The test tank is instrumented separately to monitor the instantaneous changes in pressure in the ullage, temperature in the vapor, and temperatures at various levels of the liquid.

Pressure Gages : Analog pressure gages are placed at various points along the liquid line to visually monitor the pressures in the tanks and in the associated piping. These MATHESON cryogenic pressure gages are Bordon tube type and have a pressure range of 0 to 100 psig.

Pressure Transducers : The cryogenic pressure transducers are placed in the system as to continuously monitor the ullage pressure, the pressure of the liquid at the exit of the test tank (see Figure 4), and the pressure of the vapor in the recovery tank. They are KELLER Series 420 cryogenic transducers with a range of 0 to 100 psia and are factory calibrated for -320 deg F.

Thermocouples : Flow-thru thermocouples are placed on the tanks and on the piping to monitor the temperatures of the vapor and the liquid Nitrogen in the system. They are T type (OMEGA 304-T-MO-125), 24 WG, and shielded with stainless steel.

Another set of thermocouples are placed 2 inches (5 cm) apart on a 1/2 Teflon tubing which is suspended from the instrument port at the top of the test tank (see Figure 4). These thermocouples are T type (OMEGA TT-T-30-200), 32 WG and teflon coated, and are secured to the teflon tube by a special epoxy.

Flow Meter : A turbine flow meter is placed on the liquid line at the outlet of the test tank to monitor the flow rate. It is by SPONSLER and is designed to operate at cryogenic temperatures.

Laser Doppler Anemometer : The setup is equipped with a Laser Doppler Anemometry (LDA) to measure the velocity of the liquid particles in two directions near to the liquid-vapor interface. This will enable one to determine any circulation that may be present within the liquid, especially adjacent to the interface. The LDA can also be used to determine the velocity of the bubbles (Helium or Nitrogen). The present LDA system comprises of a 2 watts Argon-Ion laser manufactured by COHERENT, LDA optics by DANTEC which include a beam waist adjuster, retarder, beamsplitter, Brag cell, PM section, beam translator, beam expander, and front lens.

Data Acquisition Systems

Three different types of data acquisition systems are used, depending on the type of signal, to

collect and analyze the data coming from the thermocouples, pressure transducers, and the LDA photomultipliers [10 and 11].

Data Acquisition with DT2801 A/D Board : A Data Translation A/D board, T2801, is used to digitize the analog signals coming from the amplifiers that are connected to the pressure transducers. The analog signals from the KELLER cryogenic pressure transducers are amplified with HONEYWELL Acudata 218 bridge amplifiers then fed into the termination board for the DT2801. The DT2801 A/D board digitizer the signals coming from the amplifiers at a 10 Hz frequency and feds them into the ZENITH Z-286 personal computer. Here a software called ADA processes the digitized signals and stores them in a user named data file. The stored data can be retrieved any time and plotted using the GRAPHER plotting software.

Data Acquisition with LabView : The LABVIEW software and the associated A/D board is used to collect and process the signals coming from the thermocouples. The very low potential signals are fed into a SC-2070 breadboard and then into the NB-MIO-16 A/D board. The digitized signals from the A/D board are fed into a MACINTOSH IIsi personal computer which runs the NATIONAL INSTRUMENT's LABVIEW software package. LABVIEW package is configured to display the temperatures by virtual instruments like thermometers or recordings on a strip-chart recorder. All the data that is processed by the system can be retrieved at a later time for further analysis and display.

Data Acquisition for LDA : The data acquisition system for the LDA is made by DANTEC and include two counter processors, a frequency shifter, a traversing mechanism for two-dimensional velocity measurements. The signals from the photomultipliers are fed into the counters for both channels through a frequency shifter. The processed data is fed into a ZENITH Z-386 personal computer which runs the enCOUNTER data acquisition software. This software package stores and analyzes the data and can represent the results in graphical form.

EXPERIMENTAL STUDY

The calibration of the instruments, preparation and execution of the experiments using LN2 as the working fluid are explained below.

Calibration

It was necessary to calibrate the temperature reference junction on the A/D bread board by using a reference thermocouple which is suspended into LN2 which is stored in a very small dewar open to atmosphere. The reference thermocouple was continuously monitored during the experiments. Furthermore, each thermocouple in the test tank was calibrated by suspending it into LN2 under atmospheric pressure and then comparing the readings to the readings of the reference thermocouple. The maximum deviation was +/- 0.5 degrees F. The data acquisition system for the thermocouples has an overall accuracy of 0.2 degree F.

The signals from the pressure transducers were also calibrated. For this purpose the vapor Nitrogen line was equipped with a pressure transducer and a analog pressure gage. A simple calibration test was conducted where the pressure in the line was reduced slowly at a controlled rate. All the readings, including the pressure gage , multimeter, and digitized signal readings, were recorded at equal time intervals. Using these recordings, calibration curves were constructed for each pressure transducer. Third order polynomials that approximate these curves were then implemented into the software (ADA) which converts the digital readings from the A/D board to psia. The accuracy of the pressure transducers is within +/- 0.2 psia.

Experimental Procedure

The 55 gallon supply tank is filled with liquid Nitrogen one hour before the experiments start.

The pressure relief line on the supply tank is connected to the exhaust line and the valve is adjusted to keep the pressure in the tank below 300 psig. Before filling the test tank with liquid Nitrogen, the liquid and vapor exhaust lines are conditioned with liquid Nitrogen. Then the liquid Nitrogen is introduced to the test tank from the bottom with the discharge valve completely open. The vent valve at the top of the test tank is opened partially to keep the pressure in the tank lower than the pressure in the discharge line so that the liquid flows into the test tank. When the required level of liquid Nitrogen in the test tank is obtained , the 1 1/2 inch liquid outlet valve is closed. Then the liquid Nitrogen is allowed to boil until the saturation temperature at atmospheric pressure is attained. At this point the 1/2 inch vent line is closed. Then the liquid Nitrogen in the test tank is pressurized with cold Nitrogen gas to a predetermined ullage pressure. The system is ready for a blowdown experiment when the pressure and temperature of the vapor in the ullage are stabilized at predetermined values.

The experiment starts by activating the data acquisition systems. Then all the ball valves in the system except the liquid outlet valve at the bottom of the test tank are opened fully. Ten seconds after the activation of the acquisition system the discharge valve is opened to a predetermined setting in one quick stroke. The temperature and pressure readings are monitored continuously while the liquid Nitrogen discharges into the dewar or the recovery tank.

Experimental Results and Discussion

A typical history of pressure in the ullage during a sudden depressurization - TESTN41 - is shown in Figure 5. The recorded history of temperature of the vapor in the ullage (TC1) and the history of the temperatures in the liquid (TC2, TC3, and TC4) for the same experiment are shown in Figure 6. Sudden depressurization causes a drop in the recorded temperatures and then an increase as the liquid turns into vapor. The existence of temperature stratification within the liquid can be easily observed from this figure.

Three different sets of experiments were conducted to determine the effect of various operational parameters on pressure recovery. A detailed description of the experimental results can be found in reference [10 and 11].

Ullage Pressure : In one set of experiments, three different initial ullage pressures were studied: 21 psia, 18 psia, and 16 psia. The tank was full with liquid Nitrogen and the discharge valve was fully opened (90 degrees) in this set of experiments. The fluid inside the test tank was observed through the viewports during one of the high pressure experiments and has been recorded by a high speed, digital video camera. The pressure histories for these experiments as registered by the pressure transducer (PT2) located on the discharge line (Figure 4) are given in Figure 7. In all of the cases studied the pressure starts to recover after a sudden, sharp decrease in pressure.

Discharge Rate : Four different discharge rates were studied in another set of experiments. Different discharge rates were attained by setting the discharge valve to four different valve opening positions: 15, 30, 60, and 90 degrees. The pressure histories for these experiments are shown in Figure 8. The initial ullage pressure was 20 psia in all of these experiments. It can easily be observed from these figures that a slower discharge rate provides a faster rate of pressure recovery.

Initial Ullage Volume : The effect of the initial ullage volume was studied during the last set of experiments. The pressure histories for each experiment is shown in Figure 9 where the tank is filled with 50 , 40, and 30 gallons of liquid Nitrogen at a time. In these experiments the ullage pressure is 20 psia and the discharge valve is fully opened. Studying these figures one observes the increase in susceptibility of the fluid to flow oscillations with increase in ullage volume.

NUMERICAL STUDY

To improve upon the numerical simulations given by the existing thermal equilibrium model [7],

it was necessary to assume the vapor and the liquid phases to be at nonequilibrium conditions which is expected to exist under sudden depressurization. Furthermore, the nonequilibrium model can be made more realistic if each phase is assumed to be made up of multiple layers of unequal temperatures. Such a model which will be referred to as "one-dimensional multi-node nonequilibrium model" is adopted for the present analytical study.

Mathematical Model

In this study the liquid and vapor phases of the cryogenic fluid in the sample tank is assumed to be separated by a well defined interface which is modelled by a film of liquid of infinitesimal thickness. The mass interaction between the phases occurs only through this well defined boundary. The location of the interface is determined by the continuity equation written for the differential volume that encloses the interface. It is assumed that vapor is located only above this interface whereas the liquid rests below.

Conservation Equations : The conservation equations of mass, momentum and energy for the liquid and the vapor phases for one-dimensional fluid flow are given by similar equations with the exception of certain terms for the liquid which are assumed to be negligible. These terms are identified by various Greek letters which take on the values -1, 0, or +1 as described in the nomenclature section of this paper.

Continuity

$$\gamma \frac{\partial}{\partial t}(\rho_k') + \frac{\partial}{\partial z}(\rho_k' u_k) = \xi \Gamma' \tag{1}$$

momentum

$$\frac{\partial}{\partial t}(\rho_k' u_k) + \gamma \frac{\partial}{\partial z}(\rho_k' u_k^2) = \rho_k' g - \frac{\partial}{\partial z}(\theta_k P) - \tau_w' + \xi \Gamma' u_k \tag{2}$$

energy

$$c_v\left(\frac{\partial}{\partial t}(\rho_k' T_k) + \frac{\partial}{\partial z}(\rho_k' u_k T_k)\right) = \eta \left(\frac{P}{\rho_k}\frac{\partial}{\partial t}(\rho_k')\right) + \eta \left(\frac{P u_k}{\rho_k}\frac{\partial}{\partial z}(\rho_k')\right) + \frac{\partial}{\partial z}\left(k\theta_k \frac{\partial}{\partial z}(T_k)\right) + \xi \Gamma' c_{p_k} T_k + \beta q_{in_k}' + q_w' \tag{3}$$

where

$$\rho_k' = \rho_k \theta_k \tag{4}$$

and

$$\theta_k = \frac{A_k}{A_{ref}} \tag{5}$$

The continuity equation for the vapor or liquid adjacent to the interface for a variable differential volume is given by

$$\eta V_k \frac{\partial}{\partial t}(\rho_k) + \xi \rho_k A_k \frac{\partial}{\partial t}(z_k) + \epsilon (\rho_k u_k A_k)_m = \xi \Gamma' \tag{6}$$

Equation of State : The thermodynamic equation of state is used to close the above set of equations. For this purpose, the vapor phase is assumed to behave like an ideal gas and the liquid phase is assumed to incompressible. Thermophysical properties of the fluid are assumed to be functions of temperature and are represented by appropriate polynomials.

Vapor generation rate : The rate of vapor generation is assumed to be a function of evaporation at the liquid-vapor interface.

Constitutive Relations for Interfacial Evaporation : The mass of evaporation term is determined from the energy balance at the interface and is given by

$$\Gamma_{eva} = \frac{-Q_{in_g} - Q_{in_l}}{h_{fg}} \tag{7}$$

where the heat transferred to any phase is given as

$$Q_{in_k} = h_{in_k} A_{in} (T_{sat} - T_k) \tag{8}$$

The heat transfer coefficient in the above equation is give in terms of Nusselt number which is function of Grashof and Prandlt numbers :

$$Nu = C Gr^a Pr^b \tag{9}$$

The coefficient C in this equation is used as a calibration parameter.

Constitutive relations for Friction : The wall drag force is given by the relation

$$\tau_w = \frac{1}{8} f \rho \, | u | \, u \tag{10}$$

where the friction factor is based on the Blassius formula.

Boundary and Initial Conditions : The above governing equations are subject to the following boundary conditions for the problem under considerations: The top of the tank is closed, therefore the velocity at this end of the domain is assumed to be zero at all times which requires the continuity, momentum, and energy equations modified for zero influx of mass, momentum, and heat. The velocity at the bottom of the tank, however, is a known quantity calculated from the given (time dependent) discharge rate. The other thermodynamic properties at the exit are extrapolated from the calculated values inside the tank. Initially, the vapor and the liquid is assumed to be at rest with specified temperature and pressure distributions. The unknown properties are determined from the equation of state for each phase at the given pressure and/or temperature.

Assumptions and Limitations of the Model

Although the mathematical model is applied to a geometrically three dimensional case , i.e., the test tank in this study, the variations in thermodynamic and physical properties are assumed to be only in one dimension which is chosen to be the direction of the flow. Certainly, one expects to have variations in all three dimensions for a process that continues for minutes under nonequilibrium conditions. Also it is very possible that the initial conditions exhibit variations of properties in all directions. However, all these factors are minor compared to the role of the heat and mass transfer at the vapor-liquid interface which is basically a one-dimensional phenomena. The assumptions that the vapor is ideal and the liquid is incompressible are valid ones considering the magnitudes of temperatures and pressures attained by each phase during the initiation (and also the continuation) of the boiling process.

The ET LOx tank has some features that were not considered in this initial study. The vapor above the liquid Oxygen contains a certain amount of Helium gas. It is understood that the mixture of Helium and GOx will have different thermodynamic properties than GOx alone. However, these variations in properties do not change the magnitude of mass and heat transfer at the interface which ultimately determines the pressure and temperature of the vapor. Also , it should be noted that the effect of the Helium will substantially decrease as GOx concentration increases due to evaporation. The existence of Helium bubbles in the liquid, initially, is also ignored in this study.

Solution Technique

Finite-Difference Formulation : The numerical technique adopted to solve the governing equations under the boundary conditions given above is an explicit one which approximates the partial differential equations of the problem by finite-differences.

Discretization : The cryogenic tank (Figure 4) with a variable area section is approximated by a function given by the user of the program. This function is then used to determine the radius of each computational cell and thus the cross sectional area. The variable area section can be divided into as many cells as one wishes. A staggered spatial mesh is used in the numerical scheme. In this scheme, the fluid properties such as density and temperature are defined at the center of the computational cells, while the liquid and vapor velocities are defined at the cell boundaries. Furthermore, a dual velocity concept is used at the cell boundaries which defines a velocity just upstream and another one just downstream of the boundary [13]. The relation between these two velocities for any phase is based on the steady state mass conservation across the interface.

Finite-Difference Approximations : The basic concepts used in developing the finite-difference approximations of the governing equations are summarized below (See reference [1] for details):

(i) The mass and energy equations are approximated by forward differencing in time and space, while momentum equations are approximated by forward differencing in time and central differencing in space.

(ii) The mass and energy conservation equations are integrated from the right boundary of each cell to the right boundary of the next cell with temperature and density held constant over the length of each cell. The velocity is assumed to vary linearly within each cell between the value at the left boundary and the value at the right boundary. Momentum conservation equation on the other hand, is integrated from the center of the computational cell to the center of the next cell.

Using the above principles the governing differential equations are approximated by finite differences and then the continuity equation is solved for the future value of density, momentum equation is solved for the future value of velocity, and energy equation is solved for the future value of temperature.

Solution Algorithm

The algorithm developed to solve the present problem using the above finite-difference

approximations of conservation equations uses a specific order of calculations. First, the velocities in the liquid and the liquid-vapor interface is calculated by a backward sweep because the exit velocity is known at all times. Then the velocities in the vapor are calculated. Next, the density and then the temperature is calculated. Knowing the temperature and density, the algorithm then uses the equation of state to determine the pressures. Finally, the continuity equation at the interface is used to predict the future location of the liquid-vapor interface. The mass of evaporation, heat transfer rates at the interface and other physical properties are updated before the next set of calculations. A flow chart of the computer program is given in reference [14].

Numerical Stability Criteria : As in all explicit finite-difference techniques, the Courant stability criteria is used to obtain numerically stable solutions.

Calibration and Model Verification

The heat transfer coefficients for the liquid and the vapor at the liquid-vapor interface are chosen to be the calibration parameters of the proposed model. The value of C in Equation 9 is determined by trial and error. This is not a very difficult task because the results are very sensitive to the magnitude of these coefficients. A plus or minus 20 to 30 % deviation in the assumed values of these parameters result in physically unreasonable temperatures and/or pressures for the vapor phase.

The analytical model has been tested, by numerical experimentation, for various possible initial and boundary conditions. First, the program was run for a case where only gaseous Nitrogen existed inside the test tank. The results were comparable to the one expected for an ideal gas going through a polytropic expansion. In the next test run the evaporation rate was taken to be zero. As in the "all gas" case, the vapor phase went through a process which resembles a polytropic process. In another study the discharge was terminated after 0.5 seconds of sudden depressurization [1]. The results showed that the pressures and temperatures attained stable values very close to the ones given by the thermal equilibrium conditions. These expected results confirm the success of the model in predicting the dynamic behavior of the fluid under sharp changes in boundary conditions.

Results of the Numerical Simulations

The results of a numerical experiment (sample run), are given in Figures 10 and 11. Figure 10 shows the variation of vapor pressure in the ullage, specifically in the second computational cell, during blowdown. During initiation of boiling the pressure drops down below 16 psia then recovers mainly due to increase in evaporation, then gradually decreases. Similarly, the temperature of the vapor in the ullage decreases very sharply during the initiation of boiling then increases considerably due to increase in pressure as shown in Figure 11. It attains its maximum value around the time the pressure is maximum and then decreases gradually. The density and velocity histories were also plotted together with the distributions of each at certain time intervals.

CONCLUSIONS

An experimental study was undertaken to determine the effect of various operational parameters on the characteristics of pressure recovery for cryogenic fluids that undergo a sudden depressurization process. It is concluded that the relative discharge rate is the most important parameter that determines the rate of pressure recovery. Lower discharge rates give more time for vapor generation which increase the rate of the recovery. Initial ullage volume is important in determining the characteristics of the discharge: a high initial ullage volume amplifies pressure oscillations that exist during the blowdown. The magnitude of the initial ullage pressure effects the discharge rate therefore plays a role in the initial stages of the recovery.

The numerical analysis was carried out using a one dimensional, multi-node, nonequilibrium thermo-hydrodynamic model. This model was also used to determine the important parameters that effect the vapor generation rate during boiloff initiation and continuous boiling. In general, the numerical study also confirms the fact that self-pressurization is possible only under certain combinations of initial and boundary conditions. Various specific conclusions can be drawn from this study: The initiation of boiling is determined by the pressure and temperature of the liquid at the vapor-liquid interface. The rate of evaporation at the interface during the initiation of boiling is largely determined by the temperature gradients that exists on both sides of the interface. These gradients are determined by the rate of heat exchange between each phases. The important parameters that effect this heat exchange are the interfacial heat transfer coefficients and the interfacial area. A higher heat transfer coefficient means higher rates of evaporation which in turn means quicker recovery in vapor pressure.

ACKNOWLEDGEMENTS

This study has been supported by Martin Marietta Manned Space Systems at New Orleans. Our special thanks go to the graduate students, R. Kesani and M. Redmond in assisting us in conducting the experiments and running the computer program for numerical simulations. Our thanks are extended to D. Coote of Martin Marietta who helped us understand the important issues of the problem. S. Malipeddi's help in preparing the manuscript is appreciated.

NOMENCLATURE

A	cross sectional	q	heat flux
C	constant, calibration parameter	q'	heat input per reference volume of fluid
D	diameter of the cell	Q	total heat input
f	friction factor	T	temperature
g	gravitational constant	t	time
h_{fg}	heat of evaporation	u	velocity
h_{ink}	interfacial heat transfer coefficient	V	volume
k	thermal conductivity	z	spatial coordinate in axial direction
P	pressure		

Greek Symbols

β	= 0, for all vapor or all liquid; = 1, for vapor or liquid at interface	η	= 0, for liquid; = 1, for vapor
γ	= 0, for liquid; = 1, for vapor	θ	area ratio
Γ	rate of mass of vapor generation	μ	dynamic viscosity
ϵ	=-1, for vapor; = 1, for liquid	ρ	density
ξ	= 0, for all vapor or all liquid; = 1, for vapor at the interface; =-1, for liquid at the interface	ρ'	density times area ratio
		τ	wall drag force
		τ'	wall drag force per reference volume

Subscripts

in	interface between liquid and vapor	m	=inlet, for vapor; =exit for liquid
g	vapor phase	ref	reference
k	k th phase: liquid or vapor	s	saturation
l	liquid phase	w	wall

REFERENCES

1. Akyuzlu, K. M. , " *Analytical Evaluation of a Cryogenic Boiloff Pressurization System: Volume I,* " Final Report, Martin Marietta Manned Space Systems, Contract No. A71412, New Orleans, LA, 1990.

2. Alamgir, M., Kan, C. Y., and Lienhard, J. H. , " *An experimental Study of the Rapid Depressurization of Hot Water,*" ASME Journal of Heat Transfer, Vol 102, p.433, 1980.

3. Deligiannis, P. and Cleaver, J. W., " *The Role of Nucleation in the Initial Phases of Rapid Depressurization of a Subcooled Liquid,*" International Journal of Multi-Phase Flow, Vol.16, No.6, p.975, 1990.

4. Lienhard, J. H. , Alamgir, M., and Trela, M., " *Early Response to Sudden Release from High Pressure,* " ASME Journal of Heat Transfer, Vol. 100. P. 473, 1978.

5. Nein, M. E. and Head, R.R., " *Experiences with Pressurized Discharge of Liquid Oxygen from Large Flight Vehicle Propellant Tanks,* " Advances in Cryogenic Engineering, Vol. ,p. 244, 19.

6. Ring, E., " *Rocket Propellant and Pressurization Systems.*" Prentice-Hall, Inc., Englewood Cliffs, N.J., 1964.

7. System Analysis Flight Evaluation Team, " *STS-31R Flight ET-MPS Predicted Performance,*" Martin Marietta Manned Space Systems, New Orleans, Louisiana, April 1990.

8. Vaughan, D. and Schmidt, G. , " *Analytical Modeling of No-Vent Fill Process,*" Proceedings of the 26th Joint Propulsion Conference, AIAA/SAE/ASME/ASEE, Orlando, FL , 1990.

9. Hochstein, J.I. et al, " *Prediction of Self-Pressurization Rate of Cryogenic Propellant Tankage,*" Journal of Propulsion and Power, AIAA, Volume 6, Number 1, 1990.

10. Redmond, M., " *An Experimental Study of the Effects of Initial Conditions on the State of Liquid Nitrogen inside a Cryogenic Tank during Sudden Depressurization,*" M.Sc. Thesis, Department of Mechanical Engineering, University of new Orleans, New Orleans, LA, 1993.

11. Akyuzlu, K. M., " *Experimental and Analytical Study of Cryogenic Propellant Boiloff, Phase II; Experimental Study and Model Calibration,* " Preliminary Report, Martin Marietta Manned Space Systems, Contract No. A71510, New Orleans, LA, December 1992.

12. Hahne, E. and Grigull, U. (Eds.) , " *Heat Transfer in Boiling,*" Hemisphere Publishing Corp., Washington, D.C., 1977.

13. Akyuzlu, K.M. and Guillot, M.J., " *Mathematical Simulation of Dynamic Oscillations in Annular Two-Phase Flows In Variable Area Pipes with Heat input Using a Separated Flow Model,*" Thermal Hydraulics of Advanced Nuclear Reactors, ASME, HTD-Vol.150, 1990.

14. Kesani, R., " *Calibration and modification of a One-Dimensional Multinode Non-Equilibrium Model to Simulate the Sudden Depressurization of Liquid Nitrogen inside a Cryogenic tank* ," M.Sc. Thesis, Department of Mechanical Engineering, University of New Orleans, New Orleans, LA, 1993.

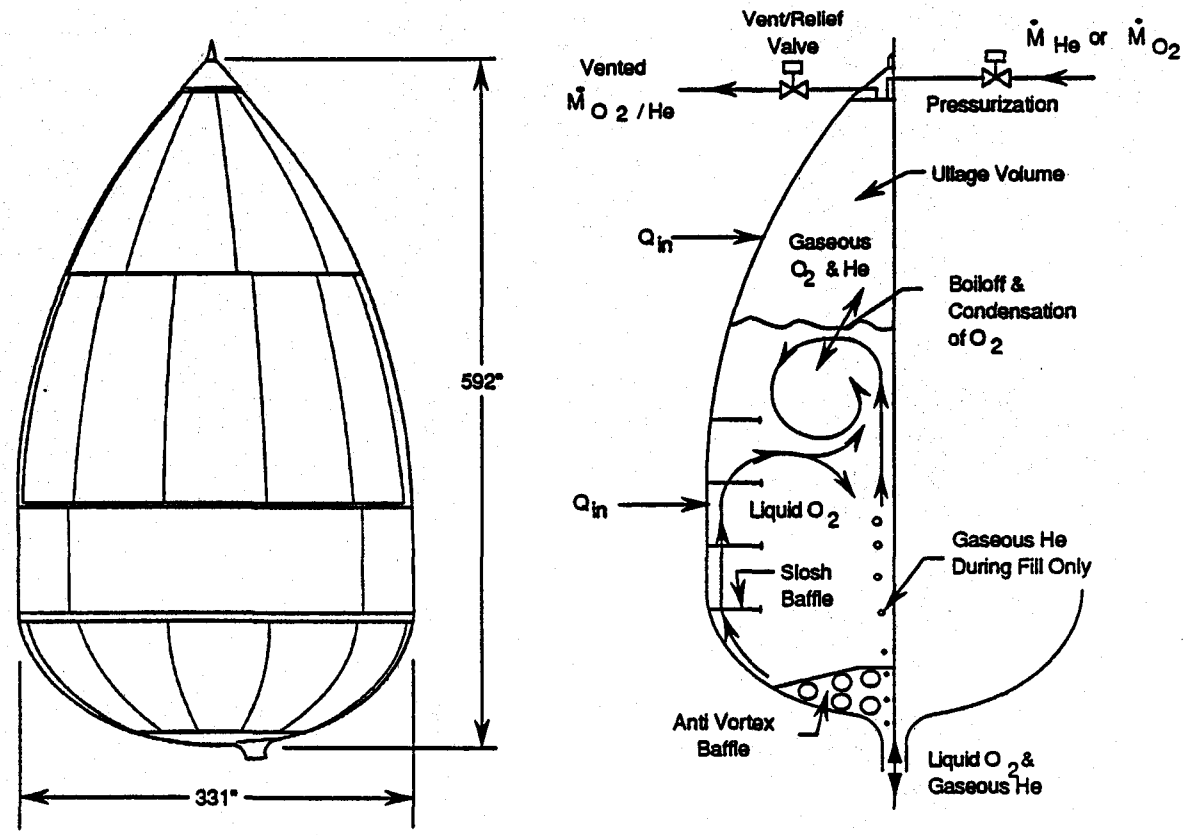

Figure 1 - Schematic of the Space Shuttle's External Liquid Oxygen Tank

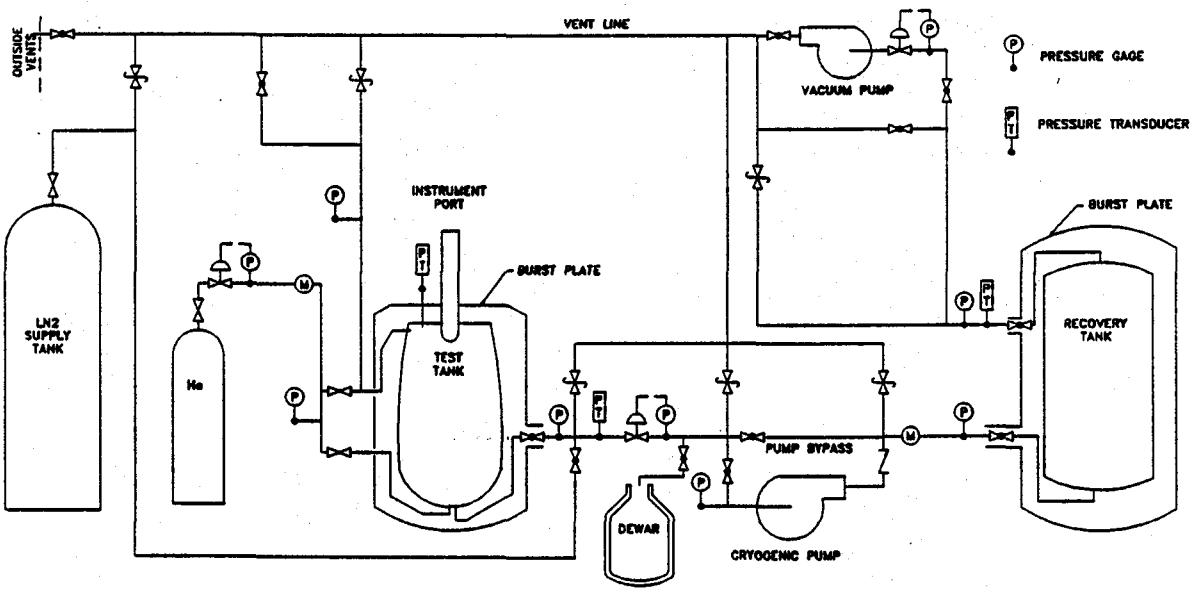

Figure 2 - Flow Diagram for the Experimental Setup

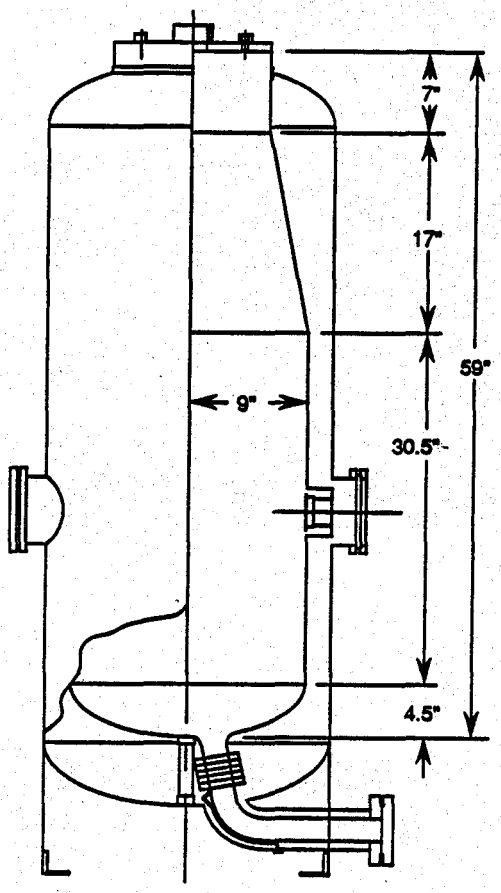

Figure 3 - Schematic Diagram of the Test Tank

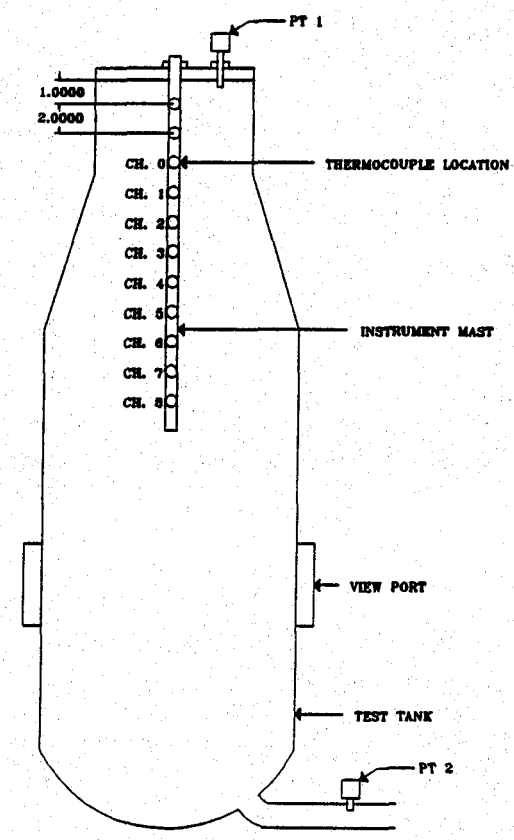

Figure 4 - Instrumentation on the Model Tank

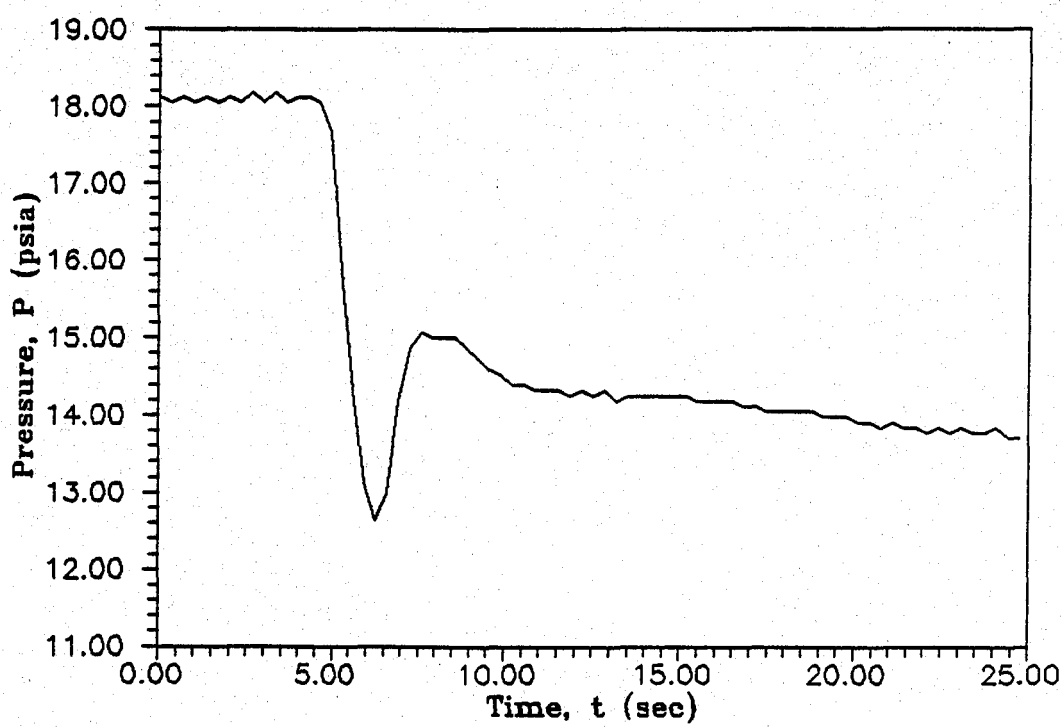

Figure 5 - Pressure Transients During Sudden Depressurization

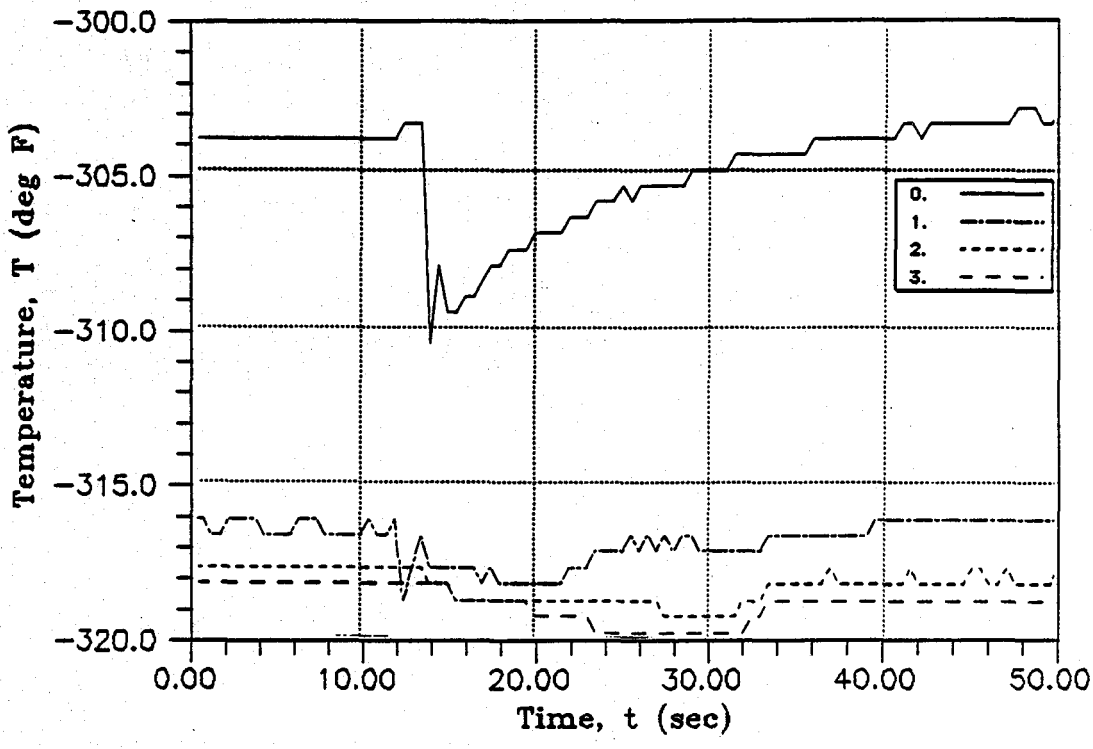

Figure 6 - Temperature Transients in Ullage During Sudden Depressurization

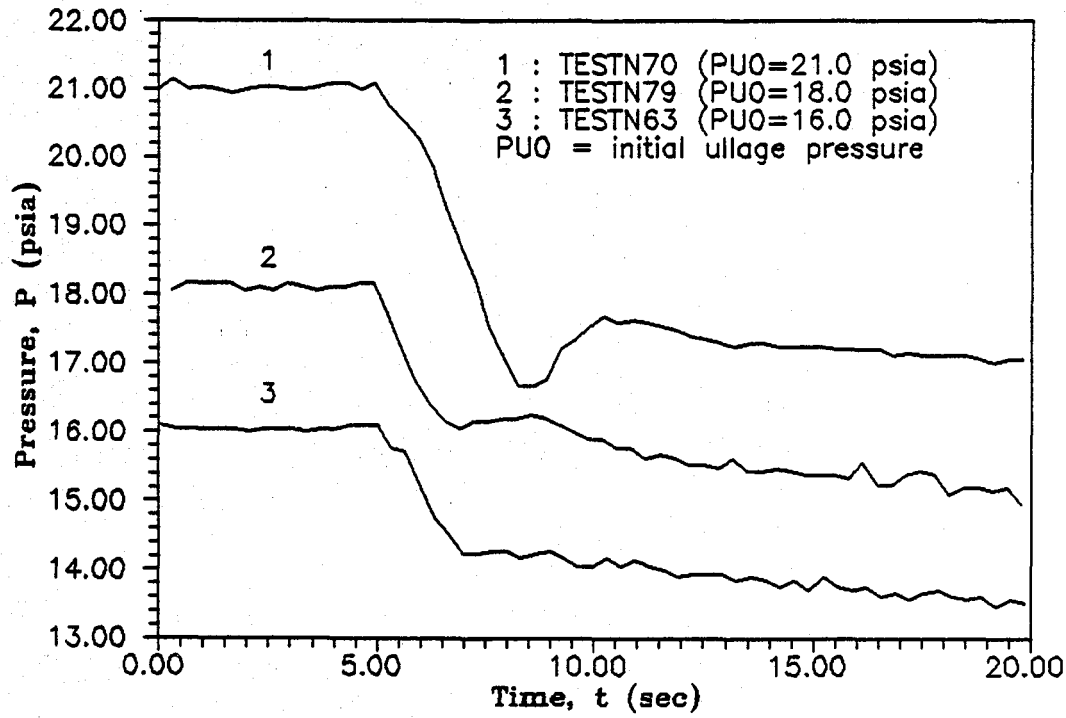

Figure 7 - Pressure Transients During Sudden Depressurization for Different Initial Ullage Pressure

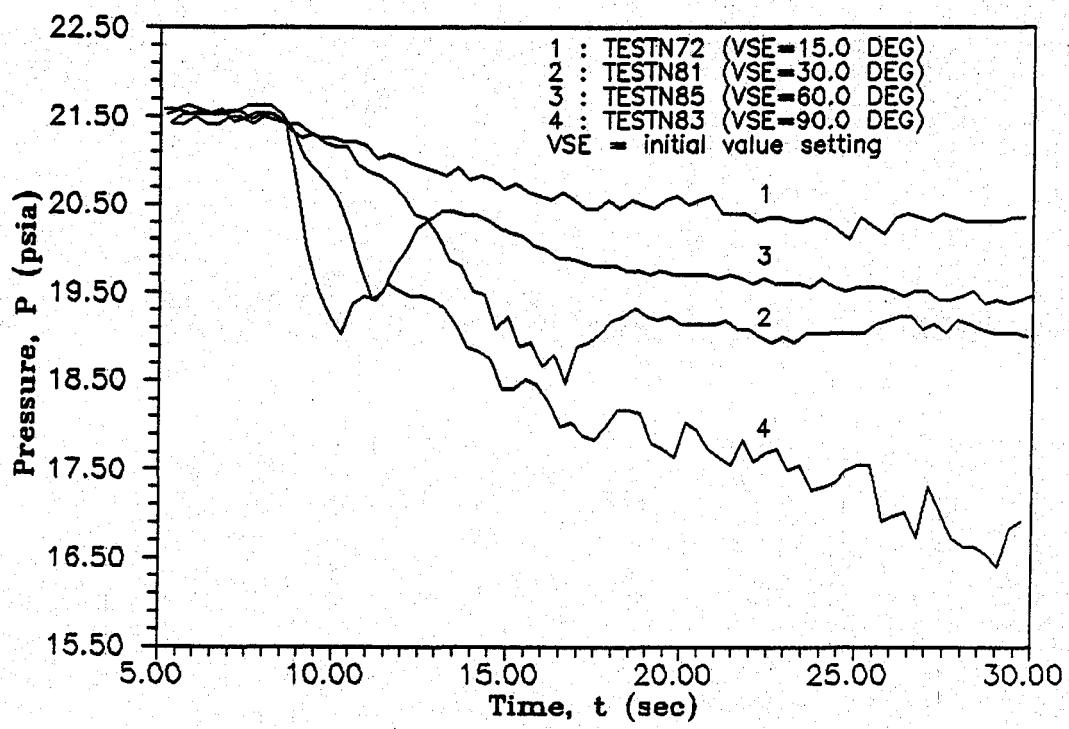

Figure 8 - Pressure Transients During Sudden Depressurization for Different Discharge Rate

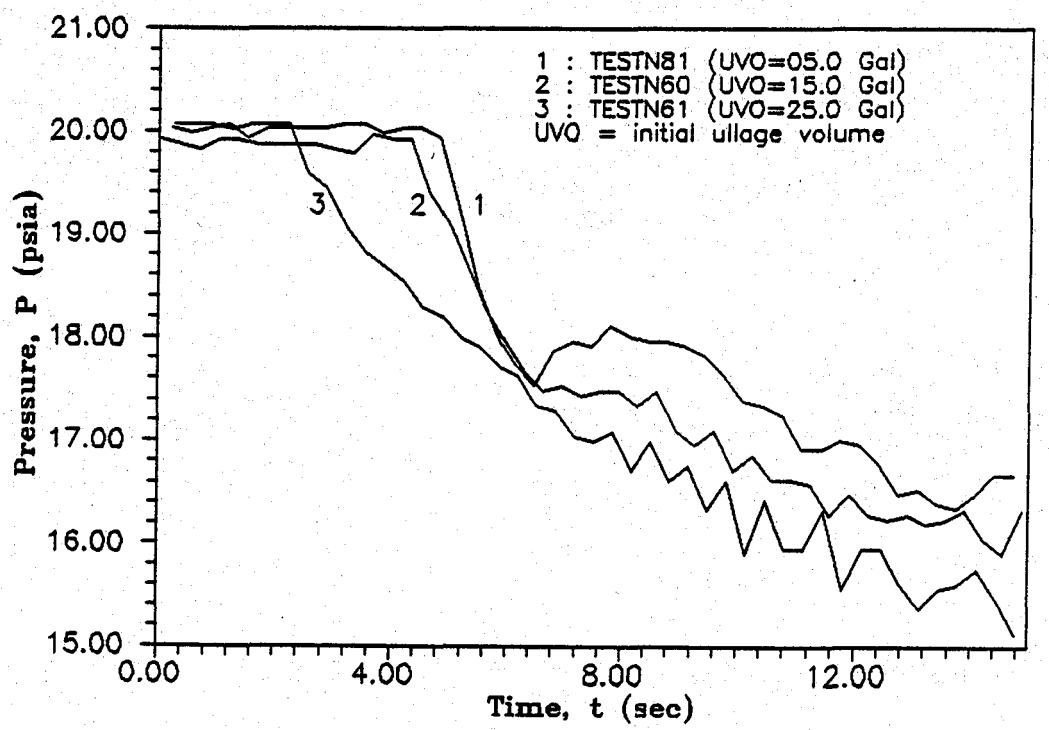

Figure 9 - Pressure Transients During Sudden Depressurization Different Initial Ullage Volume

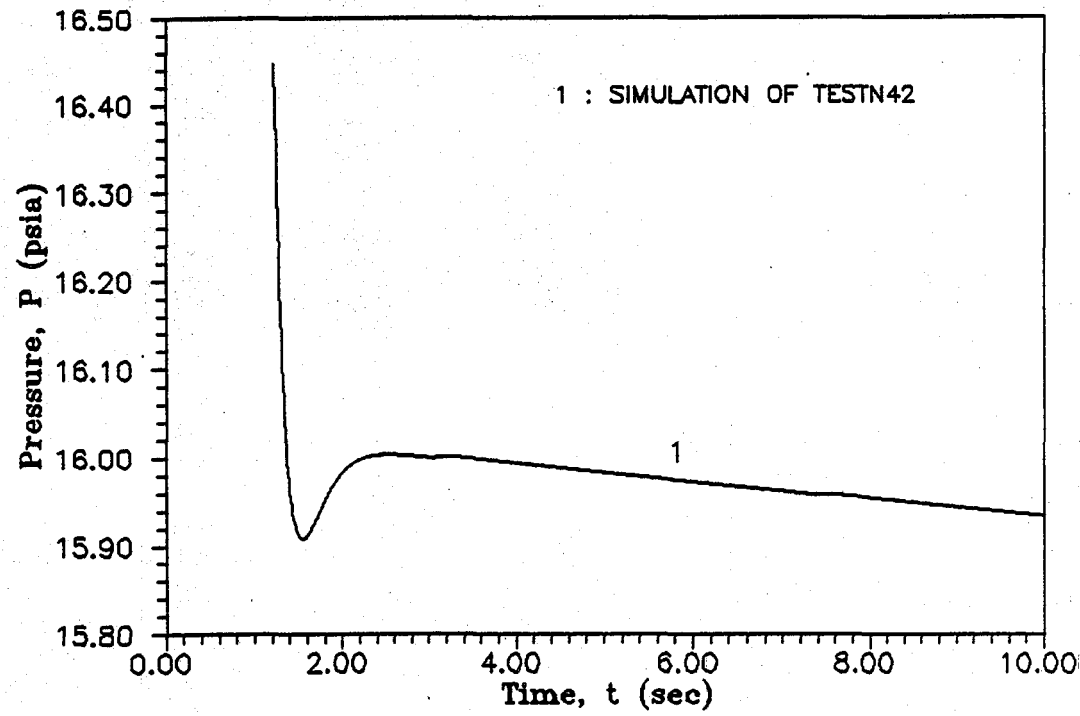

Figure 10 - Numerical Simulations of Pressure Transients in Vapor

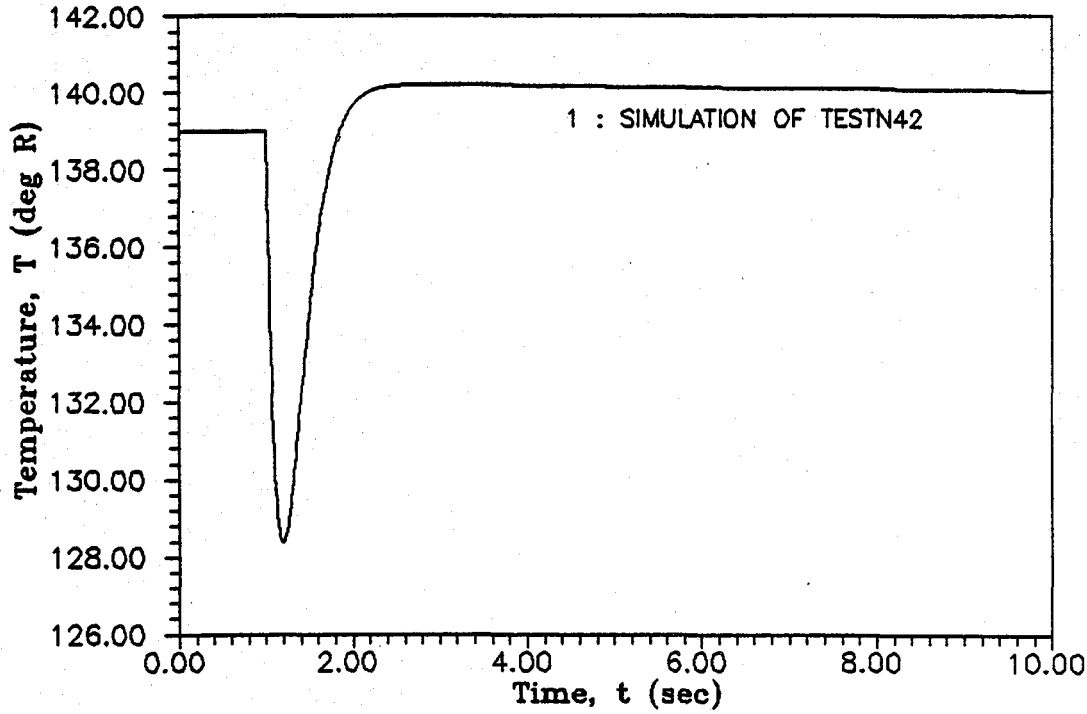

Figure 11- Numerical Simulation of the Temperature Transients in Vapor

3-D CFD MODELING OF GAS TURBINE COMBUSTOR-INTEGRAL BLEED FLOW INTERACTION

D. Y. Chen

and

R. S. Reynolds

AlliedSignal Engines
P.O. Box 52180
Phoenix, AZ 85072-2180

ABSTRACT

An advanced 3-D Computational Fluid Dynamics (CFD) model was developed to analyze the flow interaction between a gas turbine combustor and an integral bleed plenum. In this model, the elliptic governing equations of continuity, momentum and the k-e turbulence model were solved on a boundary-fitted, curvilinear, orthogonal grid system. The model was first validated against test data from public literature and then applied to a gas turbine combustor with integral bleed. The model predictions agreed well with data from combustor rig testing. The model predictions also indicated strong flow interaction between the combustor and the integral bleed. Integral bleed flow distribution was found to have a great effect on the pressure distribution around the gas turbine combustor.

INTRODUCTION

The onboard gas turbine auxiliary power unit (APU) generally is designed to deliver bleed air either from a basic APU or from a separate compressor. The bleed air supplied by the APU normally is used for starting the main engines and operating the air-cycle air conditioning and pressurization system. On the direct-bleed APU (also called integral-bleed APU), bleed air is extracted from a point between the compressor and combustor, as shown in Figure 1, and is routed to the airplane pneumatic system via a bleed valve attached to a port on the turbine plenum.

The bleed air extraction from the turbine plenum has long been recognized among APU combustor designers to have a significant effect on combustor performance. However, knowledge in this field is limited and has been acquired only as a result of rig or engine testings. No theoretical modeling has been conducted and reported in the literature. The purpose of this study is to do a comprehensive theoretical investigation into the flow interaction between a gas turbine combustor and an integral bleed plenum. Findings from this study should prove useful in the design and development of a gas turbine combustor with integral bleed.

The flow interaction between a gas turbine combustor and an integral bleed is fully three-dimensional and extremely complicated. To do 3-D Computational Fluid Dynamics (CFD) modeling of this complex flow interaction using a cylindrical grid system requires a huge number of grid nodes and complex treatment of wall boundary conditions. Recently, a large variety of numerical grid generation methods [1] have been developed to simplify wall boundary condition treatment for any complex flow geometry. These methods can generate either orthogonal or non-orthogonal boundary-fitted grid systems for any complex flow geometry. In this study, a boundary-fitted, curvilinear, orthogonal grid system is used for the two-dimensional (x,y) plane and the angular (z)

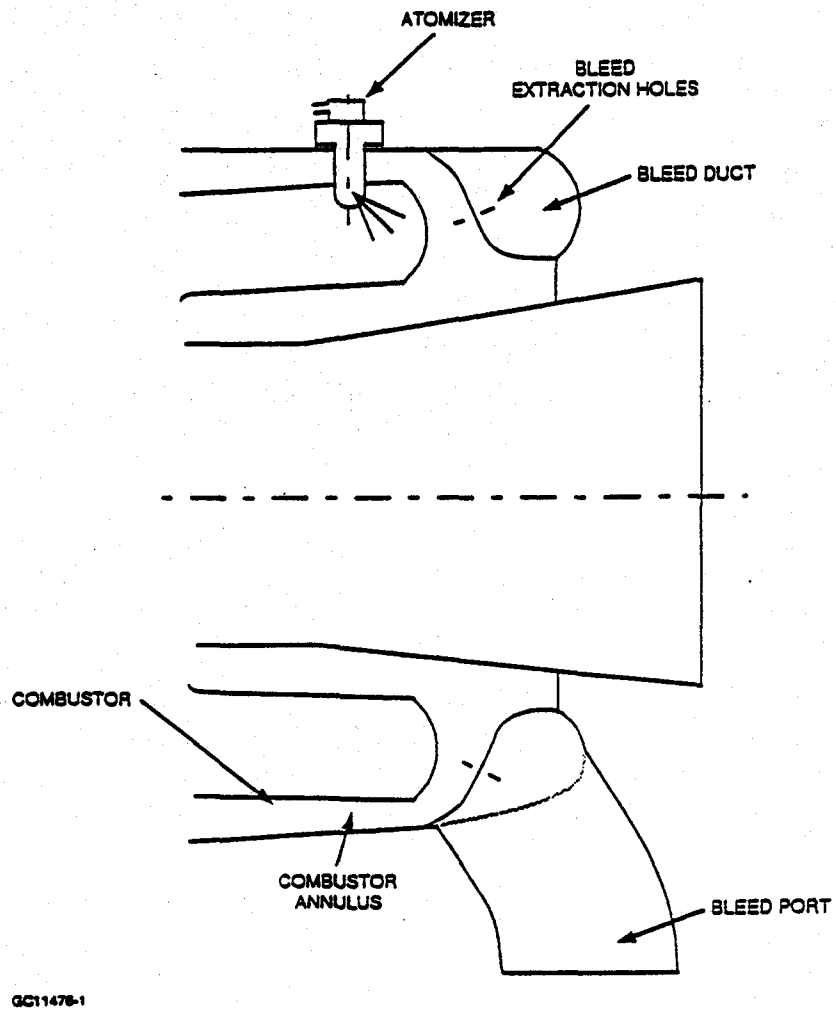

Figure 1. A Typical Gas Turbine Combustor with Integral Bleed.

dimension is considered as a body of revolution. The choice of a curvilinear orthogonal grid system in the present flow modeling is motivated by easier wall boundary condition treatment, inclusion of most of the grid nodes in the computational domain, and no extra terms of cross-derivative appearing in the transformed governing equations.

ORTHOGONAL GRID GENERATION

As mentioned above, the flow geometry of a gas turbine combustor with integral bleed is quite complex for 3-D CFD modeling. A boundary-fitted, curvilinear, orthogonal grid system is therefore used here. The orthogonal grid system used in this study was obtained numerically based on the following 2-D orthogonal grid generation model:

Governing Equations:

$$\xi_{xx} + \xi_{yy} = P \qquad (1)$$

$$\eta_{xx} + \eta_{yy} = Q \qquad (2)$$

Boundary Conditions:

$$BC1: \quad \xi_x\eta_x + \xi_y\eta_y = 0; \quad F_1(\xi,\eta) = 0 \qquad (3)$$

$$BC2: \quad \xi_x\eta_x + \xi_y\eta_y = 0; \quad F_2(\xi,\eta) = 0 \qquad (4)$$

$$BC3: \quad \xi_x\eta_x + \xi_y\eta_y = 0; \quad F_3(\xi,\eta) = 0 \qquad (5)$$

$$BC4: \quad \xi_x\eta_x + \xi_y\eta_y = 0; \quad F_4(\xi,\eta) = 0 \qquad (6)$$

where (x,y) are the Cartesian coordinates of the grid points in the physical plane, as shown in Figure 2, and (ξ,η) are the coordinates of the corresponding grid points in the transformed plane. The control functions P and Q in equations (1) and (2) are used to concentrate grid lines as desired. The function F denotes user-specified boundary curves. In order to facilitate numerical solution for the above equations (1) to (6), they were transformed into the following equations:

Governing Equations:

$$\alpha x_{\xi\xi} - 2\beta x_{\xi\eta} + \gamma x_{\eta\eta} = -J^2(x_\xi P + x_\eta Q) \qquad (1a)$$

$$\alpha y_{\xi\xi} - 2\beta y_{\xi\eta} + \gamma y_{\eta\eta} = -J^2(y_\xi P + y_\eta Q) \qquad (2a)$$

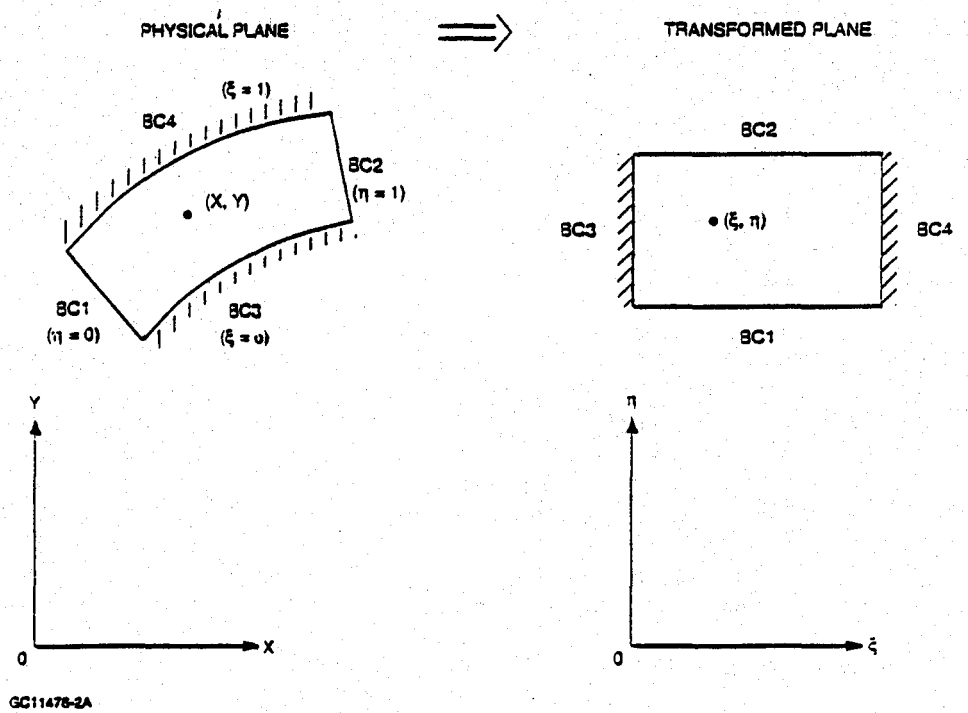

Figure 2. Coordinate Transformation.

where

$$\alpha = (x_\eta^2 + y_\eta^2)$$

$$\beta = (x_\xi x_\eta + y_\xi y_\eta)$$

$$\gamma = (x_\xi^2 + y_\xi^2)$$

$$J = x_\xi y_\eta - x_\eta y_\xi$$

Boundary Conditions:

$$BC1: \; x_\xi x_\eta + y_\xi y_\eta = 0 \; ; \; G_1(x,y) = 0 \qquad (3a)$$

$$BC2: \; x_\xi x_\eta + y_\xi y_\eta = 0 \; ; \; G_2(x,y) = 0 \qquad (4a)$$

$$BC3: \; x_\xi x_\eta + y_\xi y_\eta = 0 \; ; \; G_3(x,y) = 0 \qquad (5a)$$

$$BC4: \; x_\xi x_\eta + y_\xi y_\eta = 0 \; ; \; G_4(x,y) = 0 \qquad (6a)$$

These transformed equations are solved numerically using a finite difference technique. This grid generation model only generates a boundary-fitted, curvilinear, orthogonal grid system in two dimensions. The present flow calculation requires a 3-D orthogonal grid system, obtained by rotating this 2-D orthogonal grid system about an axis in the same plane. Using this approach, a typical 3-D grid system for the combustor with integral bleed flow calculation is shown in Figure 3.

MATHEMATICAL MODEL

The transport equations for a 3-D incompressible turbulent flow can be written as

$$\frac{\partial}{\partial x}(\rho u\phi - \Gamma\frac{\partial\phi}{\partial x}) + \frac{\partial}{\partial y}(\rho v\phi - \Gamma\frac{\partial\phi}{\partial y}) + \frac{\partial}{\partial z}(\rho w\phi - \Gamma\frac{\partial\phi}{\partial z}) = S_\phi$$

where ϕ represents a general variable, ρ is density, U, V, and W are velocities, Γ is effective turbulent diffusivity, and S_ϕ is the source term for variable ϕ .

The above transport equations are given in Cartesian coordinates (x,y,z). Prior to their numerical solution, these equations are transformed into general orthogonal coordinates (ξ, η, ζ). The resulting transport equations are expressed as follows:

$$\frac{\partial}{\partial\xi}(h_2h_3(\rho u\phi - \frac{\Gamma}{h_1}\frac{\partial\phi}{\partial\xi})) + \frac{\partial}{\partial\eta}(h_3h_1(\rho v\phi - \frac{\Gamma}{h_2}\frac{\partial\phi}{\partial\eta})) + \frac{\partial}{\partial\zeta}(h_1h_2(\rho w\phi - \frac{\Gamma}{h_3}\frac{\partial\phi}{\partial\zeta})) = h_1h_2h_3S_\phi$$

where h represents scalar coefficients.

In order to solve the above partial differential equations governing the flow of fluid through a combustor annulus with integral bleed, boundary conditions must be specified at the appropriate locations. In the present study, the boundary conditions at the annulus inlet and the bleed duct exit are

provided from the engine cycle analysis, while the airflow through the various orifices in the combustor, as shown in Table 1, are calculated using a 1-D annulus flow model.

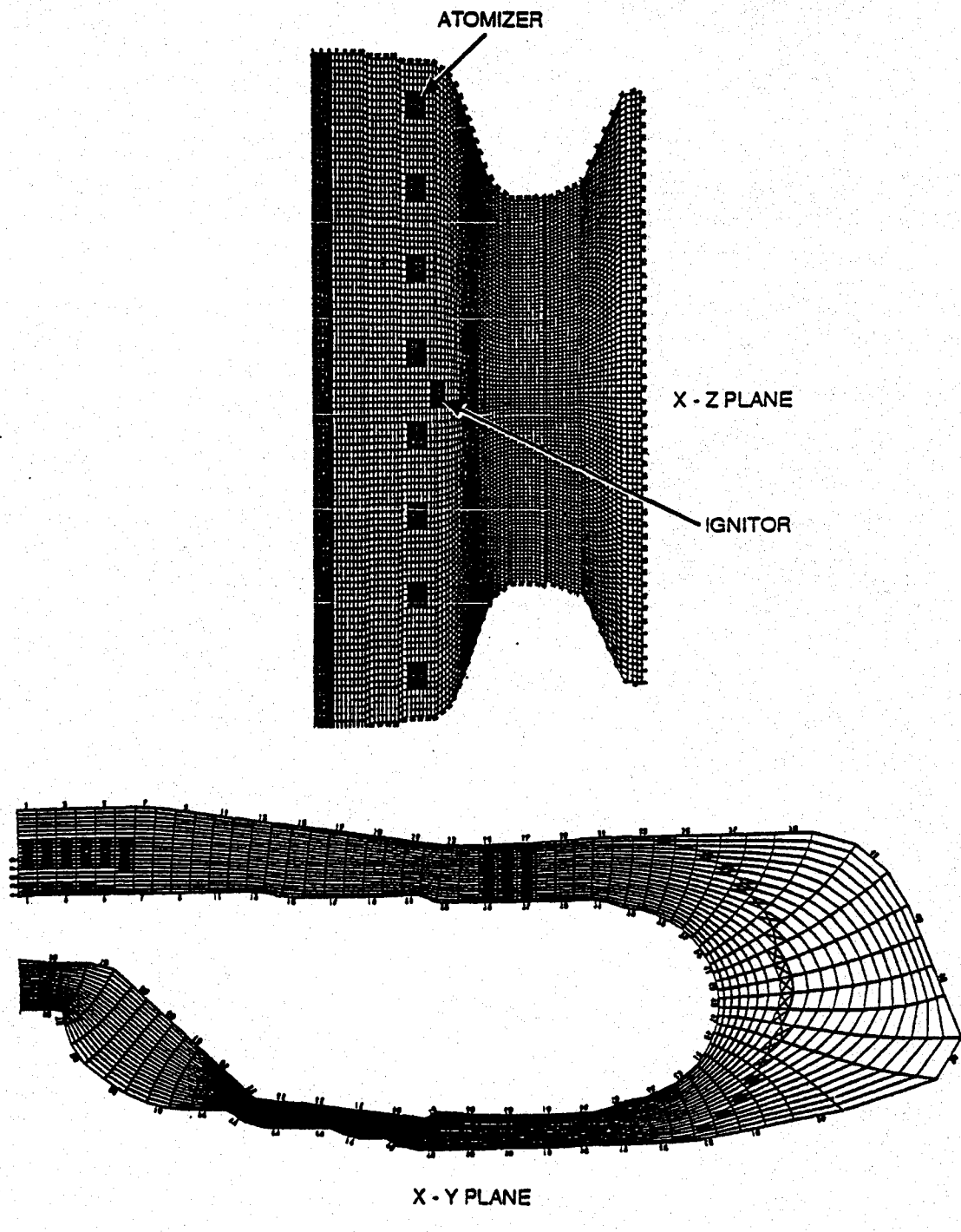

Figure 3. A Typical Orthogonal Grid System for the Combustor with Integral Bleed Flow Calculation.

TABLE 1. AIRFLOW DISTRIBUTIONS AROUND THE COMBUSTOR

	OD	ID
Primary Holes	4.28	9.90
Dilution Holes	5.59	5.69
Film Cooling	10.90	7.15
Dome Cooling	11.21	-.-
Bleed	42.01	-.-
Shroud Air	1.10	-.-
Leakage	1.28	0.89
Total	**76.37%**	**23.63%**

The solution of the curvilinear transport equations is accomplished using a finite volume, structured grid, sequential solution, numerical method. The differential equations are integrated over discrete volumes in the domain of interest using assumptions of linear and stepped profiles to obtain their numerical counterparts. Interaction between the convective and diffusive terms is handled numerically using Upwind Hybrid Differencing [2], while the coupling between the continuity and momentum equations is treated by the SIMPLER algorithm [3] and the turbulence closure is accomplished by the standard k-e model. At each iteration step, the set of linear equations is solved using the Whole Field Solver (WFS) routine of Przekwas [4]. The WFS has proven to be very efficient as it is formulated for structured grids and cyclic boundary conditions which are used in this analysis.

The use of orthogonal coordinate systems adds effort to the grid generation process, as numerical equations must be solved to determine the position of the coordinates in the physical space. It is also frequently the case that the shape of the domain is such that a completely orthogonal grid system cannot be generated and a certain amount of deviation from orthogonality must be tolerated. However, the benefits of this extra work are realized when the flow equations are solved. The terms associated with grid non-orthogonality are usually treated in an explicit manner and in situations of skewed control volumes, can be the same order of magnitude as the normal implicit convection and diffusion terms. As a result, convergence can be hindered. Orthogonal grids create a more implicit nature to the numerical equations and have inherently better convergence rates.

The combination of the SIMPLER algorithm and the orthogonal grid structure has proven to be extremely robust. In all but a very few situations, relaxation factors of 0.5 are used on all equations (except for pressure and the velocity correction which require 1.0 relaxation factors). Converged solutions using up to 400,000 cells have been obtained in the order of 750 iterations. At convergence, the sum of the absolute continuity error of all the control volumes, normalized by the total system flow rate, is less than 0.1 percent.

NUMERICAL RESULTS

The predictions of the CFD model used in this study have been compared to numerous sets of experimental data found in the literature. In order to illustrate the predictive capability of the code, two such cases have been included below, both of which are 2-D flows. For these situations, the 3-D code was run with three circumferential planes.

The first case is from the experiment of Roback and Johnson [5] and consists of two coaxial flowing water jets that discharge into a confined region (illustrated in Figure 4). The inner jets are swirling while the outer are not. Velocity data was taken at several axial stations downstream of the jet discharge. Figure 5 shows the comparison of the predicted and measured axial, radial, and tangential velocity components respectively. The comparison is as good as should be expected considering the well known deficiencies of the k-e model for swirling flow and the uncertainty in the boundary conditions of the data.

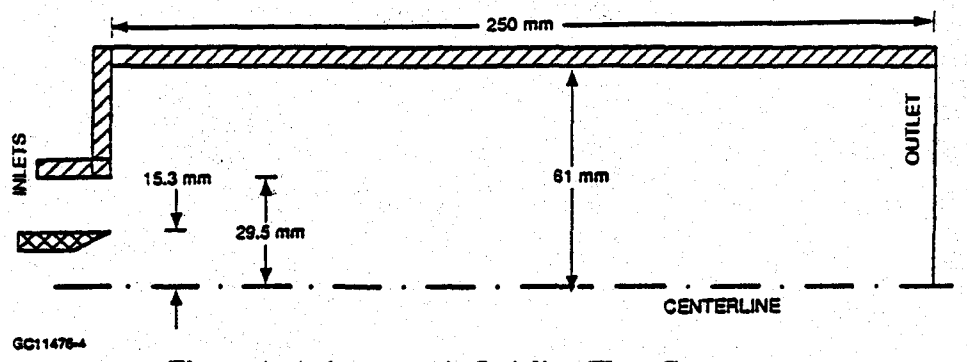

Figure 4. Axisymmetric Swirling Flow Geometry.

The second case described is that of Sovran and Klomp [6] and consists of a 6-degree wall annular diffuser with an area ratio of 1.955. The computed static pressure contours (Pascals) are shown in Figure 6. The experimental data for this case consist of the static pressure recovery coefficient, Cp. For the configuration analyzed, the measured Cp was 0.6 which should be compared to the value of 0.643 (7 percent high) calculated from the CFD model output, indicating resonable accuracy in the pressure calculation methods used in the code.

After validation of the 3-D CFD model using experimental data found in the literature, the present model was then used to simulate complex external flow of a gas turbine combustor with integral bleed. The computed results using a grid system of 91x21x97 nodes, as shown in Figure 3, are discussed in the following:

Figure 7 shows the predicted U-V velocity field at K-planes 1, 38, and 59. The predicted results illustrate a strong recirculation zone formed near the annulus inlet. The formation of this recirculation zone is due to the presence of a backward-facing step in the flow path. This recirculation zone has caused pressure loss near the combustor O.D. dilution holes. As a result, the dilution jet penetration will be reduced because of less pressure drop across dilution holes. Based on gas turbine combustor design experiences, inadequate dilution jet penetration usually cannot break up the hot gas regions efficiently and will result in high pattern factor at the combustor exit.

The predicted results, as shown in Figure 7, also illustrate non-uniform bleed air extraction from the turbine plenum. The bleed air extraction at K-plane 59, which is closer to bleed port (K-planes 61-65), is higher than that at K-plane 38. The non-uniform bleed air extraction indicates that the present integral bleed design has not been optimized and has caused some flow separations in the annulus. It is also interesting to note that bleed air enters the bleed duct like an impinged jet and creates a vortex pair in the duct.

Figure 8 shows the predicted U-W velocity field on the unwrapped surface of combustor liner. The predicted results indicate that a forward stagnation point, where the air is brought to rest with an accompanying rise in pressure, was formed upstream of a fuel atomizer or an ignitor. The predicted results also indicate that a strong wake was formed downstream of a fuel atomizer or an ignitor.

The presence of eight fuel atomizers and one ignitor has a profound effect on pressure distributions around the combustor liner. This can be seen in Figure 9, where the predicted static pressure distributions around the combustor liner is plotted using color graphics. In this figure, each fuel atomizer was found to be associated with a high pressure region upstream and a low pressure region downstream. The same pattern was observed for the ignitor. Figure 9 also shows non-uniform bleed extraction has a great effect on pressure distribution around the combustor liner. This is illustrated by results of non-uniform pressure distribution on the dome. Based on gas turbine combustor design experience, non-uniform pressure distribution around the combustor liner usually causes non-uniform airflow distribution and will result in hot and cold spots at the combustor exit.

Figure 10 shows the predicted static pressure distributions around the turbine plenum. The predicted results further illustrate that the presence of eight fuel atomizers and one ignitor has a

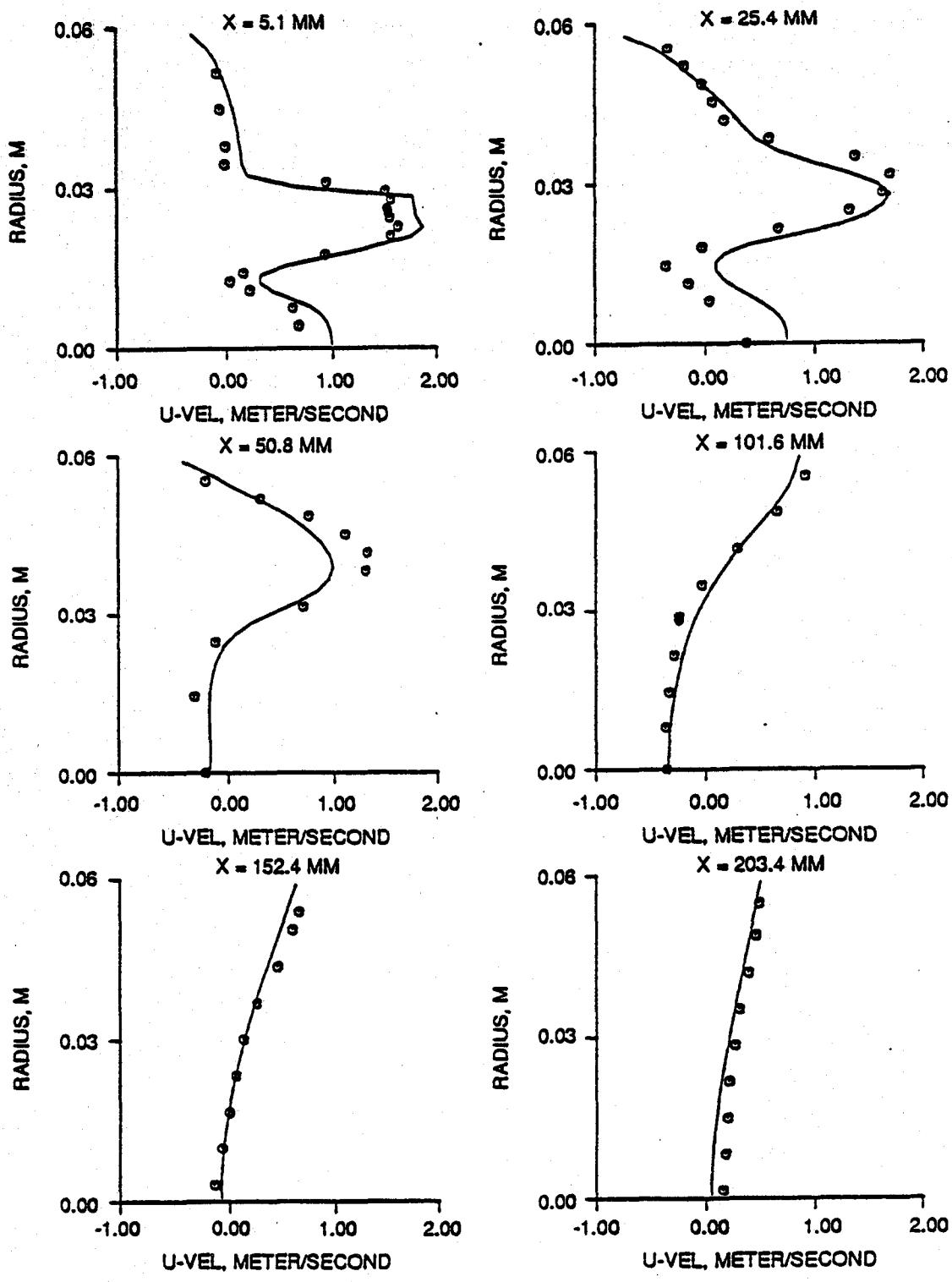

Figure 5a. Comparison of Predictions and Measurements of Velocity Distributions for Confined Coaxial Jets.

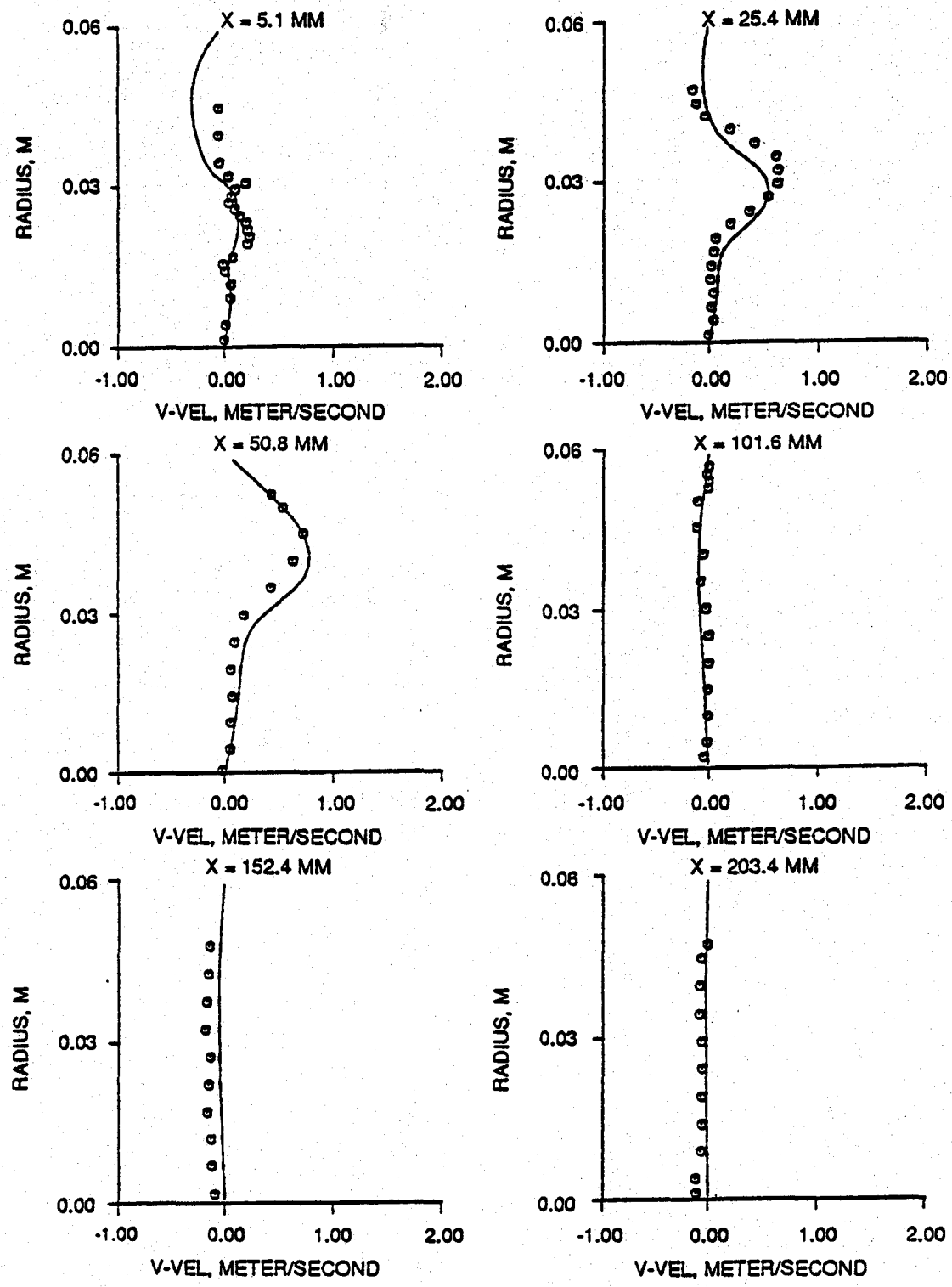

Figure 5b. Comparison of Predictions and Measurements of Velocity Distributions for Confined Coaxial Jets.

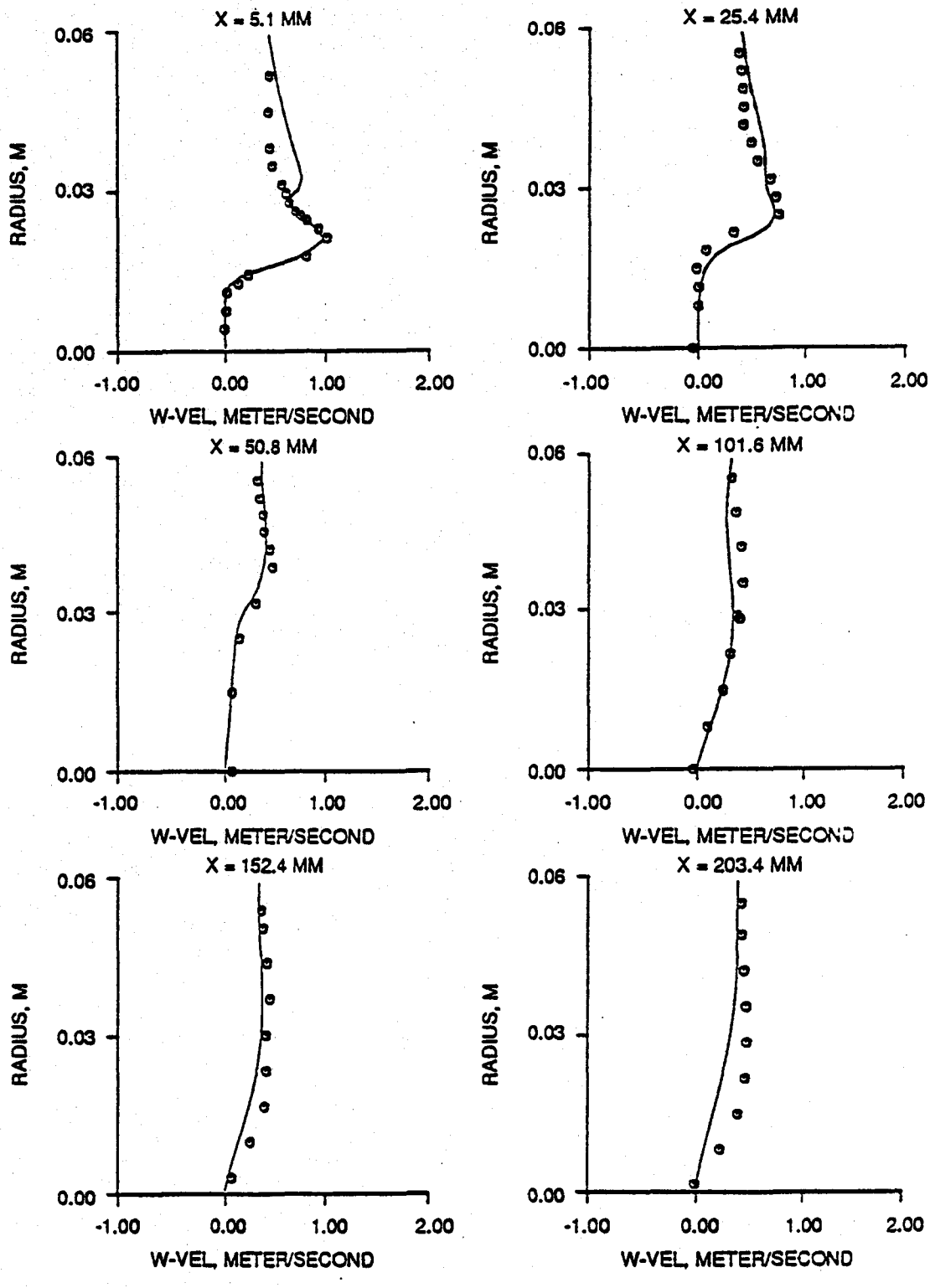

Figure 5c. Comparison of Predictions and Measurements of Velocity Distributions for Confined Coaxial Jets.

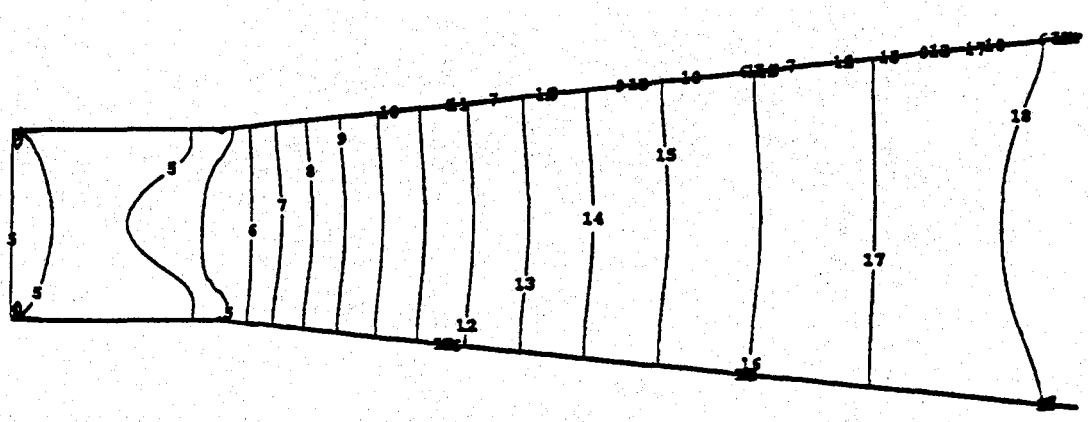

CONTOUR VALUE

1	-1200.0	11	1800.0
2	-900.0	12	2100.0
3	-600.0	13	2400.0
4	-300.0	14	2700.0
5	0.0	15	3000.0
6	300.0	16	3300.0
7	600.0	17	3600.0
8	900.0	18	3900.0
9	1200.0	19	4200.0
10	1500.0		

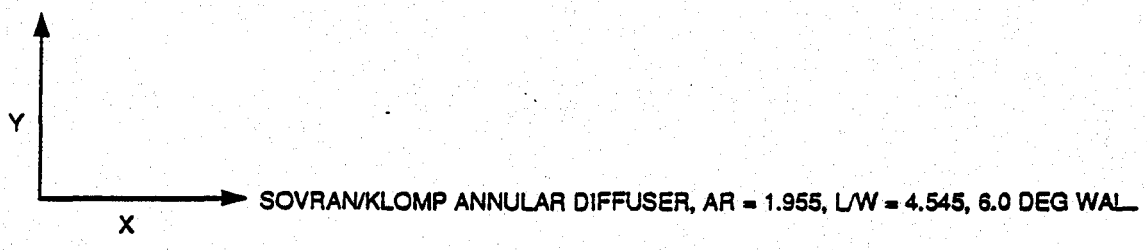

GC11476-6

Figure 6. Pressure Contours for Annular Diffuser.

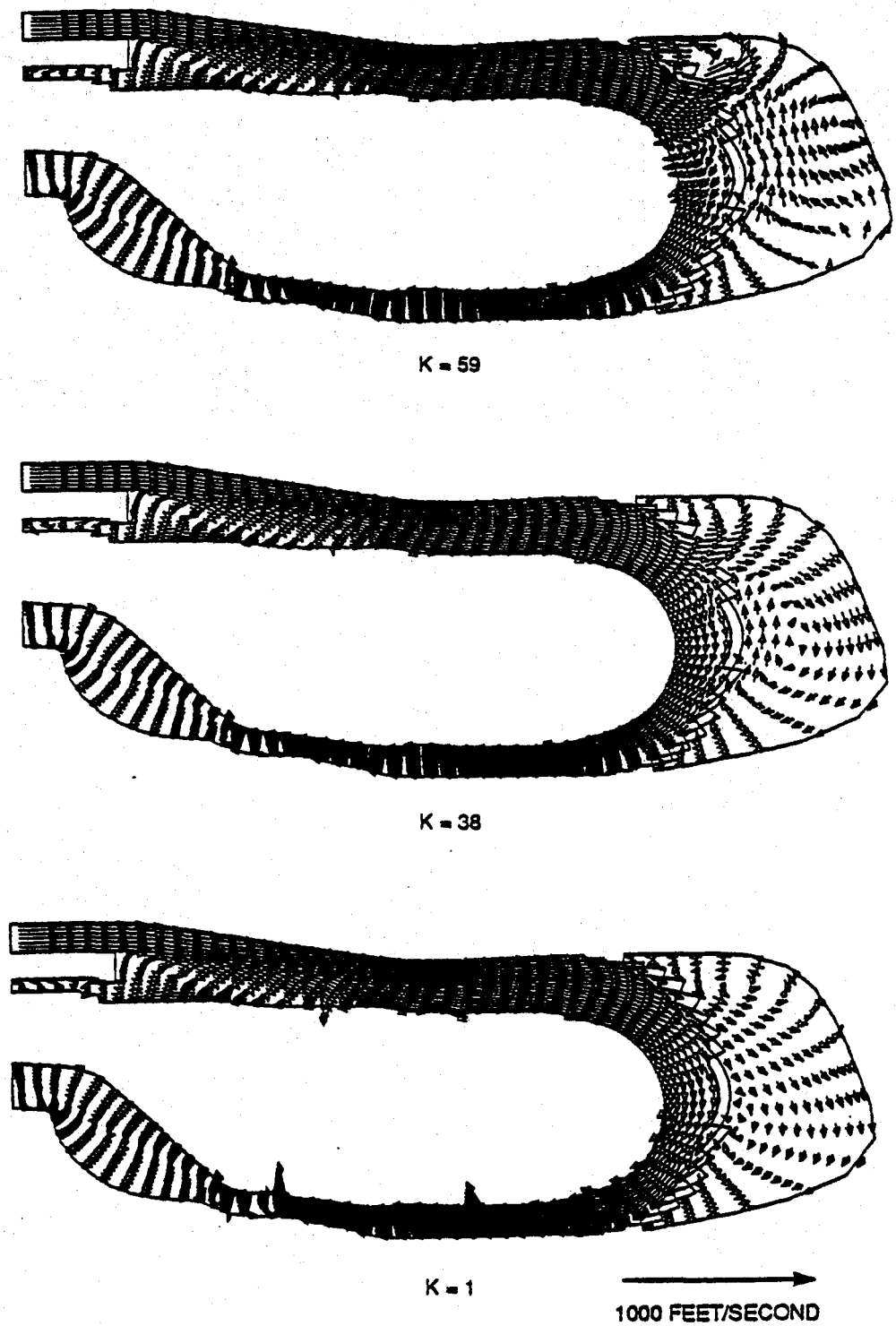

GC11476-7

Figure 7. Predicted U-V Velocity Field around Combustor.

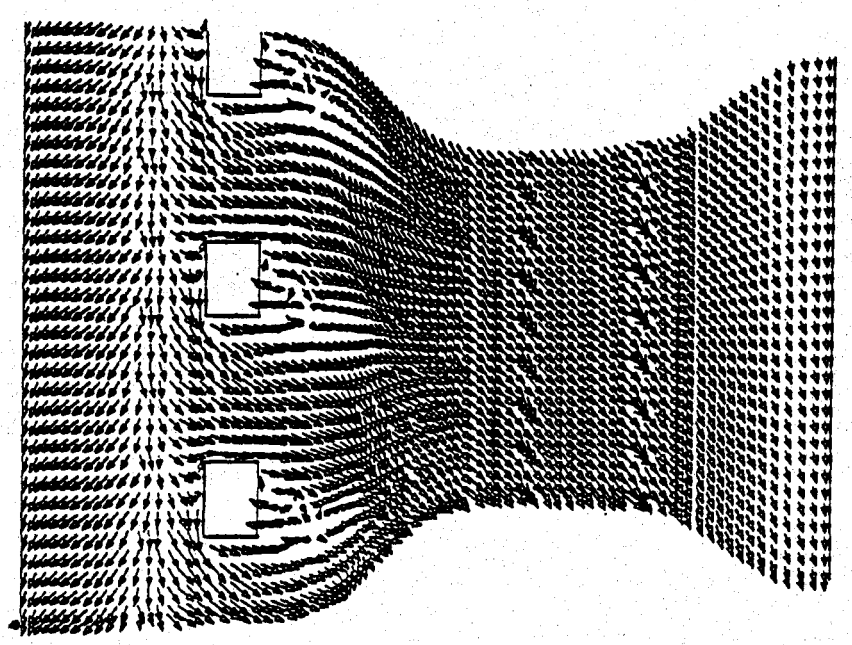

1000 FEET/SECOND

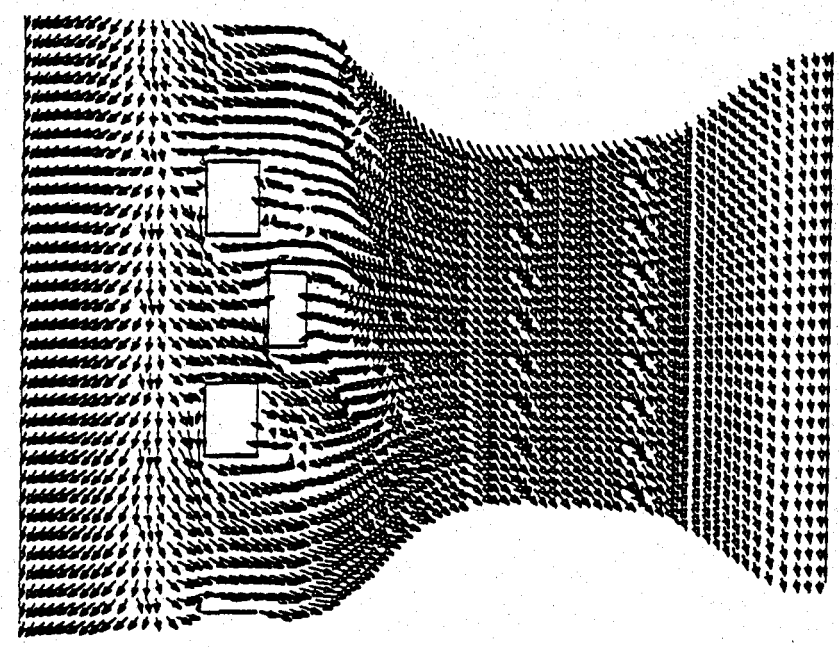

1000 FEET/SECOND

GC11476-8-1

Figure 8a,b. Predicted U-W Velocity Field around Combustor.

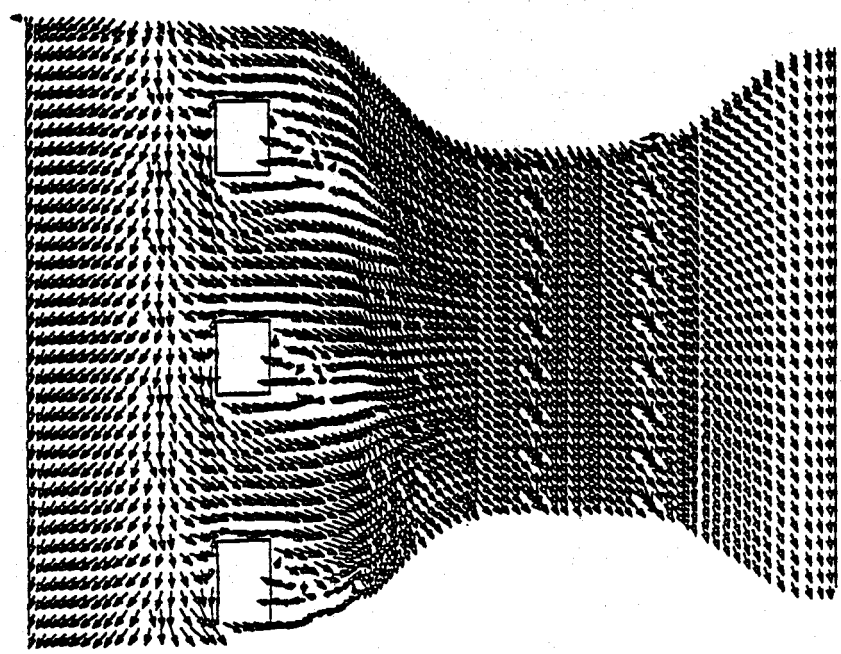

GC11476-8-2

Figure 8c. Predicted U-W Velocity Field around Combustor.

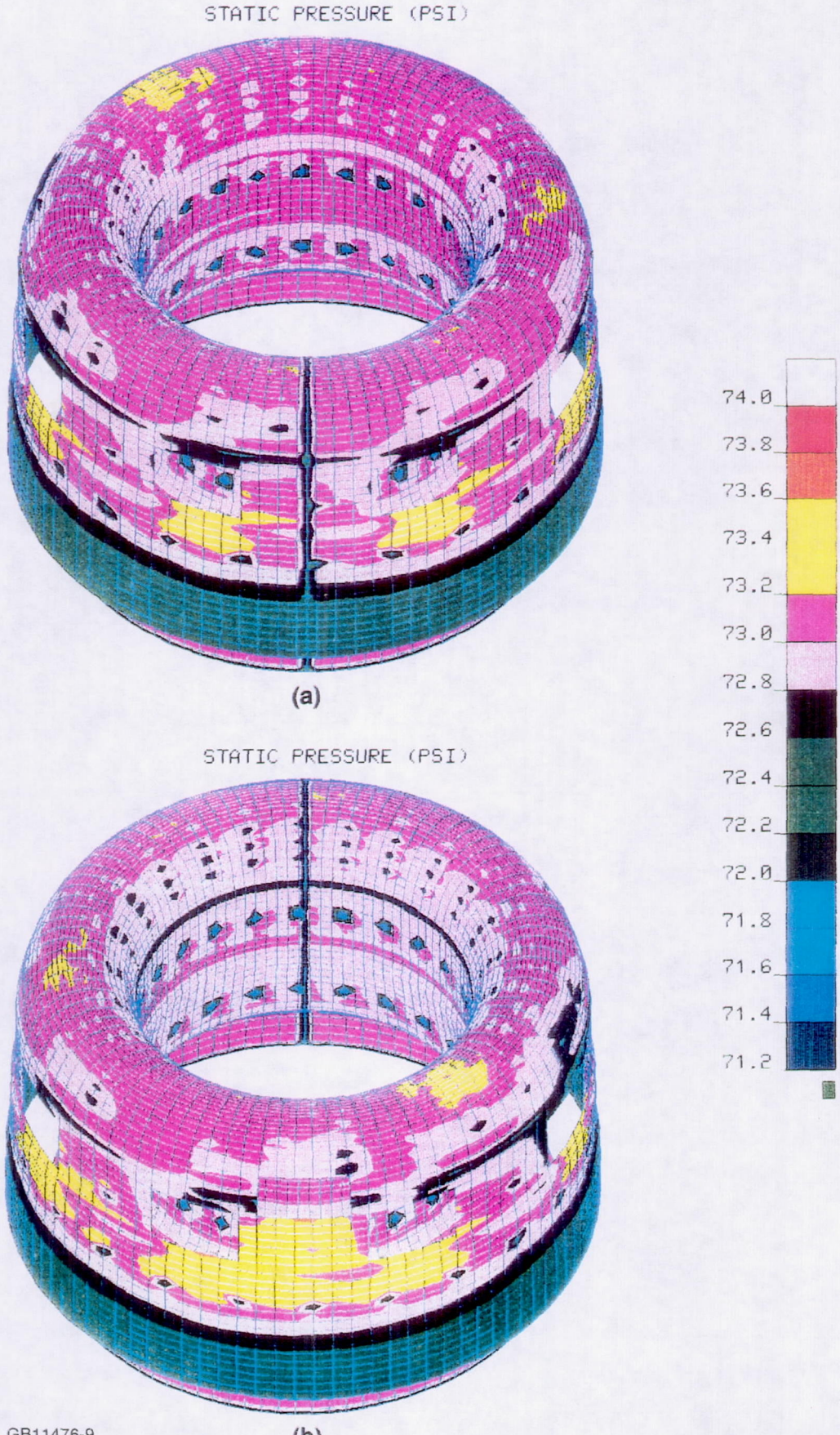

Figure 9. Predicted Pressure Distributions around Combustor.

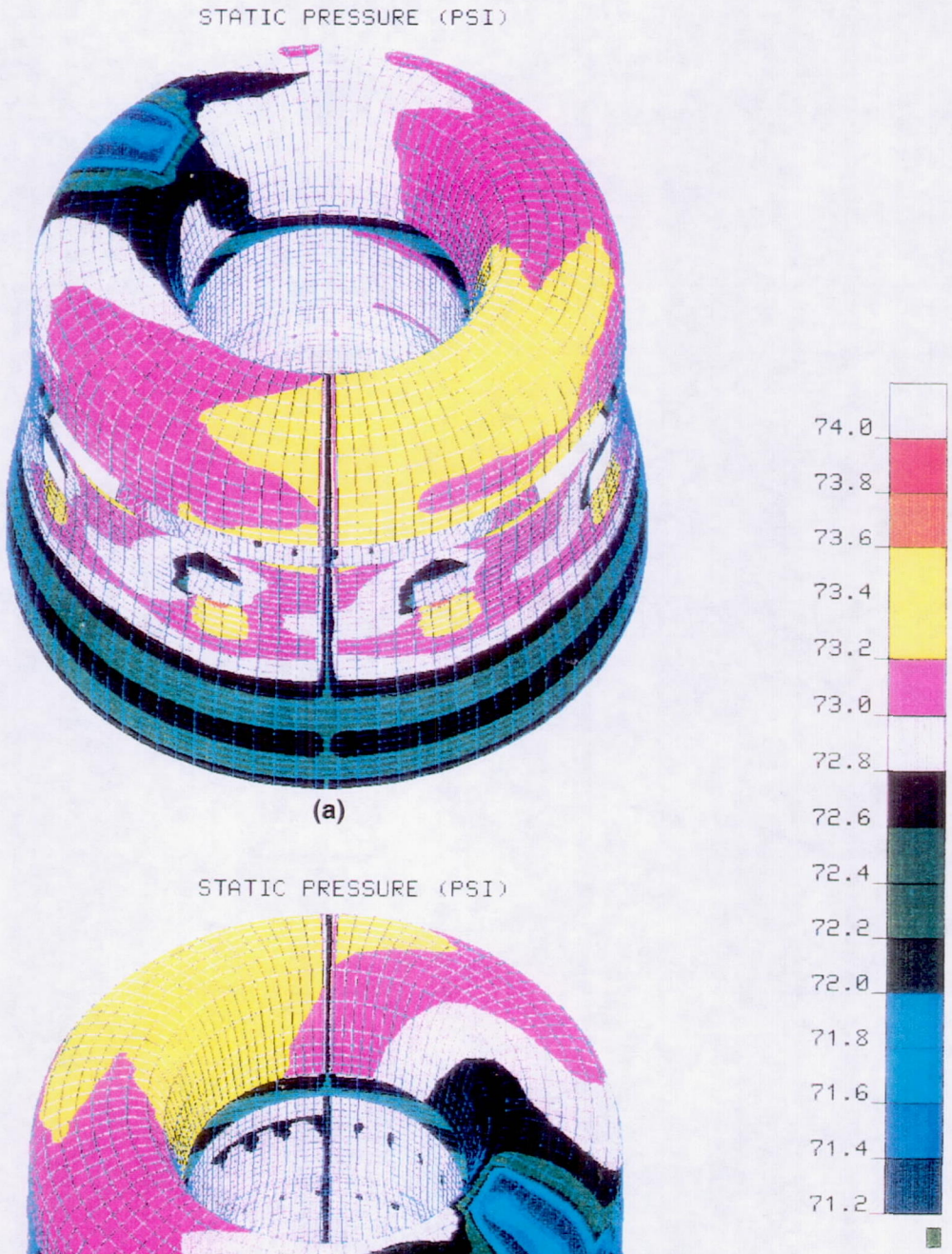

Figure 10. Predicted Pressure Distributions around Turbine Plenum.

significant effect on pressure distributions around the turbine plenum. The predicted results also show non-uniform pressure distributions on the bleed duct wall. The predicted results of non-uniform pressure distributions on the bleed duct wall (at I=43 and J=20) were compared to combustor rig test data in Figure 11. This comparison indicates model predictions agreed well with test data from combustor rig.

Having obtained good predictions of non-uniform pressure distribution on the bleed duct wall, it is then possible to consider another 3-D case run in order to study the effect of intergral bleed extraction on the pressure distributions around the combustor liner. Figures 12 and 13 show the predicted pressure distributions at various hole locations for a gas turbine combustor with and without an integral bleed. Comparison of Figures 12 and 13 confirms that integral bleed flow distribution has a great effect on the pressure distributions around the gas turbine combustor.

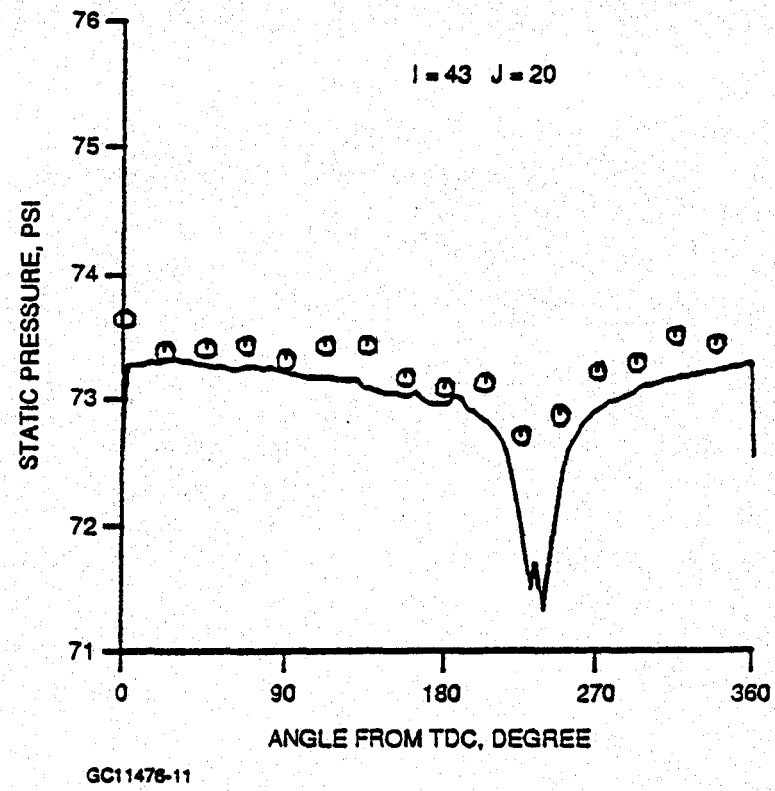

Figure 11. Comparison of Predicted and Measured Pressure Distributions on the Bleed Duct Wall.

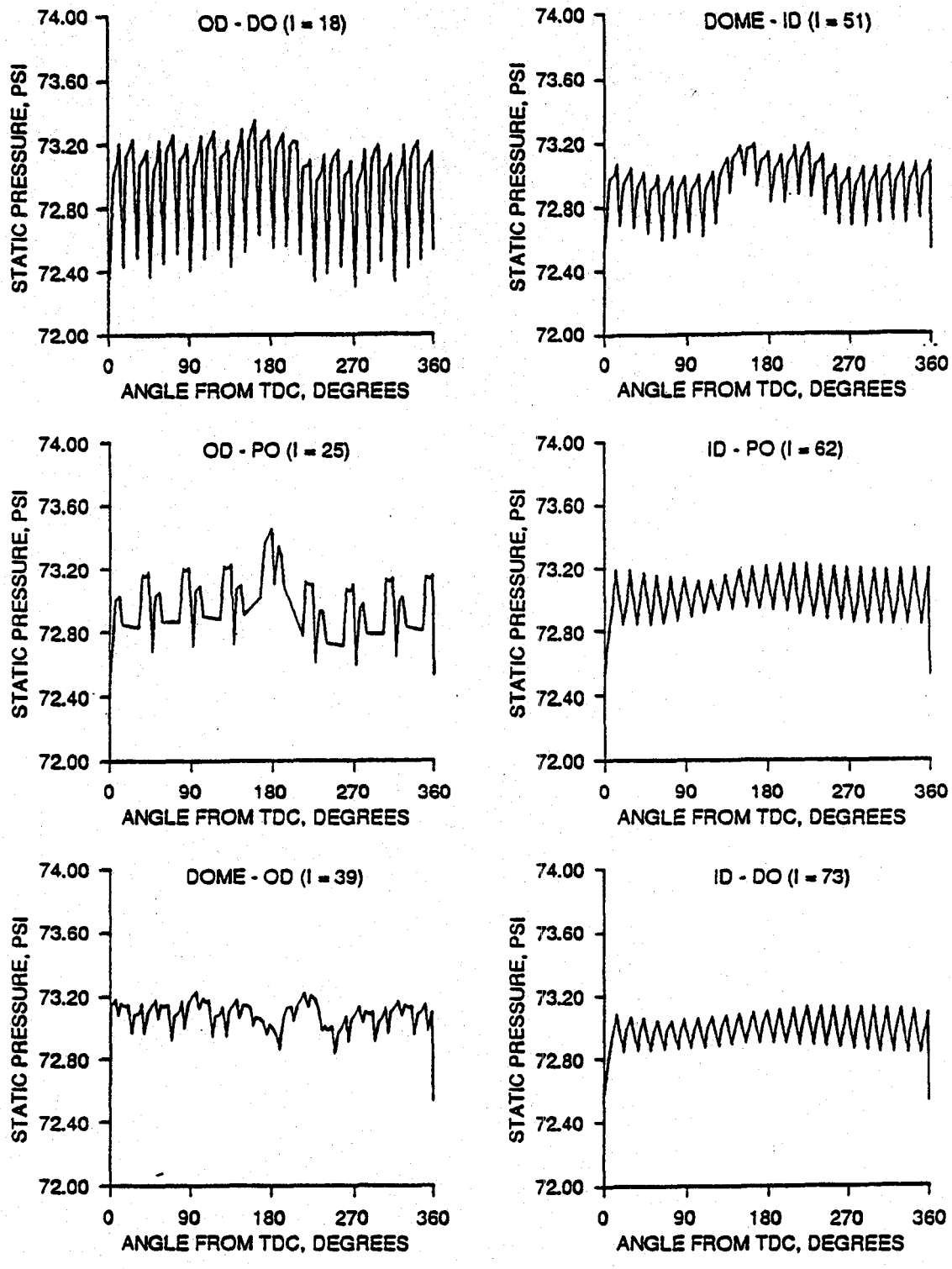

Figure 12. Predicted Pressure Distributions at Various Combustor Hole Locations.

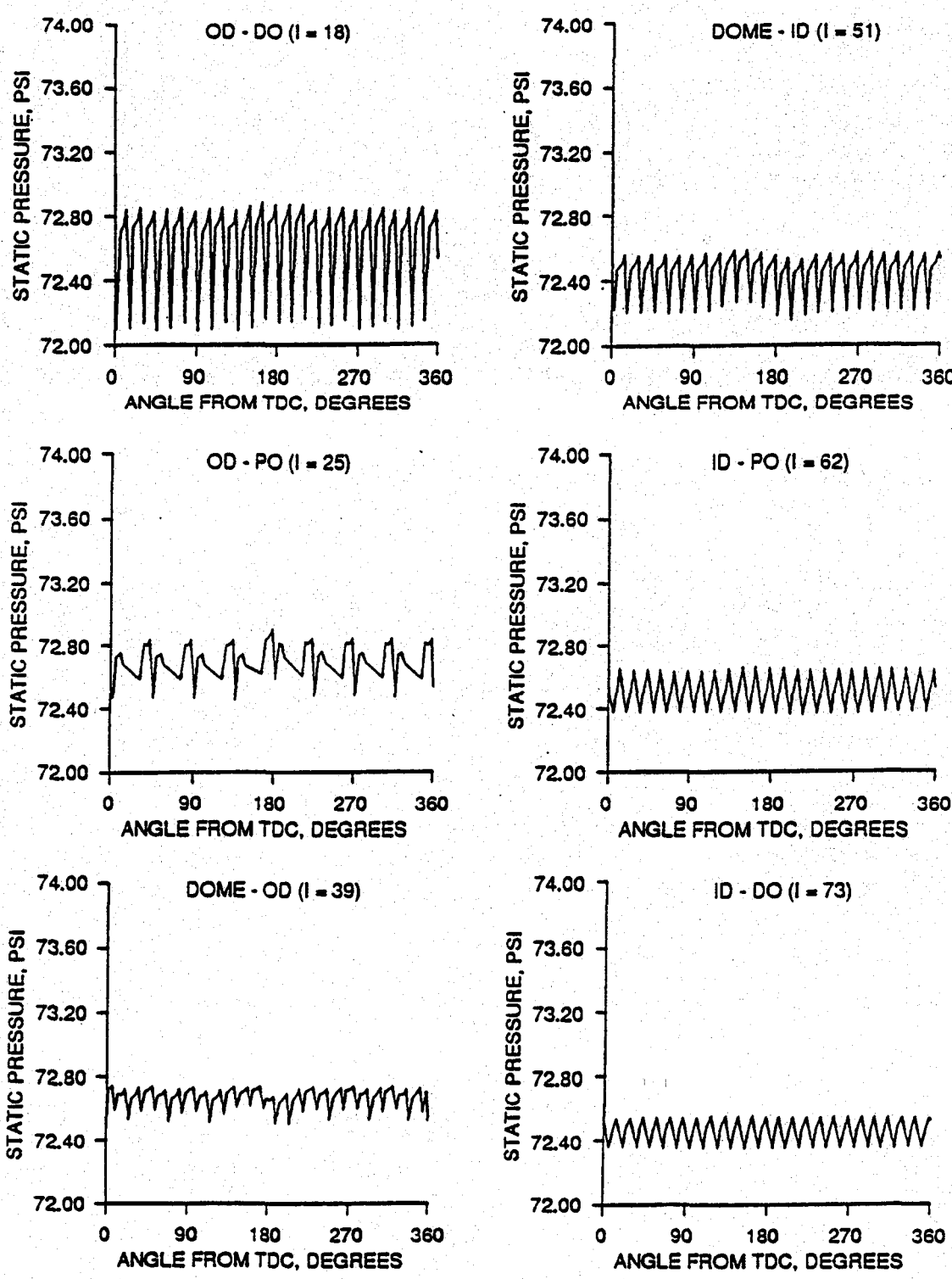

GC11476-13

Figure 13. Predicted Pressure Distribution at Various Combustor Hole Locations (without Integral Bleed).

CONCLUSIONS

An advanced 3-D CFD model based on a boundary-fitted, curvilinear, orthogonal grid system has been developed. The model is capable of predicting the complex external flow field of a gas turbine combustor with integral bleed. Several important findings from this study of Combustor-Integral Bleed flow interaction are summarized below:

(1) Integral bleed flow distribution has a great effect on the pressure distribution around the gas turbine combustor.

(2) The presence of atomizers and ignitors has a profound effect on pressure distribution around the combustor O.D. liner. Each atomizer or ignitor was found to be associated with a high pressure region upstream and a low pressure region downstream.

(3) The non-uniform pressure distribution usually causes non-uniform airflow distribution around the combustor liner and will result in hot and cold spots at the combustor exit.

(4) The recirculation zone formed near the annulus inlet has caused pressure loss near the combustor O.D. dilution holes. As a result, the dilution jet penetration is reduced and will result in high pattern factor at the combustor exit.

REFERENCES

1. Thompson, J. F., 1982, "Numerical Grid Generation," North-Holland.
2. Spalding, D. B., 1972, "A Novel Finite Difference Formulation for Differential Expressions Involving Both First and Second Derivatives," Int. J. Num. Mech. Engr., Vol. 4, pp551.
3. Patankar, S. V., 1980, "Numerical Heat Transfer and Fluid Flow," McGraw-Hill-Hemisphere.
4. Przekwas, A. J., 1984, "Whole Field Solution Method for Elliptic Difference Equations with General Boundary Conditions," Numerical Heat Transfer, Vol-, pp-.
5. Roback, R. and Johnson, J. P., 1983, "Turbulent Confined Swirling Coaxial Jets," NASA CR-168252.
6. Sovran, G. and Klomp, E.G., 1967, "Experimentally Determined Optimum Geometries for Rectilinear Diffusers with Rectangular, Conical and Annular Cross Sections," Fluid Mechanics of Internal Flow, Elsevier, New York.

ACKNOWLEDGEMENTS

The authors would like to thank Mr. Randy Williams for his encouragement of developing this 3-D Combustor-Integral Bleed Flow Interaction Model. They would also like to thank the AlliedSignal Engines management for permission to publish this paper.

NUMERICAL ANALYSIS OF A VORTEX CONTROLLED DIFFUSER

Robert E. Spall
Department of Mechanical Engineering
University of South Alabama
Mobile, AL 36688

SUMMARY

A numerical study of a prototypical vortex controlled diffuser is performed. The basic diffuser geometry consists of a step expansion in a pipe of area ratio 2.25:1. The incompressible Reynolds averaged Navier-Stokes equations, employing the $K-\varepsilon$ turbulence model, are solved. Results are presented for bleed rates ranging from 1 to 7 percent. Diffuser efficiencies in excess of 80 percent are obtained. Reattachment lengths are reduced by a factor of up to 3. These results are in qualitative agreement with previous experimental work. However, differences in some basic details of experimentally observed and the present numerically generated flowfields exist. The effect of swirl is also investigated.

INTRODUCTION

The central idea behind the vortex controlled diffuser (VCD) is that highly efficient diffusion may be achieved by bleeding off fluid through a small gap located at a region of rapid expansion. This concept appears to have been first introduced by Heskestad [1]. In that work, edge suction was applied through a slot situated at the edge of a convex corner. It was found that the flow turned the corner in a manner that significantly decreased the extent of the recirculation region. Heskestad later [2] experimented with edge suction at the step expansion of a circular pipe, evaluating the effectiveness of the configuration as a short diffuser. That study employed a uniform inlet profile with a thin boundary layer. Heskestad also [3] considered the effectiveness of edge suction in producing a short diffuser when the inlet profiles were fully developed. High static pressure recoveries were produced in both cases.

The desirability of a short diffuser between the compressor and combustor in gas turbine applications provided the incentive for further development of the VCD concept. Adkins [4] obtained data for a series of research diffusers with area ratios ranging from 1.9:1 to 3.2:1. He found that, for moderate bleed rates, efficiencies in excess of 80% could be achieved with diffuser lengths 1/3 that required with conventional conical diffusers. A hybrid diffuser (a combination VCD and conventional diffuser) was later studied by Adkins et al. [5]. Results showed that bleed rates were reduced from those required for the previously studied step VCD configurations. Most recently, Sullerey et al. [6] have investigated the effect of inlet flow distortion on a VCD. Results revealed that as inlet distortions were increased, so too were the levels of bleed required to maintain diffuser efficiency.

It appears that the only previous numerical work concerning the VCD was performed by Busnaina and Lilley [7]. In that work, the incompressible Navier-Stokes equations were solved

for the flow in a two-dimensional VCD geometry. Although the effects of turbulence were not modeled, and the grid employed was quite coarse, the general trends followed those observed experimentally.

The mechanism by which the VCD operates is still unclear. One explanation is that a region of high shear is produced resulting in a layer of turbulence that inhibits flow separation [4]. Others [3] have suggested that the primary result of suction is to simply deflect or turn the mean flow around the sharp corner, thus diminishing the length of the recirculation zone.

In the present work the performance of a prototypical VCD is investigated numerically. The incompressible, axisymmetric Reynolds averaged Navier-Stokes equations are solved for the flow through a pipe containing a step expansion of area ratio 2.25:1. The vortex chamber and bleed gap height-to-length ratio are representative of those employed in previous experimental works. The effect of turbulence is modeled using the $K-\varepsilon$ model. (The standard $K-\varepsilon$ model has predicted the reattachment length for flow in a sudden pipe expansion within experimental uncertainty [8]). Calculations are performed for bleed rates ranging from 1% to 7%. For comparative purposes, results for a step expansion without the benefits of bleed are also presented. Details of the flow structure are studied and presented using velocity vectors and contour plots of pressure, turbulence kinetic energy, and axial velocity.

NUMERICAL APPROACH

The incompressible Reynolds-averaged Navier-Stokes equations are appropriate to describe the motion within a prototypical VCD configuration. Although the governing equations are solved in cylindrical polar coordinate form, for purposes of brevity they are presented below in cartesian tensor form. The continuity and momentum equations are given as:

$$\frac{\partial u_i}{\partial x_i} = 0 \tag{1}$$

$$\frac{\partial u_i}{\partial t} + u_j\frac{\partial u_i}{\partial x_j} = -\frac{1}{\rho}\frac{\partial p}{\partial x_i} + \frac{\mu}{\rho}\nabla^2 u_i - \frac{\partial R_{ij}}{\partial x_j} \tag{2}$$

respectively, where u_i is the mean velocity, ρ is the density, μ is the viscosity, p is the mean pressure and $R_{ij} = \overline{u'_j u'_i}$ are the Reynolds stresses. The Boussinesq hypothesis provides an expression for the Reynolds stresses in terms of the gradients of the mean flow [9] as:

$$-R_{ij} = -\frac{2}{3}\delta_{ij}K + \frac{\mu_t}{\rho}\left(\frac{\partial u_i}{\partial x_j} + \frac{\partial u_j}{\partial x_i}\right) \tag{3}$$

where μ_t is the turbulent viscosity and K is the turbulent kinetic energy. The turbulent viscosity is expressed, in terms of K and the dissipation rate, ε, as:

$$\mu_t = \rho C_\mu \frac{K^2}{\varepsilon} \tag{4}$$

Transport equations for K and ε, respectively, are given as [10]:

$$\frac{DK}{Dt} = \frac{\partial}{\partial x_i}\left(\frac{\nu_t}{\sigma_k}\frac{\partial K}{\partial x_i}\right) + \nu_t\frac{\partial u_i}{\partial x_j}\left(\frac{\partial u_i}{\partial x_j} + \frac{\partial u_j}{\partial x_i}\right) - \varepsilon \tag{5}$$

$$\frac{D\varepsilon}{Dt} = \frac{\partial}{\partial x_j}\left(\frac{\nu_t}{\sigma_\varepsilon}\frac{\partial \varepsilon}{\partial x_j}\right) + C_1\nu_t\frac{\varepsilon}{K}\frac{\partial u_i}{\partial x_j}\left(\frac{\partial u_i}{\partial x_j} + \frac{\partial u_j}{\partial x_i}\right) - C_2\frac{\varepsilon^2}{K} \tag{6}$$

It remains to specify the empirical constants in the above equations. Although investigators have attempted to optimize these values for recirculating and/or swirling flows (c.f. [8]), most of these attempts have been *ad hoc*, and thus the standard values for boundary-layer flows ($C_\mu = 0.09$, $C_1 = 1.44$, $C_2 = 1.92$, $\sigma_\kappa = 1.0$ and $\sigma_\varepsilon = 1.3$) have been taken. Near the wall, it is assumed that the log-law holds.

The above equations were solved using the commercial code FLUENT [11]. FLUENT uses a control volume technique with non-staggered grids. All variables are stored at control volume centers. QUICK [12] interpolation is used to provide values of the variables on cell faces. Pressure-velocity coupling is implemented using the SIMPLE [13] algorithm. Convergence of the solution is assumed when the normalized residual for each conservation equation is decreased to 10^{-3}. (The residual for a given equation consists of the summation of the unbalance in the equation for each cell in the domain.) Since the above solution techniques are well known and widely discussed in the literature, they will not be elaborated upon here.

GEOMETRY AND BOUNDARY CONDITIONS

A prototypical axisymmetric VCD of expansion area ratio 2.25:1 is considered (see Figure 1). (The radius of the diffuser upstream of the expansion is 1 unit; downstream, 1.5 units.) The diffuser geometry is typical of that employed in dump combustors. The essence of the diffuser is the suction slot at the expansion corner. Small quantities of fluid (typically 5% of the mass flow) are bled off through the suction slot into a vortex chamber. Fluid exits the chamber through a channel (as shown in Figure 1). In the present study, the axial extent of the slot (L) is taken as 0.1 units, and the radial depth (D), 0.05 units. Thus, the slot length-to-depth ratio is 2.0, typical of those employed in experimental works appearing in the literature. The total length of the VCD configuration is 25 units, with the gap beginning 2.4 units downstream from the inflow plane. A length of 25 was chosen so that outflow boundary conditions could be specified with reasonable accuracy. The radius of the pipe upstream of the expansion is 1 unit; the radius downstream, 1.5 units. A cylindrical grid consisting of 85 cells in the axial direction and 45 cells in the radial direction is employed. Cells were clustered toward the vortex fence (the aft wall of the vortex chamber) and the lateral diffuser walls. To assure a grid converged solution, calculations are also performed using double the number of grid points in each coordinate direction (for the 5% swirl case).

For all cases, a uniform inflow axial velocity profile was specified. Previous experimental studies [2, 3] reveal that thin inlet boundary layers result in higher pressure recoveries than fully developed turbulent profiles, and thus it is expected that pressure recoveries in the present study would be somewhat decreased if fully developed turbulent inlet profiles were used. However, the underlying physical principals should not be affected. The Reynolds number, based on inflow pipe diameter and velocity is 200,000. This is representative of Reynolds numbers employed in

most experimental investigations, which range from 100,000 [4] to 840,000 [5]. The inlet turbulence intensity is 10%. Given the turbulence intensity, the turbulence kinetic energy and dissipation rates are calculated from:

$$K = \frac{3}{2}(u')^2 \tag{7}$$

$$\varepsilon = C_\mu^{\frac{3}{4}} \frac{K^{\frac{3}{2}}}{l} \tag{8}$$

where l is a turbulence length scale given as 0.07R, (R is the inlet pipe radius). At the outlet, fully developed flow conditions are assumed; that is, streamwise gradients of the flow properties are set to zero.

RESULTS

Results have been obtained for the VCD with bleed rates ranging from 1% to 7%, and for a step expansion (without the vortex chamber). In addition, results for the 5% bleed case with swirl have been obtained. For the sake of brevity, contour and velocity vector plots are provided only for the case of the step expansion, and the VCD 5% bleed case. In addition, only the portion of the domain near the suction slot is shown. (Note that grey contour lines signify negative values.)

Before delving into a description of the flowfield, it is first desirable to provide some means of quantifying improvements in diffuser effectiveness as a function of bleed rate. Toward this end, a one dimensional correction may be applied to the usual definition of diffuser effectiveness, which results in the expression [4]:

$$\eta = \frac{p_2 - p_1}{\frac{1}{2}\rho \bar{v}_1^2 \left(\alpha_1 - \left(\frac{1-B}{AR}\right)^2\right)} \tag{9}$$

where B is the bleed rate, AR is the area ratio and α is a kinetic energy coefficient. For the case of uniform inflow profiles, α equals unity. (For fully developed turbulent flows in circular pipes, $\alpha = 1.05$.) The dramatic effect of bleed on effectiveness is demonstrated in Figure 2, in which effectiveness is plotted as a function of distance downstream from the step expansion (or fence). In the case of the step expansion, the maximum effectiveness reaches approximately 52%, and is not achieved until nearly 20 step heights (H) downstream from the expansion. Maximum effectiveness increases to 67%, 82%, 90% and 92%, for VCD bleed rates of 1%, 3%, 5%, and 7%, respectively. In addition, the distance required for maximum diffusion to take place decreases from approximately 13 H for 1% bleed to 3 H for 7% bleed. The increase in effectiveness begins to asymptote as the bleed rate is increased beyond 5%. For the 3, 5, and 7% bleed rates, losses to friction cause the effectiveness of the diffuser to diminish slowly beyond about 10 H (downstream of the fence). These results are in qualitative agreement with experimental results for both tubular and annular VCD's presented by Adkins [4]. The results do differ in one important aspect. Adkins [4] suggests that at low bleed rates, diffuser effectiveness increases slowly with increased bleed. Then, at some bleed rate, fluid begins to enter the suction slot from the freestream (as opposed to entering over the vortex fence). At this point, diffuser effectiveness increases rapidly with respect

to slight increases in bleed rate. Finally, at some critical rate (described as the rate necessary for the formation of a stagnation point at the top of the fence) increases in effectiveness with increases in bleed rate become minimal. The numerical results however, show no such trends at low bleed rates. That is, at low bleed rates, numerical results indicate that diffuser effectiveness increases gradually with respect to increases in bleed rate.

One benefit of numerical solutions is that detailed flow patterns are obtained. In the remainder of this section, results in terms of contour plots and velocity vectors are examined. Velocity vectors for the step expansion and for the VCD with 5% bleed are shown in Figures 3a,b, respectively. For clarity, the vectors are plotted at every other gridpoint in both the radial and streamwise coordinate directions. The effect of bleed in reducing the extent of the recirculation region is clearly revealed in Figure 3b. A stable vortical structure within the vortex chamber is also clearly indicated. However, most important is the rapid directional change and acceleration of the fluid around the corner under the influence of bleed. For the step expansion, a clean separation from the corner is obtained.

More accurate indications of the extent of the recirculation regions, described by contours of constant axial velocity, are shown in Figures 4a,b. Figure 4a reveals that for the step expansion, the length of the recirculation zone is approximately 7 H. This value is less than the values of 8-9 H reported experimentally [c.f. 14] over a range of expansion ratios. Numerical results using the $K-\varepsilon$ model range from 7-9 H for an area expansion ratio of 4:1 [c.f. 8] which agree fairly well with the experimental results. However, as the expansion ratio diminishes, one might expect the $K-\varepsilon$ model to begin to underpredict the separation length, in accordance with well known results for the 2D backward facing step. Implementation of 5% bleed reduces the length of the separated region to 2.5 H. In addition, the rapid diffusion downstream of the expansion is well illustrated. The diffusion process appears to be nearly complete at a distance of 5 H downstream from the expansion. This correlates well with the optimum length for the diffuser predicted using wall pressure data as shown in Figure 2 (where the efficiency reaches approximately 85%). One also notes an acceleration of the fluid in the near wall region just upstream of the expansion due to the presence of the low pressure vortex chamber. This is followed by a region in which a rapid decrease in the axial velocity of the fluid occurs as it passes over the gap and, due to the expansion, encounters a strong adverse pressure gradient. The net result is the creation of a region of high localized shear.

Contours of constant pressure are shown in Figures 5a,b for the step expansion and VCD geometries, respectively. The pressure variations presented are with respect to a reference pressure located adjacent to the duct inlet (given as p_1 in Equation 9). Figure 5b reveals that, away from the wall, a significant adverse pressure gradient forms upstream of the suction slot. This occurs due to the flux of fluid through the bleed slot. That is, due to mass removal at the slot, the axial flux decreases away from the wall. Nearer the wall, the influence of the vortex chamber results in a decrease in the pressure with a corresponding increase in the axial velocity. A local minimum in the pressure occurs at the slot entrance and thus serves to deflect the oncoming fluid toward the outer wall. Of further interest is the pressure distribution on the back face of the step. Here, the pressure is not constant along the wall (as is the case with the step expansion, Figure 5a) but increases in the radial direction. To assess the effects of grid refinement, shown in Figure 5c are pressure contours computed using a 170 x 90 grid. Only very minor differences in the contours (appearing near the downstream portion of the shown flowfield) are visible. Thus, the original 85 x 45 grid is deemed sufficient for the purposes of this study.

Contours of turbulence kinetic energy are shown in Figures 6a,b. As previously men-

tioned, the region near the slot is one of high shear, and is thus responsible for the generation of considerable turbulence energy, as revealed in Figure 6b. In addition to this local maximum, an additional maximum appears downstream, near the aft portion of the recirculation region. However, the turbulence levels at this downstream point are below the levels near the slot. This may be contrasted to the case of the step expansion, shown in Figure 6a. Here, only one local maximum appears near the aft portion of the recirculation region. In addition, maximum turbulence levels are below those shown in Figure 6b.

Since many practical VCD applications involve some level of swirl in the approach flow, the effect of swirl on VCD flow patterns is briefly investigated. Again, the bleed rate is taken as 5%, and other flow field conditions remain identical to those described earlier. A solid body rotation is superimposed on the axial velocity at inflow such that the ratio of the maximum swirl velocity to axial velocity equals 0.5. This represents a significant level of swirl, although well below that at which reversed flow is expected to occur. Shown in Figure 7a are contours of constant axial velocity. By comparison with Figure 4b, it is apparent that the length of the recirculation region has been diminished. This is consistent with experimental results reported by, for instance, Dellenback [14] for the step expansion with swirl. (Apparently, no experimental or numerical results on VCD performance under the influence of swirl exist in the open literature.) Pressure contours are shown in Figure 7b. One notes that near the axial location of the bleed slot, radial variations in pressure are similar to those for the zero swirl case. However, downstream from this position, a significant radial gradient exists, as one would expect in the case of swirling flows.

DISCUSSION

The numerical results shed light on several points which have been previously discussed in the literature. The existence of a region of high shear (with corresponding turbulence) has been mentioned as one of the physical mechanisms responsible for the drastic improvements in effectiveness of the VCD over the step expansion as a diffuser [4]. That a region of high turbulence is formed near the suction slot is borne out in the present study. However, that this region is necessary or responsible for preventing flow separation seems unlikely. Indeed, the flow separates at the top of the chamber fence. It appears that the primary contribution of the suction slot is to deflect the fluid toward the outer wall.

It has been suggested [4] that at low bleed rates fluid is drawn into the vortex chamber from this lee side of the fence, resulting in only minimal improvement in diffuser effectiveness. For higher bleed rates, it has then been proposed that this process is diminished, eventually resulting in the formation of a stagnation point on the top of the fence. This bleed rate is termed the critical rate. However, results from the present study do not confirm this process. Even at the 1% bleed level, the results indicate that fluid does not enter the chamber from the lee side of the fence. In addition, a sudden increase in efficiency with respect to bleed rate is not observed, regardless of the chosen length of the diffuser.

There are several possible reasons for the discrepancy regarding the details of the process as observed experimentally, and computed numerically. Of primary concern is the ability of the $K-\varepsilon$ turbulence model to accurately predict fine flow details of this complex recirculating flowfield. Perhaps inclusion of a full Reynolds stress model could be of benefit in this respect. The present study does indicate however, that numerical solutions of the Reynolds averaged Navier-

Stokes equations provide a useful tool to aid in the analysis and design of practical VCD configurations.

ACKNOWLEDGEMENTS

The author would like to acknowledge Dr. Lanier Cauley for useful discussions regarding the vortex controlled diffuser. The Theoretical Flow Physics Branch, NASA Langley Research Center is also acknowledged for providing computer resources and access to the FLUENT code.

REFERENCES

1. Heskestad, G. "An Edge Suction Effect," AIAA J., Vol. 3, 1965, pp. 1958-1961.

2. Heskestad, G., "A Suction Scheme Applied to Flow Through a Sudden Enlargement," J. Basic Eng., Vol. 90, 1968, pp. 541-544.

3. Heskestad, G., "Further Experiments with Suction at a Sudden Enlargement in a Pipe," J. Basic Eng., Sept. 1970, pp. 437-449.

4. Adkins, R.C., "A Short Diffuser With Low Pressure Loss," J. Fluids Eng., Sept. 1975, pp. 297-302.

5. Adkins, R.C., Martharu, D.S. and Yost, J.O., "The Hybrid Diffuser," J. Eng. Power, Vol. 103, 1981, pp. 229-236.

6. Sullerey, R.K., Ashok, V., and Shantharam, K.V., "Effect of Inlet Flow Distortion on Performance of Vortex Controlled Diffusers," J. Fluids Eng., Vol. 114, 1992, pp. 191-197.

7. Busnaina, A.A. and Lilley, D.G., "A Simple Finite Difference Procedure for the Vortex Controlled Diffuser," AIAA-82-0109, AIAA 20th Aerospace Sciences Meeting, Jan. 11-14, Orlando, FL, 1982.

8. Nallasamy, M., "Turbulence Models and Their Applications to the Prediction of Internal Flows: A Review," Computers & Fluids, Vol. 15, 1987, pp. 151-194.

9. Hinze, J.O., Turbulence, New York, NY: McGraw-Hill Publishing Co., 1975.

10. Jones, W.P., and Launder, B.E., "The Prediction of Laminarization with a Two-Equation Model of Turbulence," Internat. J. Heat Mass Transfer, Vol. 15, 1972, pp. 301-314.

11. FLUENT Users Guide, Fluent, Inc., Lebanon, NH

12. Leonard, B.P., "A Stable and Accurate Convective Modeling Procedure Based on Quadratic Upstream Interpolation," Methods in Appl. Mech. Eng., Vol. 19, 1979, pp. 59-98.

13. Patankar, S.V., Numerical Heat Transfer and Fluid Flow, Washington, D.C., Hemisphere Publishing Corp., 1980.

14. Dellenback, P.A., "Heat Transfer and Velocity Measurements in Turbulent Swirling Flows Through an Axisymmetric Expansion, Arizona State University, PhD dissertation, 1986.

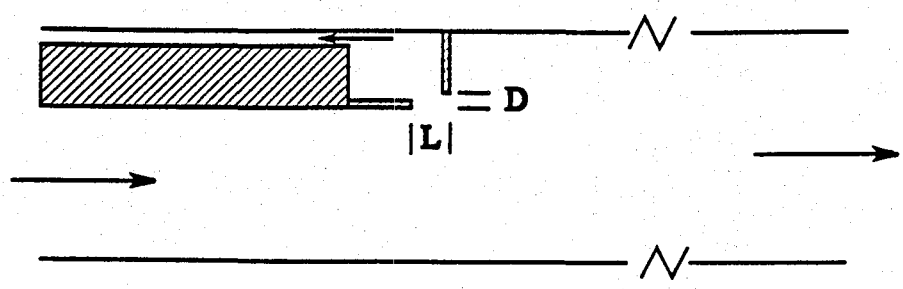

Figure 1 Vortex controlled diffuser geometry.

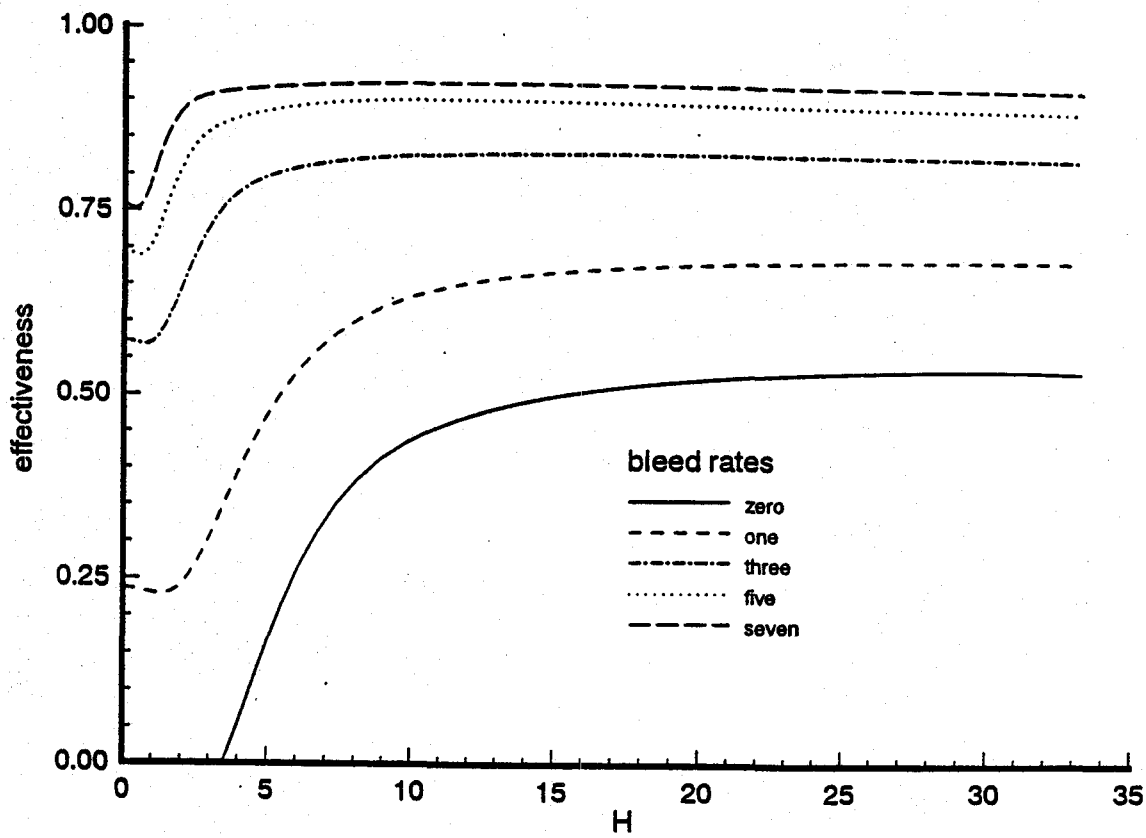

Figure 2 Diffuser effectiveness as a function of the downstream distance from the vortex fence.

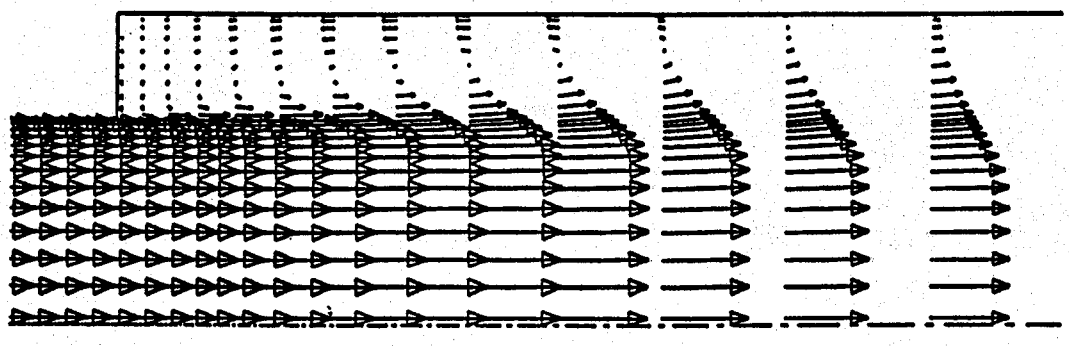

a) step expansion

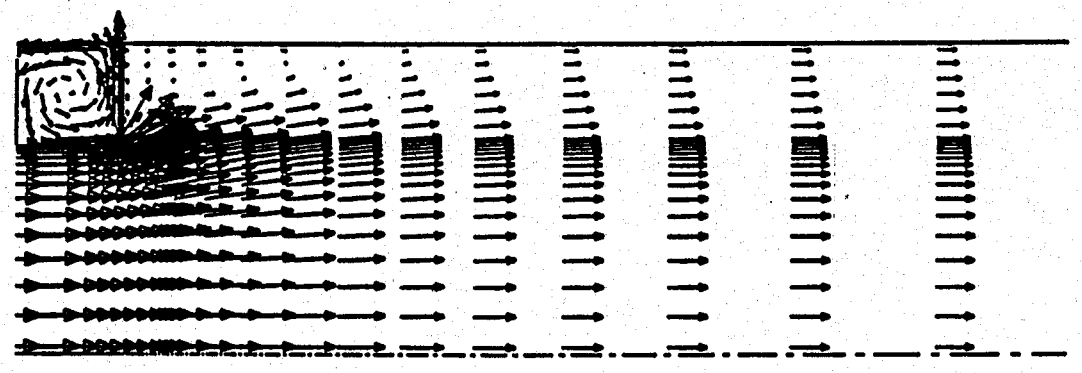

b) VCD with 5% bleed

Figure 3 Velocity vectors in region of step expansion and vortex chamber.

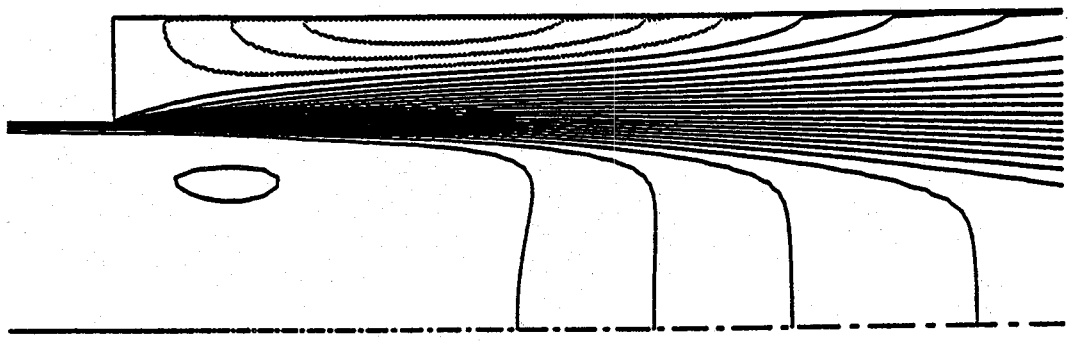

a) step expansion

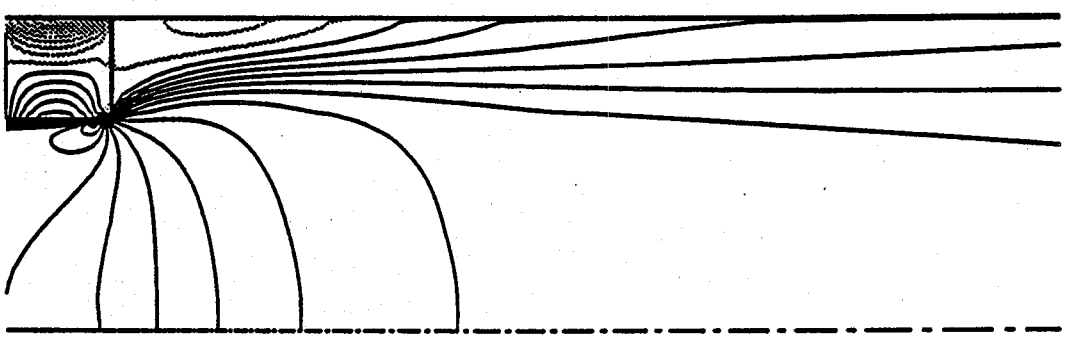

b) VCD with 5% bleed

Figure 4 Contours of constant axial velocity.

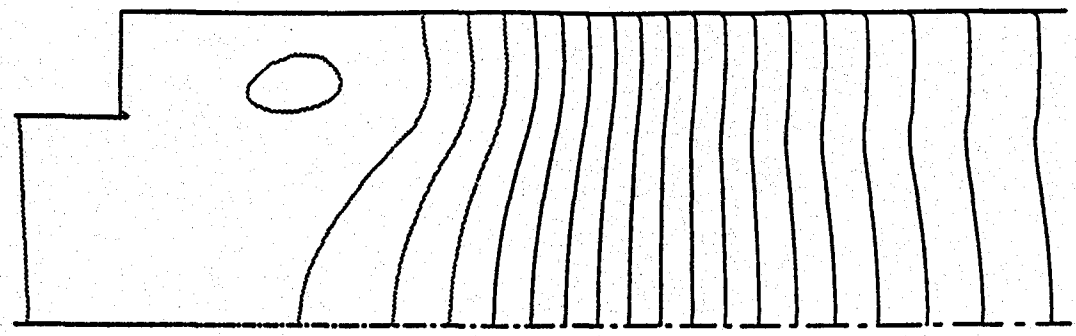

a) step expansion

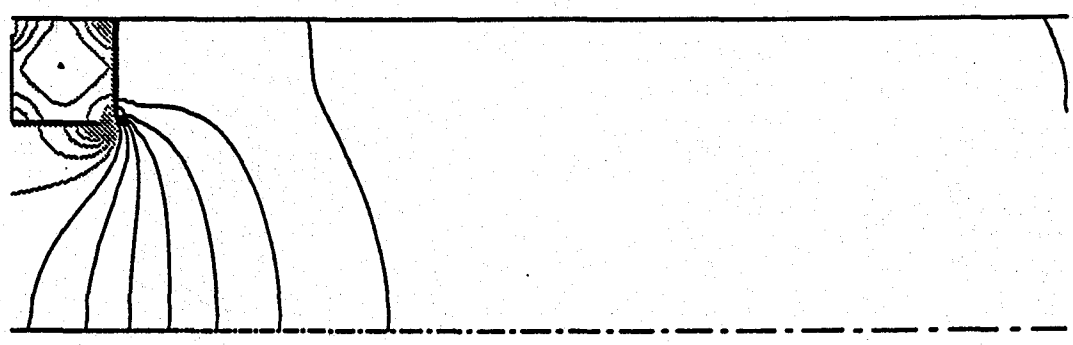

b) VCD with 5% bleed

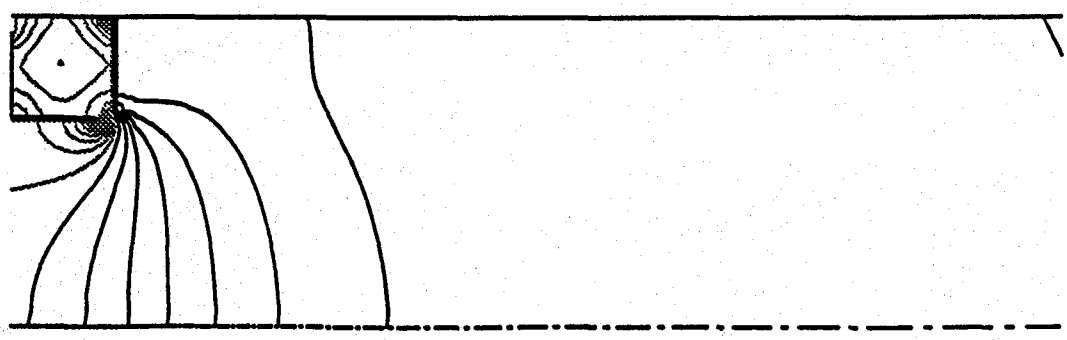

c) VCD with 5% bleed, 170 x 90 grid

Figure 5 Contours of constant pressure.

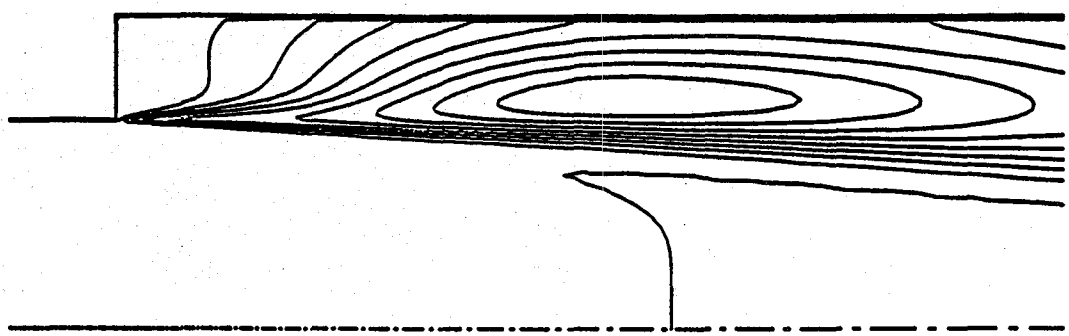

a) step expansion

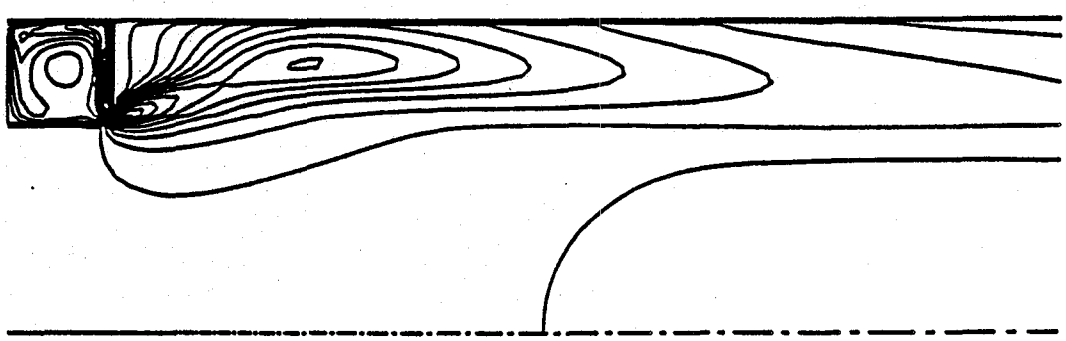

b) VCD with 5% bleed

Figure 6 Contours of turbulence kinetic energy.

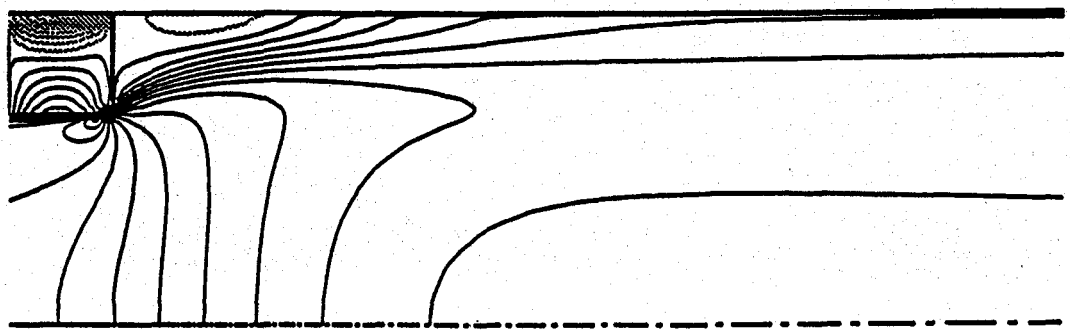

a) contours of constant axial velocity

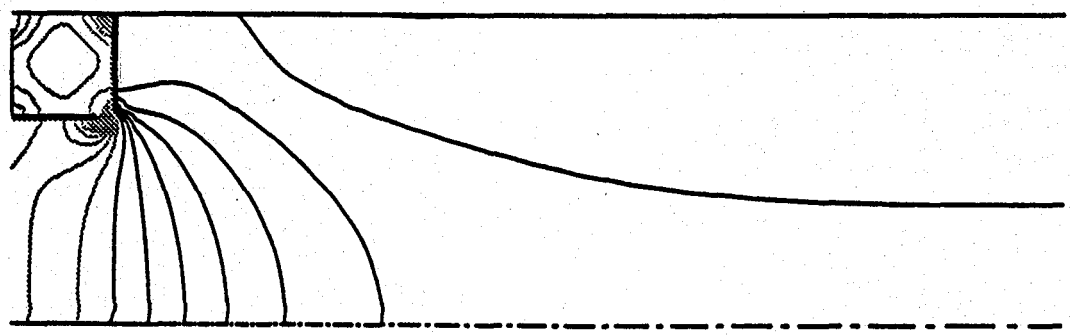

b) contours of constant pressure

Figure 7 VCD with swirl (5% bleed).

3D NUMERICAL STUDY OF AIRFLOW IN THE COMPRESSOR/COMBUSTOR PREDIFFUSER AND DUMP DIFFUSER OF AN INDUSTRIAL GAS TURBINE

Ajay K. Agrawal* and Tah-teh Yang
Department of Mechanical Engineering
Clemson University, Clemson, SC 29631-0921

SUMMARY

This paper describes the 3D computations of a flow field in the compressor/combustor diffusers of an industrial gas turbine. The geometry considered includes components such as the combustor support strut, the transition piece and the impingement sleeve with discrete cooling air holes on its surface. Because the geometry was complex and 3D, the airflow path was divided into two computational domains sharing an interface region. The body-fitted grid was generated independently in each of the two domains. The governing equations for incompressible Navier-Stokes equations were solved using the finite volume approach. The results show that the flow in the prediffuser is strongly coupled with the flow in the dump diffuser and vice versa. The computations also revealed that the flow in the dump diffuser is highly nonuniform.

INTRODUCTION

In gas turbine engines the air exiting the compressor is decelerated in the annular prediffuser before it is discharged into the dump diffuser. The dump diffuser then distributes the air to the combustor(s) through the annular jacket(s). Typical aircraft engines use an annular combustor, which extends over 360 degrees continuously around the turbine axis. In contrast, the industrial gas turbines use several can combustors discretely and equispaced in the circumferential direction. Each of these combustor cans has an annular jacket around it which receives air from the dump diffuser and then feeds it to the combustor can for combustion.

From the gas turbine's compressor exit to the combustor, frictional losses in the diffuser flow path adversely affect the efficiency of the gas turbine. The diffuser system must uniformly distribute air to the hot-sections of the turbine to maintain combustion, to improve thermal mixing and to avoid local burnout. Thus, high efficiency advanced gas turbines require an aerodynamic design of the prediffuser and dump diffuser for minimizing energy losses and for maintaining combustion stability and performance. The design of these flow systems is complicated because of two main reasons (1) the performance of the prediffuser is affected by the flow

* Present Address:
School of Aerospace and Mechanical Engineering
The University of Oklahoma, Norman, OK 73019-0601

conditions in the dump region and vice versa and (2) the flow geometry in the dump region is 3D. The complex geometry and the flow interactions between the components of the compressor/combustor region present a significant design challenge.

The test model in figure 1 depicts the air flow path in the compressor/combustor region of an industrial gas turbine. After passing through the annular prediffuser, a portion of the air flows through the cooling holes in the impingement sleeve into the space between the impingement sleeve and the transition piece; then it flows through this annular space towards the combustor can and finally mixes with the balance of the air flowing through the bypass air ports. Next, the air enters the combustor can through primary, secondary, dilution and cooling holes. Several components in the flow path disrupt the circumferential uniformity; hence, the resulting flow field is 3D. The authors of this study are aware of only one other similar investigation, which was conducted by Karki et al. (ref. 1). Their investigation considered a typical combustor-diffuser in aircraft engines. The diffuser geometry and the flow path in the present study are far more complex than that in the study by Karki et al (ref. 1).

The primary purpose of this work was to simulate the cold airflow in the test model of an industrial gas turbine. Thus, the reacting flow in the combustor can and the hot-gas flow through the transition piece were not considered. However, the geometric details of the transition piece and the surrounding impingement sleeve were included to add realism to the simulations. In computations, the airflow exited at the annular space between the combustor casing and the combustor can. In the circumferential direction, the exact same geometry of the combustor/transition piece assembly repeats cyclically. Additionally, each of these assemblies is symmetric about its midplane. Therefore, the computations in the circumferential direction were required in only one-half of the distance between the adjacent combustor/transition piece assemblies (which is 1/28th of the full 360 degrees).

COMPUTATIONAL PROCEDURE

Because the geometry was complex and 3D, the airflow path was divided into two computational domains. The lower domain included the prediffuser, a part of the combustor support strut and the lower dump diffuser. The upper domain included the details of the combustor/transition piece assembly, the upper dump diffuser and a part of the combustor support strut. These two domains shared an interface region through which boundary condition data were communicated between the two domains and updated during the computations.

Grid Generation

The body-fitted, curvilinear coordinate system was used to incorporate the geometric details in the computational analysis. Internal solid objects, such as the support struts and the surface of the impingement sleeve were, simulated by blocking the flow through the grids representing these areas. Figure 2 shows the computational grid in the two domains on a longitudinal

plane between the combustor support struts and also the midplane of the combustor/transition piece assembly. The shaded grids in figure 2 were impervious to the flow. Thus, they represent internal solid objects, such as the impingement sleeve and the transition piece. The procedure for generating the 3-D computational grid is described below.

EasyMesh-3D, a 3-D mesh-generation program (ref. 2), was used to independently generate a structured grid in each of the two domains. First, the computational domain was divided into subsections or subvolumes. These subvolumes represented specific objects inside the computational domains. The mesh was generated within each subvolume, which allowed local grid refinement and accurate representation of flow obstructions. The computational grid in the lower domain consisted of 62,208 grids with 18 in the circumferential direction, 32 in the radial direction and 108 in the axial direction.

The computational grid in the upper domain represented the complex 3-D shape of the combustor/transition piece and the combustor casing/impingement sleeve. The combustor and its casing are circular in cross-section. The transition piece and impingement sleeve are circular at the combustor end and are nearly rectangular at the turbine inlet. Moreover, the spacing between the adjacent combustor/transition piece assemblies varies along the axial direction. This spacing is maximum at the combustor end and zero at the turbine inlet. The computational grid on the surface of the combustor can/transition piece is shown in figure 3. The mesh was constructed by prescribing geometric details at 5 axial locations. Azimuthal planes at each of these axial locations were divided into 6 subsections. Therefore, a total of 30 subvolumes formed the upper computational domain. Figures 3 and 4 show, respectively, the azimuthal planes at the combustor exit and the turbine inlet. As seen in figures 4 and 5, the surface of the impingement sleeve was broken into three segments, each of which belonged to a subsection. This procedure allowed flexibility in generating the mesh and improved grid resolution and grid orthogonality. Figures 4 and 5 identify also the grids that were blocked to the flow and that represent the solid objects. The computational grid in the upper domain consisted of 63,648 grids with 18 in the circumferential direction, 52 in the radial direction and 68 in the axial direction.

In the test model, the air enters the space between the impingement sleeve/transition piece and the combustor casing/combustor through cooling air holes on the impingement sleeve and the bypass air holes on the combustor casing. The combustor casing has 3 rows of bypass air holes, and each of these rows consists of several discrete holes equally spaced in the circumferential direction. The impingement sleeve has several rows of smaller cooling air holes. The finite grid in the present analysis could not precisely and indivisibly resolve the large number of cooling holes. Therefore, only 12 holes were considered in each row. These holes were distributed nearly uniformly in the circumferential direction. Although the exact shape and orientation of the holes in a row could differ, the area of each hole was kept the same. If the actual number of holes in a row exceeded 12, then the total area of these 12 holes was made to equal the actual total area of the holes in that row. Each hole comprised of at least 1 or more grids. When the area of a grid exceeded the area of the hole it represented, the grid was partially blocked to the flow.

Because the mesh was generated independently in each of the two domains, the grids differ at the interface between these domains. Linear interpolation was used to compute boundary data at the proper interface location before the information was transferred from from one domain to another.

Governing Equations

Using Cartesian tensor notation, governing equations for incompressible turbulent flow are expressed in time-averaged form:

$$\frac{\partial}{\partial x_j}(\rho V_j) = 0 \tag{1}$$

$$\frac{\partial}{\partial x_j}(\rho V_j V_i) = -\frac{\partial p}{\partial x_i} + \frac{\partial}{\partial x_j}[\mu_{eff}\frac{\partial V_i}{\partial x_j}] \tag{2}$$

The effective viscosity, μ_{eff}, was defined by the relation

$$\mu_{eff} = \mu + \mu_t \tag{3}$$

The turbulent viscosity, μ_t, in equation (3) was obtained from the standard k-ε model of turbulence.

Boundary Conditions

Because of the symmetry, the mass flow rate and the gradients of dependent variables were specified as zero at the two circumferential boundaries.

Inlet.-- In the lower domain, the axial velocity at the inlet of the prediffuser was prescribed according to the measured data. Inlet radial and circumferential velocities were assumed to be zero. The inlet turbulence intensity was taken as 10%. The inlet turbulent energy dissipation was calculated from

$$\varepsilon = [C_D^{0.75} k^{1.5}]/\ell \tag{4}$$

where the length scale, ℓ, was the annular gap. The axial diffusion at the prediffuser inlet was ignored.

The interface between the domains was also the inlet to the upper domain. Values of all the dependent variables at the inlet to the upper domain were determined from flow computations in the lower domain. The diffusion at the interface was neglected.

Walls.-- The wall function approach for turbulent flow was employed. This approach requires that the logarithmic velocity profile bridge the region between a wall and a near wall node on the outside of the viscous sublayer. Turbulence in the near wall region was in local equilibrium.

Outlet.-- The fluid leaves the upper domain through the annular gap between the combustor and the combustor casing. A constant static pressure was specified at this outlet. The axial diffusion at the outlet was ignored.

The interface between the domains was also the outlet to the lower domain. The static pressure at this outlet was determined from flow computations in the upper domain. The radial diffusion at the interface was neglected.

Solution Procedure

The governing equations for each dependent variable could be reduced to a single general form:

$$\nabla.(\rho\, V\phi + J_{\phi}) = S_{\phi} \qquad (5)$$

where ϕ represents the dependent variable, V is the velocity vector, J_{ϕ} is the diffusive flux vector ($-\Gamma_{\phi}\nabla\phi$) and S_{ϕ} is the volumetric source of ϕ. Integration of the generalized equation (5) over control volumes resulted in the finite difference equations of a general form. Convection-diffusion terms in the governing equations were discretized using the upwind scheme. The set of coupled nonlinear equations was solved implicitly in an iterative manner. Coupling between velocity and pressure fields was provided by a variant of the SIMPLE algorithm (ref. 3) called SIMPLEC.

The computational steps to implement the subdomain procedure can be described as follows:

(1) Prescribe a guess pressure distribution at the outlet of the lower domain (or the interface)
(2) Compute the flow field in the lower domain
(3) Compute the flow field in the upper domain. The flow solution in the lower domain provides boundary condition data at the inlet to the upper domain (or the interface).
(4) Return to step 2 with an updated guess for the pressure distribution at the interface obtained from the solution in the upper domain. Continue these trials until the pressure distribution at the interface no longer changes.

It was necessary to underrelax the changes in the pressure distribution at the interface. Underrelaxing prevented large differences between the successive updates of the pressure field at the interface which otherwise led to oscillations. In the present work, an underrelaxation value of 0.2 was used. The computations proceeded serially on a single CPU. Thus, at the end of computations in a domain, both geometric and flow field data were saved on disk files before computations were initiated for another domain. Each trial took approximately 120 flow iterations. The flow field calculated for an earlier trial served as the initial guess for the new trial. The flow field converged after 6 to 10 trials. Each trial took 6 to 8 CPU hours on a Sun Sparkstation 10 Model 30.

RESULTS AND DISCUSSIONS

Flow Field

The computed flow field at the midplane of the combustor/transition piece assembly (also in between the combustor support struts) is shown in Figure 6. The air in the prediffuser's outer region accelerates as it exits the prediffuser. Then, it turns almost 180 degrees to enter the bypass air holes on the combustor casing. This short-circuiting of the diffuser flow is referred to as the sink effect of the combustor bypass air holes on the flow field in the pre- and dump diffusers. Flow acceleration is detrimental to a diffuser's performance because the primary function of a diffuser is to diffuse or decelerate the flow.

The flow separates underneath the impingement sleeve close to the turbine inlet. Nearly half the distance between the prediffuser exit and the turbine inlet is occupied by the recirculating flow. The flow separates also in the lower dump diffuser at the tip of the prediffuser's outer wall and in the space between the combustor casing and the prediffuser's outer wall. However, the size and strength of these eddies are relatively small. All recirculating flows dissipate the energy received from the main flow, thus contributing to frictional losses.

The flow field at the midplane of the strut and also in between the combustor/transition piece assembly is shown in Figure 7. The combustor support strut completely blocks the prediffuser flow, which is then redirected in the circumferential direction. Thus, the flow in the pre- and dump diffusers is 3-D. The flow remains separated underneath the impingement sleeve near the turbine inlet.

Figures 8 and 9 show projections of velocity vectors on axial planes P1 and P2 identified in Figure 6. At plane P1 (figure 8), the support struts block a large portion of the flow area, and the impingement sleeve is nearly circular in cross-section. The fluid underneath the support struts turns azimuthally before joining the fluid flowing towards the impingement sleeve. Fluid velocity near the side panel (3 or 9 o'clock position) of the impingement sleeve is high while that near the outer panel (12 o'clock position) is relatively small. Thus, the outer region of the dump diffuser behaves as a large reservoir. At plane P2, the blockage due to the support strut is reduced, and the impingement sleeve is nearly rectangular in cross-section. The flow field at

plane P2, shown in Figure 9, is similar to that at plane P1, except that the fluid velocity near the side panel is even higher because of the smaller gap between the adjacent impingement sleeves.

Overall System Performance

Performance Parameters.-- At any plane the mass flow rate, $\dot{m}$ was obtained as

$$\dot{m} = \int \rho \, u \, dA = \rho \, \bar{u} \, A \tag{6}$$

where u is the velocity component perpendicular to the flow area.

The mass-averaged pressures at a plane were derived as

$$\bar{P} = \frac{1}{\dot{m}} \int P \rho \, u \, dA \tag{7}$$

and

$$\bar{p} = \frac{1}{\dot{m}} \int p \rho \, u \, dA \tag{8}$$

where P and p are the local total and static pressures, respectively.

The total pressure P at a point is related to the static pressure p at that point as

$$P = p + 0.5 \rho V^2 \tag{9}$$

where V is the total velocity at that point.

The wall static pressure recovery coefficient (C_p) and the total pressure loss coefficient (λ) are defined as

$$C_p = [p - \bar{p}_a]/h_d \tag{10}$$

and

$$\lambda_{a\text{-}c} = [\bar{P}_c - \bar{P}_a]/h_d \tag{11}$$

where h_d is the dynamic head at the prediffuser inlet $[\bar{P}_a - \bar{p}_a]$.

Prediffuser Wall Static Pressure Recovery.-- Figure 10 shows the static pressure recovery coefficients along the inner and outer walls of the prediffuser. The pressure increases linearly along the inner wall of the prediffuser, and a C_p of nearly 0.6 is reached at the prediffuser exit.

The prediffuser outer wall C_p is nearly zero owning to the flow acceleration at the prediffuser exit because of the sinkeffect.

Because the prediffuser flow is highly coupled with the flow in the dump diffuser, the wall pressure recovery coefficients may not appropriate performance parameters. The mass-averaged total pressure loss coefficients presented below provide a quantitative description of the prediffuser performance.

Total Pressure Loss.-- The mass-weighted total pressure loss coefficients in the diffuser systems are summarized in Table 1. The computations indicate that more than 1 dynamic head at the prediffuser inlet (or the compressor discharge) is lost in the diffusers. Approximately 80% of this loss occurs in the upper dump diffuser where the fluid must pass through the narrow gaps and pathways between the adjacent combustor/transition piece assemblies. The total pressure loss in the prediffuser is relatively small: only 3% of the total pressure loss in the diffusers. The remaining 17% of the pressure loss occurs in the lower dump diffuser.

Flow Uniformity around the Impingement Sleeve

Figure 11 shows the static pressure distributions along the impingement sleeve at 3 circumferential locations: 12 o'clock, 3 o'clock and 6 o'clock. The reference pressure in Figure 11 is the static pressure at a point on the 12 o'clock position. Figure 11 shows that the static pressure varies both along the length and the periphery of the sleeve. The pressure is highest at the 6 o'clock position and is lowest at the 3 o'clock position. At the 12 o'clock position, the pressure is nearly constant along the length of the sleeve, indicating that the outer most dump diffuser behaves as a plenum. At the 3 o'clock position (or the side panel), the pressure decreases along the length of the sleeve because of the increased venturi effect induced by a smaller space between adjacent sleeves. Three-D computations indicate reverse flow from the side panel. When the reverse flow occurs, the air exits into the dump diffuser through cooling holes on the impingement sleeve.

REFERENCES

1. Karki, K.C., Oechsle, V.L., and Mongia, H.C., "A Computational Procedure for Diffuser-Combustor Flow Interaction Analysis," ASME Paper No. 90-GT-35, 1990.
2. CFD2000 User Manual, Adaptive Research Corporation, Huntsville, Alabama, 1992.
3. Patankar, S.V., Numerical Heat Transfer and Fluid Flow, Hemisphere, 1980.

Table 1. Mass-Averaged Pressure Loss Coefficient

Prediffuser	0.04 (3%)
Dump Diffuser	
Lower Part	0.22 (19%)
Upper Part	0.93 (78%)
Total	1.19 (100%)

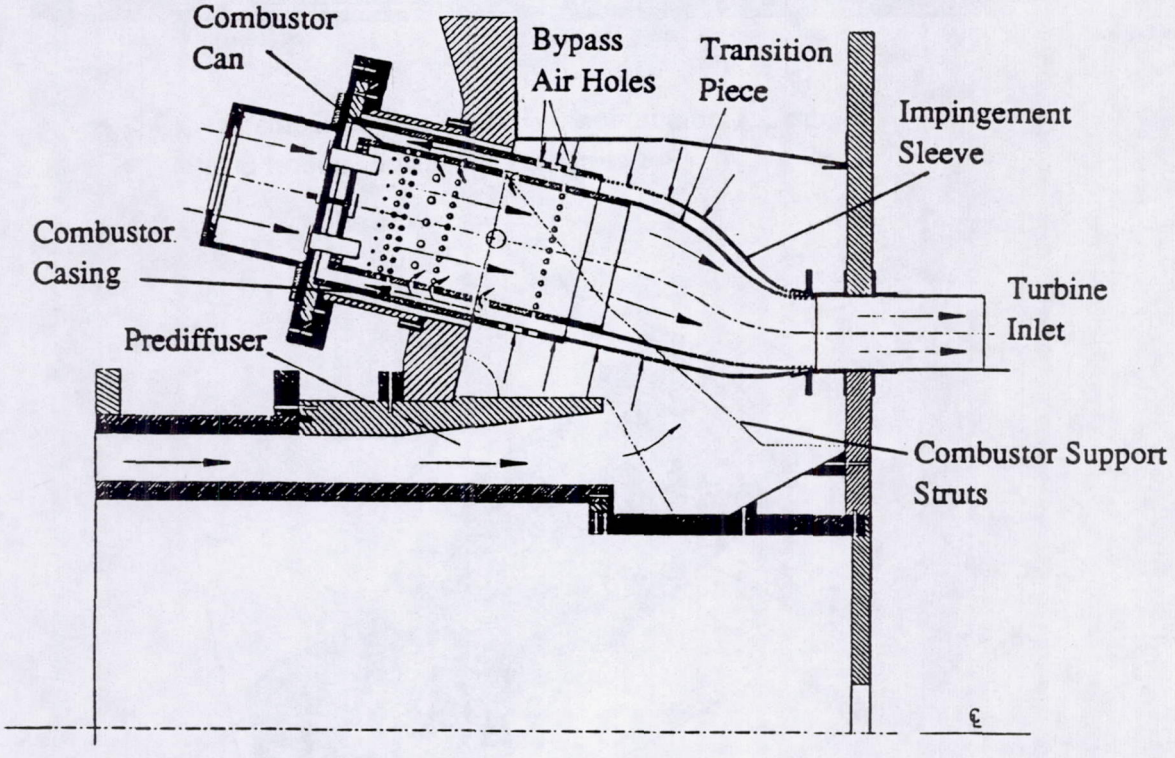

Figure 1. Airflow Path in the Compressor/Combustor Region of an Industrial Gas Turbine

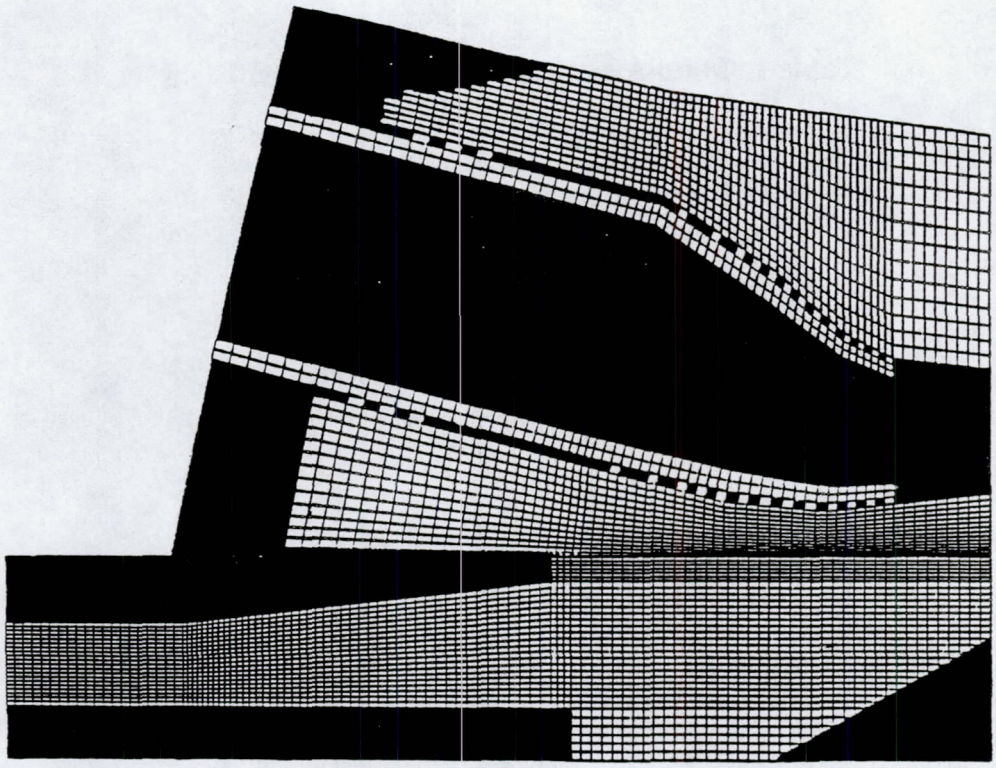

Figure 2. Computational Grid in the Two Domains
(Between the Combustor Support Struts)

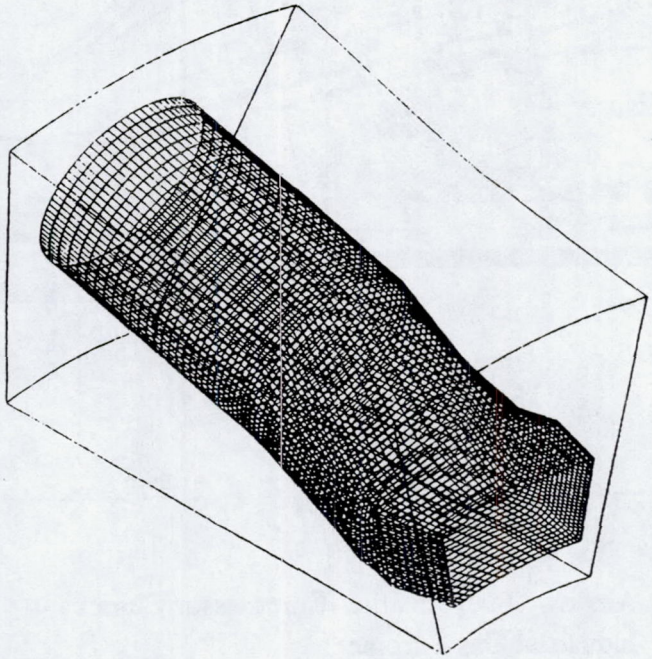

Figure 3. Computational Grid on the Surface of the Impingement Sleeve

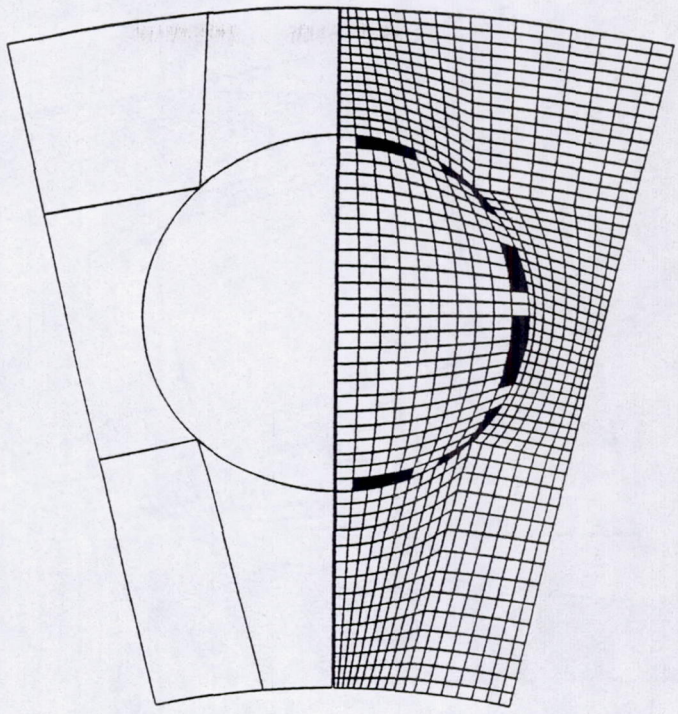

Figure 4. Upper Computational Domain Divided into 6 Subvolumes
(Azimuthal Plane Near the Combustor Can)

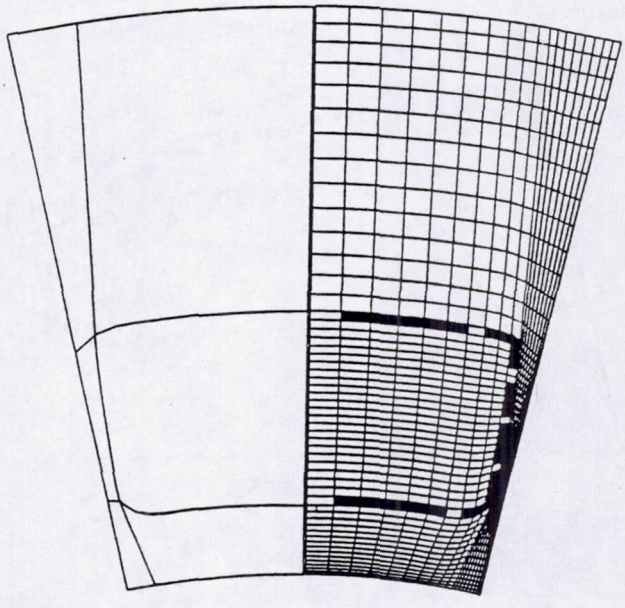

Figure 5. Upper Computational Domain Divided into 6 Subvolumes
(Azimuthal Plane Near the Turbine Inlet)

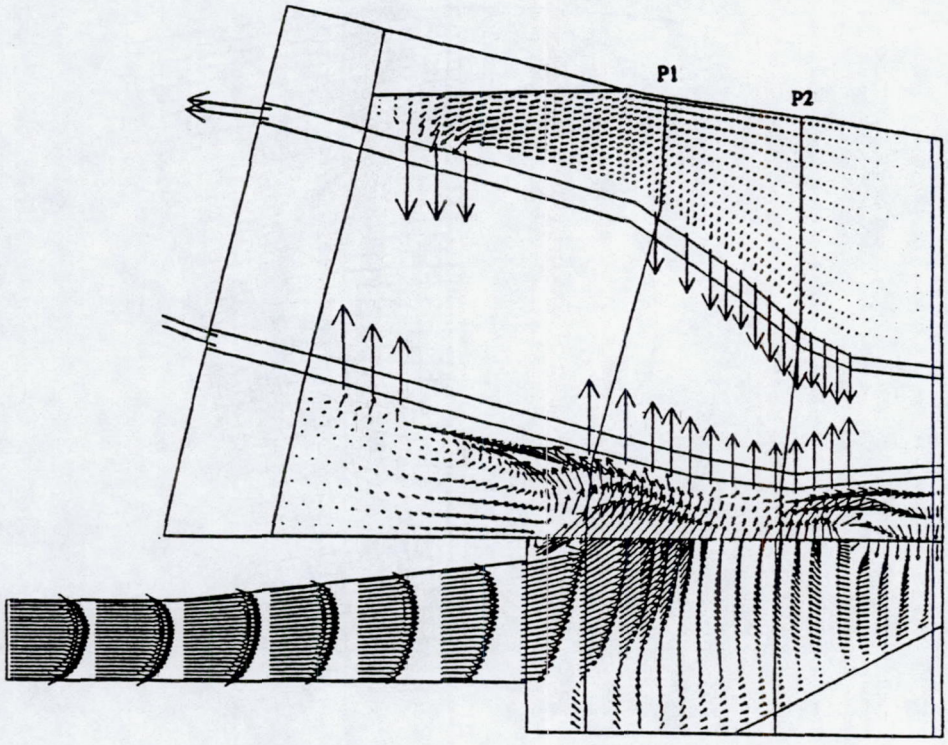

Figure 6. Velocity Vectors on a Longitudinal Plane
(Between the Combustor Support Struts)

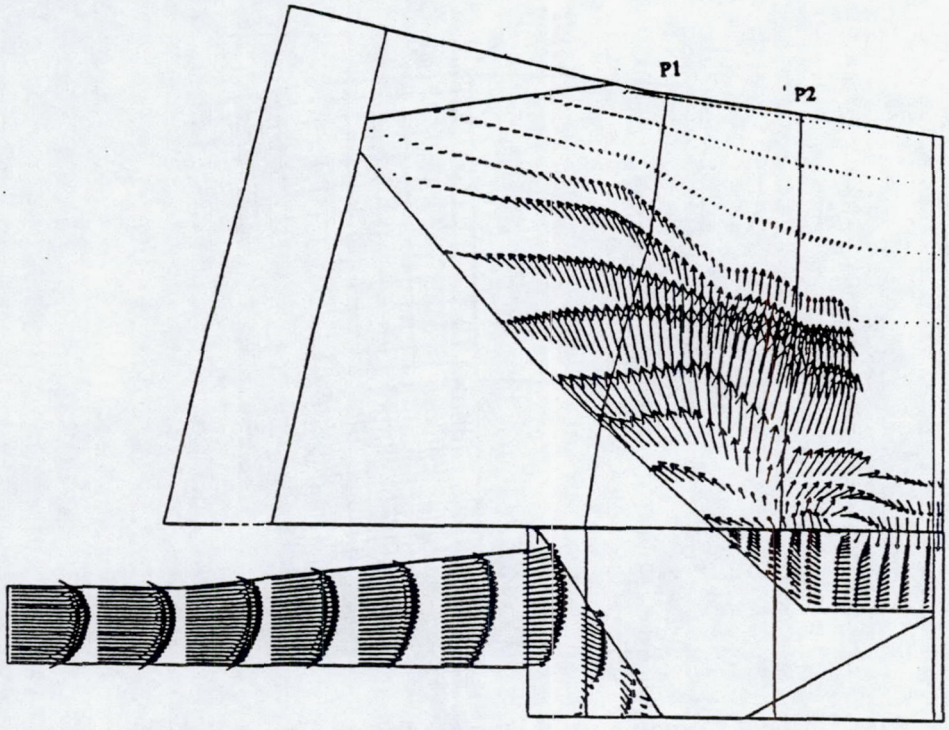

Figure 7. Velocity Vectors on a Longitudinal Plane
(Midplane of the Combustor/Transition Piece Assembly)

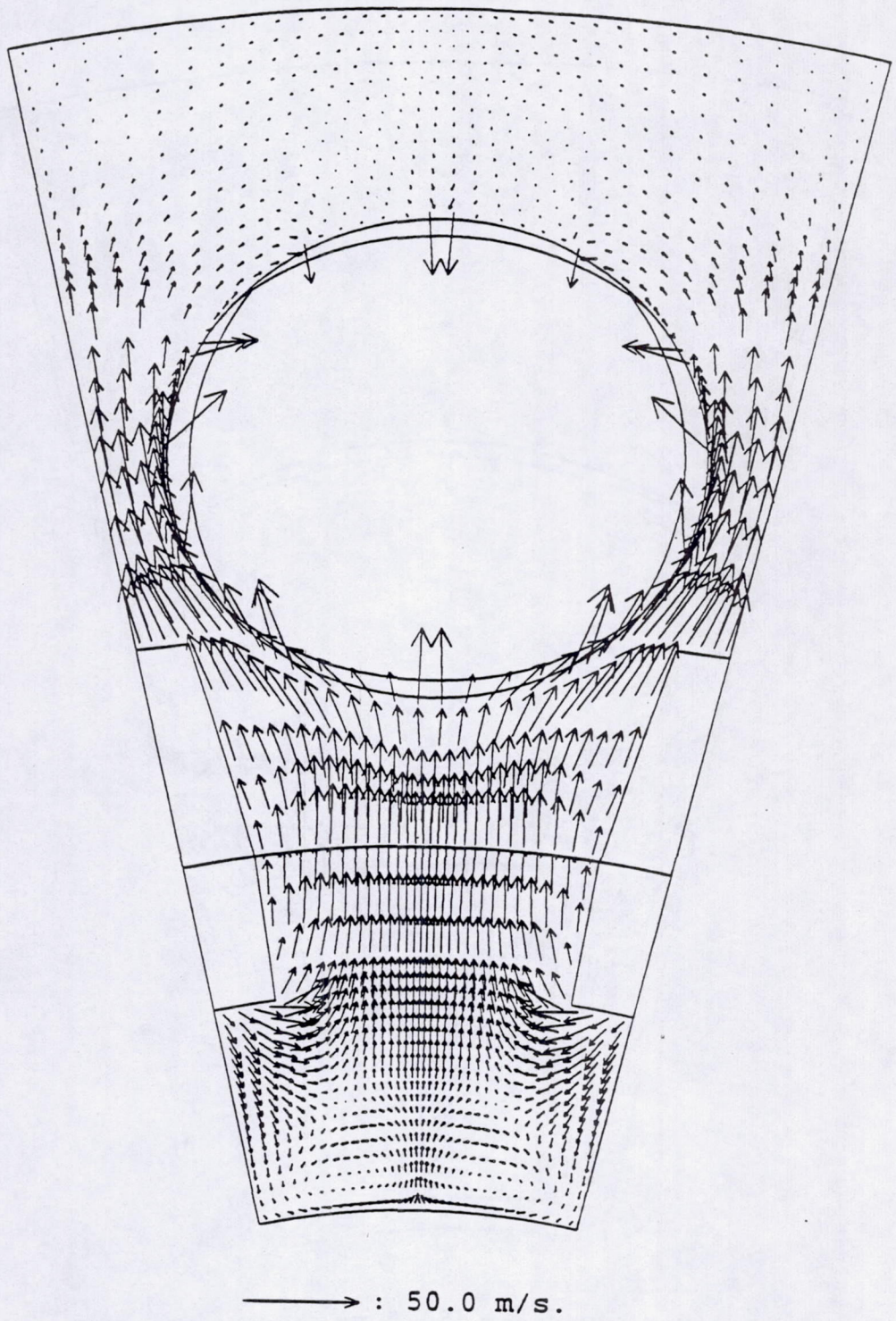

Figure 8. Velocity Vectors on an Azimuthal Plane
(Axial Location P1)

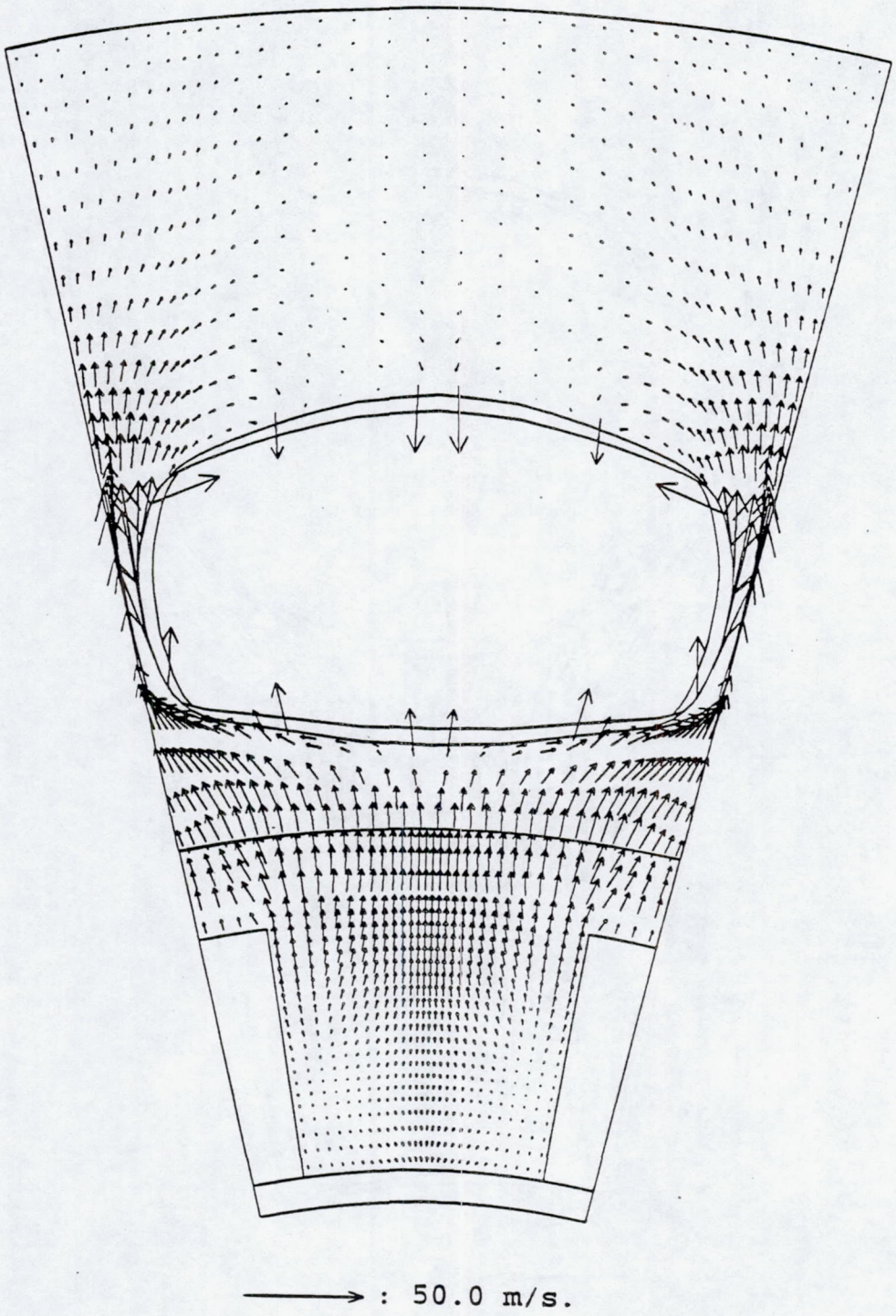

Figure 9. Velocity Vectors on an Azimuthal Plane
(Axial Location P2)

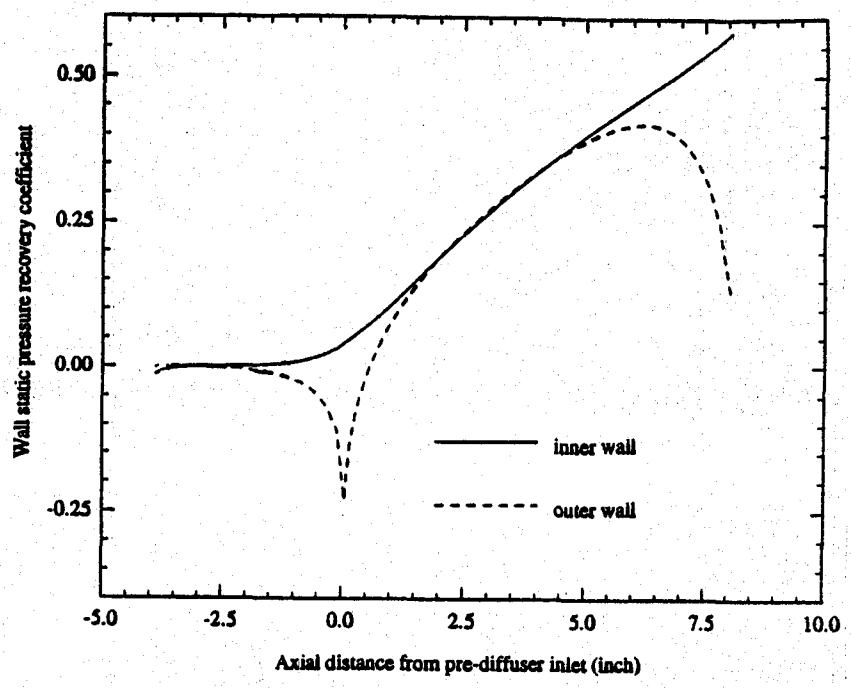

Figure 10. Prediffuser Wall Static Pressure Recovery Coefficients

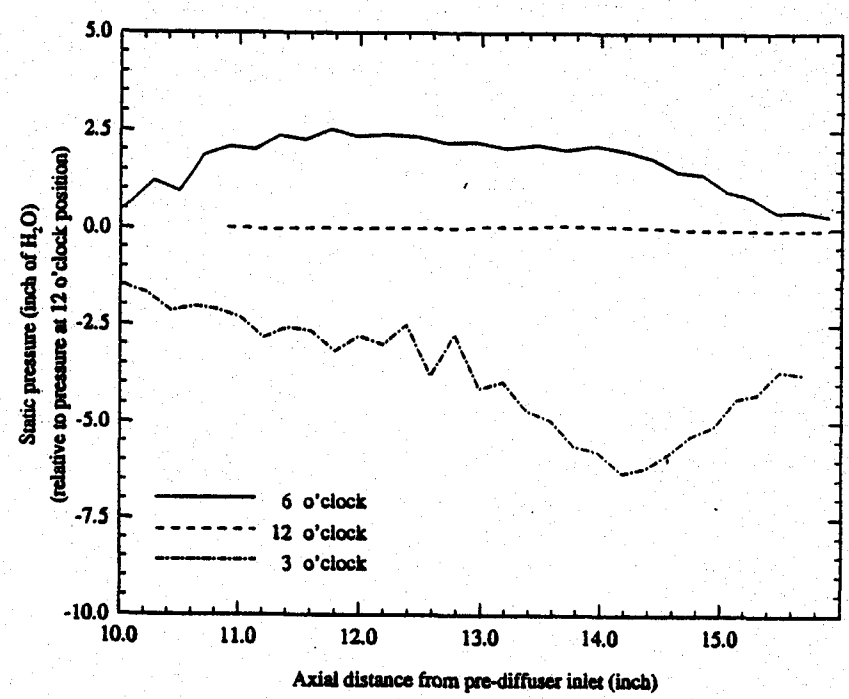

Figure 11. Static Pressure Distribution Along the Impingement Sleeve

Session
Five

Multiphase Flow

AN ANALYTIC STUDY OF A TWO-PHASE LAMINAR AIRFOIL IN SIMULATED HEAVY RAIN

by

Yu Kao Hsu
Professor of Mathematics
Division of Mathematics
University College of the University of Maine
Orono, Maine
May, 1993

Nomenclature

English letters

- a = indicates air
- c = chord length
- D = drop
- f = subscript, denotes fog or vapor state
- i = subscript, denotes incident
- L = characteristic length
- t = time
- U_2 = free stream velocity
- u,v = velocity components along x-y-directions respectively
- w = subscript, denotes water
- x,y = physical coordinates

Greek letters

- α = angle of attack, or non-dimensional ration = W_1/ρ_w
- β = droplet incident angle
- ρ = density of the fluid
- ρ_v = density of the vapor
- ρ_1 = density of the liquid
- μ = coefficient of viscosity
- δ = thickness of the boundary layers
- υ = kinematic coefficient of viscosity = μ/ρ

SUMMARY

A mathematical model for a two-phase flow laminar airfoil in simulated heavy rain has been established.

The set of non-linear partial differential equations has been converted into a set of finite difference equations; appropriate initial and boundary conditions are provided. The numerical results are compared with the experimental measurements. They show good agreement in quality.

I. INTRODUCTION

This paper investigates the rain effects to the airfoil during landing and take-off. When the heavy rain hits the airfoil, the fine water drops near to the wing surface form a liquid film while the water vapor above the wing surface establishes a gaseous fog. The former is in liquid state, the latter is in gaseous state. This is the so-called two-phase phenomenon. The thin liquid film close to the wing surface usually forms a laminar boundary layer. However, the heavy rain fall may cause a premature turbulent boundary layer. That is, the heavy rain effects may cause the laminar boundary layer transit into turbulent boundary layer. As a result, the lift is appreciably decreased, while the drag is considerably increased. In a a more serious situation, the decrease in lift and increase in drag may develop into wind shear which causes an airplane catastrophe involving loss of human life and property damage. This important knowledge should keep the pilot well-informed as a precaution of flight safety. A variety of experimental and analytic methods used to investigate the heavy rain effects on airfoil may be referred to in previous works, notably references # 1 through # 13. This paper has established a mathematical model for the airfoil under the simulated heavy rain. The said mathematical model consists of a set of non-linear partial differential equations for which a numerical solution has been obtained. A comparison between theory and experiment has been made and will shed some light on flight safety.

II. FORMULATION

As in the following figure, the two-phase-flow around an airfoil is clearly

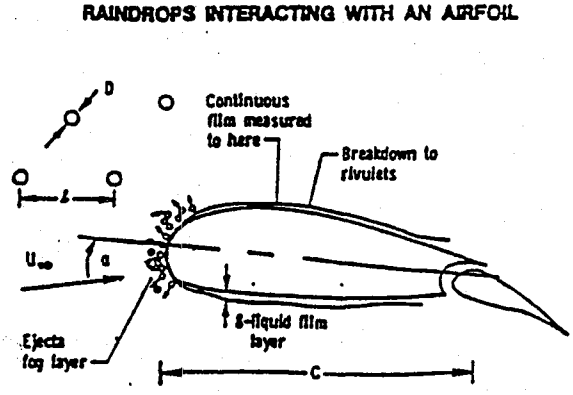

FIGURE(1)

described. To simplify the problem the following assumptions are made:

1. The fluid flow is non-steady, viscous, and incompressible.
2. There is laminar boundary in the flow region.
3. The airfoil is represented by a flat plate. The physical coordinates are shown in Figure (2).

For a two-dimensional, nonsteady two-phase flow, we obtain the following sets of fundamental equations under boundary layer approximation: For the liquid phase

Equation of Continuity: $$\frac{\partial u}{\partial x}+\frac{\partial v}{\partial y} = \frac{W_L}{\rho_\omega}\frac{V_1 \sin\beta}{\delta} \quad \ldots\ldots \quad (1)$$

Equation of Momentum : $$\frac{\partial u}{\partial t} + u\frac{\partial u}{\partial x}+ v\frac{\partial u}{\partial y} = \frac{\mu}{\rho_w}\frac{\partial^2 u}{\partial y^2}\frac{W_L V_1^2 \sin\beta\cos\beta}{\rho_w \delta} \quad \ldots\ldots \quad (2)$$

Film thickness: $$\delta = 5\sqrt{\upsilon x / U_2} \quad \ldots\ldots \quad (3)$$

For the fog phase Equation of Continuity: $$\frac{\partial u}{\partial x} + \frac{\partial v}{\partial y} = 0 \quad \ldots\ldots \quad (4)$$

Equation of Momentum: $$\frac{\partial u}{\partial \tau} + u\frac{\partial u}{\partial x} + v\frac{\partial u}{\partial y} = \frac{\mu}{\rho_f}\frac{\partial^2 u}{\partial y^2} \quad \ldots\ldots \quad (5)$$

The initial conditions are:

at $t = 0, u = U_2(x,O), V = 0, \delta = 0$ $\ldots\ldots$ (6)

The boundary conditions are:

$y = 0$, for the liquid phase
$u = 0, v = 0$ (no slip condition) $\}$ $\ldots\ldots$ (7)

at $y = \delta$ (liquid-fog interface)

$(u)1 = (u)f \qquad (v)1 = (v)f$

$$\left(\mu\frac{\partial u}{\partial y}\right)_1 = \left(\mu\frac{\partial u}{\partial y}\right)_f$$

$\}$ $\ldots\ldots$ (8)

In other words, U, V, and $\partial u/\partial y$ for both liquid and fog must be compatible at the interface, as $y \to \infty$ (for the fog phase), $u = U(x,t)$ ... ... (9)

III. NON-DIMENSIONALIZATION

In order to non-dimensionalize the set of fundamental equations, we introduce the following:

$$\left.\begin{aligned} \bar{x} &= \frac{x}{L} \quad \bar{y} = \frac{y}{L} \quad \bar{u} = \frac{u}{U_c} \quad \bar{v} = \frac{v}{U_c} \\ \bar{\delta} &= \frac{\delta}{L} \quad \tau = \frac{U_c T}{L} \quad \bar{v_i} = \frac{V_i}{U_c} \end{aligned}\right\} \quad \ldots \ldots \qquad (10)$$

where Uc is the reference velocity, and L is the chord length of the airfoil. Substituting the above relations into Equations (1), (2), (3), (4) and (5), and omitting the bar notations, we obtain:

$$\frac{\partial u}{\partial x} + \frac{\partial v}{\partial y} = \frac{W_1}{\rho_w} \frac{V_1}{\delta} \sin\beta \quad \ldots \ldots \qquad (11)$$

$$\frac{\partial u}{\partial \tau} + u\frac{\partial u}{\partial x} + v\frac{\partial u}{\partial y} = \frac{1}{(RN)_1} \frac{\partial^2 u}{\partial y^2} + \frac{W_\ell}{\rho_w} \frac{V_i^2 \sin\beta\cos\beta}{\delta} \quad \ldots \ldots \qquad (12)$$

$$\delta = 5\sqrt{\frac{\nu x}{U_2}} / L \qquad \ldots \ldots \qquad (13)$$

In Equ. (12), W_1 has the dimension of M/L^3, so does the density ρ. W_1/ρ_W is a non-dimensional quantity, where $(RN)_1 = \rho_W U_2 x/\mu$ Reynolds number of the liquid water. We let $\alpha = W_1/\rho_W$ = non-dimensional ratio of the liquid water content to the water density.

For the fog phase

Equation of Continuity:

$$\frac{\partial u}{\partial x} + \frac{\partial v}{\partial y} = 0 \ \ldots \ldots \qquad (14)$$

Equation of momentum

$$\frac{\partial u}{\partial \tau} + u\frac{\partial u}{\partial x} + v\frac{\partial u}{\partial y} = \frac{1}{(RN)_f}\frac{\partial^2 u}{\partial y^2} \ldots\ldots \quad (15)$$

where $(RN)_f = \frac{\rho_f U_2 L}{\mu}$ = Reynolds number of the fog.

The corresponding initial and boundary conditions are:

at $\tau = 0$, $u = U(x,o)$, $V = 0$

$\delta = 0$ } . . . . . (6.a)

for the liquid phase, at $y = 0$, $u = v = o$ (No slip condition) . . . . . (7.a)

at $y = \delta/L$ (Liquid-vapor interface)

$(u)_1 = (u)_f \qquad (V)_1 = (V)_f$

$$\left(\mu\frac{\partial u}{\partial y}\right)_1 = \left(\mu\frac{\partial u}{\partial y}\right)_f$$

} . . . . . (8.a)

As $y \to \infty$ $u = U(x,\tau)$ . . . . . (9.a)

IV. FINITE DIFFERENCE EQUATIONS

The previously derived set of non-dimensional partial differential equations can be transformed into the finite difference equations in the following manner: An explicit method is used. Let U', V' and δ' denote the values of U, V and δ at the end of a time-step. Then the appropriate sets of finite difference equations are:

For the liquid

Equation of Continuity:

$$\frac{U'_{i,j} - U'_{i-1,j}}{\Delta x} + \frac{V'_{i,j} - V'_{i,j-1}}{\Delta y} = \alpha \frac{V_1}{\delta'_{i,j}} \sin\beta \ldots\ldots \quad (11.a)$$

Equation of Momentum:

$$\frac{U'_{ij} - U_{ij}}{\Delta\tau} + U_{ij} \frac{(U'_{ij} - U'_{i-1,j})}{\Delta x} + V_{ij} \frac{(U_{i,j+1} - U_{ij})}{\Delta y}$$

$$= \frac{1}{(RN)_1} \frac{(U_{i,j+1} - 2U_{ij} + U_{i,j-1})}{(\Delta y)^2} + \frac{\alpha}{\delta'_{ij}} V_1^2 \sin\beta\cos\beta \ldots\ldots \quad (12.a)$$

Film thickness:

$$\delta'_{i,j} = 5 \sqrt{\frac{\nu I \Delta x}{U_2}} / L \ldots\ldots \quad (13.a)$$

For the fog

Equation of Continuity:

$$\frac{U'_{i,j} - U'_{i-1,j}}{\Delta x} + \frac{V'_{i,j} - V'_{i,j-1}}{\Delta y} = 0 \ldots\ldots \quad (14.a)$$

Equation of Momentum:

$$\frac{U'_{i,j} - U_{i,j}}{\Delta\tau} + U_{i,j} \frac{(U_{i,j} - U_{i-1,j})}{\Delta x} + V_{i,j} \frac{(U_{i,j+1} - U_{i,j})}{\Delta y}$$

$$= \frac{1}{(RN)_f} \frac{(U_{i,j+1} - 2U_{i,j} + U_{i,j-1})}{(\Delta y)^2} \ldots\ldots\ldots \quad (15.a)$$

The boundary conditions are

$$\left.\begin{array}{llll} \text{at} & \tau = 0, & u = U_2, & v = 0 \\ & & \zeta = 0 & \end{array}\right\} \ldots\ldots \quad (16)$$

for the liquid phase, y = 0, U=V=0 . . . . . (17) . At the interface $0 < x < L$, $O < y < \delta_{max}$. We choose integers M_x and M_y such that

$$\left.\begin{aligned} (V_{o,j})_1 &= (V_{o,j})_f \quad (V_{M_x,j})_1 = (V_{M_x,j})_f \\ (V_{i,o})_1 &= (V_{i,o})_f \quad (V_{i,M_y})_1 = (V_{i,M_y})_f \end{aligned}\right\} \ldots\ldots\ldots \quad (16.a)$$

$$\left.\begin{aligned} (U_{o,j})_1 &= (U_{o,j})_f \quad (U_{M_x,j})_1 = (U_{M_x,j})_f \\ (U_{i,o})_1 &= (U_{i,o})_f \quad (U_{i,M_y})_1 = (U_{i,M_y})_f \end{aligned}\right\} \ldots\ldots\ldots \quad (16.b)$$

All the points denoted by Equations (16.a) and (16.b) are boundary points at which the values of U and V are already known. Furthermore the shearing force of the interface is denoted by the following relation

$$\left[\mu \frac{(U_{i,j+1} - U_{i,j})}{\Delta y}\right]_1 = \left[\mu \frac{(U_{i,j+1} - U_{i,j})}{\Delta y}\right]_f \ldots\ldots \quad (17.a)$$

V. THE STABILITY OF THE FINITE-DIFFERENCE EQUATIONS

Since an explicit procedure is used, we wish to know the largest time-step consistent with stability. Equation of continuity is ignored since $\Delta\tau$ does not appear in it. The general terms of the Fourier expansion for U at a time arbitrarily called $\tau=0$ are both $e^{i\alpha x}\, e^{i\beta y}$, apart from a constant (Here $i = \sqrt{-1}$). At a time τ later, these terms will become

$$U: \psi(\tau)\, e^{i\alpha x} \cdot e^{i\beta y}$$

Substituting the above into Equation (12.a), regarding the coefficients U and V as constants over any one step, and denoting the values after time-step by ψ' gives

$$\frac{\psi'-\psi}{\Delta\tau} + U\frac{\psi\left[1-e^{i\alpha\Delta x}\right]}{\Delta x} + V\frac{\psi\left[e^{i\beta\Delta y}-1\right]}{\Delta y}$$

$$= \frac{1}{RN}\,\frac{2\psi(\tau)[\cos(\beta\Delta y)-1]}{(\Delta y)^2} + \frac{\alpha}{\delta_{i,j}}\, V_i^2\, \sin\beta\cos\beta e^{-i(\alpha x+\beta y)} \quad (18)$$

Through a very tedious algebraic manipulation, there obtains the criterion of stability:

$$U\frac{\Delta\tau}{\Delta x} - V\frac{\Delta\tau}{\Delta y} + \frac{2\Delta\tau}{R_N(\Delta y)^2} \leq 1 \quad \ldots\ldots\ldots \qquad (19)$$

In the present research, R_N, the Reynolds number, is in the order of 10^6. Equation (19) follows automatically. However, the coefficients U and V, treated as constants over any one time-step, will vary from one time-step to the next in a manner which cannot be predicted as a priori. That is the maximum permissible time-step consistent with stability and is itself variable, but its value can always be checked during computation if necessary.

VI. CALCULATION OF LIFT COEFFICIENT

According to Glauert, the lift coefficient is given by

$$C_L = \pi(\alpha+\varepsilon_o) \qquad \ldots\ldots \qquad (20)$$

where d is the angle of attack,

$$\varepsilon_o = \int_o^1 \left(\frac{y}{c}\right) f_1\left(\frac{x}{c}\right) d\left(\frac{x}{c}\right) \qquad \ldots\ldots \qquad (21)$$

$$\text{and } f_1(x/c) = \frac{1}{\pi\left(1-\frac{x}{c}\right)\sqrt{\frac{x}{c}\left(1-\frac{x}{c}\right)}} \qquad \ldots\ldots \qquad (22)$$

The relationship between (x/c) and f (x/c) is :

(x/c)	0.025	0.05	0.10	0.20	0.30	0.40
$f_1(x/c)$	2.090	1.54	1.18	1.00	0.99	1.08
(x/c)	0.50	0.60	0.70	0.80	0.90	0.95
$f_1(x/c)$	1.27	1.62	2.31	3.98	10.60	29.20

For Wortmann airfoil, the value of (y/c) for each (x/c) can be found. The integration can be performed easily. However, for flat plate airfoil, $\varepsilon_o = O$, the lift coefficent reduces to $C_L = \pi\alpha$.

VII. CALCULATION OF DRAG COEFFICIENT

A body of buff form, particularly if it has sharp edges like a flat plate (which is the case here) will shed strong vortices and will have a large form drag. As a first approximation, the form drag coefficient may be written

$$C_D = 2.83\left(\frac{h}{b}\right)\cdot\frac{U}{V} = 0.281\,\frac{K}{bV} \quad \cdots \cdots \qquad (23)$$

where $K = 2\sqrt{2}\ a\ U$, is the strength of each point vertex, the so- called Karman vortex street, a is the distance separating the successive vortices of each row, U is the induced velocity, h is the distance between the two rows, i.e. the breadth of the street. A sketch for von Karman vortex street is given as follows :

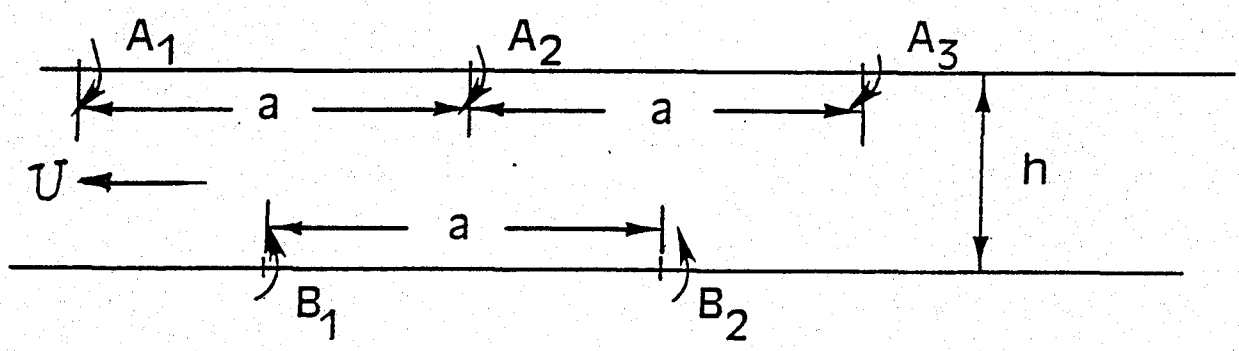

Two Vortex Rows

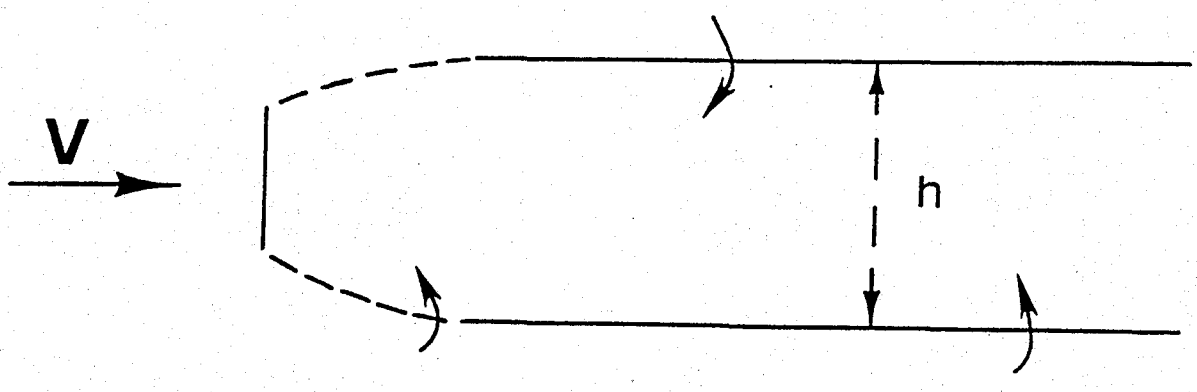

Von Karman Vortex Street

Figure (3).

The skin frictional drag coefficient of a flat plate is given by a classical formula:

$$Cd = 1.328/\sqrt{RN} \quad \ldots \ldots \quad (24)$$

The historical results and the current computation are tabulated as follows:

Reynolds No.	1.14×10^4	0.57×10^4	3×10^5	10^6	7×10^6
Experimental Measurement			0.0057	0.0047	0.0035
Karman			0.0058	0.0045	0.0031
Blasius			0.0024	0.0013	0.0005
Current Computation	0.0_3124 (Dry)	0.0176 (Wet)			

As shown in the above table, the drag coefficient of the airfoil with rain is higher than that without rain. The computed results are much lower than those measured by Hansman(in references 5,and 6).The reason for this is that the over-simplified mathematical model of an airfoil by a flat plate does not cover the physical reality of a true airfoil which has proper thickness and suitable chord length.

Also the premature transition of laminar flow into turbulent flow may cause higher drag coefficient . This possible turbulent phenomenon is not covered due to our previous assumptions.

The superposition of form drag to the skin frictional drag should improve the agreement in quantity with the experimental measurement. However, the analytic determination of form drag in Eq.(23) remains to be a difficult task for further investigation.

VIII Conclusion and Discussion

The set of finite difference equations has been converted into Fortran language, and a numerical solution is obtained. The complexity and computation time are far beyond the investigator's anticipation. For the numerical results it was found that there is decrease in lift and increase in drag due to the heavy rain effects. The reason for this is that the heavy rain causes roughness on the wet surface of the airfoil. A comparison of the present numerical calculation with Hansman's (6) experimental measurement is shown in Figure (5). According to Hansman, the Wortmann section had the greatest lift degradation: nearly 25%. The computed decrease in lift and increase in drag are both lower than that of the experimental measurements. The reason may be that the over-simplified mathematical model could not cover the physical reality, such as the premature boundary layer transition near the leading edge of the airfoil and the three-dimensional effects.

The laminar layer thickness of both the liquid film and fog is shown in Figure (6). The velocity profile near the surface of the airfoil is shown in Figure (4). It is evident that the U-component of the velocity near the surface of the airfoil is decreased due to the rain-effects.

It requires further investigation for a turbulence model and three-dimensional wing in order to accomplish perfect agreement between analytical investigation and experimental measurements.

IX. Acknowledgements

The mathematical formulation was completed in the summer of 1989 through a NASA Summer Faculty Fellowship at Langely Research Center, whose hospitality and financial aid is greatly appreciated. The preliminary calculation was done at the University of Maine with the aid of a Summer Faculty Research Award, for which I am very grateful to the Research Funds Committee at the University of Maine. The author would like to express his sincere gratitude to Dr. Charles MacRoy, Dr. Kay Storch and Professor Stephen Hyatt for their encouragement and endorsement of this research. The final draft was completed in May, 1993 during the author's visit to Princeton University. The hospitality shown there by Professor Gary Brown, Professor Antony Jameson, Dr. Timothy Baker and Professor Sau-Hai Lam is greatly appreciated. Thanks are due also to Betty Adam and Henry MacAdam for typing this paper.

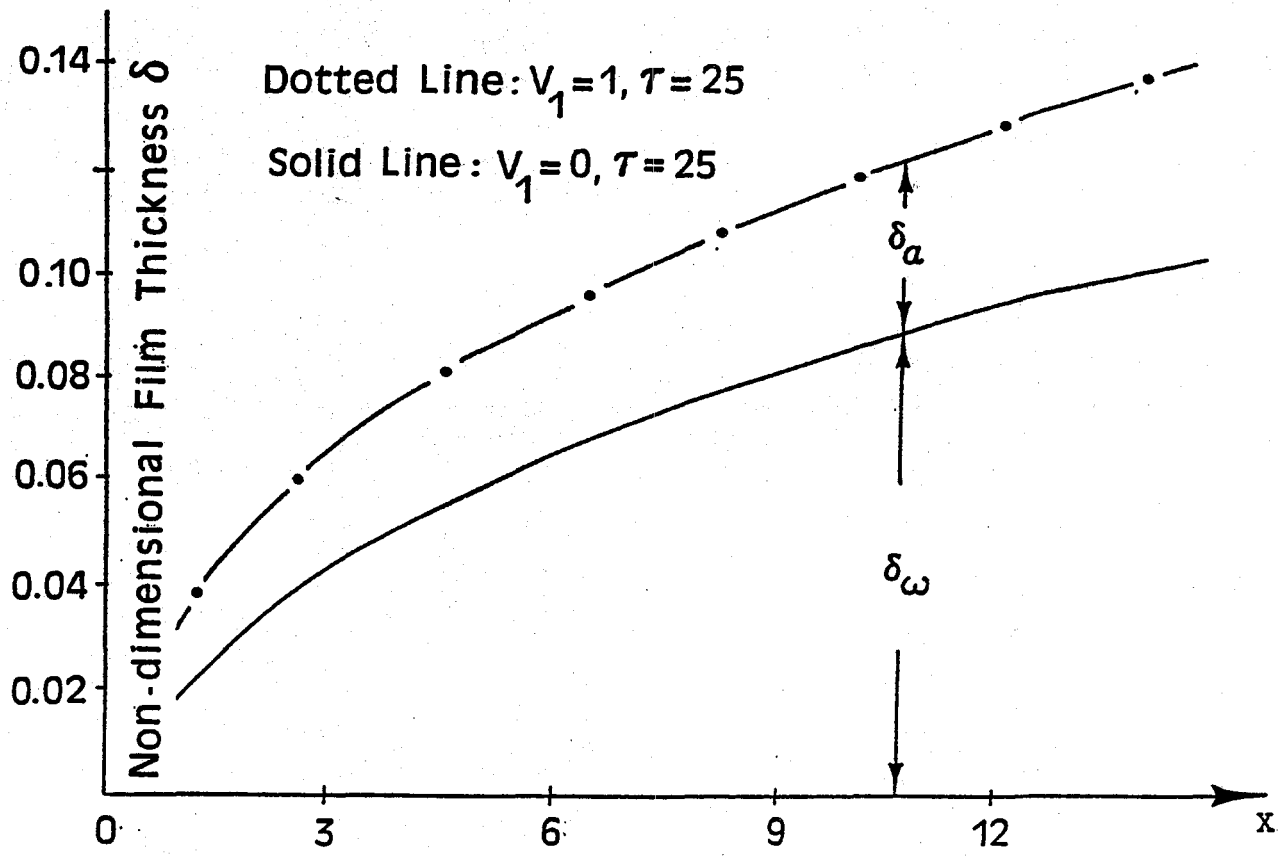

Figure (6). X-chordwise Length.

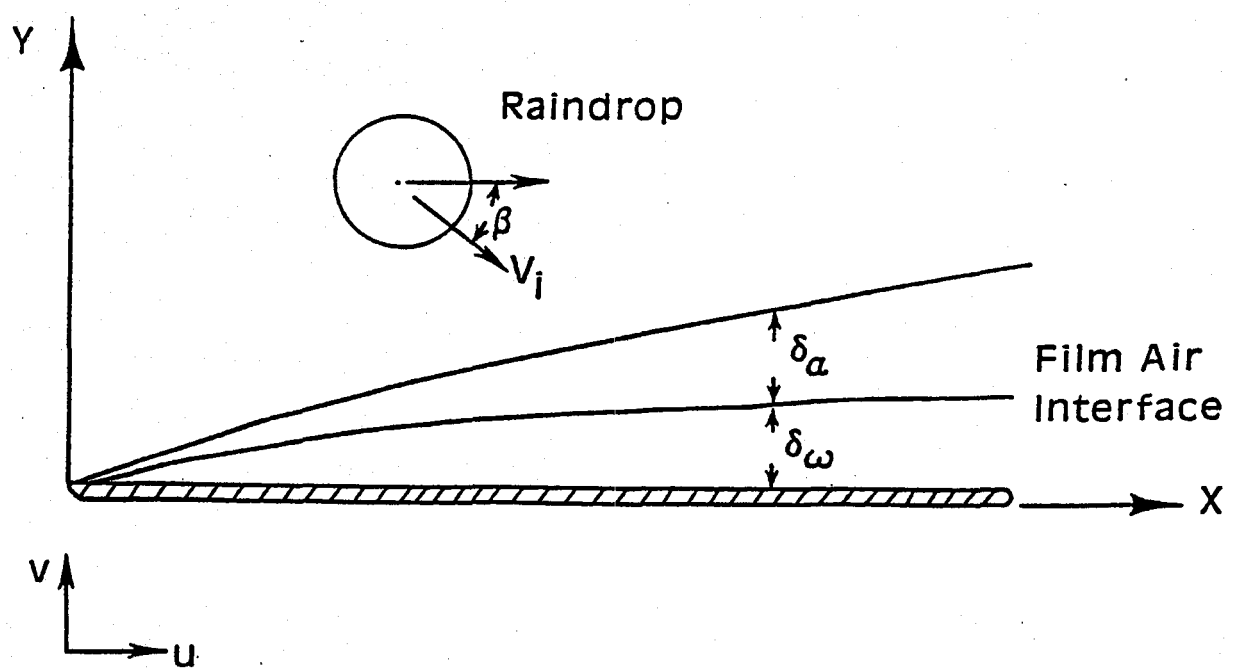

Figure (2). Physical Coordinates of Boundary Layer.

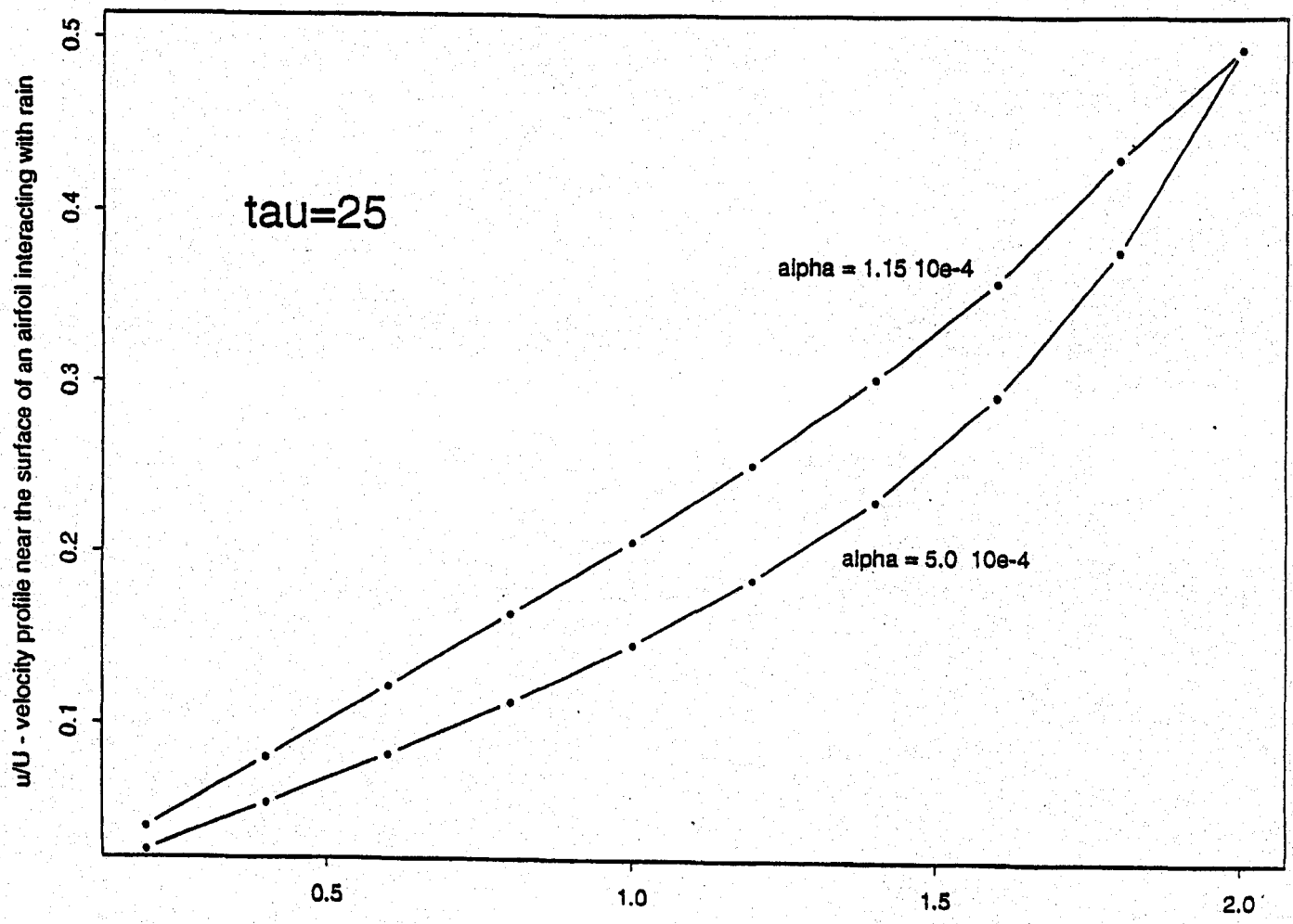

Figure(4) u/U versus y

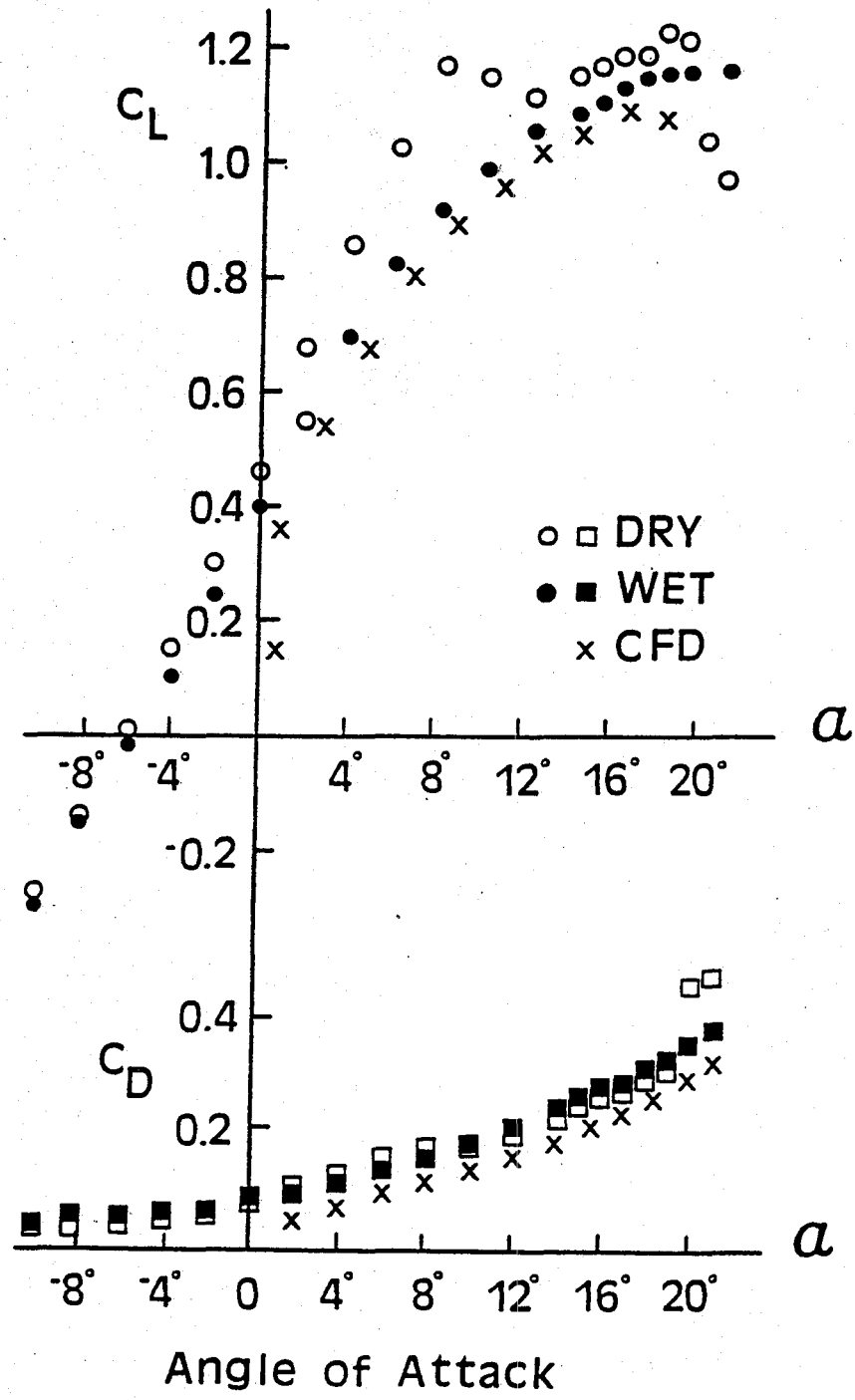

Figure (5). Lift and drag coefficients vs angle of attack for the Wortmann FX67-K170 airfoil in dry and wet conditions.

BIBLIOGRAPHY

1. Rhode, R.V.: Some Effects of Rain Fall on Flight of Airplanes and on Instrument Indications. NACA TN No. 803, April, 1941.

2. Bergrun, N.R.: A Method for Numerically Calculating the Area and Distribution of Water Impingement on the Leading Edge of an Airfoil in a Cloud. NACA TN No. 1397, August 1947.

3. Roys, G.P.; and Kessler, E.: Measurements by Aircraft of Condensed Water in Great Plains Thunderstorms. National Severe Storms Laboratory Publication TN-49-NSSP-19, 1966.

4. Luers, J.K.; and Haines, P.A.: The Effect of Heavy Rain on Wind Shear Attributed Accidents. AIAA paper # 81-0390, January 12-15, 1981.

5. Haines, P.A.; and Luers, J.K.: Aerodynamic Penalties of Heavy Rain on a Landing Aircraft. NASA Contact Report No. 156885, July, 1982.

6. Hansman, R.J.; and Barsotti, M.F.: Surface Wetting Effects on a Laminar Flow Airfoil in SimulatedHeavy Rain. Journal of Aircraft Vol. 22, No. 12, Dec. 1985.

7. Hansman, R.J.; and Craig, A.P. "Low Reynolds Number Tests of NACA 64-210, NACA 0012, and Wortmann FX67-K170 Airfoils in Rain. Journal of Aircraft Vol. 24, No. 8, August, 1987.

8. Marchman III, J.F.; Robertson, E.A.; and Emsley, H.T.: Rain Effect of Low Reynolds Number. Journal of Aircraft Vol. 24, No. 9, Sept. 1987.

9. Dunhamm, R.E.: The Potential Influence of Rain on Airfoil Performance. Lecture presented at the von Karman Institute for Fluid Dynamics, February, 1987.

10. Dunham, R.E. Jr.; Bezos, G.M.; Gentry, C.L.; and Melson, W.E. Two-Dimensional Wind Tunnel Tests of a Transport Type Airfoil in a Water Spray. AIAA-85-0258, January, 1985.

11. Bezos, G.M.; Campbell, B.A.; and Melson, W.E.: The Development of a Capability for Aerodynamic Testing of Large-Scale Wing Sections in a Simulated Natural Rain Environment. AIAA paper - 89-0762, January, 1989.

12. Henry, R.; Pasemehmetoglu, K.; Eno, B.; and Anderson, L. A von Karman Integral Approach to a Two-Phase Boundary Layer Problem. AIAA Paper--87-0256, January, 1987.

13. Bilanin, A.J.: Scaling Laws for Test of High Lift Airfoils Under Heavy Rainfall. AIAA paper--85-0257, January, 1985.

14. Bilanin, A.J.: Feasibility of Predicting Performance Degradation of Airfoils in Heavy Rain. Report under contract No. NASI-18302 for NASA Langley Research Center, April, 1989.

TRANSIENT STUDIES OF CAPILLARY-INDUCED FLOW

M. K. Reagan*
W. J. Bowman**
Air Force Institutue of Technology
AFIT/ENY
Wright-Patterson AFB OH 45433

SUMMARY

This paper presents the numerical and experimental results of a study performed on the transient rise of fluid in a capillary tube. The capillary tube problem provides an excellent mechanism from which to launch an investigation into the transient flow of a fluid in a porous wick structure where capillary forces must balance both adverse gravitational effects and frictional losses. For the study, a capillary tube, initially charged with a small volume of water, was lowered into a pool of water. The behavior of the column of fluid during the transient that followed as more water entered the tube from the pool was both numerically and experimentally studied.

INTRODUCTION

A capillary tube, initially charged with a small volume of distilled water, is lowered into a pool of distilled water to initiate the experiment. The amount of time required for the water within the capillary tube to reach steady-state, the final height of the column at steady-state and the behavior of the column during the transient were all sought. The solution to the problem will be accomplished both numerically and experimentally. The numerical solution will be discussed first. The experimental portion will be used to provide data to verify the numerical solution.

THEORY AND NUMERICAL SOLUTION

One dimensional, unsteady continuity and momentum equations were derived for the capillary tube flow problem. The energy equation was not used since this problem had no measurable transfer of energy taking place (ie., no external heat addition or subtraction).

Consider the cylindrical control volume seen in Figure 1. This control volume encompasses all of the fluid within the capillary structure at any given time. The lower boundary is the only one which mass can flow across and is the interface between the pool of fluid and the bottom of the tube. The upper boundary of the control volume is the bottom of the meniscus which is formed due to surface tension effects between the water in the tube and the tube wall. No mass transfer is allowed to occur across the meniscus. The distance between the bottom of the control volume and the bottom of the meniscus is defined as h. The unsteady, one-dimensional continuity equation applied to this control volume, assuming a constant density fluid, is

$$\frac{dh}{dt} = V_l \tag{1}$$

* Doctoral Candidate
** Associate Professor of Aerospace Engineering

where V_l is the velocity of water entering the bottom of the tube.

Figure 2 depicts the same control volume with the appropriate forces and momentum fluxes present. The capillary force ($\sigma 2\pi r \cos\theta$), is depicted as a single force acting on the top of the control volume. This assumption results partly from the work done by Swanson and Herdt (1:434-441), who investigated the evaporating meniscus in a capillary tube, and partly from observations from this work on the behavior of the meniscus during the early portion of the transient. Swanson and Herdt's numerical study showed that the local capillary pressure remained constant for varying degrees of superheat and that the mean curvature of the meniscus asymptotically approached that of a hemispherical meniscus. In the experimental portion of this study, a capillary tube with a small volume of water was lowered into a pool of water *just* until the transient began (ie., fluid began climbing up the capillary tube). From observations of the very early portion of this transient, the column of fluid began to rise immediately after coming in contact with the fluid in the reservoir. This implied that the capillary force was present at the onset of the transient. Close observation of the meniscus revealed that it did not appreciably change shape throughout the entire transient, implying that the magnitude of the capillary force remained relatively constant. Based on these observations, the capillary force was therefore treated as a constant that formed instantaneously at time equal to zero.

The unsteady, one-dimensional momentum equation for the control volume in Figure 2 yields,

$$\frac{d}{dt}(hV_l) - V_l^2 + hg + \frac{2\tau h}{\rho_l r} - \frac{2\sigma\cos\theta}{\rho_l r} = 0 \qquad (2)$$

Where g is the acceleration due to gravity, ρ_l is the water density, σ is the water surface tension, θ is the contact angle between the fluid and the tube wall, and r is the capillary tube radius. The shear stress, τ, represents the overall shear between the fluid and the capillary tube. Note at steady-state conditions, the time derivative, velocity and shear stress go to zero, and Eq. [2] reduces to,

$$h = \frac{2\sigma\cos\theta}{\rho_l g r} \qquad (3)$$

which is the classic equation given in any physics text, describing the steady-state height rise of a column of water in a capillary tube (2:30).

Combining Eqs. [1] and [2] into the matrix form required by the time integrating scheme used in this work (3:357-372) yields the following forms for the U and F matrices,

$$U = \begin{bmatrix} h \\ hV_l \end{bmatrix}$$

$$F = \begin{bmatrix} V_l \\ V_l^2 - hg - \frac{2\tau h}{\rho_l r} + \frac{2\sigma\cos\theta}{\rho_l r} \end{bmatrix}$$

The integrating scheme was,

$$U^{n+1} = U^n + \Delta t F^n \qquad (4)$$

which is a forward-time integrating scheme using values for F at the previous timestep.

The initial conditions of this problem are easily specified. The initial height of fluid in the groove is known, ie., h(t=0) is a measurable or specifiable quantity, and the velocity of the fluid in the groove is initially zero, $V_l(t=0)=0$. The only thing left to be determined is the shear stress, τ. An expression given in White (4:292) provides a correlation for the *apparent* friction factor for laminar flow in a circular tube,

$$f_{app}Re_D = \frac{3.44}{\xi^{1/2}} + \frac{fRe_D + K_\infty/(4\xi) - 3.44/\xi^{1/2}}{1 + c/\xi^2} \tag{5}$$

where Re_D is the hydraulic Reynold's number, $\xi = (h/D)/Re_D$, $fRe_D = 16.0$ from the Hagen-Poiseuille flow solution, and K_∞ and c are constants given as 1.25 and 0.000212 respectively. The apparent friction factor is the local friction factor, integrated over the length of channel of interest, taking into account the entrance region effects. The overall shear stress can then be calculated from,

$$\tau = \frac{1}{2} f_{app} \rho_l V_l^2 \tag{6}$$

While Eqs. [5] and [6] provide a compact, closed-form solution to the shear stress, they are somewhat lacking for this work. The reason is that the flow in a capillary tube is not really accelerating tube flow, as is implied by Eq. [5]. In the region of the tube entrance, the equations should apply; however, the fact that the meniscus does not change shape throughout the transient implies that the velocity profile in the vicinity of the meniscus is uniform and equal in magnitude to the average velocity in the tube (from continuity). Boundary layer growth begins at the tube entrance but must disappear by the top of the fluid column. The difficulty is explaining what happens to the velocity profile between the entrance to the tube and the meniscus region.

Consider a shock wave passing over a flat plate through a medium initially at rest. It is known that a boundary layer forms *behind* the shock as it passes over the plate. A second boundary layer can be seen at the leading edge of the plate where the flow is fully developed. If we consider the rise of the meniscus to be similar to the shock as it passes down the plate, then it is reasonable to assume that a boundary layer may form behind the meniscus as it rises in the tube. If this is true, then the discrepancy noted above can be explained. During the initial portion of the transient, a boundary layer is formed as fluid enters the tube. Additionally, as the meniscus rises, another boundary layer forms behind it. These two boundary layers combine to form a kind of diffuser shape within the capillary tube, which basically allows the boundary layer to grow, and then diminish, with approximately uniform velocity profiles at the tube entrance and top of the fluid column.

Assuming merging boundary layers exist, then an approximate expression for the overall shear stress may be derived by dividing the length of the tube into two regions, one where the boundary layer grows from the tube entrance, the other where the boundary layer grows from the advancing meniscus (see Figure 3). The force on each region is given simply as $F_i = \tau_i \pi r h$ (i = 1 or 2) and the overall force is given as $F = F_1 + F_2$. If it is further assumed that the two boundary layers grow at the same rate, then $f_{app1} \approx f_{app2}$ and the overall friction coefficient is simply the Shah friction coefficient, Eq. [5], evaluated at (h/2) instead of h. This method of calculating the shear stress results in an overall increase in the total shear on the fluid element and is referred to as the *modified* Shah friction model.

EXPERIMENTAL SETUP

The experimental equipment consisted of two glass capillary tubes, approximately 0.15 m in length with diameters equal to 0.876 and 1.778 mm (flush cut at each end), a small reservoir full of distilled water, and a mechanism for precisely lowering the capillary tubes into the pool of water. The wetting angle between the glass and water was assumed to be zero radians. A Kodak SP2000 high-speed video motion analyzer (5) was utilized to capture the transient rise of water height within the capillary structure. The SP2000 was capable of capturing from 60 to 2000 frames per second (fps); 60 fps provided adequate resolution of the transient and was utilized in this study. Calibration of the internal clock was accomplished by videotaping a precision stopwatch and comparing the watch movement to the videotape movement at 60 fps. Accuracy of the time measurement was ± 0.01 sec. Length calibration was done by videotaping a precision ruler and comparing the distance between ruler markings on the videotape with the SP2000 crosshair movements. Accuracy of length measurements was ± 0.1 mm.

EXPERIMENTAL PROCEDURE

Prior to insertion into the pool of water, the tubes were thoroughly cleaned with a general cleaning detergent and rinsed with several distilled water baths. The tubes were initially charged with small amounts of distilled water and placed in the lowering mechanism and clamped in place. The video was activated and the capillary tubes lowered into the pool of water until the column of water began to rise, at which point the tube lowering was halted. The video was stopped after the fluid rise transient was over. A quick review of the video after each experimental run indicated whether or not the run was valid. The method of determining a valid run consisted of measuring the height to which the column of water rose in the video and comparing this to the steady-state value calculated from Eq. [3]. If the measured height was equal to the calculated value, the run was deemed valid. If however, the final rise height was lower, then the run was discarded and the video erased. A rise height lower than that predicted by Eq. [3] indicated a fault with the cleaning procedure described above.

RESULTS AND DISCUSSION

Close observation of initial data runs indicated that the formation of the meniscus occurred over a time increment much shorter than what was able to be measured with the equipment at hand. Additionally, the general shape of the meniscus on a macroscopic level, did not change appreciably throughout the transient, whether the fluid was rising or falling within the tube. Therefore, the assumption of a fully-formed meniscus throughout the transient, modeled as a constant capillary force, appeared to be valid.

Figures 4 through 6 show the results of three data runs with the large bore tube, each figure representing a different initial charge. Several general observations are made. For the range of initial charges investigated, the transient was oscillatory in nature, with the behavior essentially damped out after 0.8 seconds. Additionally, the final height rise for all the cases was identical to that predicted by Eqn [3]. This basically answered two of the three questions posed by the problem statement. The last question dealt with how the fluid achieved its final steady-state height. The dashed line indicates the numerical solution using the *modified* Shah friction model. In all three cases, the oscillatory nature of the solution was predicted by the *modified* Shah model; however, it predicted an overshoot of the final rise height slightly greater than what was observed, indicative of insufficient numerical friction. The lower than

predicted rise height during the transient was not believed to be caused by a "dirty" capillary tube, since the final rise height was consistent with that predicted by the steady-state solution. The anomalous behavior was suspected to be caused by either an incorrect assumption in the modeling of the boundary layers or in the omission of additional loss mechanisms. The boundary layer modeling was believed to be accurate due to experimental observations of the meniscus behavior, so additional loss mechanisms were investigated in order to explain the discrepancies.

In all pipe flow systems, there are *major* losses, primarily due to the friction associated with long, straight sections of pipe. These losses are calculated by well-established friction models. However, there are additional losses, termed *minor* losses, that occur due to the presence of valves, bends and obstructions to the flow. In most cases, these losses are small compared to the major losses. The minor losses are generally categorized as to their effect on the recovery of the flow kinetic energy, and are given as head loss coefficients, ϕ. The loss coefficient is a percentage of the incoming kinetic energy that is lost due to the obstruction and is defined as,

$$\phi = \frac{\Delta p}{\frac{1}{2}\rho_l V_l^2} \tag{7}$$

The loss coefficient is proportional to a friction factor, and for this example, that factor, f_ϕ, is easily shown to be,

$$f_\phi = \frac{\phi r}{2h} \tag{8}$$

This friction factor is then added to the *modified* Shah friction factor calculated previously, and the sum is used in the calculation of the overall shear stress.

The only minor loss present in this experiment is that due to the method in which the flow enters the capillary tube. The entrance of the tube was flush cut; in other words, there was little, if any, rounding of the inlet, which meant the flow had to turn a relatively sharp angle at the entrance to the tube. Based on the level of rounding at the entrance, the loss coefficient could vary anywhere from 0.004 (well-rounded) to 0.500 (no rounding) (2:504-517). Because of the flush cut, this loss coefficient was expected to be closer to 0.5 than to 0.004.

Using a conservative value of ϕ=0.5, the improvement in the friction model is seen as the solid line in Figures 4 through 6. The trend is obviously in the correct direction; the match with the experimental data was better than with no minor losses included. There was still some discrepancy between this model and the data; however, the difference was well within the experimental scatter.

Figures 7 and 8 show the comparison of the *modified* Shah friction model with the experimental data for the small bore capillary tube. The obvious difference between this and the large bore tube was the exponential shape of the transient curve. In this case, there was no overshoot, but a smooth rise to the final steady-state value predicted by Eq. [3]. The fact that there was no overshoot in this case was most probably due to the fact that because the small bore tube rise height was much greater than the large bore, the overall friction was greater, and the greater friction prevented the overshoot. Including the minor losses improved the match with the experimental data, although the difference between including and not including the minor losses was much less pronounced in the small bore tube as compared to the large bore tube. This was because the losses due to the flush cut acted over a greater percentage of the total rise height in the large bore tube than the small bore, hence their effect was more pronounced.

CONCLUSIONS

Control volume analysis was utilized to numerically study the behavior of a simple, capillary-induced flow. The steady-state rise height, along with the transient behavior of the flow, was accurately modeled with numerical techniques. The nature of the fluid rise in a capillary tube was highly dependant on the tube geometry; the smaller diameter tubes providing higher rise heights and less overshoot during the transient to steady-state. The majority of the frictional losses in capillary tube flow were handled with simple friction models that provided adequate results. Inclusion of minor flow losses in the numerical model improved the correlation between theory and experiment.

The use of high speed video was used to provide transient experimental data on capillary-induced flow. Because of the short transient times in capillary tube flow, a means of capturing the flow behavior was necessary. High speed video was shown to be a viable means of collecting transient data.

Finally, the importance of properly preparing capillary tubes for the experimental portion of the work was perhaps the most valuable lesson learned. Inadequate cleaning of the tubes resulted in several invalid data runs. The only means of verifying proper cleaning of the tubes was an *a priori* knowledge of the steady-state rise height solution for the given tube geometry. Without this, there was no means of determining if the tubes were properly cleaned prior to testing. However, this knowledge did provide a means of choosing a preferred cleaning procedure and once this procedure was followed, few problems were encountered in obtaining valid transient data.

REFERENCES

1. Swanson, L.W. and G.C. Herdt, "Model of the Evaporating Meniscus in a Capillary Tube," Journal of Heat Transfer, 114 n2: 434-441 (May 1992).

2. Munson, Bruce R. et al., Fundamentals of Fluid Mechanics. New York: John Wiley & Sons Inc., 1990.

3. Roe, P.L., "Approximate Reimann Solvers, Parameter Vectors, and Difference Schemes," Journal of Computational Physics, 43 n2: 357-372 (November 1981).

4. White, Frank M., Viscous Fluid Flow (Second Edition). New York: McGraw-Hill Book Company, 1991.

5. Spin Physics Division. SP2000 Motion Analysis System Users Manual, Manual P/N 4000016, Spin Physics Division, Eastman Kodak Company, San Diego, CA, November 1986.

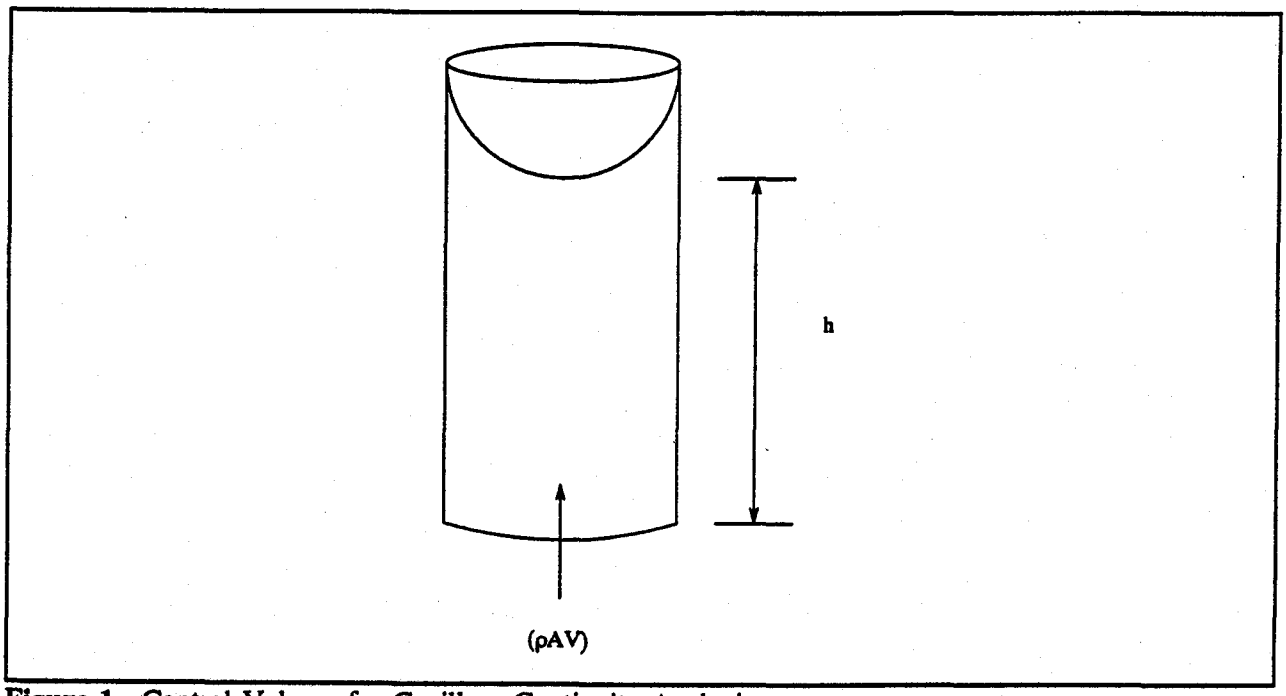

Figure 1. Control Volume for Capillary Continuity Analysis

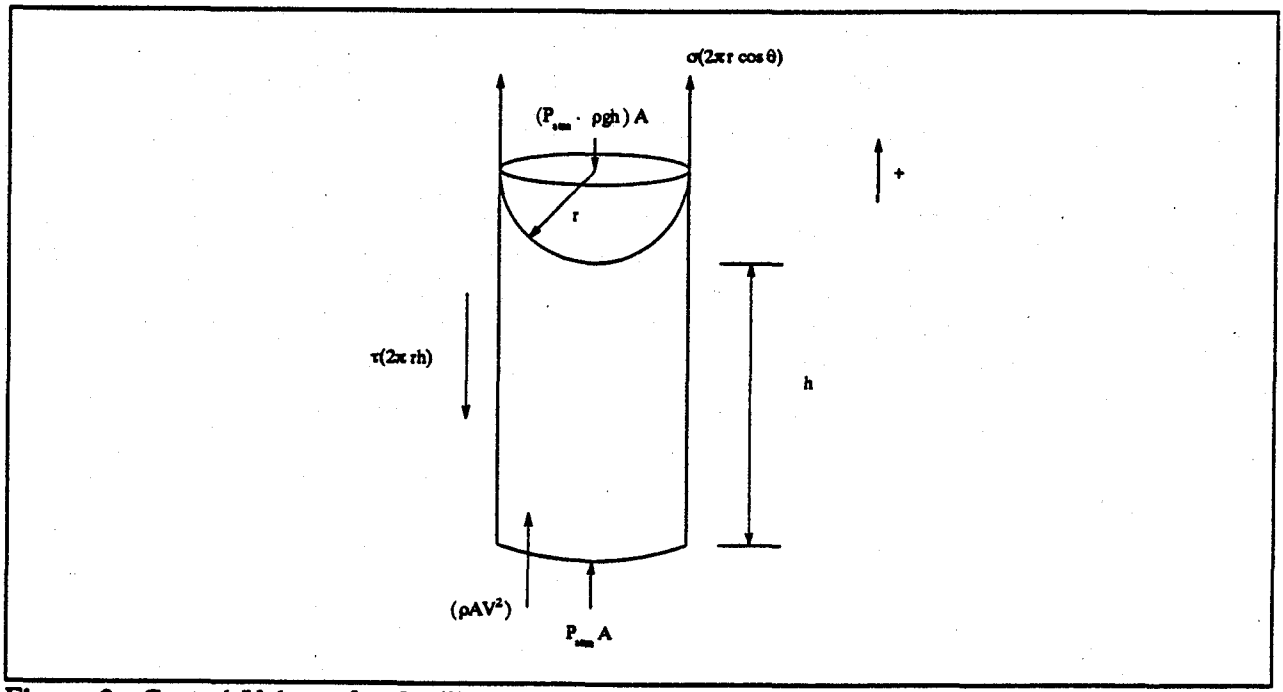

Figure 2. Control Volume for Capillary Momentum Analysis

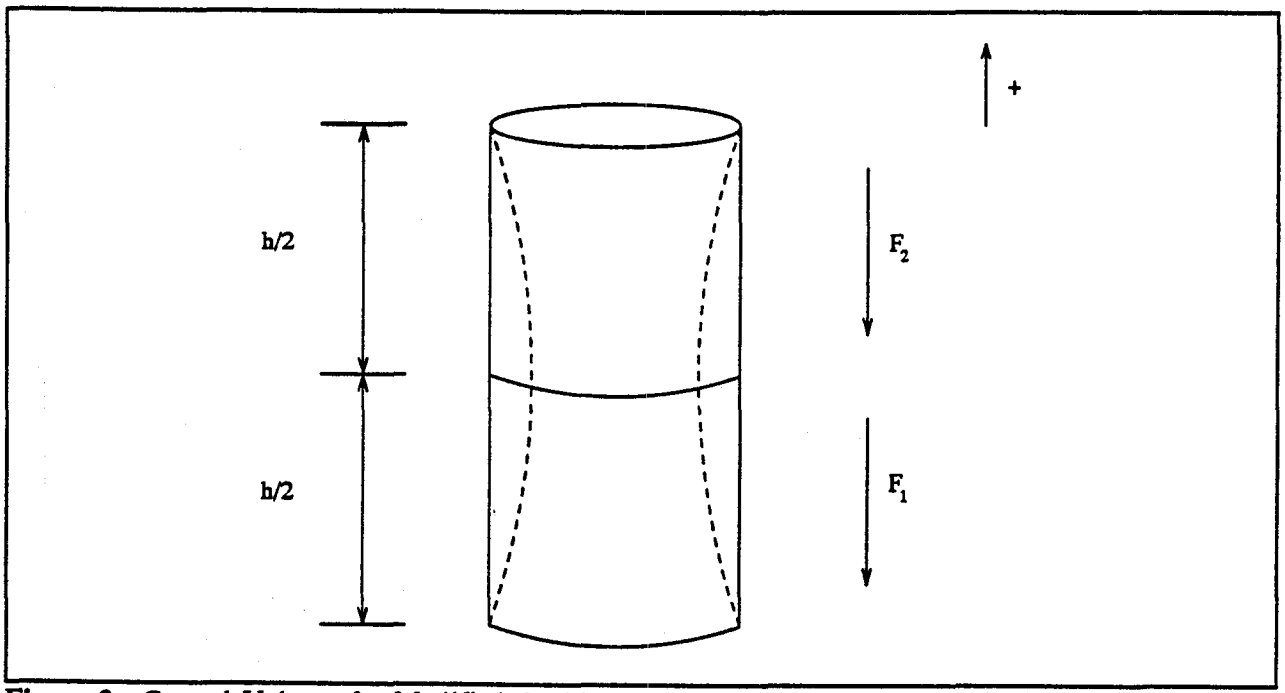

Figure 3. Control Volume for Modified Capillary Shear Analysis

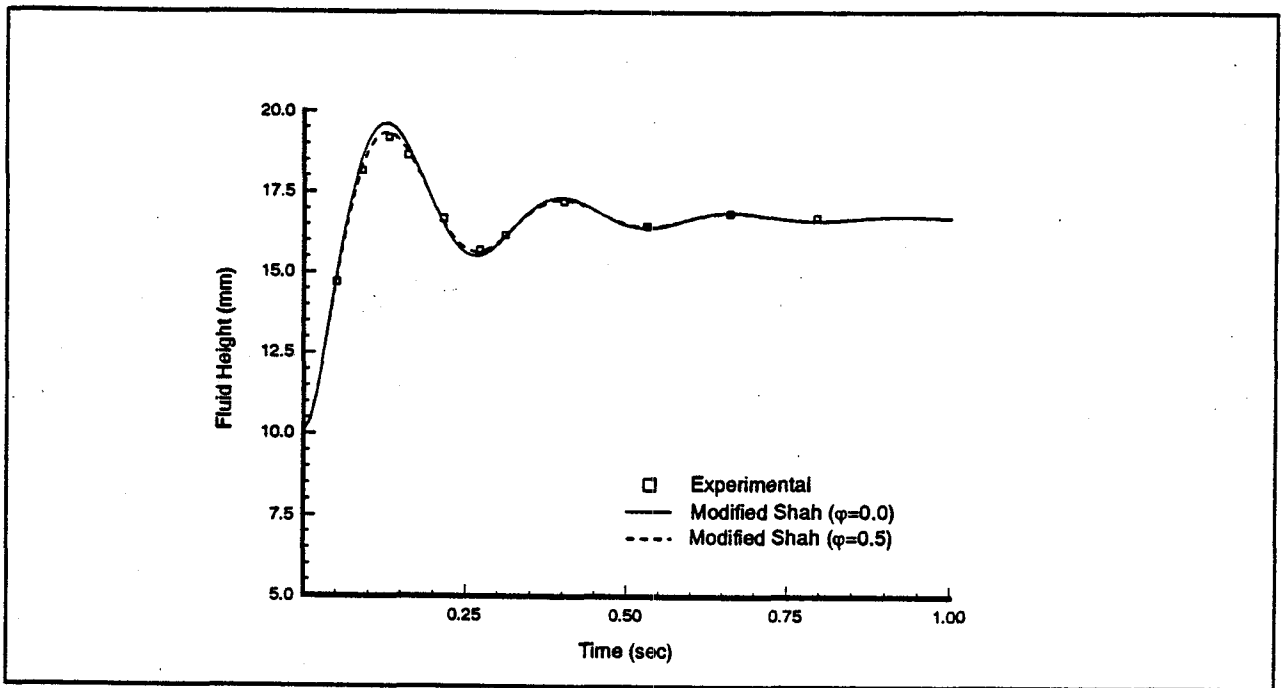

Figure 4. Transient Capillary Rise--Glass/Water r=0.889mm h_i=10.073mm

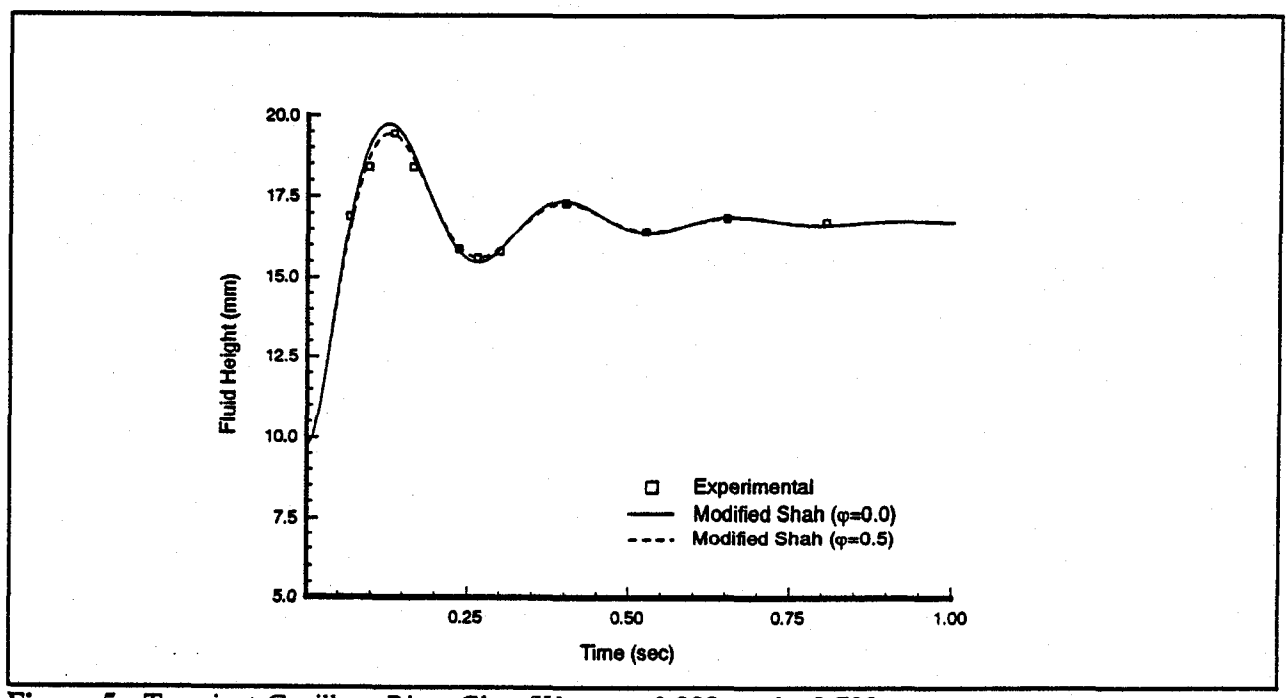

Figure 5. Transient Capillary Rise--Glass/Water r=0.889mm h_i=9.709mm

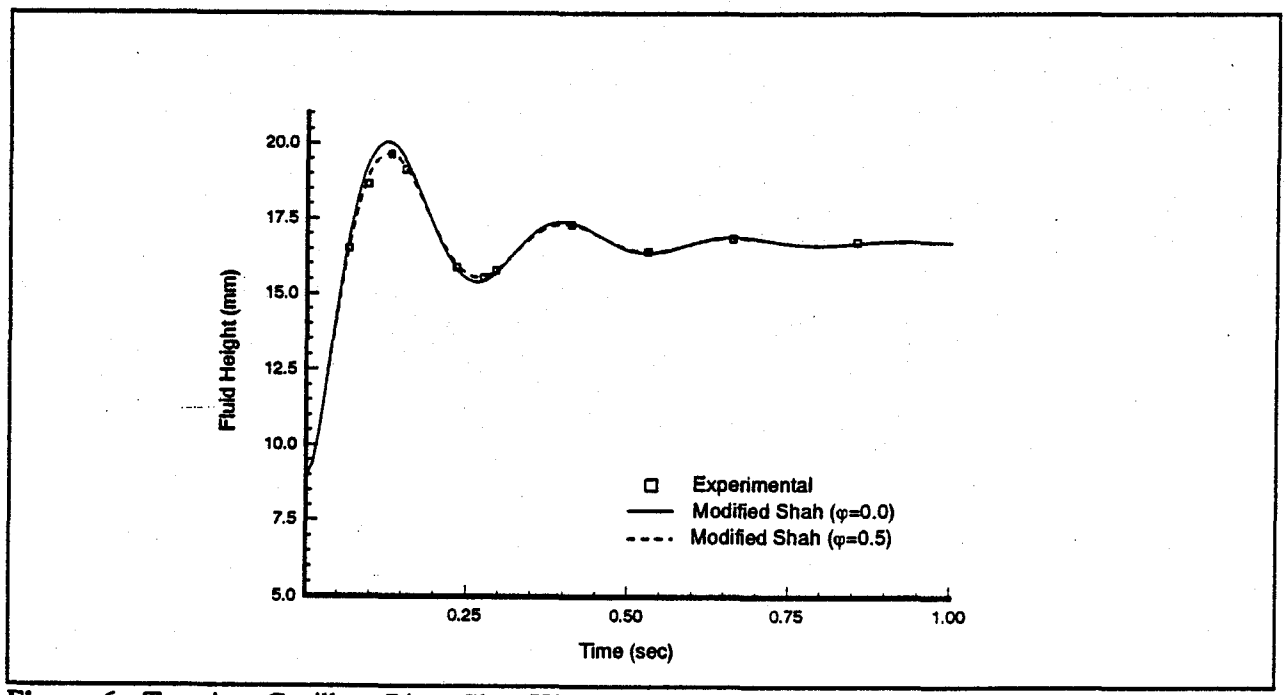

Figure 6. Transient Capillary Rise--Glass/Water r=0.889mm h_i=8.932mm

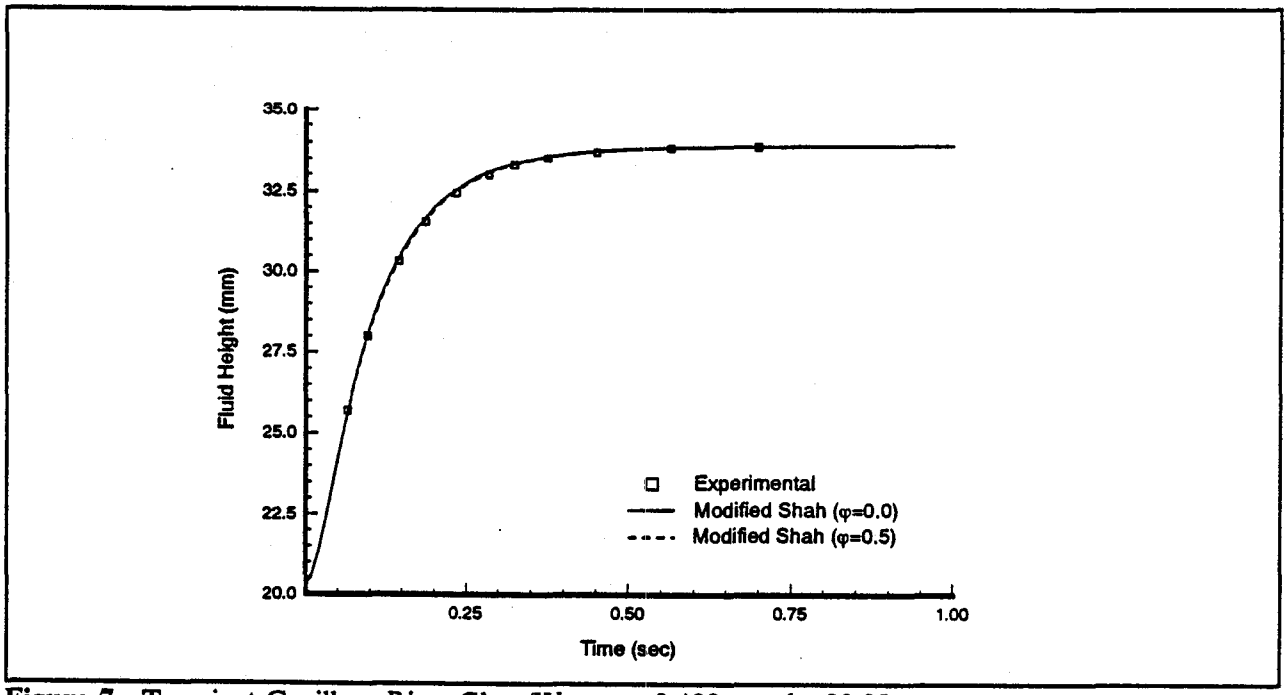

Figure 7. Transient Capillary Rise--Glass/Water r=0.438mm h_i=20.32mm

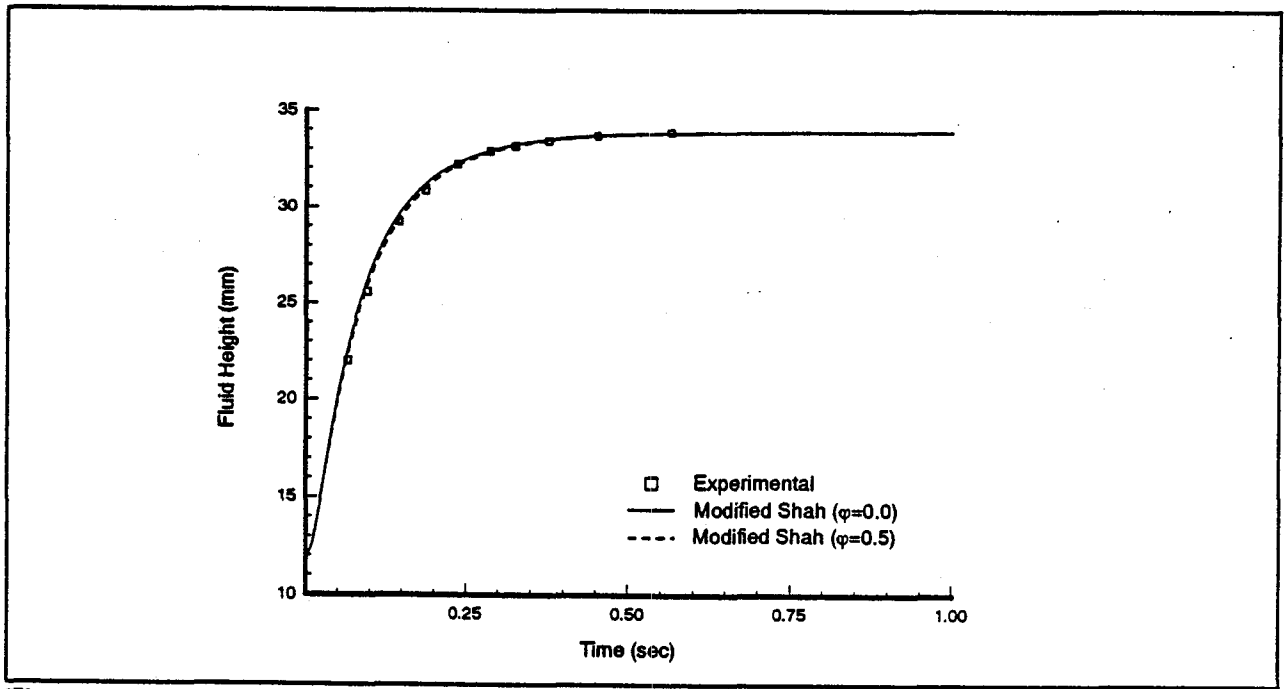

Figure 8. Transient Capillary Rise--Glass/Water r=0.438mm h_i=11.73mm

ON THE DETERMINATION OF LOCAL INSTANTANEOUS AVERAGES IN PARTICULATE FLOW MEASUREMENTS

R. E. Van de Wall and S. L. Soo
Department of Mechanical and Industrial Engineering
University of Illinois at Urbana-Champaign
1206 West Green Street
Urbana, IL 61801-2906

SUMMARY

Determination of instantaneous local average particle density of a gas-particle suspension requires satisfying both the time scale relation and the volume scale relation or its continuum counter part of time averaging. This procedure was validated by comparing simultaneous velocity and mass flux measurements and the laser phase Doppler measurements.

INTRODUCTION

In an earlier discussion, the corresponding scale relations of both volume- and time-averaging were identified (Soo, 1991). It was noted that almost all measuring techniques in particulate flows are based on time-averaging. Recent work on laser phase Doppler particle analyzer (PDPA) (Aerometrics, 1987) raised the question of probing volume or characteristic dimension of probe in relation to the particle size. This is because the collecting volume of laser beams of the dimension of 100 μm was used to determine the density from mass flux measurement of particles of similar diameters. The long time average density thus determined, with some careful consideration of the effective flow area (Saffman, 1987), is accurate when the flow is nearly fully developed. The same is true in the use of an electrical conductance probe of diameter small than that of bubbles in liquid (Nassos and Bankoff, 1963). This is true as long as the criterion of time-scale relation based on passage of interfaces at an observation point is satisfied according to (Soo, 1991):

$$U_s/(dU_s/dt) > T > \Delta t_k \qquad (1)$$

where U_s is the velocity of an interface, t is the time, such that the acceleration time be longer than the averaging time T, and Δt_k is the passage time of a phase. There is no question that Eq. (1) is sufficient when dealing with one-dimensional motion. It is also sufficient for determining long time averages, such as isokinetic sampling of the average mass flux of particles of a suspension. However, no provision was made for determining the local instantaneous density.

EFFECT OF DIMENSION OF PROBES

Previous experience has been that most of the characterisitc dimensions of probes for particle mass flux such as isokinetic sampling (Soo et al., 1969) and electrostatic ball probe (Cheng and Soo, 1970; Zhu and Soo, 1992) were much larger than the size of

particles. Therefore, the concept of volume- or area- averaging given in Soo (1989) were satified first of all, or

$$L > v^{1/3} > v_k^{1/3} \qquad (2)$$

for volume-averaging of local instantaneous flow properties, where L is the charactristic dimension of the physical system, v is the control volume, and v_k is the characteristic volume of phase k. It was taken for granted that the inlet opening (diameter D) of the isokinetic sampling probe be larger than the particle (diameter d). Fig. 1(a) shows that this condition is conceptically significant in measurements based on time-averaging, with mass flux of particles of various sizes determined by the area $\pi D^2/4$. However, when d is large compared to D, as illustrated in Fig. 1(b), the accuracy of measured mass flux and the deduced density from average velocity of particles become questionable when the former is based on the probe diameter. This is because many large particles which are within the projected area of the area of exclusion of the probe and the particle would be excluded.

When the electrostatic probe is calibrated by the isokinetic sampling probe, the above large (compared to probe diameter) particle effect are not readily corrected from the results of one to the other when dealing with long time averages of density or mass flux. By using a larger probe diameter than the particle diameter, one effectively satisfy the scale relation in Eq. (2) to average the electrostatic charge transfer of a number of particles over the projected area of the probe. The electrostatic probe thus calibrated can be used to determine the instantaneous mass flux of particles based on the projected area $\eta\pi D^2/4$; η being the fraction impacted based on the projected area of exclusion of particles (see for instance, Soo, 1989). This relation is shown in Fig. 2(a) for D>>d. Instantaneous mass flux is given by the probe current due to simultaneous collision of particles of average number N_c given by:

$$N_c = \lambda_B / n^{-1/3} \qquad (3)$$

where λ_B is the collision free path of the probe by particles, n is the number density of particles, and $n^{-1/3}$ is the mean interparticle spacing (Zhu and Soo, 1992). This number is of order 10 for the present example of 2.4 mm diameter probe and 44-62 μm glass particles at a mass flux to give nearly 1 kg particles/kg of air, or an inter-particle spacing of 10 particle diameters.

A different situation arises when the particle size is large when compared to the diameter of an electrostatic probe (Fig. 2); the effective projected probe area would be $\eta\pi(D+d)^2/4$. This illustrates the significance of probe dimension in comparison to the particle size in the above calibration procedure. One also has to rely on the the average from a number of longitudinal spacings of particles to attain a corresponding averaging time to the area average for the instantaneous mass flux.

FLUCTUATIONS OF DENSITY FROM PDPA OUTPUT

To improve the theoretical basis of determining fluctuating density of particles by phase Doppler particle analyzer (PDPA), we have to extend the scaling relation of volume averaging (see Soo, 1989), given by Eq. (2). Because the collecting volume had a characteristic length of, say, 102 μm, it does not satisfy the criterion of volume averaging (Eq. 2) for particles of 44-62 μm diameter. Its counterpart in local instantaneous time averaging is seen to be over Δt with (Fig. 3):

$$\Delta t_i < \Delta t < T \qquad (4)$$

where Δt_i is the duration allotted to the passage of a particle i, Δt is the duration corresponding to a "continuum" sampling frequency over a number of particles in say, ms, and T is the overall averaging time in seconds. In Fig. 3, the phase difference between two detectors in PDPA gives the particle size, and the width indicating passage of a particle i gives its velocity U_{pi}; $\Delta t_i\, U_{pi} A_i$ gives its averaging volume. A_i is the corresponding cross-section of the path of particles and is a function of a given particle size d_i as shown in Fig. 4 (Saffman, 1987). Correspondence to the case in Fig. 2(b) is noted. The average density given by the procedure of Aerometrics (1987), for a total of N particle over the duration T:

$$\langle \rho_p \rangle = (1/T)\Sigma_i\, m_{pi}(N_i/\langle U_p \rangle)(L/v)_i = (1/T)\Sigma_i\, m_{pi}(N_i/\langle U_p \rangle A_i) \qquad (5)$$

where m_{pi} is the mass of particle of diameter d_i ($m_{pi} = \pi \rho_p d_i^3/6$, ρ_p is density of particle material), L_l is the characteristic path length in the laser collecting volume v. The local instantaneous density is given by, over the duration Δt corresponding to (schematically shown in Fig. 3):

$$\Delta t = \sum_{i=1}^{i=n} \Delta t_i \qquad (6)$$

$$\rho_p = \langle \rho_p \rangle + \rho_p' = \sum_{i=1}^{i=n} (N_i m_{pi}/\Delta t_i\, U_{pi})(L_l/v)_i = \sum_{i=1}^{i=n} (N_i m_{pi}/\Delta t_i\, U_{pi} A_i) \qquad (7)$$

Fluctuation in density of particles affects the transport processes in a suspension.

EXPERIMENTAL PROCEDURE

A complete description of the cyclone-standpipe recirculating pipe flow loop system for a dense suspension of particles and metering is given in Chapter 9 of Roco (1993), Plumpe et al. (1993), or Zhu and Soo (1992a). The Lexel laser facility (5 W two-color argon laser) for laser Doppler (LDV) and phase Doppler particle analyzer (PDPA) (Liljegren and Vlachos, 1990) has been modified for vertical traverse in a horizontal pipe of 127 mm diameter (in a cyclone-standpipe recirculating test loop). The LDV has the capability of measuring fluctuating velocity in two dimensions (longitudinal and transverse).

This system, in combination with an electrostatic probe (Fig. 5), was used in the determination of local velocity and density fluctuations by Slaughter in his thesis (1992) and in Soo et al. (1993). This provides a check for the PDPA measurements of instantaneous local density. The use of a 2.4 mm diameter electrostatic probe gave area average in determining mass flow or density fluctuations with time.

The PDPA has been placed for forward scattering as shown in Fig. 6. The Aerometric software has been modified to give density fluctuation besides average density according to the theory of continuum counterpart of time averaging following Eq. (7).

EXPERIMENTAL RESULTS

The PDPA gives density fluctuations from a continuum approximation in time corresponding to sampling time in the electrostatic probe. These results on glass particles of 44-62 μm diameter at a mean air velocity of 15 m/s and mass flow ratio m* of 1.5 kg particles/kg of air are shown in Fig. 7. Fig. 7(a) gives the long time average density as determined by PDPA, the data for large mass flow ratio m* of 1.5 did not extend to positions close to the bottom of the pipe because of interference of the bottom dense layer of particles with the PDPA position in Fig. 6. Fig. 7(b) compares the results of PDPA with the electrostatic probe and LDV measurements, showing general agreement for a sufficient averaging time Δt (1/256 s) in Eq. (7) for averaging, while Δt_i (Fig. 3) may be less than 1/10-th of that. The frequencies of fluctuations of the two measurements are comparable. Fig. 8 shows the mean particle size distribution for various m* over the height of the vertical diameter as measured by PDPA; large particle tend to sink toward the bottom of the pipe as expected. Table 1 compares the average particle density and RMS fluctuation of density as determined by the PDPA and the LDV - electrostatic (ball) probe at two averaging times of 1/256 s and 1/128 s for m* = 0.4 and 1.5, showing that the continuum scale relation was satisfied.

Table 1 Comparison of the average particle density <rp> and RMS density flucturation $\langle \rho_p' \rho_p' \rangle^{1/2}$ as determined by PDPA

Method	$\langle \rho_p \rangle$, kg/m^3	$\langle \rho_p' \rho_p' \rangle^{1/2}$, kg/m^3	Averaging time, s
	m* = 0.4		
PDPA	0.95	1.02	1/256
LDV- Ball Probe	0.95	0.62	1/256
PDPA	0.95	0.98	1/128
LDV- Ball Probe	0.95	0.48	1/128
	m* = 1.5		
PDPA	1.68	1.14	1/256
LDV- Ball Probe	1.70	1.12	1/256
PDPA	1.68	0.95	1/128
LDV- Ball Probe	1.70	0.99	1/128

CONCLUSIONS

Measurements of instantaneous local particle density calls for satisfying the criteria of both time and volume averaging or its continuum counter part.

The PDPA provides a means for determining the instantaneous local particle density when the soft ware satisfies the criterion of continuum counter part of time averaging.

The present procedure as applied to PDPA provides a primary standard for particle density measurement.

ACKNOWLEDGEMENT

This study was supported by the National Science Foundtion under Grant CTS-9014914 of the Fluid, Particulate and Hydraulic System Program directeD by Dr. M. C. Roco.

REFERENCES

Aerometrics Corp., 1987, PDPA Operations Manual Release 3.0.

Cheng, C., and Soo, S. L., 1970, "Charging of Dust Particles by Impact," *J. Appl. Phys.*, Vol. 41, 585-591.

Liljegren, L. M., and Vlachos, N. S., 1990, "Laser Velocimetry Measurements in a Horizontal Gas-Solid Pipe Flow," *Experiments in Fluids*, Vol. 9, 205-212.

Nassos, G. P., and S. G. Bankoff, 1967, "Local Resistivity probe for study of Point Properties of Gas-liquid Flows," The Canadian J. Chem. Eng., Vol. 45, pp. 271-274.

Roco, M. C., 1993, *Particualte Two-phase Flow*, Butterworth-Heinemann, Boston.

Saffman, M., 1987, "Automatic Calibration of LDA Measurement Volume Size," *Applied Optics*, Vol. 26, (13), pp. 2592-2597.

Slaughter, M. C., 1992, *Experiments on Particle-Gas Suspension Flow*, M. S. Thesis, University of Illinois at Urbana-Champaign, Urbana, IL 61801.

Slaughter, M. C., C. Zhu, and S. L. Soo, 1992, "Measurement of Local Statistical Properties of Particle Motion in a Dense Gas-solid Suspension," *Advanced Powder Tech.*, Vol. 3, pp.1-10.

Soo, S. L., 1989, *Particulates and Continuum - Multiphase Fluid Dynamics*, Hemisphere, DC.

Soo, S. L. 1991, "Comparisons of Formulations of Multiphase Flow," *Powder Technology*, Vol. 66(1): 1-7.

Soo, S. L., J. J. Stukel, and J. M. Hughes, 1969, "Measurement of Mass Flow and Density of Aerosols in Transfer," *Environmental Sci. and Tech., Ind. Engr. Chem.*, Vol. 3(4), 386-393.

Soo, S. L., M. C. Slaughter, and J. G. Plumpe, 1993, "Instrumentation for Flow Properties of Gas-Solid Suspensions," *ASME Symposium Recent Advances in Mechanics of Structured Continua, II*, Charlottesville, VA, June 6-9, 1993.

Zhu, C. , and S. L. Soo, 1992,"A Modified Theory for Electrostatic Probe Measurements of Particle Mass Flows in Dense Gas-Solid Suspensions," *J. Appl. Phys.*, Vol. 72(5), pp. 2060-2062.

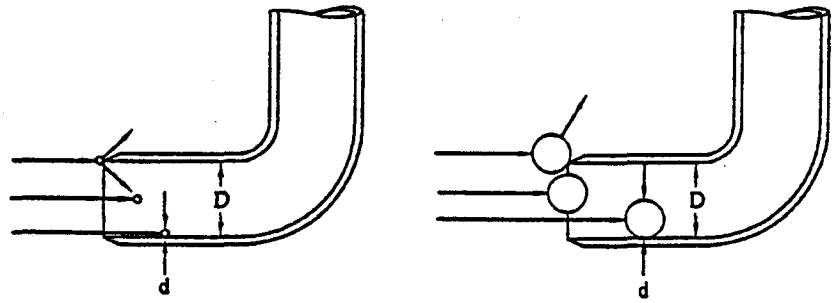

(a) D>>d, $\pi D^2/4$ gives sampling flow area.

(b) D~d, meaningful sampling flow area < $\pi D^2/4$ (many large particles are lost).

Fig. 1 Influence of probe size in isokinetic sampling.

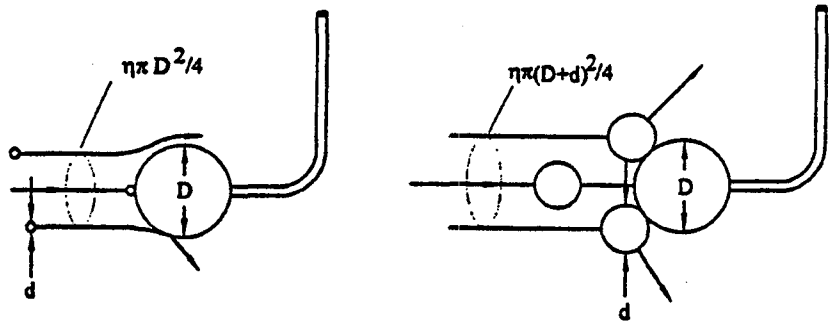

(a) D>>d, $\eta\pi D^2/4$ gives sampling flow area.

(b) D~d, meaning ful sampling area > $\eta\pi D^2/4$.

Fig. 2 Influence of size of electrostatic ball probe.

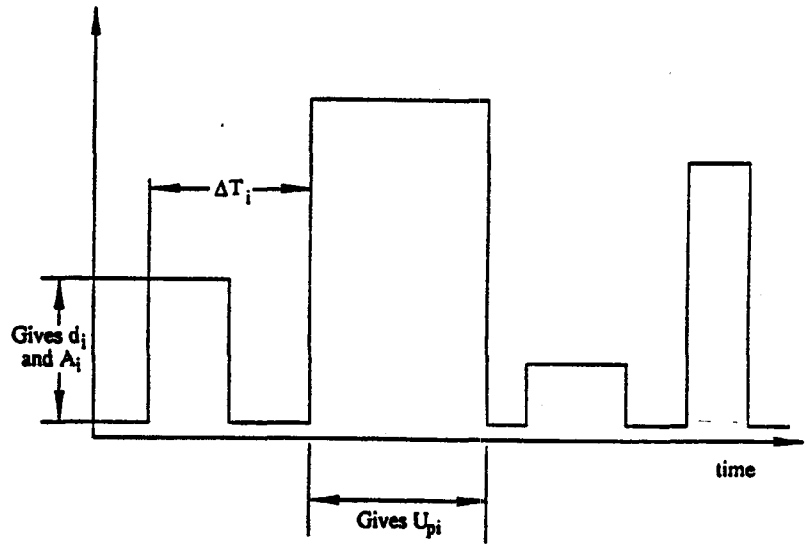

Fig. 3 Time scale relation in determining local density from phase Doppler particle analyzer output.

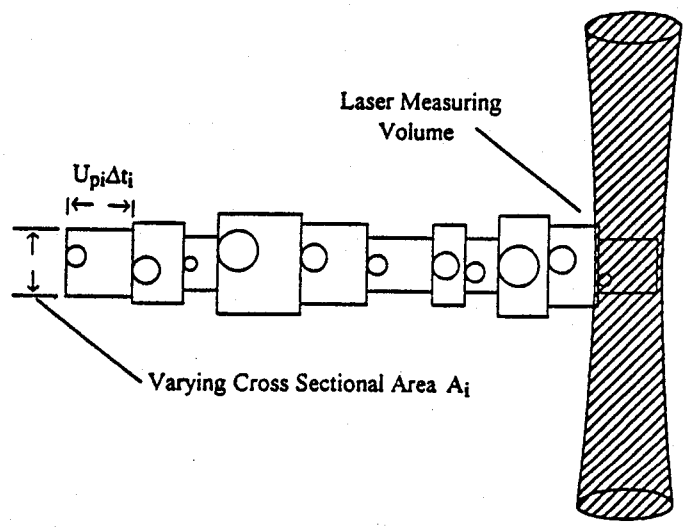

Fig. 4 Passage of particles through collecting area of beam and the equivalent flow areas.

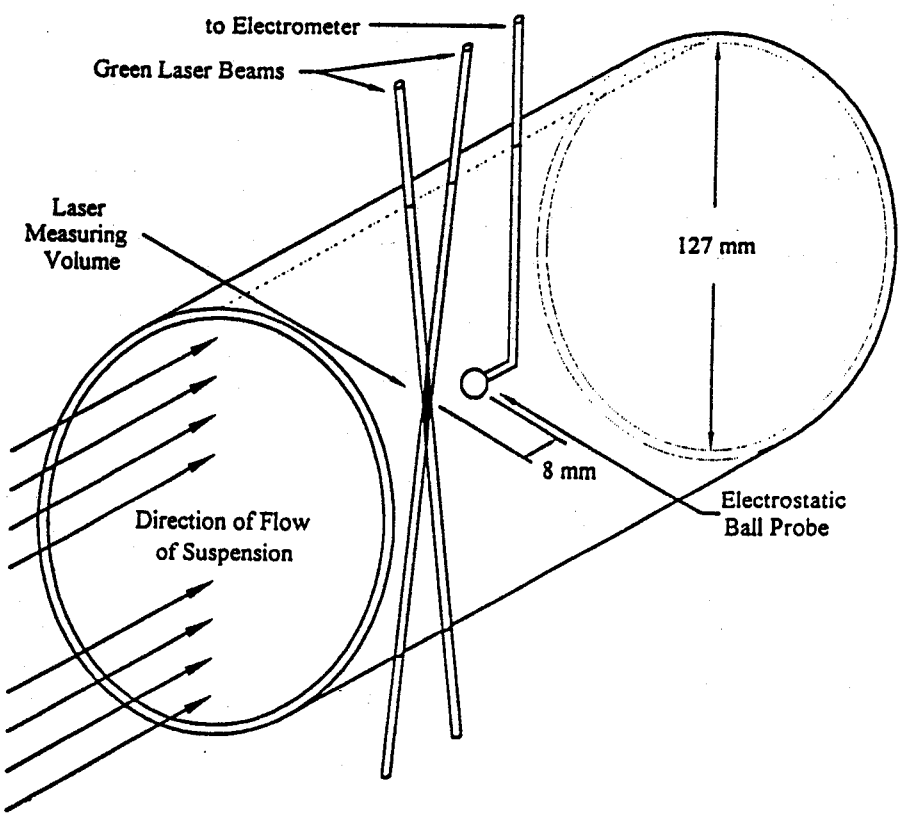

Fig. 5 LDV and electroatatic ball probe immediately behind the LDV collecting volume in a 127 mm diameter horizontal pipe.

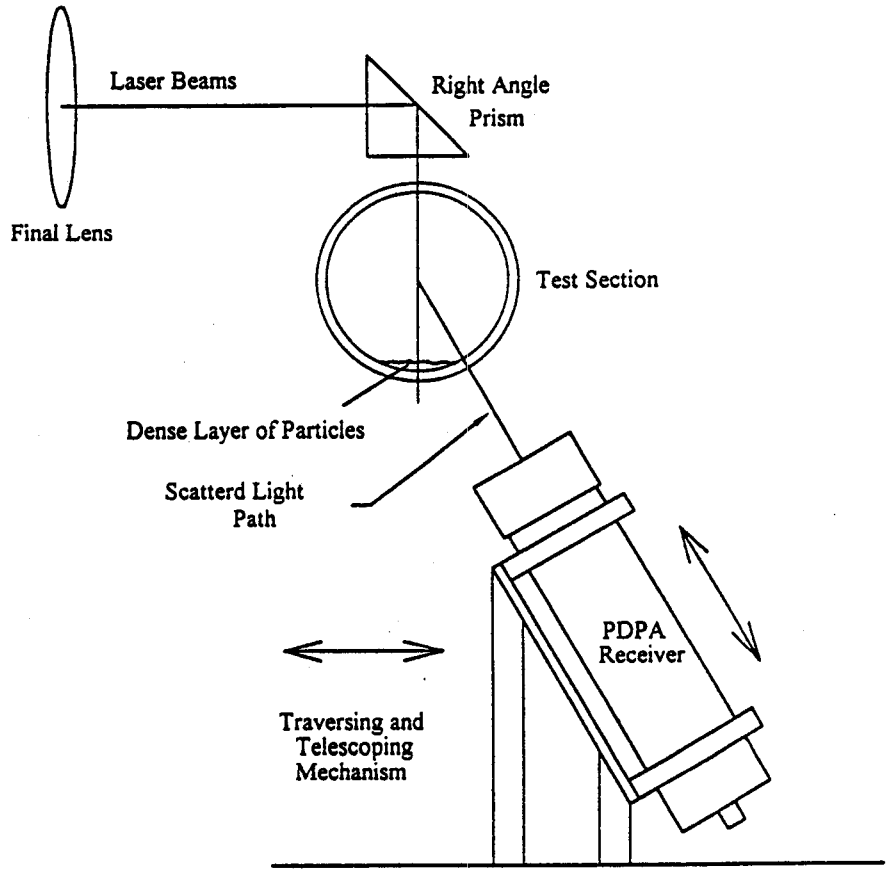

Fig. 6 PDPA system oriented for forward scattering measurement of particle density along vertical diameter.

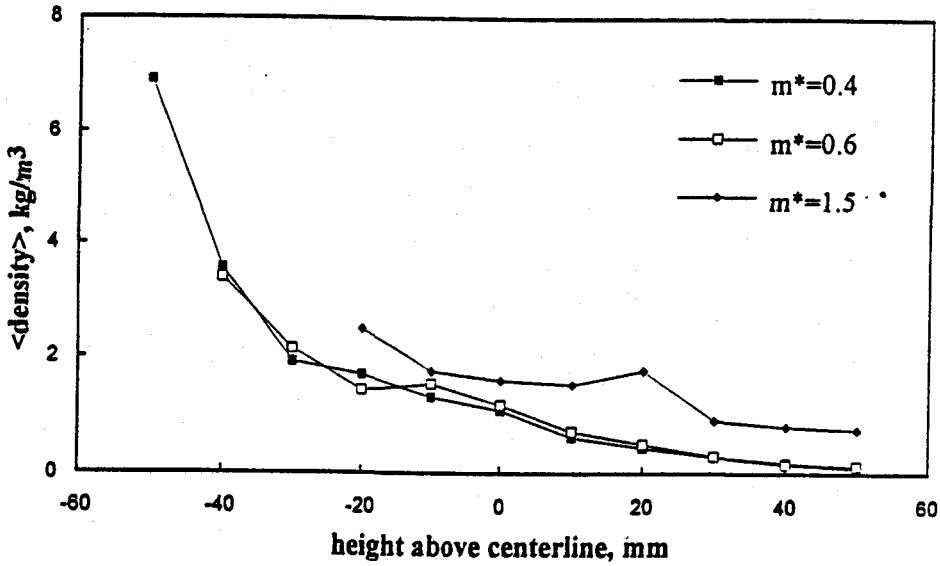

(a) Average particle density over the pipe height at various mass flow ratios as given by PDPA.

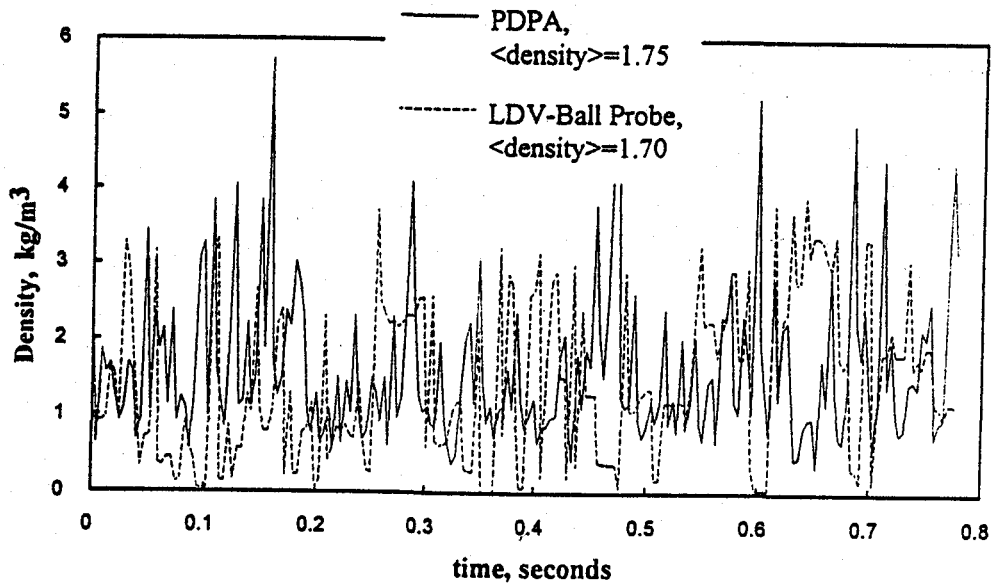

(b) Density fluctuation as given by the PDPA at 1/256 s averaging time and the electrostatic ball probe at mass flow ratio of 1.5 along the center line of the pipe.

Fig. 7 Particle density distribution $\langle \rho_p \rangle$ at 15 m/s mean air velocity and glass particles of 44-62 μm diameter in 127 mm diameter pipe.

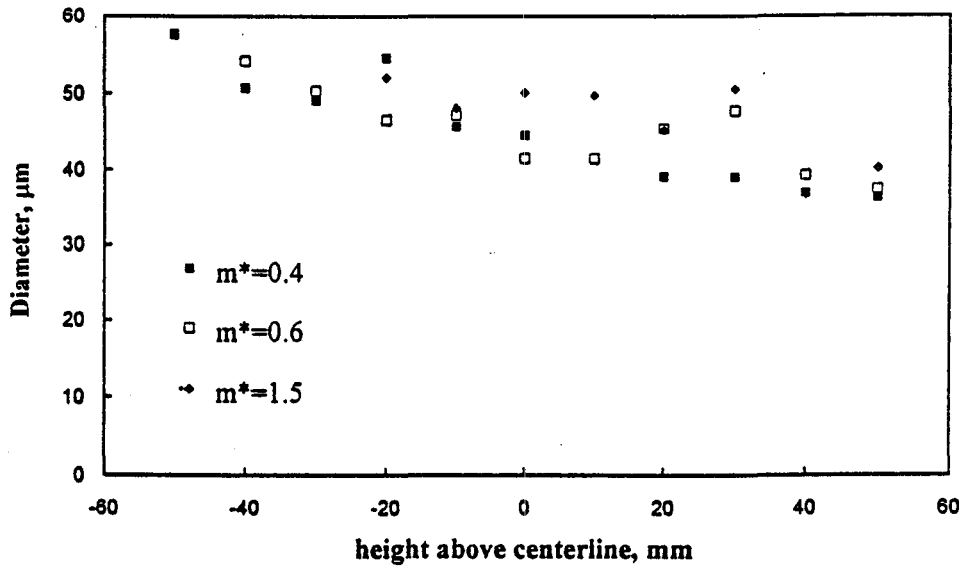

Fig. 8 Mean particle diameter at various heights along the vertical diameter as determined by PDPA for particle size from 44-62 μm and 15 m/s mean air velocity at various mass flow ratio of solid to air m*.

THREE-DIMENSIONAL SOLIDIFICATION AND MELTING USING MAGNETIC FIELD CONTROL

George S. Dulikravich* and Vineet Ahuja**
Department of Aerospace Engineering
The Pennsylvania State University, University Park, PA 16802, USA

ABSTRACT

A new two-fluid mathematical model for fully three-dimensional steady solidification under the influence of an arbitrary acceleration vector and with or without an arbitrary externally applied steady magnetic field have been formulated and integrated numerically. The model includes Joule heating and allows for separate temperature-dependent physical properties within the melt and the solid. Latent heat of phase change during melting/solidification was incorporated using an enthalpy method. Mushy region was automatically captured by varying viscosity orders of magnitude between liquidus and solidus temperature. Computational results were obtained for silicon melt solidification in a parallelepiped container cooled from above and from a side. The results confirm that the magnetic field has a profound influence on the solidifying melt flow field thus changing convective heat transfer through the boundaries and the amount and shape of the solid accrued. This suggests that development of a quick-response algorithm for active control of three-dimensional solidification is feasible since it would require low strength magnetic fields.

INTRODUCTION

Possible means of devising controlling mechanisms for solidification and bulk single crystal growth from a melt is of practical importance to many industrial processes [Kosovic, Dulikravich and Lee 1991; Dulikravich, Kosovic and Lee 1992]. We will demonstrate the quantified effects of a fully three-dimensional solidification control using magnetic fields. If there are no electric charges in the melt and no external electric field is applied, a magnetohydrodynamic (MHD) model [Stuetzer 1962] can be applied. MHD flows without solidification have already been numerically analyzed in three-dimensions [Ozoe and Okada 1989; Lee and Dulikravich 1991]. It was only recently that various researchers have demonstrated numerically the effects of the magnetic field in two-dimensional [Salcudean and Sabhapathy 1990; Dulikravich, Kosovic and Lee 1991; Kosovic and Dulikravich 1991] and in three-dimensional [Dulikravich, Ahuja and Lee 1993a, 1993b; Dulikravich and Ahuja 1993] solidification.

Our objective is to use a single system of governing equations in the entire domain which could consist of the melt, mixture of the melt and the solid (mushy region), or the solid alone. In other words, we want to use a single system of partial differential equations that treats both the melt and the solid as liquids, while allowing each of the two liquids to have its own set of temperature-dependent physical properties (density, heat capacity, thermal conductivity, electric permitivity, thermal expansion, magnetic permeability, etc.). A crucial difference between the two liquids is that the liquid which models the solid phase ($T < T_{solidus}$) must be assigned extremely high viscosity. Hence, velocities interior to the regions occupied by the liquid that models the solid phase will be practically zero. Consequently, we will refer to this artificially extremely viscous liquid as "solid", while the pure melt ($T > T_{liquidus}$) will be called "liquid".

---

* Associate Professor.

** Graduate Research Assistant.

Mass fraction of the liquid at any point in the domain determines locally to what extent should physical properties of the liquid or the solid be taken into account. Since latent heat released or absorbed per unit mass of the mushy region is proportional to the local volumetric fraction, f, occupied by the liquid in a particular computational cell, this ratio is often modeled [Voller and Swaminathan 1991] as

$$f = \frac{V_{liquid}}{V_{liquid} + V_{solid}} = \left(\frac{\theta - \theta_{solidus}}{\theta_{liquidus} - \theta_{solidus}}\right)^n \qquad (1)$$

where the exponent "n" is typically $0.2 < n < 5$. Here, the non-dimensional temperature is defined as $\theta = (T - T_0)/\Delta T_o$ where T is the temperature measured in degrees. Typically, either $\Delta T_o = T_{liquidus} - T_{solidus}$ and $T_0 = T_{solidus}$ or $\Delta T_o = T_{hot} - T_{cold}$ and $T_0 = T_{cold}$. The latent heat, L, is released in the mushy region (where $T_{liquidus} > T > T_{solidus}$) in proportion to the fraction f of the liquid in the mixture. Liquid density, ρ_l is assumed to vary linearly as a function of non-dimensional temperature

$$\rho_l' = 1 + \left.\frac{\partial(\rho_l/\rho_{0l})}{\partial\theta}\right|_0 (\theta - \theta_0) = 1 - \alpha^*_{0l}(\theta - \theta_0) \qquad (2)$$

with a similar expression for the solid phase. We will use subscripts "l" and "s" to designate liquid and solid phase, respectively. If subscript "o" designates reference values, then the non-dimensionalization can be performed as follows

$$v^* = \frac{v}{|v_o|} \qquad g^* = \frac{g}{|g_o|} \qquad H^* = \frac{H}{|H_o|} \qquad x^* = \frac{x}{l_o} \qquad t^* = \frac{t\,|v_o|}{l_o} \qquad p^* = \frac{p}{\rho_o\,|v_o|^2} \qquad (3)$$

$$\rho_l^* = \frac{\rho_{0l}}{\rho_o}\rho_l' \qquad \mu_l^* = \frac{\mu_{0l}}{\mu_o}\mu_l' \qquad k_l^* = \frac{k_{0l}}{k_o}k_l' \qquad c_l^* = \frac{c_{0l}}{c_o}c_l' \qquad \alpha_l^* = \frac{\alpha_{0l}}{\alpha_o}\alpha_l' \qquad (4)$$

with similar expressions for the solid phase. Here, v, g, H and x are vectors of velocity, gravity acceleration, magnetic field and spatial position vector, respectively. Similarly, μ, k, c and α are coefficients of viscosity, heat conductivity, heat capacity and thermal expansion, respectively. Hydrodynamic pressure, coefficients of electric conductivity and magnetic permeability are designated with p, σ and γ, respectively. In this work we assumed that σ and γ do not vary with temperature ($\sigma_l^* = \sigma_{0l}/\sigma_o$, $\sigma_s^* = \sigma_{0s}/\sigma_o$, $\gamma_l^* = \gamma_{0l}/\gamma_o$ and $\gamma_s^* = \gamma_{0s}/\gamma_o$). Since the reference values designated with the subscript "o" are arbitrary, the non-dimensional numbers can be defined as

$$Re = \frac{\rho_o\, v_o\, l_o}{\mu_o} \qquad Fr^2 = \frac{|v_o|^2}{|g_o|\, l_o} \qquad Ec = \frac{|v_o|^2}{c_o\, \Delta T_o} \qquad (5)$$

$$Pr = \frac{\mu_o\, c_o}{k_o} \qquad S_{te} = \frac{c_o\, \Delta T_o}{L_o} \qquad P_m = \frac{\gamma_o\, \sigma_o\, \mu_o}{\rho_o} \qquad (6)$$

$$Gr = \frac{\rho_o^2 \alpha_o |g_o| \Delta T_o l_o^3}{\mu_o^2} \qquad H_t = \gamma_o |H_o| l_o \left(\frac{\sigma_o}{\mu_o}\right)^{1/2} \tag{7}$$

Then, adopting an extended Boussinesq approximation [Gray and Giorgini 1976] to MHD flows, the non-dimensional Navier-Stokes equations for phase-changing mixtures of two liquids [Dulikravich and Ahuja 1993] become:
Mass conservation for two-phase MHD flows

$$\nabla^* \cdot v^* = 0 \tag{8}$$

Linear momentum conservation for two-phase MHD flows with thermal buoyancy and magnetic force

$$\bar{\bar{\rho}} \frac{\partial v^*}{\partial t^*} + f \rho_l^* \nabla^* \cdot (v^* v^* + \bar{\bar{p}}_l^* I) + (1-f) \rho_s^* \nabla^* \cdot (v^* v^* + \bar{\bar{p}}_s^* I)$$

$$= f [\nabla^* \cdot (\frac{\mu_l^*}{Re} (\nabla^* v^* + (\nabla^* v^*)^T)) + \rho_l^* (\gamma_l^* \frac{H_t^2}{P_m Re^2} (\nabla^* \times H^*) \times H^* + \alpha_l^* \frac{Gr\theta}{Re^2} g^*)]$$

$$+(1-f)[\nabla^* \cdot (\frac{\mu_s^*}{Re} (\nabla^* v^* + (\nabla^* v^*)^T)) + \rho_s^* (\gamma_s^* \frac{H_t^2}{P_m Re^2} (\nabla^* \times H^*) \times H^* + \alpha_s^* \frac{Gr\theta}{Re^2} g^*)] \tag{9}$$

Energy conservation for incompressible two-phase MHD flows including Joule heating

$$(f \rho_l^* (c_{el}^* \theta)_{,\theta} + (1-f) \rho_s^* (c_{es}^* \theta)_{,\theta}) \frac{\partial \theta}{\partial t^*} + f \rho_l^* \nabla^* \cdot (c_{el}^* \theta v^*) + (1-f) \rho_s^* \nabla^* \cdot (c_{es}^* \theta v^*)$$

$$= f (\frac{1}{RePr} \nabla^* \cdot (k_l^* \nabla^* \theta) + \frac{\gamma_l^*}{\sigma_l^*} \frac{H_t^2 Ec}{P_m^2 Re^3} (\nabla^* \times H^*) \cdot (\nabla^* \times H^*))$$

$$+ (1-f) (\frac{1}{RePr} \nabla^* \cdot (k_s^* \nabla^* \theta) + \frac{\gamma_s^*}{\sigma_s^*} \frac{H_t^2 Ec}{P_m^2 Re^3} (\nabla^* \times H^*) \cdot (\nabla^* \times H^*)) \tag{10}$$

Magnetic field transport equations for two-phase MHD flows

$$\frac{\partial H^*}{\partial t^*} - \nabla^* \times (v^* \times H^*) = \frac{f/(\sigma_l^* \gamma_l^*) + (1-f)/(\sigma_s^* \gamma_s^*)}{P_m R_e \bar{\bar{\rho}}} \nabla^{*2} H^* \tag{11}$$

Here, $\bar{\bar{\rho}} = f \rho_l^* + (1-f) \rho_s^*$, where $f = 1$ for $\theta > \theta_{liquidus}$ and $f = 0$ for $\theta < \theta_{solidus}$. Non-dimensional hydrostatic, hydrodynamic, and magnetic pressures were combined to give

$$\overset{=}{p}_l^* = \frac{p^*}{\rho_l^*} + \frac{\phi^*}{Fr^2} + \frac{\gamma_l^* H_t^2}{P_m Re^2} H^* \cdot H^* \qquad \overset{=}{p}_s^* = \frac{p^*}{\rho_s^*} + \frac{\phi^*}{Fr^2} + \frac{\gamma_s^* H_t^2}{P_m Re^2} H^* \cdot H^* \qquad (12)$$

where ϕ^* is the non-dimensional gravity potential defined as $g^* = \nabla^* \phi^*$. We used an enthalpy method to formulate the equivalent specific heat coefficients in the liquid and the solid phases are $c_{el}^* = c_l^* - \frac{1}{S_{te}} \frac{\partial f}{\partial \theta}$ and $c_{es}^* = c_s^* - \frac{1}{S_{te}} \frac{\partial f}{\partial \theta}$, respectively. This expression allows latent heat to be released in the mushy region according to the empirical law given in equation (1).

At the solid walls, the velocity components were set to zero and the wall pressure was determined from the normal momentum equation. Wall temperatures were either specified or obtained from the specified wall heat fluxes and the points on the first grid layer off the walls. Magnetic field was either specified as uniform on a particular wall, or its normal derivative to the wall was set to zero. The governing system of eight partial differential equations (8-11) was transformed into a non-orthogonal curvilinear coordinate system compatible with a typical three-dimensional boundary-conforming structured computational grid. In such a way, the resulting finite difference algorithm for an iterative integration of the system can be applied to relatively arbitrary three-dimensional configurations. Since the system is singular (its time-dependent term in the mass conservation equation is zero), it can be integrated simultaneously only after introducing an artificially time-dependent term [Chorin 1967] in the mass conservation. Consequently, such an "artificial compressibility" iterative process does not follow physical time, but rather an artificial time coordinate. As a result, intermediate solutions are not time-accurate pictures of the flow field, but the final converged steady solution is accurate since the artificial compressibility term variation with iterations then becomes zero.

We are using an explicit four-step time-integration and central differencing in space. Since the magnetic field transport equations (11) are strongly parabolic (for the given velocity field), their allowable integration time step is much smaller than in the case of the Navier-Stokes equations (7-10). Consequently, we coded the three magnetic transport equations separately from the three-dimensional Navier-Stokes equations [Lee and Dulikravich 1991] so that we can use different time steps for the two systems. Communication between the two systems based on periodically updating source terms (thermal buoyancy and magnetic effect s) in the Navier-Stokes system.

NUMERICAL RESULTS

Based on this analytical model for a two-fluid MHD solidification, a fully three-dimensional MHD flow analysis computer program was developed. Numerical results from this code were compared with known three-dimensional MHD analytical solutions in the case of no heat transfer [Lee and Dulikravich 1991] and in the case of heat transfer but without solidification [Ozoe and Okada 1991]. In both cases the code proved to be highly accurate [Dulikravich, Ahuja and Lee 1993a]. This code was then augmented to incorporate temperature-dependent physical properties of the melt and the solid phase and the effects of latent heat release with an adequate account of the mushy region.

We decided to study the three-dimensional MHD effects on solidification by numerically analyzing an MHD solidification in a parallelepipedal closed container initially filled with molten silicon. The container was discretized with $40 \times 20 \times 20$ grid cells that were clustered symmetrically towards all the walls (Figure 1). Gravity was assumed to act vertically downward in the positive z-direction. If not indicated otherwise, the solid walls were thermally insulated. The values of the reference parameters were: $|v_o| = 0.02342$ m s^{-1}, $l_o = 0.02$ m, $|g_o| = 9.81$ m s^{-2}. Physical properties for silicon were compiled from a number of references (Table 1) which lead to

the following values of the non-dimensional numbers: Gr = 2.89 x 10^6, Re = $Gr^{1/2}$ = 1702, Ec = 2.589 x 10^{-8}, Pr = 0.01161, Pr = 4.255 x 10^{-6} and Ht = 837.3 Bo, where Bo is measured in Teslas. The exponent used in the model for latent heat release (1) was n = 5. Test cases were run with Ht = 0, 20, 30, 60 corresponding to the magnetic fields having strengths of 0 Tesla, 0.02389 Tesla, 0.03583 Tesla and 0.07166 Tesla, respectively.

Solidification From the Top

In this case the container had dimensions 0.04 m x 0.02 m x 0.02 m. Top wall was uniformly cooled below freezing temperature (θ = - 0.5) and the bottom wall was uniformly heated (θ = 0.5). A solidification case was first run without the magnetic field (Ht = 0). The computed contours of equal vertical velocity magnitude evaluated in the z^* = 0.3 horizontal plane (Fig. 2a) indicate strong upward melt motion mainly along the short vertical walls and a centrally located downward jet. This is more evident in Figures 2b (evaluated at y^* = 0.5 vertical mid-plane) and 2c (evaluated at x^* = 0.5 vertical mid-plane) where it is clear that almost one-third (4926 solidified cells out of 16000 computational cells in the container) solidified starting from the top wall [Kerr et al. 1990]. Evidently, heat transfer is carried out by both conduction and convection. The computed isotherms in the vertical y^* = 0.5 mid-plane (Fig. 2d) and in the vertical x^* = 0.5 mid-plane (Fig. 2e) indicate that the solid/melt interface is somewhat pulled down in the central part of the container due to the strong centrally located downward melt jet. After reaching the bottom of the container, the jet spreads out and starts mowing upwards along the side walls thus forming a deformed vertical thoroidal melt motion.

A uniform steady magnetic field of Ht = 20 was then assigned in the vertically downward direction (same as the gravity direction). The computed contours of equal vertical velocity magnitude evaluated in the z^* = 0.25 horizontal plane (Fig. 3a) now indicate that the peak upward melt motion is mainly along the long vertical walls, while the centrally located downward jet became narrower and developed a non-parabolic profile. It is especially important to notice that the velocity profiles close to the walls and the solid/melt interface became steeper (Fig. 3b and 3c) which is typical of MHD flows. This in turn caused enhanced heat convection in the mushy region resulting in less accrued solid (4773 solidified computational cells). Because of the stronger downward centrally located jet the computed isotherms in the vertical mid-planes indicate slight sagging of the solid/melt interface (Fig. 3d and 3e).

Finally, a uniform steady magnetic field of Ht = 60 was assigned in the vertically downward direction. The computed contours of equal vertical velocity magnitude evaluated in the z^* = 0.25 horizontal plane (Fig. 4a) indicate a dramatic change as compared to the two previous cases. Specifically, the peak upward melt motion is contained in a narrow region along the short vertical walls, while the centrally located downward jet became wider and developed a strongly double-parabolic profile (Fig. 4a). The magnitudes of velocity vector components in the entire flow field were substantially reduced (Fig. 4b and 4c) to about 30% of those in the case with Ht = 20. Because of the weaker and less concentrated downward centrally located jet the computed isotherms in the vertical mid-planes indicate that the solid/melt interface is more planar (Fig. 4d and 4e). In this case there were 4676 solidified computational cells.

Solidification From a Side

The solidification was then tested for the case where one vertical wall (x^* = 0) was kept uniformly hot (θ = 0.5) and the opposite vertical wall (x^* = 1) was at a uniformly below freezing temperature (θ = - 0.5). Three runs were performed; one without the magnetic field (Ht = 0) and the other two with a uniform external magnetic field (Ht = 30) applied in the vertical z-direction and horizontal x-direction, respectively. The container size in this case was 0.01 m x 0.01 m x 0.02 m.

In the case of no magnetic field (Ht = 0), the computed contours of equal z-momentum evaluated in the $z^* = 0.5$ horizontal mid-plane indicate (Fig. 5a) a single large vortex that rises the melt at the hot wall and descends it at the solid/melt interface (Fig. 5b). The computed isotherms in the vertical $y^* = 0.5$ (Fig. 5c) and $x^* = 0.5$ (Fig. 5d) mid-planes show that the solid/melt interface is highly curved and three-dimensional. In this case there were 3990 solidified computational cells.

When the uniform magnetic field of Ht = 30 was applied downward, the computed contours of equal z-momentum evaluated in the $z^* = 0.5$ horizontal mid-plane indicate (Fig. 6a) that the intensity of the single large vortex decreased (Fig. 6b). Also, a recirculation mini-vortex that existed at the lower corner of the hot vertical wall in the case without a magnetic field (Fig. 5b) was now eliminated. Computed isotherms in the vertical mid-planes (Fig. 6c and 6d) indicate that the solid/melt surface in this case became essentially two-dimensional. The number of solidified computational cells in this case increased significantly to 4283.

A uniform magnetic field of Ht = 30 was then applied horizontally in the hot-to-cold x-direction. The computed contours of equal z-momentum evaluated in the $z^* = 0.5$ horizontal mid-plane indicate (Fig. 7a) that the intensity of the single large vortex decreased even further (Fig. 7b). Computed isotherms in the vertical mid-planes (Fig. 7c and 7d) indicate that the solid/melt interface became essentially two-dimensional. The number of solidified computational cells in this case increased significantly to 4311.

REFERENCES

Chorin, A.: A Numerical Method for Solving Incompressible Viscous Flow Problems, Journal of Computational Physics. vol. 2, 1967, pp. 12-26.

Dulikravich, G.S., Ahuja, V. and Lee, S.: Three-Dimensional Solidification With Magnetic Fields and Reduced Gravity. AIAA paper 93-0912, Aerospace Sciences Meeting, Reno, Nevada, January 11-14, 1993a.

Dulikravich, G.S., Ahuja, V. and Lee, S.: Three-Dimensional Control of Crystal Growth Using Magnetic Fields, SPIE paper 1916-07, Proceedings of Smart Structures and Materials Conference, Albuquerque, N. M., February 1-4, 1993b.

Dulikravich, G.S. and Ahuja, V.: Modeling Three-Dimensional Solidification With Magnetic Fields and Reduced Gravity. To appear in Internat. J. of Heat and Mass Transfer, 1993.

Dulikravich, G.S., Kosovic, B. and Lee, S.: Solidification in Reduced Gravity With Magnetic Fields and Temperature-Dependent Physical Properties, Symposium on Heat and Mass Transfer in Solidification Processing, Editors: S.G. Advani and C. Beckermann, ASME WAM'91, Atlanta, GA, Dec. 1-6, 1991, ASME HTD-Vol. 175/MD-Vol.25, 1991, pp. 61-73,

Dulikravich, G.S., Kosovic, B. and Lee, S.: Magnetized Fiber Orientation Control in Solidifying Composites: Numerical Simulation, 28th ASME National Heat Transfer Conference, San Diego, CA., August 9-12, 1992, Symposium on Transport Phenomena in Materials Processing and Manufacturing, Editors: M. Charmchi et al., ASME HTD-Vol. 196, 1992, pp. 135-144; also in Journal of Heat Transfer. vol.115, 1993, pp. 255-262.

Gray, D.D. and Giorgini, A.: The Validity of the Boussinesq Approximation for Liquids and Gases, International Journal of Heat and Mass Transfer, vol. 19, 1976, pp. 545-551.

Kerr,R.C., Woods, A.W., Worster, M.G. and Huppert, H.E.: Solidification of an Alloy Cooled From Above. Part 1. Equilibrium Growth. Journal of Fluid Mechanics, vol. 216, 1990, pp. 323-342.

Kosovic, B., Dulikravich, G.S. and Lee, S.: Freezing Under the Influence of a Magnetic Field: Computer Simulation, Proceedings of ICHMT International Symposium on Macroscopic and Microscopic Heat & Mass Transfer in Biomedical Engineering, Editors: K.Diller and A. Shitzer, Athens, Greece, Sept. 2-6, 1991, Elsevier Press, 1992, pp. 307-326.

Lee, S. and Dulikravich, G.S.: Magnetohydrodynamic Steady Flow Computations in Three Dimensions, Internat. Journal for Numerical Methods in Fluids. vol. 13, No. 8, 1991, pp. 917-936.

Ozoe, H. and Okada, K.: The Effect of the Direction of the External Magnetic Field on the Three-Dimensional Natural Convection in a Cubical Enclosure, International Journal of Heat and Mass Transfer. vol. 32, No. 2, 1989, pp. 1939-1954.

Poirier, D. and Salcudean, M.: On Numerical Methods Used in Mathematical Modeling of Phase Change in Liquid Metals. ASME paper 86-WAM/HT-22, Anaheim, CA, Dec. 7-12, 1986.

Salcudean, M. and Sabhapathy, P.: Numerical Study of Liquid Encapsulated Czochralski Growth of Gallium Arsenide With and Without an Axial Magnetic Field, ASME MD-Vol. 20, Symposium on Computer Modeling and Simulation of Manufacturing Processes, Editors: Singh, B., Im,Y. T., Haque, I. and Altan, C., Book No. G00552, 1990, pp. 115-127.

Stuetzer, O.M.: Magnetohydrodynamics and Electrohydrodynamics, The Physics of Fluids. vol. 5, No. 5 , 534-544 (1962).

Voller, V.R. and Swaminathan, C.R.: General Source-Based Method for Solidification Phase Change. Numerical Heat Transfer, Part B. vol. 19, 1991, pp. 175-189.

ρ_l [kg m^{-3}]	2550
ρ_s [kg m^{-3}]	2330
c_l [J kg^{-1} K^{-1}]	1059
c_s [J kg^{-1} K^{-1}]	1038
k_l [W m^{-1} K^{-1}]	64
k_s [W m^{-1} K^{-1}]	22
T_l [K]	1685
T_m [K]	1683
T_s [K]	1681
μ [kg m^{-1} s^{-1}]	7.018×10^{-4}
α_l [K^{-1}]	1.41×10^{-4}
α_s [K^{-1}]	1.41×10^{-4}
L [J kg^{-1}]	1803000
σ_l [W^{-1} m^{-1}]	12.3×10^5
σ_s [W^{-1} m^{-1}]	4.3×10^4
γ [Tm A^{-1}]	$4\pi \times 10^{-6}$

Table 1. Physical properties used for silicon.

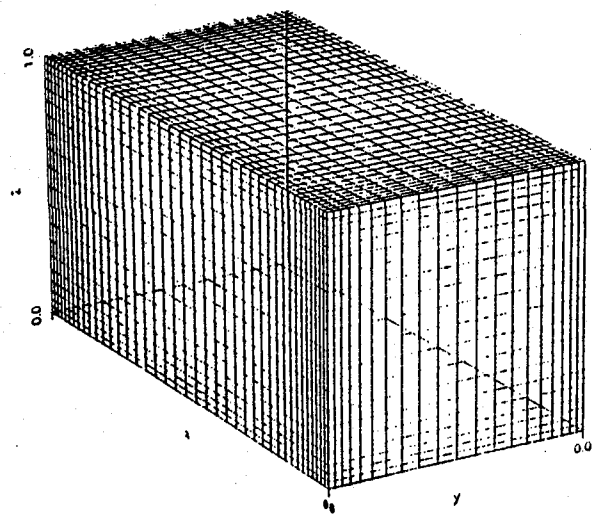

Figure 1. Computational grid and coordinate system

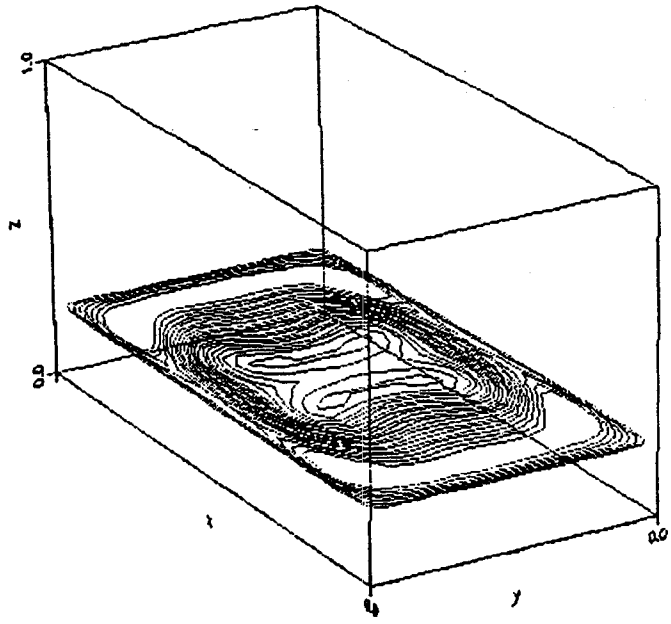

a

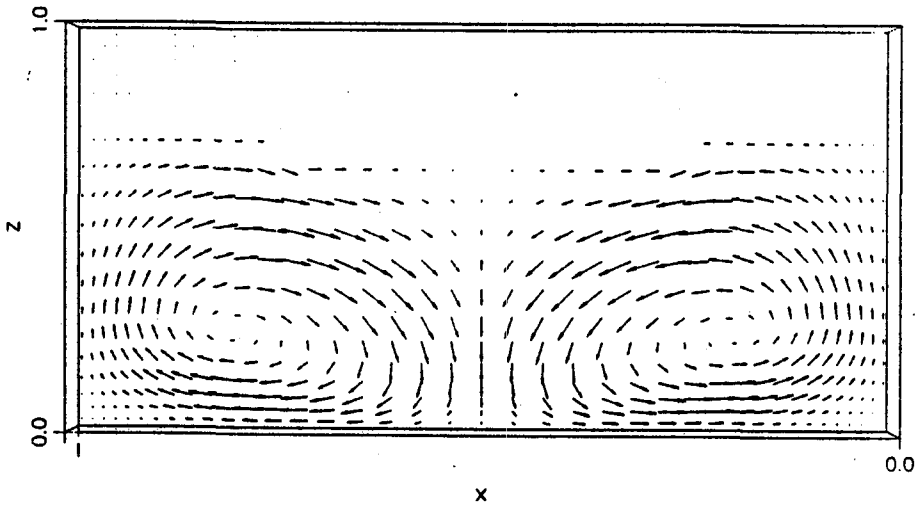

b

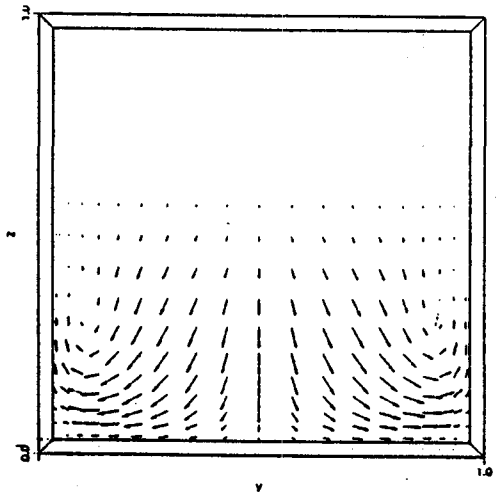

c

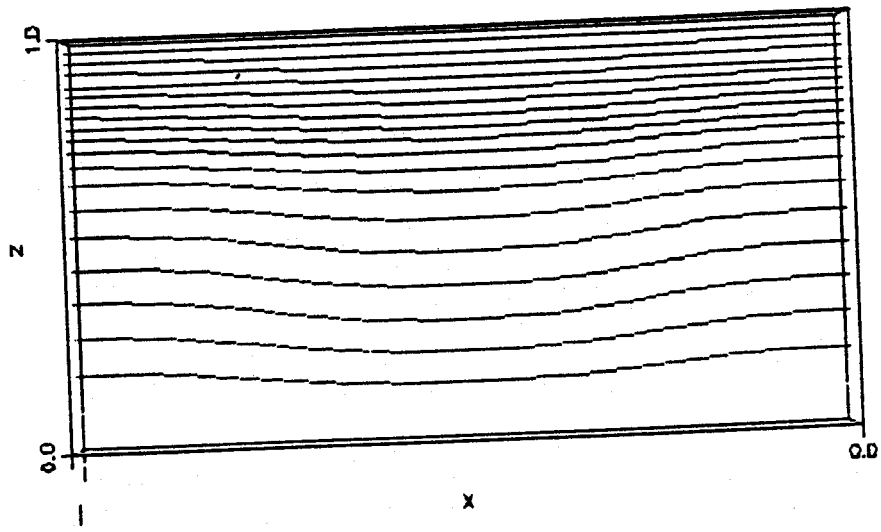

d

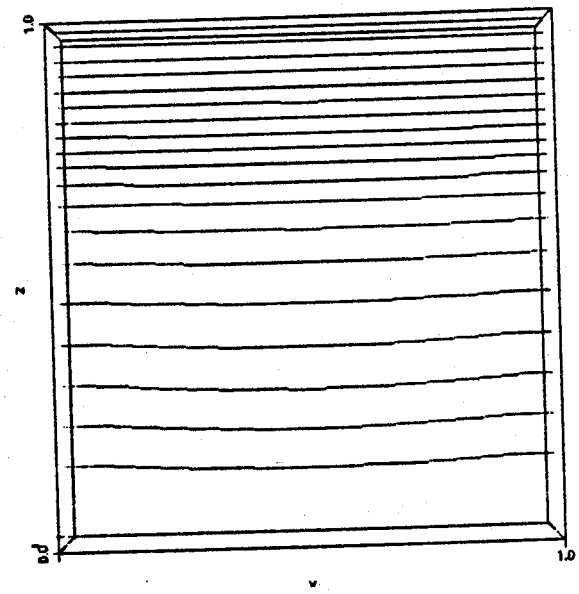

e

Figure 2. Solidification from the top: Ht = 0.
a) constant vertical velocity component contours at $z^* = 0.3$ horizontal plane; b) velocity vector field in vertical $y^* = 0.5$ mid-plane; c) velocity vector field in vertical $x^* = 0.5$ mid-plane; d) isotherms in vertical $y^* = 0.5$ mid-plane; e) isotherms in vertical $x^* = 0.5$ mid-plane.

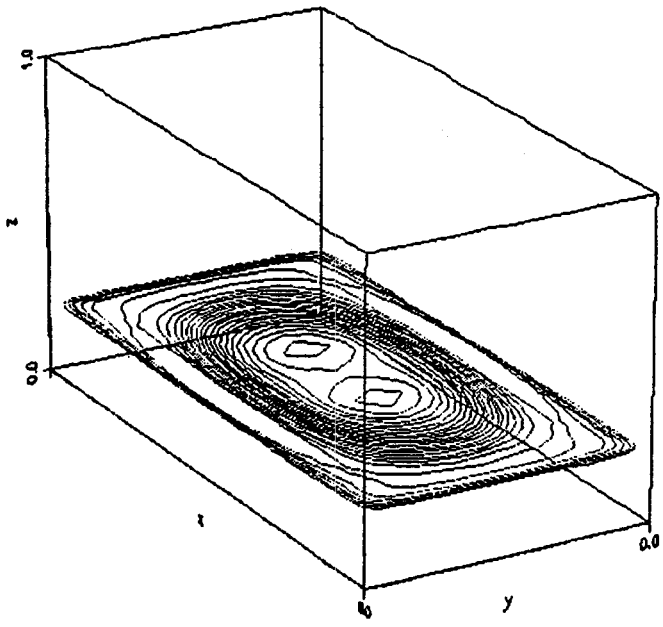

a

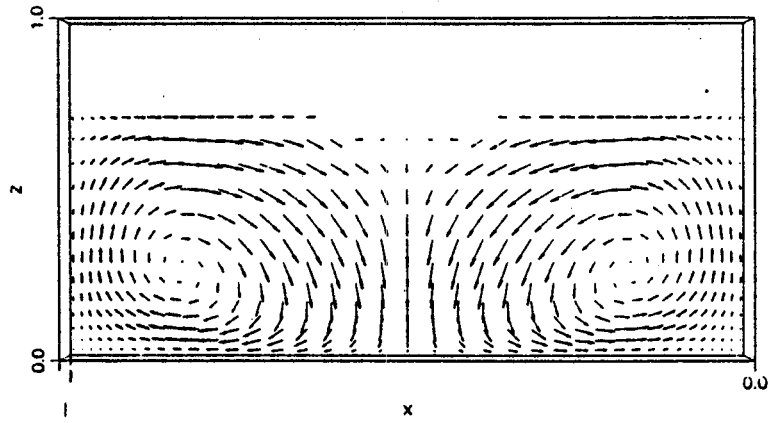

b

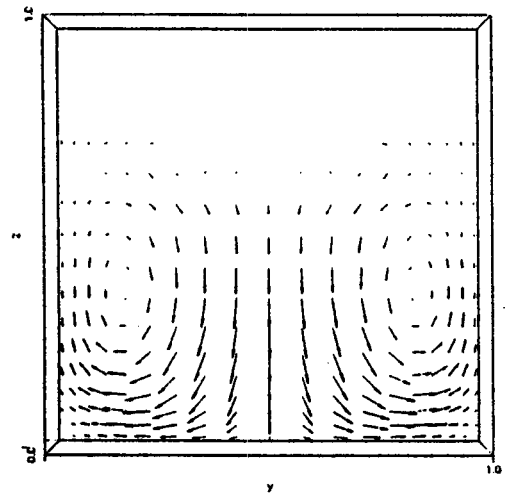

c

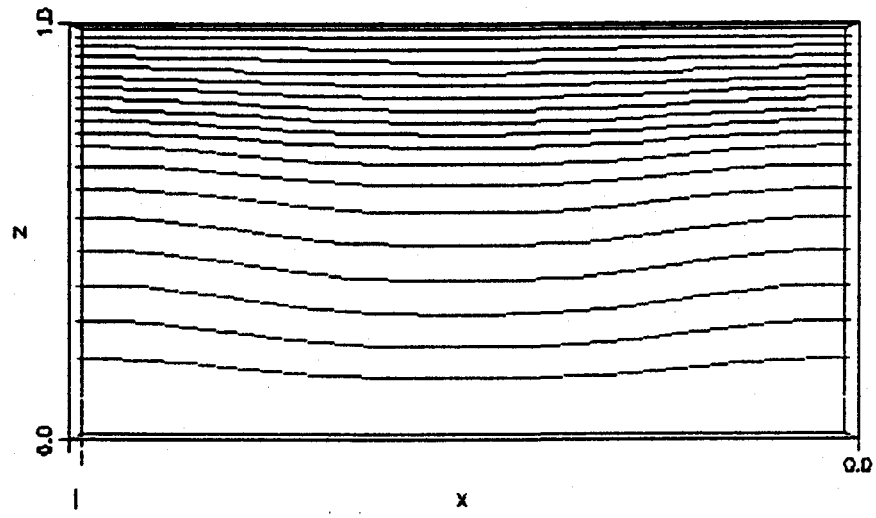

d

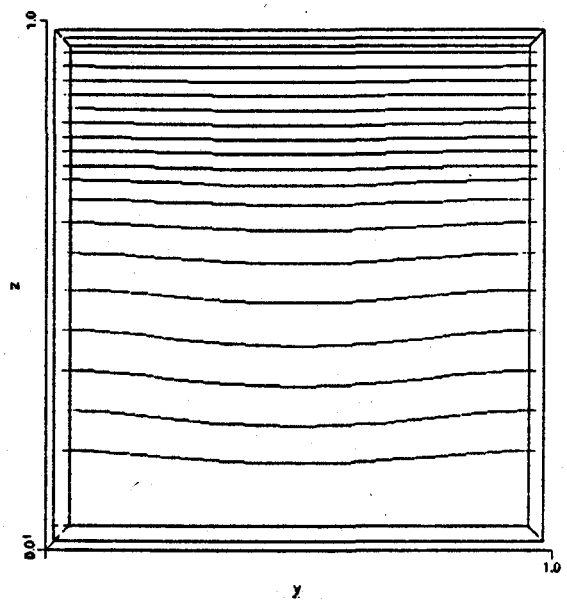

e

Figure 3. Solidification from the top: Ht = 20.
a) constant vertical velocity component contours at $z^* = 0.3$ horizontal plane; b) velocity vector field in vertical $y^* = 0.5$ mid-plane; c) velocity vector field in vertical $x^* = 0.5$ mid-plane; d) isotherms in vertical $y^* = 0.5$ mid-plane; e) isotherms in vertical $x^* = 0.5$ mid-plane.

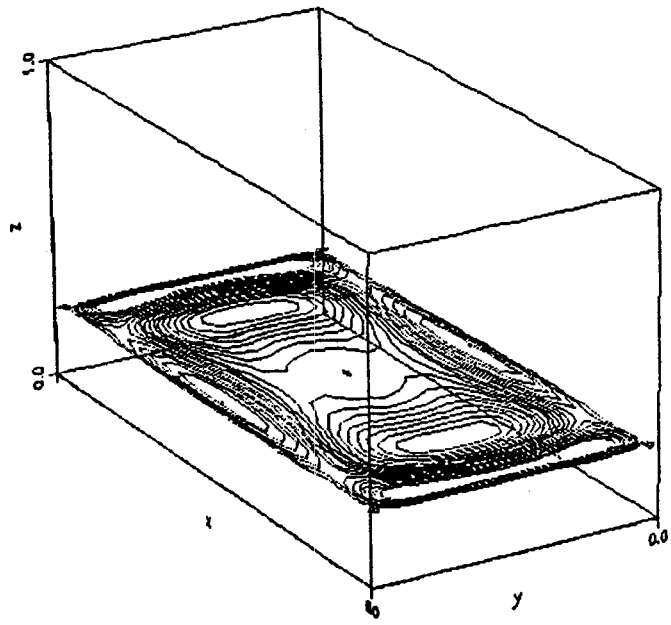

a

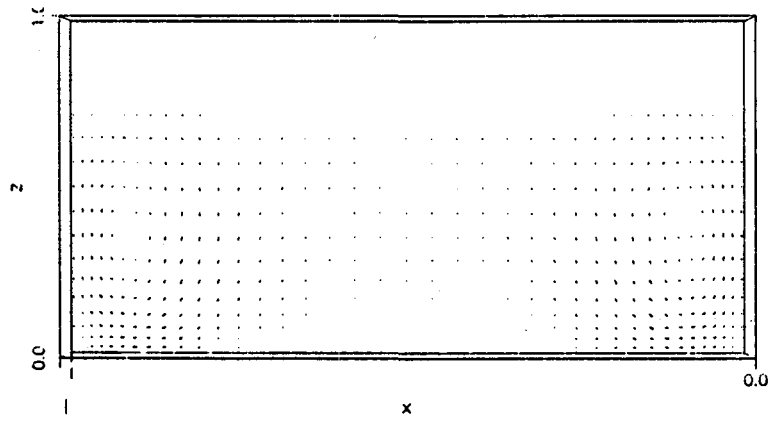

b

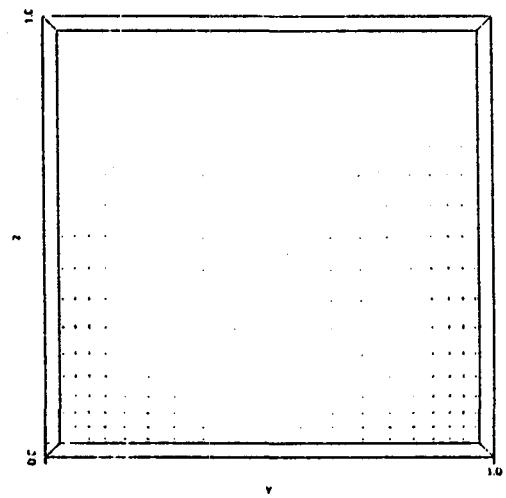

c

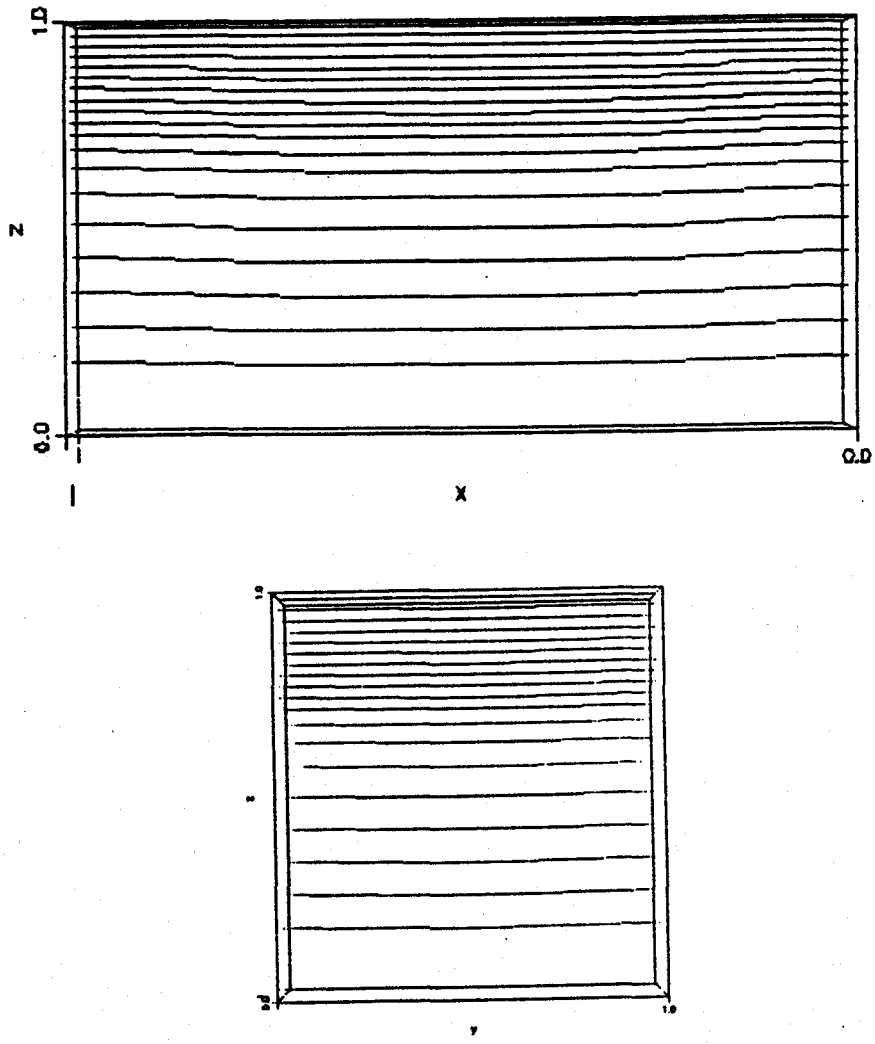

Figure 4. Solidification from the top: Ht = 60.
a) constant vertical velocity component contours at $z^* = 0.3$ horizontal plane; b) velocity vector field in vertical $y^* = 0.5$ mid-plane; c) velocity vector field in vertical $x^* = 0.5$ mid-plane; d) isotherms in vertical $y^* = 0.5$ mid-plane; e) isotherms in vertical $x^* = 0.5$ mid-plane.

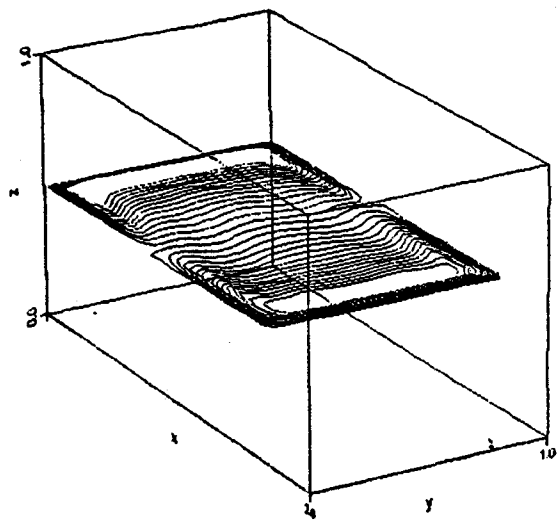

a

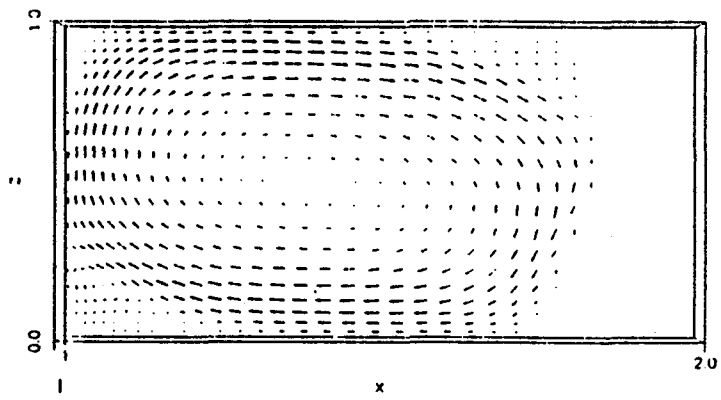

b

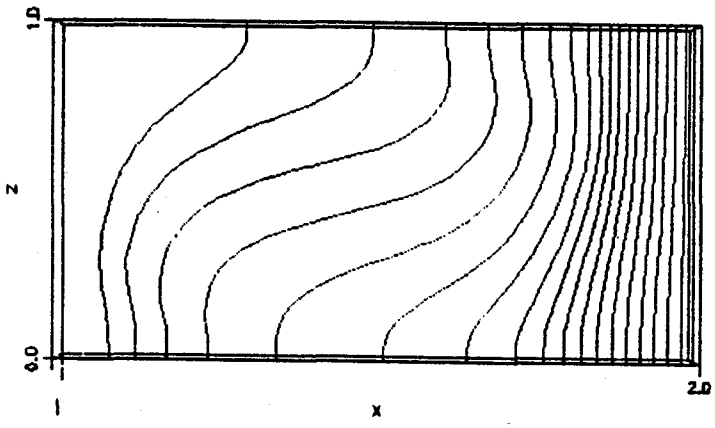

c

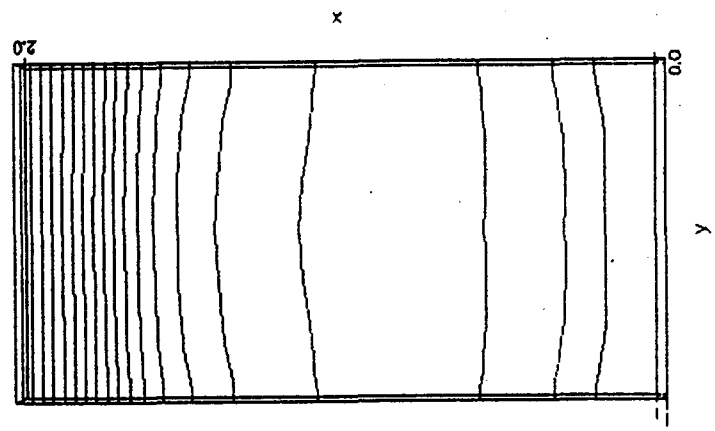

d

Figure 5. Solidification from the side: Ht = 0.
a) constant vertical velocity component contours at $z^* = 0.5$ horizontal mid-plane; b) velocity vector field in vertical $y^* = 0.5$ mid-plane; c) isotherms in vertical $y^* = 0.5$ mid-plane; d) isotherms in vertical $x^* = 0.5$ mid-plane.

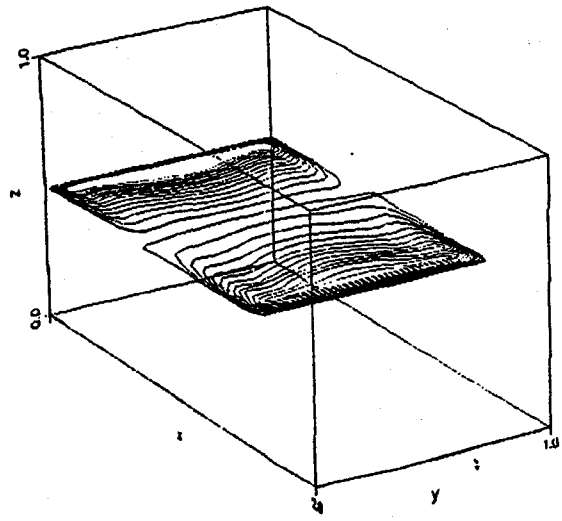

a

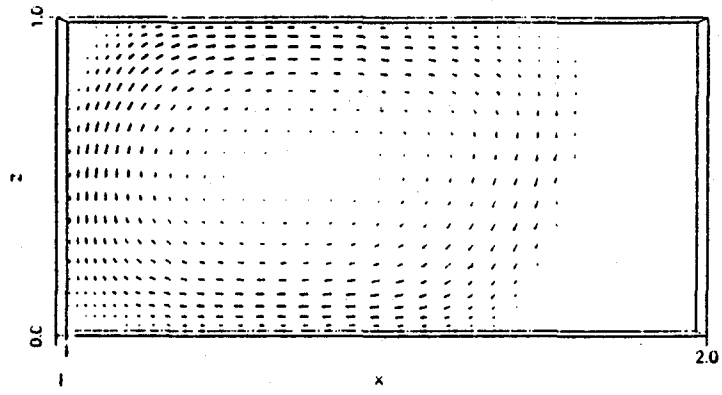

b

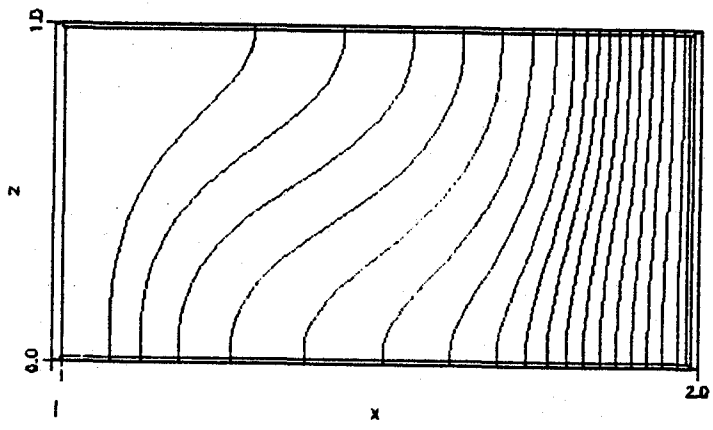

c

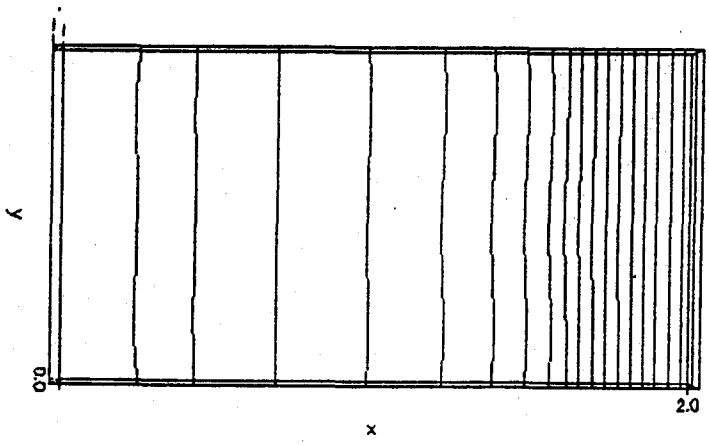

d

Figure 6. Solidification from the side: Ht = 30 applied vertically.
a) constant vertical velocity component contours at $z^* = 0.5$ horizontal mid-plane; b) velocity vector field in vertical $y^* = 0.5$ mid-plane; c) isotherms in vertical $y^* = 0.5$ mid-plane; d) isotherms in vertical $x^* = 0.5$ mid-plane.

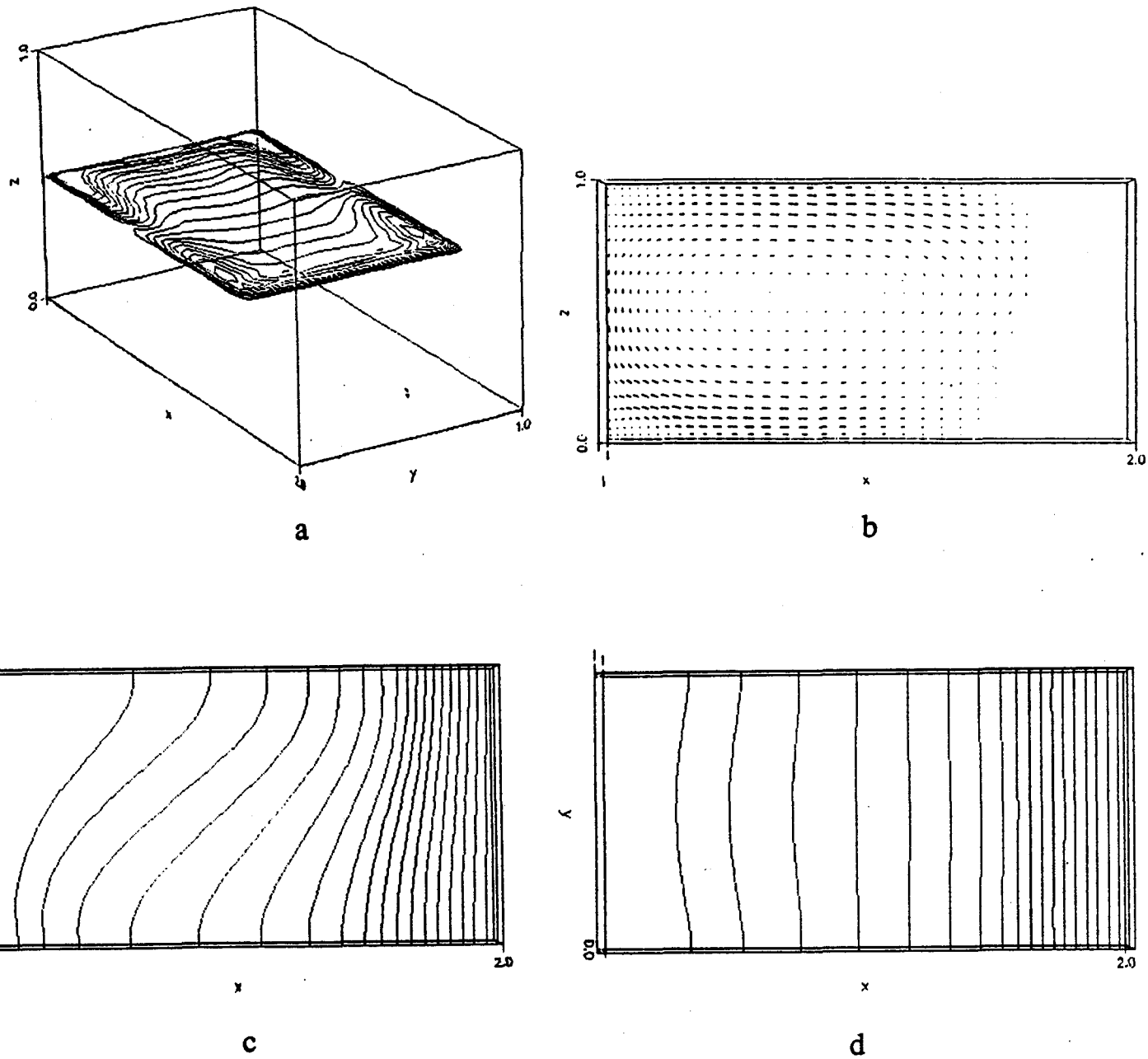

Figure 7. Solidification from the side: Ht = 30 applied in hot-to-cold direction.
a) constant vertical velocity component contours at $z^* = 0.5$ horizontal mid-plane; b) velocity vector field in vertical $y^* = 0.5$ mid-plane; c) isotherms in vertical $y^* = 0.5$ mid-plane; d) isotherms in vertical $x^* = 0.5$ mid-plane.

Session
Six

Analysis Techniques

UNSTEADY THREE-DIMENSIONAL THERMAL FIELD PREDICTION IN TURBINE BLADES USING NONLINEAR BEM

Thomas J. Martin* and George S. Dulikravich*
Department of Aerospace Engineering
The Pennsylvania State University, University Park, PA 16802, USA

SUMMARY

A time-and-space accurate and computationally efficient fully three-dimensional unsteady temperature field analysis computer code has been developed for truly arbitrary configurations. It uses Boundary Element Method (BEM) formulation based on an unsteady Green's function approach, multi-point Gaussian quadrature spatial integration on each panel, and a highly clustered time-step integration. The code accepts either temperatures or heat fluxes as boundary conditions that can vary in time on a point-by-point basis. Comparisons of the BEM numerical results and known analytical unsteady results for simple shapes demonstrate very high accuracy and reliability of the algorithm. An example of computed three-dimensional temperature and heat flux fields in a realistically shaped internally cooled turbine blade is also discussed.

INTRODUCTION

For linear boundary-value and initial-value problems it is computationally more efficient to use BEM rather than finite differencing or finite element technique. An additional benefit is that the BEM requires a relatively coarse grid and that it can be easily extended to non-linear conduction problems via Kirchoff's transformation. Probably the most important fact is that the BEM is essentially a non-iterative technique thus making the BEM codes more reliable [Dulikravich and Hayes 1988; Dargush and Banerjee 1991].

THEORY OF 3-D BOUNDARY ELEMENTS

The governing equation for heat conduction in the absence of heat generators is

$$\frac{\partial u}{\partial t} = \alpha \nabla^2 u \tag{1}$$

where α is the thermal diffusivity such that $\alpha = k/\rho c$, k is the thermal conductivity, ρ is the mass density, and c is the specific heat. As the problem is now time-dependent, the weighted residual statement must be integrated with relation to time and space. After integration by parts twice [Brebbia and Dominguez 1989], one obtains

$$\int_{t_0}^{t}\int_{\Omega}\left(\nabla^2 u^* - \frac{1}{\alpha}\frac{\partial u^*}{\partial t}\right) u \, d\Omega \, d\tau + \int_{t_0}^{t}\int_{\Gamma} q\, u^* \, d\Gamma \, d\tau = \int_{t_0}^{t}\int_{\Gamma} u\, q^* \, d\Gamma \, d\tau + \left[\int_{\Omega} u\, u^* \, d\Omega\right]_{\tau=t_0}^{\tau=t} \tag{2}$$

where $t_0 < \tau < t$ and the $\partial u^*/\partial t$ term was obtained integrating by parts with respect to time.

---

* Graduate Research Assistant.

* Associate Profesor.

The corresponding fundamental solution for this equation is

$$u^* = \frac{1}{[4\pi\alpha(t-\tau)]^{D/2}} \exp\left[\frac{-r^2}{4\alpha(t-\tau)}\right] \tag{3}$$

where D is the number of spatial dimensionality, that is, D = 3 for three-dimensional problems and r is the distance from the point of integration, x_j, to the observation point, x_i. The fundamental solution satisfies the auxiliary equation

$$\nabla^2 u^* - \frac{1}{\alpha}\frac{\partial u^*}{\partial t} = 0 \tag{4}$$

and for $t = \tau$,

$$\int_\Omega u^* \, d\Omega = \begin{cases} 0 \text{ for } r \neq 0 \\ 1 \text{ for } r = 0 \end{cases} \tag{5}$$

Using these relations, one obtains the boundary element equation for the ith control point

$$c_i u_i + \int_{t_0}^{t}\int_\Gamma u\, q^* \, d\Gamma \, d\tau = \int_{t_0}^{t}\int_\Gamma q\, u^* \, d\Gamma \, d\tau + \left[\int_\Omega u\, u^* \, d\Omega\right]_{\tau=t_0} \tag{6}$$

The last term in the above formula represents the contribution of the initial state at $t = t_0$. Since the fundamental solution is time dependent, one does not need to solve this equation with an iterative scheme as is usually done in finite elements or finite differences. Instead, this equation can be solved for any time step after a known initial state although small time intervals are recommended. In the latter case, the potential at each node within the domain needs to be evaluated at the end of each time step in order to determine the initial conditions for the next time step. Although the primary advantage of boundary elements is lost (for unsteady problems, the discretization of the volume is necessary), the matrix is much smaller than those in finite elements and the inversion needs only be performed once if time-independent boundary conditions are enforced.

The region, Ω, and bounding surface, Γ, are discretized into N_{CELL} volume cells utilizing a total of N_{TOT} nodes and N_{SP} surface elements using a total N nodes. Nodal quantities are interpolated linearly across each individual cell or surface panel. One also needs to assume a variation in time for the functions u and q. If these functions do not vary significantly with respect to time, they may be treated as constant over small time intervals and the time integration may be performed stepwise. If greater accuracy is required, these functions may be assumed to vary linearly such that

$$u(x_i, x_j, t, \tau) = \frac{\tau - t_0}{\Delta t} u + \frac{t - \tau}{\Delta t} u_0 \tag{7}$$

where the subscript 0 indicate the variable at the previous time level and t is the current time level. The time step is defined as $\Delta t = t - t_0$. Once fully discretized, the boundary element equation may be expressed as

$$[H]\, U = [G]\, Q + P \tag{8}$$

for constant time elements. If linearly varying time elements are used, the boundary element

equation becomes

$$[H]\,U + [H_0]\,U_0 = [G]\,Q + [G_0]\,Q_0 + P \tag{9}$$

The term $U = (u_1,u_2,u_3,...,u_N)$ is the vector of potentials and $Q = (q_1,q_2,q_3,...,q_{Nsp})$ is a vector of fluxes where each term q_i contains four potential derivatives corresponding to the corner vertices of the N_{SP} quadrilateral surface panels. In addition, each term in the [G] matrix contains four terms corresponding to each q_i term. The terms in the [H] matrix are the properly summed coefficients corresponding to the potential at a specific node. The boundary element algorithm developed for use in three-dimensions with the inverse design code was formulated with isoparametric, quadrilateral surface panels and eight-point linearly deformed parallelepiped volume cells. Integration in space was done numerically with Gaussian quadrature and time integration was performed numerically using the trapezoid rule. Since the fundamental solutions contain a singularity at the end of each time step (at the time level $\tau = t$), the time integration points were clustered strongly near the singularity, $\tau = t$.

A transformation from the global (ξ,η,ζ) coordinate system is necessary to a localized (ξ_1,ξ_2) coordinate system defined over the surface of the body or to a (ξ,η,ζ) coordinate system defined for the volume cell of integration. The volume integrals are transformed such that

$$\int_{\Omega} u\,u^*\,d\Omega = \iiint u\,u^*\,|J|\,d\xi\,d\eta\,d\zeta \tag{10}$$

where $|J|$ is the determinant of the Jacobian matrix of the transformation, that is,

$$|J| = \det\left(\frac{\partial(x,y,z)}{\partial(\xi,\eta,\zeta)}\right). \tag{11}$$

The terms of the G and H matrices for constant time elements may be written as

$$H_{im} = \sum_{k=1}^{N_c} \int_{to}^{t} \int_{\Gamma_j} \phi_k\,q^*\,d\Gamma_j\,d\tau \quad \text{and} \quad G_{ijk} = \int_{to}^{t} \int_{\Gamma_j} \phi_k\,u^*\,d\Gamma_j\,d\tau \tag{12}$$

for the jth surface panel. The subscript m indicates the node number corresponding to the kth vertex of the jth surface panel and N_C is the number of surface panels connected to the mth node. The function f_k is the kth interpolation function corresponding to the value at the kth corner vertex of the jth surface panel. Discretization of the surface is identical to that described in section 2.2. If linearly varying time elements are used, the terms of the [G] and [H] matrices are similar and are formed into pairs of coefficient matrices due to the initial state and the current time level at the boundary.

$$H_{im0} = \sum_{k=1}^{N_c} \int_{to}^{t} \int_{\Gamma_j} \phi_k \frac{\tau - t_0}{\Delta t}\,q^*\,d\Gamma_j\,d\tau \tag{13}$$

$$H_{im} = \sum_{k=1}^{N_C} \int_{t_0}^{t} \int_{\Gamma_j} \phi_k \frac{t - \tau}{\Delta t} q^* \, d\Gamma_j \, d\tau \tag{14}$$

The vector P indicates the contribution of the initial state throughout the domain on the ith observation point and is of the form

$$P_i = \sum_{j=1}^{N_{CELL}} \sum_{k=1}^{8} u_{0jk} \int_{\Omega_j} \phi_k \, u^* \, d\Omega_j \tag{15}$$

where ϕ_k is the kth trilinear interpolation function of the linearly deformed parallelepiped cell and is of the form

$$\phi_k = \frac{1}{8}(1 \pm \xi)(1 \pm \eta)(1 \pm \zeta) \tag{16}$$

The term u_{0jk} is the potential on the kth vertex of the jth parallelepiped volume cell at time $\tau = t_0$. In discretized form, the fundamental solution contains the term r representing the distance from the point of integration on the jth volume cell or surface panel to the ith control point. The normal derivative of the fundamental solution may be determined as

$$q^* = \frac{\partial u^*}{\partial r} \frac{\partial r}{\partial n} = \frac{-d}{[4\pi\alpha(t-\tau)]^{D/2} 2\alpha(t-\tau)} \exp\left[\frac{-r^2}{4\alpha(t-\tau)}\right] \tag{17}$$

where d is defined by the normal distance from the ith point under consideration to the surface panel. If the control point is on the surface of integration, then $q^* = 0$ and the diagonal of [H] may be computed implicitly by the application of a uniform potential over the whole domain, which will give zero normal fluxes at the boundaries such that

$$H_{ii} = -\sum_{j=1}^{N_N} H_{ij} + P_i \tag{18}$$

NUMERICAL RESULTS

The accuracy and reliability of the BEM formulation governing three-dimensional, unsteady heat transfer problems has been verified versus the analytical solution for a finite length rod. Total surface of a cylinder of 0.5 m radius and 1.0 m in length was modeled with 216 nodes and 108 surface panels as shown in Figure 1. The thermal diffusivity, α, was specified to be 1.0 $m^2 s^{-1}$. The initial temperature of the cylinder was uniformly 0 °C and contained no heat sources or sinks. Then, suddenly, the boundary conditions on the cylinder were specified as 100 °C on the front face, 0 °C on the back face while the outer radial surface was kept adiabatic. The BEM algorithm used constant time interpolation, 3-point Gaussian quadrature for the surface and volume integration and a linear variation of the temperature and heat flux along the surface panels and volume cells. The analytic solution for this test case corresponded to the one-dimensional unsteady heat flow in a finite thin rod. Temperatures were obtained at various time levels and at several axial locations and are compared to the analytic results shown in Figure 2. As seen in this figure, there is a discrepancy between the numerical and analytic solutions averaging about 6 °C.

The geometry of the cylinder was then modeled differently by slightly clustering the surface panels and volume cells near the hot end. Figure 3 shows the results of the BEM in this case.

Notice that the average error has reduced to about 4 °C. The unsteady BEM algorithm was then developed with a linear variation within each time step for the temperatures and heat fluxes. This test case used the same slightly clustered geometry with identical boundary and initial conditions. A single BEM analysis run using linear time interpolation consumed about 15% more CPU time than the BEM formulation with constant time interpolation. It resulted in a solution which averaged a 3 °C error compared to the analytic solution. Figure 4 shows the computed temperatures from the BEM using linear time interpolation against the analytic solution at several axial locations. Figure 5 is a plot of the error between the BEM and the analytic solution.

The accuracy of the BEM algorithm could not be improved further while using the cylinder test case. Instead, a different and simpler geometry was developed and the BEM solution with this new geometry showed that much of the error in the previous tests was due to the cylindrical geometry. That is, since the BEM uses flat quadrilateral surface panels, the exact geometry of the cylinder surface could not be modeled properly. Figure 1 shows a discretized cross section of the circular cylinder and clearly depicts the inability of a limited number of flat surface panels to properly capture the surface curvature of the cylinder. Besides, elements surrounding the cylinder axis are nearly triangular in shape. These situations produce surface and volume integrals which behave somewhat singularly. The result is that the integrals are not properly integrated and may involve ill-conditioned BEM solution matrices.

The new geometry, a rectangular box of 0.1 m x 0.1 m base cross section and 1.0 m in length, was then used instead of the cylinder. The geometry was divided into 10 axial cells of equal size. The entire surface of the box was discretized with 44 nodes (four nodes per each section) and 44 flat quadrilateral surface panels (four side panels per each section). The boundary conditions on the box were specified as 100 °C on the front face, 0 °C on the back face while the side surfaces were kept adiabatic. The BEM algorithm used linear time interpolation, 5-point Gaussian quadrature and a linear variation of the temperature and heat flux along the surface panels and volume cells. Temperatures obtained with the unsteady BEM algorithm for the rectangular box were compared to the analytic solution at several axial locations. Figure 6 illustrates that the BEM solution for the box was much more accurate than those for the cylinder. Figure 7 shows the absolute value of the error in the temperatures computed using the BEM. These results indicate that the BEM generates an error of 0.5 °C with the maximum error below 0.9 °C.

The unsteady BEM algorithm was then modified to incorporate temperature-dependent material properties. Although the BEM solution of the linear heat conduction equation is quite fast (requiring less than 10 CPU seconds for 25 time steps on an IBM 3090 for the rectangular box), the addition of temperature-dependent material properties greatly increases the computational effort. Normally the BEM solution matrices need only to be computed once if the time intervals and diffusivity are constant. Since the diffusivity is now a function of temperature, the BEM solution matrices need to be developed at each time interval using temperatures computed at each source point in the surface and volume integrands.

The same rectangular box geometry and boundary conditions were used to test the accuracy of the three-dimensional, unsteady BEM algorithm with temperature-dependent material properties. The reference thermal conductivity was $\lambda_o = 1.0$ kcal m^{-1} s^{-1} K^{-1} and it varied linearly with temperature as $\lambda = \lambda_o + C\,T$. The temperature variations in time at a single axial location were collected for various degrees of nonlinearity given by the parameter C. These results are shown in Figure 8 and compare well with published computational results involving finite elements [Tanaka, Kikuta and Togoh 1987]. Total CPU time for 25 time steps with the temperature-dependent physical properties was approximately 300 seconds on an IBM 3090.

CONCLUSIONS

A fully three-dimensional unsteady heat conduction analysis code has been successfully developed and tested against known analytical solutions. The code is computationally efficient and reliable and can be used on arbitrary configurations. A modification involving temperature-dependent thermal diffusivity was also incorporated and shown to produce good results.

REFERENCES

Brebbia, C.A. and Dominguez, J.: Boundary Elements: An Introductory Course. McGraw-Hill Book Company, 1989.

Dargush, G.F. and Banerjee, P.K.: Application of the Boundary Element Method to Transient Heat Conduction. International Journal for Numerical Methods in Engineering, Vol. 31, 1991, pp. 1231-1247.

Dulikravich, G.S. and Hayes, L.J.; Control of Surface Temperatures to Optimize Survival in Cryopreservation, ASME Winter Annual Meeting", Proceedings of the Symposium on Computational Methods in Bioengineering, Editors: R.L. Spilker and B.R. Simon, Nov. 27-Dec. 2, 1988, ASME BED-Vol. 9, 1988, pp. 255-265.

Tanaka, M., Kikuta, M. and Togoh, H.: Boundary Element Analysis of Nonlinear Transient Heat Conduction Problems. Computer Methods in Applied Mechanics and Engineering, Vol. 62, No. 3, June 1987, pp. 321-329.

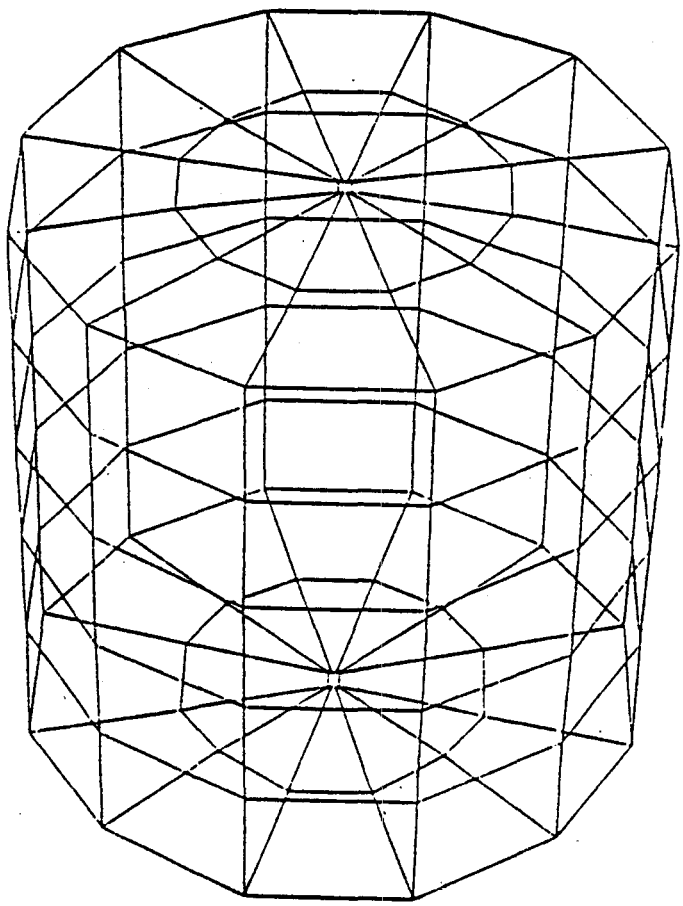

Figure 1. Geometry of a cylinder for the verification of the three-dimensional, unsteady BEM formulation.

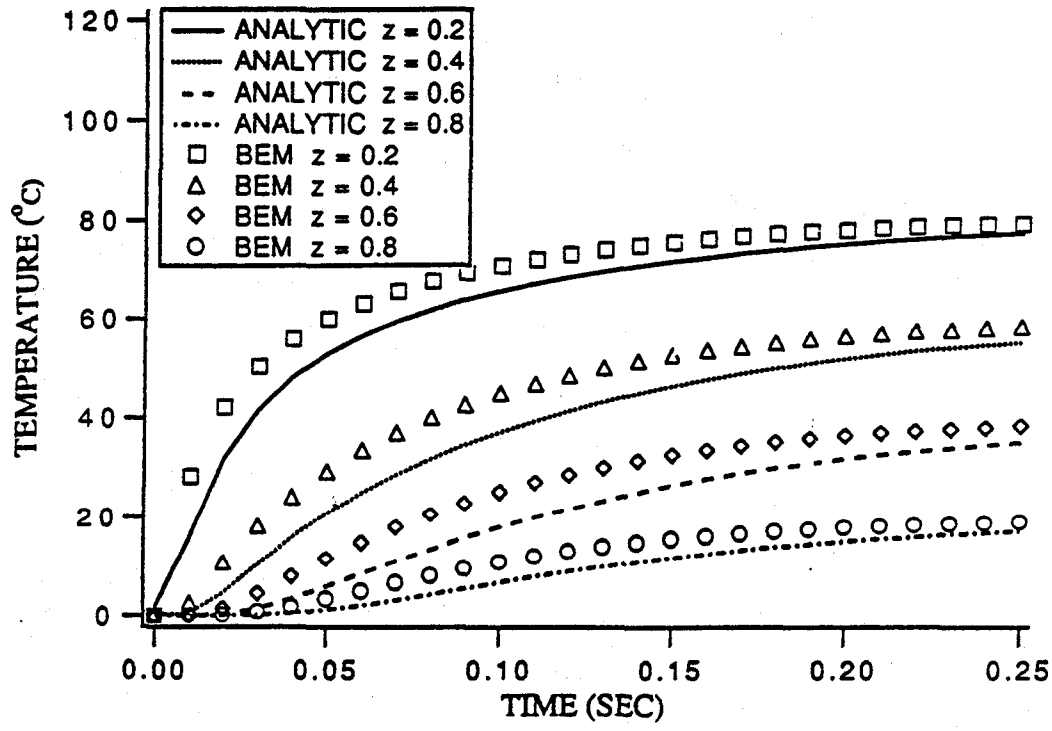

Figure 2. Comparison of temperatures between the unsteady BEM solution and the analytic solution using constant time elements.

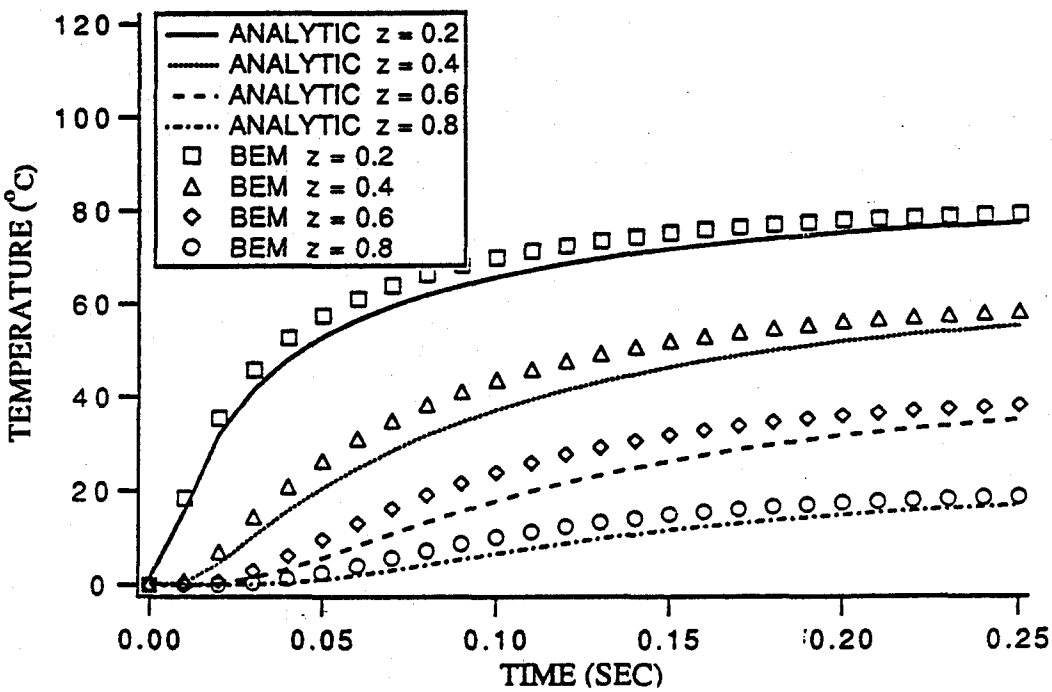

Figure 3. Comparison of temperatures between the unsteady BEM solution and the analytic solution using a refined grid and constant time elements.

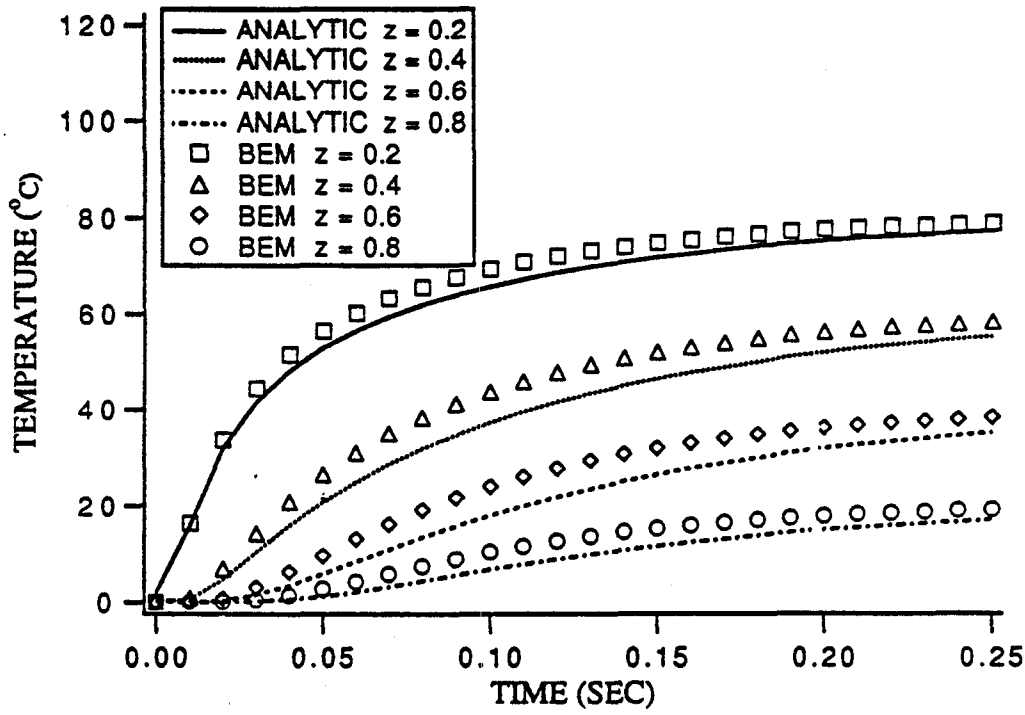

Figure 4. Comparison of temperatures between the unsteady BEM solution and the analytic solution using a refined grid and linear time elements.

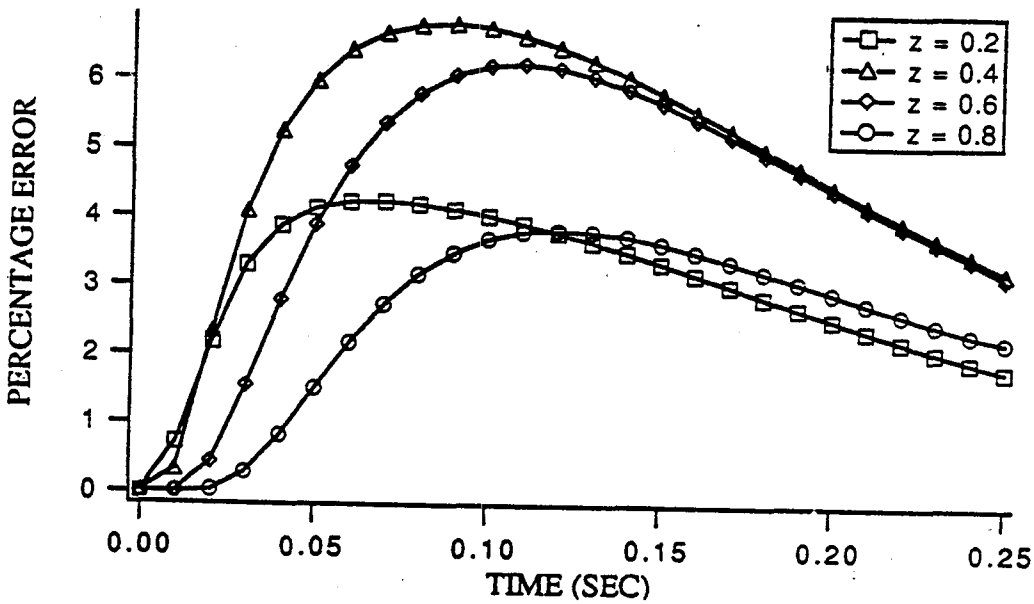

Figure 5. Relative error in temperature between the unsteady BEM solution and the analytic solution using a refined grid and linear time elements.

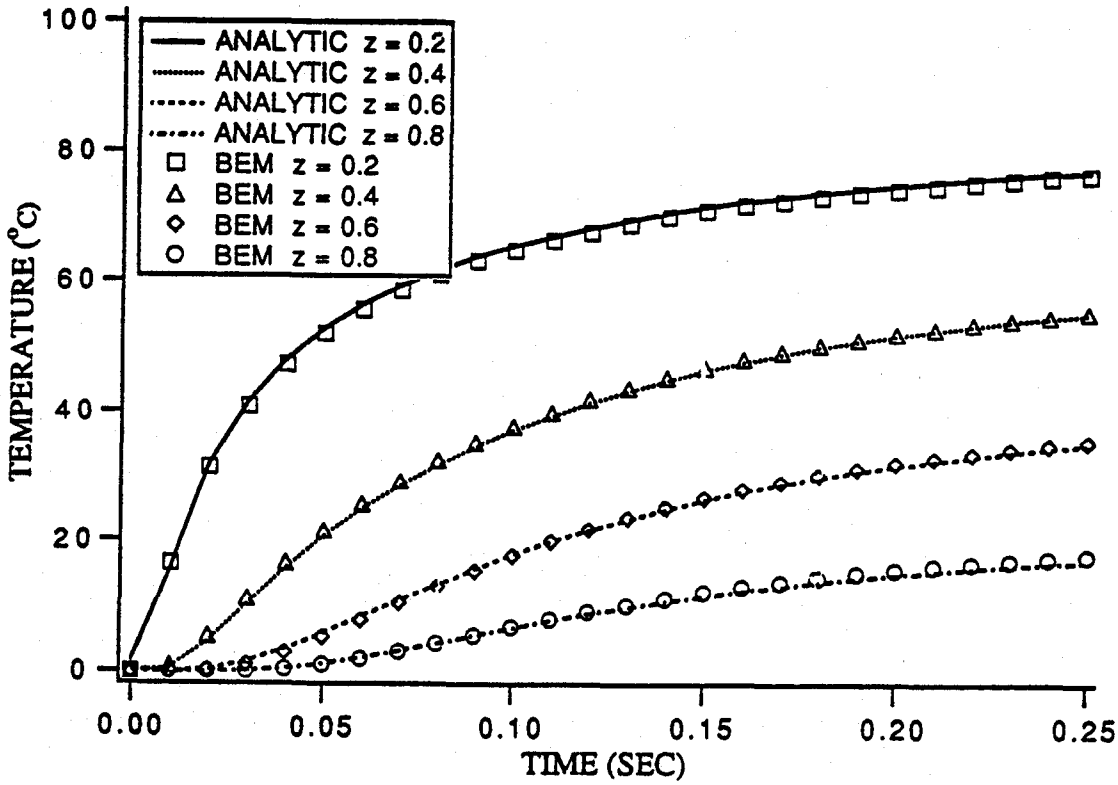

Figure 6. Comparison of temperatures between the unsteady BEM solution of a rectangular box and the analytic solution using linear time interpolation and accurate quadrature integration.

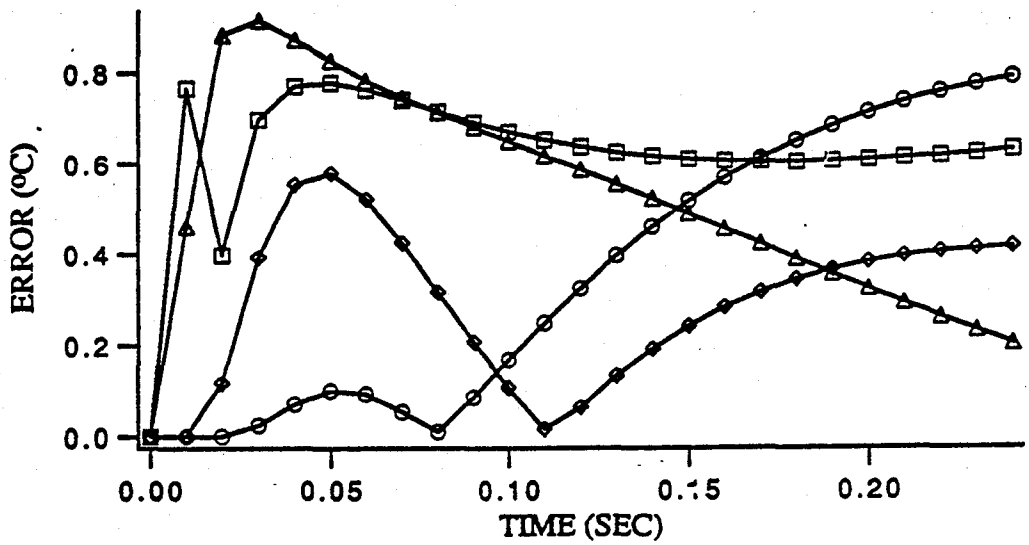

Figure 7 . Error in temperature between the unsteady BEM solution of a rectangular box and the analytic solution.

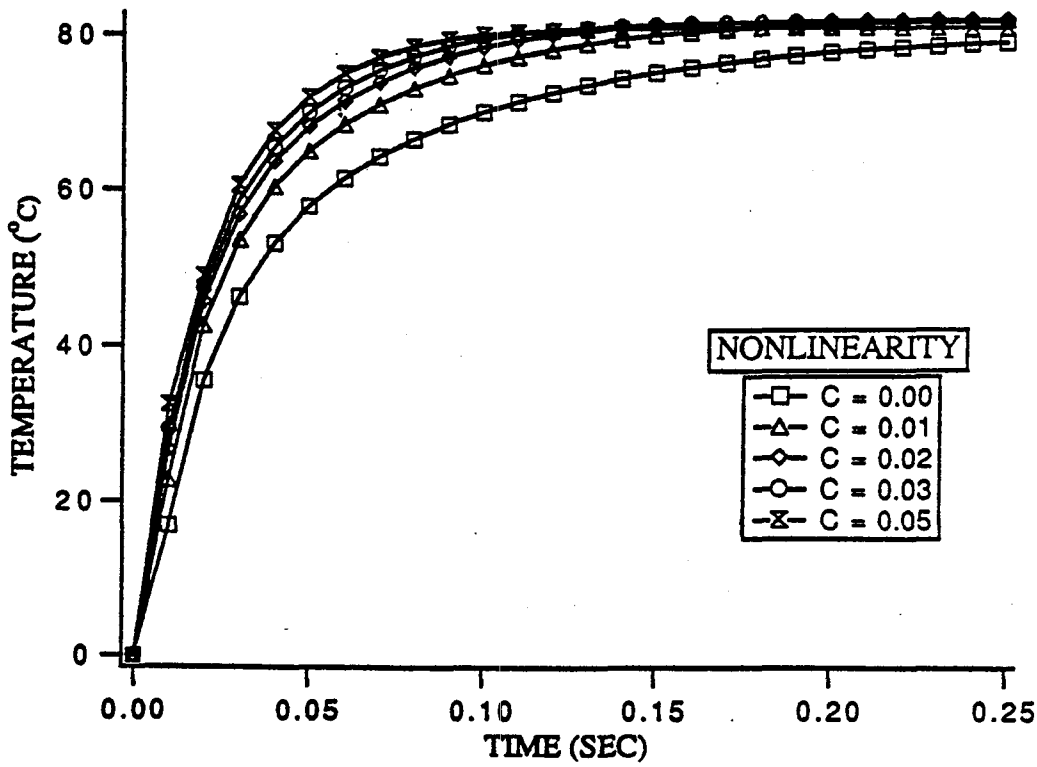

Figure 8 Results of the unsteady BEM algorithm with temperature-dependent material properties. The figure shows temperatures versus time at the z = 0.2 m axial location for various ranges of nonlinearity.

A DUAL RECIPROCAL BOUNDARY ELEMENT FORMULATION FOR VISCOUS FLOWS

Olu Lafe[1]
OLTech Corporation
Innovative Computing Group
11795 Sherwood Trail
Chesterland, Ohio 44026-1730

SUMMARY

The advantages inherent in the Boundary Element Method (BEM) for potential flows are exploited to solve viscous flow problems. The trick is the introduction of a so-called Dual Reciprocal technique in which the convective terms are represented by a global function whose unknown coefficients are determined by collocation. The approach, which is necessarily iterative, converts the governing partial differential equations (PDEs) into integral equations via the distribution of fictitious sources or dipoles of unknown strength on the boundary. These integral equations consist of two parts. The first is a boundary integral term, whose kernel is the unknown strength of the fictitious sources and the fundamental solution of a convection-free flow problem. The second part is a domain integral term whose kernel is the convective portion of the governing PDEs. The domain integration can be transformed to the boundary by using the Dual Reciprocal (DR) concept. The resulting formulation is a pure boundary integral computational process.

INTRODUCTION

The major advantage the BEM approach enjoys over other techniques is the confinement of the computation to the boundary. The result is the reduction in the effective dimension of the problem. The efficiency with which linear problems in continua can be solved using BEM has received considerable mention in the literature during the past decade. Apart from the reduced dimensionality and the need for no special domain discretization, other derived advantages include:

1. the ability to handle infinitely large domains;
2. a much reduced coefficient matrix;
3. the ease with which singularities are handled;
4. the restriction of the discretization errors to the boundary, so that the solution is as good as the description of the boundary geometry;
5. the robustness when complex geometries are involved;
6. the ability to find solutions *a posteriori* at desired points, not at nodes predetermined by the domain discretization;

[1] President

7. the great latitude in solving transient problems by a) using the appropriate time dependent fundamental solution in the formulation: b) applying the technique in a transform domain (*e.g.*, Laplace or Fourier): or c) using a time marching procedure.

Efforts at applying boundary integral techniques to nonlinear problems are quite recent. For over a decade the main focus was largely on linear problems such as potential flows (see *e.g.*, *Brebbia et al.*, [1984]. *Liggett & Liu* [1984]). BEM formulations for nonlinear (*e.g.*, *Lafe et al.*, [1981]; *Lafe & Cahan* [1990]) or those in heterogeneous continua (*e.g.*, *Cheng* [1984]; *Lafe et al.*, [1987-1992] have relied heavily on iterative methods which still require some domain integration. The *Dual Reciprocal* technique creates a major path for exploiting the advantages of BEM to solve nonlinear problems such as convective flows. No domain integration is involved when the *Dual Reciprocal* approach is followed.

The original credit for *Dual Reciprocal* BEM concept goes to *Nardini & Brebbia* [1982] who first suggested an innovative approach for transforming domain integrals to the boundary. However, until recently, prior investigations (see *e.g.*, *Brebbia* [1991]; *Partridge et al.*, [1992]) did not make use of a complete set of global functions. A series of local radial functions were utilized. This made convergence difficult or impossible for a class of nonlinear problems. This author and his co-workers (see *Cheng et al.*, [1993]) have recently derived a set of complete coordinate functions which have been tested on a family of strongly nonlinear PDEs. Excellent results have been obtained with the complete set. This work opens the door to the application of BEM to a wide spectrum of complex flow problems.

In this paper, we present the full formulation of the Dual Reciprocal Boundary Element Method (DRBEM), for incompressible convective flows.

GOVERNING EQUATIONS

Let the flow region is represented by Ω and the boundary is Γ. The pertinent flow equations are:

- *Continuity Equation*

$$\nabla \cdot \mathbf{v} = 0 \tag{1}$$

- *Conservation of Momentum*

$$\frac{\partial \mathbf{v}}{\partial t} + (\mathbf{v} \cdot \nabla)\mathbf{v} = -\frac{1}{\rho}\nabla p + \frac{1}{\rho}\nabla \cdot \tau + \mathbf{g} \tag{2}$$

where $\mathbf{v}$ is the velocity, p is pressure, $\mathbf{g}$ is the gravitational accelerator vector, τ is the viscous stress tensor. If μ is viscosity, then for a Newtonian fluid, τ is expressible in the form:

$$\tau = \mu \nabla \mathbf{v}$$

Dimensionless Equations

Let L = characteristic length scale, $\bar{v}$ = mean velocity, and η is the elevation of the point $(\mathbf{x})$. We can define the following dimensionless variables:

$$\mathbf{x}_* = \mathbf{x}/L \tag{3}$$

$$\mathbf{v}_* = \mathbf{v}/\bar{v} \tag{4}$$

$$p_* = (p + g\eta)/\left(\rho \bar{v}^2\right) \tag{5}$$

$$t_* = t\bar{v}/L \tag{6}$$

With these, the above conservation statements can be made dimensionless:

$$\nabla \cdot \mathbf{v}_* = 0 \tag{7}$$

$$\frac{\partial \mathbf{v}_*}{\partial t_*} + (\mathbf{v}_* \cdot \nabla)\mathbf{v}_* = -\nabla p_* + \frac{1}{R_e}\nabla^2 \mathbf{v}_* \tag{8}$$

where

$$R_e = \rho \bar{v} L/\mu = \text{Reynolds Number} \tag{9}$$

The governing equations can be rearranged and written in the pseudo-Poisson form:

$$\nabla^2 \Phi(\mathbf{x}_*, t_*) = F(\mathbf{x}_*, t_*) \tag{10}$$

where

$$\Phi = \begin{cases} \mathbf{v}_* & \textit{Velocity} \\ p_* & \textit{Pressure} \end{cases} \tag{11}$$

and

$$F = \begin{cases} R_e\left[\partial \mathbf{v}_*/\partial t_* + (\mathbf{v}_* \cdot \nabla)\mathbf{v}_* + \nabla p_*\right] & \textit{Velocity Equation} \\ -\nabla \cdot [(\mathbf{v} \cdot \nabla)\mathbf{v}] & \textit{Pressure Equation} \end{cases} \tag{12}$$

The pressure equation is obtained by introducing the continuity equation into the divergence of the momentum equation. Note that in the velocity equation, Φ and F are vectors with two (for 2-D and axi-symmetric problems) or three (for 3-D problems) components. We will now drop the $*$ prefix in the dimensionless variables, for convenience.

For most flow problems the boundary conditions will generally consist of three types:

- **Dirichlet Boundary** (Γ_Φ)

$$\Phi = \Phi_b$$

- **Neumann Boundary** (Γ_Q)

$$Q = \frac{\partial \Phi}{\partial n} = Q_b$$

  where $\partial\Phi/\partial n = \nabla\Phi \cdot \mathbf{n}$, and $\mathbf{n}$ is the unit vector normal to the boundary.

- **Mixed** (Γ_M)

$$\zeta(\Phi, \nabla\Phi, \mathbf{x}, t) = 0$$

where ζ is some specified function. A free-surface will be an example of the third. In most iterative schemes it is usual to recast the *Mixed* boundary condition in the form of either the *Dirichlet* or the *Neumann* types.

BOUNDARY INTEGRAL EQUATIONS

We will use equation (10) as the representative PDE in developing the integral equations. If fictitious sources of strength w are distributed around Γ. equation (10) can be converted into the integral expression (see *Jaswon & Symm* [1977]):

$$\Phi(\mathbf{x}) = \int_{\Gamma} w(\mathbf{x}')g(\mathbf{x},\mathbf{x}')\,d\mathbf{x}' + \int_{\Omega} F(\mathbf{x}'')g(\mathbf{x},\mathbf{x}'')\,d\mathbf{x}'' \tag{13}$$

where g is the free-space Green's function which must satisfy:

$$\nabla^2 g(\mathbf{x},\mathbf{x}') = \delta(\mathbf{x},\mathbf{x}') \tag{14}$$

where δ is the Dirac delta function applied at a point $\mathbf{x}'$ and felt at $\mathbf{x}$. The closed form solution to equation (14) is (*Greenberg* [1971]):

$$g(\mathbf{x},\mathbf{x}') = \begin{cases} \ln r/2\pi & \text{in two-dimensions} \\ \\ 1/(4\pi r) & \text{in three-dimensions} \end{cases} \tag{15}$$

in which $r = |\mathbf{x} - \mathbf{x}'|$. The last term in equation (13) represents a domain integral. To convert this into an integration on the boundary we introduce the *Dual Reciprocal* concept (*Cheng* et al.. [1993]).

DUAL RECIPROCAL TECHNIQUE

Consider n_T points on Γ and in Ω. We introduce a family of coordinate functions $M_j(\mathbf{x})$ $(j = 1, 2, \cdots n_T)$ such that:

$$F(\mathbf{x}) \approx \sum_{j=1}^{n_T} \beta_j M_j(\mathbf{x}) \tag{16}$$

where β_j are coefficients to be determined by collocation. We assume for each function $M_j(\mathbf{x})$. there exists an associated function $\Psi_j(\mathbf{x})$ such that:

$$\nabla^2 \Psi_j(\mathbf{x}) = M_j(\mathbf{x}) \tag{17}$$

It can be shown (*Cheng & Ouazar* [1993]) that for a two- dimensional problem for which $M_j = x^m y^n$ the function Ψ_j is given by:

$$\Psi_j = \begin{cases} \sum_{k=1}^{[\frac{n+2}{2}]} (-1)^{k-1} \frac{m!n!x^{m+2k}y^{n-2k+2}}{(m+2k)!(n-2k+2)!} & m \geq n \\ \\ \sum_{k=1}^{[\frac{m+2}{2}]} (-1)^{k-1} \frac{m!n!x^{m+2-2k}y^{n+2k}}{(m-2k+2)!(n+2k)!} & m < n \end{cases} \tag{18}$$

where the square brackets in the upper limit of the summation denote the integer part of the argument. Solutions for other possible families of coordinate functions are presented in Table 1.

Table 1			
$\mathcal{L}$	Dim.	M_j	Ψ_j
∇^2	2D	$\cos(nx)\cos(my)$	$\frac{-M_j}{(n^2+m^2)}$
∇^2	Axi	$K_0(nr)\cos(kz)$	$\frac{-M_j}{(n^2+k^2)}$
∇^2	3D	$\cos(nx)\cos(my)\cos(kz)$	$\frac{-M_j}{(n^2+m^2+k^2)}$
∇^2	2D	$e^{(nx+my)}$	$\frac{M_j}{(n^2+m^2)}$
∇^2	Axi	$K_0(nr)e^{kz}$	$\frac{M_j}{(n^2+k^2)}$
∇^2	3D	$e^{(nx+my+kz)}$	$\frac{M_j}{(n^2+m^2+k^2)}$
$\nabla^2-\lambda^2$	2D	$\cos(nx)\cos(my)$	$\frac{-M_j}{(n^2+m^2-\lambda^2)}$
$\nabla^2-\lambda^2$	Axi	$K_0(nr)\cos(kz)$	$\frac{-M_j}{(n^2+k^2-\lambda^2)}$
$\nabla^2-\lambda^2$	3D	$\cos(nx)\cos(my)\cos(kz)$	$\frac{-M_j}{(n^2+m^2+k^2-\lambda^2)}$
$\nabla^2-\lambda^2$	2D	$e^{(nx+my)}$	$\frac{M_j}{(n^2+m^2-\lambda^2)}$
$\nabla^2-\lambda^2$	Axi	$K_0(nr)e^{kz}$	$\frac{M_j}{(n^2+k^2-\lambda^2)}$
$\nabla^2-\lambda^2$	3D	$e^{(nx+my+kz)}$	$\frac{M_j}{(n^2+m^2+k^2-\lambda^2)}$

in which K_0 is the zeroth order modified Bessel function of the first kind. When equations (16) and (17) are used in (10). and we distribute the fictitious sources on Γ we can obtain the 'pure' boundary integral equation:

$$\Phi(\mathbf{x}) = \int_\Gamma w(\mathbf{x}')g(\mathbf{x},\mathbf{x}')\,d\mathbf{x}' + \sum_{j=1}^{n_T} \beta_j \Psi_j(\mathbf{x}) \tag{19}$$

An expression for the gradient of Φ, which is required in equation (12) can be obtained from equation (19) as:

$$\nabla\Phi(\mathbf{x}) = \int_\Gamma w(\mathbf{x}')\nabla g(\mathbf{x},\mathbf{x}')\,d\mathbf{x}' + \sum_{j=1}^{n_T} \beta_j \nabla\Psi_j(\mathbf{x}) \tag{20}$$

The normal derivative $\partial\Phi/\partial n = \nabla\Phi \cdot \mathbf{n}$ is given by:

$$\frac{\partial\Phi}{\partial n}(\mathbf{x}) = \int_\Gamma w(\mathbf{x}')\frac{\partial g}{\partial n}(\mathbf{x}, \mathbf{x}')\, d\mathbf{x}' + \sum_{j=1}^{n_T} \beta_j \frac{\partial\Psi_j}{\partial n}(\mathbf{x}) \tag{21}$$

Assuming β_j $(j = 1.2\cdots n_T)$ are known, the only unknown in equations (19) and/or (21) is the source strength distribution w on Γ. The trick is to start with a trial distribution of $F(\mathbf{x})$ and to obtain the coefficients β_j $(j = 1.2\cdots n_T)$ by collocation using equation (16). When applied to all n_T selected points the result of the collocation is the matrix equation:

$$\sum_{j=1}^{n_T} M_{ij}\beta_j = F_i \quad i = 1.2.\cdots n_T \tag{22}$$

where $M_{ij} = M_j(\mathbf{x}_i)$ and $F_i = F(\mathbf{x}_i)$. The matrix system (22) is also expressible in the form:

$$\mathbf{M}\beta = \mathbf{F} \tag{23}$$

which can be inverted to give:

$$\beta = \mathbf{M}^{-1}\mathbf{F} \tag{24}$$

Once β has been determined, equations (19) and/or (21) are then combined with the prescribed boundary conditions and solved for w on Γ. A better estimate of $\mathbf{F}$ is then obtained by using equations (19) and (20) in (12). The solution process continues until a specified convergence criterion is satisfied.

DISCRETIZATION

We subdivide the boundary into n_b elements. Let $N_k(\mathbf{x})$ $(k = 1.2.\cdots n_b)$ represent the boundary shape functions describing the distribution of w on Γ. By selecting each of the n_b boundary points as successive origins of integration, equations (19) and (21) can be assembled into the system:

$$\sum_{k=1}^{n_b} a_{ik}w_k = b_i, \quad i = 1.2.\cdots.n_b \tag{25}$$

where

$$a_{ik} = \begin{cases} \int_{\Gamma_k} N_k(\mathbf{x}')g(\mathbf{x}', \mathbf{x}_i)\, d\mathbf{x}' & \mathbf{x}_i \in \Gamma_\Phi \\ \int_{\Gamma_k} N_k(\mathbf{x}')\partial g/\partial n(\mathbf{x}', \mathbf{x}_i)\, d\mathbf{x}' & \mathbf{x}_i \in \Gamma_Q \end{cases} \tag{26}$$

$$b_i = \begin{cases} \Phi(\mathbf{x}_i) - \sum_{j=1}^{n_T} \beta_j\Psi_{ij} & \mathbf{x}_i \in \Gamma_\Phi \\ \partial\Phi/\partial n(\mathbf{x}_i) - \sum_{j=1}^{n_T} \beta_j\partial\Psi_{ij}/\partial n & \mathbf{x}_i \in \Gamma_Q \end{cases} \tag{27}$$

Therefore, we have n_b equations to determine w_k $(k = 1.2.\cdots n_b)$. Symbolically equation (25) can be written in the alternative form:

$$\mathbf{aw} = \mathbf{b} \tag{28}$$

which can be inverted to give:

$$\mathbf{w} = \mathbf{a}^{-1}\mathbf{b} \tag{29}$$

The whole process boils down to the iterative solution of equations (24) and (29), with repeated updating of $\mathbf{F}$ using (12). At each time level t, the iterative steps are:

1. Start with a trial $\mathbf{F}$ (*i.e.*, F_i values for $i = 1.2.\cdots n_T$).

2. Obtain β from equation (24).

3. Obtain $\mathbf{w}$ using equation (29).

4. Use discretized forms of equations (19) and (20) to compute Φ, $\nabla\Phi$ at all n_T points. This provides a better estimate for $\mathbf{F}$.

5. Go back to Step 2 if convergence condition is still unsatisfied.

Note that the matrix inversions in equations (24) and (29) need only be performed once, for fixed boundary problems. The vectors $\mathbf{w}$ and β are the quantities whose values change during the iterative process. Once convergence is reached, equations (19) and (20) can be used routinely to obtain $\Phi = (\mathbf{v}_*, p_*)$ or the gradient at any point $(\mathbf{x})$ of interest.

Treatment of Time Derivatives

We now need to address the treatment of the local acceleration term $\partial\mathbf{v}/\partial t$ as occurs when equation (11) is written for the velocity. We discuss two efficient approaches for handling this term. The first is based on the use of a time- dependent fundamental solution. The second utilizes a simple time-marching procedure.

Time-dependent Fundamental Solution

Equation (11), written for the velocity (*i.e.*, $\Phi = \mathbf{v}$), can be re-arranged into the alternative form

$$\mathcal{L}\Phi(\mathbf{x}, t) = F(\mathbf{x}, t) \tag{30}$$

where

$$\mathcal{L} = \nabla^2(\cdot) - R_e \frac{\partial(\cdot)}{\partial t}$$

$$F = R_e\,[(\mathbf{v}\cdot\nabla)\mathbf{v} + \nabla p]$$

The boundary integral equation in this case is

$$\Phi(\mathbf{x}, t) = \int_0^t \int_\Gamma w(\mathbf{x}', t') g(\mathbf{x}, t, \mathbf{x}', t')\, d\mathbf{x}'\, dt' + \sum_{j=1}^{n_T} \beta_j \Psi_j(\mathbf{x}, t) \tag{31}$$

where the functions g and Ψ_j must respectively satisfy the following PDEs

$$\mathcal{L}g(\mathbf{x}, t, \mathbf{x}', t') = \delta(\mathbf{x}, t, \mathbf{x}', t') \tag{32}$$

$$\mathcal{L}\Psi(\mathbf{x}, t) = M_j(\mathbf{x}, t) \tag{33}$$

The closed-form solution for (32) is (see *Greenberg* [1971])

$$g(\mathbf{x}, t, \mathbf{x}', t') = \begin{cases} \dfrac{H(t-t')}{(t-t')} \exp\left\{-\dfrac{R_e r^2}{4(t-t')}\right\} & \text{in two-dimensions} \\ \dfrac{\sqrt{R_e}\,H(t-t')}{(t-t')^{3/2}} \exp\left\{-\dfrac{R_e r^2}{4(t-t')}\right\} & \text{in three-dimensions} \end{cases} \tag{34}$$

where H is the Heaviside function.

The extra computational effort required here is the time integration, $\int_0^t(\cdot)$, at each time level. However, this approach has the major advantage that no difference approximation is introduced in the evaluation of the time derivative, and the exact time-dependent fundamental solution is utilized in the integral equation.

Time-marching Procedure

In this approach we assume the time derivative can be approximated by the difference equation

$$\frac{\partial \mathbf{v}}{\partial t} = \frac{\mathbf{v} - \mathbf{v}_0}{\Delta t}$$

where $\mathbf{v}_0$ is the velocity at a previous time level. The velocity equation (30) is still valid but the differential operator $\mathcal{L}$ and forcing function F now become

$$\begin{aligned} \mathcal{L} &= \nabla^2(\cdot) - \frac{R_e}{\Delta t}(\cdot) \\ F &= R_e\left[-\frac{\mathbf{v}_0}{\Delta t} + (\mathbf{v}_0 \cdot \nabla)\mathbf{v}_0 + \nabla p\right] \end{aligned}$$

The boundary integral equation in this case is

$$\Phi(\mathbf{x}, t) = \int_\Gamma w(\mathbf{x}', t')g(\mathbf{x}, \mathbf{x}'')\, d\mathbf{x}' + \sum_{j=1}^{nT} \beta_j \Psi_j(\mathbf{x}, t) \tag{35}$$

where the functions g and Ψ_j must respectively satisfy

$$\mathcal{L}g(\mathbf{x}, \mathbf{x}') = \delta(\mathbf{x}, \mathbf{x}') \tag{36}$$

$$\mathcal{L}\Psi(\mathbf{x}, t) = M_j(\mathbf{x}, t) \tag{37}$$

It is easily shown that

$$g(\mathbf{x}, \mathbf{x}') = \begin{cases} K_0\left(\sqrt{\frac{R_e}{\Delta t}}r\right) & \text{in two-dimensions} \\ \frac{1}{r}\exp\left\{-\left(\sqrt{\frac{R_e}{\Delta t}}r\right)\right\} & \text{in three-dimensions} \end{cases} \tag{38}$$

The time-marching approach has the obvious advantage of not requiring an explicit time integration, as in the first method. Furthermore, for fixed boundary problems, the free-space function g need not be calculated at each time level. The iterative scheme can now be replaced by the time-marching process. However, the presence of Δt and R_e in the argument of the Green's function creates the need for extreme caution in the numerical evaluation of g. As the time step is reduced to improve accuracy, or as the flow moves away from the laminar regime, the numerical value of g reduces very rapidly.

CONCLUSIONS

New concepts in boundary element modeling provide excellent approaches for solving convective transport problems. A formal determination of the advantages inherent in the new DRBEM formulation can easily be accomplished. In general, we expect optimum n_T (=total number of collocation points selected to evaluate coefficients β) to be of the same order as the number, n_b, of boundary elements. Therefore, the largest matrix size in BEM will be of order $n_b \times n_b = n_b^2$. By comparison, the domain techniques, because of the need to discretize the entire region, will produce a global matrix size of order $n_b^2 \times n_b^2 = n_b^4$. The advantage in terms of storage requirements is obvious. Moreover, the much reduced size of the global matrix has a more pronounced advantage in total CPU time.

For example, in a 2-D flow problem discretized with 100 boundary elements, the matrix size using the domain methods (if no special consideration is given to matrix bandedness) will be 10^4 larger than that of BEM. Even with the sparseness of the global matrix taken into account in the domain methods, a boundary element approach still enjoys a size advantage proportional to the bandwidth of the matrix. The computational advantage in 3-D is more significant because of the much increased number of meshes in the domain techniques.

These computational advantages are key to effective modeling of convective flows. The compactness of BEM matrices allows for a greater freedom to experiment, even on computers of average memory. DRBEM provides an excellent platform for optimizing system geometry.

REFERENCES

1. Brebbia, C.A., *Two Different Approaches for Transforming Domain Integrals to the Boundary*, Mathl Comput. Modelling, Vol. 15, No. 3-5, pp. 43-58, 1991.

2. Brebbia, C.A., J.C.F. Telles, and L.C. Wrobel, **Boundary Element techniques - Theory and applications in Engineering**, Springer-Verlag, 1984.

3. Cahan, B.D., and O. Lafe, *On the Iterative Boundary Element Method*, in Proc. 5th Int. Conf. on Boundary Element Technology, Vol. 2: solid and Computational Problems, eds. A. H- D. Cheng, C.A. Brebbia and S. Grilli, Univ. of Delaware, July 10- 12, 1990.

4. Cheng, A. H-D., *Darcy's Flow with Variable Permeability - A Boundary Integral Solution*, water Resour. Res., 20(7), 1984.

5. Cheng, A. H-D., and O.E. Lafe, *Boundary Element Solution for Stochastic Groundwater Flow: Random Boundary Condition and Recharge*, Water Resour. Res., **27**, 1991:

6. Cheng, A. H-D., S. Grilli, and O. Lafe, *Dual Reciprocity Boundary Element Based on Complete Set Global Shape Functions*, To be presented at the 15th Boundary Element International Conference, Worcester, Massachusetts, Aug. 10-12, 1993.

7. Cheng, A. H-D., and D. Ouazar, *Groundwater*, To appear as Chapter 9 in **Boundary Element Techniques in Geomechanics**, eds. G.D. Manolis and T.G. Davies, CMP/Elsevier, 1993.

8. Greenberg, M.D., **Applications of Green's Functions in Science and Engineering**, Prentice-Hall, Englewood Cliffs, New Jersey, 1971.

9. Jaswon, M.A., and G.T. Symm, *Integral Equation Methods in Potential Theory and Elastostatics*, Academic, San Diego, Calif., 1977.

10. Lafe, O.E., J.A. Liggett, and P. L-F. Liu, *BIEM Solutions to Combination of Leaky, Layered, Confined, Unconfined, Anisotropic Aquifers*, Water Resour. Res., 19(5), 1431-1444, 1981.

11. Lafe, O.E., A. Adeniran, and H.K. Johnson, *Three-dimensional Flows Around Kinks in Zoned and Leaky Aquifers*, ASCE/EMD Specialty Conference, Purdue University, May, 1983.

12. Lafe, O.E., and A. H-D. Cheng, *A Perturbation Boundary Element Code for Groundwater Flow in Heterogeneous Aquifer*, (with A. H-D. Cheng), Water Resour. Res., **23**, 1987;

13. Lafe, O.E., O. Owoputi, and A. H-D. Cheng, *Two Perturbation Boundary Element Codes for Steady Groundwater Flow in Heterogeneous Aquifers*, Computational Methods in Water Resources, Vol.1 Modeling Surface and Sub-surface Flows, Proceedings of the 7th International Conference, MIT, eds. M.A. Celia, et al., CMP/Elsevier, June, 1988;

14. Lafe, O.E., and A. H-D. Cheng, *A Stochastic Boundary Element Method for Groundwater Flow with Random Boundary Conditions and Recharge*, Boundary Element techniques: Applications in Engineering, Proceedings of BETECH90 Conference, Windsor, canada, eds. C.A. Brebbia, and N.G. Zamani, pp. 271- 280, June 6-8, 1989.

15. Lafe, O., *Fourier Transform and Boundary Element Simulation of 3D Flow in a Leaky Porous Medium*, **2**, Solid and Computational Problems, BETECH90, eds. by A. H-D. Cheng, C.A. Brebbia, and S. Grilli, Computational Mechanics Publishers, Southampton, Mass., 1990.

16. Lafe, O.E., and A. H-D. Cheng, *Stochastic Analysis of Groundwater Flow*, in **Computational Water Resources**, eds. D. Benasari, C.A. Brebbia & D. Ouazar, Computational Mechanics Publication, Southampton, Boston, 1991.

17. Lafe, O., and A. H-D. Cheng, *Stochastic Indirect Boundary Element Method*, To appear in Computational Stochastic Mechanics, eds. A. H-D. Cheng and C.Y. Yang, Comp. Mech. Pub., 1993.

18. Liggett, J.A., and P. L-F. Liu, **The Boundary Integral Equation Method for Porous Media Flow**, Allen and Unwin, London, 1983.

19. Nardini, D., and C.A. Brebbia, *A New Approach to Free Vibration Analysis using Boundary Elements*, in **Boundary Element Methods in Engineering**, Proc. 4th Int. Sem., Southampton, ed. C.A. Brebbia, Spriger-Verlag, 312-326, 1982.

20. Partridge, P.W., C.A. Brebbia, and L.C. Wrobel. *The Dual Reciprocity Boundary Element Method*. CMP/Elsevier, 1992.

A THEOREM REGARDING ROOTS OF THE ZERO-ORDER BESSEL FUNCTION OF THE FIRST KIND

X.A. Lin and O.P. Agrawal
Department of Mechanical Engineering and Energy Processes
Southern Illinois University at Carbondale
Carbondale , IL 62901

ABSTRACT

This paper investigates a problem on the steady-state, conduction-convection heat transfer process in cylindrical porous heat exchangers. The governing partial differential equations for the system are obtained using the energy conservation law. Solution of these equations and the concept of enthalpy lead to a new approach to prove a theorem that the sum of inverse squares of all the positive roots of the zero order Bessel function of the first kind equals to one-forth. As a corollary, it is shown that the sum of one over pth power ($p \geq 2$) of the roots converges to some constant.

NOMENCLATURE

W specific mass flow rate , $Kg/m^2.s$

C_p specific heat of fluid at constant pressure , J/Kg.$^\circ C$

h convective heat transfer coefficient , $W/m^2.^\circ C$

R radius of cylindrical board , m

r radial coordinate , m

z axial coordinate , m

T_s solid temperature , $^\circ C$

T_{s0} solid temperature at circumference , $^\circ C$

T_f fluid temperature , $^\circ C$

T_{f0} inlet fluid temperature , $^\circ C$

A WC_pR/λ_r , dimensionless parameter

B $\beta hR/WC_p$, dimensionless parameter

t $(T_s - T_{f0})/(T_{s0} - T_{f0})$, dimensionless temperature of solid media

T $(T_f - T_{f0})/(T_{s0} - T_{f0})$, dimensionless temperature of fluid

x z/R , dimensionless axial coordinate

y r/R , dimensionless radial coordinate

Greek Letters

β specific area of heat transfer , m^2/m^3

γ λ_z/λ_r , ratio of the axial and radial thermal conductivity

λ_z axial thermal conductivity of solid , $W/m.^\circ C$

λ_r radial thermal conductivity of solid , $W/m.^\circ C$

INTRODUCTION

Porous heat exchangers play a significant role in many engineering applications, such as cryogenics, thermal storage systems, and chemical reactors. Such systems lead to a set of Partial Differential Equations (PDEs) with a strong coupling between equations for the solid and the fluid phases. Analytical schemes to solve a general class of problems in this area include the method of separation of variables (refs. 1 and 2), Riemann method (ref. 3), orthogonal collocation techniques (ref. 4) and collocation-perturbation scheme for packed beds (ref. 5). Siegwarth and Radebough (ref. 6) present a numerical technique to solve the above problems with variable physical properties. Lin, Guo, and Wang (ref. 7) present a combined orthogonal collocation-perturbation method to solve the temperature field in a cylindrical porous heat exchanger.

In this paper, the physical problem presented in (Ref. 7) is reconsidered. Using the approach of separation of variables, the PDEs associated with the problem are reduced to two Boundary Value Problems (BVPs) of Ordinary Differential Equations (ODEs). Solution of the resulting BVPs leads to a new method to prove a theorem regarding roots of the zero-order Bessel function of the first kind. As a corollary, it is shown that the sum of one over pth power ($p \geq 2$) of the roots converges to some constant.

The theory of Bessel functions and related functions is well established and the main results are summarized in textbooks and mathematical manuals (refs. 8

to 10). The properties of Bessel functions concerning operations of differentiation and integration with respect to their order have also been studied by Apelblat and Kravitsky (ref. 11). However, little is known about the convergence and summation of series for roots of Bessel functions due to no explicit expressions for the roots except for $\pm 1/2$ order Bessel functions. Although in 1874 Rayleigh derived a general form of the theorem discussed here by applying an Euler's formula (ref. 8), his approach is suitable for even power series only. Furthermore, he did not study the convergence of such series for a general case. Therefore, research is needed to further understand the properties of Bessel functions. The new method to prove the theorem stated above is based on the mathematical model of a cylindrical porous heat exchanger. A brief description of this model is presented next.

MATHEMATICAL MODELING

The model considered here is a semi-infinite cylindrical porous heat exchanger as shown in (fig. 1). Let r and z be the radial and the axial coordinates, and R be the radius of the cylinder. A fluid flows through the porous media in axial direction from left to right. The inlet temperature of the fluid is T_{f0} which can be higher or lower than the board circumference temperature T_{so}. Let W, C_p, and h be the specific mass flow rate, the specific heat of fluid at constant pressure, and the convective heat transfer coefficient respectively.

Porous materials used in such applications exhibit anisotropic behavior. It is assumed that the thermal conductivity of the solid is symmetric about the axis of the cylinder. Let β be the specific area of heat transfer , k_z and k_r be the axial and the radial thermal conductivities of the solid, and γ be the ratio of k_z and k_r.

In the derivation to follow, we assume that: 1) the physical properties and convective heat transfer coefficient between porous substance and fluid are constants, 2) the dimensions of the porosity and solid particles are very small compared to the overall dimension of the heat exchanger, and therefore, the porous material can be treated as continuous media, 3) the fluid thermal conductivities are negligible compared to the solid thermal conductivities, and 4) the inner wall temperature is kept constant, and there are no thermal resistances between wall

and porous media or fluid. Finally, for simplicity, it is considered that $T_{s0} > T_{f0}$. However, the formulation presented here equally holds for $T_{s0} < T_{f0}$.

The differential equations of the system may be obtained by applying the energy conservation law to a micro unit volume (ref. 7). Nondimensional forms of these equations and the boundary conditions are given as follows:

Solid Phase :

$$\frac{\partial^2 t}{\partial y^2} + \frac{1}{y}\frac{\partial t}{\partial y} + \gamma\frac{\partial^2 t}{\partial x^2} = A\frac{\partial T}{\partial x} \tag{1}$$

Fluid Phase :

$$\frac{\partial T}{\partial x} = B(t - T) \tag{2}$$

Boundary Conditions :

$$\begin{cases} t = 1, & y = 1 & (3a) \\ T = 0, & x = 0 & (3b) \\ t = 1, & x \to +\infty & (3c) \end{cases}$$

where $t(= (T_s - T_{f0})/(T_{s0} - T_{f0}))$ and $T(= (T_f - T_{f0})/(T_{s0} - T_{f0}))$ are dimensionless temperatures of the solid and the fluid, $x(= z/R)$ and $y(= r/R)$ are dimensionless radial and axial coordinates, and $A(= WC_pR/k_r)$ and $B(= \beta hR/WC_p)$ are dimensionless parameters. Here T_s and T_f are the solid and the fluid temperature distributions. It should be noted that an additional boundary condition is required to completely define the problem. However, it is not needed here and therefore it is not considered.

Equations (1) to (3) can be used to find the temperature distributions of the solid and the fluid phases. It will be shown that these equations can also be used to prove the following theorem:

Theorem: Let α_n denote the nth positive root of the zero-order Bessel function of the first kind, then

$$\sum_{n=1}^{+\infty} \frac{1}{\alpha_n^2} = \frac{1}{2^2} \tag{4}$$

Corollary: For $p \geq 2$, series $\sum_{n=1}^{+\infty} \frac{1}{\alpha_n^p}$ converges to a constant $C(p)$ which depends on p.

Proof: In order to prove the above theorem, we begin by eliminating T from Eqs. (1) and (2). This leads to

$$\frac{\partial}{\partial x}(\frac{\partial^2 t}{\partial y^2}+\frac{1}{y}\frac{\partial t}{\partial y}+\gamma\frac{\partial^2 t}{\partial x^2})=AB\frac{\partial t}{\partial x}-B(\frac{\partial^2 t}{\partial y^2}+\frac{1}{y}\frac{\partial t}{\partial y}+\gamma\frac{\partial^2 t}{\partial x^2}) \tag{5}$$

Let

$$t=1-XY \tag{6}$$

where X and Y are functions of x and y respectively. Using Eqs. (3) and (5) and the method of separation of variables, we obtain the following two equivalent boundary value problems of ordinary differential equation:

$$\begin{cases} Y''+\frac{1}{y}Y'-\lambda Y=0 & (7a) \\ Y=0, \quad y=1 & (7b) \\ |Y|<\infty, \quad y=0 & (7c) \end{cases}$$

and

$$\begin{cases} \gamma X'''+\gamma BX''+(\lambda-AB)X'+\lambda BX=0 & (8a) \\ X=0, \quad x\to+\infty & (8b) \end{cases}$$

where a prime($'$) on X (Y) represents the derivative with respect to x (y), and λ is a separation constant. Equation (7c) suggests that Y is bounded at its center. Equation (7) can be brought to standard Bessel equation form by a simple linear transformation. This is a general Sturm - Liouville eigenvalue problem (ref. 14). It has nontrivial solutions only when $\lambda_n=-\alpha_n^2(\alpha_n\neq 0)$. Using the properties of Bessel functions, the solution of Eq. (7) for any α_n may be written as

$$Y_n=c_nJ_0(\alpha_n y) \tag{9}$$

where $J_0(x)$ is the zero order *Bessel* function of the first kind, α_n is the nth positive root of $J_0(x)$, and c_n is an undetermined constant.

Let the trial solution of Eq. (8) be given as

$$X=a'e^{\beta x} \tag{10}$$

Substitution of Eq. (10) into Eq. (8) leads to the following characteristic equation,

$$\gamma\beta^3 + \gamma B\beta^2 - (\alpha_n^2 + AB)\beta - \alpha_n^2 B = 0 \tag{11}$$

Equation (11) is cubic in β. The discriminant Δ of this equation is given as

$$\Delta = -\frac{1}{4\gamma^3}\{4\alpha_n^2(B^2\gamma - \alpha_n^2)^2 + 18AB^2\alpha_n^2\gamma + AB^3(AB + 2\alpha_n^2) +$$

$$4AB(A^2B^2 + 3\alpha_n^4 + 3\alpha_n^2 AB)\} \tag{12}$$

Equation (12) suggests that $\Delta < 0$. Thus, using the theory of cubic equations, it follows that all roots of Eq. (11) are real (ref. 12). Let these roots be given as β_{n1}, β_{n2}, and β_{n3}. From Eq. (11), it follows that

$$\beta_{n1} + \beta_{n2} + \beta_{n3} = -B < 0 \tag{13}$$

and

$$\beta_{n1} \cdot \beta_{n2} \cdot \beta_{n3} = \alpha_n^2 B/\gamma > 0 \tag{14}$$

Equation (13) suggests that atleast one of the roots is negative and Eq. (14) indicates that negative roots appear in pair. Thus, it is concluded that Eq. (11) has two negative roots and one positive root for each α_n. From physical consideration (or Eq. (8b)), the positive root is disregarded. The general solution for X may now be written as

$$X_n = \sum_{i=1}^{2} a'_{ni} e^{\beta_{ni} x} \tag{15}$$

Substituting Eqs. (9) and (15) into Eq. (6), we get

$$t = 1 - \sum_{n=1}^{\infty} J_0(\alpha_n y) \cdot \sum_{i=1}^{2} a_{ni} e^{\beta_{ni} x} \tag{16}$$

where $a_{ni} = c_n a'_{ni}$. From Eqs. (1), (2) and (16), we obtain

$$T = 1 - \frac{1}{AB} \cdot \sum_{n=1}^{\infty} J_0(\alpha_n y) \cdot \sum_{i=1}^{2} a_{ni} e^{\beta_{ni} x} \cdot (\alpha_n^2 - \gamma\beta_{ni}^2 + AB) \tag{17}$$

Differentiation of Eq. (17) with respect to x yields,

$$\frac{\partial T}{\partial x} = -\frac{1}{AB} \cdot \sum_{n=1}^{\infty} J_0(\alpha_n y) \cdot \sum_{i=1}^{2} a_{ni}\beta_{ni} \cdot (\alpha_n^2 - \gamma\beta_{ni}^2 + AB) e^{\beta_{ni} x} \tag{18}$$

Using Eq. (17), the inlet condition (Eq. (3b)), and the property of orthogonality of $J_0(\alpha_n y)$ in the interval $[0,1]$, we derive

$$\sum_{i=1}^{2} a_{ni}(\alpha_n^2 - \gamma\beta_{ni}^2 + AB) = \frac{2AB}{\alpha_n \cdot J_1(\alpha_n)} \tag{19}$$

where $J_1(x)$ is a *Bessel* function of the first kind of order one.

ENTHALPY RELATIONS

Some enthalpy relations help prove the above theorem. Let $H(x)$ and $H(x+dx)$ be quantities of enthalpy carried by the fluid across the axial planes at x and $x+dx$ respectively (Figure 1). Expression for $H(x)$ is given as

$$H(x) = WC_p \cdot \int_0^R \{rdr \cdot \int_0^{2\pi} d\theta \cdot [T_{f0} + T(T_{s0} - T_{f0})]\} \tag{20}$$

A closed form expression for $H(x)$ can be obtained by substituting Eq. (17) into Eq. (20), and integrating the resulting equation. Expanding $H(x+dx)$ in a Taylor's series, and neglecting the second and the higher order terms, we obtain

$$dH(x) = H(x+dx) - H(x) = \frac{\partial H(x)}{\partial x} \cdot dx \tag{21}$$

where $dH(x)$ is the enthalpy variation of the fluid passing through the control volume between x and $x+dx$ (Figure 1). The total change in enthalpy of the fluid is obtained by integrating Eq. (21) over the length of the heat exchanger. Thus,

$$\Delta H_0^{+\infty} = \int_0^{+\infty} dH(x) = \int_0^{+\infty} \frac{\partial H(x)}{\partial x} \cdot dx \tag{22}$$

Using Eqs. (18), (20), and (22), we obtain

$$\Delta H_0^{+\infty} = \frac{2\pi R^2 WC_p(T_{s0} - T_{f0})}{AB} \cdot \sum_{n=1}^{\infty} \{\frac{J_1(\alpha_n)}{\alpha_n} \cdot \sum_{i=1}^{2} a_{ni}(\alpha_n^2 - \gamma\beta_{ni}^2 + AB)\} \tag{23}$$

$\Delta H_0^{+\infty}$ can also be evaluated directly by subtracting the enthalpy of the fluid at the inlet ($= H(0)$) from that at the outlet ($= H(\infty)$). Expressions for $H(0)$ and $H(\infty)$ are given as

$$H(0) = WC_p\pi R^2 \cdot T_{f0}$$

and

$$H(\infty) = WC_p\pi R^2 \cdot T_{s0}$$

Hence,

$$\Delta H_0^{+\infty} = WC_p\pi R^2 \cdot (T_{s0} - T_{f0}) \tag{24}$$

Comparing Eqs. (23) and (24), we obtain

$$\frac{2}{AB} \cdot \sum_{n=1}^{\infty} \frac{J_1(\alpha_n)}{\alpha_n} \cdot \{\sum_{i=1}^{2} a_{ni}(\alpha_n^2 - \gamma\beta_{ni}^2 + AB)\} = 1 \tag{25}$$

Finally, substituting Eq. (19) into Eq. (25) and simplifying, we obtain

$$\sum_{n=1}^{+\infty} \frac{1}{\alpha_n^2} = \frac{1}{2^2}$$

This proves the theorem. Since function $J_0(y)$ is symmetrical, it follows that

$$\sum_{n=-\infty}^{+\infty} \frac{1}{\alpha_n^2} = \frac{1}{2} \tag{26}$$

In order to prove the corollary, observe that all positive roots of $J_0(x)$ are greater than 1 (ref. 8). This implies that for $p \geq 2$

$$\frac{1}{\alpha_n^p} \leq \frac{1}{\alpha_n^2} \tag{27}$$

Equations (4) and (27) suggest that the series

$$C_n(p) = \sum_{i=1}^{n} \frac{1}{\alpha_i^p}$$

increases monotonically and it is bounded. Thus, by monotone convergence theorem (ref. 13), it follows that the series $C_n(p)$ $(n \to \infty)$ is convergent.

CONCLUSION

A mathematical model for a steady-state conduction-convection heat transfer processes in a cylindrical porous heat exchanger has been investigated. It has been shown that the equations resulting in this model may be used to prove a theorem and a corollary regarding roots of the zero-order Bessel function of the first kind.

Research reported in this paper provides an alternate approach to prove a theorem in this area. The advantages of this physical approach are that it enriches physical understanding of a theorem, and that we may avoid difficulties emerging from rigid mathematical arguments.

ACKNOWLEDGMENT

The authors wish to thank Prof. M. Tarabek, Department of Mathematics, Southern Illinois University at Carbondale for his valuable suggestions and comments.

REFERENCES

1. Pust, L.: Investigation of Temperature Field in Heat Exchanger of Porous Cylindrical Board. *Int. J. Heat Mass Transfer*, vol. 20, Nov. 1977, pp. 1255-1257.

2. Maiorov, V.A.; Polyaev, V.M.; Vasiliev, L.L.; and Kiselev, A.I.: Augmentation of Convective Heat Transfer in Conduits with High Temperature Porous Matrix. Part 1. Heat Transfer in case of Local Heat Balance in Matrix. J. Eng. Phys. (in Russian), vol. 47, Jan. 1984, pp. 13-24.

3. Montakhab, A.: Convective Heat Transfer in Porous Media. *J. Heat Transfer*, vol. 101, Aug. 1979, pp. 507-510.

4. Finlayson, B.A.: Packed-Bed Reactor Analysis by Orthogonal Collocation. *Chem. Eng. Sci.*, vol. 26, Jul. 1971, pp. 1081-1091.

5. Dixon, A.G.; and Cresswell, D.L.: Theoretical Prediction of Effective Heat Transfer Parameters in Packed Beds. *AICHE J.*, vol. 25, Jul. 1979, pp. 663-676.

6. Siegwarth, J.D.; and Radebaugh, R.: Analysis of Heat Exchangers for Dilution Refrigerators. *Rev. Sci. Instrum.*, vol. 42, Aug. 1971, pp. 1111-1119.

7. Lin, X.A.; Guo, F.Z.; and Wang, H.: Solution to Temperature Fields of Porous Heat Exchangers. Song-Jiu Deng ed. in chief: *Heat Transfer Enhancement and Energy Conservation.* 1990, pp. 559-565, Hemisphere Publ. Corp.

8. Watson, G.N.: *A Treatise on the Theory of Bessel Functions.* Cambridge Univ. Press, 1944.

9. Abramowitz, A.; and Stegun, I.E.: *Handbook of Mathematical Functions.* U.S. National Bureau of Standards, 1965.

10. Gary, A.; and Macrobert, T.M.: *A Treatise on Bessel Functions and Their Applications to Physics*, Macmillan, 1922.

11. Apelblat, A.; and Kravitsky, N.: Integral Representations of Derivatives and Integrals With Respect To the Order of the Bessel Functions $J_{v(t)}, I_{v(t)}$, the Anger Function $J_{v(t)}$ and the Integral Bessel Function $J_{v(t)}$. *IMA J. Applied Math.*, vol. 34, Mar. 1985, pp. 187-210.

12. Condon, E.U.; and Odishaw, H.: *Handbook of Physics.* McGraw-Hill, 1967.

13. Bartle, R.G.: *The Elements of Real Analysis.* Wiley, 1976.

14. Haberman, R.: *Elementary Applied Partial Differential Equations.* pp. 134-135, pp. 216-217, Prentice - Hall, 1987.

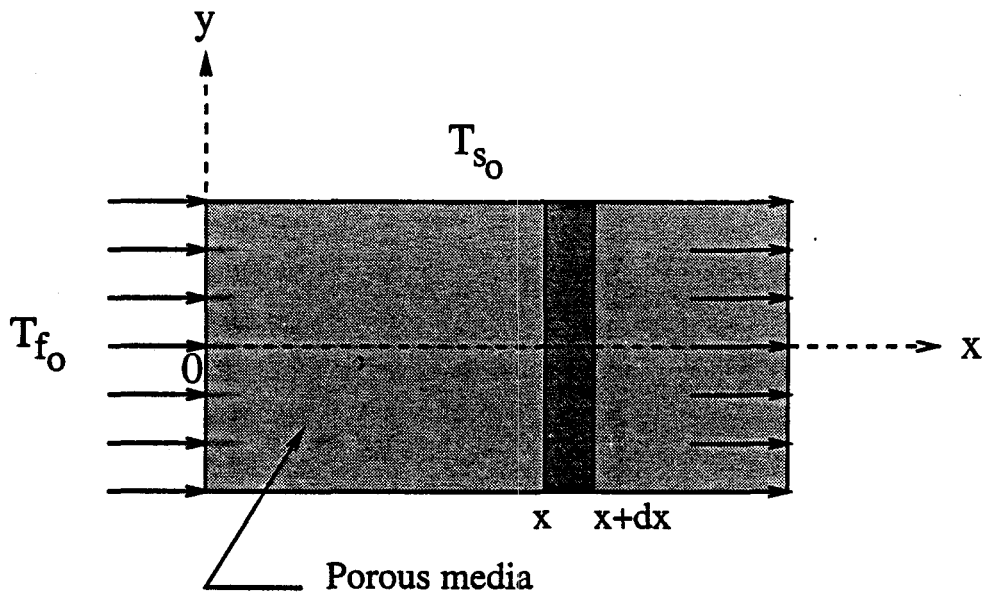

Figure 1. Porous heat exchanger model

AN APPLICATION OF SMALL-GAP EQUATIONS IN SEALING DEVICES

Carlos A. Vionnet and Juan C. Heinrich
Department of Aerospace and Mechanical Engineering
University of Arizona
Tucson, Arizona 85721

SUMMARY

The study of a thin, incompressible Newtonian fluid layer trapped between two almost parallel, sliding surfaces has been actively pursued in the last decades. This subject includes lubrication applications such as slider bearings or the sealing of non-pressurized fluids with rubber rotary shaft seals. In the present work we analyze numerically the flow of lubricant fluid through a micro-gap of sealing devices. The first stage of this study is carried out assuming that a 'small-gap' parameter δ attains an extreme value in the Navier-Stokes equations. The precise meaning of small-gap is achieved by the particular limit $\delta = 0$ which, within the bounds of the hypotheses, predicts transport of lubricant through the sealed area by centrifugal instabilities. Numerical results obtained with the penalty function approximation in the finite element method are presented. In particular, the influence of inflow and outflow boundary conditions, and their impact in the simulated flow are discussed.

INTRODUCTION

Most seals are relatively simple elements widely employed in diverse types of rotary machines. This sealing component is often used to seal rotating shafts at low oil pressures, avoiding the transport of contaminant to, or lubricant from, the equipment it protects. The seal, bonded to the oil reservoir, is stationary and presents a narrow section that slides over the moving surface of the rotary shaft. Fig.1 shows a cross section of the geometry under consideration.

The device is designed to have an interference with the shaft. Therefore, once the piece is mounted, the compliance of the elastic body ensures a perfect fit between the seal and the cylindrical surface of the shaft. Under these conditions, some of the initial asperities of the seal wear out after a brief period of time, leaving an extremely thin layer of lubricant fluid that separates the surfaces in contact. This was first noticed by Jagger (ref.1) and, ever since, numerous explanations attempted to account for two consequences of this experimental fact: the hydrodynamic force able to sustain a gap between the two bodies and the mechanisms that prevent the fluid from leaking through. Jagger proposed that the surface tension of the sealed fluid controls leakage thanks to a meniscus formed on the air side. Kawahara and Hirabayashi (ref.2) observed that a properly installed and functional seal leaked when the installation is reversed.

With the assumption of relative parallel sliding between two rough surfaces, lubrication theory has been the chosen tool by many researchers to answer these fundamental problems (see e.g. ref.3). The load-carrying capacity of parallel sliding of rough surfaces was first studied by Davies (ref.4). Later on, Jagger and Walker (ref.5) assumed that the asperities act as micro-bearings pads in the contact area. However, Lebeck (refs.6 and 7) concluded that none of the existing models can fully explain the sliding motion as commonly observed in experiments. Gabelli and Poll (ref.8) studied the dominant action of the surface microgeometry in the formation of the lubricant

film. They found that the contribution of mechanical pressure to the load-carrying capacity due to body contact is very small and indeed negligible. Salant (ref.9) claimed that micro-undulations in the lip surface restrict leakage by virtue of a 'reverse-pumping' process in which fluid is driven from the low to the high pressure side. However, no one has really observed such micro-undulations, either in static or dynamic conditions (ref.10).

Combinations of angular velocity and system eccentricity beyond the ability of the sealing device to maintain contact with the shaft would cause the seal to leak profusely. It has been suggested that an inherent pumping mechanism (ref.11), sufficient to counterbalance those influences promoting leakage, would be given by a relative motion between the sealing surfaces. Besides all these explanations, at present there is a wide gap between theory and practice, and a feasible explanation of the mechanism involved in the sealing action is still pending, even though elastomeric seals have been used extensively since the 1940's.

In the next section, we establish the small-gap equations using a rather simple order-of-magnitude analysis. This is followed by numerical examples showing the validity of the proposed model and the influence of the boundary conditions in the numerical predictions.

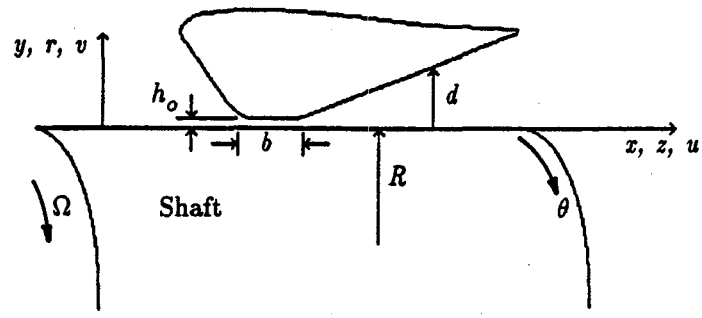

fig. 1 - Cross section of a typical sealing device

ANALYTICAL MODEL

We assume an oil-film already formed ignoring any mechanical contact between the sealing device and the shaft, as well as any distortion of the upper elastic seal. We consider a thin viscous liquid layer bounded above by a smooth surface and below by a perfectly rounded shaft, without including edge effects such as the meniscus experimentally observed on the air-side (ref.1). Despite the fact that the film within the gap is very thin, we assume it to be thick enough to conform to the continuum hypothesis. There is no local rupture of the film such as cavitation or dry spots in the contact area, and the layer consists of an incompressible Newtonian fluid with constant properties under isothermal conditions.

We begin with the Navier-Stokes equations written in cylindrical coordinates (ref.12), setting the direction of the line $r = 0$ coincident with the shaft axis

$$\frac{1}{r}\frac{\partial(ru_r)}{\partial r} + \frac{1}{r}\frac{\partial u_\theta}{\partial \theta} + \frac{\partial u_z}{\partial z} = 0 \tag{1}$$

$$\frac{\partial u_r}{\partial t} + \vec{u}.grad(u_r) - \frac{u_\theta^2}{r} = -\frac{1}{\rho}\frac{\partial p}{\partial r} + \nu\left(\Delta u_r - \frac{2}{r^2}\frac{\partial u_\theta}{\partial \theta} - \frac{u_r}{r^2}\right) \tag{2}$$

$$\frac{\partial u_\theta}{\partial t} + \vec{u}.grad(u_\theta) + \frac{u_r u_\theta}{r} = -\frac{1}{\rho r}\frac{\partial p}{\partial \theta} + \nu\left(\Delta u_\theta + \frac{2}{r^2}\frac{\partial u_\theta}{\partial \theta} - \frac{u_\theta}{r^2}\right) \tag{3}$$

$$\frac{\partial u_z}{\partial t} + \vec{u}.grad(u_z) = -\frac{1}{\rho}\frac{\partial p}{\partial z} + \nu\,\Delta u_z \tag{4}$$

where

$$\vec{u} = (u_r,\, u_\theta,\, u_z) \quad , \quad grad = \left(\frac{\partial}{\partial r}\,,\, \frac{1}{r}\frac{\partial}{\partial \theta}\,,\, \frac{\partial}{\partial z}\right) \quad , \quad \Delta = \frac{1}{r}\frac{\partial}{\partial r}\left(r\frac{\partial}{\partial r}\right) + \frac{1}{r^2}\frac{\partial^2}{\partial \theta^2} + \frac{\partial^2}{\partial z^2}$$

In absence of a free surface the gravitational body force is expressed as the gradient of a scalar quantity and, therefore, it has been included in the pressure gradient term.

The analysis of the lubricant flow in the micro-gap involves, roughly speaking, three disparate length scales, namely, the radius R of the shaft ($\sim 0.04m$), the much smaller thickness h_o of the fluid ($\sim 10\mu m$) and an intermediate length b characterizing the axial extent of the contact region ($\sim 200\mu m$) (see fig. 1). Next, the Navier-Stokes equations, once recasted with the aforementioned scales, are simplified by letting the ratio between the gap height and the radius of the shaft formally approach zero.

Inner region: lubrication regime

Given the tiny thickness of the lubricant film, radial oscillations proportional to the gap height will alter considerably the flow inside the micro-gap. To analyze this effect, consider a shaft rotating at angular velocity Ω and separated an average distance h_o from the stationary seal (fig.1). Introducing now

$$(x, y, \xi) \rightarrow \left(\frac{z}{h_o}\,,\, \frac{r-R}{h_o}\,,\, \theta\right) \qquad , \qquad \tau \rightarrow \Omega t \tag{5}$$

$$(u, v, w) \rightarrow \left(\frac{u_z}{\Omega h_o}\,,\, \frac{u_r}{\Omega h_o}\,,\, \frac{u_\theta}{\Omega R}\right) \quad , \quad p^* \rightarrow \frac{(p - p_a)}{\rho \nu \Omega} \tag{6}$$

into the equations of motion (1)-(4), and letting $\delta = \frac{h_o}{R}$ formally approach zero while holding everything else fixed, we get

$$\nabla.\vec{u} = 0 \tag{7}$$

$$\sigma\,(\,\partial_\tau + \vec{u}.\nabla)\,\vec{u} \;-\; R_e\, w^2\,\hat{j} = -\nabla p^* + \nabla^2\vec{u} \tag{8}$$

$$\sigma\,(\,\partial_\tau + \vec{u}.\nabla)\,w = \nabla^2 w \tag{9}$$

where

$$\vec{u} = (u, v) \quad , \quad \nabla = \left(\frac{\partial}{\partial x}\,,\frac{\partial}{\partial y}\right) \quad , \quad \hat{j}=(0,1)$$

and

$$R_e = \frac{\Omega R h_o}{\nu} \quad : \text{Reynolds number} \tag{10}$$

$$\sigma = \frac{\Omega h_o^2}{\nu} \quad : \text{squeezing Reynolds number} \tag{11}$$

Several other scaling are possible (ref.13), but this particular choice seems to be consistent with Gabelli and Poll observations (ref.8). They stated that the average

pressure gradient in the circumferential direction is indeed negligible when compared with the pressure gradient across the sealing contact. The squeezing Reynolds number σ is commonly so small that inertia terms can be neglected and the classical lubrication theory can be applied. Moreover, for small R_e, as it turns out to be in most applications, the flow is stable to small perturbations (ref.14). In the absence of mechanical vibrations, no secondary flow is possible at this level, the circumferential flow being stable and mostly of Couette type.

Outer region: centrifugal effects

The loss of contact between seal and shaft, combined with changes in the geometry, will introduce different features in the flow behavior as we go farther away from the gap. For a slowly-varying channel of height $d(z)$ on the outside (fig.1), we rescale the flow field by writing

$$(x, y, \xi) \to \left(\frac{z}{d} , \frac{r-R}{d} , \theta \right) \quad , \quad \tau \to \frac{\nu t}{d^2} \tag{12}$$

$$(u, v, w) \to \left(\frac{d}{\nu} u_z , \frac{d}{\nu} u_r , \frac{u_\theta}{\Omega R} \right) \quad , \quad p^* \to \frac{(p - p_a) d^2}{\rho \nu^2} \tag{13}$$

where d is some mean value of $d(z)$. It can be shown that the equations of motion, in the limit $\delta = d/R \to 0$, become

$$\nabla . \vec{u} = 0 \tag{14}$$

$$(\partial_\tau + \vec{u} . \nabla) \vec{u} - T_a w^2 \hat{j} = - \nabla p^* + \nabla^2 \vec{u} \tag{15}$$

$$(\partial_\tau + \vec{u} . \nabla) w = \nabla^2 w \tag{16}$$

where

$$T_a = \frac{\Omega^2 R d^3}{\nu^2} \text{ : Taylor number} \tag{17}$$

Note that the above system of equations are the so-called 'small-gap' equations, widely used in the context of the stability of axisymmetric Taylor-Couette flows (ref.15). Again, while the curvature effects are almost completely neglected, they are retained through the centrifugal term by imposing the Taylor number be held fixed as $\delta \to 0$. It follows that a rigid seal separated from a rotary shaft by a thin lubricating film is subject to centrifugal instabilities in a neighborhood of the contact area, driving eventually a secondary flow across the gap. Had we used these scales in the inner region

$$T_a = \frac{\Omega^2 R d^3}{\nu^2} \to \frac{\Omega^2 R h_o^3}{\nu^2} = \left(\frac{\Omega R h_o}{\nu} \right)^2 \frac{h_o}{R} = R_e^2 \, \delta \to 0 \quad \text{as } \delta \to 0 \tag{18}$$

outer region | *inner region*

and the Taylor number indicates where curvature effects must be retained, regardless of the scales chosen.

In principle, the flow of lubricant fluid is governed by a set of equations similar to those of a stratified flow, where the centripetal acceleration plays the role of the buoyancy force, although for rotating flows whose inner surface moves the basic state could be unstable to small disturbances.

The domain under consideration is typically unbounded, and clearly some

difficulties arise with the introduction of artificial boundaries. It is known that isothermal flows with open boundaries can be successfully modeled employing the so-called natural boundary conditions, but other techniques are needed to solve the more complicated problem of buoyancy-driven flows, where the use of the natural boundary conditions is precluded by the additional pressure gradient generated by the buoyancy term (refs. 16 to 18).

In the next section we address the appropriate use of the penalty formulation in the finite element method for unbounded flows in presence of variable body forces. Finally, we will see how different open boundary conditions can lead to contradictory predictions in the flow behavior.

PENALTY FUNCTION FORMULATION FOR THE N-S EQUATIONS

In what follows, we denote the coordinate directions as (x,y) or (x_1,x_2), the transverse velocity components as (u,v) or (u_1,u_2), the azimuthal component of the velocity as w, and the pressure as p; δ_{ij} is the Kronecker delta. For convenience in the treatment of the boundary conditions, we rewrite the equations of motion as

$$\frac{\partial u_i}{\partial x_i} = 0 \tag{19}$$

$$\frac{\partial u_i}{\partial t} + u_j \frac{\partial u_i}{\partial x_j} = T_a \, w^2 \, \delta_{i2} + \frac{\partial \sigma_{ij}}{\partial x_j} \tag{20}$$

$$\frac{\partial w}{\partial t} + u_j \frac{\partial w}{\partial x_j} = \frac{\partial^2 w}{\partial x_j \partial x_j} \tag{21}$$

The Taylor number T_a is defined in equation (17), and the stress in the fluid is given now by

$$\sigma_{ij} = -p\delta_{ij} + \left(\frac{\partial u_i}{\partial x_j} + \frac{\partial u_j}{\partial x_i} \right) \tag{22}$$

A weak form is obtained by taking the inner product of the transverse momentum equations (20) with a weighting function $\vec{W} = (W_1, W_2)$, and multiplying the azimuthal momentum equation (21) by a scalar function W. The penalty method is implemented by introducing the pseudo-constitutive relation (ref.19)

$$p = p_s - \lambda \frac{\partial u_j}{\partial x_j} \tag{23}$$

where p_s is the hydrostatic pressure for a fluid at rest and λ is the penalty parameter. Upon application of Green's theorem and substituting p by the above expression, we get

$$\int_\Omega \left(\frac{\partial u_i}{\partial t} + u_j \frac{\partial u_i}{\partial x_j} \right) W_i \, d\Omega + \lambda \int_\Omega \frac{\partial u_j}{\partial x_j} \frac{\partial W_i}{\partial x_i} \, d\Omega + \int_\Omega \left(\frac{\partial u_i}{\partial x_j} + \frac{\partial u_j}{\partial x_i} \right) \frac{\partial W_i}{\partial x_j} \, d\Omega = V_f + S_f \tag{24}$$

$$\int_\Omega \left(\frac{\partial w}{\partial t} + u_j \frac{\partial w}{\partial x_j} \right) d\Omega + \int_\Omega \frac{\partial w}{\partial x_j} \frac{\partial W}{\partial x_j} \, d\Omega = \int_{\partial\Omega} W \frac{\partial w}{\partial x_j} n_j \, ds \tag{25}$$

where the surface forces S_f and the volume forces V_f are defined by

$$S_f = \int_{\partial\Omega} \left[-p \, W_i \, n_i + W_i \left(\frac{\partial u_i}{\partial x_j} + \frac{\partial u_j}{\partial x_i} \right) n_j \right] ds \tag{26}$$

$$V_f = \int_{\Omega} T_a \, w^2 \, \delta_{i2} \, W_i \, d\Omega \tag{27}$$

and $\hat{n} = (n_1, n_2)$ is the unit vector normal to the boundary $\partial\Omega$ and pointing outwards. On a vertical boundary with normal $\hat{n} = (1, 0)$, the integrand of S_f reduces to

$$\vec{W} = (W_1, 0): \quad -p + 2\frac{\partial u}{\partial x} \tag{28}$$

for normal traction, and

$$\vec{W} = (0, W_2): \quad \frac{\partial u}{\partial y} + \frac{\partial v}{\partial x} \tag{29}$$

for shear traction, in a weak rather than a pointwise sense.

Boundary conditions

The boundary conditions are the usual no-slip and no mass penetration at solid walls on the physical boundaries. This is, $u = v = 0$ and $w = 1$ at the lower boundary $y = 0$, which represents the outer surface of the rotating shaft, and $u = v = w = 0$ at the upper boundary, which is stationary.

At the open boundaries, on both sides of the contact region, the following two open boundary conditions (OBC) are employed for the flow field.

(*i*) Stress-free or natural boundary condition (NBC). We set the normal and shear stresses in equation (26) equal to zero.

(*ii*) Free-boundary condition (FBC). We evaluate the line integrals (26) of the weak form of the momentum equations using values computed on the outflow elements. Then, we force the line integrals into the right-hand-side of the discretized equations until convergence is achieved (refs. 17 and 18).

The natural boundary condition $\partial w/\partial n = 0$ is used in the weak form of the transport equation (25) instead.

FINITE ELEMENT METHOD

We discretize the domain into M elements and N nodes, and we expand the velocity components using bilinear quadrilateral elements and piecewise constant elements for pressure. All terms of the weak form of the governing equations are evaluated with full Gaussian quadrature, except the penalty term, where selective reduced integration is used (ref.20). The weighting functions are set equal to the basis functions, except in the convective terms, where perturbed Petrov-Galerkin functions with balancing tensor diffusivity are employed (refs.21 and 22). The time integration is based on the theta method with lumped mass matrices in the time derivatives. The numerical evaluation of the weighted residuals of the momentum equations leads to a nonlinear system of equations that is solved by Newton iteration using a direct solver based on Gauss elimination for unsymmetric banded matrices (ref.23). A convergence tolerance less than 1% of the relative change $\|\Delta \boldsymbol{u}^{\nu}\|/\|\boldsymbol{u}^{\nu}\|$ in the velocity field is imposed to terminate each full ν-th Newton iteration. The pressure p_e over each element Ω_e is calculated using the weak form of the relation (23)

$$p_e = -\frac{\lambda}{\Omega_e} \int_{\Omega_e} \nabla \cdot \vec{u} \, d\Omega \tag{30}$$

where the cross bar denotes selective reduced integration.

To march in time we use the velocity field $\boldsymbol{u}^n$ and pressure p^n at time t_n to evaluate the terms of S_f and V_f of the buoyancy force vector $\boldsymbol{b}^n$. Having determined $\boldsymbol{b}^n$, we compute the velocity field using the Newton linearization algorithm. Once $\boldsymbol{u}^{n+1}$ is known, we update the pressure by means of the equation (30) and solve the transport equation for w^{n+1}. The scheme is repeated until steady state is achieved. Time integration is terminated when the relative change between time steps is

$$\left\| \frac{\boldsymbol{u}^{n+1} - \boldsymbol{u}^n}{\boldsymbol{u}^{n+1}} \right\| < \epsilon_1 \quad \text{and} \quad \left\| \frac{w^{n+1} - w^n}{w^{n+1}} \right\| < \epsilon_2 \tag{31}$$

where

$$\|\boldsymbol{u}\| = \sum_{j=1}^{2N} |u_j|$$

for some prescribed error tolerances ϵ_1 and ϵ_2. All the following results are obtained with the fully implicit algorithm starting from zero initial conditions.

NUMERICAL EXAMPLES

Preliminary computations showed the necessity of using mesh grading as the contact region is approached from both sides. Transition elements are also employed to avoid extremely small elements in the contact area.

The geometry and the finite element mesh employed for the present calculations are shown in fig. 2. Details of the discretization can be appreciated in fig.3. The mesh contains 2035 nodes and 1864 elements, and the penalty parameter λ is equal to 10^8 in all cases. The relevant lengths are $b = 200\mu m$, which is used as reference length, $h_o = 10\mu m$, and $R = 0.035m$.

The pressure is adjusted at every time step in such a way that is always zero at the first element (located at $x = -11$, $y = 0$), and the line integrals (26) are evaluated, if the OBC requires so, with values computed on the outflow elements.

Results of the transverse velocity field, the azimuthal component of the velocity, and the pressure obtained with the FBC at the open boundaries are all shown in fig.4, and continues up to fig.7. The simulation corresponds to a Taylor number $T_a = 15$. The steep pressure gradient developed across the gap is shown in fig.5, and the resultant flux of lubricant flowing from the air-side to the oil-side is observed in fig.6. Streamline contours are plotted in fig.7. Similar results obtained with the NBC at the outlets can be seen from fig.8 to fig.11. The striking differences in the numerical predictions of both OBC are better illustrated in fig.7 and fig.11. The former clearly shows that an improper treatment of the open boundary conditions causes backflow into the computational domain. The intensity of the returning flow due to the NBC at the air-side outflow boundary induces a cell structure in an otherwise almost plane Couette flow (see w in fig.4).

CONCLUSIONS

The geometry and, in particular, the tiny size of the gap imposes a severe constraint in the numerical simulation. Furthermore, we have seen that an improper specification of the outflow boundary condition can cause artificial returning flow which, for the present problem, spoils the solution in the whole computational domain. Both boundary conditions show that centrifugal instabilities play an important role in the

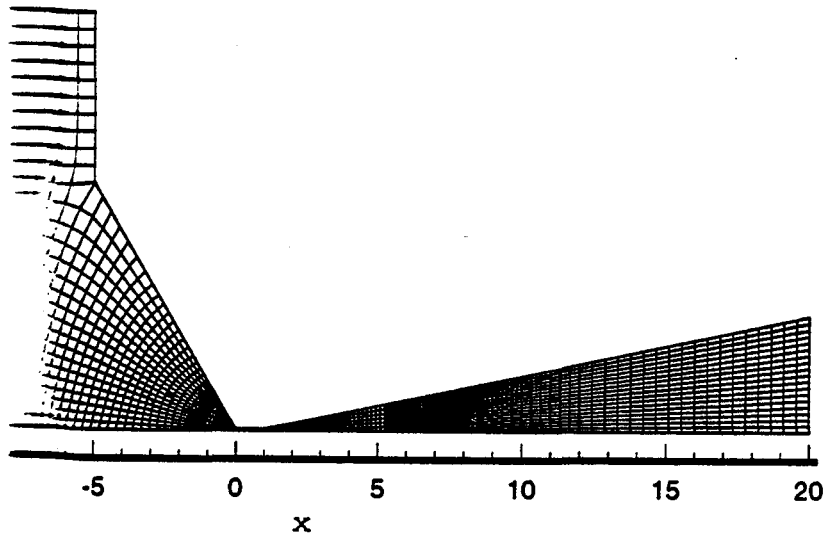

figure 2

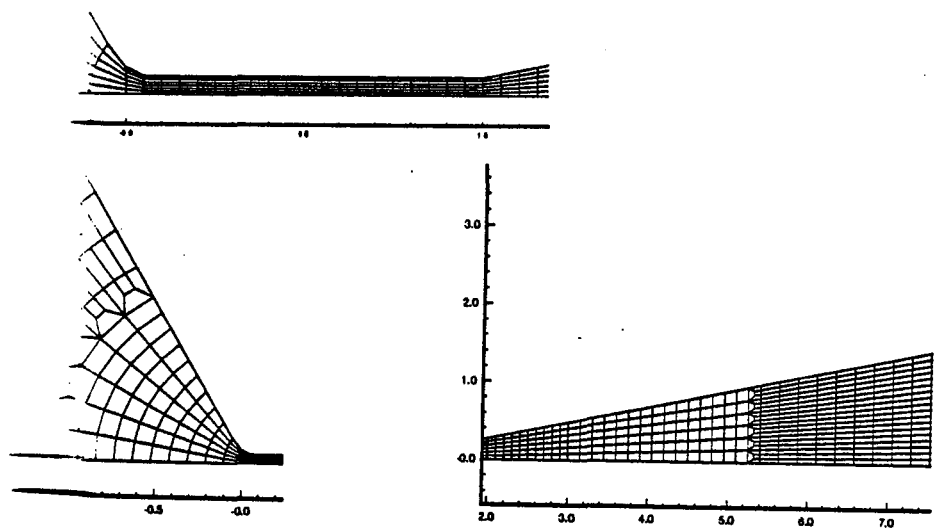

figure 3

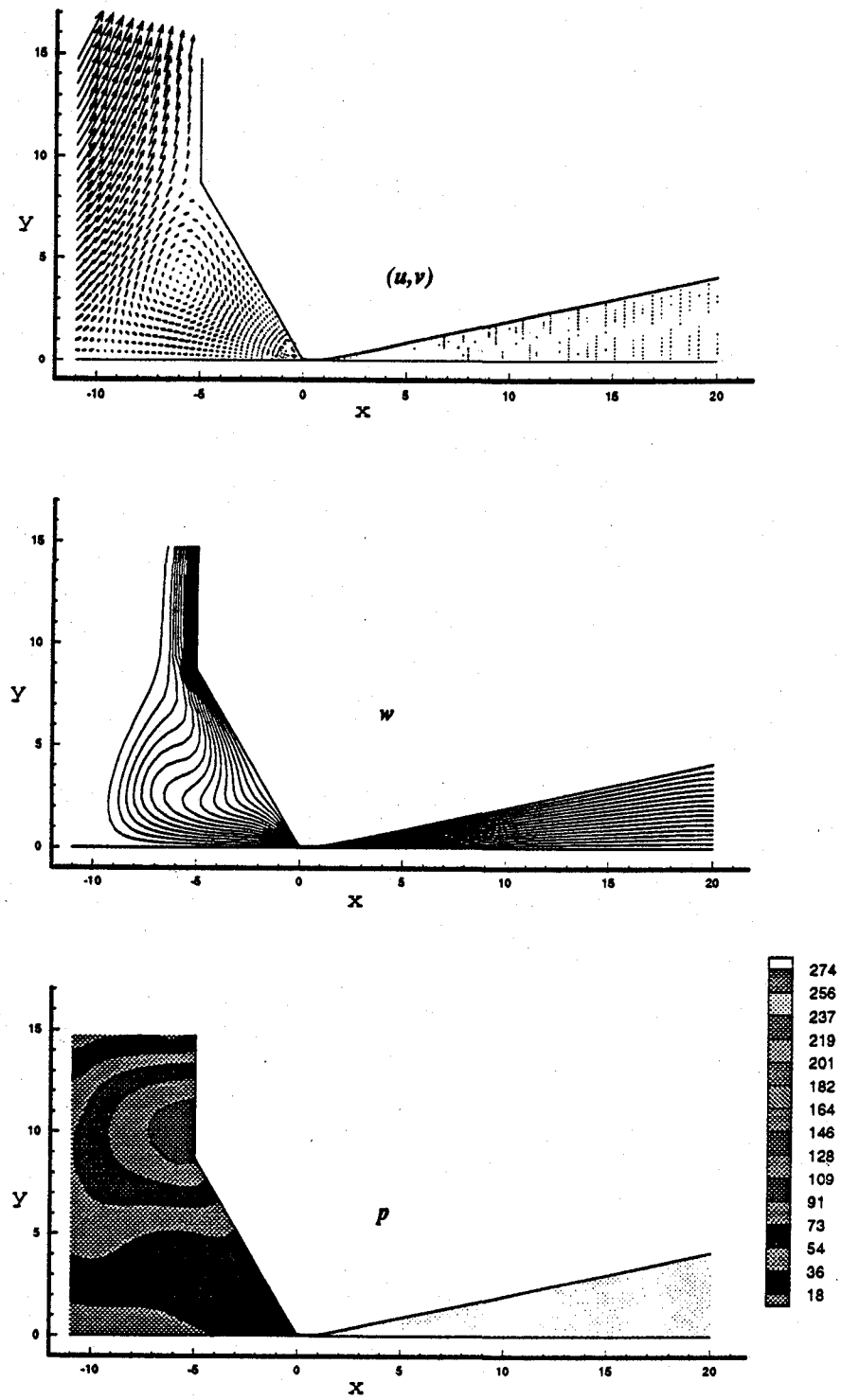
(u,v)
w
p
Y
X
15
10
5
0
-10
-5
0
5
10
15
20
274
256
237
219
201
182
164
146
128
109
91
73
54
36
18

figure 4

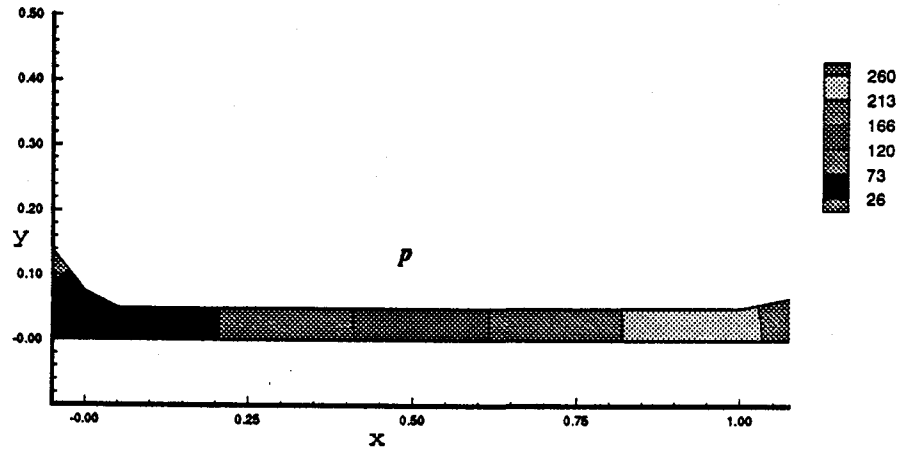

figure 5

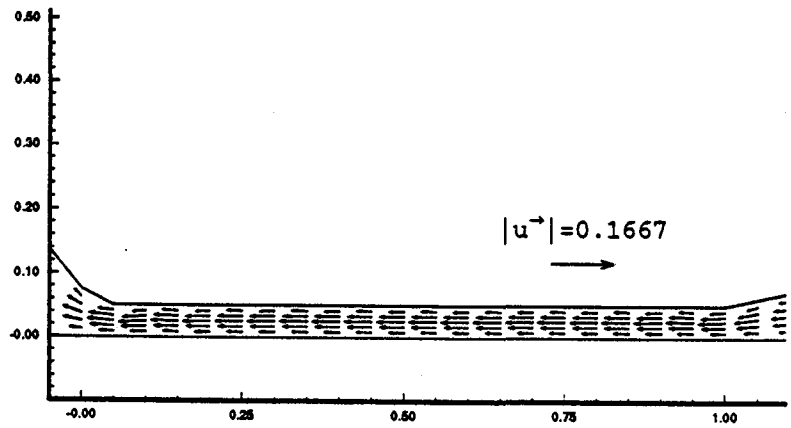

figure 6

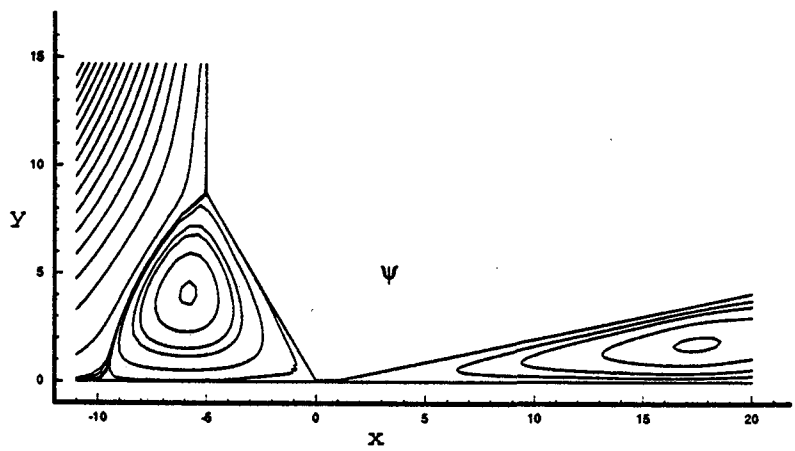

figure 7

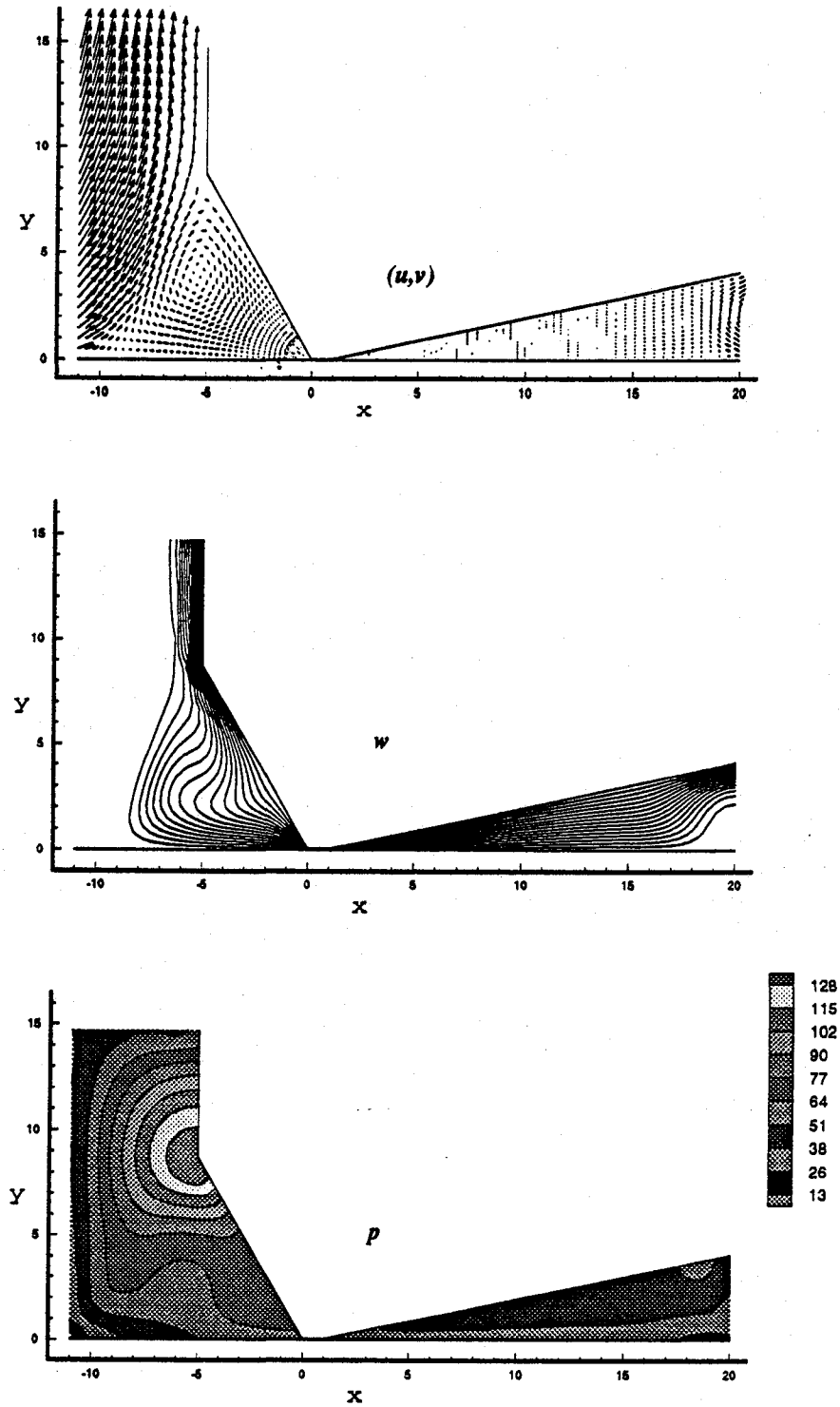

figure 8

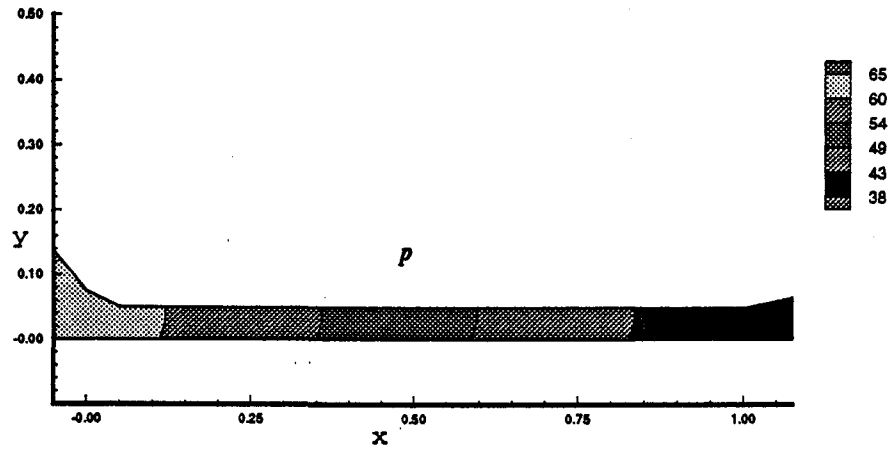

figure 9

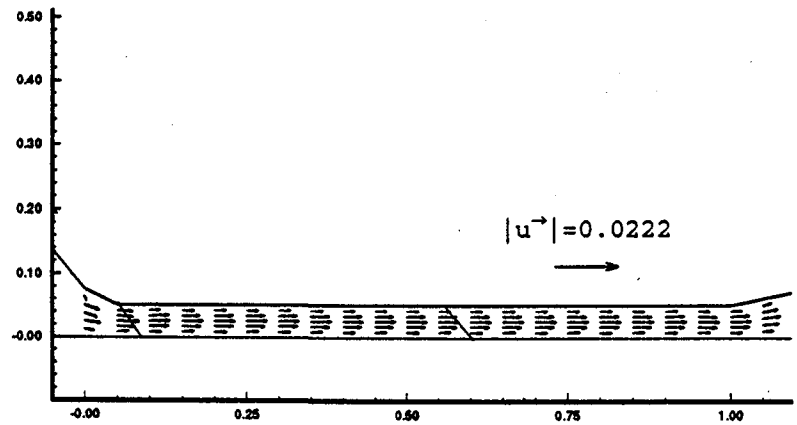

figure 10

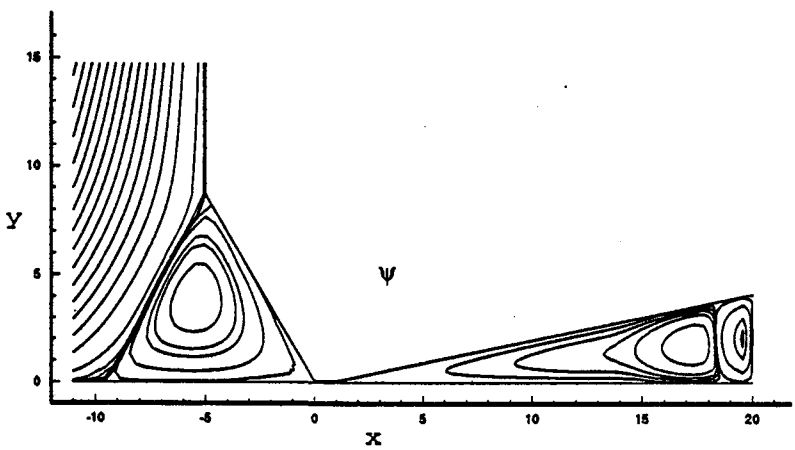

figure 11

sealing mechanisms of the type of devices here studied, even when their predictions are contradictory. While the NBC suggests leakage, the FBC indicates that sealing is achieved by pumping oil from the air-side, where the azimuthal flow is stable, to the oil-side, where centrifugal instabilities set in.

It is known that the use of the NBC in presence of variable body forces leads to erroneous results (refs.16 and 18). On the contrary, the application of the FBC is equivalent to a radiating boundary able to filter unwelcome reflections towards the interior of the computational domain (ref.24).

Besides its simplicity, the capability of the small-gap limit in incorporating the physics of the flow of lubricant fluid through the micro-gap of sealing devices has been established. Other effects, such as capillary forces on the oil-air interface and temperature variations should be included in future works.

REFERENCES

1. Jagger, E.T.: Study of the Lubrication of Synthetic Rubber Rotary Shaft Seals. Proc. Conf. on Lubrication and Wear. Inst. of Mech. Eng., 1957, pp.409-415.
2. Kawahara, Y.; and Hirabayashi, H.: A Study of Sealing Phenomena on Oil Seals. ASLE 77-LL-5B-2, 1977.
3. Hirano, F.; Ishiwata, H.; and Kambayashi, H.: Frictional Sealing Characteristics of Oil Seals. Proc. 1st. Int. Conf. on Fluid Sealing, BHRA, 1961, pp. 698-709.
4. Davies, M.G.: The Generation of Lift by Surfaces Roughness in Radial Face Seals. Int. Conf. on Fluid Sealing. B.H.R.A., 1961, Cranfield, England.
5. Jagger, E.T.; and Walker, P.S.: Further Studies of the Lubrication of Synthetic Rubber Shaft Seals. Proc. Inst. Mech. Engrs. Vol.181, 1966-1967, pp. 101-204.
6. Lebeck A.O.: Parallel Sliding Load Support in the Mixed Friction Regime. Part 1. The Experimental Data. *ASME Journal of Tribology*, 1986, Vol. 109.
7. Lebeck A.O.: Parallel Sliding Load Support in the Mixed Friction Regime. Part 2. Evaluation of the Mechanisms. *ASME Journal of Tribology*, 1986, Vol. 109.
8. Gabelli A.; and Poll, G.: Formation of Lubricant Film in Rotary Sealing Contacts: Part I - Lubricant Film Modeling. Paper No.90-Trib-64, ASME/STLE Tribology Conference, 1990, Toronto, Canada.
9. Salant R.F.: Numerical Analysis of the Flow Field within Lip Seals Containing Microundulations. Paper No.91-Trib-45, STLE/ASME Tribology Conference, 1990, St. Louis, Mo.
10. Gabelli A.: Private communication, 1992.
11. Johnston D.E.: Theoretical Analysis of a Pumping Mechanism Between Relatively Moving Surfaces. Proc. BHRA 12th. Int. Conf. Fluid Sealing. 1989, Brighton, UK.
12. Batchelor G.K.: An Introduction to Fluid Dynamics. Cambridge University Press, 1967.
13. Krueger E.R.; Gross, A.; and Di Prima, R.C.: On the Relative Importance of Taylor-vortex and Non-axisymmetric Modes in Flow Between Rotating Cylinders. *J. Fluid Mech.*, Vol.24, part 3, 1966, pp.521-538.
14. Drazin P.G.; and Reid, W.H.: Hydrodynamic Stability. Cambridge University Press, 1981.
15. Hall P.: The Stability of Unsteady Cylinder Flows. *J. Fluid Mech.*, Vol.67, part 1, 1975, pp.29-63.
16. Leone J. M.: Open Boundary Condition Symposium. Benchmark Solution: Stratified Flow over a Backward-facing Step. *Int. J. Num. Meth. in Fluids* Vol.11, 1990, pp 969-984.
17. Papanastasiou T.C.; Malamataris N.; and Ellwood, K.: A New Outflow Boundary

Condition. *Int. J. Num. Meth. Fluids*, Vol.14, 1992, pp.587-608.
18. Vionnet, C.A.; and Heinrich, J.C.: Open Boundary Conditions for Viscous Flows with Variable Body Forces. To be presented at the ASME WAM 93, Advances in Finite Element Analysis in Fluid Dynamics III. Nov. 1993, New Orleans, Louisiana.
19. Heinrich, J.C.; and Marshall, R.S.: Viscous Incompressible Flow by a Penalty Function Finite Element Method. *Computer and Fluids*, Vol.9, 1981, pp 73-83.
20. Carey G.F.; and Oden, J.T.: Finite Elements. Fluid Mechanics. Vol. VI, 1986, Prentice-Hall, Inc.
21. Brooks A.N.; and Hughes, T.J.R.: Streamline Upwind/Petrov Galerkin Formulations for Convection Dominated Flows with Particular Emphasis on the Incompressible Navier-Stokes Equations. *Comp. Meth. in Appl. Mech. and Eng.*, Vol.32, 1982, pp.199-259.
22. Heinrich, J.C.; and Yu, C.C.: Finite Element Simulation of Buoyancy-Driven Flows with Emphasis on Natural Convection in a Horizontal Circular Cylinder. *Comp. Meth. Appl. Mech. Eng.*, Vol.69, 1988, pp.1-27.
23. Dongarra, J.J.; Bunch, J.R.; Moler, C.B.; and Stewart, G.W.: LINPACK User's Guide, SIAM, 1979, Philadelphia.
24. Heinrich, J.C.; and Vionnet, C.A.: On Boundary Conditions for Unbounded Flows. Submitted for publication to *Communications in Applied Numerical Methods*. Wiley and Sons.

COMPARISON OF NUMERICAL SIMULATION AND EXPERIMENTAL DATA FOR STEAM-IN-PLACE STERILIZATION

Jack H. Young
William C. Lasher
Pennsylvania State University at Erie
Erie, PA 16563

SUMMARY

A complex problem involving convective flow of a binary mixture containing a condensable vapor and noncondensable gas in a partially enclosed chamber was modelled and results compared to transient experimental values. The finite element model successfully predicted transport processes in dead-ended tubes with inside diameters of 0.4 to 1.0 cm. When buoyancy driven convective flow was dominant, temperature and mixture compositions agreed with experimental data. Data from 0.4 cm tubes indicate diffusion to be the primary air removal method in small diameter tubes and the diffusivity value in the model to be too large.

NOMENCLATURE

C_p = mixture specific heat at constant pressure, J/kg-°C
C_1 = mass fraction of air
g = gravitational vector, m/s^2
h = convective heat transfer coefficient, W/m^2-°C
k = thermal conductivity, W/m-°C
P = mixture total pressure, Pa
P_{sat} = saturated water vapor pressure, Pa
q = heat transfer rate, W
t = time, s
T = mixture temperature, °C
T_{amb} = ambient temperature, °C
T_{sat} = saturated steam temperature, °C
u = velocity vector, m/s
μ = mixture dynamic viscosity, Pa-s
u_x = x-component of velocity, m/sec
ρ = mixture density, kg/m^3
ρ_0 = mixture density at reference temperature and concentration, kg/m^3
ρ^* = mixture density used in momentum equation, kg/m^3
ρ_{sat} = saturated water vapor density, kg/m^3
α = binary mass diffusivity, m^2/s
β_C = mixture coefficient of concentration expansion
β_T = mixture coefficient of thermal expansion

Subscripts

f = fluid
t = tube

INTRODUCTION

Availability of commercial computational fluid dynamic (CFD) packages have made finite element modeling available for use as a tool in studying complex real-world fluid engineering problems. Previously most CFD work involved selection of a problem based on availability of software or study of simple geometries and very idealized problem formulations. This study describes application of a commercial CFD package to a complex problem, compromises made during model development and how the model was used in conjunction with experimental data to gain an understanding and start in quantizing the important physical parameters.

Steam-in-place (SIP) sterilization has arisen in the biotechnology and pharmaceutical industries as result of the increased need to sterilize large devices which can not be placed in an autoclave. SIP offers the additional advantage of sterilizing complete systems (i.e., filters, holding tanks and interconnecting piping) without the need for aseptic assembly of individually sterilized components. This provides greater sterility assurance, improved productivity and reduced cost over convectional sterilization in an autoclave.

SIP sterilization requires that an adequate amount of moisture at the proper temperature be delivered for a required time to all sterilization sites. The factor most often resulting in sterilization failure is air entrapment which results in inadequate temperature and moisture. Failures are most likely to occur in dead-ended geometries, deadlegs, such as safety valves, gauges/transducers and closed inlet/outlet lines. Displacement of air can result from molecular diffusion and/or buoyancy driven convective flow resulting from temperature and solutal gradients.

Published studies have focused on general SIP principles (refs. 1 and 2) or recommendations for specific pieces of equipment (ref. 3). Recently experimental data have been reported describing effect of deadleg tube orientation (ref. 4) and diameter (ref. 5) on sterilization, but no quantitative guidelines exist for design engineers and scientists. Currently, biological testing is conducted to determine if sterilization has occurred. This is time-consuming and expensive. A mathematical model is needed for the transient air/steam mixing process occurring during SIP sterilization. The model would predict temperatures and steam concentrations at locations within various deadleg geometries and could be used to determine general transport processes and critical parameters.

EXPERIMENTAL METHODS

Temperature and biological measurements were taken in tubes

orientated vertically up or 5 degrees above horizontal. Inside diameters (IDs) of the tubes were 0.4, 1.0 and 1.7 cm with tube lengths ranging from 7.8 to 18.0 cm. Thermocouples or biological indicators were attached to a nylon string which ran along the tube centerline. The test fixture was pressurized with saturated steam having an average temperature of 122.4°C and pressure of 217 kPa. Details of experimental methods are given elsewhere (ref. 5).

Linear regression analysis was performed on the segment of the semi-logarithmic plots of surviving population versus time showing decreasing population. Slope of the regression line was used to determine time required to reduce the population by one log. This was termed cycle log reduction (CLR) time. Time at which the regression line intersected the initial population was termed time to start of kill (TSK). These two parameters characterized experimental kill at a location within a tube.

NUMERICAL SIMULATION

Simulation of deadleg SIP sterilization required:

1. Compressibility of air be taken into account
2. Development of expressions for physical properties of air/steam mixtures over wide ranges of composition (C_1 equal 0 to 1) and temperature (27 to 123°C).
3. Modeling of condensation from a mixture containing a noncondensable gas and condensable vapor.

Major effects associated with compressibility occur during initial pressurization with steam since the pressure is constant thereafter. This allows inclusion of these effects into the initial conditions for the problem (fig. 1b). It was assumed that all air was removed from the cross by steam flow and that the air in the tube was isentropically compressed to 217 kPa with no mixing of air and steam. This results in the top 56% of the tube initially containing all air at 100°C. The mixture was then considered to be incompressible with density ρ_o and the Boussinesq approximation applied to the momentum equation to account for temperature and concentration induced density variations.

Actual mixture density at 217 kPa is given by :

$$\rho = \frac{217}{0.287\ T\ C_1 + \frac{P_{sat}\ (1-C_1)}{\rho_{sat}}} \qquad (1)$$

Density used to calculate buoyant forces in the momentum equation was determined by assuming density to be a linear function of temperature and mass fraction with coefficient of

volume expansion due to concentration to be a function of temperature. Least squares analysis resulted in:

$$\rho^* = \rho_o \, (0.00407 \, T + (0.01638 - 0.00178 \, T) \, C_1) \qquad (2)$$

Variations in other mixture properties were determined using published values for steam and air at 25 to 125°C and assuming properties to be proportional to mass fraction of each component. Published diffusivity values could not be found for air/steam mixtures at 217 kPa and over the appropriate temperature and mass fraction ranges. A semiemperical equation for diffusivity of low density gases which depends on total pressure, temperature and molecular properties of constituent gases was used. Diffusivity was evaluated at 217 kPa and 123°C and assumed constant (0.15 cm^2/s).

Heat transfer resulting from condensation of a condensable vapor from a binary mixture containing a noncondensable gas is complex and depends on mixture composition , as well as, fluid flow near condensation sites. Convective heat transfer coefficients can vary from 24 to 2500 W/m^2-°C as composition varies from C_1 equals 0 to 1. Heat transfer reductions of over 50% can result when only 2 to 5% mass of air is present during free convection (ref. 6 and 7). Substantially higher heat transfer occurs if forced flow is present and condensation is minimal (ref. 8 and 9).

The condensation model was kept simple since this represented a first attempt at modeling SIP sterilization and substantial computational time was required. The tube was divided into six segments and temperature of a tube wall segment was set equal to the saturated steam temperature corresponding to steam concentration in that segment when the mass fraction of air was less than 0.1 (fig. 1a). This simulates the high convective heat transfer associated with condensation and availability of an infinite steam supply. When C_1 was greater than 0.1, the mixture was treated as a simple mixture of two noncondensable gases and a constant convective heat transfer coefficient of 7 W/m^2-°C corresponding to free convection was specified on external surfaces of the tube segment. Heat transfer between the tube wall and mixture within the tube was specified as:

$$k_t \left.\frac{\partial T}{\partial y}\right|_{t@wall} = k_f \left.\frac{\partial T}{\partial y}\right|_{f@wall} \qquad (3)$$

The commercially available CFD package FIDAP Version 6 (Fluid Dynamics International, Inc.) was used on a Silicon Graphics 4D35 workstation with 48 mg of memory. The governing equations were:

Continuity equation

$$\nabla \cdot u = 0 \tag{4}$$

Concentration equation

$$\frac{\partial C_1}{\partial t} + u \cdot \nabla C_1 = \alpha \nabla^2 C_1 \tag{5}$$

Momentum equation

$$\rho_0 \left[\frac{\partial u}{\partial t} + u \cdot \nabla u\right] = -\nabla P + \mu \nabla^2 u - \rho_0 g\left[\beta_T T + \beta_C C_1\right] \tag{6}$$

Energy equation

$$\rho_0 C_p \left[\frac{\partial T}{\partial t} + u \cdot \nabla T\right] = k_f \nabla^2 T \tag{7}$$

Quadrilateral finite elements were used with non-uniform meshes containing 1923 to 3464 nodes. A preliminary study was performed to evaluate the effect of two versus three dimensional modeling and to ensure grid-independence. The three-dimensional model required two weeks of CPU time to simulate 2.56 seconds of actual fluid flow, whereas the two-dimensional required 12 hours. Comparison of tube centerline temperatures showed a maximum average difference of 9.4%. Doubling the number of elements in the two dimensional model resulted in a 2.0% difference in average temperatures. Since five different tube simulations covering up to 40 minutes of real time were needed, two-dimensional models were used.

RESULTS AND DISCUSSION

Typical model velocity vector plots show steam rising at the tube centerline and the cooler air being displaced downward along the tube walls (fig. 2a). This results in a pair of counterrotating vortices. A second pair of vortices develop below the initial interface and the shear layers between the

vortices become unstable (fig. 2b). The vortices pair and roll up resulting in a more homogeneous mixture in the tube (fig. 2c). The buoyant forces eventually diminish until only weak structures remain (fig. 2d).

Magnitude of convective flow is indicated by mean fluid speed (Table I). 0.4 cm ID tubes were predicted to have minimal flow. This was experimentally investigated by comparing centerline temperature profiles and biological results from vertically orientated tubes and those positioned 5 degrees above horizontal. Average temperatures were within 3.7% and neither tube showed significant biological kill above the interface after 2 hours, thereby confirming diffusion to be the primary mode of air removal.

The model predicted significant increases in convective flow with increasing tube diameter (Table I). Since mixture density depends on temperature and mixture composition (eq. (1)) and not diameter, buoyant forces are independent of diameter. Viscous or retarding forces increase with decreasing tube diameter and tend to damp out convective flow. In the case of 0.4 cm ID tubes, viscous forces quickly damp out flow and diffusion dominates. Temperature and biological data confirmed diameter to be a critical parameter for sterilization. Sterilization was achieved throughout an 18 cm long tube with 1.7 cm ID within 75 minutes whereas 185 minutes were required for a 7.8 cm long tube with 1.0 cm ID (fig. 3). Sterilization could be achieved in only the lower half of 0.4 cm ID tubes with lengths of 7.8 cm.

Model predicted and experimental temperature profiles were quantitatively compared for three different lengths of 1.7 cm ID tubes, as well as, 7.8 cm long tubes with diameters from 0.4 to 1.7 cm (fig. 4). % differences were less than 12% for all lengths of 1.7 cm ID tubes with average differences increasing with increasing tube length. % differences increased with decreasing tube diameter. Model temperatures were higher than experimental values for 0.4 and 1.0 cm tubes with % differences as high as 28%.

The model must quantitatively predict transient mixture composition, in addition to temperature, if it is to be used to predict sterilization times. Mixture composition can not be measured experimentally but can be inferred from CLR times and TSK. Young (ref. 5) has shown a correlation between CLR and saturated steam temperatures for vertical deadlegs. Therefore, experimental CLR times can be used to calculate mixture mass fraction. Model predictions of time required to reach this mass fraction can then be compared to experimental TSK. Due to % differences in temperatures for 0.4 and 1.0 cm tubes, comparisons of predicted and experimental TSK were carried out for 1.7 cm ID tubes only. % differences increased with increasing tube length. For the shortest tube, 7.8 cm, experimental TSK for the uppermost location was 2.6 minutes while the model predicted 2.2 minutes. Experimental values for 13.0 and 18.0 cm tubes were 10.2 and 17.5 minutes. Corresponding predicted values were 5.4 and 7.9

minutes.

Model and experimental data show diffusion to be the primary transport process in 0.4 cm ID tubes, but the value of diffusivity used in the model was too large. A smaller value would result in a greater time required for steam to diffuse to top of the tubes when convective flow is not present. In the case of 7.8 cm long tubes with 1.7 cm IDs, a smaller diffusivity will have minimal effect on temperatures and TSK since air is removed from the tubes within 2-3 minutes by buoyant driven convective flow. In the longer 1.7 cm tubes, convective flow dies out prior to complete removal of air. Therefore, diffusion becomes important in these 1.7 cm tubes. A smaller diffusivity would increase model predicted TSK and thereby increase agreement between model and experimental data. A similar argument can be made for 1.0 cm tubes.

An empirical value for diffusivity can be obtained by comparison of model and experimental results for 0.4 cm tubes. This value could be used in the model as a next level of refinement.

The present condensation model does not allow for accumulation of non-condensable gas at the site of condensation. This does not appear to be a problem when convective flow is present, but may present a problem in 0.4 cm tubes and larger diameter tubes when convection is minimal.

CONCLUSIONS

Although many simplifying assumptions had to be made, use of a commercial CFD package has been extremely useful in understanding transport processes and critical parameters in SIP sterilization. It correctly predicted diffusion to be the primary air removal mechanism in 0.4 cm ID tubes and diameter to have a significant effect on magnitude of buoyant driven convective flow. When convective flow is the only significant transport mechanism the model and experimental data were in good agreement. Interactive use of numerical model and experimental data has proven effective towards development of quantitative SIP guidelines.

REFERENCES

1. Berman, D., Myers, T. and Suggy, C., Factors Involved in Cycle Development of a Steam-in-Place System, *J. Parenter. Sci. Technol.*, Vol.40, No. 4, 1986, 119-121.
2. Agalloco, J., Steam Sterilization-in-Place Technology, *J. Parenter. Sci. Technol.*, Vol.44, No. 5, 1990, 253-256.
3. Myers, T. and Chrai, S., Steam-in-Place Sterilization of Cartridge Filters In-Line with a Receiving Tank. *J. Parenter. Sci. Technol.*, Vol. 36, No. 3, 1982, 108-112.
4. Young, J. H., Ferko, B. L., Temperature Profiles and Sterilization Within a Dead-ended Tube. *J. Parenter. Sci. Technol.* Vol. 46, No. 4, 1992, 100-107.

5. Young, J. H., Sterilization of Varying Diameter Dead-ended Tubes. *Biotechnology and Engineering*. Vol. 42, No. 1, 1993, 125-132.
6. Mori, Y., Hijikata, K., Free Convective Condensation Heat Transfer with Noncondensable Gas on a Vertical Surface. *Int. J. Heat Mass Transfer*. Vol. 16, 1973, 2229-2240.
7. Sparrow, E. M., Lin, S. H., Condensation Heat Transfer in the Presence of a Noncondensable Gas. *J. of Heat Transfer*. August 1964, 430-436.
8. Al-Diwany, H. K, Rose, J. W., Free Convection Film Condensation of Steam in the Presence of Non-condensing Gas. *Int. J. Heat Mass Transfer*. Vol. 16, 1973, 1359-1369.
9. Sparrow, E. M., Mincowycz, W. J. and Saddy, M., Forced Convection Condensation in the Presence of Non-Condensables and Interfacial Resistance. *Int. J. Heat Mass Transfer*. Vol. 93, No. 3, 1967, 1829-1838.

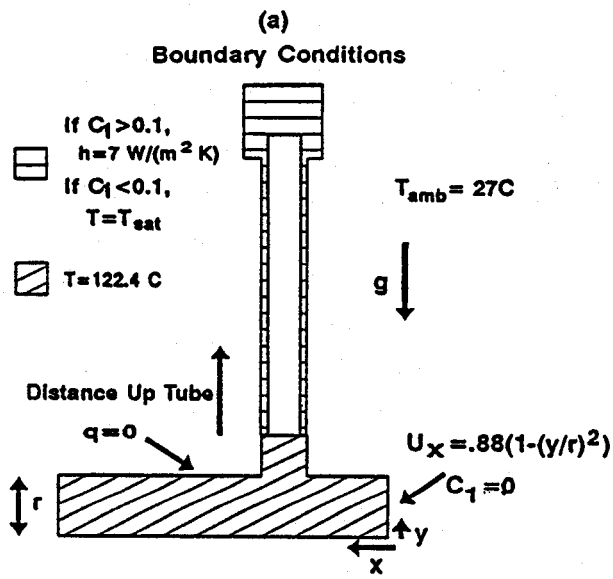

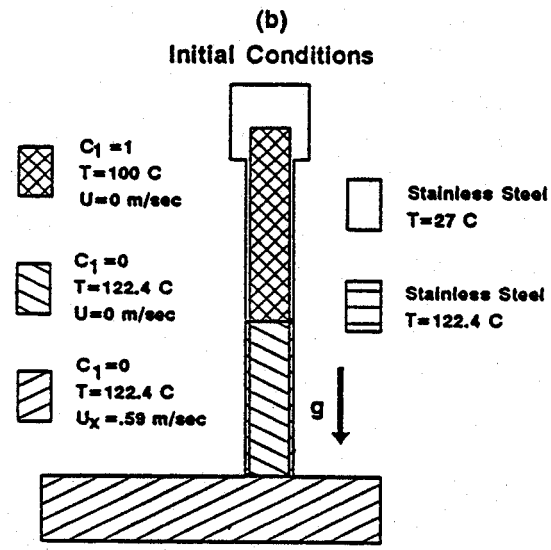

Figure 1- Schematic representation of numerical model (a) boundary conditions and (b) initial conditions.

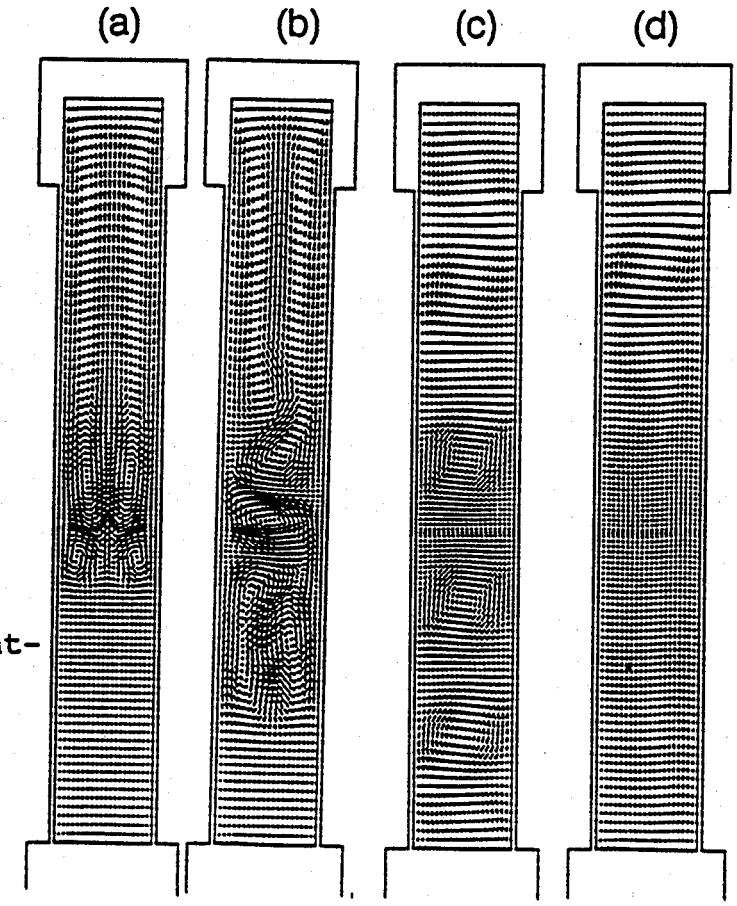

Figure 2- Velcity vector plots from 13.0 cm long tubes with 1.7 cm ID; (a) 0.48 seconds, (b) 1.75 seconds, (c) 1.02 minutes and (d) 4.75 minutes after pressurization with steam.

Time (Minutes)	Mean Speed (cm/sec)		
	0.4 cm ID Tube	1.0 cm ID Tube	1.7 cm ID Tube
0.02	0.029	1.43	3.55
0.05	0.007	0.97	3.42
0.50	0.005	1.14	2.37
1.0	0.005	0.89	2.05
3.0	0.005	0.74	0.11
5.0	0.005	0.02	0.03

Table I- Transient mean fluid speed for 7.8 cm long tubes.

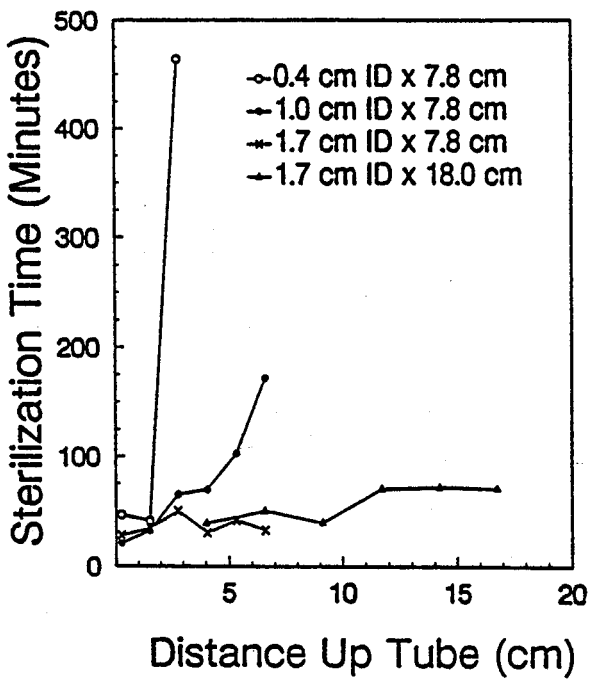

Figure 3- Time required for 12 log reduction of *B. stearothermophilus* spores

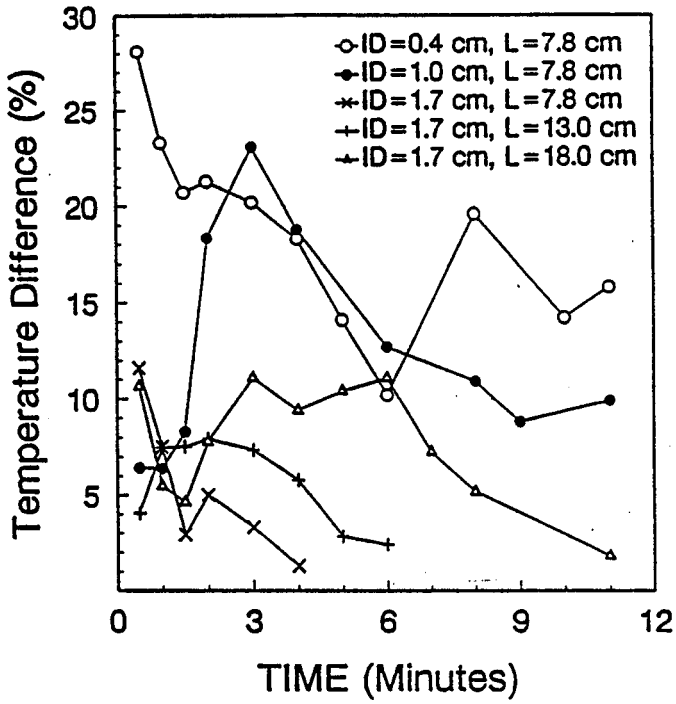

Figure 4- % difference between model and experimentally measured centerline temperatures.

A COMPARATIVE STUDY OF COMPUTATIONAL SOLUTIONS TO FLOW OVER A BACKWARD-FACING STEP

M. Mizukami, N. J. Georgiadis and M. R. Cannon
National Aeronautics and Space Administration
Lewis Research Center
Cleveland, Ohio 44135

SUMMARY

A comparative study was conducted for computational fluid dynamic solutions to flow over a backward-facing step. This flow is a benchmark problem, with a simple geometry, but involves complicated flow physics such as free shear layers, reattaching flow, recirculation, and high turbulence intensities. Three Reynolds-averaged Navier-Stokes flow solvers with k-ε turbulence models were used, each using a different solution algorithm: finite difference, finite element, and hybrid finite element - finite difference. Comparisons were made with existing experimental data. Results showed that velocity profiles and reattachment lengths were predicted reasonably well by all three methods, while the skin friction coefficients were more difficult to predict accurately. It was noted that in general, selecting an appropriate solver for each problem to be considered is important.

INTRODUCTION

In the application of computational fluid dynamic (CFD) methods, some considerations are the relative accuracy, efficiency, and applicability of different flow solvers. Selecting an appropriate solver for a given problem based on those criteria is an important factor in the successful use of CFD. Conversely, selecting an inappropriate solver can result in an inaccurate solution, a waste of computer resources, excessive user effort, a solution with insufficient detail, a solution with overwhelming detail, or a failure to obtain any solution at all.

Validation is a first step in applying CFD to any problem. This is accomplished by running the solver on appropriate benchmark cases and comparing the solutions with experimental results, or better yet, by identifying such validation cases that have already been performed. The benchmark cases, which can vary in complexity and size, should encompass the main fluid dynamic features contained in the problem to be investigated.

For air breathing propulsion systems, separated-reattaching flows are of interest, especially as they apply to areas such as diffusers and nozzle boattails, because the presence and characteristics of separated-reattaching flow on these components can drastically alter their performance. In these flows, the separation is driven by boundary layer development and pressure gradients in the flow over a complex geometry, so predicting the separation point is a difficult task.

A classic benchmark case used for validating CFD codes for turbulent separated-reattaching flows is the flow over a backward-facing step (BFS). The geometry of the configuration is simple, but the flow is still complex and challenging to simulate, involving flow physics such as free shear layers, reattaching flow, and recirculation. Proper modeling of turbulence is needed for accurate simulation of the flow, and many studies applying different turbulence models to BFS flows have been conducted, such as in references 1-3. In BFS flow,

the separation point is fixed at the corner of the step; the separation is not driven by boundary layer development and adverse pressure gradients. Thus the problem is simplified considerably, facilitating study of the reattachment itself.

In order to assess the application of different CFD solvers to separated-reattaching flows, a comparative study was conducted for solutions to flow over BFS. Three Reynolds-averaged Navier-Stokes flow solvers incorporating two-equation k-ε turbulence models were used, each one using a different solution algorithm: a finite difference method (FDM) solver originally oriented to aeropropulsion flows, a computer aided engineering (CAE) oriented finite element method (FEM) code, and a CAE oriented hybrid finite element - finite difference method (HM) solver. FDM used a low Reynolds number k-ε turbulence (LR k-ε) model, whereas FEM and HM used versions of high Reynolds number k-ε turbulence (HR k-ε) models. Solutions were compared with each other, and with existing experimental data. This is not a comparison between numerical algorithms of finite differences and finite elements, due to a number of factors, and particularly because of differences in the turbulence models used.

EXPERIMENTAL STUDY

The experimental study of flow over BFS conducted by Driver and Seegmiller (4) was selected for use in the present work, because of the extensive quantitative measurements made, the relatively high flow speeds, and the low streamwise pressure gradient of the flow. The freestream velocity was 145 ft/s (Mach number = 0.128) in standard atmosphere, and the step height was 0.5 inches, giving a step height Reynolds number of 33420. The Reynolds number of the boundary layer momentum thickness 4 step heights upstream of the step was 5000, producing a fully turbulent boundary layer. The ratio of step height to tunnel exit height was 1:9 for the parallel wall case, so the streamwise pressure gradient due to the step was relatively small. Mean and turbulent flow velocity components were obtained using two component laser doppler velocimetry (LDV), wall static pressures downstream of the step were measured by static taps, and wall friction coefficients were obtained from oil-flow laser interferometry. Turbulence intensities, correlations, and dissipation were computed from LDV data.

COMPUTATIONAL METHODS

Three Reynolds-averaged Navier-Stokes flow solvers with k-ε turbulence models were used to solve BFS flow, each using a different solution algorithm: FDM with LR k-ε, FEM with HR k-ε, and HM with HR k-ε. HR k-ε assumes law-of-the-wall profiles in the boundary layer, whereas LR k-ε requires a large number (20+) of grid points near the wall to numerically resolve the boundary layer. Therefore, although LR k-ε is much more computationally intensive than HR k-ε, LR k-ε is usually expected to be more accurate for separated flows, because it does not assume the law-of-the-wall profiles that are based on attached flat plate boundary layers. The computational domain, schematically depicted in figure 1, begins four step heights upstream of the step where an incoming boundary layer velocity profile is specified, and ends far downstream of the step. HM and FEM use the same grid; FDM uses a much finer grid in order to accommodate the LR k-ε model.

Finite Difference Method (FDM)

The finite difference solver used in this study is PARC, an internal flow Navier-Stokes code used extensively by government and industry to analyze propulsion flows (5,6). Two-

dimensional / axisymmetric (2D), and three-dimensional (3D) versions are available. PARC was derived from the ARC Navier-Stokes code (7) which has been used for external flow calculations.

The governing equations of motion are the time dependent Reynolds averaged Navier-Stokes equations using a perfect gas relationship and Fourier's heat conduction law. These equations are discretized in conservation law form with respect to general curvilinear coordinates and solved with the Beam and Warming approximate factorization algorithm (8). Although the time dependent formulation of the equations is used, the code is intended for steady state flow simulations. The LR k-ε model of Chien (9), including modifications for compressibility by Nichols (10), was used in these calculations using the 2D version of the code.

A 11,341 point grid was used, with 111 points in the horizontal direction and 131 points in the vertical direction downstream of the step. In the boundary layers, the grid was packed to the walls such that downstream of the reattachment point, on the average, the first grid point off the wall was approximately at $y+ \sim 1.0$.

Finite Element Method (FEM)

The finite element solver used is FIDAP Version 5.04 by Fluid Dynamics International (11). It is intended to handle a wide variety of applications, including: internal and external aerodynamics, heat transfer, crystal growth, extrusion, injection molding, chemical mixing, chemical vapor deposition, etc. The code includes its own pre and post-processors to form a complete, integrated analysis package. Files can also be imported from, or exported to, other finite element pre/post-processors such as PATRAN, ANSYS, and SUPERTAB.

FEM uses the incompressible, Reynolds-averaged Navier-Stokes equations in either dimensional or non-dimensional form. Non-inertial frames of reference are supported, as are free surfaces. The Galerkin method of weighted residuals is used for finite-element formulation of the problem. A streamline upwinding capability is included to handle the numerical instabilities posed by Galerkin's method. Also, the standard pressure discretization can be replaced by a penalty function approximation. Several methods are available for solving the discrete system of equations including successive substitution, Newton-Raphson, and modified Newton-Raphson methods.

The HR k-ε model of Launder and Spalding (12), generally considered the 'standard' HR k-ε model, is used. However the treatment at the wall differs from that used in the HM (to be discussed later). In order to solve the full set of elliptic equations down through the viscous sublayer to the wall, a one-element thick layer of special wall elements are used adjacent to the physical boundary. These wall elements specify shape functions based on the law-of-the-wall profiles to characterize the variations in the mean flow variables. Then, van Driest's mixing length approach is used to model the variations of turbulent quantities. Alternatively, a user-defined algebraic turbulence model (based on mixing-length theory) could be created and used in place of HR k-ε; however, this option was not exercised in the present study.

The computational grid was generated using the mesh generator integrated with the FEM system. With the exception of the additional wall elements, the grid is identical to the one used with HM, consisting of 2751 nodes and 2796 elements, with 70 elements in the horizontal direction, and 40 elements in the vertical direction downstream of the step.

Hybrid Method (HM)

FLOTRAN version 2.0, by Compuflo, Inc. (13) uses a hybrid finite-element / finite-difference method. The solution algorithm is based on finite element methods. However, certain modifications make the computational efficiency and storage requirements more competitive with finite difference / finite volume codes, while still retaining the geometric flexibility of finite

element codes. This program consists of the flow solver only; grid generation and post processing are handled by finite element pre/post processors, such as PATRAN, ANSYS and I-DEAS.

The governing equations are the steady, Reynolds averaged Navier-Stokes equations, used in the incompressible form for the present problem. Galerkin's method of weighted residuals is used to discretize the diffusion and source terms. A monotone streamline upwind method is used to discretize the advection terms, in order to avoid oscillations in the advection terms, called dispersion errors, caused by the Galerkin's method. The intent of streamwise upwinding is to minimize the 'crosswind' numerical diffusion that may occur when the fluid flows diagonally across the cell. Pressure is derived from a velocity-pressure relation.

As in FEM, the Launder and Spalding HR k-ε turbulence model is used (11). Analytical law of the wall and log law of the wall velocity profiles are used, but the exact treatment near the wall differs from that used in FEM.

The grid used by HM in the present study was generated using PATRAN. In order to check the grid sensitivity, two grids were created: a coarse grid with 2640 elements, and a fine grid with about 6000 elements. However, both produced nearly identical solutions, therefore results shown herein are with the coarse grid, which is nearly identical to the grid used by FEM.

RESULTS

Reattachment Length

A sensitive parameter often used to quantify the accuracy of solutions to BFS flow is the reattachment length, defined as the distance downstream of the step where the flow separating at the step corner reattaches with the bottom wall. Reattachment occurs where the velocity gradient off the wall is zero, or in other words, where the wall shear stress is zero. However, there appears to be an inconsistency in the experimental results (4). Driver and Seegmiller report a reattachment length of $x/H = 6.25$, as measured by laser interferometry. On the other hand, velocity profiles measured by LDV indicate a reattachment point just downstream of $x/H = 5$, and the profile at $x/H=6$ appears clearly attached. Driver & Seegmiller speculate the discrepancy may be due to a long, thin separated region along the wall with very small length scales; but no such flow was indicated even in FDM results using LR k-ε (which is expected to better resolve near-wall flows than HR k-ε). Based on the reattachment length determined from oil-flow interferometry, FDM gives a good prediction, whereas FEM and HM underpredict by about 12% and 17%, respectively (table 1). However, if one were to consider the reattachment length inferred by the LDV velocity profiles, FEM and HM give the better predictions.

Wall Shear Stresses

Present results concur with studies in the literature (1-3) that wall shear stresses downstream of the step are difficult to predict accurately, yet in general, accurate prediction of skin friction is important for calculating the drag of practical configurations. Figure 2 depicts the present results. FDM created significant under and over shoots of skin friction coefficients, behind and ahead of the reattachment point, respectively. FEM produced a reasonable looking curve, but it was slightly shifted to the left due to a short reattachment length. HM underpredicted the skin friction, and the curve was also shifted to the left due to a short reattachment length. Neither FEM nor HM appeared to reproduce the secondary recirculation zone near the base of the step, indicated experimentally by positive C_f values in that region.

Mean Velocity Profiles

Axial velocity profiles were predicted reasonably well by all three methods, at the stations x/H = 3, 6 and 12 downstream of the step (fig. 3). At x/H = 3, all three solutions look qualitatively similar, with the 'corner' in the velocity profile at the correct y height. At x/H = 6 and x/H = 12, the velocity profile corners are still at the correct heights, but all three methods slightly underpredict the velocity near the wall, with FDM having the greatest discrepancy, and HM the least.

DISCUSSION

Turbulence is a major phenomena in BFS flow, and as expected, turbulence models have been observed to significantly impact the CFD solutions. Because the turbulence models used in FDM, FEM and HM are not exactly the same, differences in the solutions are likely due at least in part to different turbulence models. Using LR k-ε, Avva, et al. (1) observed strong sensitivity of the skin friction results to grid refinement in the inner layer, by varying the number of grid points in the inner layer between 5 and 30. In the present study, for FDM with LR k-ε, approximately 18 grid points were in the inner layer, so the skin friction results may change with changes in the boundary layer grid. Conventional wisdom holds that HR k-ε is not accurate for separated flow, because it assumes an attached velocity profile at the wall. Failure of solvers equipped with HR k-ε (FEM and HM) to reproduce the secondary recirculation zone at the base of the step seems to support this assertion. However, when the overall situation is considered, the present study concurs with Avva, et al. (1) and Steffen (3) that high Re k-ε may actually be preferable to LR k-ε for some cases such as BFS flow, because HR k-ε uses less computer resources, is less grid-resolution sensitive, and produces results of similar quality overall, when compared to LR k-ε.

Computational efficiency is a consideration, since these codes may be applied to large, complex problems; to this end, simple benchmark cases should not consume large quantities of computer resources. To obtain the present solutions, FDM used 50,000 Cray Y-MP CPU seconds, FEM consumed 615 Y-MP CPU seconds, and HM used 2000 seconds on a VAX9000. FEM and HM appear to be substantially more CPU efficient than FDM, but some other factors need to be considered. This particular FDM code is known to be very slow to converge for low speed flows (freestream Mach number < 0.2). Convergence is much faster for higher Mach numbers that are more typical of aerospace applications. Furthermore, as discussed above, LR k-ε, used in FDM, is inherently more computer intensive than HR k-ε, used in FEM and HM. Therefore, if the problem under consideration has higher freestream velocities as is more typical of aerospace applications, or if a HR k-ε model is successfully integrated with FDM, the relative computational efficiency of FDM should improve substantially.

The present study is only one test case, with a single fixed flow regime and a certain set of flow features; to draw generalized conclusions regarding the merit or performance of the three codes based on this one case only would be misleading. The original objective of this work--which was not fully realized due to time and code capability constraints--was to investigate a number of geometrically simple benchmark cases encompassing most of the flow regimes and flow physics encountered in air breathing propulsion inlet and nozzle flows, using a number of different flow solvers. Compressible and supersonic flows are aspects of those flows, therefore a simple low angle 'bent wall' was selected as a benchmark case to evaluate solver performance at high subsonic and supersonic Mach numbers. However, the FEM version available at the time did not handle compressible or supersonic flow, and attempts to run this case on HM were unsuccessful. Therefore, it becomes clear that an appropriate flow solver must be chosen for each problem to be investigated, and that there is no one code that is ideal for solving all types of flow.

The U.S. Government does not endorse any commercially available program with respect to any other program.

ANSYS is a registered trademark of Swanson Analysis Systems, Inc.

FIDAP is a registered trademark of Fluid Dynamics International, Inc.

FLOTRAN is a registered trademark of Compuflo, Inc.

I-DEAS and SUPERTAB are registered trademarks of Structural Dynamics Research Corp.

PATRAN is a registered trademark of PDA Engineering.

REFERENCES

1. Avva, R., Smith, C. and Singhal, A., "Comparative Study of High and Low Reynolds Number Versions of k-e Models," AIAA Paper 90-0246, 1990.
2. Georgiadis, N. J., Drummond, J. E., and Leonard, B. P., "Development of an Algebraic Turbulence Model for Analysis of Propulsion Flows," AIAA Paper 92-3861 or NASA TM-105701, 1992.
3. Steffen, C. J. Jr., "A Critical Comparison of Several Low Reynolds Number k-ε Turbulence Models for Flow Over a Backward-Facing Step", NASA TM to be published, 1993.
4. Driver, D. M. and Seegmiller, H. L., "Features of a Reattaching Turbulent Shear Layer in Divergent Channel Flow," *AIAA Journal*, Vol. 24, No. 2, 1985, pp. 163-171.
5. Cooper, G. K. and Sirbaugh, J. R., "PARC Code: Theory and Usage," AEDC-TR-89-15, 1989.
6. Cooper, G.K. and Sirbaugh, J.R., "The PARC Distinction: A Practical Flow Simulator," AIAA Paper 90-2002, 1990.
7. Pulliam, T.H., "Euler and Thin Layer Navier-Stokes Codes: ARC2D, ARC3D," Notes for Computational Fluid Dynamics User's Workshop, The University of Tennessee Space Institute, Tullahoma, Tennessee, (UTSI Publication E02-4005-023-84), 1984, pp. 15.1-15.85.
8. Beam, R.M., and Warming, R.F., "An Implicit Finite-Difference Algorithm for Hyperbolic Systems in Conservation-Law Form–Application to Eulerian Gasdynamic Equations," *Journal of Computational Physics*, Vol. 22, No. 1, 1976, pp. 87-110.
9. Chien, K.-Y., "Predictions of Channel and Boundary-Layer Flows with a Low-Reynolds-Number Turbulence Model," *AIAA Journal*, Vol. 20, No. 1, 1982, pp. 33-38.
10. Nichols, R.H., "A Two-Equation Model for Compressible Flows," AIAA Paper 90-0494, 1990.
11. *FIDAP Theoretical Manual: Revision 5.0*, Fluid Dynamics International, Inc., Evanston, IL, 1990.
12. Launder, B. E., and Spalding, D. B., "The Numerical Computation of Turbulent Flows," *Comp. Methods in Appl. Mech Engr.*, Vol. 3, 1974, pp. 269-289.
13. *FLOTRAN Theoretical Manual*, Compuflo, Inc. Charlottesville, VA., 1992.

Table 1. Reattachment lengths

Method	reattachment length (x/H)
Driver-Seegmiller Data	6.25
FDM	6.26
FEM	5.47
HM	5.22

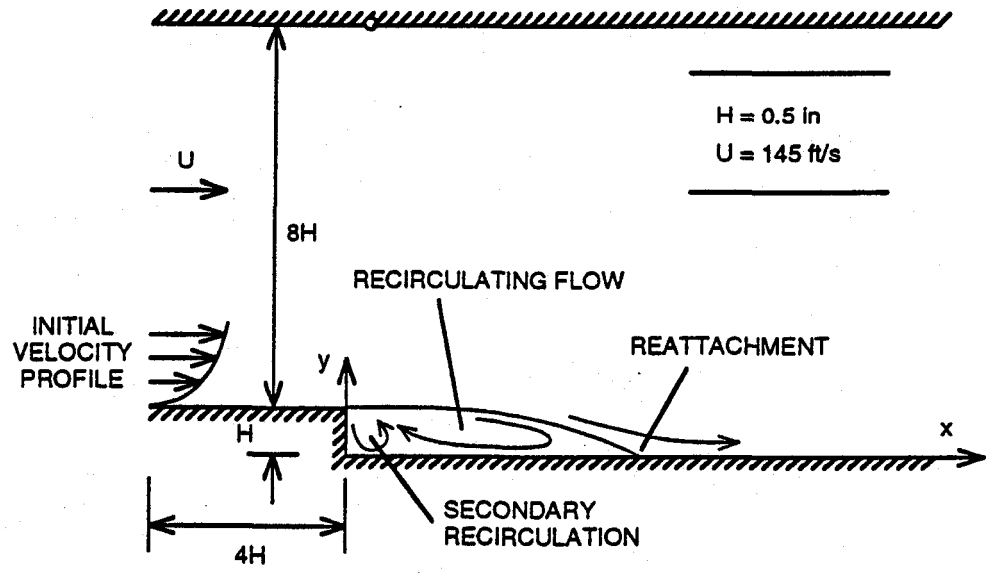

Figure 1. Schematic diagram of backward-facing step

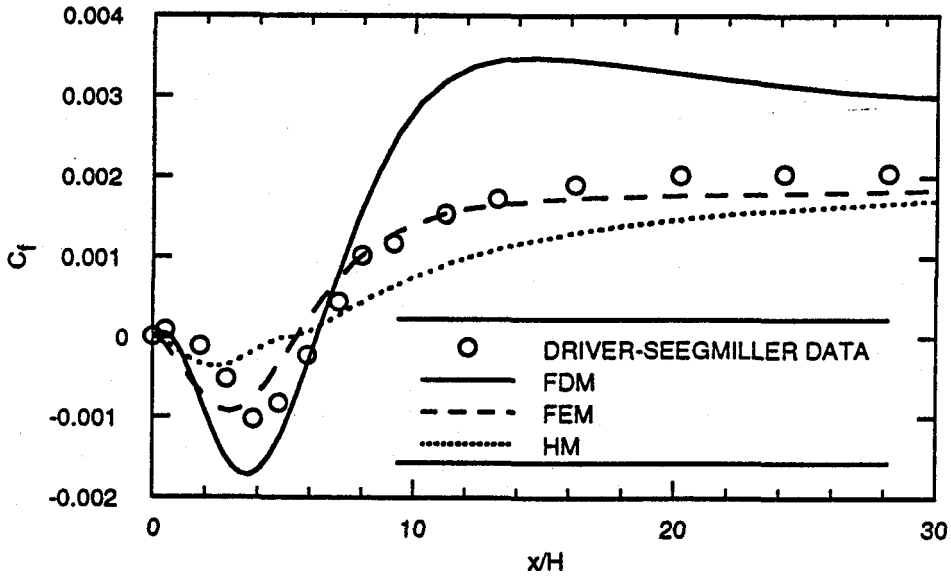

Figure 2. Wall skin friction coefficient distributions

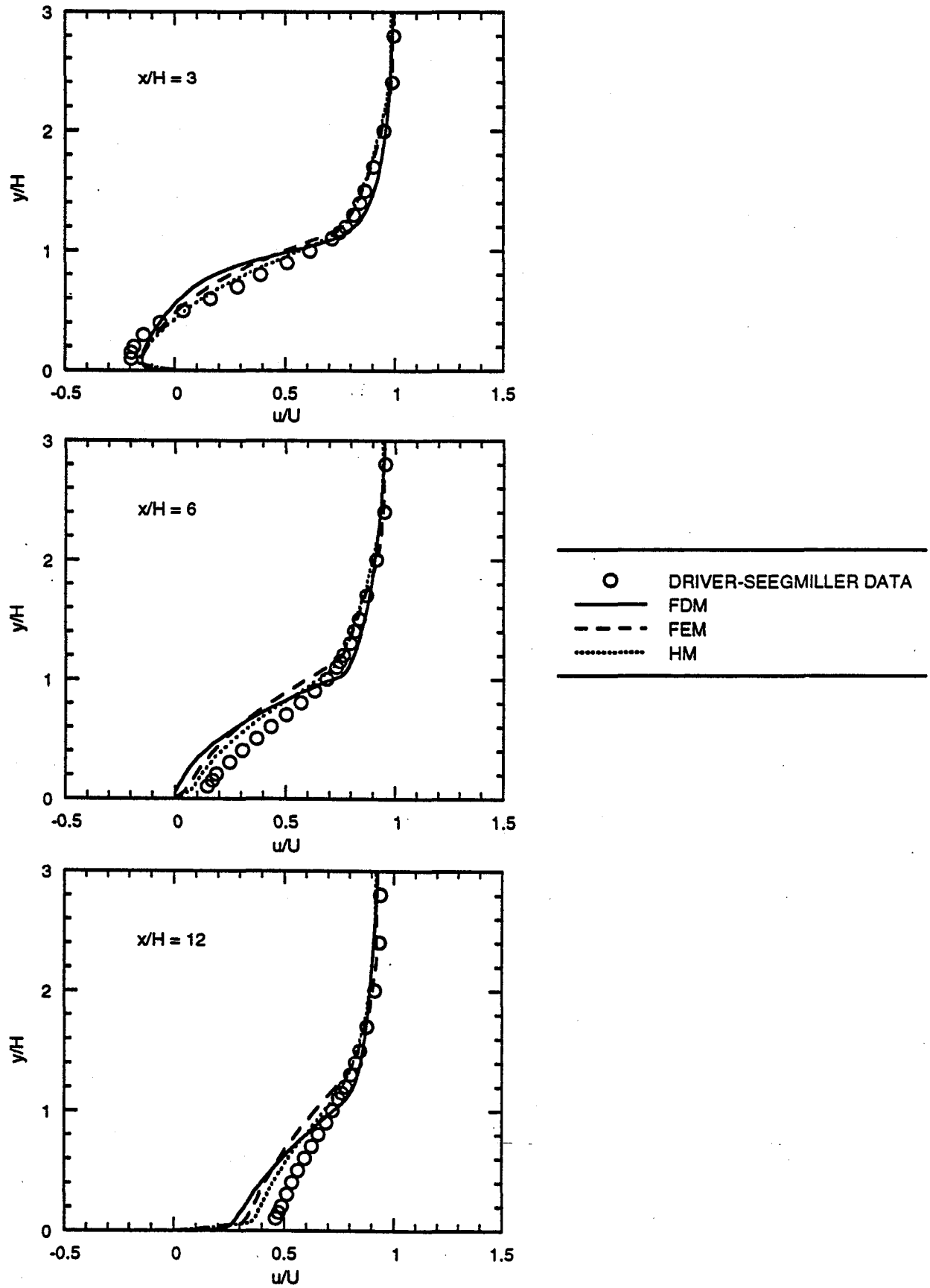

Figure 3. Mean velocity profiles in the separated and reattached regions

RESPONSE-COEFFICIENT METHOD FOR HEAT-CONDUCTION TRANSIENTS WITH TIME-DEPENDENT INPUTS

Tamer Ceylan
University of Wisconsin-Platteville
Department of Mechanical Engineering
Platteville, WI 53818

SUMMARY

A theoretical overview of the response-coefficient method for heat-conduction transients with time-dependent input forcing functions is presented with a number of illustrative applications. The method may be the most convenient and economical if the same problem is to be solved many times with different input-time histories or if the solution time is relatively long. The method is applicable to a wide variety of problems (including irregular geometries, position-dependent boundary conditions, position-dependent physical properties, and nonperiodic irregular input histories). Nonuniform internal energy generation rates within the structure can also be handled by the method. The area of interest is long-time solutions (in which initial condition is unimportant) and not the early transient period. The method can be applied to one-dimensional problems in cartesian, cylindrical, and spherical coordinates as well as to two-dimensional problems in cartesian and cylindrical coordinates.

THEORETICAL OVERVIEW

The analytical formulation of the heat-conduction problems (in cartesian coordinates) covered by this paper is given in the appendix A (ref. 3). A problem may have any combination of the following four time-dependent inputs: specified boundary temperature, specified boundary heat flux or heat flow, specified ambient temperature in a convective boundary condition, and specified internal energy generation rate within the structure. One may be required to determine outputs such as selected surface temperatures or boundary heat fluxes as a function of time in response to the time-dependent input forcing functions in the problem.

After the problem is discretized spatially by using either finite differences or finite elements, the resulting system of first-order ordinary differential equations in time with constant coefficients can be expressed as (ref. 2)

$$\underline{H}\,\underline{T}' + \underline{S}\,\underline{T} = \underline{F} \qquad (1)$$

where $\underline{H}$ is the capacitance matrix, $\underline{T}$ is the temperature vector containing nodal temperatures, $\underline{S}$ is the conductance matrix, and $\underline{F}$ is the input vector containing time-dependent and constant input values. The vector $\underline{T}'$ contains time derivatives of nodal temperatures. The matrices $\underline{H}$ and $\underline{S}$ are constant but the vector $\underline{F}$

is time dependent.

The response-coefficient method utilizes the exact solution to equation (1) rather than following the standard approach used by the finite-difference or finite-element method. This involves using an integrating factor or Duhamel's theorem , and solving a generalized eigenvalue problem. Since this paper will also discuss a number of response-coefficient applications, see ref. 3 for the details of theoretical development.

After expressing the input vector $\underline{F}$ in equation (1) as a function of time-dependent and constant inputs, the integration in the exact solution can be carried out. If a time interval is selected and if each time-dependent input is assumed to be linear within the time interval, it is possible to obtain current values of nodal temperatures as a function of current and previous values of time-dependent inputs as well as constant input values. The initial condition will not be important for long-time solutions because only the most recent input history should be relevant in finding current values of the selected outputs.

Typically one is interested only in a selected temperature or heat flow in the system. There are two ways of writing the output equations. It is possible to express current values of the desired outputs in terms of current and previous values of time-dependent inputs as well as constant input values. It is also possible to incorporate previously-computed outputs into the computations of the current outputs to facilitate calculations. Equations (B1) and (B2) for these two options are given in the appendix B. Equation (B2) is preferred because it involves much fewer calculations compared to equation (B1). The coefficients in equation (B2) (the $\underline{B}$, the C, and $\underline{D}$) are called "response coefficients".

Once all of the response coefficients have been determined in a problem, it is possible to keep track of the desired outputs as a function of time by the repeated use of equation (B2). It should be noted that equation (B2) can handle multiple inputs and multiple outputs. If there is only one input and one output, then the $\underline{B}$ will become scalar numbers.

ONE-DIMENSIONAL EXAMPLE (CARTESIAN COORDINATES)

The response-coefficient method can be used to handle one-dimensional composite wall structures with nonuniform internal energy generation within the structure. Consider a homogeneous wall with convective boundaries on both sides given in the appendix C. The ambient temperature on the left-hand side is the time-dependent input and the ambient temperature on the right-hand side is constant. Let the desired output be the heat flux at the right-hand side. We have one time-dependent input, one constant input, and one output in this problem. Therefore, the response coefficients will all be scalars, as can be seen in the appendix C. A detailed discussion of this example problem and the computation of the output based on a given input history can be found in ref. (3).

ONE-DIMENSIONAL EXAMPLE (CYLINDRICAL COORDINATES)

The response-coefficient method can be used to handle one-dimensional composite cylinders (solid or hollow) with nonuniform internal energy generation within the structure. Consider a long circular cylinder made of steel (Appendix D). Let the surface temperature be time dependent. The output is the surface heat flow per unit length. We have one time-dependent input and one output in this problem. Therefore, the response coefficients will all be scalars, as can be seen in the appendix D. More details of this example problem and the computation of the output based on a given nonperiodic input history can be found in ref. (4).

ONE-DIMENSIONAL PROBLEM (SPHERICAL COORDINATES)

The response-coefficient method can be used to handle one-dimensional composite spheres (solid or hollow) with nonuniform internal energy generation within the structure. Ref. (5) describes a hollow steel sphere covered with asbestos. The inner surface of this composite structure has a time-dependent specified temperature and the outer surface is exposed to a time-dependent ambient temperature (convective heat-transfer coefficient known). Assuming that the input-time histories are given on an hourly basis, it is desired to find the hourly variation of the heat flux at the outer surface. There are two time-dependent inputs and one output in this problem. More details of this example problem and the response coefficients are given in ref. (5).

TWO-DIMENSIONAL EXAMPLE PROBLEM (CYLINDRICAL COORDINATES)

The response-coefficient method can be used to handle two-dimensional composite structures in cylindrical coordinates (r,z) with nonuniform internal energy generation within the structure. Ref. (6) determines the annual heat loss through the walls and floor of a buried solar energy storage tank with water as the storage medium. In this example, a vertical cylindrical tank has a water level at the ground surface. The insulation and the earth surrounding the tank is the conduction system. The temperature variation is in the r- and z-directions in this axially-symmetric problem. Some assumptions need to be made to find the solution. A time interval of two weeks is used to approximate the yearly variation of the ambient temperature. The data for the problem, the response coefficients, and the variation of the instantaneous heat loss (from which annual heat loss is determined) are given in ref. (6).

DISCUSSION

For a given problem and time interval, the response coefficients need to be found only once. They do not depend on any particular input-time history. For this reason, if the same

problem is to be solved many times with different input-time histories, the response-coefficient method may be advantageous. If the solution is needed for a very long period of time, this would also make the response-coefficient method advantageous because arithmetical operations required by equation (B2) can be carried out easily once the coefficients are found. Moreover, there is no stability problem in this method since the exact solution to equation (1) is utilized.

The response-coefficient method can be used to handle three-dimensional problems as well; however, currently it has not been developed to do that. The method has not been developed to handle time- or temperature-dependent thermal conductivity or convective heat-transfer coefficient. Another limitation is that radiation boundary condition cannot be handled at the present time.

REFERENCES

1. Carslaw, H.S.; and Jaeger, J.C.: Conduction of Heat in Solids, 2nd edition. Oxford University Press, 1959.
2. Myers, G.E.: Analytical Methods in Conduction Heat Transfer. McGraw-Hill, 1971.
3. Ceylan, H.T.; and Myers, G.E.: Long-Time Solutions to Heat-Conduction Transients with Time-Dependent Inputs, ASME Journal of Heat Transfer, vol.102, pp. 115-120.
4. Ceylan, T.: Transient Heat Transfer in Long Cylinders with Time-Dependent Surface Temperature, ASHRAE Transactions, vol. 93, part 2, 1987.
5. Ceylan, T.: Response Coefficients for Composite Cylinders and Spheres, ASHRAE Transactions, 1991.
6. Ceylan, H.T.; and Myers, G.E.: Application of Response-Coefficient Method to Heat-Conduction Transients, ASHRAE Transactions, part 1A, pp. 30-39, 1985.

APPENDIX A

This paper is concerned with heat-conduction transients described by the partial differential equation:

$$\frac{\partial}{\partial x}\left(k\frac{\partial t}{\partial x}\right) + \frac{\partial}{\partial y}\left(k\frac{\partial t}{\partial y}\right) + \frac{\partial}{\partial z}\left(k\frac{\partial t}{\partial z}\right) + g''' = \rho c \frac{\partial t}{\partial \theta} \qquad (A1)$$

where k, ρ, and c can be position dependent and g''' may depend upon both position and time. There will be no restriction to simple geometrical shapes. The conditions on the boundaries of the region may be combinations of convection, specified heat flux, or specified temperature as shown by equations (A2-A4).

$$\textit{Convection:} \quad -k\frac{\partial t}{\partial n} = h(t_\infty - t) \qquad (A2)$$

$$\textit{Specified heat flux:} \quad -k\frac{\partial t}{\partial n} = q''_s \qquad (A3)$$

$$\textit{Specified temperature:} \quad t = t_s \qquad (A4)$$

The convective heat-transfer coefficient may depend upon position but not upon time. The quantities t_∞, q''_s, and t_s may depend upon both position and time. In fact, the primary purpose of this paper is to discuss problems in which t_∞, q''_s, t_s, and g''' are prescribed functions of time. Since long-time solutions rather than initial transients are of interest, the initial condition will be unimportant.

APPENDIX B

The output vector for current values ($\underline{u}^{(0)}$) can be expressed as a function of the input vectors for current ($\underline{s}^{(0)}$ and previous values ($\underline{s}^{(\mu)}$) as well as constant input vector ($\underline{p}$) as follows:

$$\underline{u}^{(0)} = \underline{A}_0\underline{s}^{(0)} + \sum_{\mu=1} \underline{A}_\mu\underline{s}^{(\mu)} + \underline{E}\underline{p} \qquad (B1)$$

In this equation, μ is a time-step index that is zero at the present time and increases by one for each time-step backward in time. See ref. (1) for the expressions for the coefficient matrices (the $\underline{A}$ and $\underline{E}$).

After incorporating previously-computed outputs into the computation of the current outputs, equation (B1) takes the form:

$$\underline{u}^{(0)} = \underline{B}_0\underline{s}^{(0)} + \sum_{\mu=1} \underline{B}_\mu\underline{s}^{(\mu)} + \sum_{\mu=1} C_\mu\underline{u}^{(\mu)} + \underline{D}\underline{p} \qquad (B2)$$

In this equation $\underline{u}^{(\mu)}$ represents the previous output vector at the time index μ. See ref.(1) for the expressions for the $\underline{B}$, the C, and $\underline{D}$; which are named as "response coefficients". The summations have a finite number of terms because the $\underline{B}$ and the C get smaller and smaller as μ increases. The total number of the $\underline{B}$ and the C in equation (B2) is much smaller than the total number of the $\underline{A}$ in equation (B1). The number of rows in the $\underline{B}$ will be equal to the number of different outputs desired and the number of columns in $\underline{B}$ will be equal to the number of different time-dependent inputs.

APPENDIX C

Length and physical properties of the homogeneous wall

$L = 8$ in.
$k = 0.6$ Btu/hr-ft-F
$\rho = 61$ ℓbm/ft^3
$c = 0.2$ Btu/ℓbm-F

Convective heat-transfer coefficient on each side

$h = 1.46$ Btu/hr-ft^2-F

Time interval

$\Delta\theta = 1$ hr

Response coefficients

$B_0 = 0.004$
$B_1 = 0.044$
$B_2 = 0.031$
$B_3 = 0.002$
$C_1 = 0.944$
$C_2 = -0.144$
$C_3 = 0.001$
$D = -0.080$

APPENDIX D

Radius and physical properities of long circular cylinder

$R = 10$ cm
$k = 0.03$ kW/m-C
$\rho = 8000$ kg/m^3
$c = 0.5$ kJ/kg-C

Time interval

$\Delta\theta = 5$ minutes

Response coefficients

$B_0 = -0.340$
$B_1 = 0.376$
$B_2 = -0.036$
$C_1 = 0.274$

UPWIND MACCORMACK EULER SOLVER WITH NON-EQUILIBRIUM CHEMISTRY

Scott E. Sherer James N. Scott
Department of Aeronautical & Astronautical Engineering
The Ohio State University, Columbus, Ohio 43210

ABSTRACT

A computer code, designated UMPIRE, is currently under development to solve the Euler equations in two dimensions with non-equilibrium chemistry. UMPIRE employs an explicit MacCormack algorithm with dissipation introduced via Roe's flux-difference split upwind method. The code also has the capability to employ a point-implicit methodology for flows where stiffness is introduced through the chemical source term. A technique consisting of diagonal sweeps across the computational domain from each corner is presented, which is used to reduce storage and execution requirements. Results depicting one-dimensional shock tube flow for both calorically perfect gas and thermally perfect, dissociating Nitrogen are presented to verify current capabilities of the program. Also, computational results from a chemical reactor vessel with no fluid dynamic effects are presented to check the chemistry capability and to verify the point-implicit strategy.

INTRODUCTION

The role of Computational Fluid Dynamics (CFD) for engineering applications has become widespread in various disciplines within technology. This growth can be attributed to the development of advanced solution algorithms and computer architectures. One area of recent particular interest is the application of CFD codes with non-equilibrium chemistry to high-performance propulsion systems such as ramjets and scramjets.[1,2] The use of CFD in such situations is especially appealing due to the challenges associated with obtaining experimental data. CFD can provide substantial information regarding the physics of flows associated with these systems that may be either impractical or impossible to obtain from ground or flight-based experiments.

The Euler equations which govern inviscid fluid dynamics provide a good initial point for the development of computational methods. They describe significant features in the physics of fluid dynamics, but are easier to work with than the full Navier-Stokes equations. In the past, the standard method for solving the Euler equations numerically was to use central differences to evaluate the spatial derivatives with second-order accuracy. This approach produces good results everywhere except in the vicinity of discontinuities such as shock waves, slip lines, or contact discontinuities. Near these features, central differencing generates spurious oscillations, resulting in corrupted, non-physical solutions. Numerical dissipation is usually introduced through artificial viscosity, but this method requires repeated "knob-turning" to determine satisfactory amounts of dissipation necessary for different applications.

Recently, upwind schemes have become popular in dealing with flows possessing discontinuities. Upwind schemes exhibit the ability to reduce spurious oscillations by incorporating physical characteristics of the flow into the discretization process. They are naturally dissipative, and thus the "knob-turning" required by central differencing schemes is unnecessary. One of the standard upwind-type schemes is the flux-difference split method of Roe. Formulated first for a calorically-perfect gas,[3] it has been modified for both equilibrium and non-equilibrium chemically-reacting gases.[4,5,6] Roe's flux-difference split method utilizes exact solutions to a series of local, approximate Riemann problems at computational cell interfaces. Roe's method in its basic form results in a spatially first-order

accurate scheme, since the state of the fluid is assumed constant across the entire cell. It can be extended to second-order accuracy through a array of techniques that use either variable extrapolation[7] or flux extrapolation.[8,9] In general, however, by raising the accuracy to second-order, some oscillations will be produced.[10] This difficultly can usually be overcome through the application of flux limiters in the algorithm to smooth oscillations without additional smearing of any discontinuities.[11]

As part of an effort to acquire the capability to model high-speed, reacting flows, a computer code was developed to solve the Euler equations including non-equilibrium chemistry. The code, designated UMPIRE (for Upwind MacCormack Point-Implicit) uses a scheme similar to the one presented by White, et.al.[12] This method is based on the explicit, predictor-corrector MacCormack scheme with upwind dissipation terms introduced through Roe's flux-difference split method and extended to second-order accuracy using the Szema-Chakravarthy method[8] and a minmod flux limiter. The point-implicit method presented by Bussing and Murman[13] for dealing with a stiff chemical source term is also utilized to speed convergence for steady-state applications. The motivation behind UMPIRE is to create a code that can accurately and efficiently model inviscid flows with non-equilibrium chemistry for a wide variety of different conditions, and to have the code to serve as a basis for future development of more advanced codes to solve the Parabolized or Full Navier-Stokes equations. Also, the educational benefits and practical experience obtained in developing such a code from the ground up cannot be overlooked.

GOVERNING EQUATIONS

Fluid Dynamics Model

The governing fluid dynamic equations currently utilized in the UMPIRE code are the two-dimensional, time-dependent, compressible Euler equations in chemical non-equilibrium. They may be written in compact vector form for Cartesian coordinates as

$$\frac{\partial \boldsymbol{Q}}{\partial t} + \frac{\partial \boldsymbol{E}}{\partial x} + \frac{\partial \boldsymbol{F}}{\partial y} + \boldsymbol{H} = 0 . \qquad (1)$$

The dependent vector **Q**, the inviscid flux vectors **E** and **F**, and the chemical source term **H** are given by

$$\boldsymbol{Q} = \begin{bmatrix} \rho f_1 \\ \rho f_2 \\ \vdots \\ \rho f_N \\ \rho u \\ \rho v \\ \varepsilon_o \end{bmatrix} \quad \boldsymbol{E} = \begin{bmatrix} \rho f_1 u \\ \rho f_2 u \\ \vdots \\ \rho f_N u \\ \rho u^2 + p \\ \rho uv \\ u(\varepsilon_o + p) \end{bmatrix}$$

$$\boldsymbol{H} = \begin{bmatrix} \dot{\omega}_1 \\ \dot{\omega}_2 \\ \vdots \\ \dot{\omega}_N \\ 0 \\ 0 \\ 0 \end{bmatrix} \quad \boldsymbol{F} = \begin{bmatrix} \rho f_1 v \\ \rho f_2 v \\ \vdots \\ \rho f_N v \\ \rho vu \\ \rho v^2 + p \\ v(\varepsilon_o + p) \end{bmatrix} , \qquad (2)$$

where ρ is the density, f_i is the mass fraction of specie i, $\dot{\omega}_i$ is the production rate of specie i, p is the pressure, u and v are the x- and y-components of the velocity, respectively, and ε_o is the total energy per unit volume. In order to close the set of equations, additional relationships are required. For a mixture consisting of independent, thermally perfect gases in thermodynamic equilibrium, the equations for pressure, specie enthalpy, and total energy may be defined as

$$p = \rho \Re T \sum_{i=1}^{N} \frac{f_i}{M_i} \qquad (3)$$

$$h_i = (\Delta h_f)_i^{T_s} + \int_{T_s}^{T} c_{p,i}(\tau)\, d\tau \qquad (4)$$

$$\varepsilon_o = \rho \sum_{i=1}^{N} h_i f_i - p + \frac{\rho}{2}(u^2+v^2) , \quad (5)$$

where $\Re$ is the universal gas constant, $(\Delta h_f)_i^{T_s}$ is the formation enthalpy of specie i at reference temperature T_s, T is the temperature, and $c_{p,i}$ is the specific heat at constant pressure of specie i. The final equation necessary to complete the system is given by

$$\sum_{i=1}^{N} f_i = 1 . \quad (6)$$

Equations 1 and 2 are best suited for solving on an orthogonal grid with constant spacing. Since the Cartesian x-y coordinate system does not provide such a grid for most physical applications, Equations 1 and 2 were transformed into a general computational ξ-η coordinate system possessing the above qualities. Carrying out this transformation and manipulating the resulting equations into conservation-law form yields[14]

$$\frac{\partial \overline{Q}}{\partial t} + \frac{\partial \overline{E}}{\partial \xi} + \frac{\partial \overline{F}}{\partial \eta} + \overline{H} = 0 , \quad (7)$$

where the transformed vectors are given by

$$\overline{Q} = \frac{1}{J}\begin{bmatrix} \rho f_1 \\ \rho f_2 \\ \vdots \\ \rho f_N \\ \rho u \\ \rho v \\ \varepsilon_o \end{bmatrix} \quad \overline{E} = \frac{1}{J}\begin{bmatrix} \rho f_1 U \\ \rho f_2 U \\ \vdots \\ \rho f_N U \\ \rho uU+\xi_x p \\ \rho vV+\xi_y p \\ U(\varepsilon_o+p) \end{bmatrix} \quad (8)$$

$$\overline{H} = \frac{1}{J}\begin{bmatrix} \dot{\omega}_1 \\ \dot{\omega}_2 \\ \vdots \\ \dot{\omega}_N \\ 0 \\ 0 \\ 0 \end{bmatrix} \quad \overline{F} = \frac{1}{J}\begin{bmatrix} \rho f_1 V \\ \rho f_2 V \\ \vdots \\ \rho f_N V \\ \rho uV+\eta_x p \\ \rho vV+\eta_y p \\ V(\varepsilon_o+p) \end{bmatrix}$$

In Equation 8, J represents the Jacobian of the transformation, ξ_x, ξ_y, η_x, and η_y are the transformation metrics, and U and V are defined as

$$U = \xi_x u+\xi_y v \quad V = \eta_x u+\eta_y v . \quad (9)$$

Equations 7 and 8 are the equations that are actually differenced and solved by the UMPIRE code. For the remainder of this paper, the bar over the transformed vectors will be dropped and it will be assumed that they are being used unless otherwise noted.

Thermodynamic Model

The thermodynamic model utilized by UMPIRE consists of a fourth-order polynomial for the specific heat at constant pressure,

$$c_{p,i} = A_i+B_i T+C_i T^2+D_i T^3+E_i T^4 . \quad (10)$$

The coefficients A_i, B_i, C_i, D_i, and E_i are found for each specie of interest using a least-squares curve-fitting routine and thermodynamic data up to 6000 K as given in the JANAF tables[15].

A thermodynamic quantity required for the calculation of the chemical equilibrium constant is the Gibbs free energy per mole of specie i at one atmosphere pressure. From its definition, the Gibbs free energy may be found from

$$g_i^{p=1} = A_i(T-T\ln T) - \frac{B_i}{2}T^2 - \frac{C_i}{6}T^3 - \frac{D_i}{12}T^4 - \frac{E_i}{20}T^5 - F_i + G_i T \quad (11)$$

where the coefficients F_i and G_i are functions of T_s, $(\Delta h_f)_i^{T_s}$, A_i, B_i, C_i, D_i, E_i, and the specie entropy at T_s. All of this information may be easily obtained for the species from the JANAF tables.

Chemistry Model

To obtain the specie production rates required in the calculation of chemical source

vector, it was assumed that the reaction method employed consists of J chemical reactions involving N species, and that the j^{th} reaction may be written in the generic form

$$\sum_{i=1}^{N} \nu'_{i,j} X_i \rightleftharpoons \sum_{i=1}^{N} \nu''_{i,j} X_i . \qquad (12)$$

In the above equation, $\nu_{i,j}$ is the stoichiometric coefficient for the i^{th} species in the j^{th} chemical reaction, where i = 1, 2,..., N, and j = 1, 2,..., J. The source term for specie i is found by summing its production rate over all reactions. If the forward and backward rate expressions are defined as

$$\sigma^f_{i,j} = k_{f,j} \prod_{m=1}^{N} \left(\frac{\rho f_m}{M_m} \right)^{\nu'_{i,j}}$$
$$\sigma^b_{i,j} = k_{b,j} \prod_{m=1}^{N} \left(\frac{\rho f_m}{M_m} \right)^{\nu''_{i,j}} \qquad (13)$$

then the source term becomes

$$\dot{\omega}_i = M_i \sum_{j=1}^{J} (\nu''_{i,j} - \nu'_{i,j}) [\sigma^f_{i,j} - \sigma^b_{i,j}] \qquad (14)$$

The forward rate constant of reaction j, $k_{f,j}$, is calculated using the Arrhenius model equation

$$k_{f,j} = A_j T^{N_j} \exp\left(-\frac{E_j}{\Re T}\right) \qquad (15)$$

where A_j, N_j, and E_j are empirically determined constants for each reaction. The backwards reaction rate and equilibrium constants are

$$k_{b,j} = \frac{k_{f,j}}{k_{eq,j}} \qquad (16)$$

$$k_{eq,j} = \left(\frac{101,325}{\Re T}\right)^{\Delta n} \exp\left(\frac{\Delta G_j^{p-1}}{\Re T}\right) \qquad (17)$$

where

$$\Delta G_j^{p-1} = \sum_{i=1}^{N} (\nu''_{i,j} - \nu'_{i,j}) g_i^{p-1} \qquad (18)$$

and

$$\Delta n = \sum_{i=1}^{N} (\nu''_{i,j} - \nu'_{i,j}) . \qquad (19)$$

NUMERICAL METHODS

Roe's Flux-Difference Split Method

The upwinding present in the UMPIRE code is introduced through Roe's flux-difference split method. For a one-dimensional situation in Cartesian coordinates, the approximate Riemann problem

$$\frac{\partial Q}{\partial t} + [A'] \frac{\partial Q}{\partial x} = 0 \qquad (20)$$

with the initial conditions given by

$$Q(x,0) = Q_L \quad for \quad x \le 0$$
$$Q(x,0) = Q_R \quad for \quad x > 0 \qquad (21)$$

is solved at each cell interface to yield a new distribution of the dependant variables across a computational cell. The matrix [A'] is a special form of the flux Jacobian matrix, $\partial E/\partial Q$, that is assumed to be a constant function of Q_R and Q_L over a computational cell and must satisfy certain properties as shown by Roe[3]. For the non-reacting, calorically perfect gas case, these properties are satisfied by the "Roe-averaging" of the flow variables, given for a general flow variable q as

$$\hat{q}_{i+\frac{1}{2}} = \frac{q_{i+1}\sqrt{\rho_{i+1}} + q_i\sqrt{\rho_i}}{\sqrt{\rho_{i+1}} + \sqrt{\rho_i}} \qquad (22)$$

For the non-equilibrium reacting gas case, this averaging process becomes more involved due to the added complexities of the system of equations.

Grossman and Cinnella[4] presented Roe-averaged expressions for a reacting gas that satisfy the conditions prescribed by Roe exactly, and these are the relationships used by UMPIRE.

In Roe's flux-difference split method, the first-order numerical flux at the cell interfaces in the ξ-direction may be defined by[16]

$$E^*_{i-\frac{1}{2},j} = E_{i,j} + de^-_{i+\frac{1}{2},j} = E_{i+1,j} - de^+_{i+\frac{1}{2},j} \quad (23)$$

where

$$de^*_{i+\frac{1}{2},j} = (\hat{S}_\xi \hat{\Lambda}^*_\xi \hat{S}^{-1}_\xi)_{i+\frac{1}{2},j} (Q_{i+1,j} - Q_{i,j}) \quad (24)$$

In Equation 23, S_ξ is the matrix whose columns consist of the right eigenvectors of $\partial E/\partial Q$, S_ξ^{-1} is the inverse of S_ξ, Λ^*_ξ is a matrix consisting either of the positive or negative eigenvalues of $\partial E/\partial Q$ on its diagonal, and the ^ represents evaluation at the Roe-averaged state. The first-order numerical flux for the interface at i-½,j is defined similarly as

$$E^*_{i-\frac{1}{2},j} = E_{i-1,j} + de^-_{i-\frac{1}{2},j} = E_{i,j} - de^+_{i-\frac{1}{2},j} \quad (25)$$

where

$$de^*_{i-\frac{1}{2},j} = (\hat{S}_\xi \hat{\Lambda}^*_\xi \hat{S}^{-1}_\xi)_{i-\frac{1}{2},j} (Q_{i,j} - Q_{i-1,j}) \quad (26)$$

For two-dimensional calculations, one-dimensional flux-difference splitting may be applied in each direction independently, and the results then combined. This method is fairly straight-forward, but does have some limitations when waves oblique to the computational grid are present.[6,17] The first-order numerical fluxes in the η-direction at the interfaces i,j±½ are given by equations similar to Equations 23 through 26.

Upwind MacCormack Method

The numerical algorithm used by UMPIRE is the MacCormack predictor-corrector scheme with flux-difference split, upwind dissipation terms as presented by White, et.al.[12] The derivation of the upwind MacCormack scheme begins with the spatially and temporally second-order accurate form of the modified Euler method for the Euler equations

$$\Delta Q^{\tau+1}_{i,j} = -\Delta t [(E^\tau_{i+\frac{1}{2},j} - E^\tau_{i-\frac{1}{2},j}) + (F^\tau_{i,j+\frac{1}{2}} - F^\tau_{i,j-\frac{1}{2}}) + H^\tau_{i,j}] \quad (27)$$

where τ+1 = p and τ = n for the predictor step, and τ+1 = c and τ = p for the corrector step. The change in Q for the entire time step from n to n+1 is then given by

$$\Delta Q^{n+1}_{i,j} = \frac{1}{2}(\Delta Q^p_{i,j} + \Delta Q^c_{i,j}) \quad (28)$$

$$Q^{n+1}_{i,j} = Q^n_{i,j} + \Delta Q^{n+1}_{i,j}$$

The numerical fluxes at the cell interfaces (± ½) are calculated by Roe's flux-difference split method as represented in Equations 23 through 26. Since there are two expressions that yield the numerical flux at each interface, the expression $E_{i+½,j} - E_{i-½,j}$ may be written in four different ways. The two ways that are of interest here are

$$E_{i+\frac{1}{2},j} - E_{i-\frac{1}{2},j} = E_{i+1,j} - de^+_{i+\frac{1}{2},j} - (E_{i,j} - de^-_{i-\frac{1}{2},j}) \quad (29)$$

$$= \Delta_\xi E_{i,j} - (de^+_{i-\frac{1}{2},j} - de^-_{i-\frac{1}{2},j})$$

and

$$E_{i+\frac{1}{2},j} - E_{i-\frac{1}{2},j} = E_{i,j} + de^{-}_{i+\frac{1}{2},j} - (E_{i-1,j} + de^{-}_{i-\frac{1}{2},j}) \quad (30)$$

$$= \nabla_\xi E_{i,j} + (de^{-}_{i+\frac{1}{2},j} - de^{-}_{i-\frac{1}{2},j})$$

Similar equations may also be written for $F_{i,j+½}$ - $F_{i,j-½}$. Inserting these expressions into Equation 27 yields the MacCormack predictor-corrector scheme with upwind terms to provide dissipation. For example, if forward differences are inserted into the predictor step while backwards differences are inserted into the corrector step, the resulting equation is

$$\Delta Q^{p}_{i,j} = -\Delta t [\Delta_\xi E^{n}_{i,j} - (de^{+\,n}_{i+\frac{1}{2},j} - de^{+\,n}_{i-\frac{1}{2},j}) + \Delta_\eta F_{i,j} - (df^{+\,n}_{i,j+\frac{1}{2}} - df^{+\,n}_{1,j-\frac{1}{2}}) + H^{n}_{i,j}]$$

$$\Delta Q^{c}_{i,j} = -\Delta t [\nabla_\xi E_{i,j} + (de^{-\,p}_{i+\frac{1}{2},j} - de^{-\,p}_{i-\frac{1}{2},j}) + \nabla_\eta F_{i,j} + (df^{-\,p}_{i,j+\frac{1}{2}} - df^{-\,p}_{i,j-\frac{1}{2}}) + H^{p}_{i,j}] \quad (31)$$

In the UMPIRE code, the forward and backward differences for the predictor and corrector steps are cycled according to Table 1[14] to prevent build-up of directional bias. This method is stable for a CFL number ≤ 1, as is the standard MacCormack scheme when applied to the Euler equations.

Second Order Terms

Thus far, the upwind MacCormack scheme as presented is only first-order accurate in space because the state of the fluid is assumed to be constant across a computational cell. There are several methods available for extending the spatial accuracy of the upwind MacCormack scheme, but UMPIRE currently uses the Szema-Chakravarthy method[8], based on the work of Lawerance, et.al.[19]

First, in the ξ-direction, intermediate variables α are defined as

$$\alpha_{1,i+\frac{1}{2},j} = (S_\xi^{-1})_{i+\frac{1}{2},j}(Q_{i,j} - Q_{i-1,j})$$

$$\alpha_{2,i+\frac{1}{2},j} = (S_\xi^{-1})_{i+\frac{1}{2},j}(Q_{i+1,j} - Q_{i,j}) \quad .$$

$$\alpha_{3,i+\frac{1}{2},j} = (S_\xi^{-1})_{i+\frac{1}{2},j}(Q_{i+2,j} - Q_{i+1,j}) \quad (32)$$

Then, these vectors are limited relative to each other using a minmod flux limiter function in order to reduce spurious oscillations. The resulting equations are given by

$$A_{1,i+\frac{1}{2},j} = mm[(\alpha_1)_{i+\frac{1}{2},j}, \beta(\alpha_2)_{i+\frac{1}{2},j}]$$

$$A_{2,i+\frac{1}{2},j} = mm[(\alpha_2)_{i+\frac{1}{2},j}, \beta(\alpha_1)_{i-\frac{1}{2},j}]$$

$$A_{3,i+\frac{1}{2},j} = mm[(\alpha_2)_{i+\frac{1}{2},j}, \beta(\alpha_3)_{i+\frac{1}{2},j}]$$

$$A_{4,i+\frac{1}{2},j} = mm[(\alpha_3)_{i+\frac{1}{2},j}, \beta(\alpha_2)_{i+\frac{1}{2},j}] \quad (33)$$

where the minmod function of two values x and y is defined as

$$mm = sgn(x)\max[0, \min\{|x|, ysgn(x)\}] \quad (34)$$

and

$$\beta = \frac{(3 - \phi)}{(1 - \phi)} \quad . \quad (35)$$

ϕ is known as the accuracy parameter, and was assumed equal to -1 throughout this study, corresponding to a fully-upwind method.[19]

The intermediate vectors are then multiplied by the eigenvalues and eigenvectors to obtain the limited upwind fluxes

$$
\begin{aligned}
\tilde{de}^{+}_{1,i+\frac{1}{2},j} &= S_{i+\frac{1}{2},j}\Lambda^{+}_{i+\frac{1}{2},j}A_{1,i+\frac{1}{2},j} \\
\tilde{de}^{+}_{2,i+\frac{1}{2},j} &= S_{i+\frac{1}{2},j}\Lambda^{+}_{i+\frac{1}{2},j}A_{2,i+\frac{1}{2},j} \\
\tilde{de}^{-}_{1,i+\frac{1}{2},j} &= S_{i+\frac{1}{2},j}\Lambda^{-}_{i+\frac{1}{2},j}A_{3,i+\frac{1}{2},j} \\
\tilde{de}^{-}_{2,i+\frac{1}{2},j} &= S_{i+\frac{1}{2},j}\Lambda^{-}_{i+\frac{1}{2},j}A_{4,i+\frac{1}{2},j}
\end{aligned}
\qquad (36)
$$

Finally, the total second-order contribution to the numerical flux is defined by

$$
\begin{aligned}
dee_{i+\frac{1}{2},j} = \frac{1-\phi}{4}\tilde{de}^{+}_{1,i+\frac{1}{2},j} + \frac{1+\phi}{4}\tilde{de}^{+}_{2,i+\cdot} \\
- \frac{1+\phi}{4}\tilde{de}^{-}_{1,i+\frac{1}{2},j} - \frac{1-\phi}{4}\tilde{de}^{-}_{2,i+\frac{1}{2}}
\end{aligned}
\qquad (37)
$$

Similar second-order terms may be found for the i-½,j interface as well as for the interfaces in the η-direction.

The second-order upwind MacCormack scheme is obtained by adding Equation 37 and its counterparts at i-½,j and i,j±½ evaluated at time level n to their corresponding first-order numerical fluxes defined by Equations 23 through 26 in the corrector step only.[12,16] For example, to raise Equation 31 to second-order spatial accuracy, the predictor step would remain unchanged while the corrector step would become

$$
\begin{aligned}
\Delta Q^{c}_{i,j} = -\Delta t\,[\nabla_{\xi}E_{i,j} &+ (de^{-\,p}_{i+\frac{1}{2},j} - de^{-\,p}_{i-\frac{1}{2},j}) \\
&+ (dee^{n}_{i+\frac{1}{2},j} - dee^{n}_{i-\frac{1}{2},j}) \\
&+ \nabla_{\eta}F_{i,j} + (df^{-\,p}_{i,j+\frac{1}{2}} - df^{-\,p}_{i,j-\frac{1}{2}}) \\
&+ (dff^{n}_{i,j+\frac{1}{2}} - dff^{n}_{1,j-\frac{1}{2}}) \\
&+ H^{p}_{1,j}]
\end{aligned}
\qquad (38)
$$

Point-Implicit Treatment of Source Vector

When dealing with numerical solutions of chemically reacting systems, the problem of stiffness often arises. Stiffness in a chemically reacting system is a result of the widely varying characteristic time scales between the chemical and the fluid dynamic processes being modelled. If left untreated, stiff problems require prohibitively long solution times, due to the fact that the solution must be advanced at its smallest time step to remain stable. A popular method for treating the chemical source term is to evaluate it implicitly, which introduces the chemical source Jacobian as a premultiplying matrix to the left-hand side of the predictor and corrector equations. Continuing with the forward predictor, backwards corrector example in both coordinate directions, Equation 38 becomes

$$
\begin{aligned}
\left[I + \Delta t\left(\frac{\partial H}{\partial Q}\right)^{n}\right]\Delta Q^{p}_{i,j} &= RHS\ Eq.\ 38 \\
\left[I + \Delta t\left(\frac{\partial H}{\partial Q}\right)^{p}\right]\Delta Q^{c}_{i,j} &= RHS\ Eq.\ 38
\end{aligned}
\qquad (39)
$$

Thus, at each grid point, an N+3 system of equations must be solved. Bussing and Murman[13] have shown that by evaluating the source term implicitly, the disparity between the characteristic times is removed, thus allowing each process to advance towards the steady-state at its own rate. Point-implicit capability has been included in the UMPIRE code for use in steady-state problems which contain stiff chemical source terms.

Coding of Upwind MacCormack Method

The coding of the upwind MacCormack method was given much consideration while constructing UMPIRE. A technique where the computational domain is swept diagonally in varying directions was felt to be the most efficient application of the upwind MacCormack method. By examining Equation 44 and its counterparts, it can be seen that $\Delta Q_{i,j}^{p}$ and $\Delta Q_{i,j}^{c}$ each rely on information from two of the four surrounding grid

points and all four of the surrounding cell interfaces. The two grid points providing information depend upon whether forward or backward differences are currently being employed for each of the coordinate directions. For example, in the predictor step of Equation 38, which will be referred to as an FF step since the finite differences in both directions are forward, the grid points i+1,j and i,j+1 are used in the calculation. By inspecting Figure 1, a model 6 x 6 grid in computational space, it can be seen that, for an FF step, a diagonal line of grid points (Line A) relies on the information found along the next diagonal line of grid points to the upper right (Line B) and the two surrounding diagonal lines of cell interfaces (Lines F and G). Similarly, for a BB step, Line A relies on the information from Line C and Lines F and G, for a FB step, Line D and Lines H and I, and for a BF step, Line E and Lines H and I. Thus, for any combination of differences, only four lines of data need be stored, two for the fluxes at the grid points, and two for the numerical fluxes at the cell interfaces. This reduces storage requirements when compared with calculating and storing data for each grid point and interface in the domain, and it reduces execution time when compared to calculating data at each node and interface as needed and discarding, especially when considering the computational effort necessary to calculate the interface fluxes. There are some additional coding requirements as well as an increase in code complexity with this method, but it was felt that these were insignificant when compared to the disadvantages associated with either of the other methods. Also, this method should improve vectorization ability when the code is ported to vector machines such as the Cray Y-MP.

For each predictor or corrector step, the code first determines the category of the current step; FF, FB, or BF, BB (see Table 1). With this information, an initial starting grid point is defined; lower left for FF, upper right for BB, upper left for FB, and lower right for BF. The code then sweeps towards the corner of the computational domain opposite to its starting point, stepping one diagonal at a time. The same lines of code are used for all of the categories, with the only difference being the value of a few integer variables to make the distinction between sweep directions. Only the data for the current grid point and interface diagonal and for the previous grid point and interface diagonal are stored in the computer's memory. If the step is a predictor step, then the second-order terms from Equation 37 are calculated and stored for the entire domain, while if the step is a corrector step, the previously calculated second-order terms are added to the interface flux as indicated Equation 38. Care must be taken when calculating and adding the second-order flux terms using this method to insure that all of the signs are correct when performing both forward and backward sweeps.

RESULTS

Three test cases that were solved using the UMPIRE code are presented here; a shock tube containing calorically perfect gas, a well-stirred chemical reactor with dissociating Nitrogen, and a shock tube containing dissociating Nitrogen.

Shock Tube (Calorically Perfect Gas)

Shown in Figure 2 are the density profiles obtained by UMPIRE for a shock tube with calorically perfect gas. This example was run until the time was equal to 5×10^{-4} seconds, with γ = 1.4, a CFL number of 0.5, a pressure ratio of 2:1, and a temperature ratio of 1:1. There were 101 grid points taken along the length of the tube, and, even though the problem is essentially one-dimensional, 5 grid points were taken along the width of the tube to test the code's basic structure in two dimensions. Figure 2 was generated by running UMPIRE in four different modes; no upwinding (MacCormack scheme with no added dissipation), first-order upwinding, second-order upwinding with no flux limiters, and second-order upwinding with minmod flux limiters. A modest

2:1 pressure ratio was selected here to contrast the results from the standard MacCormack scheme with no dissipation to those from the MacCormack scheme with upwind dissipation, since at higher pressure ratios, the former produces such wild oscillations that negative pressures and temperatures develop. The effect of the upwind dissipation on the oscillations present in the standard MacCormack scheme can be easily seen. Also, the second-order scheme appears to resolve the shock and contact discontinuity better that the first-order scheme. In this case, the difference between the limited and unlimited second-order scheme are minimal because of the low pressure ratio, which causes only minor oscillations to be produced by the unlimited scheme. Other pressure and temperature ratios were examined for the case of a shock tube with calorically perfect gas, and they yielded results that similarly matched those obtained exactly from one-dimensional gas-dynamics[20].

Chemical Reactor (Dissociating Nitrogen)

The second case presented here is the chemical reactor containing dissociating Nitrogen. In this model reactor, it is assumed that there are no fluid dynamic effects present, and that the only change in the system is caused by the presence of chemical reactions. This case was investigated to check the ability of the code to handle a simple reaction mechanism decoupled from the fluid dynamics, and to examine some of the features of the point-implicit method.

The reactor was assumed to be a square box, and a simple 5 x 5 grid was used. An initial temperature and pressure were selected, and values for the mass fractions of N_2 and N were chosen so as to not correspond with the equilibrium conditions. For the case shown here, these values were taken to be 4000 K, 10 MPa, .9, and .1, respectively. UMPIRE was then used to march the solution forward in time to a steady-state, equilibrium condition, using both the point-implicit and non-point-implicit methods and a variety of CFL numbers. The reaction used to drive this system and its Arrhenius coefficients are shown in Table 2[21]. The results are shown in Figure 3, which are graphs of the length of time and the number of steps required to reduce the norm of the residual vector to 10^{-8}. When the point implicit method is not used, it can be seen that the length of time required to reach the equilibrium point is about the same no matter what CFL number is used. This represents the physical time required for the dissociation reaction of Nitrogen to equilibrate. However, the results for the point-implicit method show no such constant time is found for different CFL numbers. The time in the point-implicit method is no longer a physical time, but a "psuedotime"[13] used to advance towards the steady-state. The point-implicit method was found to converge to an equilibrium value for CFL numbers as high as 0.9, while for the non-point-implicit method, CFL numbers under 0.01 were required for stability. This example demonstrates the potential of the point-implicit method for solving equations where the chemical and fluid dynamic time scales vary widely. The point-implicit method has allowed the reaction to be separated from its physical time scale and instead be associated with a psuedotime scale, which will be of the same order as the fluid time scale. It should also be noted that, for the initial conditions presented earlier, the code converged to practically the same equilibrium point no matter what CFL number or whether the point-implicit or the non-point-implicit was used. For the given initial conditions, this equilibrium point is given by T = 6067.8 K, p = 1,426,811 Pa, f_{N2} = 0.965355, and f_N = 0.034644.

Shock Tube (Dissociating Nitrogen)

Once some confidence was established for the chemistry capabilities of UMPIRE for the simple Nitrogen dissociation reaction, it was applied to the shock tube case. In this case, a pressure ratio of 8:1 was used (10 MPa : 1.25 MPa), with a temperature ratio of 1:1 (T = 4000

K). Again, the grid was 101 x 5 and a CFL of 0.5 was used. The code was marched up to 1 x 10^{-4} seconds, and the second-order, limited, upwind MacCormack method was used to solve the equations. The profile of the mass fractions for the two species of Nitrogen are shown in Figure 4. At 4000 K, molecular Nitrogen is just starting to dissociate, and thus we do not see much atomic Nitrogen present. As the shock wave propagates to the right into the lower pressure gas, the mass fraction of the molecular Nitrogen drops while the mass fraction of atomic Nitrogen rises. The non-equilibrium effects are clearly seen in the overshoots and undershoots present in the mass fractions immediately following the shock. Downstream of the shock, the chemical composition is given the chance to equilibrate, and returns to its equilibrium composition.

CONCLUSIONS

In this study, a computer code named UMPIRE has been presented for solving the Euler equations with non-equilibrium chemistry. The code employees a MacCormack predictor-corrector scheme with upwind dissipation terms provided by Roe's flux-difference split method to smooth out spurious numerical oscillations. A technique involving diagonal sweeps across the computational domain that is especially suited for use with this method is used to reduce storage and speed execution time. Three test cases have been investigated to verify the current capabilities of UMPIRE; a shock tube with calorically perfect gas, a chemical reactor with dissociating Nitrogen, and a shock tube with dissociating Nitrogen. All three cases compare well with exact results or results from other sources. Current work involving UMPIRE includes examining true two-dimensional cases, such as inlets and blunt bodies, and incorporating more advanced reaction mechanisms, such as reacting air, or hydrogen-air mixtures.

REFERENCES

[1] White, M.E., Drummond, J.P., and Kumar, A., "Evolution and Application of CFD Techniques for Scramjet Engine Analysis", *Journal of Propulsion and Power*, Vol. 3, No. 5, 1987, pp. 423-439.

[2] Barber, T.J., and Cox, Jr., G.B., "Hypersonic Vehicle Propulsion: A CFD Application Case Study", AIAA Paper 88-0475, January 1988.

[3] Roe, P.L., "Approximate Riemann Solvers, Parameter Vectors, and Difference Schemes", *Journal of Computational Physics*, Vol. 43, 1981, pp. 357-372.

[4] Grossman, B., and Cinnella, P., "Flux-Split Algorithms for Flows with Non-Equilibrium Chemistry and Vibrational Relaxation", *Journal of Computational Physics*, Vol. 88, 1990, pp. 131-168.

[5] Vinokur, M., and Montagne, J.-L., "Generalized Flux-Vector Splitting and Roe Averaging for an Equilibrium Real Gas", *Journal of Computational Physics*, Vol. 89, 1990, pp. 276-300.

[6] Shuen, J.-S., Liou, M.-S., and van Leer, B., "Inviscid Flux-Splitting Algorithms for Real Gases with Non-equilibrium Chemistry", *Journal of Computational Physics*, Vol. 90, 1990, pp. 371-395.

[7] van Leer, B., "Towards the Ultimate Conservation Difference Scheme V, A Second-Order Sequel to Godunov's Method", *Journal of Computational Physics*, Vol. 32, 1979, pp.101-136.

[8] Chakravarthy, S.R., and Szema, K.Y., "An Euler Solver for Three-Dimensional

Supersonic Flows with Subsonic Pockets", AIAA Paper 85-1703, July 1985.

[9] Chakravarthy, S.R., and Osher, S., "A New Class of High Accuracy TVD Schemes for Hyperbolic Conservation Laws", AIAA Paper 85-0363, January 1985.

[10] Engquist, B. and Osher, S., "One-sided Difference Approximations for Nonlinear Conservation Laws", *Mathematics of Computation*, Vol. 36, pp. 321-352.

[11] Scott, J.N., and Niu, Y.-Y., "Comparison of Limiters in Flux-Split Algorithms for Euler Equations", AIAA Paper 93-0068, January 1993.

[12] White, J.A., Korte, J.J., and Gaffney, Jr., R.L., "Flux-Difference Split Parabolized Navier-Stokes Algorithm for Nonequilibrium Chemically Reacting Flows", AIAA Paper 93-0534, January 1993.

[13] Bussing, T.R.A., and Murman, E.M., "Finite-Volume Method for the Calculation of Compressible Chemically Reacting Flows", *AIAA Journal*, Vol. 26, No. 9, 1988, pp. 1070-1078.

[14] Anderson, D.A., Tannehill, J.C., Pletcher, R.H., *Computational Fluid Mechanics and Heat Transfer*, Hemisphere Publishing Corporation, New York, 1984.

[15] Chase, M.W., et.al., "JANAF Thermochemical Tables, Third Edition, Part II, Cr-Zr", *Journal of Physical and Chemical Reference Data*, Vol. 14, Supplement 1, American Chemical Society and American Institute of Physics, 1985.

[16] Hirsch, C., *Numerical Computation of Internal and External Flows, Volume 2: Computational Methods for Inviscid and Viscous Flows*, John Wiley and Sons, New York, 1988.

[17] Leck, C.L., and Tannehill, J.C., "A New Rotated Upwind Difference Scheme for the Euler Equations", AIAA Paper 93-0066, January 1993.

[18] Lawerance, S.L., Tannehill, J.C., and Chausee, D.S., "Upwind Algorithm for the Parabolized Navier-Stokes Equations", *AIAA Journal*, Vol. 27, No. 9, 1989, pp. 1175-1183.

[19] Yee, H.C., and Shinn, J.L., "Semi-Implicit and Fully Implicit Shock Capturing Methods for Nonequilibrium Flows", *AIAA Journal*, Vol. 27, No. 3, 1989, pp. 299-307.

[20] Anderson, J.A., *Modern Compressible Flow With Historical Perspective*, McGraw-Hill Book Company, New York, 1982.

[21] Vincenti, W.G., and Kruger, Jr., C.H., *Introduction to Physical Gas Dynamics*, Robert E. Krieger Publishing Company, Malabar, Florida, 1965.

Cycle	Predictor		Corrector	
Direction	ξ	η	ξ	η
1	F	F	B	B
2	F	B	B	F
3	B	F	F	B
4	B	B	F	F

Table 1 - Cycling of MacCormack Scheme
F -> forward difference, B-> backward difference

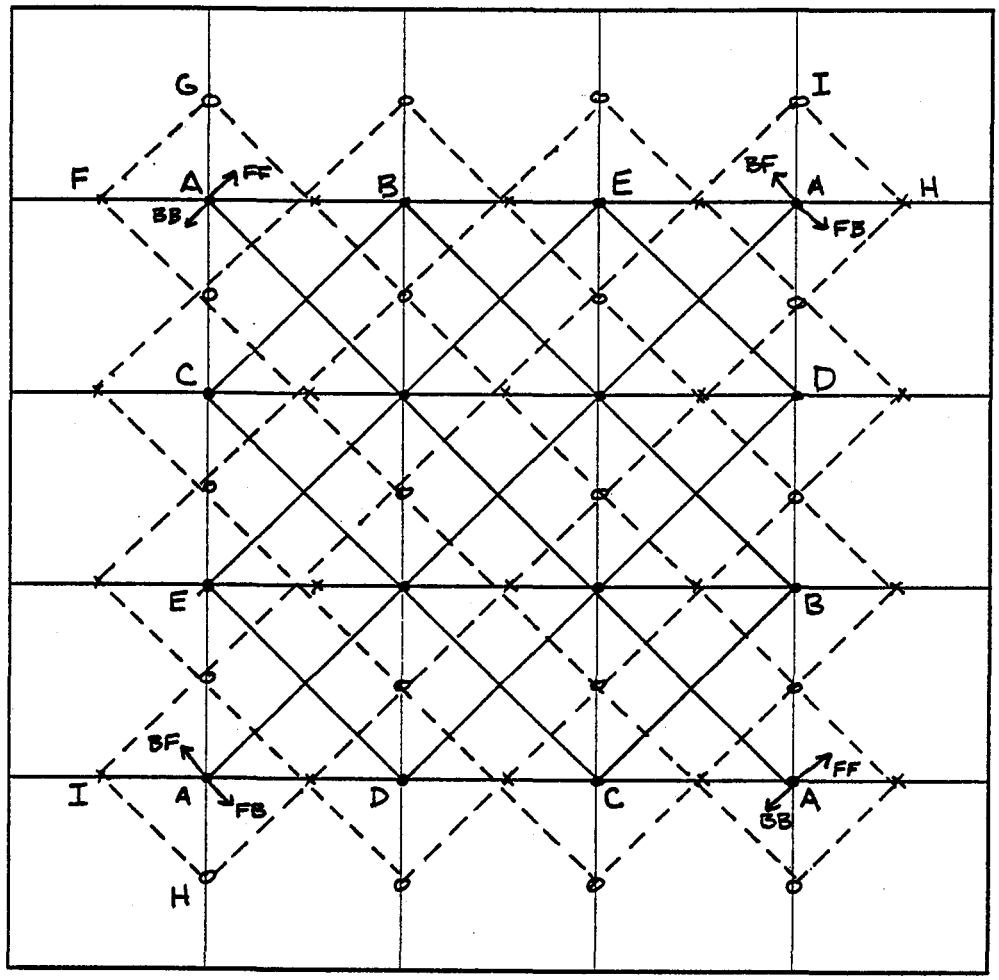

Figure 1 - Diagonal Sweeping of Computational Domain

$N_2 + N_2 \leftrightarrow 2N + N_2$	$A = 4.8 \times 10^{14}$
	$N = -0.5$
	$E = 9.3951929 \times 10^8$
$N_2 + N \leftrightarrow 2N + N$	$A = 4.1 \times 10^{19}$
	$N = -1.5$
	$E = 9.3951929 \times 10^8$

Table 2 - Reaction Mechanism for Dissociating N_2
k_f in units of $m^3/(kmol \cdot s)$

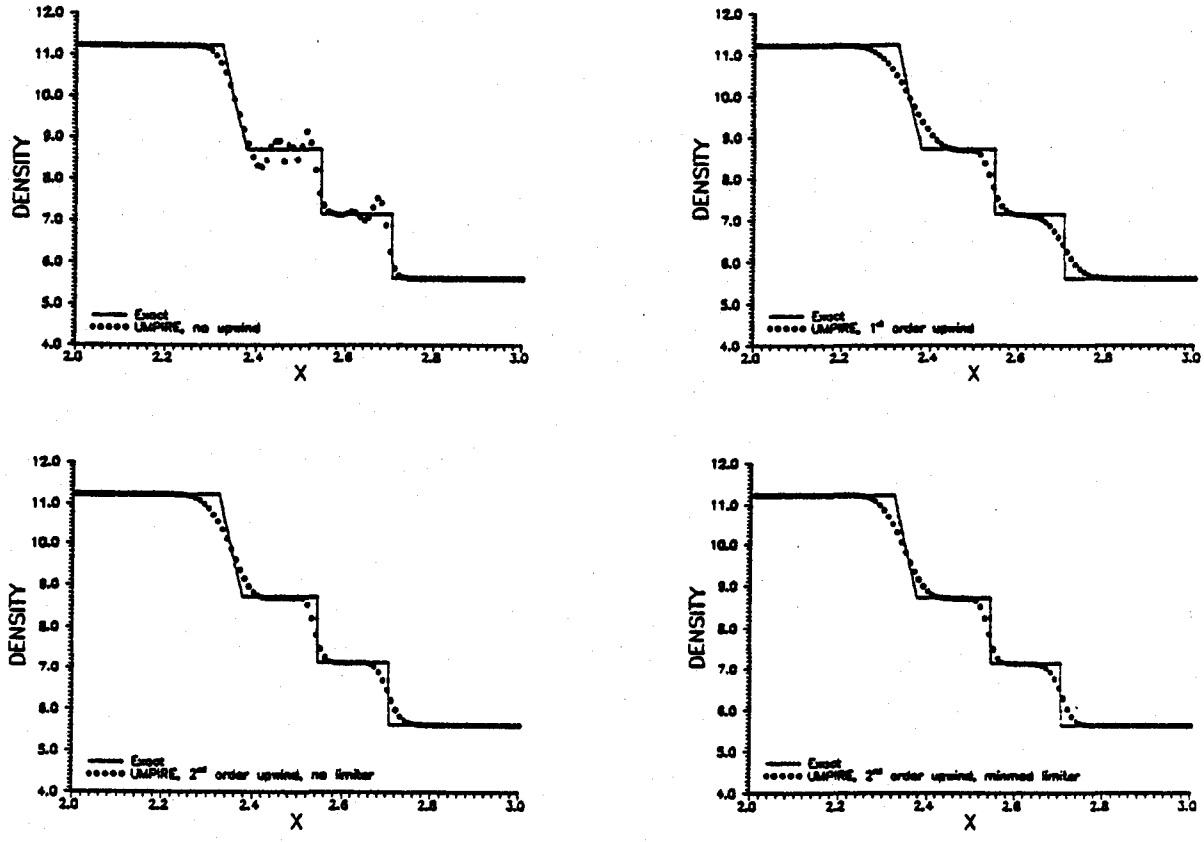

Figure 2 - Shock Tube, Calorically Perfect Gas

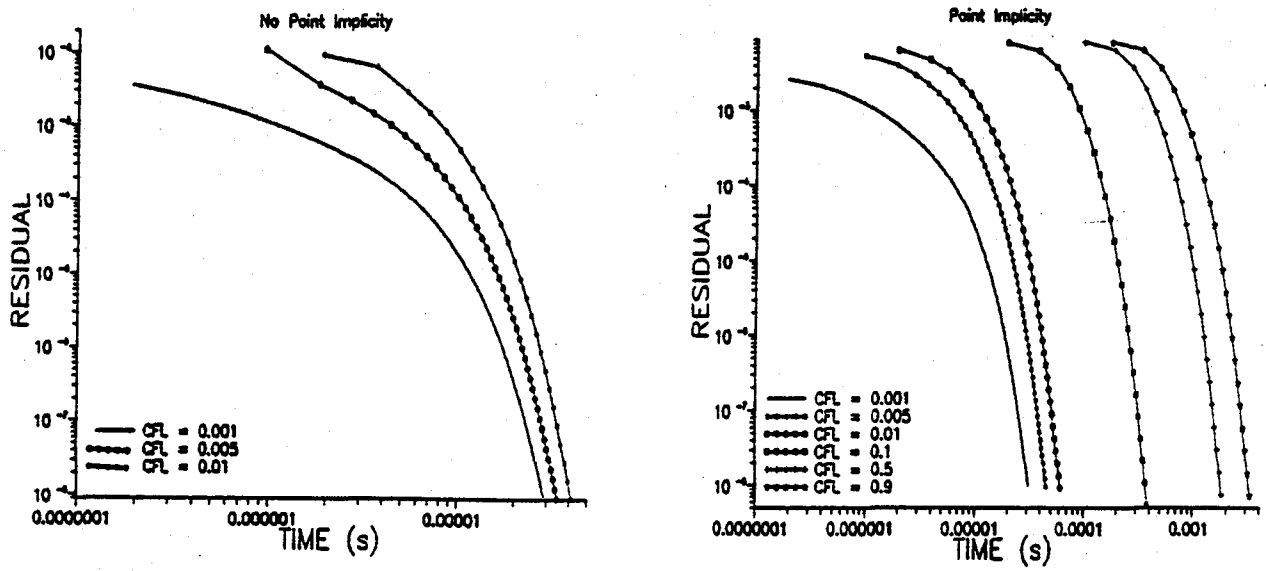

Figure 3 - Chemical Reactor, Dissociating Nitrogen

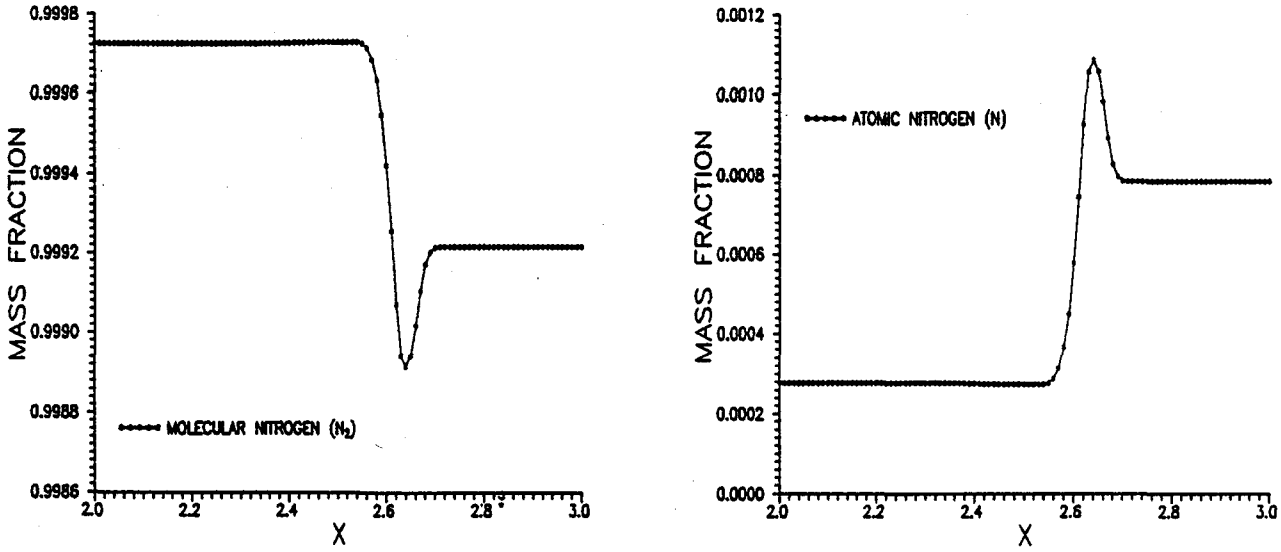

Figure 4 - Shock Tube, Dissociating Nitrogen

REPORT DOCUMENTATION PAGE

Form Approved
OMB No. 0704-0188

1. AGENCY USE ONLY (*Leave blank*)	2. REPORT DATE	3. REPORT TYPE AND DATES COVERED
	November 1993	Conference Publication

4. TITLE AND SUBTITLE

Fifth Annual Thermal and Fluids Analysis Workshop

5. FUNDING NUMBERS

6. AUTHOR(S)

7. PERFORMING ORGANIZATION NAME(S) AND ADDRESS(ES)

National Aeronautics and Space Administration
Lewis Research Center
Cleveland, Ohio 44135–3191

8. PERFORMING ORGANIZATION REPORT NUMBER

E–8094

9. SPONSORING/MONITORING AGENCY NAME(S) AND ADDRESS(ES)

National Aeronautics and Space Administration
Washington, D.C. 20546–0001

10. SPONSORING/MONITORING AGENCY REPORT NUMBER

NASA CP–10122

11. SUPPLEMENTARY NOTES

Responsible person, Doug Darling, (216) 433–8273.

12a. DISTRIBUTION/AVAILABILITY STATEMENT

Unclassified - Unlimited
Subject Category 01, 61, 64, and 34

12b. DISTRIBUTION CODE

13. ABSTRACT ***(Maximum 200 words)***

The Fifth Annual Thermal and Fluids Analysis Workshop was held at the Ohio Aerospace Institute, Brook Park, Ohio, cosponsored by NASA Lewis Research Center and the Ohio Aerospace Institute, August 16–20, 1993. The workshop consisted of classes, vendor demonstrations, and paper sessions. The classes and vendor demonstrations provided participants with the information on widely used tools for thermal and fluids analysis. The paper sessions provided a forum for the exchange of information and ideas among thermal and fluids analysts. Paper topics included advances and uses of established thermal and fluids computer codes (such as SINDA and TRASYS) as well as unique modeling techniques and applications.

14. SUBJECT TERMS	15. NUMBER OF PAGES
Thermal simulation; Fluid mechanics; Computer programs	566
	16. PRICE CODE: A24

17. SECURITY CLASSIFICATION OF REPORT	18. SECURITY CLASSIFICATION OF THIS PAGE	19. SECURITY CLASSIFICATION OF ABSTRACT	20. LIMITATION OF ABSTRACT
Unclassified	Unclassified	Unclassified	